Proceedings of CJJC2025

The 14th China-Japan Joint Conference on Material Recycling and Waste Management

Oct, 27-31 2025, Toyama, Japan

九州大学
KYUSHU UNIVERSITY

北京科技大学
University of Science and Technology Beijing

参加大学・機関・企業

日本： 九州大学　東京科学大学　国立環境研究所　明星大学　北九州市立大学
カナデビア㈱　JFE エンジニアリング㈱　栗田工業㈱　(一財) 九州環境管理協会
㈱安藤・間　五洋建設㈱　㈱クボタ　三ツ星ベルト㈱　㈱奥村組
NPO 法人廃棄物地盤工学研究会　環境・遮水管理センシング技術研究会

中国： 同済大学　北京科技大学　青島理工大学　清華大学　北京林業大学　浙江大学
広州大学　安徽大学　瀋陽航空航天大学　哈爾濱工業大学　浙江工商大学

（参加者数順、協賛口数順）

CONTENTS

Session 1 Waste Management Systems, Environmental Impacts p1-p57

Chair : Prof. Kentaro Miyawaki (Meisei University)

1-1 Overlooked risk of microplastics from municipal solid waste–storage site, Yuyang Long (Zhejiang Gongshang University **1**

1-2 Using cognitive dissonance induced by waste presented as art to improve perceptions of waste, Bo Wang (Institute of Science Tokyo) **15**

1-3 Study on atmospheric CO_2 neutralization of high-PH leachate at offshore disposal sites, Kentaro Miyawaki (Meisei University) **20**

1-5 Spectral discrimination of landfill sites in Africa: an analysis using HISUI hyperspectral data, Leeme Arther Baruti (Kyushu University) **24**

1-6 Environmental economic modeling of sustainable marine litter collection activities by fisherman ～ Focusing on Tsushima city, Daiki Nakagawara (Kyushu University) **33**

1-7 Optimization of municipal solid waste collection and transportation routes in Odawara City, Nanako Ohno (Kanadevia Corporation) **41**

1-8 Nutrient recovery from anaerobic digestate through struvite precipitation: process performance and economic analysis, Shunchang Yang (The Institute of Zhejiang University-Quzhou) **45**

Session 2 Hazardous Waste, Innovative Treatment p58-p138

Chair : Prof. Sun Yingjie (Qingdao University of Technology)

2-2 Optimization of wet alkali hydrolysis process for treating dead livestock and poultry, Hongzhi Ma (University of Science and Technology Beijing) **58**

2-3 Evaluation of heavy-metal leaching in returned and crushed concrete aggregates, Mitali Nag (National Institute for Environmental Studies) **62**

2-4 Aeration-enhanced acid leaching of heavy metals from municipal solid waste incineration fly ash, Pengfei Li (Kyushu University) **70**

2-5 Crystallization process enhanced by quaternary ammonium salt surfactant for dewaterability improvement of waste-activated sludge, Yawen Ye (Tongji University) **83**

2-6 Low-temperature, ambient-pressure and rapid mineralization of per- and polyfluoroalkyl substances by molten alkali, Huan Zhang (Tongji University) **113**

Poster session 1 p139-p228

P1-2 machine learning framework for optimization and inverse design of catalytic pyrolysis of plastics, Zhengyu Wang (Tongji University) **139**

P1-3 Effect of load on temperature measurement using optical sensors, Yuto Yamakawa (Kyushu University) **150**

P1-4 Speciation analysis and extractability Potential of rare earth elements in landfill humus soil, Linhai Ye (Tongji University) **156**

P1-5 Risk assessment of long-term leaching of heavy metals during solidification/stabilization of MSWI fly ash landfill disposal under the coupling effect of freeze-thaw cycle and carbonation, Xue Li (Qingdao University of Technology) **164**

P1-6 Facilitating anaerobic digestion of kitchen waste through diatomite-mediated spatial ecological niches construction, Dong Li (Tongji University) **165**

P1-7 Destabilization of colloidal particles induced by in-situ calcium carbonate crystallization with implications on highly efficient removal of insoluble matter from anaerobic digestate liquor, Jieling Feng (Tongji University) **176**

P1-8 Fundamental study on drying treatment of incineration residues using non-power-generating solar energy, Yosuke Tsuru (Kyushu University) **178**

P1-9 Micro-granular sludge driven by powder carrier in membrane bioreactor: Highly efficient N & P removal and membrane fouling alleviation, Junqian Zhong (Tongji University) **182**
P1-10 Research on material flows of agricultural plastic materials by product type and region, Ryotaro Kawanishi (Kyushu University) **184**
P1-11 Molecular transformation mechanisms of humus soil biomaterial in enhancing humification process of anaerobic digestate composting, Zhengliang Du (Tongji University) **190**
P1-12 Emission characteristics and control mechanism of dioxins during the synergistic treatment of waste incineration fly ash during the sintering process, Rongrong Lei (University of Science and Technology Beijing) **192**
P1-13 Towards sustainable municipal solid waste treatment: Life cycle environmental-economic analysis under waste sorting, Rongxing Bian (Qingdao University of Technology) **195**
P1-14 Impact of biochar on greenhouse gas emissions: A literature review, Xiaona Wang (University of Science and Technology Beijing) **218**
P1-15 Study of the mechanism of hydrolysis of hemicellulose by density functional theory and experiment, Weiyun Wang (Shenyang Aerospace University) **219**

Session 3 Recycling Technologies and Circular Economy p229-p263
Chair : Prof. Fumitake Takahashi (Institute of Science Tokyo)

3-1 Life cycle assessment of the effective utilization of low-grade plastics in melt separation systems for municipal solid waste incineration and non-combustible residues, Shuta Kawakami (Kyushu University) **229**
3-2 Using large language models and machine learning to enable sustainable electrochemical conversion of biomass-derived HMF into value-added BHMF, Cheng Zeng (Tongji University)**233**
3-3 Prediction of airborne bacterial concentrations and identification of critical factors in contaminated waste facilities Insights into interpretable machine learning models, Yanyan Guo (Tongji University) **243**
3-4 Proper evaluation of environmentally safe municipal solid waste incineration bottom ash as a material for artificial stone, Koshiro Ikaruka (Kyushu University) **251**
3-6 Design and validation of a novel contraction–expansion array conical grit remover for grit removal in wastewater sludge, Yi Xiong (Tongji University) **255**
3-7 From brewery wastewater to bio-olefins: a comprehensive tea and LCA, Na Wu (The Institute of Zhejiang University-Quzhou) **260**

Session 4 Resource Recovery and Thermal Processes p264-p282
Chair : Prof. Song Liyan (Anhui University)

4-1 Resource utilization potential of waste glass in a typical city of China and its carbon reduction and economic benefits evaluation, Jinfeng Tang (Guangzhou University) **264**
4-2 Research on the characteristics and kinetics of co-pyrolysis of sludge and biogas residue, Jun Zhang (Harbin Institute of Technology) **272**
4-3 Anti-fouling application for air-cooled condensers to improve power efficiency at waste-to-energy plant, Ryo Nakajima (Kurita Water Industries Ltd.) **276**
4-4 Recycling Li from spent LiFePO4 batteries through an economical and highly efficient strategy, Minhua Su (Guangzhou University) **278**
4-5 Recovery of valuable metals from incineration ash as non-ferrous refining materials using melting technology, Motohiro Sakamoto (Kubota Corporation) **279**

Poster session 2 p283-p368

P2-1 Bioaerosol contamination binds to PM2.5 during leachate treatment: Occurrence characteristics of human pathogens, virulence factor genes and antibiotic resistance genes, Yanan Wang (Qingdao University of Technology) **283**
P2-2 Mechanism of iron release from steel slag induced by denitrifying microorganisms and

optimization of its phosphorus removal performance in wastewater, Yan Guo (University of Science and Technology Beijing) **299**
P2-5 Bioremediation of coking contaminated soil: MnOB boosts the degradation of high-molecular-weight PAHs, Huawei Wang (Qingdao University of Technology) **301**
P2-6 Efficiency optimization and mechanistic insights into microbial electrosynthesis of methane from CO2 under high current density conditions, Yan Dang (Beijing Forestry University) **320**
P2-7 Automated two-stage partial nitrification/anammox system for treating actual dewatered liquid from food waste methane fermentation: Pilot-scale performance and control strategy optimization, Yuanyuan Ren (University of Science and Technology Beijing) **334**
P2-9 Study on detection method of waste disposal sites using object detection technology (YOLO) with satellite remote sensing in Japan, Yasuhiro Sugisaki (Kyushu University) **335**
P2-10 Study on synthesis of ethyl lactate by microbial-enzyme coupling esterification, Qunhui Wang (University of Science and Technology Beijing) **339**
P2-11 Enhancement of anaerobic fermentation for acid production and synergistic CO2 fixation by granular activated carbon (GAC) in distillery's grains, Dezhi Sun (Beijing Forestry University)**347**
P2-13 Straw-induced carbon dynamics in saline soils: insights from CO_2 emissions to soil organic carbon sequestration, Wenjun Xie (School of Environment and Municipal Engineering) **353**
P2-14 Construction and technological progress of a comprehensive carbon reduction system for CCUS in the steel industry, Yang Zheng (University of Science and Technology Beijing) **354**
P2-15 Research on social implementation of lithium-ion batteries (LIBs) detection methods using RFID tags, Koji Sakakibara (Kyushu University) **356**
P2-16 Process optimization for dissolving hemicellulose form corn bran in dilute acid pretreatment, Qunhui Wang (University of Science and Technology Beijing) **360**
P2-17 Porous polymethyl methacrylate monolith fabricated without organic solvent for cationic pollutantremoval: A preliminary study, Fumitake Takahashi (Institute of Science Tokyo) **366**

Oher papers **p369-p371**

O-1 Root-mediated oxygen transfer drives methylobacter Enrichment and secondary alcohol metabolism to Strengthen chlorobenzene degradation in rhizosphere Systems, Zhilin Xing (Chongqing University of Technology) **369**

CONTENTS

Session 1 Waste Management Systems, Environmental Impacts p1-p57

Chair : Prof. Kentaro Miyawaki (Meisei University)

1-1 Overlooked risk of microplastics from municipal solid waste–storage site, Yuyang Long (Zhejiang Gongshang University **1**

1-2 Using cognitive dissonance induced by waste presented as art to improve perceptions of waste, Bo Wang (Institute of Science Tokyo) **15**

1-3 Study on atmospheric CO_2 neutralization of high-PH leachate at offshore disposal sites, Kentaro Miyawaki (Meisei University) **20**

1-5 Spectral discrimination of landfill sites in Africa: an analysis using HISUI hyperspectral data, Leeme Arther Baruti (Kyushu University) **24**

1-6 Environmental economic modeling of sustainable marine litter collection activities by fisherman ～ Focusing on Tsushima city, Daiki Nakagawara (Kyushu University) **33**

1-7 Optimization of municipal solid waste collection and transportation routes in Odawara City, Nanako Ohno (Kanadevia Corporation) **41**

1-8 Nutrient recovery from anaerobic digestate through struvite precipitation: process performance and economic analysis, Shunchang Yang (The Institute of Zhejiang University-Quzhou) **45**

Session 2 Hazardous Waste, Innovative Treatment p58-p138

Chair : Prof. Sun Yingjie (Qingdao University of Technology)

2-2 Optimization of wet alkali hydrolysis process for treating dead livestock and poultry, Hongzhi Ma (University of Science and Technology Beijing) **58**

2-3 Evaluation of heavy-metal leaching in returned and crushed concrete aggregates, Mitali Nag (National Institute for Environmental Studies) **62**

2-4 Aeration-enhanced acid leaching of heavy metals from municipal solid waste incineration fly ash, Pengfei Li (Kyushu University) **70**

2-5 Crystallization process enhanced by quaternary ammonium salt surfactant for dewaterability improvement of waste-activated sludge, Yawen Ye (Tongji University) **83**

2-6 Low-temperature, ambient-pressure and rapid mineralization of per- and polyfluoroalkyl substances by molten alkali, Huan Zhang (Tongji University) **113**

Poster session 1 p139-p228

P1-2 machine learning framework for optimization and inverse design of catalytic pyrolysis of plastics, Zhengyu Wang (Tongji University) **139**

P1-3 Effect of load on temperature measurement using optical sensors, Yuto Yamakawa (Kyushu University) **150**

P1-4 Speciation analysis and extractability Potential of rare earth elements in landfill humus soil, Linhai Ye (Tongji University) **156**

P1-5 Risk assessment of long-term leaching of heavy metals during solidification/stabilization of MSWI fly ash landfill disposal under the coupling effect of freeze-thaw cycle and carbonation, Xue Li (Qingdao University of Technology) **164**

P1-6 Facilitating anaerobic digestion of kitchen waste through diatomite-mediated spatial ecological niches construction, Dong Li (Tongji University) **165**

P1-7 Destabilization of colloidal particles induced by in-situ calcium carbonate crystallization with implications on highly efficient removal of insoluble matter from anaerobic digestate liquor, Jieling Feng (Tongji University) **176**

P1-8 Fundamental study on drying treatment of incineration residues using non-power-generating solar energy, Yosuke Tsuru (Kyushu University) **178**

P1-9 Micro-granular sludge driven by powder carrier in membrane bioreactor: Highly efficient N & P removal and membrane fouling alleviation, Junqian Zhong (Tongji University) **182**
P1-10 Research on material flows of agricultural plastic materials by product type and region, Ryotaro Kawanishi (Kyushu University) **184**
P1-11 Molecular transformation mechanisms of humus soil biomaterial in enhancing humification process of anaerobic digestate composting, Zhengliang Du (Tongji University) **190**
P1-12 Emission characteristics and control mechanism of dioxins during the synergistic treatment of waste incineration fly ash during the sintering process, Rongrong Lei (University of Science and Technology Beijing) **192**
P1-13 Towards sustainable municipal solid waste treatment: Life cycle environmental-economic analysis under waste sorting, Rongxing Bian (Qingdao University of Technology) **195**
P1-14 Impact of biochar on greenhouse gas emissions: A literature review, Xiaona Wang (University of Science and Technology Beijing) **218**
P1-15 Study of the mechanism of hydrolysis of hemicellulose by density functional theory and experiment, Weiyun Wang (Shenyang Aerospace University) **219**

Session 3 Recycling Technologies and Circular Economy p229-p263
Chair : Prof. Fumitake Takahashi (Institute of Science Tokyo)

3-1 Life cycle assessment of the effective utilization of low-grade plastics in melt separation systems for municipal solid waste incineration and non-combustible residues, Shuta Kawakami (Kyushu University) **229**
3-2 Using large language models and machine learning to enable sustainable electrochemical conversion of biomass-derived HMF into value-added BHMF, Cheng Zeng (Tongji University)**233**
3-3 Prediction of airborne bacterial concentrations and identification of critical factors in contaminated waste facilities Insights into interpretable machine learning models, Yanyan Guo (Tongji University) **243**
3-4 Proper evaluation of environmentally safe municipal solid waste incineration bottom ash as a material for artificial stone, Koshiro Ikaruka (Kyushu University) **251**
3-6 Design and validation of a novel contraction–expansion array conical grit remover for grit removal in wastewater sludge, Yi Xiong (Tongji University) **255**
3-7 From brewery wastewater to bio-olefins: a comprehensive tea and LCA, Na Wu (The Institute of Zhejiang University-Quzhou) **260**

Session 4 Resource Recovery and Thermal Processes p264-p282
Chair : Prof. Song Liyan (Anhui University)

4-1 Resource utilization potential of waste glass in a typical city of China and its carbon reduction and economic benefits evaluation, Jinfeng Tang (Guangzhou University) **264**
4-2 Research on the characteristics and kinetics of co-pyrolysis of sludge and biogas residue, Jun Zhang (Harbin Institute of Technology) **272**
4-3 Anti-fouling application for air-cooled condensers to improve power efficiency at waste-to-energy plant, Ryo Nakajima (Kurita Water Industries Ltd.) **276**
4-4 Recycling Li from spent LiFePO4 batteries through an economical and highly efficient strategy, Minhua Su (Guangzhou University) **278**
4-5 Recovery of valuable metals from incineration ash as non-ferrous refining materials using melting technology, Motohiro Sakamoto (Kubota Corporation) **279**

Poster session 2 p283-p368

P2-1 Bioaerosol contamination binds to PM2.5 during leachate treatment: Occurrence characteristics of human pathogens, virulence factor genes and antibiotic resistance genes, Yanan Wang (Qingdao University of Technology) **283**
P2-2 Mechanism of iron release from steel slag induced by denitrifying microorganisms and

optimization of its phosphorus removal performance in wastewater, Yan Guo (University of Science and Technology Beijing) **299**
P2-5 Bioremediation of coking contaminated soil: MnOB boosts the degradation of high-molecular-weight PAHs, Huawei Wang (Qingdao University of Technology) **301**
P2-6 Efficiency optimization and mechanistic insights into microbial electrosynthesis of methane from CO2 under high current density conditions, Yan Dang (Beijing Forestry University) **320**
P2-7 Automated two-stage partial nitrification/anammox system for treating actual dewatered liquid from food waste methane fermentation: Pilot-scale performance and control strategy optimization, Yuanyuan Ren (University of Science and Technology Beijing) **334**
P2-9 Study on detection method of waste disposal sites using object detection technology (YOLO) with satellite remote sensing in Japan, Yasuhiro Sugisaki (Kyushu University) **335**
P2-10 Study on synthesis of ethyl lactate by microbial-enzyme coupling esterification, Qunhui Wang (University of Science and Technology Beijing) **339**
P2-11 Enhancement of anaerobic fermentation for acid production and synergistic CO2 fixation by granular activated carbon (GAC) in distillery's grains, Dezhi Sun (Beijing Forestry University)**347**
P2-13 Straw-induced carbon dynamics in saline soils: insights from CO_2 emissions to soil organic carbon sequestration, Wenjun Xie (School of Environment and Municipal Engineering) **353**
P2-14 Construction and technological progress of a comprehensive carbon reduction system for CCUS in the steel industry, Yang Zheng (University of Science and Technology Beijing) **354**
P2-15 Research on social implementation of lithium-ion batteries (LIBs) detection methods using RFID tags, Koji Sakakibara (Kyushu University) **356**
P2-16 Process optimization for dissolving hemicellulose form corn bran in dilute acid pretreatment, Qunhui Wang (University of Science and Technology Beijing) **360**
P2-17 Porous polymethyl methacrylate monolith fabricated without organic solvent for cationic pollutantremoval: A preliminary study, Fumitake Takahashi (Institute of Science Tokyo) **366**

Oher papers **p369-p371**

O-1 Root-mediated oxygen transfer drives methylobacter Enrichment and secondary alcohol metabolism to Strengthen chlorobenzene degradation in rhizosphere Systems, Zhilin Xing (Chongqing University of Technology) **369**

OVERLOOKED RISK OF MICROPLASTICS FROM MUNICIPAL SOLID WASTE–STORAGE SITE

Ying Hu, Shuli Guo, Dongsheng Shen, Jiali Shentu, Li Lu, Shengqi Qi, Min Zhu, Yuyang Long *
Zhejiang Provincial Key Laboratory of Solid Waste Treatment and Recycling, Zhejiang Engineering Research Center of Non-ferrous Metal Waste Recycling, School of Environmental Science and Engineering, Zhejiang Gongshang University, Hangzhou, China

ABSTRACT

Municipal solid waste (MSW) storage sites are potential and overlooked contributors to microplastic (MP) pollution. Herein, the distribution and dispersion characteristics of MPs at MSW storage sites were investigated through modeling, sampling analysis, and prediction methodologies. The results indicated a notable adsorption phenomenon of MPs on smooth surfaces within such sites, achieving high saturation levels and making MPs prone to re-release by airflow disturbance. Quantitative analysis revealed that the MP concentrations on these surfaces varied from 4.48×10^5 to 1.90×10^6 $n \cdot m^{-3}$ and that MPs predominantly accumulated in the corner areas. Notably, MP accumulation on wall surfaces can be reduced by 76.4% using washing procedures. The majority of MPs were under 50 μm in size and were primarily in fragment form. Operational activities such as ventilation and waste handling were identified to amplify the airborne spread of MPs. The atmospheric concentrations of MPs peaked seasonally, with concentrations of 28.25 $n \cdot m^{-3}$ in summer and 3.90 $n \cdot m^{-3}$ in winter, and the spatial dispersion ranged from 14.98 to 124.08 km² per station. This study highlights that MSW storage sites are substantial yet overlooked sources of MP pollution, where wall surfaces play a critical role in MP adsorption and dispersal. The implementation of robust management and cleaning protocols is essential to mitigate the environmental footprint of MPs emanating from these locations. This study also provides a typical case for the precise prevention and control of MPs in the environment.

KEYWORDS

MSW storage sites; Microplastic; Adsorption; Dispersion; Emerging pollution

1 INTRODUCTION

Up to now more than 8,300 million tons of plastic has been produced globally, with 60% entering terrestrial ecosystems as municipal solid waste (MSW) (Staplevan and Hai, 2024). Plastics can be gradually broken down into microplastics (MPs) through physical, chemical, and biological processes; these MPs are then dispersed through soil, water, and air (Luo et al., 2024). The resulting dispersion of MPs can impact ecosystems (Porter et al., 2023; Wu et al., 2024), necessitating thorough investigation.

Up to now more than 8,300 million tons of plastic has been produced globally, with 60% entering terrestrial ecosystems as municipal solid waste (MSW) (Staplevan and Hai, 2024). Plastics can be gradually broken down into microplastics (MPs) through physical, chemical, and biological processes; these MPs are then dispersed through soil, water, and air (Luo et al., 2024). The resulting dispersion of MPs can impact ecosystems (Porter et al., 2023; Wu et al., 2024), necessitating thorough investigation.

In recent years, studies into MPs in MSW have mainly focused on the generation of MPs during end-of-pipe disposal. The dynamic succession of MPs in two typical scenarios, landfill and incineration, has been reported (Zhang et al., 2024). However, the generation of MPs before these stages has received less attention. It has been found that the airborne concentration of MPs in the waste reception halls of six MSW transfer stations in Shanghai reached up to 7.3 $n \cdot m^{-3}$ (Hu et al., 2022), which is approximately 5.1 times higher than the concentration in the atmosphere of Shanghai (Liu et al., 2019a; Liu et al., 2024b). However, the distribution and dispersion mechanisms of MPs in these semienclosed environments are not well understood. MPs, with their irregular shapes and large specific surface areas, easily adhere to surfaces due to capillary, van der Waals, and electrostatic forces (Witzmann et al., 2022; Liu et al., 2024c). Owing to their small size (1 μm–5 mm) and low density (0.85–2.20 $g \cdot cm^{-3}$) (Luo et al., 2024), MPs are readily transported through the atmosphere (Chen et al., 2023; Chen et al., 2024). The detection of high MP concentrations in the reception halls of MSW transfer stations indicates a hidden risk, pointing to the possibility of MPs migrating within these enclosed spaces or even dispersing outside before the waste is disposed of. It has been found that MPs deposited in central London migrated up to 60 km away to the south-east of England (Wright et al., 2020), and their presence in the French Pyrenees provides further evidence of this migratory behavior (Allen et al., 2019). Therefore, MSW

storage sites, which serve as staging areas, are critical environments for exploring the generation and dispersion of MPs. Compared to MSW transfer stations, MSW storage sites are smaller, typically semi-enclosed structures, where waste is concentrated before it is transferred to transfer stations. These sites remain mostly sealed, except during waste handling operations and routine indoor ventilation. MPs are continuously generated and released during waste compression and crushing at these sites (Wang et al., 2024). Over time, MPs may agglomerate in the storage site (Kefer et al., 2022; Li et al., 2022), forming a potential source of high-density MP release. Workers involved in waste collection, sorting, and recycling within these environments face an unavoidable risk of MP exposure (Sun and Wang, 2023). In addition, the inherent properties of MPs, including their small particle size and low density, make them prone to atmospheric diffusion. The transport and deposition of MPs are influenced by wind dynamics (Preston et al., 2023), posing health risks to nearby residents and even contributing to regional or larger-scale pollution concerns (Parashar and Hait, 2023; Rao et al., 2024). Thus, the environmental risks associated with MPs in the confined spaces of MSW pre-disposal sites should not be overlooked.

This study is the first to investigate the distribution and environmental dispersion characteristics of MPs in MSW storage sites in depth. Through laboratory simulations and field sampling, the study highlights these sites as potential high-density MP emitters, posing health risks to workers and residents. This research fills a gap in the knowledge about MP dynamics during waste handling and offers key insights for pollution control strategies.

In recent years, studies into MPs in MSW have mainly focused on the generation of MPs during end-of-pipe disposal. The dynamic succession of MPs in two typical scenarios, landfill and incineration, has been reported (Zhang et al., 2024). However, the generation of MPs before these stages has received less attention. It has been found that the airborne concentration of MPs in the waste reception halls of six MSW transfer stations in Shanghai reached up to 7.3 $n \cdot m^{-3}$ (Hu et al., 2022), which is approximately 5.1 times higher than the concentration in the atmosphere of Shanghai (Liu et al., 2019a; Liu et al., 2024b). However, the distribution and dispersion mechanisms of MPs in these semi-enclosed environments are not well understood. MPs, with their irregular shapes and large specific surface areas, easily adhere to surfaces due to capillary, van der Waals, and electrostatic forces (Witzmann et al., 2022; Liu et al., 2024c). Owing to their small size (1 μm–5 mm) and low density (0.85–2.20 $g \cdot cm^{-3}$) (Luo et al., 2024), MPs are readily transported through the atmosphere (Chen et al., 2023; Chen et al., 2024). The detection of high MP concentrations in the reception halls of MSW transfer stations indicates a hidden risk, pointing to the possibility of MPs migrating within these enclosed spaces or even dispersing outside before the waste is disposed of. It has been found that MPs deposited in central London migrated up to 60 km away to the south-east of England (Wright et al., 2020), and their presence in the French Pyrenees provides further evidence of this migratory behavior (Allen et al., 2019). Therefore, MSW storage sites, which serve as staging areas, are critical environments for exploring the generation and dispersion of MPs. Compared to MSW transfer stations, MSW storage sites are smaller, typically semi-enclosed structures, where waste is concentrated before it is transferred to transfer stations. These sites remain mostly sealed, except during waste handling operations and routine indoor ventilation. MPs are continuously generated and released during waste compression and crushing at these sites (Wang et al., 2024). Over time, MPs may agglomerate in the storage site (Kefer et al., 2022; Li et al., 2022), forming a potential source of high-density MP release. Workers involved in waste collection, sorting, and recycling within these environments face an unavoidable risk of MP exposure (Sun and Wang, 2023). In addition, the inherent properties of MPs, including their small particle size and low density, make them prone to atmospheric diffusion. The transport and deposition of MPs are influenced by wind dynamics (Preston et al., 2023), posing health risks to nearby residents and even contributing to regional or larger-scale pollution concerns (Parashar and Hait, 2023; Rao et al., 2024). Thus, the environmental risks associated with MPs in the confined spaces of MSW pre-disposal sites should not be overlooked.

This study is the first to investigate the distribution and environmental dispersion characteristics of MPs in MSW storage sites in depth. Through laboratory simulations and field sampling, the study highlights these sites as potential high-density MP emitters, posing health risks to workers and residents. This research fills a gap in the knowledge about MP dynamics during waste handling and offers key insights for pollution control strategies.

2 MATERIALS AND METHODS

2.1 Simulation of MP Release Process in MSW Storage Site

To understand the actual situation of the MSW storage site, the scene of the MSW storage site was simulated in the laboratory (Fig. 1A). An experimental model with dimensions of 30 cm × 10 cm × 10 cm (L × W × H) was constructed using tiles in a ratio of 1:30. Specimen piles of MPs (polyethylene, PE; 0.002 g) were placed

equidistantly in the interior to simulate the scenario of the waste stacking state to produce MPs. To mimic daily ventilation at the storage site (Hu et al., 2022), an external exhaust fan (2.5 w) was installed on the model's top side, with the wind speed controlled at 3 m s^{-1}. The air inlets of the model were rectangular, with dimensions of 6 cm × 2 cm (L × W) and a height of 8 cm. Adjacent to these were square air outlets (2 × 2 cm) positioned at the same height as the inlet. The ventilation study was conducted in eight time intervals: 2, 4, 5, 6, 7, 8, 9, and 12 h. After each interval, MPs were collected from the inner surface of the model to assess their level of accumulation on the walls of the storage site.

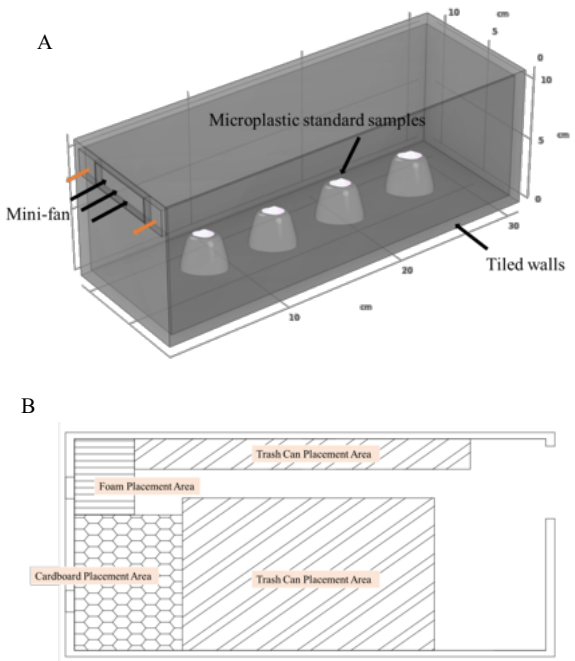

Fig. 1. Simulated adsorption model (A) and internal zoning of MSW storage sites (B). (In Fig. 1A, three black arrows represent the air inlets, and the orange arrow indicates the air outlet)

2.2 Distribution Analysis of MPs in a Typical MSW Storage Site

2.2.1 Sample Collection Point

A community MSW storage site in Hangzhou City, Zhejiang Province, China (30.291175°N, 120.131281°E) was studied to analyze the distribution characteristics of MPs. The site has a volume of approximately 150 m^3 and an elevation of 5 m. The site contains two axial fans to renew the indoor gases, with an outlet wind speed of 4.44 $m \cdot s^{-1}$. The waste types include domestic waste and plastic waste and include waste items from the community's supporting supermarkets, such as food packaging and foam boxes. The interior is divided into three zones for bins, foam, and cardboard (Fig. 1B).

2.2.2 Experimental Design

MSW storage sites are typically isolated, closed compartments. Within these compartments, MPs tend to readily adhere to the inner walls. This study directly and dynamically examined the distribution characteristics of wall-bound MPs in the storage sites by collecting them in stages under different scenarios. The experimental scenarios included:

(1) Wall washing: The MSW storage site's walls are washed daily at 12:00. With waste collection and transportation peaking between 18:30 and 22:00, samples are collected at these times to represent MP deposition during natural settling and strongly disturbed phases.

(2) Ventilation: Ventilation runs from 12:00 to 22:00 daily. MP sampling of the walls occurs at 18:30 and 22:00 to assess the impact of continuous air flow. (3) Combined washing and ventilation: Walls are washed at 12:00, coinciding with the start of daily ventilation, which lasts until 22:00. Sampling at 18:30 and 22:00 captures the combined effects of these actions on MP deposition.

In each experimental scenario, a pre-wetted filter membrane (Φ50 mm 0.45 μm, Zinten) was used to sample the wall-bound MPs. A hydrophilic filter membrane was first pre-wetted with deionized water, ensuring the entire membrane was damp without any dripping. Using stainless steel tweezers, the moistened membrane was gently pressed against the wall at the sampling site, ensuring it adhered closely without falling off. Then, the membrane was carefully peeled off using tweezers, keeping the side that was in contact with the wall facing up, and then placed into a clean aluminum box for preservation. To ensure comprehensive coverage, nine sampling points with different horizontal and vertical heights were set up on four walls, creating two parallel groups. The distribution of the specific sampling points is shown in Fig. S1.

2.3 MP Detection, Analysis, And Quality Control Requirements

In each experimental setup, the MP samples collected from tiles and walls were rinsed three times with deionized water. The rinse was collected in a 150-mL beaker and then vacuum-filtered through a 0.45-μm pore size filter membrane to capture the MPs. To avoid interference of organic matter, wall-derived MP samples were digested with hydrogen peroxide (15 mL of a 30% solution at 60°C for 30 min) and then vacuum-extracted after cooling to room temperature, transferring the MPs onto a flesh membrane. The MPs on the membrane were

stained with 10 mg L^{-1} of a Nile red solution and sequentially incubated at 25 ℃ for 10 min, 50 ℃ for 20 min, and 75 ℃ for 30 min (Guo et al., 2024). After staining, the MPs were vacuum-filtered through a 0.45-μm polytetrafluoroethylene membrane and stored in an aluminum box for microscopic analysis. MPs were detected using a fluorescence microscope (DM2500, Lycra), and the morphology of the MPs was determined based on the FIJI ImageJ software (Schneider et al., 2012), followed by the calculation of particle size and shape.

Rigorous protocols were implemented to ensure experimental accuracy. The experimental apparatus (stainless steel tweezers and glass beakers) were rinsed with deionized water and oven-dried at 55°C before use, then sealed with aluminum foil to avoid air exposure. During filtration, the experimental apparatus was rinsed at least thrice with deionized water to minimize the loss of MPs. The researchers wore nitrile gloves and 100% cotton lab coats during the operation to prevent contamination from external MPs. Given the small number of MPs adsorbed by the membranes, a control test was performed to offset potential interference, accounting for an average background of 6–7 MPs per membrane, equating to approximately 47.75–55.70 n·m $^{-2}$. This value was taken as the background value and was deducted during MP counting to ensure the reliability of the experimental results.

2.4 Data Analyses

For the analysis of airflow and spatial distribution of MPs within the MSW storage sites, simulations were conducted using COMSOL Multiphysics. The dispersion of MPs due to exhaust ventilation at these sites was calculated using the Aermod View software (v.8.9.0), incorporating meteorological data from the Hangzhou region of China. This data spanned a complete natural year, from January 1 to December 31, 2019. The data source selected was the Xiaoshan meteorological station in China (station number: 58459). Inputs included meteorological data for both surface and upper air, encompassing time, temperature, wind speed and direction, cloud cover, weather type, precipitation, and relative humidity. The predictive process assumed the following:

(1) The MSW storage site was treated as a point source, considering only the static adhesion of MPs on the inner walls.

(2) A dynamic equilibrium was presumed between the concentration of wall-adsorbed MPs and the concentration of MPs within the MSW storage site, denoted as $n_{wall} = n_{indoor}$.

Therefore, the equations for calculating the average rate of release of MPs from the MSW storage site were as follows:

$$C_i = \frac{n_{walli}}{V} \quad (1)$$

$$C_m = 0.0000024 C_i \quad (2)$$

$$V_0 = \frac{2.4 \times 10^{-6} \sum_{i=1}^{n=4} C_i V}{3600 V t} \quad (3)$$

where C_i (N·m^{-3}) represents the cumulative particle concentration released from each wall into the MSW storage site during the sampling period; V (m^3) represents the volume of the MSW storage site; n_{walli} is the total number of MPs corresponding to each interior wall; C_m (g·m^{-3}) represents the cumulative particle concentration during the sampling period; V_0 (g·s^{-1}) represents the MP release rate, and t (h) represents the stage sampling period. Equation (1) is based on the relation between the number of PE standard samples and mass as a reference (see Fig. S2) based on the universal transverse mercator grid system and the base map data imported into the air dispersion model by Google Earth Pro 2023. The receptor types used a unified cartesian receptor grid to evaluate the maximum ground-level pollutant concentrations. This involved a grid of 21 × 21 evenly spaced receptors, with all receptors spaced at 500 m. The terrain is flat, with a base of 5 m. The emission source height is 2.4 m, and the emission temperature was set to 25°C. The hourly average pollutant concentration at each receptor for different seasons was predicted using Aermod View based on the parameters of $PM_{2.5}$. It incorporated hourly meteorological data at the ground level and meteorological data at high altitudes for different seasons. Referring to the background MP concentration values in the clean environment, the MP concentration contained in the western Pacific Ocean surface (Liu et al., 2019b) was chosen as the standard in this study, and the boundary limit of MP diffusion concentration was set at 0.01 n·m^{-3}.

3 RESULTS AND DISCUSSION

3.1 Characteristics of MP Release from Simulated MSW Storage Sites

In the simulated MSW storage site scenario, between 4.30 × 10^3 and 2.09 × 10^4 n·m^{-2} MPs were detected on the wall surface, which indicates that MPs can be adsorbed on smooth walls. As can be seen in Fig. 2A, the accumulation of wall-bound MPs within the simulated MSW storage site varied over time. This suggests that the adhesive strength between MPs and the wall surfaces may be influenced by the microstructure of the surfaces. Persson's study (Persson, 2006) revealed that surfaces, even if seemingly smooth, can possess intricate roughness at the microscale, subtly affecting the adhesion of MPs. The initial rapid accumulation indicates an abundance of adhesion sites on newly exposed walls, which may become increasingly rough

due to the accumulating MPs, thereby altering the adhesion dynamics (Alfaro et al., 2012). Kinetic fitting to a first-order model showed that with increasing ventilation time, the adhesion rate climbed swiftly before gradually stabilizing, with an average equilibrium time of about 10 h. This dynamic likely mirrors the interplay between the characteristics of the MP particles and the evolving microstructure of the wall surface. Due to the symmetrical characteristics of the simulated walls at the MSW storage site, the Wall1 and Wall4 curves were in good agreement. Comparing Wall2 with Wall3 revealed a considerable difference in MP accumulation, with the leeward wall exhibiting a notably higher quantity and adsorption rate. This suggests a close correlation between the direction of gas flow and the distribution of suspended MPs but differs from the higher abundance of MPs in the windward part of the estuary observed by Browne et al. (Browne et al., 2010). This difference is possibly due to the ability of airflow in confined spaces to drive the recirculation of particles within the interior space (Zhang et al., 2020). This can also be mirrored from the internal wind field of the MSW storage site model (Figs. 2B and C). As airflow enters the interior of the MSW storage site model from the air inlet, it initially travels horizontally for a certain distance; then the airflow carrying MPs changes its direction of movement due to the obstruction of the windward wall. Consequently, only a small portion of the airflow reaches the windward wall, while the majority undergoes a downward gyration toward the leeward wall, forming a double-rotation reflux within the narrow channel. Due to the air resistance and the obstruction of the wall, energy loss occurs during the movement of the airflow. Eventually, MPs are deposited onto the wall surface, with a greater accumulation observed on the leeward wall compared to the windward wall. The observed distribution pattern may indicate how air currents control the behavior of MPs. While the simulation did not incorporate human activities, actual operations at waste storage facilities, such as personnel traffic and waste handling, can alter these dynamics. Factors such as personnel movement and waste transport may disturb the established patterns of MP behavior. Such activities might lead to the resuspension of MPs that were previously adhered to wall surfaces, thus initiating a cycle of MPs (Zhang et al., 2020). This cycle not only increases the mobility of MPs but also escalates the associated risks. It has been reported that human activities (e.g., movement of people, vacuum cleaning, etc.) can cause resuspension of particulate matter in indoor air (Lewis et al., 2018; Wang et al., 2021). This process heightens the risk of MP exposure via inhalation, ingestion, and dermal contact (Sun and Wang, 2023). Therefore, contrasting the MP deposition patterns seen in the simulation with those in active waste storage sites is essential for a thorough assessment of the environmental and health risks.

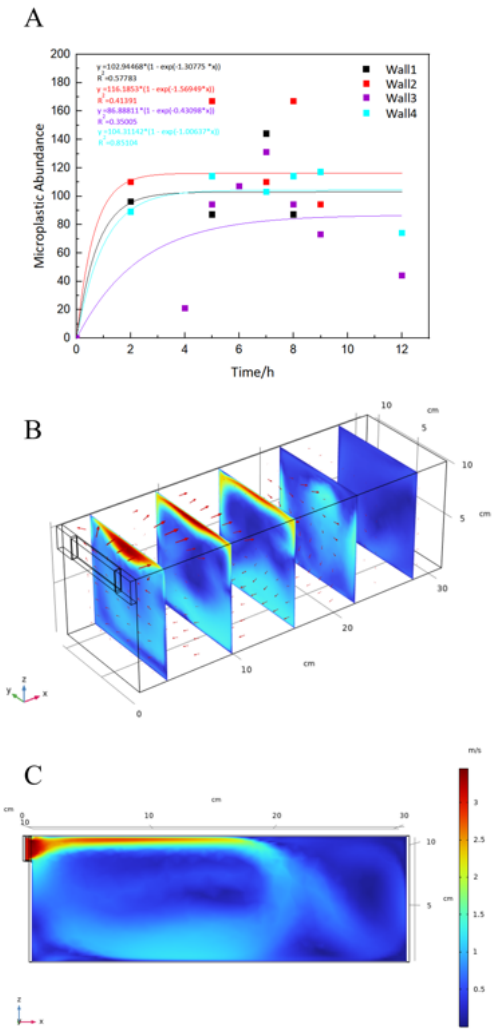

Fig. 2. Adsorption curves of MPs on the WSM storage site's internal walls (A) and the modeled wind field sections: transverse (B) and longitudinal (C). (In Fig. 2A, Wall1 and Wall4 are adjacent to the air intake, while Wall2 is near the exhaust outlet and Wall3 is the furthest. The legend in C indicates wind speed, with red for higher and blue for lower speeds.)

3.2 Influence of the Operational Status of MSW Storage Sites on the Distribution of MPs

The results of the MSW storage site model indicated that the risk of MP exposure in such confined spaces should not be underestimated. To further delineate the formation process, multi-scenario sampling and analysis were conducted at the actual site. The statistical analysis of the total MPs collected under three experimental scenarios (washing, ventilation, or a combination of both)

showed that the abundance of wall-bound MPs at the MSW storage site ranged from 4.48×10^5 to 1.90×10^6 $n \cdot m^{-2}$. This concentration is considerably higher than the levels reported in previous studies in Shanghai (1.50×10^3 to 9.90×10^3 $n \cdot m^{-2}$), New Zealand State (6.20×10^3 to 1.96×10^4 $n \cdot m^{-2}$), and St. Paulite (3.09×10^2 $n \cdot m^{-2}$), where the indoor air MPs concentration over one day was several orders of magnitude lower (Zhang et al., 2020; Amato-Lourenço et al., 2022; Yao et al., 2022). This notable difference in MP abundance can be primarily attributed to the much higher density of plastic waste at the MSW storage site compared to typical indoor environments. The accumulation of substantial amounts of plastic waste in these storage areas considerably increases the concentration of MP particles in air, transforming them into high-risk zones for MP pollution. Consequently, it is crucial and necessary to improve the management of MP pollution sources at MSW storage sites and similar enclosed spaces.

From the MSW storage site washing scenario (comparing E and I in Fig. 3), it can be seen that washing the wall surface reduced the accumulation of MPs by 76.40% compared with the unwashed condition. Evidently, the adsorption of MPs on wall surfaces is mitigated by washing. This reduction subsequently diminishes their potential for rerelease into the ambient air, ultimately lowering the associated health risks. This outcome aligns with the findings conducted by Hu et al (Hu et al., 2022). The washing process can affect MP adsorption and release, primarily through physical removal and alterations to the wall's surface properties (Tiwari et al., 2019; Burrows et al., 2020). These changes may impact the re-adsorption capacity of the MPs. Increased moisture from rinsing can change the surface energy (Henry, 2017; Moreno Baqueiro Sansao et al., 2021), affecting how MPs re-attach to the wall. A moistened surface reduces direct contact between MPs and the wall, lessening the particles' ability to re-adsorb. Fig. 3A shows that, after rinsing, MPs settle less during strongly disturbed phases than during natural settling, likely due to increased humidity reducing adsorption. However, the presence or absence of ventilation presents a completely different phenomenon. Figs. 3E and I show that under ventilation, the quantity of MPs adsorbed on the wall was higher during strongly disturbed phase than during the natural settling phase. In scenarios of ventilation alone and ventilation combined with rinsing, adsorption increased by 16.52% and 11.50%, respectively. This indicates that both passive and active airflow perturbations, caused by waste handling and ventilation, respectively, contribute to wall-bound MP accumulation. Previous research corroborates the notable role of ventilation and human activities in modulating indoor MP levels (Zhang et al., 2020; Wang et al., 2021). It has been suggested that airflow turbulence caused by air conditioning can lead to secondary suspension of settled MPs, which also coincides with the phenomenon found in this study. During waste handling, a substantial number of MPs were released into the air, with ventilation enhancing air disturbance and convective circulation, which further increased the likelihood of suspended MPs contacting the walls with the airflow. Figs. 3A, E, and I reveal that combined rinsing and ventilation on walls resulted in substantially fewer MPs compared to either method alone. This demonstrates their combined efficacy for MP reduction. Rinsing mainly removes MPs physically from surfaces, whereas ventilation aids in expelling them indoors. Although turbulence might increase MP resuspension, ventilation effectively eliminates these particles via the exhaust, thus lowering the indoor MP burden. In reality, MPs in confined spaces do not disappear but merely migrate, whether adsorbed on walls or not.

In this study, the distribution of MPs in the confined space of the MSW storage site was further analyzed by numerical simulation. As shown in Fig. S3, the distribution of MPs in a MSW storage site showed different accumulation patterns due to washing and ventilation actions, contrasting with simulation experiments where MPs mainly accumulated on the leeward wall. The real-life scenario used negative pressure from exhaust fans for ventilation, as opposed to the positive pressure ventilation used in the simulations. When comparing the distribution of MPs during natural settling (A, B, C) and that during strongly disturbed phases (D, E, F) under three cleaning scenarios (Fig. S3), it was observed that the leeward wall showed higher MP abundance during the strongly disturbed phase. This is likely due to the increased input of MPs from waste handling activities, with the indoor trash can arrangement impeding airflow (Fig. 1B), thereby reducing the impact of air movement on the leeward side. The distribution of the MP field inside the MSW storage site indicated that most of the MPs' abundance extremes were located at corner positions, suggesting that corners are the main accumulation areas of MPs. Airflow turbulence causes air–wall variations in the concentration of MPs, and MPs that settle in corners or other locations may be resuspended, thus increasing the risk of MP exposure to operational workers. Studies on occupational exposure have shown that exposure to plastic dust may lead to an increased risk of lung damage and cancer (Mastrangelo et al., 2003; Murashov et al., 2021). This suggests that care should be taken to avoid direct contact and maintain necessary protection to avoid inhalation risk when carrying out waste handling operations within the MSW storage site. In particular, the cleaning of corners and other areas should be strengthened when washing is carried out.

In addition to abundance, the size and shape of MPs also

affect their transport and residence time in the air and determine their environmental risks (Koelmans et al., 2022; Preston et al., 2023). As shown in Figs. 3B, F, and J, the majority of MPs within the MSW storage site were predominantly found in sizes ranging from 1–100 μm, and were particularly concentrated in the 1–50-μm range. Size is a key factor influencing the spatial transport of MPs (Preston et al., 2023). Most of the wall-bound MPs were observed to be of small particle size, suggesting the presence of numerous MPs in the air capable of remaining suspended for extended periods. This poses potential health risks to humans and facilitates the diffusion of other chemical pollutants from MSW storage sites. Referring to the method proposed by Tong et al. (Tong et al., 2022), MPs are classified into fibers (roundness: 0.0–0.3 mm), fragments (roundness: 0.3–0.6 mm), and particles (roundness: 0.6–1.0 mm). As shown in Figs. 3C, G, and K, the upper and lower quartiles of roundness for the three scenarios did not fluctuate much, indicating a minimal impact of these conditions on the shape distribution of wall-bound MPs. The ventilation system in the waste storage facility does not specifically target MPs for removal, allowing MPs of various sizes and shapes to be transported by airflow. This led to a uniform distribution of MPs in terms of size and shape across different scenarios, aligning with the findings of Hu et al. (Hu et al., 2022). Although fibers are typically associated with atmospheric transport, fragments also commonly occur in ambient air (Klein and Fischer, 2019; Xu et al., 2024). In this study, fragments were the predominant shape of MPs on the walls (Figs. 3D, H, and L), which may mainly come from the fragmentation of large plastic products, such as plastic bottles and disposable fast food packaging (Huang et al., 2024). Plastics tend to undergo compression and stretching operations before disposal and are prone to release fragments due to breakage. For example, hot beverage plastic containers (soaking in 100 °C hot water for 60 min) release 1.07×10^6–2.24×10^6 n·mL^{-1} MPs, most of which are irregular in shape, While silicone pacifiers can release 0.99×10^5–5.00×10^5 particles per rupture due to steam sterilization or surface etching (Su et al., 2022). MPs detected in mineral water are primarily from bottle caps and necks, predominantly in flake shapes (Praveena et al., 2022), releasing 6.34×10^4–3.30×10^5 particles per bottle cap under mechanical stress(opening and closing the bottle cap 100 times) (Winkler et al., 2019). By analogy, the complex environment of the MSW storage site, with factors such as predisposal plastic deformation, waste compression, and high temperature and humidity, promotes the release of mainly fragment-shaped MPs.

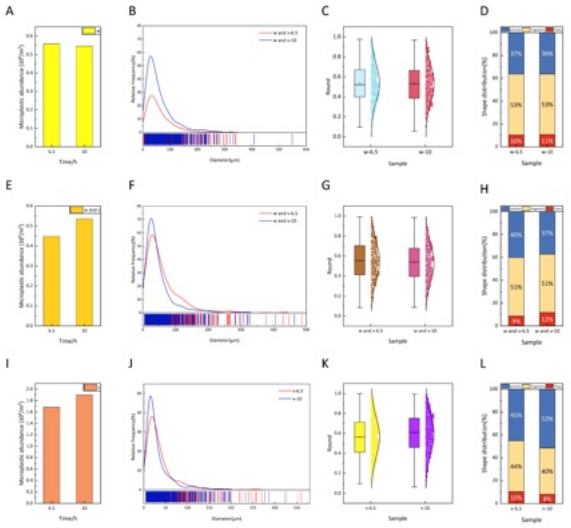

Fig. 3. Distribution of number, particle size, roundness, and shape for MPs under different treatments at MSW storage sites. (A, E, and I for quantity distributions of MPs after washing treatment (w), combined washing and ventilation treatment (w and v), and ventilation treatment (v) respectively; B, F, and J for particle size distributions; C, G, and K for roundness distributions; and D, H, and L for shape distributions corresponding to each treat

3.3 Environmental Dispersion Behavior of MPs in MSW Storage Sites

Indoor MP levels always surpass those outdoors (Liao et al., 2021; Choi et al., 2022; Yuan et al., 2022), suggesting considerable atmospheric MP contributions from indoors. Waste storage sites, disturbed by ventilation, likely serve as major MP sources. Our data show these MPs are mostly under 100 μm in size and are fragmentary in shape, indicating high mobility. Klein and Fischer (Klein and Fischer, 2019) found that 95% of MPs in Hamburg's air were fragmentary, mostly below the size of 63 μm, with wind speed and direction affecting MP distribution and transport. Similarly, Xu et al. (Xu et al., 2024) observed that in eastern China's mountains, approximately 60% of cloud water MPs were fragmentary and under 100 μm in size. Research in Kerala, India (Kannankai and Devipriya, 2024), pinpointed landfills and waste facilities as key MP sources, with the highest nearby deposition in winter, highlighting the migration potential of MPs from waste sites. These studies also highlighted the importance of meteorological factors in the atmospheric transport and deposition of MPs. Therefore, understanding the impact of waste sites on air quality and health is crucial. Consequently, the dispersion of MPs emanating from this source was predicted under varied seasonal meteorological conditions (spring, summer, autumn, and

winter). Fig. 4 indicates that during strong disturbances, the MPs' dispersion ranges were 2.4–8.0 km for rinsing, 2.0–5.6 km for rinsing with ventilation, and 4.8–17.2 km for ventilation alone, far exceeding the range of the natural settling phase (Fig. S5). During the natural settlement phase, the dispersion range of MPs is generally small, with the maximum dispersion distance being 0.4 km and being concentrated in several blocks near the storage site. These activities substantially increased the MP spread, making the waste site a potent MP source. Hangzhou's developed water network suggests that MPs could reach main water bodies such as West Lake and Qiantang River. This is consistent with the findings of Chen Hao et al.'s study (Chen et al., 2022) in Shanghai, which showed atmospheric deposition caused 21.7% of MPs to enter waterways. Similarly, Sun Jing et al. (Sun et al., 2022) found that atmospheric transport and deposition substantially contributed to urban water MPs and were closely related to $MP_{2.5}$ levels. Thus, atmospheric MP dispersion likely escalates their transfer to aquatic systems.

After cleaning at the waste storage site, the MP concentrations were 1.32–9.53 $n \cdot m^{-3}$ for washing, 1.11–8.03 $n \cdot m^{-3}$ for washing with ventilation, and 3.90–28.25 $n \cdot m^{-3}$ for ventilation alone. These figures are below the levels found in Beijing, China (Li et al., 2020) (5,650 $n \cdot m^{-3}$) and London, UK (Levermore et al., 2020) (2,502 $n \cdot m^{-3}$) but similar to those in Bushehr, Iran (Akhbarizadeh et al., 2021) (2.1–10.3 $n \cdot m^{-3}$), Paris, France (Allen et al., 2020) (2.9–9.6 $n \cdot m^{-3}$), Nanjing, China (Rao et al., 2024) (0.29–4.88 $n \cdot m^{-3}$), and Shanghai, China (Liu et al., 2019a) (1.4 $n \cdot m^{-3}$). This reflects how location and environment can affect atmospheric MP levels. The notable differences could also stem from the high variability in daily particulate sampling, with Beijing's high levels potentially linked to abundant surface dust and construction materials such as asbestos, gypsum, and man-made mineral fibers. London's high concentrations might be due to its sampling sites being near busy roads, where tire wear generates more MPs. Comparable concentrations were noted in port or bay areas, where air renewal dilutes MPs. It has been established previously that atmospheric migration of MPs is influenced by wind transport (Allen et al., 2019; Liu et al., 2019a; Liao et al., 2021). The extensive range and southeast-northwest contour orientation in Fig. 4 may primarily be due to the year's predominant northeast winds in Hangzhou. Additionally, previous studies (Wright et al., 2020; Luo et al., 2024; Xu et al., 2024) have indicated that precipitation, monsoons, and human activities (e.g., industry and traffic) also affect MP dispersion, meriting further detailed investigation in future research.

In terms of season, MP spread was greatest in the winter, reaching 124.08 km^2 and affecting approximately 1.6 million people, far exceeding other seasons. Spring and fall had moderate spreads, while summer saw the least, with only 14.98 km^2 affected, impacting around 273,100 people. This variation may be due to Hangzhou's climate, with less wind and convection in summer, and dry, windy conditions in winter aiding MP migration. Hangzhou, a mega-city in China, has a study site located in a densely populated area containing 6,214 $people \cdot km^{-2}$, calculated from the maximum dispersion range. Liu Kai et al. (Liu et al., 2024a) suggest that 80% of MP intake comes from residential areas, influenced by human activities. Thus, the MPs released from waste storage sites pose a considerable risk to nearby residents

In response to the critical aspects of our findings, enhancing the cleaning and ventilation of inner walls at waste storage sites is recommended to reduce the release of MPs into the atmosphere. Consideration should also be given to the fate of MPs in wastewater generated from site washing activities. Equipping workers with appropriate personal protective equipment is crucial to minimize health risks associated with exposure to MPs. Additionally, it is suggested that the emission of MPs from waste storage sites be included when accounting for sources of microplastics in urban atmospheric environments. Controlling MPs at the source may effectively involve reducing the consumption and breakage of unnecessary plastic products, along with strengthening the segregation and recycling of plastic materials.

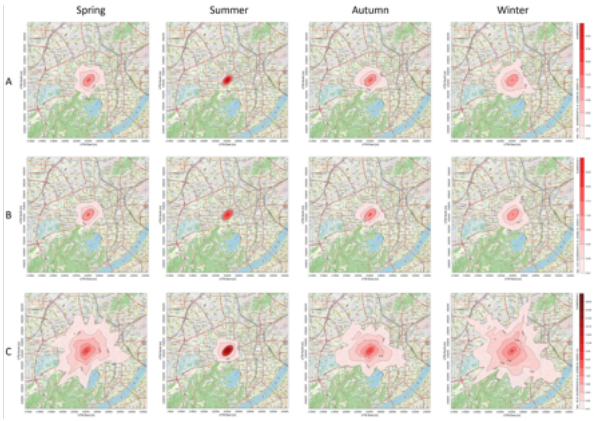

Fig. 4. Concentration distribution of MPs in the strongly disturbed phase at WSM storage sites. (A for washing treatment, B for washing combined with ventilation, C for ventilation treatment) (The legend represents microplastic abundance, with darker red colors increasing abundance in $n \cdot m^{-3}$)

4 CONCLUSIONS

In the typical confined space of MSW storage sites, MPs

are quickly adsorbed on smooth wall surfaces, reaching saturation; however, MPs remain vulnerable to rerelease due to airflow disturbance. The particle size of wall-bound MPs at the MSW storage site was primarily 1–50 μm, predominantly in the fragment form. The abundance of wall-bound MPs ranged from 4.48×10^5 to 1.90×10^6 $n \cdot m^{-2}$ under different operating conditions, with the corners of the walls being the main accumulation area of MPs. The accumulation of wall-bound MPs can be reduced by 76.4% through washing; however, airflow disturbance caused by ventilation or human activities contributes to the adsorption and accumulation of well-bound MPs. Measures should be implemented for improving the protection of cleaning operators during waste handling and for ensuring timely cleaning. The diffuse concentration of MPs substantially differs with season, with the peak concentrations in summer and winter being 28.25 $n \cdot m^{-3}$ and 3.90 $n \cdot m^{-3}$, respectively. The corresponding diffuse coverage areas are 14.98 and 124.08 km^2 per station. Prevention and control of MPs pollution from MSW storage sites should be taken in terms of potential health risks to surrounding residents. In future work, the prevention and control of MP pollution from MSW storage sites should be prioritized owing to the potential health risks faced by the surrounding residents. This includes assessing how city-wide waste management influences MP levels and devising ways to reduce their atmospheric release, improving our knowledge of urban MP behavior and pollution control.

REFERENCES

Akhbarizadeh R, Dobaradaran S, Amouei Torkmahalleh M, Saeedi R, Aibaghi R, Faraji Ghasemi F (2021). Suspended fine particulate matter (PM2.5), microplastics (MPs), and polycyclic aromatic hydrocarbons (PAHs) in air: Their possible relationships and health implications. Environmental Research, 192(1): 110339https://doi.org/https://doi.org/10.1016/j.envres.2020.110339

Alfaro S C, Chabas A, Lombardo T, Verney-Carron A, Ausset P (2012). Predicting the soiling of modern glass in urban environments: A new physically-based model. Atmospheric Environment, 60(15): 348-357https://doi.org/https://doi.org/10.1016/j.atmosenv.2012.06.050

Allen S, Allen D, Moss K, Le Roux G, Phoenix V R, Sonke J E (2020). Examination of the ocean as a source for atmospheric microplastics. PLOS ONE, 15(5): e0232746https://doi.org/10.1371/journal.pone.0232746

Allen S, Allen D, Phoenix V R, Le Roux G, Durántez Jiménez P, Simonneau A, Binet S, Galop D (2019). Atmospheric transport and deposition of microplastics in a remote mountain catchment. Nature Geoscience, 12(5): 339-344https://doi.org/10.1038/s41561-019-0335-5

Amato-Lourenço L F, Dos Santos Galvão L, Wiebeck H, Carvalho-Oliveira R, Mauad T (2022). Atmospheric microplastic fallout in outdoor and indoor environments in São Paulo megacity. Science of The Total Environment, 821(20): 153450https://doi.org/https://doi.org/10.1016/j.scitotenv.2022.153450

Browne M A, Galloway T S, Thompson R C (2010). Spatial Patterns of Plastic Debris along Estuarine Shorelines. Environmental Science & Technology, 44(9): 3404-3409https://doi.org/10.1021/es903784e

Burrows S D, Frustaci S, Thomas K V, Galloway T (2020). Expanding exploration of dynamic microplastic surface characteristics and interactions. TrAC Trends in Analytical Chemistry, 130(9): 115993https://doi.org/https://doi.org/10.1016/j.trac.2020.115993

Chen H, Jia Q, Sun X, Zhou X, Zhu Y, Guo Y, Ye J (2022). Quantifying microplastic stocks and flows in the urban agglomeration based on the mass balance model and source-pathway-receptor framework: Revealing the role of pollution sources, weather patterns, and environmental management practices. Water Research, 224: 119045https://doi.org/https://doi.org/10.1016/j.watres.2022.119045

Chen Q, Shi G, Revell L E, Zhang J, Zuo C, Wang D, Le Ru E C, Wu G, Mitrano D M (2023). Long-range atmospheric transport of microplastics across the southern hemisphere. Nature Communications, 14(1): 7898https://doi.org/10.1038/s41467-023-43695-0

Chen Y, Jing S, Wang Y, Song Z, Xie L, Shang X, Fu H, Yang X, Wang H, Wu M, Chen Y, Li Q, Zhang Y, Wang W, Zhang L, Wang R, Fang M, Zhang Y, Li W, Zhao D, Li C, Rudich Y, Wang L, Zhang R, Liu W, Wanger T C, Yu S, Chen J (2024). Quantification and Characterization of Fine Plastic Particles as Considerable Components in Atmospheric Fine Particles. Environmental Science & Technology, 58(10): 4691-4703https://doi.org/10.1021/acs.est.3c06832

Choi H, Lee I, Kim H, Park J, Cho S, Oh S, Lee M, Kim H (2022). Comparison of Microplastic Characteristics in the Indoor and Outdoor Air of Urban Areas of South Korea. Water, Air, & Soil Pollution, 233(5): 169-178https://doi.org/10.1007/s11270-022-05650-5

Guo S, Wu Z, Li X, Shen D, Shentu J, Lu L, Qi S, Zhu M, Long Y (2024). Microplastic, a possible trigger of landfill sulfate reduction process. Science of The Total Environment, 906(1): 167662https://doi.org/https://doi.org/10.1016/j.scitotenv.2023.167662

Henry C (2017). Particles in Wall-Bounded Turbulent Flows: Deposition, Re-Suspension and Agglomeration. Minier, J.-P. and Pozorski, J. (eds). Cham: Springer International Publishing, 209-261

Hu T, He P, Yang Z, Wang W, Zhang H, Shao L, Lü F (2022). Emission of airborne microplastics from municipal solid waste transfer stations in downtown. Science of The Total Environment, 828(27): 154400https://doi.org/https://doi.org/10.1016/j.scitotenv.2022.154400

Huang Y-Q, Zeng Y, Mai J-L, Huang Z-S, Guan Y-F, Chen S-J (2024). Disposable Plastic Waste and Associated Antioxidants and Plasticizers Generated by Online Food Delivery Services in China: National Mass Inventories and Environmental Release. Environmental Science & Technology, 58(7): 3098-3107https://doi.org/10.1021/acs.est.3c06345

Kannankai M P, Devipriya S P (2024). Atmospheric microplastic deposition in a coastal city of India: The influence of a landfill source on monsoon winds. Science of The Total Environment, 908(3): 168235https://doi.org/https://doi.org/10.1016/j.scitotenv.2023.168235

Kefer S, Friedenauer T, Langowski H C (2022). Characterisation of different manufactured plastic microparticles and their comparison to environmental microplastics. Powder Technology, 412(18): 117960https://doi.org/https://doi.org/10.1016/j.powtec.2022.117960

Klein M, Fischer E K (2019). Microplastic abundance in atmospheric deposition within the Metropolitan area of Hamburg, Germany. Science of The Total Environment, 685(40): 96-103https://doi.org/https://doi.org/10.1016/j.scitotenv.2019.05.405

Koelmans A A, Redondo-Hasselerharm P E, Nor N H M, De Ruijter V N, Mintenig S M, Kooi M (2022). Risk assessment of microplastic particles. Nature Reviews Materials, 7(2): 138-152https://doi.org/10.1038/s41578-021-00411-y

Levermore J M, Smith T E L, Kelly F J, Wright S L (2020). Detection of Microplastics in Ambient Particulate Matter Using Raman Spectral Imaging and Chemometric Analysis. Analytical Chemistry, 92(13): 8732-8740https://doi.org/10.1021/acs.analchem.9b05445

Lewis R D, Ong K H, Emo B, Kennedy J, Kesavan J, Elliot M (2018). Resuspension of house dust and allergens during walking and vacuum cleaning. Journal of Occupational and Environmental Hygiene, 15(3): 235-245https://doi.org/10.1080/15459624.2017.1415438

Li S, Yang M, Wang H, Jiang Y (2022). Adsorption of microplastics on aquifer media: Effects of the action time, initial concentration, ionic strength, ionic types and dissolved organic matter. Environmental Pollution, 308(17): 119482https://doi.org/https://doi.org/10.1016/j.envpol.2022.119482

Li Y, Shao L, Wang W, Zhang M, Feng X, Li W, Zhang D (2020). Airborne fiber particles: Types, size and concentration observed in Beijing. Science of The Total Environment, 705(8): 135967https://doi.org/https://doi.org/10.1016/j.scitotenv.2019.135967

Liao Z, Ji X, Ma Y, Lv B, Huang W, Zhu X, Fang M, Wang Q, Wang X, Dahlgren R, Shang X (2021). Airborne microplastics in indoor and outdoor environments of a coastal city in Eastern China. Journal of Hazardous Materials, 417(17): 126007https://doi.org/https://doi.org/10.1016/j.jhazmat.2021.126007

Liu K, Li Q, Andrady A L, Wang X, He Y, Li D (2024a). Underestimated activity-based microplastic intake under scenario-specific exposures. Environmental Science and Ecotechnology, 18(2): 100316https://doi.org/https://doi.org/10.1016/j.ese.2023.100316

Liu K, Wang X, Fang T, Xu P, Zhu L, Li D (2019a). Source and potential risk assessment of suspended atmospheric microplastics in Shanghai. Science of The Total Environment, 675(30): 462-471https://doi.org/https://doi.org/10.1016/j.scitotenv.2019.04.110

Liu K, Wu T, Wang X, Song Z, Zong C, Wei N, Li D (2019b). Consistent Transport of Terrestrial Microplastics to the Ocean through Atmosphere. Environmental Science & Technology, 53(18): 10612-10619https://doi.org/10.1021/acs.est.9b03427

Liu P, Shao L, Zhang Y, Silvonen V, Oswin H, Cao Y, Guo Z, Ma X, Morawska L (2024b). Comparative study on physicochemical characteristics of atmospheric microplastics in winter in inland and coastal megacities: A case of Beijing and Shanghai, China. Science of The Total Environment, 912(7): 169308https://doi.org/https://doi.org/10.1016/j.scitotenv.2023.169308

Liu Q, Wu D, Chen Y, Chen Z, Yuan S, Yu H, Guo Y, Xie Y, Qian H, Yao W (2024c). Interaction and mechanistic studies of thiram and common microplastics in food and associated changes in hazard. Journal of Hazardous Materials, 461(): 132464https://doi.org/https://doi.org/10.1016/j.jhazmat.2023.132464

Luo D, Chu X, Wu Y, Wang Z, Liao Z, Ji X, Ju J, Yang B, Chen Z, Dahlgren R, Zhang M, Shang X (2024). Micro- and nano-plastics in the atmosphere: A review of occurrence, properties and human health risks. Journal of Hazardous Materials, 465(5): 133412https://doi.org/https://doi.org/10.1016/j.jhazmat.2023.133412

Mastrangelo G, Fedeli U, Fadda E, Milan G, Turato A, Pavanello S J O, Medicine E (2003). Lung cancer risk in workers exposed to poly (vinyl chloride) dust: a nested case-referent study. 60(6): 423-428

Moreno Baqueiro Sansao B, Kellar J J, Cross W M, Romkes A (2021). Separation of particles of different surface energies through control of humidity. Minerals

Engineering, 160(1): 106680https://doi.org/https://doi.org/10.1016/j.mineng.2020.106680
Murashov V, Geraci C L, Schulte P A, Howard J (2021). Nano- and microplastics in the workplace. Journal of Occupational and Environmental Hygiene, 18(10-11): 489-494https://doi.org/10.1080/15459624.2021.1976413
Parashar N, Hait S (2023). Plastic rain—Atmospheric microplastics deposition in urban and peri-urban areas of Patna City, Bihar, India: Distribution, characteristics, transport, and source analysis. Journal of Hazardous Materials, 458(18): 131883https://doi.org/https://doi.org/10.1016/j.jhazmat.2023.131883
Persson B N J (2006). Contact mechanics for randomly rough surfaces. Surface Science Reports, 61(4): 201-227https://doi.org/https://doi.org/10.1016/j.surfrep.2006.04.001
Porter A, Godbold J A, Lewis C N, Savage G, Solan M, Galloway T S (2023). Microplastic burden in marine benthic invertebrates depends on species traits and feeding ecology within biogeographical provinces. Nature Communications, 14(1): 8023https://doi.org/10.1038/s41467-023-43788-w
Praveena S M, Shamsul Ariffin N I, Nafisyah A L (2022). Microplastics in Malaysian bottled water brands: Occurrence and potential human exposure. Environmental Pollution, 315(24): 120494https://doi.org/https://doi.org/10.1016/j.envpol.2022.120494
Preston C A, Mckenna Neuman C L, Aherne J (2023). Effects of Shape and Size on Microplastic Atmospheric Settling Velocity. Environmental Science & Technology, 57(32): 11937-11947https://doi.org/10.1021/acs.est.3c03671
Rao W, Fan Y, Li H, Qian X, Liu T (2024). New insights into the long-term dynamics and deposition-suspension distribution of atmospheric microplastics in an urban area. Journal of Hazardous Materials, 463(3): 132860https://doi.org/https://doi.org/10.1016/j.jhazmat.2023.132860
Schneider C A, Rasband W S, Eliceiri K W (2012). NIH Image to ImageJ: 25 years of image analysis. Nature Methods, 9(7): 671-675https://doi.org/10.1038/nmeth.2089
Staplevan M J, Hai F I (2024). Recycling process produces microplastics. Science, 383(6686): 958-958https://doi.org/10.1126/science.ado1473
Su Y, Hu X, Tang H, Lu K, Li H, Liu S, Xing B, Ji R (2022). Steam disinfection releases micro(nano)plastics from silicone-rubber baby teats as examined by optical photothermal infrared microspectroscopy. Nature Nanotechnology, 17(1): 76-85https://doi.org/10.1038/s41565-021-00998-x
Sun A, Wang W X (2023). Human Exposure to Microplastics and Its Associated Health Risks. Environment & Health, 1(3): 139-149https://doi.org/10.1021/envhealth.3c00053
Sun J, Peng Z, Zhu Z-R, Fu W, Dai X, Ni B-J (2022). The atmospheric microplastics deposition contributes to microplastic pollution in urban waters. Water Research, 225(18): 119116https://doi.org/https://doi.org/10.1016/j.watres.2022.119116
Suzuki G, Uchida N, Tanaka K, Higashi O, Takahashi Y, Kuramochi H, Yamaguchi N, Osako M (2024). Global discharge of microplastics from mechanical recycling of plastic waste. Environmental Pollution: 123855https://doi.org/https://doi.org/10.1016/j.envpol.2024.123855
Tiwari A, Wang A, Müser M H, Persson B N J (2019). Contact Mechanics for Solids with Randomly Rough Surfaces and Plasticity. Lubricants, 7(10): 90-108 https://doi.org/10.3390/lubricants7100090
Tong H, Zhong X, Duan Z, Yi X, Cheng F, Xu W, Yang X (2022). Micro- and nanoplastics released from biodegradable and conventional plastics during degradation: Formation, aging factors, and toxicity. Science of The Total Environment, 833(32): 155275https://doi.org/https://doi.org/10.1016/j.scitotenv.2022.155275
Wang B, Tang Z, Li Y, Cai N, Hu X (2021). Experiments and simulations of human walking-induced particulate matter resuspension in indoor environments. Journal of Cleaner Production, 295(18): 126488https://doi.org/https://doi.org/10.1016/j.jclepro.2021.126488
Wang R, Wang H, Zhan L, Xu Z (2024). Pollution characteristics and release mechanism of microplastics in a typical end-of-life vehicle (ELV) recycling base, East China. Science of The Total Environment, 916(11): 170306https://doi.org/https://doi.org/10.1016/j.scitotenv.2024.170306
Winkler A, Santo N, Ortenzi M A, Bolzoni E, Bacchetta R, Tremolada P (2019). Does mechanical stress cause microplastic release from plastic water bottles? Water Research, 166(19): 115082https://doi.org/https://doi.org/10.1016/j.watres.2019.115082
Witzmann T, Ramsperger A F R M, Wieland S, Laforsch C, Kress H, Fery A, Auernhammer G K (2022). Repulsive Interactions of Eco-corona-Covered Microplastic Particles Quantitatively Follow Modeling of Polymer Brushes. Langmuir, 38(29): 8748-8756https://doi.org/10.1021/acs.langmuir.1c03204
Wright S L, Ulke J, Font A, Chan K L A, Kelly F J (2020). Atmospheric microplastic deposition in an urban environment and an evaluation of transport. Environment International, 136(3): 105411https://doi.org/https://doi.org/10.1016/j.envint.2019.105411
Wu F, Ha X, Wang S, Li J, Gao Y (2024). Microplastic occurrences, transport, and quantification and associated

effects on primary productivity and carbon cycling processes in freshwater ecosystems. TrAC Trends in Analytical Chemistry, 172(3): 117611https://doi.org/https://doi.org/10.1016/j.trac.2024.117611
Xu X, Li T, Zhen J, Jiang Y, Nie X, Wang Y, Yuan X-Z, Mao H, Wang X, Xue L, Chen J (2024). Characterization of Microplastics in Clouds over Eastern China. Environmental Science & Technology Letters, 11(1): 16-22https://doi.org/10.1021/acs.estlett.3c00729
Yao Y, Glamoclija M, Murphy A, Gao Y (2022). Characterization of microplastics in indoor and ambient air in northern New Jersey. Environmental Research, 207(5): 112142https://doi.org/https://doi.org/10.1016/j.envres.2021.112142
Yuan Z, Li H-X, Lin L, Pan Y-F, Liu S, Hou R, Xu X-R (2022). Occurrence and human exposure risks of atmospheric microplastics: A review. Gondwana Research, 108(8): 200-212https://doi.org/https://doi.org/10.1016/j.gr.2022.02.001
Zhang L, Zhao W, Yan R, Yu X, Barceló D, Sui Q (2024). Microplastics in different municipal solid waste treatment and disposal systems: Do they pose environmental risks? Water Research, 255(8): 121443https://doi.org/https://doi.org/10.1016/j.watres.2024.121443
Zhang Q, Zhao Y, Du F, Cai H, Wang G, Shi H (2020). Microplastic Fallout in Different Indoor Environments. Environmental Science & Technology, 54(11): 6530-6539https://doi.org/10.1021/acs.est.0c00087

SUPPLEMENTARY MATERIALS

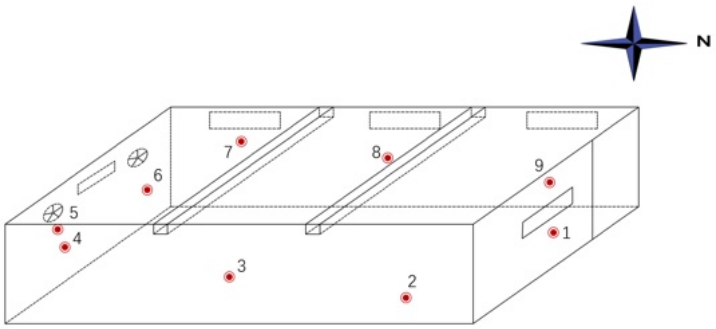

Fig. S1. Specific sampling points for waste storage sites (The red dots represent sampling points)

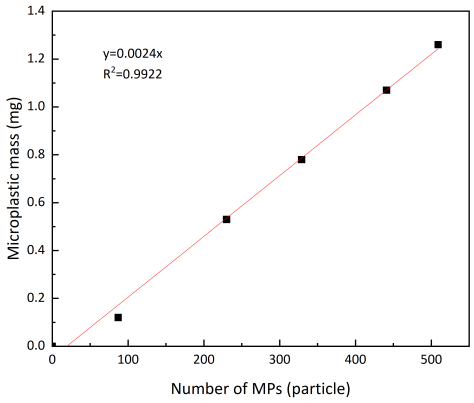

Fig. S2. Relationship between the number and quality of PE standard samples

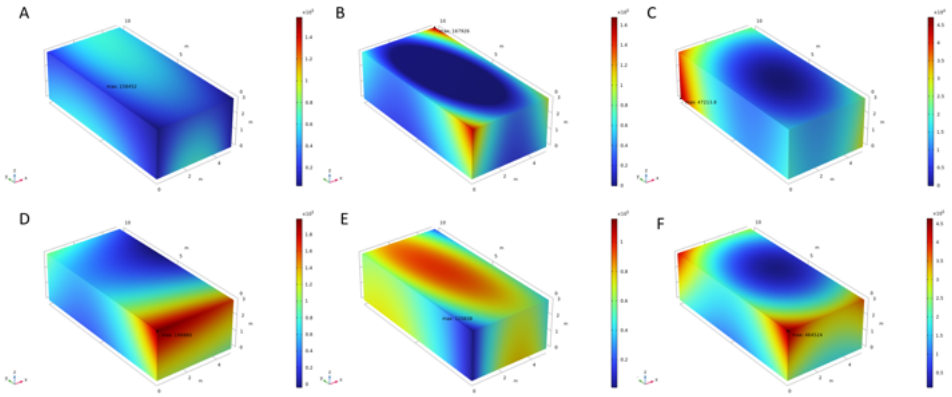

Fig. S3. Concentration field of MPs inside the MSW storage site. (A, B, and C for the natural settling phase following washing, ventilation, and combined washing-ventilation treatments, respectively; D, E, and F for the strongly disturbed phase after the same sequence of treatments.)

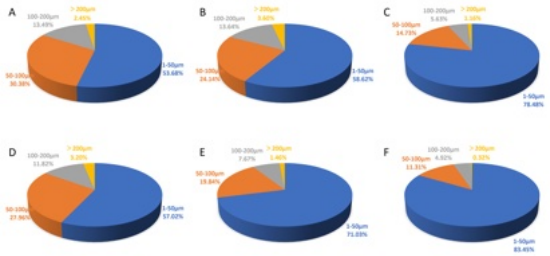

Fig. S4. Particle size distribution of MPs at MSW storage sites. (A, B, and C for the natural settling phase following washing, ventilation, and combined washing-ventilation treatments, respectively; D, E, and F for the strongly disturbed phase after the same sequence of treatments.)

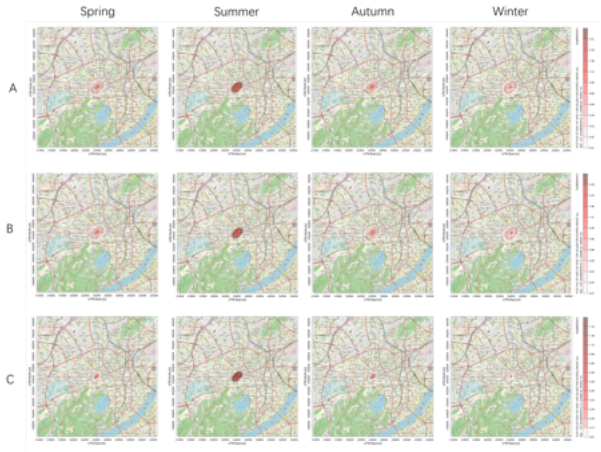

Fig. S5. Concentration distribution of MPs in the natural settling phase at the MSW storage site. (A for cleaning treatment, B for cleaning and ventilation treatment, C for ventilation treatment) (The legend represents microplastic abundance, with darker red colors increasing abundance in n·m-3)

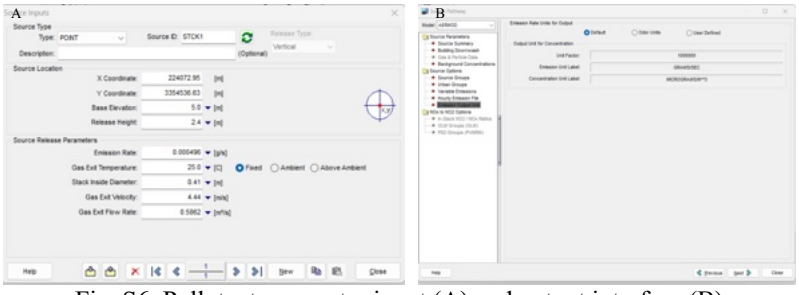

Fig. S6. Pollutant parameter input (A) and output interface (B)

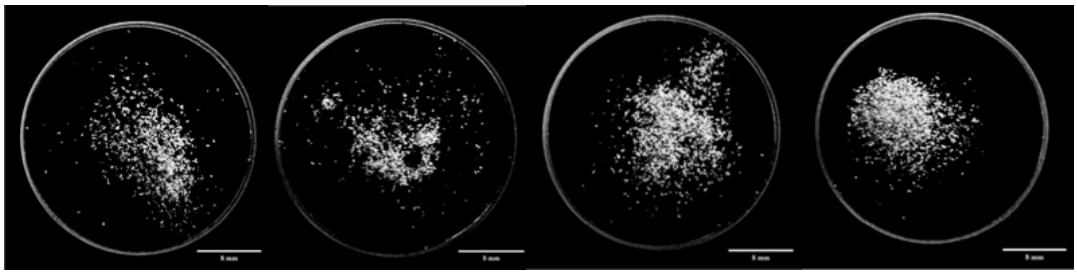

Fig. S7 Morphological distribution of four microplastic stacks

Using Cognitive Dissonance Induced by Waste Presented as Art to Improve Perceptions of Waste

Bo Wang[1], Vinayak Gupta[1], Fumitake Takahashi[1]

[1]Department of Transdisciplinary Science and Engineering, Institute of Science Tokyo, Suzukake, 4259, Nagatsuta, Midori-ku, Yokohama, 226-8503 JAPAN

ABSTRACT

Disgust is a major psychological barrier to waste-related behaviors; aestheticizing waste may reframe perceptions. Guided by the stimulus–organism–response (S-O-R) model and a cognitive-dissonance mechanism, we conducted three pilots with online participants in China (Credamo®; N_1=30, N_2=30, N_3=50). Stimuli contrasted real waste versus waste-as-art (plastic/food/metal); all measures used 7-point scales, including recycling intention (RI), purchase intention for recycled products (PI), inspiration (INS), an adapted DS-R for waste disgust sensitivity, and baseline perceptions via a semantic differential. Pilot 1, which modeled transformation salience in an SEM, did not yield the hypothesized main effects. Pilot 2 produced ceiling effects, likely due to strong unified persuasive text. Under minimal text in Pilot 3, food-waste artworks significantly increased RI relative to real waste, whereas for plastic and metal both RI and PI were generally higher under real-waste images; overall, aestheticization did not effectively raise PI. Open-ended responses suggested two additional behaviors—participating in trash-art creation and sharing related information. Findings indicate a waste-type–dependent effect whereby aestheticization more reliably elevates recycling rather than purchase intentions; perception change may operate through dissonance–guilt, anticipated disgust, self-efficacy, and inspiration. Offline replications in Japan and India will test robustness and cross-national structural differences.

1. INTRODUCTION

Negative impressions toward waste are one of the factors that hinder recycling behavior, and among them, disgust plays a significant role in lowering recycling intention. Disgust is a basic emotion directed toward decayed matter and pathogens, and it carries a psychological "contaminating potency" that influences even objects that contact with them. Therefore, even if recycled water or recycled materials are in fact clean and safe, they tend to be avoided due to the influence of disgust [1]. In addition, the influence of disgust extends even to workers engaged in waste-related occupations and is reflected in their social evaluation and treatment. On the other hand, although doctors and nurses are professions that meet pathogens—which are objects of disgust—they receive high social evaluation due to their clean image [2], suggesting that appearance and context influence feelings of disgust.

Art can be used to improve negative perceptions of waste. When negative scenes (e.g., a person being attacked) are presented in an artistic rather than a realistic form, they are more likely to be selected for viewing and are viewed for longer on average [3], suggesting that an artistic context can make negative images—such as those of waste—more likely to be seen. In order to improve the image of sanitation workers, artist Mierle Laderman Ukeles photographed herself shaking hands with them and exhibiting these photographs in an art museum [4]. The positive attributes associated with art were transmitted to the sanitation workers through physical contact, demonstrating that art can enhance people's

perceptions of negative objects through positive contamination [5].

2. HYPOTHESIS

According to cognitive dissonance theory, when individuals hold contradictory cognitions, they experience psychological discomfort, which motivates them to modify their beliefs or behaviors to restore consistency [6]. People often hold negative perceptions of waste—particularly perceiving it as disgusting—which may constitute a major psychological barrier to addressing waste-related problems. Artworks made from waste place waste within an artistic context and present it in a beautified form, which creates an inconsistency with people's usual cognitions about waste. This inconsistency may lead to an improvement in their perception of waste, which in turn may increase their willingness to engage in solving waste-related issues.

3. METHODS

This study first conducts psychological questionnaire surveys by recruiting participants from China via the online survey platform Credamo®. Following the stimulus–organism–response model [7], the study employs two types of visual stimuli: images of real waste and images of artwork created from the same types of waste. By comparing participants' responses to these stimuli, the study examines whether presenting waste in a beautified form within an artistic context can influence behavioral intentions—specifically, their intentions to participate in waste recycling, share waste-related information, and purchase recycled products.

Following the identification of the main effect, the study proceeds to explore the underlying psychological mechanisms. Feelings of guilt are employed as indicators of cognitive dissonance [8], while several psychological variables—including anticipated disgust toward waste-related behaviors, self-efficacy, and inspiration—are assessed as potential mediators of the observed relationship.

Following the validation of the conceptual model through the initial online survey, the study will undertake follow-up offline surveys in Japan and India. These subsequent investigations are designed both to assess the robustness of the model and to examine potential cross-national differences in structural relationships among the three countries.

4. RESULTS

To date, three pilot experiments have been conducted.

4.1 Pilot 1

Design and measures: Based on the study hypothesis, we specified a structural equation model (SEM; Figure 1) and recruited N = 30 participants. All items used 7-point Likert scales. Exogenous variables were transformation salience (with ③,④ vs. without ①,②; manipulated via text) and aesthetic perception (waste-as-art ①,③ vs. real waste ②,④) [9, 10]. The visual stimuli are shown in Figure 2. For endogenous constructs, we used established items for Inspiration (INS1–INS3) [11], Recycling Intention (RI1–RI3) [11], and Purchase Intention for Recycled Products (PI1–PI3)

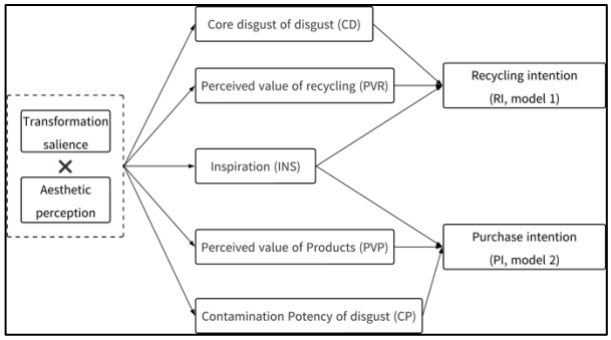

Figure 1 Sem models of pilot 1

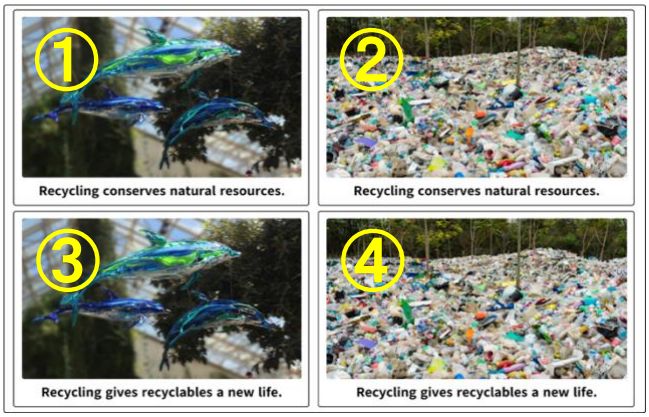

Figure 2 Stimuli used in pilot 1

[12]. Disgust sensitivity was based on Disgust Scale-Revise adaptation to waste, covering Core Disgust (CD1–CD6) and Contamination Potency (CP1–CP4) [13]. Perceived value was operationalized as Perceived Value of Waste Recycling (PVR1–PVR3) [14] and Perceived Value of Recycled Products (PVP1–PVP5) [12]. Analyses were conducted in R. Table 1 reports Cronbach's α for all latent variables; Table 2 summarizes condition-wise means and p-values.

Table 1 The Cronbach's α of latent values

Scale	CD	PVR	INS	PVP	CP	RI	PI
Cronbach's α	0.5	0.79	0.77	0.77	0.72	0.85	0.79

Results: Contrary to the hypothesis, both RI and PI tended to be higher for real plastic-waste images than for plastic waste artworks; however, differences were not statistically significant.

4.2 Pilot 2

Design adjustments: We removed transformation salience from the exogenous set and made minor questionnaire refinements while keeping the rest of the model unchanged. We recruited N = 30 participants and used real food-waste images versus food-waste artworks as stimuli. The text was unified across conditions and contained persuasive content encouraging purchase of biodegradable PHA products and support for producing PHA from food waste via recycling (Figure 3). All items again used 7-point Likert scales.

Results and interpretation: The extensive persuasive text likely overwhelmed the image manipulation: both RI and PI were extremely high in both conditions with minimal between-condition differences. We additionally measured initial perceptions of waste, which indicated that most participants perceived waste as disgusting yet possessing some value. The latter pattern contradicted our perceived-value assumption, suggesting removing perceived value from the model in subsequent work.

4.3 Pilot 3

Purpose and design: Given the inconclusive confirmation of the main effect, Pilot 3 focused explicitly on main-effect detection while minimizing textual influence. We recruited N = 50 participants, reused the plastic and food stimulus pairs, and added a metal-waste pair. The text was reduced to a minimal prompt asking participants to consider recycling and purchasing recycled products.

Pre-stimulus checks: Before exposure, we administered an SD (semantic differential) scale to reconfirm initial perceptions of waste. Replicating Pilot 2, most participants rated waste as disgusting (vs. pleasant), with value (vs. without value), ugly (vs. beautiful), and bad (vs. good). These checks established a priori inconsistency between participants' negative baseline perceptions and the aestheticized presentation of waste in artworks (Figure 4).

Results: Overall RI and PI decreased relative to Pilot 2, consistent with the weakened persuasive text. Food waste: RI was significantly higher for artworks than for

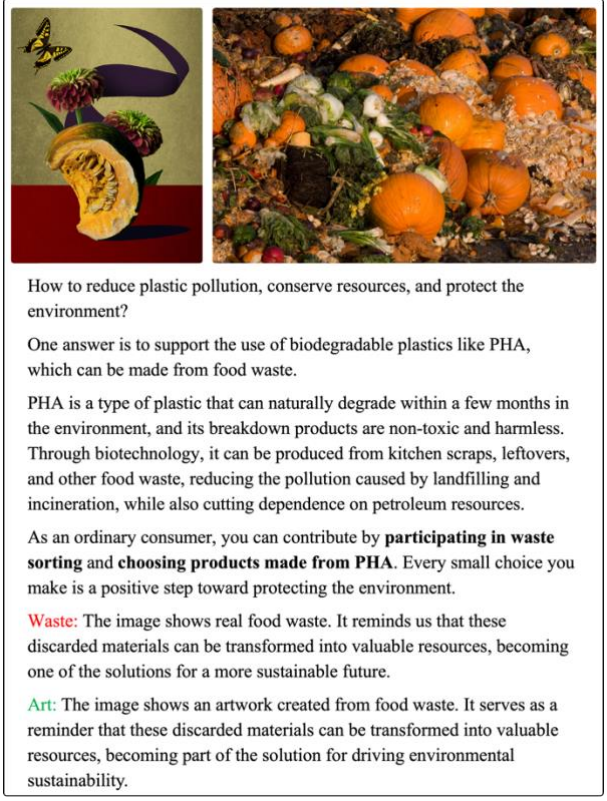

Figure 3 stimuli used in pilot 2 [15, 16]

real waste; however, PI in this group was higher for real waste. Plastic and metal: Both RI and PI were higher for real waste than for artworks.

Interpretation: The effectiveness of aesthetic transformation appears waste-type dependent and may not reliably increase PI (Table 3).

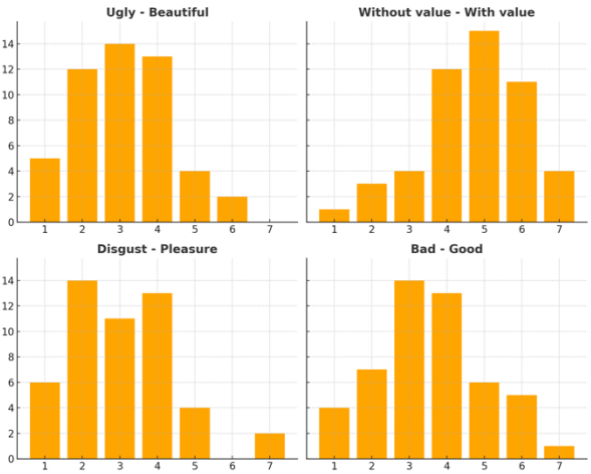

Figure 4. The initial perception of waste in pilot 3

Table 2 Results of main effect tests

		Art	Waste	p-value
Pilot 1	RI	5.65	5.75	(0.77)
	PI	5.37	5.56	(0.55)
Pilot 2	RI	6.02	6.04	(0.91)
	PI	5.78	5.80	(0.94)
Pilot 3	RI	5.87	5.69	(0.50)
	PI	5.38	5.67	(0.19)
Pilot 3 (food waste)	RI	6.41	5.37	**(0.02)***
	PI	5.44	5.52	(0.83)

4.4 Post-Pilot Exploratory Responses (Pilot 3)

After Pilot 3, participants answered two open-ended questions in Chinese:

1) Can trash art contribute to solving waste-related problems? Why? (Meaning)

2) After seeing trash art, what would you like to do to help solve waste-related problems? (Actions)

Coding and summary indicated that viewing trash art increased willingness to recycle, but did not translate into stronger purchase intentions for recycled products. Two additional behavior tendencies emerged: (a) interest in participating in the creation of trash art and (b) willingness to share related information (Table 3).

Table 3 Summarize of exploratory responses

	Contents	Freq.
Meaning	Make the possibility of recycling/circular use visible	22
	Value reappraisal —"waste → resource/treasure"	12
	Raise environmental awareness and sense of responsibility	9
	Reframe waste as a resource, highlight environmental benefits	9
	Breaks the "useless/dirty" stereotype	4
Actions	Participate in and cooperate with recycling programs	18
	Diligent waste sorting	17
	Re-use/DIY or create recycled art	17
	Share with others (recycling & environmental awareness)	9
	Purchase recycled art, or recycled/biodegradable products	5

References

[1] Rozin, P. (2015). Disgust, Psychology of. In J. D. Wright (Ed.), International Encyclopedia of the Social & Behavioral Sciences (Second Edition) (pp. 546–549). Elsevier. https://doi.org/10.1016/B978-0-08-097086-8.26020-0

[2] Hodge, R. W., Siegel, P. M., & Rossi, P. H. (1964). Occupational prestige in the united states, 1925-63. American Journal of Sociology, 70(3), 286–302. https://doi.org/10.1086/223840

[3] Ozbay, Y., Stamkou, E., & Oosterwijk, S. (2025). Art promotes exploration of negative content. Proceedings of the National Academy of Sciences, 122(5), e2412406122. https://doi.org/10.1073/pnas.2412406122

[4] Mierle Laderman Ukeles, Touch Sanitation Performance: "Handshake and Thanking Ritual" with Sanitation Workers of New York City Department of Sanitation, 1979-1980. © Mierle Laderman Ukeles.

Courtesy the artist and Ronald Feldman Gallery, New York

[5] Meng, M. D., & Leary, R. B. (2021). It might be ethical, but I won't buy it: Perceived contamination of, and disgust towards, clothing made from recycled plastic bottles. Psychology & Marketing, 38(2), 298–312. https://doi.org/10.1002/mar.21323

[6] Festinger, L. (1957). A theory of cognitive dissonance (pp. xi, 291). Stanford University Press.

[7] Mehrabian, A., & Russell, J. A. (1974). An approach to environmental psychology (pp. xii, 266). The MIT Press.

[8] Vaidis, D. C., & Bran, A. (2019). Respectable Challenges to Respectable Theory: Cognitive Dissonance Theory Requires Conceptualization Clarification and Operational Tools. Frontiers in Psychology, 10. https://doi.org/10.3389/fpsyg.2019.01189

[9] Explorers. (n.d.). SAYAKA GANZ. Retrieved August 5, 2025, from https://sayakaganz.com/plastics/explorers

[10] Guglielmi, G. (2017, July 19). In the next 30 years, we'll make four times more plastic waste than we ever have. https://www.science.org/content/article/next-30-years-we-ll-make-four-times-more-plastic-waste-we-ever-have

[11] Winterich, K. P., Nenkov, G. Y., & Gonzales, G. E. (2019). Knowing What It Makes: How Product Transformation Salience Increases Recycling. Journal of Marketing, 83(4), 21–37. https://doi.org/10.1177/0022242919842167

[12] Yadav, R., & Pathak, G. S. (2017). Determinants of Consumers' Green Purchase Behavior in a Developing Nation: Applying and Extending the Theory of Planned Behavior. Ecological Economics, 134, 114–122. https://doi.org/10.1016/j.ecolecon.2016.12.019

[13] Olatunji, B. O., Williams, N. L., Tolin, D. F., Abramowitz, J. S., Sawchuk, C. N., Lohr, J. M., & Elwood, L. S. (2007). The Disgust Scale: Item analysis, factor structure, and suggestions for refinement. Psychological Assessment, 19(3), 281–297. https://doi.org/10.1037/1040-3590.19.3.281

[14] Verma, S., Yadav, R., De Souja Andrade, H., & Yadav, S. K. (2025). Understanding household hesitancy: Analysis Of E-waste recycling application adoption among indian recyclers. Cleaner Waste Systems, 11, 100265. https://doi.org/10.1016/j.clwas.2025.100265

[15] MASUDA S. (n.d.). HANAFUDA SHOUZOKU. SHINYA MASUDA / 増田伸也 -PHOTOGRAPHY-. Retrieved May 25, 2025, from http://www.shinyamasuda.com/works/hanafudashouzoku/

[16] Facebook. (2024). Retrieved September 16, 2025, from https://www.facebook.com/photo?fbid=943138494512234&set=a.236040348555389

STUDY ON ATMOSPHERIC CO_2 NEUTRALIZATION OF HIGH-PH LEACHATE AT OFFSHORE DISPOSAL SITES

Kentaro Miyawaki[1], Riho IIzuka[1], Futa Moritani[1], Yoshiki Sato[2]
1 Department of Interdisciplinary Science and Engineering, Meisei University, 2-1-1 Hodokubo, Hino-city, Tokyo, Japan
2 Japan Waste Research Foundation

INTRODUCTION

Within Japan, there are 23 offshore landfills for municipal solid waste and 39 offshore landfills for industrial waste (some also accepting general waste) as of 2023. Offshore landfills generally have relatively large landfill capacities. Offshore landfills are isolated from the open sea by a combination of impermeable revetments and a bottom clay layer. The retained water inside is treated before being discharged into the open sea. The primary landfill material for municipal solid waste is incinerator ash, which contains a large quantity of alkaline substances. Industrial waste materials such as mineral residues, incinerator ash, and fly ash may also contain alkaline substances. The pH of the retained water (leachate) from these offshore landfills often exceeds the upper limit of the discharge standard (pH 9). In some cases, the pH of the retained water reaches 11 or higher. The pH of the effluent from such disposal sites does not reach the closure standard over the long term. The need for long-term continuous water treatment poses challenges, including increased environmental impact from electricity and chemical usage, as well as rising water treatment costs.

Indeed, many facilities continuously treat residual seawater (inner ponds, control reservoirs, effluent outlet in the future) over extended periods, and the authors are conducting ongoing water quality surveys at these sites. This study reports part of preliminary experiments concerning pH reduction through carbonate neutralization, based on the concept of absorbing atmospheric carbon dioxide from the surface of inner ponds (control reservoirs).

Using a pond simulation tank (acrylic water tank), we varied surface area, volume, and retention time (capacity/daily inflow) while measuring water quality parameters such as pH. We also attempted to calculate approximate values for the carbon dioxide absorption flux using the measurement results and a simplified calculation model.

METHOD

Experimental Apparatus:

An acrylic water tank (sealable type) was used as a pond simulation tank. A virtual inner pond was assumed (surface area 1500m², depth 2m, volume 3000m³, inflow volume 300m³/day, outflow volume 300m³/day, retention time: 10 days, $A/V \times \Delta T = 5$). $A/V \times \Delta T$ was also set incrementally to progressively reduce the area and volume. The experimental apparatus consisted of an acrylic tank, a pump, and bottles for collecting inflow and outflow water samples. The experimental apparatus is shown in Figure 1. A photograph of the apparatus is shown in Photo 1. The water surface was covered with polystyrene foam to prevent contact with the atmosphere, and the opening size was adjustable.

Simulated Pond Water:

Artificial seawater was diluted 4-fold (Artificial Seawater: Marine Art SF-1). The tank was filled with 5L or 10L of this solution (varying by test condition).

Simulated Retained Water:

The 4-fold diluted artificial seawater solution was adjusted to pH 11 using calcium hydroxide $Ca(OH)_2$.

Test Conditions:

Test conditions are shown in Table 1. Tests were conducted with $A/V \times \Delta T = 5$, 2.5, and 1.25.

Tests were also conducted with atmospheric contact (normal) and without atmospheric contact (control).

Water Quality Measurement Items:

pH, EC (electrical conductivity), and ORP (oxidation-reduction potential) were measured every 24 hours.

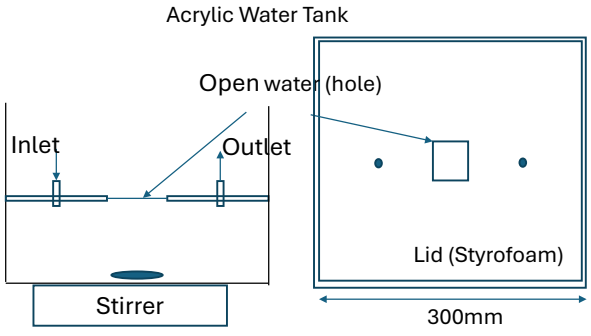

Figure 1 Experiment Apparatus (Water tank)

Photo 1 Experiment Apparatus (Water tank)

Table 1

Condition	No.1	No.2	No.3
Volume (m^3)	0.01	0.01	0.005
Surface area (m^2)	0.005	0.005	0.0025
Retensiton time (day)	10	5	5
Retain water inlet (m^3/day)	0.001	0.002	0.002
A/V× ΔT	5	2.5	1.25

RESULTS AND DISCUSSION

Experiment results

Figure 2 shows pH changes in the pond simulation tank. Under the condition where artificial seawater (adjusted to pH 11 with $Ca(OH)_2$) was inflowed relative to artificial seawater (1/4 concentration), the initial pH of the artificial seawater was around pH 7.5, as it was in equilibrium with atmospheric CO_2. Under both conditions, the pH gradually increased due to the inflow of pH 11 artificial seawater. At A/V×ΔT=5, the pH reached approximately 7.6 by day 11 (the initial pH rise followed by a drop was attributed to potential equipment issues during the inflow and mixing of the pH 11 artificial seawater). At A/V×ΔT=2.5, the pH reached 9.5 by day 3. Furthermore, at A/V×ΔT=1.25, the pH showed 10.5 by day 6.

Figure 3 shows Difference of pH changes atmospheric contact and without conditions. On A/V×ΔT=2.5 condition, compared to non-contact atmospheric conditions, under atmospheric contact conditions, CO_2 absorption caused the pH inside the tank to be approximately 1 unit lower at equilibrium.

Figure 4 shows the changes in EC (electrical conductivity). The tank contained artificial seawater, and although the pH 11 artificial seawater contains a high amount of Ca, no significant impact was observed, confirming the experimental system was functioning properly. Notably, under the A/V×ΔT=5 condition, when the pH rose sharply initially, the EC also showed a similar trend, confirming the possibility of an issue with the inflow operation.

Figure 5 shows the change in ORP (Oxidation-Reduction Potential). Initially, it decreased due to the influence of the inflow water ORP (47 mV), but it generally stabilized at atmospheric equilibrium. It was inferred that the smaller the A/V×ΔT, the lower the steady-state value tended to be.

Figure 6 shows the relationship between A/V×ΔT and pH, which is at atmospheric equilibrium. From the approximate straight line, it was inferred that A/V×ΔT ≈ 3.59 corresponds to a pH of 9 in the tank. The pH did not stabilize under the A/V×ΔT=5 condition, and the data reliability is low. By improving the precision of this test system, it can be said that the general relationship between area, volume, retention time, and pH can be determined.

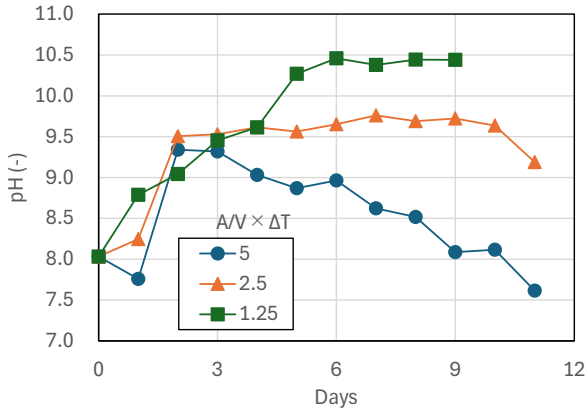

Figure 2 pH changes of effluent

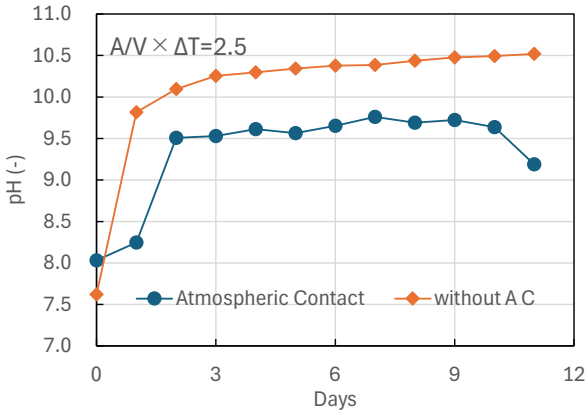

Figure 3 Difference of pH changes atmospheric contact and without conditions

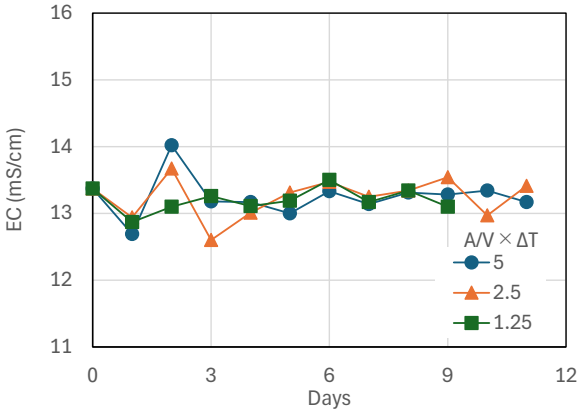

Figure 4 EC changes of the effluent

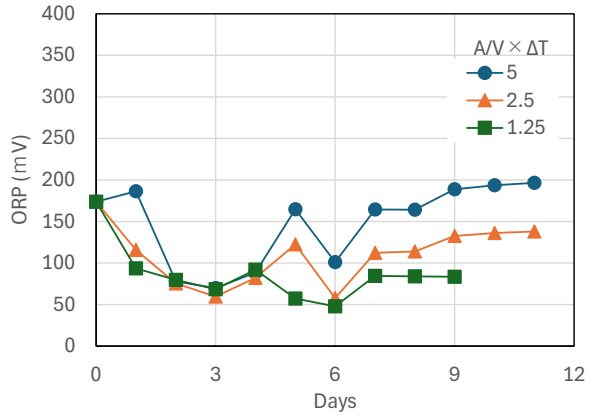

Figure 5 ORP changes of the effluent

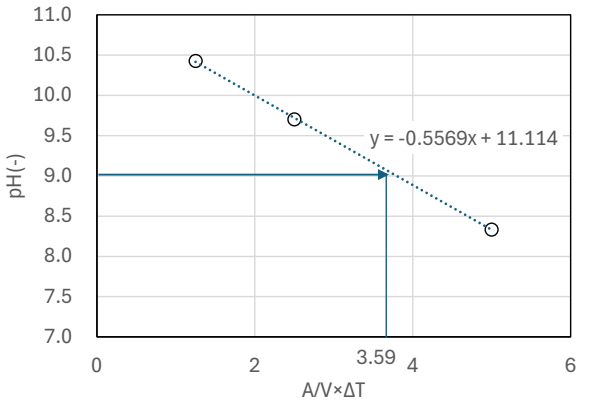

Figure 6 A/V×ΔT vs Equilibrium pH

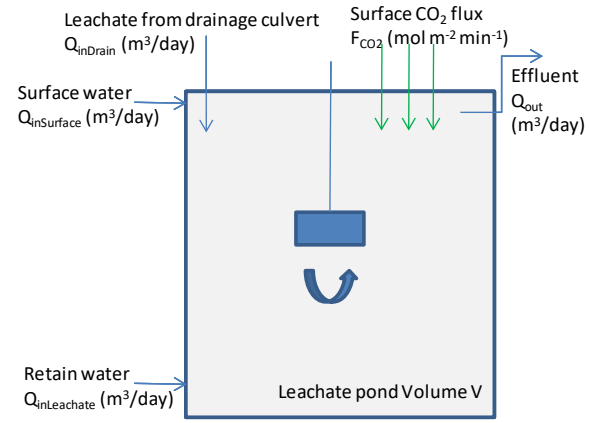

Figure 7 Simplified model overview

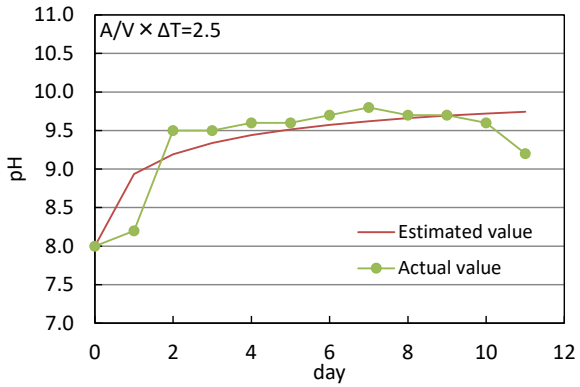

Figure 8 Simplified Model Calculation Results

Simplified Model

Simulated test conditions were set for simplified model calculations. Figure 7 shows the model overview, while Figure 8 displays pH changes between measured and calculated values. Fluxes were set to achieve pH values close to experimental data. In the simplified model, water discharged from the collection culvert is termed "leachate," while water inflowing from the pond sides and bottom is termed "retained water." The required CO_2 absorption flux in the simplified model is 6.94×10^{-5} mol/m²·min (A/V×ΔT=5), 1.33×10^{-4} mol/m²·min (A/V×ΔT=2.5) and 1.70×10^{-4} mol/m²·min (A/V×ΔT=1.25). The A/V×ΔT=5 condition showed a value close to the maximum observed in the real offshore landfill (Endo et al.). Under A/V×ΔT=2.5 and 1.25 conditions, the flux was one order of magnitude higher, resulting in a discrepancy between the calculated and measured values. Furthermore, the surface CO_2 absorption flux under each condition was of the same order of magnitude as last year, confirming a certain degree of reproducibility.

The finding that the equilibrium pH in the pond was higher and the flux was largest under the A/V×ΔT=1.25 condition was consistent with previous findings by Watanabe et al..

SUMMARY

Preliminary testing of this experimental apparatus estimated the A/V×ΔT condition meeting discharge standards to be 3.59. The test apparatus demonstrated the potential to set conditions for neutralization via carbon dioxide absorption.

Examination of carbon dioxide absorption flux at the pond surface using a simplified model yielded a value of approximately 6.9×10^{-5} mol/m²·min at A/V×ΔT=5.

Under small A/V×ΔT= conditions, it was confirmed that the flux increases due to the high pH within the apparatus.

Future work will focus on verifying the accuracy and reproducibility of the test apparatus, as well as confirming the reliability of the indicators through tests under the same A/V×ΔT= conditions but with different areas and volumes.

ACKNOWLEDGMENTS

We express our gratitude to the members of the Environmental Conservation Measures Investigation Committee at the Osaka Bay Regional Offshore Environment Improvement Center for their advice on experimental conditions and testing.

REFERENCES

Endo et al. (2018), Survey for carbon dioxide absorbed flux of seashore landfill pond, The 29th Annual Conference of Japan Society of Material Cycles and Waste Management (In Japanese), https://www.jstage.jst.go.jp/article/jsmcwm/29/0/29_451/_article/-char/en

Miyawaki et al. (2028), pH Decrease at Pond of offshore landfill by atmospheric carbon dioxide, The 29th Annual Conference of Japan Society of Material Cycles and Waste Management (In Japanese), https://www.jstage.jst.go.jp/article/jsmcwm/29/0/29_463/_article/-char/en

Watanabe et al. (2014), Rate of CO_2 absorption to aqueous alkali suspension, The 25th Annual Conference of Japan Society of Material Cycles and Waste Management (In Japanese), https://www.jstage.jst.go.jp/article/jsmcwm/25/0/25_359/_article/-char/en

SPECTRAL DISCRIMINATION OF LANDFILL SITES IN AFRICA: AN ANALYSIS USING HISUI HYPERSPECTRAL DATA

Leeme A. BARUTI[1], Yasuhiro SUGISAKI[2], Hirofumi NAKAYAMA[3] and Takayuki SHIMAOKA[4]

[1]Dept. of Urban and Environmental Engineering, Kyushu University 744 Motooka, Nishi-ku, Fukuoka 819-0395, Japan

[2]Dept. of Urban and Environmental Engineering, Kyushu University 744 Motooka, Nishi-ku, Fukuoka 819-0395, Japan

[3]Dept. of Urban and Environmental Engineering, Kyushu University 744 Motooka, Nishi-ku, Fukuoka 819-0395, Japan

[4]Kyushu Environmental Management Association 1-10-1 Rosindai, Higashi-ku, Fukuoka 813-0004, Japan

ABSTRACT

Hyperspectral imaging offers the potential to isolate distinctive material mixtures that characterise landfill surfaces, yet the spectral heterogeneity of African landfills remains largely underexplored. We analyse eight (8) landfill sites across seven (7) African countries using HISUI (20m) surface reflectance corrected with a Py6S-based pipeline. We quantify pairwise class contrast by (i) directional differences (sign-aware), (ii) signed area A_k within the spectral segments and (iii) spectral angle mapper (SAM) globally and per segment. Cross-site medians and dispersion summarise consistency. Finally, we rank separability relative to landfill_active (most to least) using mean segment SAM and identify the best segment to separate the three least-separable classes at each site. We find that across sites, water and vegetation were consistently the most separable in shape, whereas landfill_disposal and urban were the closest to landfill_active; soil was intermediate but variable. The best discriminating window for the least-separable classes was typically the VNIR Segment 1 (≈405–895 nm) for landfill_disposal and soil, and often the SWIR Segment 4 (≈1963–2475 nm) for urban. Brightness A_k emphasized strong overall contrast with water, while SAM isolated shape differences relevant to material composition. These patterns constitute practical spectral "fingerprints" and segment priorities to guide supervised classification and target detection in continental landfill mapping.

Key Words: *landfill, dumpsite, hyperspectral, satellite imagery, remote sensing, HISUI*

INTRODUCTION

Rapid urbanisation and changing consumption patterns are driving the expansion of landfills and open dumps across the African continent. More than 90% of African countries use landfills and or dumpsites as the only viable option for waste disposal [1]. These sites concentrate a complex mixture of materials such as plastics, textiles, food waste, soil, ash from frequent burning, and leachate whose spatial and temporal variability complicate monitoring. One of the major challenges of the waste sector in Africa is poor management of landfills as well as the emergence of informal dumpsites [2]. The environmental stakes are substantial: uncontrolled combustion degrades air quality, exposed waste and fires alter soil properties, and leachate threatens surface and groundwater [3]. An international team commissioned by the United Nations (UN) highlighted the urgent need for improved availability and reliability of waste and resource data [1]. Municipal authorities need recurrent, scalable information on where waste is actively exposed, where disposal areas are covered and how surrounding land covers respond. Traditional methods such as field surveys are time consuming and labour-intensive, posing challenges for large-scale landfill detection and monitoring [4]. Satellite remote sensing offers a practical option to meet these information needs over national and potentially continental extends, yet reliably distinguishing landfill surfaces from common neighbours such as bare land, urban fabric, vegetation and water bodies remains challenging.

Most landfill investigations [6,7,8,9] studies have relied on multispectral sensors (e.g. Sentinel-2 and Landsat) and image classification methods. While these data provide frequent coverage, their broad bands dilute narrow absorption features that can potentially be

diagnostic material residues, and they entangle brightness and shape information. Spectral signatures, defined as the characteristic pattern of an object's spectral reflectance across different wavelengths, form the basis for classifying remotely sensed imagery by providing critical qualitative and quantitative data. Crucially, these signatures are defined by both their specific spectral values and the overall shape of their spectral curve. However, most classification techniques that use spectral signatures have placed a disproportionate emphasis on spectral values, neglecting the informative nature of the curve's shape [10]. Hyperspectral imaging, sampling from visible to near infrared (VNIR) and shortwave infrared (SWIR) at fine spectral resolution offers an opportunity to analyse spectral curve shapes to a greater degree for feature resolution.

This study assesses the discriminability of landfill surfaces using spaceborne hyperspectral imagery from the Hyperspectral Imager Suite (HISUI) abroad the International Space Station (ISS). HISUI provides contiguous VNIR-SWIR coverage at 20m ground sampling distance and twenty-kilometre (20km) swath as shown in Table 1, offering a unique balance of spectral richness and spatial detail that can be tested on complex, heterogenous scenes. We assemble eight (8) HISUI scenes corresponding to 8 landfill sites spanning seven (7) African countries and implement a consistent processing chain that includes (i) atmospheric correction; (ii) ROI extraction of per-class mean spectra for *landfill_active, landfill_disposal, urban, vegetation, soil, and water;* (iii) and spectral analysis.

Table 1. HISUI sensor specifications

Launch date	6 December 2019
Spatial resolution	20m x 20m
Swath	20km x 30km
Bands	185 VNIR: 58 SWIR: 127
Spectral range	400 nm – 2500nm VNIR: 400 – 970nm SWIR: 900 – 2500nm
Spectral resolution	VNIR: 10nm SWIR: 12.5nm

Our objectives are therefore threefold. First, we characterise the spectral signatures of landfill_active relative to common neighbouring classes at each site, identifying specific wavelengths and segments with large directional (positive or negative) differences, large signed areas or high segment SAM. Second, we evaluate the consistency of those discriminative regions across sites using cross-site medians and dispersion. Third, we synthesize a practical 'fingerprint' that pairs visual summaries with compact tables of segment metrics suitable for downstream classification or target-detection models. The overall premise is that if HISUI consistently resolves VNIR and SWIR features linked to distinct materials (such as plastics, ash, organics) over multiple landfill sites, then those features can serve as reliable priors for automated landfill mapping at scale.

DATA AND METHODS

Study Sites and imagery

To obtain landfill and dumpsites in Africa, a desktop search was carried out. Firstly, names of African countries were searched and listed out. Then beginning from south to north searches of "landfill" and "dumpsite" in each country were carried out on Google Search as well as Bing Search. The names and or addresses of the sites where then searched for on Google Maps and a visual inspection was carried out. The inclusion criteria was:

- Presence of open dump or unmanaged landfill activities.
- Availability of HISUI L1G overpasses with minimal (< 5%) cloud cover.
- Access to high-resolution reference data (Google Earth imagery, Sentinel-2) for validation.

This yielded 8 sites across 7 different countries as shown in figure 1.

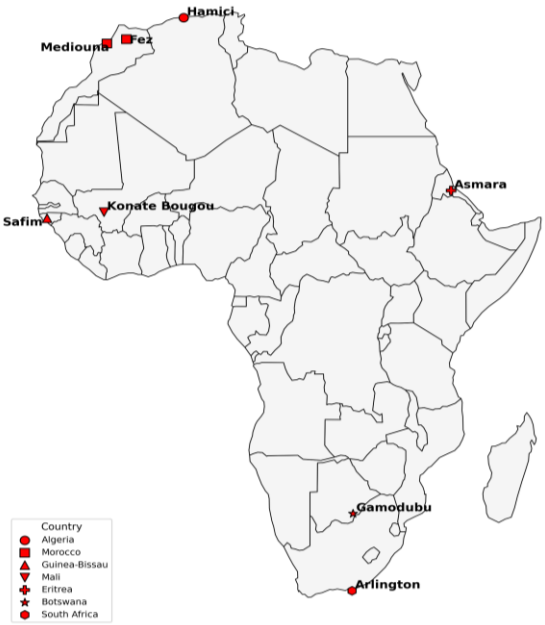

Fig. 1. Location of study sites (n=8) across Africa

Subsequently, 8 HISUI scenes that include the study sites were obtained. The data was provided as Level 1G (L1G) product, which is geometrically corrected and orthorectified top-of-atmosphere spectral radiance product [11]. An example of one of the scenes from Botswana with the landfill site indicated by red polygon is shown in figure 2. Table 2 shows the scene IDs and date of acquisition of the data.

Table 2. HISUI scenes for the 8 sites

Country	**Site Location (Name)**	**Date**	**HISUI Scene**
Algeria	Hamici	12/06/2021	HSHL1G_N366E0029_20210612091401_20231230220328
Morocco	Fez	01/05/2022	HSHL1G_N339W0049_20220501092748_20230914220642
Morocco	Mediouna	10/04/2022	HSHL1G_N335W0076_20220410101018_20230913180858
Guinea - Bissau	Safim	04/10/2022	HSHL1G_N119W0157_20221004110918_20230916012623
Mali	Konate Bougou	02/01/2021	HSHL1G_N126W0078_20210102103144_20221013224340
Eritrea	Asmara	07/04/2023	HSHL1G_N153E0390_20230407063235_20231211161555
Botswana	Gamodubu	26/09/2022	HSHL1G_S246E0257_20220926093250_20230912175523
South Africa	Arlington	08/09/2021	HSHL1G_S340E0255_20210908084126_20240109103134

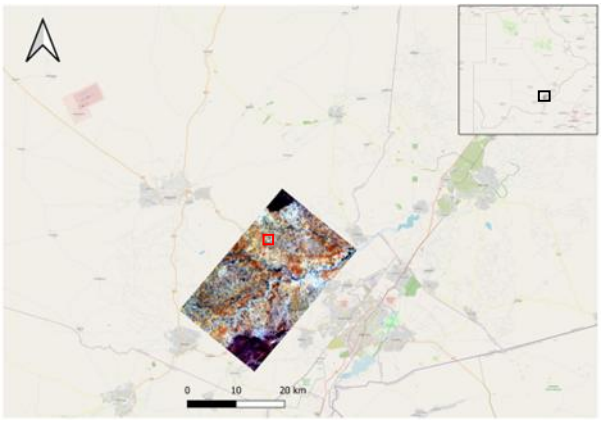

Fig. 2. HISUI scene RGB (B27,B17,B7) showing location of the Gamodubu Landfill site in Botswana

Atmospheric Correction

All scenes were converted to surface reflectance using a Py6S-based workflow [12]. Inputs included HISUI metadata and atmospheric parameters (aerosol optical depth, ozone, and water vapour) and digital elevation model estimated from Google Earth Engine. Py6S is a python based radiative transfer model using 6S (Second Simulation of a Satellite Signal in the Solar Spectrum) p_i C_i L_i.

Concept: converts at-sensor radiance *(L)* to surface reflectance *(p)* for each band using correction factor *(C_i):*

$$p_i = C_i \, . \, L_i \qquad (1)$$

p_i = Surface reflectance (TOA) for band *i* (dimensionless)

L_i = At-sensor radiance for band *i* (W/m^2/sr/µm)

C_i = Correction factor for band i (sr.µm/W), calculated:

$$C_i = p_{6s}/L_{6S} \qquad (2)$$

p_{6s} *and* L_{6S} are the 6S-simulated reflectance and radiance for band *i's* wavelength and geometry.

So, for wavelength λ and scene geometry (solar/view angles, atmosphere), the corrected reflectance becomes:

$$R_{(x,y,\lambda)} = D_{(x,y,\lambda)} \, . \, (p_{6s}/L_{6S}) \qquad (3)$$

$D_{(x,y,\lambda)}$ = Digital number (DN) or radiance at pixel (x, y) and wavelength λ

$R_{(x,y,\lambda)}$ = Corrected surface reflectance

ROI definition and spectral extraction

For each site, vector regions of interest (ROIs) were digitised in ArcGIS Pro to represent from figure 3:

- landfill_active – a part of the landfill disposal area where waste is exposed and dumping/disposal is currently occurring (black circle)

- landfill_disposal – a part of the landfill site that is used for dumping/disposing waste (purple circle)
- urban – buildings and pavements (red polygon)
- vegetation – trees, plants, shrubs and related vegetal (green circle)
- soil – an area of bare land (orange circle)
- water – any body of water (not shown)

Using Rasterio + GeoPandas (python), we extracted the per-ROI mean spectrum (and basic dispersion) from the surface reflectance cube. These per-class spectra form the basis of all subsequent analysis.

a

b

Fig. 3. Showing (a) HISUI (RGB) ROIs and (b) Google Earth Pro of Algeria around Hamici site

To reduce high-frequency noise and isolate diagnostic shape features, we applied:

- Smoothing – Savtzky-Golay (window = 9, poly =2) with a moving-average fallback used where needed
- Masking – HISUI is consists of two sensors, VNIR and SWIR and the two sensors overlap between 901 – 975nm. As a result, we masked out this region due to its potential instability. Furthermore, known water-absorbing regions (1340 – 1440, 1810 – 1960nm) were masked out as indicated in figure 4.
- Shape normalisation – when analysing shape, each spectrum r was L2-normalised ($\hat{r} = r/\|r\|_2$) to emphasize curve from albedo.

We use the term brightness (raw reflectance) and shape (L2-normalised) to distinguish analyses performed in each space.

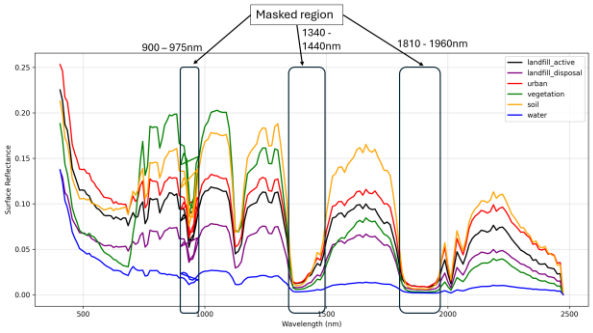

Fig. 4. Spectral reflectance curve showing masked regions.

Directional pairwise comparison

For any ordered pair of classes (A, B), we compute the directional difference:

$$\Delta R(\lambda) = R_A(\lambda) - R_B(\lambda) \qquad (4)$$

Directional difference ΔR clarifies whether A is brighter than B at a given wavelength. Overall, all valid (unmasked) bands we report global, NaN-safe metrics:
Mean ΔR, MAD, RMSE on ΔR.
Spectral Angle Mapper (SAM) in degrees, measuring shape dissimilarity; for brightness analyses SAM is reported as NaN by design.

Segmenting the spectrum

To localise separability and avoid artefacts across masked gaps, we partition the spectrum into contiguous unmasked segments bounded by the sensor-overlap and water windows (S1 – S4 in our configuration). For each segment k we derive:
Extrema: maximum positive/negative ΔR and their wavelengths.
Signed area:

$$A_k = \int_{\lambda \epsilon k} \Delta R(\lambda) d\lambda \qquad (5)$$

(implemented by a NaN-safe trapezoid rule). Ak qualifies net dominance of A over B within the segment (positive: A > B; negative: A < B).
Segment-level SAM (SAM_k) computed only over the bands in segment k (requires ≥ 2 finite points). SAM_k captures local shape mismatch even when positive/negative lobes of ΔR cancel in area.

Cross-site aggregation

To test robustness across countries, we aggregate both

curves and segment metrics:
Common grid: each site's spectra are interpolated to a shared wavelength grid
Class curves: we compute cross-site median curves per class with interquartile range (IQR); we also provide median $\Delta R(\lambda)$ for *landfill_active* versus other comparators.
Metrics: for each comparator x segment, we summarise Ak and SAMk with mediam IQR, mean, std, and n. We rank comparators by the median of $\sum_k |A_k|$ across sites to indicate which classes are on average, most separable from *landfill_active* and where.

RESULTS AND DISCUSSION

Spectral Characteristics of landfill (per site)

Across the eight (8) study sites (Hamici, Fez, Mediouna, Safim, Konate Bougou, Asmara, Gamodubu, Arlington) overlaid VNIR-SWIR curves (figure 5) reveal a repeatable "landfill_active" shape despite local heterogeneity.

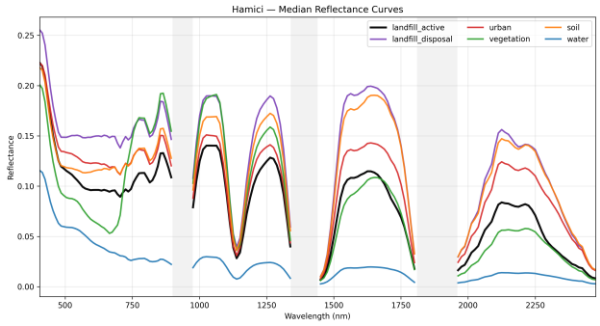

(a)

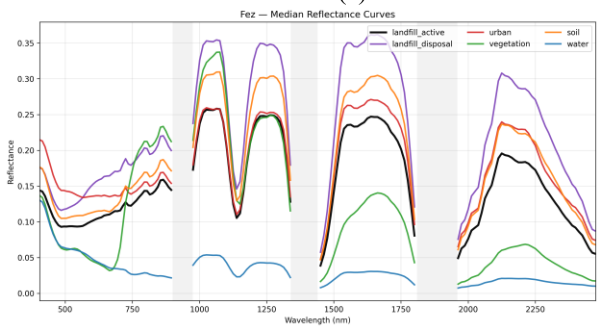

(b)

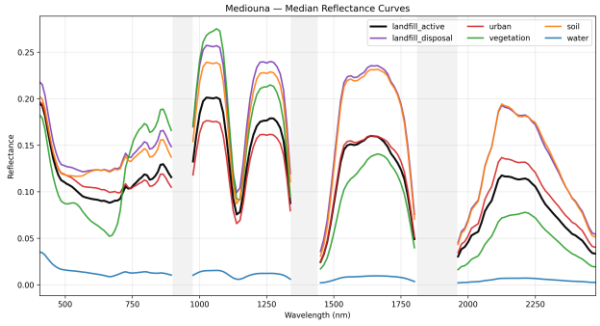

(c)

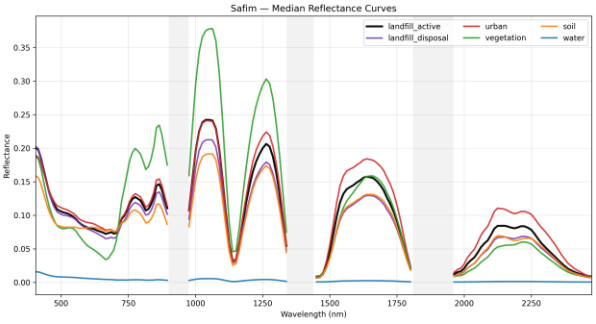

(d)

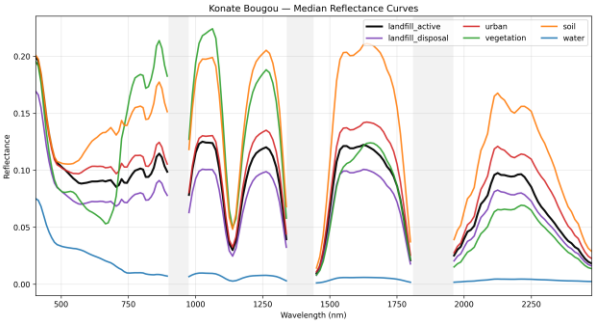

(e)

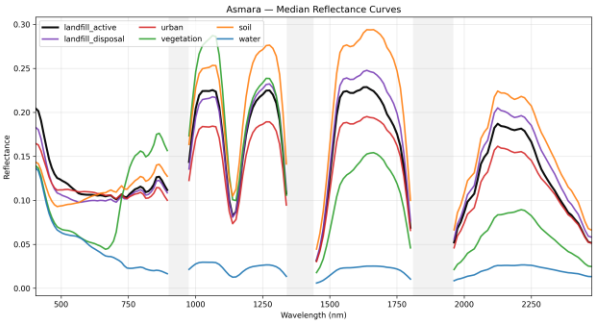

(f)

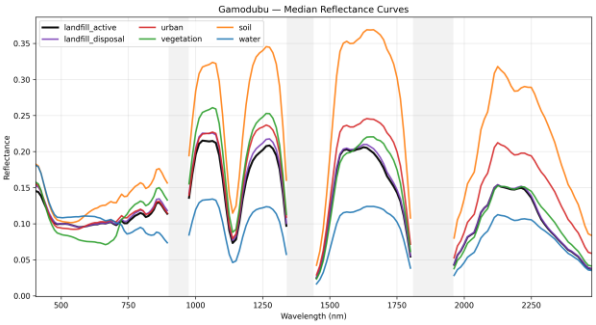

(g)

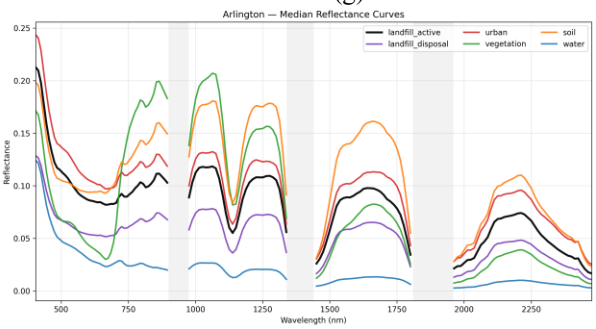

(h)

Fig. 5. Showing median reflectance curves for (a) Hamici, (b) Fez, (c) Mediouna, (d) Safim, (e) Konate Bougou, (f) Asmara, (g) Gamodubu, and (h) Arlington scenes.

Per-Site Separability of Land Cover Classes

The Spectral Angle Mapper (SAM) and brightness metrics ($\Sigma|A_k|$) demonstrate that water and vegetation are the most separable classes from landfill-active areas, while landfill-disposal sites are the most spectrally similar, as anticipated. Water was the most separable class, consistently ranking first or second in mean SAM across all sites (figure 6). This separability is driven by a combination of distinct spectral shape in the SWIR (Segment 4) and high brightness contrast. *Supporting Evidence:* High per-segment SAM values against water were observed in Segment 4 (SWIR) at sites like Safim (12.34°) and Konate Bougou (11.57°). Even at sites with lower mean SAM (e.g., Mediouna, 5.47°), separability was maintained by a high brightness contrast (179.54).

Vegetation was typically the second-most separable class, primarily due to its unique spectral shape in the SWIR region. Mean SAM values were consistently high (e.g., Arlington: 11.22°, Fez: 11.12°). This was confirmed by elevated Segment 4 SAM values when comparing landfill-active areas to vegetation (e.g., Fez: 6.43°, Hamici: 6.79°), indicating that the presence of plastics, ash, or organics alters the SWIR signature deterministically.

Soil & Urban classes showed more modest shape similarity (mean SAM: 1.32–5.01° for soil; 1.79–3.52° for urban). However, brightness remained a useful discriminator (e.g., soil $\Sigma|A_k|$_bright up to 154.60 at Gamodubu). Crucially, the signed area (A_k) in Segment 4 provided a consistent diagnostic rule: at Hamici, for instance, the landfill-active signature was consistently *below* that of soil (A_4 = -8.83) and urban (A_4 = -7.04) in the SWIR.

Landfill-Disposal sites, as expected, were the most spectrally similar to landfill-active areas, often ranking last in mean SAM (e.g., Gamodubu: 0.55°, Konate Bougou: 0.99°). The key to their discrimination lay not in the SWIR but in the VNIR (Segment 1), which was consistently the most effective segment for this challenging separation (e.g., Hamici: 6.55°, Mediouna: 4.23°). This suggests the VNIR slope and convexity of fresher, exposed waste is a critical diagnostic feature.

Cross-Site Consistency of Diagnostic Features

A key finding is the remarkable consistency in the rank-order of class separability across all eight geographically diverse sites (figure 6):

Water > Vegetation > Soil ≈ Urban > Landfill-Disposal

This hierarchy confirms the robustness of the spectral signature approach. Furthermore, specific spectral segments demonstrated generalizable utility:

- Segment 4 (SWIR: 2.0–2.5 µm): Most effective for separating water and vegetation.
- Segment 1 (VNIR: 0.40–0.90 µm): Most effective for distinguishing landfill-active from landfill-disposal.
- Segment 3 (SWIR: 1.45–1.8 µm): Provided complementary shape information for vegetation and water.

The direction of contrast, given by the signed area (A_k), adds a deterministic, rule-based layer to the analysis. For example, at Hamici in Segment 4, the landfill-active signature is consistently *below* soil and urban but *above* vegetation and water. This "who is above whom" relationship is a powerful feature for developing classification rules.

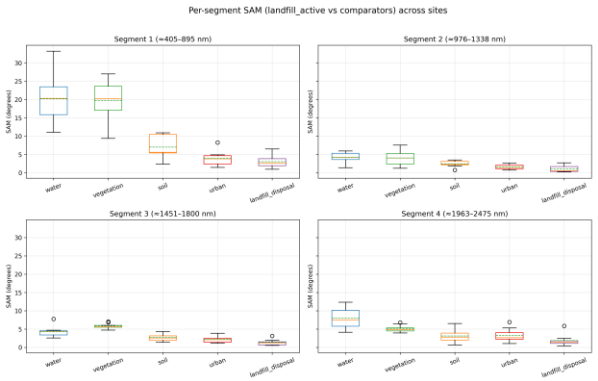

Fig. 6. Per-segment SAM boxplots across sites

The Integrated Spectral Fingerprint for Classification

We synthesise these findings into an integrated spectral fingerprint for landfill-active areas. This fingerprint combines three elements:

1. Spectral Curve Shape (figure 5): The overall profile, including characteristic features like water absorption gaps.
2. Per-Segment Metrics (Table S1; figure 6): The maxima, signed areas (A_k), and per-segment SAM values that quantify shape differences.
3. Global Similarity Metrics (figure 7): The mean SAM and brightness values.

This fingerprint directly informs a hierarchical classification strategy. For any given site, the most challenging spectral pairs can be addressed by targeting their "best segment":

- Example from Hamici: To separate the most confusable classes, use:
    - Segment 4 for Urban (SAM 6.91°, A_4

= -7.04)

- Segment 1 for Landfill-Disposal (SAM 6.55°, A_1 = +3.22)
- Segment 4 for Soil (SAM 6.52°, A_4 = -8.83)

This approach moves beyond relying on mean SAM alone, leveraging the full power of the spectral signature's shape and brightness across specific wavelength ranges to build a more robust and interpretable classification model.

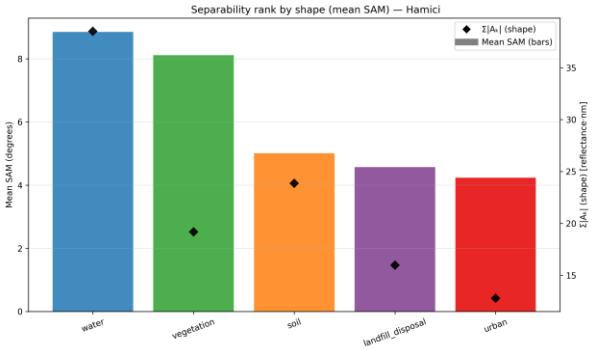

(a)

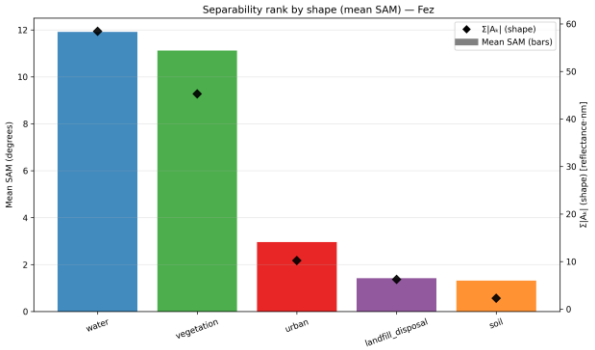

(b)

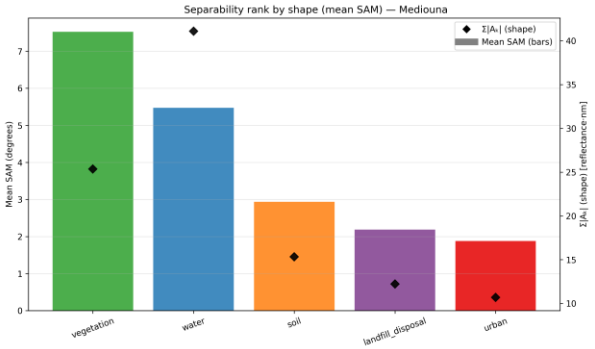

(c)

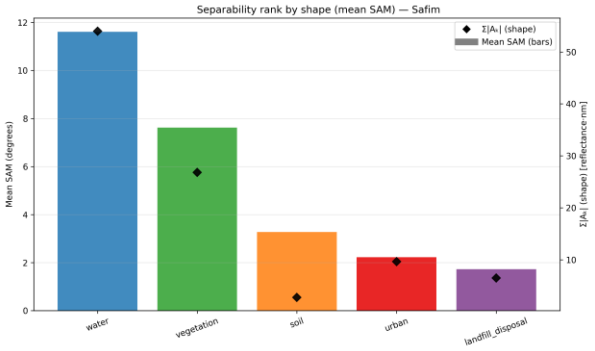

(d)

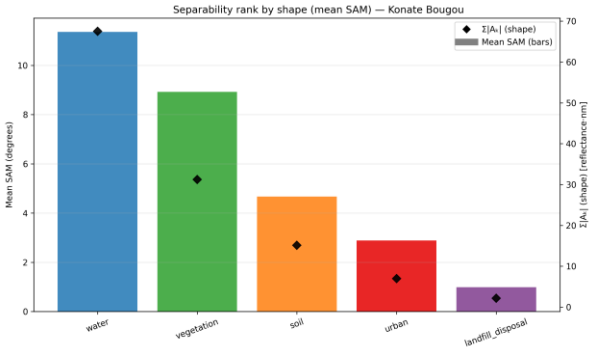

(e)

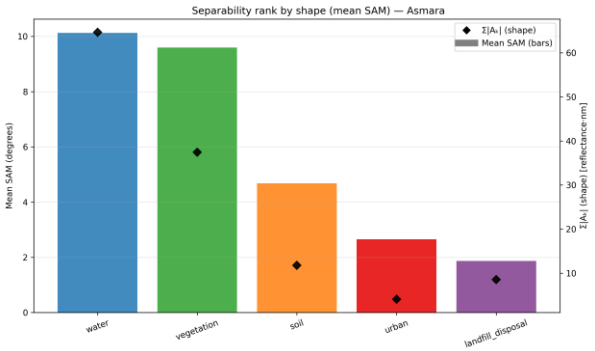

(f)

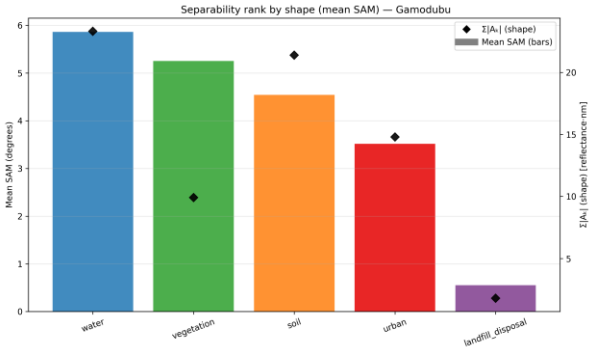

(g)

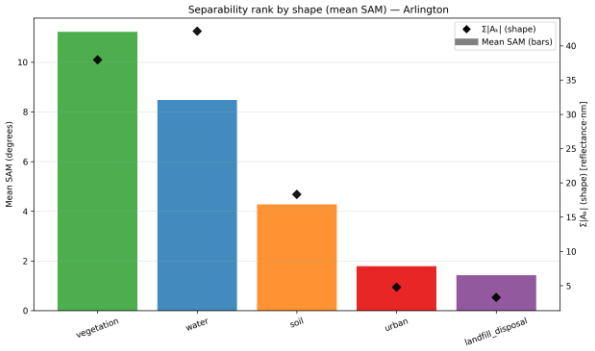

(h)

Fig. 7. Per-site separability ranks (bars = mean SAM; diamonds = $\Sigma|A_k|$_shape).

Conclusion and Outlook

This study demonstrates that spaceborne hyperspectral data from HISUI, coupled with a simple but interpretable set of curve-shape and brightness metrics, can reliably discriminate landfill-active surfaces from common neighbouring classes across diverse African sites. Using masked VNIR–SWIR spectra, L2 normalization (shape), signed area by segment (A_k), and Spectral Angle Mapper (SAM), we established a consistent separability hierarchy: water and vegetation are most separable, soil and urban are moderately separable, and landfill_disposal is the closest look-alike—in line with expectations about material overlap. Segment-wise analysis clarified *where and why* separation occurs. SWIR Segment 4 (≈2.0–2.5 µm) repeatedly carried high shape separability for water and vegetation, whereas Segment 1 (≈0.40–0.90 µm) was most informative for teasing apart landfill_active vs. landfill_disposal, reflecting differences in VNIR slope/convexity of fresher exposed waste. These patterns held across sites and were borne out by numeric summaries (e.g., per-class mean SAM and $\Sigma|A_k|$), providing both diagnostic rules (polarity and magnitude of A_k) and defensible thresholds (segment SAM) that are portable between locations.

Beyond per-site diagnostics, our cross-site aggregation showed that median spectra and segment metrics yield a *robust spectral fingerprint* for landfill-active surfaces. Practically, this translates into a simple recipe for analysts: (i) mask water bands, (ii) compute segment-level SAM and A_k versus candidate classes, (iii) apply rule-based tests using segment SAM (for separability) and A_k polarity (for direction of contrast), and (iv) prioritize Segment 4 when separating from vegetation/water and Segment 1 when separating from landfill_disposal. We also showed how to turn these diagnostics into ranked separability summaries per site and to surface the "best segment" for the three most confusable classes—outputs that are immediately usable for mapping decisions or for selecting features in supervised learning.

Limitations are clear. First, HISUI's spatial resolution (20 m) and ISS viewing geometry constrain detection of very small or heterogeneous patches; sub-pixel mixtures likely dilute class contrast. Second, although Py6S-based correction and QA masks were applied consistently, residual atmospheric and adjacency effects may vary among scenes. Third, ROIs represent site-specific waste states; operational mapping will face greater temporal and compositional variability than captured here. Finally, our analysis emphasized shape and directional differences without explicit material unmixing; some features (e.g., plastics vs. ash vs. soil coatings) may require higher-fidelity spectral libraries or meso-scale field spectra to fully disambiguate.

Outlook. Several immediate extensions follow:

1. Operational classifiers. Use the fingerprint as an interpretable feature set: per-segment SAM, A_k magnitude and sign, and a small number of segment maxima. A two-stage scheme is promising—first, coarse filtering (landfill vs. non-landfill) using Segment 4 shape + brightness, then fine discrimination of landfill_active vs. landfill_disposal emphasizing Segment 1 (and optionally textural cues from companion multispectral data).
2. Cross-sensor transfer. Map the most stable segments and polarity rules to EnMAP/PRISMA band passes and evaluate transferability; where needed, derive narrow-band indices approximating the discriminative shapes in Segment 4 and Segment 1.
3. Temporal robustness. Repeat the analysis across seasons or revisit dates to test the persistence of the fingerprint under moisture and operational changes (e.g., fresh tipping, covering, burning).
4. Mixture-aware modelling. Incorporate linear/nonlinear unmixing or constrained target detection to handle mixed pixels at the landfill fringe; the observed A_k polarity by segment can guide priors in these models.
5. Reference libraries and validation. Expand with in-situ spectra (plastics, burned residues, cover soils) to anchor feature interpretation and to calibrate thresholds; pair with independent map products or field audits for accuracy assessment.

In sum, our results establish a segment-aware, interpretable spectral fingerprint for landfill-active surfaces that is consistent across countries and readily operationalized. By combining median spectra (for context), per-segment SAM and A_k (for mechanism), and ranked separability summaries (for decisions), the approach provides both scientific insight and a practical

pathway toward scalable monitoring of waste sites with current and forthcoming hyperspectral missions.

REFERENCES

1. United Nations (2024). World population prospects 2024. Department of Economic and Social Affairs Population Division. Available at: https://population.un.org/wpp/ (Accessed: 01 November 2024).
2. Tomita, A., Cuadros, D. F., Burns, J. K., Tanser, F., & Slotow, R. (2020). Exposure to waste sites and their impact on health: A panel and geospatial analysis of nationally representative data from South Africa, 2008–2015. The Lancet Planetary Health, 4(6), e223-e234.
3. Aliu, I. R. (2021). Socio-Environmental, Residential and Health Effects of Waste Dumpsites in Igando-Alimoso area of Lagos, Nigeria. Journal of Applied Sciences and Environmental Management, 25(6), 977-984.
4. Yong, Q., Wu, H., Wang, J., Chen, R., Yu, B., Zuo, J., & Du, L. (2023). Automatic identification of illegal construction and demolition waste landfills: A computer vision approach. Waste Management, 172, 267-277.
5. Singh, A. (2019). Remote sensing and GIS applications for municipal waste management. Journal of environmental management, 243, 22-29.
6. Lucendo-Monedero, A. L., Jordá-Borrell, R., & Ruiz-Rodríguez, F. (2015). Predictive model for areas with illegal landfills using logistic regression. Journal of Environmental Planning and Management, 58(7), 1309-1326.
7. Quesada-Ruiz, L. C., Rodriguez-Galiano, V., & Jordá-Borrell, R. (2019). Characterization and mapping of illegal landfill potential occurrence in the Canary Islands. Waste Management, 85, 506-518.
8. Akinina, N. V., Akinin, M. V., Taganov, A. I., & Nikiforov, M. B. (2017, June). Methods of detection in satellite images of illegal dumps by using a method based on tree classifier. In 2017 6th Mediterranean Conference on Embedded Computing (MECO) (pp. 1-3). IEEE.
9. K. Themistocleous, C. Papoutsa, S. Michaelides, and D. Hadjimitsis, 'Investigating detection of floating plastic litter from space using sentinel-2 imagery', *Remote Sens (Basel)*, vol. 12, no. 16, Aug. 2020, doi: 10.3390/RS12162648.
10. Chen, Y., Wang, Q., Wang, Y., Duan, S. B., Xu, M., & Li, Z. L. (2016). A spectral signature shape-based algorithm for landsat image classification. *ISPRS International Journal of Geo-Information*, *5*(9), 154.
11. J-spacesystems, HISUI-Hyperspectral Imager Suite, Instruments, Product Description, hisui.go.jp/en/product/index
12. R. T. Wilson, 'Py6S: A Python interface to the 6S Radiative Transfer Model', 2012
13. Kotaridis, I., & Lazaridou, M. (2021). Remote sensing image segmentation advances: A meta-analysis. ISPRS Journal of Photogrammetry and Remote Sensing, 173, 309-322.

ENVIRONMENTAL ECONOMIC MODELING OF SUSTAINABLE MARINE LITTER COLLECTION ACTIVITIES BY FISHERMAN ～ FOCUSING ON TSUSHIMA CITY

Daiki Nakagawara[1], Hirofumi Nakayama[2], and Satoquo Seino[3]

[1] Department of Civil Engineering, Graduate School of Engineering, Kyushu University (744 Motooka, Nishi-ku, Fukuoka 819-0395, Japan)

[2] Department of Environment and Society, Graduate School of Engineering, Kyushu University (744 Motooka, Nishi-ku, Fukuoka 819-0395, Japan)

[3] Department of Environment and Society, Graduate School of Engineering, Kyushu University (744 Motooka, Nishi-ku, Fukuoka 819-0395, Japan)

This study aims to clarify the actual situation and contributions of fishermen engaged in marine litter collection activities in the Tsushima area of Nagasaki Prefecture. Furthermore, to evaluate the sustainability of the marine litter collection project in Tsushima City from 2020 to 2050, an environmental-economic model was developed using a system dynamics approach and assessed under four scenarios, including a Business-as-Usual (BAU) case.

The results revealed that fishermen account for 97.0% of the total marine litter collection in Tsushima, with an efficiency exceeding the national average. Simulation results from the system dynamics model indicated that, if the number of fishermen continues to decline, the amount of marine litter collected will decrease from the current 7,968 m³ to 4,172 m³ by 2050.

Three countermeasure scenarios were evaluated: (1) increasing fishermen's collection workload, (2) outsourcing to industrial waste contractors, and (3) maintaining the number of fishermen through economic incentives. The analysis suggested that maintaining the number of fishermen through economic incentives would be the most effective strategy for ensuring the long-term sustainability of marine litter collection in Tsushima City.

Introduction

According to surveys conducted by the Ministry of the Environment, more than 30% of the coastal debris collected at model beaches across Japan originates from fishing activities. Thus, fisheries are recognized as one of the major sources of marine litter. On the other hand, many Japanese fishers have a strong normative awareness of preventing gear loss and actively collect lost fishing nets or equipment to minimize the environmental impact of their operations on the marine ecosystem.

One of the primary reasons for this proactive behavior is that drifting marine litter often entangles with fishing vessels or fishing gear, causing operational damage such as fouling. Fishermen must respond to such incidents, as these directly interfere with their daily fishing operations. Therefore, fishers can be seen not only as potential contributors to marine litter but also as victims of it. It is not appropriate to view them unilaterally as polluters. In fact, they often contribute to marine conservation by voluntarily collecting marine litter encountered during fishing operations.

In Japan, many local governments have entrusted the implementation of coastal debris collection projects to local fishermen. This is because fishers possess deep knowledge and experience regarding the characteristics of coastal litter and the local environment. Using their vessels, they are also capable of accessing coastal areas that are otherwise difficult to reach from land, thereby ensuring high collection efficiency. However, in recent years, depopulation and aging have led to a decline in the number of fishers, particularly in remote island areas. As a result, maintaining the current structure of marine litter collection projects in the future may become increasingly difficult.

2. Contribution of Fishermen to Marine Conservation and Economic Burdens Caused by Marine Litter

2.1 Survey Methods on the Contribution of Fishermen to Marine Conservation in Tsushima

To understand the contribution of fishermen in Tsushima

to marine conservation and to identify the economic costs associated with marine litter, literature reviews and interview surveys were conducted. The surveys targeted three main entities:

Table1: Information on Survey Subjects

Survey Target	the Environmental Policy Division of Tsushima City Office	the Tsushima CAPPA (a local intermediary organization)	fishermen of the Saikai Fishery Cooperative Association in Mitsushima Town
Position (Number)	Assistant Section Manager (1 person)	Director (1 person)	– (8 people)
Survey Date	November 19, 2024	November 19, 2024	December 17, 2024

The Environmental Policy Division is responsible for environmental administration in Tsushima City and serves as the commissioning body for coastal litter collection projects conducted by fishermen. It also implements other initiatives related to coastal debris management.

The Tsushima CAPPA (General Incorporated Association) is an organization that supports the implementation of Tsushima City's *Action Plan for Promoting Coastal Debris Countermeasures*. Acting as a bridge between the municipal government and local citizens, Tsushima CAPPA promotes community participation in marine litter management. The organization coordinates with volunteers and private organizations both inside and outside the island, assists in administrative operations, and disseminates information on marine litter collection and treatment.

The fishermen, as key implementers of coastal litter collection in Tsushima, are also directly affected by marine litter through operational disturbances, such as gear entanglement and navigation hazards. In this study, interviews were conducted with fishermen and cooperative staff belonging to the Saikai Fishery Cooperative Association in Mitsushima Town.

2.2 Contribution of Fishermen to Marine Conservation:

Proportion of Collected Coastal Debris and Participant Composition

In Tsushima City, coastal debris is collected primarily through two types of activities:

(1) official Coastal Debris Countermeasure Projects implemented by the municipality, and(2) volunteer-based cleanup activities.

To estimate the share of debris collected by fishermen,

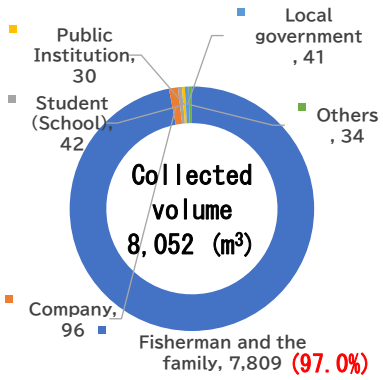

Figure1: Collected Volume by Attribute of Coastal Debris Collectors

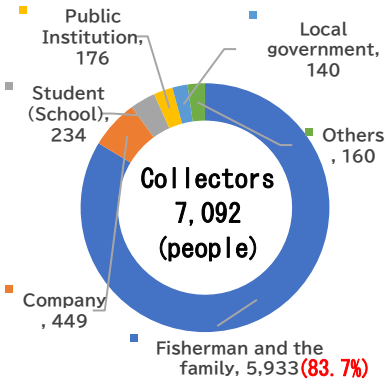

Figure2: Number of Collectors by Attribute of Coastal Debris Collectors

records provided by Tsushima City were analyzed — including the city's coastal cleanup logs, reports from fisherman-led projects, and volunteer activity reports.

As shown in Figure 1, the total amount of coastal debris collected in fiscal year 2023 (Reiwa 5) was 8,052 m³ (equivalent to 899.98 tons). Among this, 7,809 m³ (869.69 tons), or 97.0%, was collected by fishermen and their families.

Regarding the number of participants (Figure 2), out of 7,092 total participants, 5,933 (83.7%) were fishermen or their family members.

These results demonstrate that fishermen play a central role in marine litter collection activities in Tsushima City, both in terms of collected volume and labor participation. Their contribution to local marine conservation efforts is therefore highly significant.

2.3 Comparison Between Marine Litter Collected and Lost by Fishermen

As described earlier, fishermen in Tsushima play a leading role in marine litter collection. However, unintentional leakage of fishing gear into the sea also occurs during operations. To evaluate their net contribution, this study compared the amount of litter

collected by fishermen with the estimated amount of plastic fishing gear lost during fishing activities.
The collected volume was based on the fisherman-led coastal debris collection data.
For estimating the loss of fishing gear, unit outflow rates of plastic gear obtained from previous studies were multiplied by Tsushima's total fish catch in fiscal year 2023.
As shown in Figure 3, fishermen collected 782.7 tons of marine litter in 2023. Among this, plastic litter (including fishing nets, plastic waste, and Styrofoam) accounted for 376.6 tons (48.1%).
In contrast, the estimated amount of plastic fishing gear lost was 22.1 tons.
Thus, the collected volume exceeded the lost volume by 760.6 tons, equivalent to 35.5 times the estimated loss.
This finding indicates that fishermen in Tsushima collect far more litter than they release, making a remarkable contribution to marine environmental conservation.

2.4 Comparison of Collection Efficiency: Tsushima vs. National Average

Using interview data from Tsushima fishermen, the study calculated collection efficiency (m^3 per person per hour) based on collection time, collected volume, and participant numbers. These results were compared with national data from the *Manual for Coastal Cleaning Projects* (Ministry of the Environment, 2011).
As shown in Figure 4, while collection efficiency and total volume varied among areas, the three surveyed sites in Tsushima — Kashi, Imazato, and Hirugaura — all recorded over 100 m^3 of collected debris, indicating large-scale operations.
The collection efficiency was 0.84 m^3/h/person in Kashi, 0.76 m^3/h/person in Imazato, and 0.41 m^3/h/person in Hirugaura.
These values are 2.16 to 4.95 times higher than the national average of 0.19 m^3/h/person, confirming the superior efficiency of Tsushima's fisherman-led cleanup activities.
Interviews revealed that fishermen in Tsushima have been continuously commissioned for coastal cleanup for over 20 years, allowing them to develop extensive knowledge of debris accumulation sites and seasonal patterns. This experience enables them to optimize timing and methods, enhancing collection efficiency. Moreover, the ability to use fishing vessels provides access to otherwise unreachable rocky coastlines, giving them a unique advantage over land-based collectors.

2.5 External Economic Costs Incurred by Fishermen Due to Marine Litter

While fishermen in Tsushima make significant contributions to marine conservation, they also face

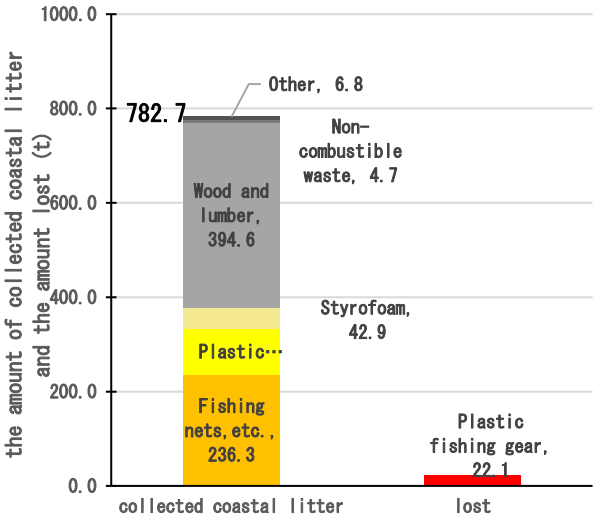

Figure3: Comparison the amount of coastal litter collected by fishermen and the amount lost

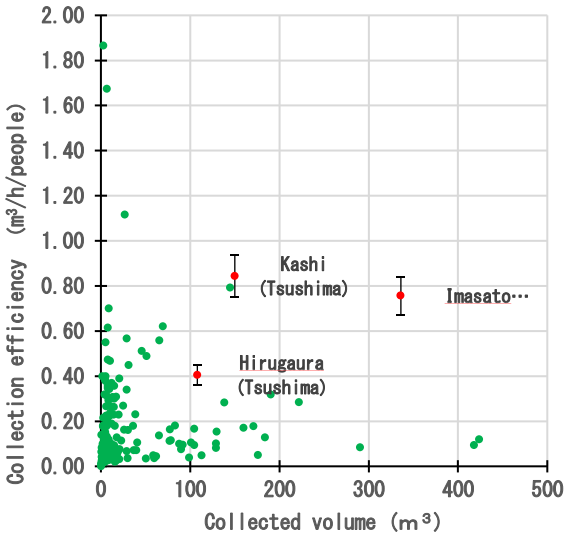

Figure4: Comparison of Collection Efficiency and Volume between Tsushima Fishermen's Projects and National Model Beaches

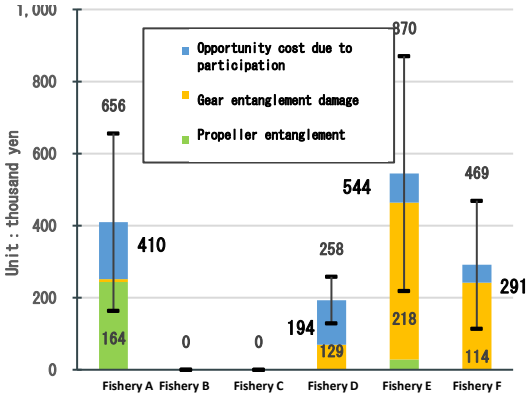

Figure5: Marine litter-related cost

economic burdens caused by marine litter that interferes with fishing operations. To evaluate this negative externality, the study defined and calculated the marine litter-related costs borne by fishermen

The cost components were defined as follows:

1. Opportunity cost due to participation in cleanup projects — estimated as the loss of income from reduced fishing days.
2. Gear entanglement damage — estimated as the reduction in catch caused by time lost removing litter entangled with fishing lines or gear (e.g., longline or trolling fisheries).
3. Propeller entanglement damage — estimated as the production loss caused by time spent removing drifting litter entangled in propellers during navigation.

Unit production values per hour and average annual income per fishing day were derived from the 2022 Fishery Management Statistics Survey (MAFF, 2024).

As shown in Figure 5, the average marine litter-related cost per fisherman was estimated at 240,000 yen (ranging from 0 to 870,000 yen), accounting for 2.8% of total fishing expenses (range: 0–8.8%).

The largest cost components were gear and propeller entanglement, which varied depending on fishing method, fishing grounds, and operational patterns.

In contrast, subsidies paid by Tsushima City for fisherman-led cleanup projects were estimated at 57,000–119,000 yen, meaning the financial burden on fishermen exceeded the compensation they received.

These results indicate that fishermen in Tsushima bear significant economic losses due to marine litter, even as they actively contribute to marine conservation.

3. Environmental Economic Analysis of Marine Litter Collection Activities by Fishermen in Tsushima Using System Dynamics

3.1 Overview of Environmental Economic Analysis Using System Dynamics

As described in the previous chapter, the coastal debris collection project in Tsushima City is largely supported by the contributions of local fishermen. However, due to demographic challenges such as aging and population decline, the number of fishermen on the island has been steadily decreasing. This raises concerns about the sustainability of current collection efforts in the future.

To address this issue, this study developed a system dynamics (SD) model to represent the structural dynamics of Tsushima's coastal debris collection project. The model simulates long-term changes in collection volume under various conditions and examines the effectiveness of different strategies for maintaining debris collection capacity.

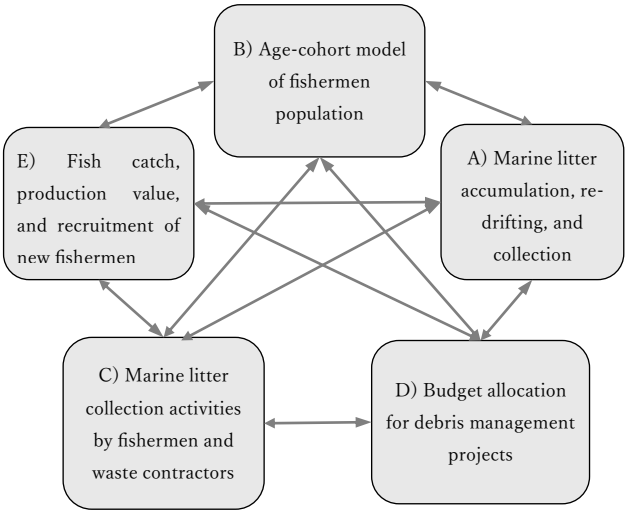

Figure6: Overall structure of the system

The model integrates quantitative indicators of fishermen's contributions and external economic losses derived from previous chapters, as well as additional information obtained through interviews and literature reviews. The model was built using Vensim PLE (Windows x64) software (Ventana Systems) and simulates the overall structure and future trajectory of coastal litter collection efforts in Tsushima City.

3.2 Structure of the Coastal Debris Collection System Model

The developed system consists of five interrelated **subsystems**:

A) Marine litter accumulation, re-drifting, and collection

B) Age-cohort model of fishermen population

C) Marine litter collection activities by fishermen and waste contractors

D) Budget allocation for debris management projects

E) Fish catch, production value, and recruitment of new fishermen

Interactions among these subsystems collectively reproduce the dynamic behavior of the debris collection project. The overall structure is shown in Figure 6.

3.3 Subsystem A: Marine Litter Accumulation, Re-drifting, and Collection

According to Tsushima City, approximately 45,850 m³ of coastal debris drifts ashore annually, of which 94.3% re-enters the sea.

During this process, some debris is collected and processed—mainly by fishermen—while the remainder either re-drifts offshore or reaccumulates along the coastline. This re-drifting generates external costs for fishermen, such as operational interference and additional cleanup time.

The total collected volume was modeled as a function of

collection efficiency and number of collectors. The number of collectors was assumed to depend on the municipal budget for debris collection and consists of both fishermen and industrial waste contractors.
Average collection efficiency was derived from interviews with fishermen. Age-related differences in efficiency were qualitatively estimated based on interview findings: elderly fishers tend to have lower efficiency due to the physically demanding nature of cleanup work, whereas middle-aged fishers, drawing on accumulated experience, achieve higher efficiency.
External costs were modeled as factors that negatively affect the production value per fisherman, representing losses due to interference from marine litter.

3.4 Subsystem B: Fishermen Age-Cohort Model

In many remote islands, including Tsushima, the number of active fishermen has been declining due to aging and depopulation.
In this model, fishermen were divided into three age cohorts — young, middle-aged, and elderly. Future changes in population by cohort were simulated based on demographic trends.
The number of new entrants in the young cohort was determined by two factors:

1. a fixed ratio reflecting the island's population decline, and
2. an economic incentive factor, proportional to the profitability of fishing (measured by fishery production value).

Initial population values were based on demographic statistics from the National Institute of Population and Social Security Research (2023). Cohort transitions were modeled to account for aging, mortality, and withdrawals from the fishery each year.

3.5 Subsystem C: Marine Litter Collection by Fishermen and Waste Contractors

In some simulated scenarios, a portion of debris collection was assumed to be outsourced to contractors to compensate for the reduction in fishermen.
Average collection efficiency values were derived from interview data. Fishermen demonstrated higher efficiency due to long experience and the ability to use vessels for collecting debris from inaccessible coastlines. Based on these findings, the model assigned higher collection efficiency and unit collection cost to fishermen compared to contractors.

3.6 Subsystem D: Project Budget Allocation

According to Tsushima City records and interview results, the annual budget for coastal debris countermeasures is approximately 300 million yen. Of this, 180 million yen is allocated to collection activities, and 120 million yen to waste processing, facility maintenance, and other expenses.
In the model, the total annual budget was fixed at 300 million yen, which is distributed between collection and processing expenditures. The collection budget was assumed to fund the fisherman-led debris removal project.

3.7 Subsystem E: Fish Catch, Production Value, and Recruitment of New Fishermen

The number of new fishermen entering the industry was modeled as a function of:
(1) a baseline recruitment rate relative to the island's population, and
(2) additional recruitment driven by economic incentives—specifically, higher fish catch and sales prices.

3.8 Scenario Settings and Assumptions

It summarizes the conditions and adjustable variables for the environmental-economic model scenarios considered in this study.
In the study, four scenarios were evaluated:

- BAU (Business as Usual) – No policy changes
- Scenario 1: Increased collection workload for fishermen
- Scenario 2: Outsourcing to industrial waste contractors
- Scenario 3: Maintaining the number of fishermen through economic incentives (fish price increase)

3.9 Results and Discussion

Figures 7–10 illustrate the simulation results, including trends in fishermen population, total collected volume, accumulated debris, re-drifting volume, fish catch, fishermen's workload, production value per fisherman, and collection cost per m^3 under each scenario.
(1) BAU Scenario
Under the Business-as-Usual scenario, the total number of fishermen is projected to decline from 1,982 in 2020 to 1,095 in 2050. Consequently, the marine litter collection volume decreases from 7,968 m^3 (2020) to

4,172 m³ (2050).
By 2050, accumulated coastal debris reaches 5,573 m³, and re-drifting debris reaches 5,257 m³. This indicates a negative feedback structure where declining fishermen numbers lead to reduced collection capacity and increasing litter accumulation along the coastline.
(2) Scenario 1 – Increased Fishermen Workload
In this scenario, fishermen's collection time per person was increased to maintain total collection volume. As a result, the 2050 collection volume slightly rose to 8,571 m³.
Since all debris was collected, both accumulated and re-drifting debris reached zero.
However, the increased workload caused fishermen's labor burden to double (2.06 times current levels), reducing their average production value.
This suggests that although expanding fishermen's workload can sustain collection volume, it imposes significant economic strain and reduces time available for fishing.
(3) Scenario 2 – Outsourcing to Waste Contractors
In this scenario, industrial waste contractors were introduced to compensate for the declining number of fishermen. However, due to lower efficiency and budget constraints, the 2050 collection volume only reached 7,595 m³, which is higher than BAU but lower than Scenario 1.
By 2050, accumulated debris remained at 1,237 m³, and re-drifting volume at 1,167 m³.
Sensitivity tests showed that lowering the contractors' unit cost increased collection volume, but maintaining the current level of collection would require equal unit costs to those of fishermen—raising concerns about budget feasibility.
Thus, simple substitution by contractors is not a sustainable solution under current budget constraints.
(4) Scenario 3 – Maintaining Fishermen Numbers via Economic Incentives
This scenario simulated a fish price increase from 1,025 yen/kg to 1,100 yen/kg to improve profitability and retain fishermen.
As a result, the 2050 collection volume increased to 8,191 m³, with 486 m³ of accumulated debris and 459 m³ of re-drifting debris.
Raising the fish price helped stabilize the number of fishermen, preventing further decline. When prices exceeded 1,100 yen/kg, the number of fishermen even began to rise.
However, excessive price increases could burden consumers and affect market sustainability.
Therefore, moderate economic incentives appear to be the most viable long-term strategy, reducing the need for additional outsourcing and maintaining stable collection capacity.

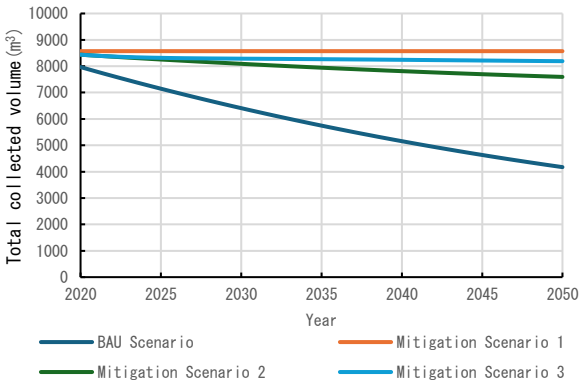

Figure7: Total collected volume

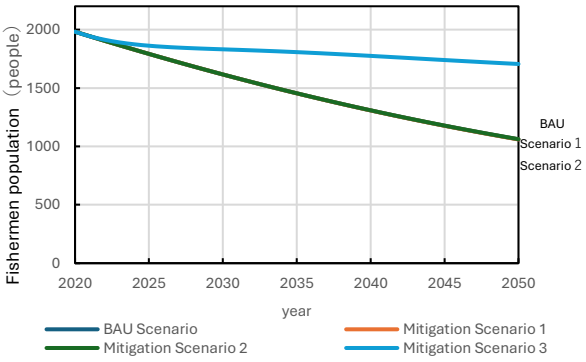

Figure8: Fishermen population

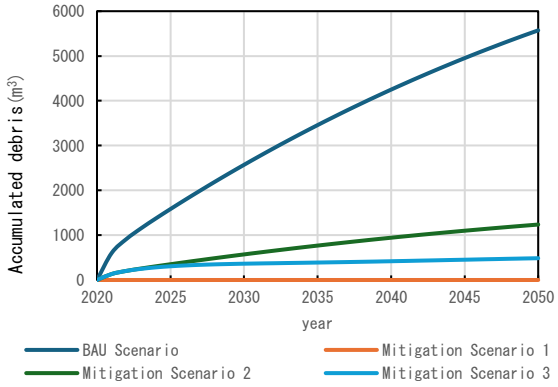

Figure9: Accumulated debris

(5) Sensitivity Analysis
To identify key determinants of collection outcomes, a sensitivity analysis was conducted for three variables:

- Project budget for collection
- Unit cost of waste contractors
- Fish sales price

Each parameter was varied from 0.8× to 1.4× its baseline value under Scenario 3.
Results (Figure 7) showed that collection volume

increased linearly with budget, while contractor unit cost exhibited a negative inverse relationship with collection volume.
Fish price followed a logistic growth curve, with diminishing returns beyond a 1.3× increase.
Among these, fish price had the strongest influence on collection volume, demonstrating that maintaining the number of fishermen is crucial for ensuring stable coastal litter collection in Tsushima.

4. Conclusion and Acknowledgements

4.1 Conclusion

The key findings of this study are summarized as follows:

1. In Tsushima City's coastal debris collection project, 97.0% of the total collected volume and 83.7% of the total participants** were fishermen or their family members**, indicating their substantial involvement and contribution to marine conservation efforts.
2. The total amount of marine litter collected by fishermen (782.7 tons) greatly exceeded the estimated amount of plastic fishing gear lost during operations (22.1 tons), demonstrating that fishermen remove far more debris than they generate.
3. The collection efficiency of fishermen in Tsushima ranged from 0.41 to 0.84 m^3 per hour per person, which is significantly higher than the national average of 0.19 m^3/h/person. This high efficiency is attributed to over 20 years of continuous involvement in debris collection, which has allowed local fishermen to accumulate experience and local knowledge that improve their effectiveness in marine litter management.
4. The average annual cost burden borne by fishermen due to marine litter (including opportunity costs and gear damage) was estimated at 240,000 yen (range: 0–870,000 yen), accounting for 2.8% of total fishery expenditures. This confirms that fishermen face economic losses caused by marine litter, despite their substantial contribution to marine conservation.
5. The system dynamics simulation revealed that the current debris collection project in Tsushima City may not be sustainable in the long term if current trends continue. Three countermeasure scenarios were examined:
    - (a) increasing fishermen's collection workload,
    - (b) outsourcing to industrial waste contractors, and
    - (c) maintaining fishermen numbers through economic incentives.

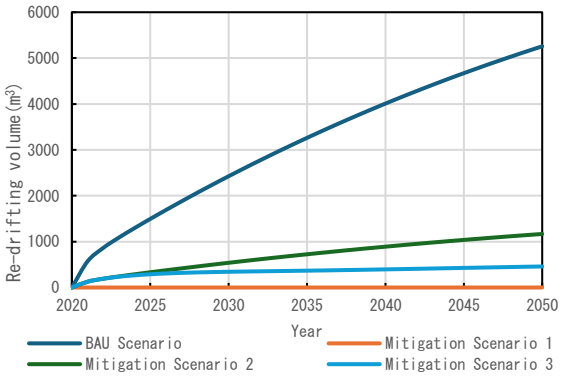

Figure9: Re-drifting volume

Among these, scenario (c)—maintaining the number of fishermen through improved economic incentives (e.g., higher fish prices)—was identified as the most effective and sustainable option for ensuring the continuity of marine litter collection in Tsushima.
Nevertheless, some limitations remain in this study. For example, age-specific collection efficiency values were qualitatively estimated rather than derived from quantitative data, and determinants of new fishery entrants were limited to fishery income without considering other social or institutional factors. Future research should address these limitations to improve model accuracy and policy applicability.

4. 2 Acknowledgements

This research was conducted as part of the Environmental Research and Technology Development Fund (S-19), titled *"Comprehensive Research on Building a System for Sustainable Plastic Resource Circulation and Marine Leakage Control"* (Project No. JPMEERF21S11900).
The authors express their sincere gratitude to the Environmental Policy Division of Tsushima City, the General Incorporated Association Tsushima CAPPA, and the Saikai Fishery Cooperative Association in Mitsushima Town for their valuable cooperation and support.

References

1. **Japan NUS Co., Ltd.** (2024). *Comprehensive Study on the Actual Conditions and Efficient Collection of Marine Debris in FY2023*. Ministry of the Environment, Japan.
   Retrieved May 6, 2025, from https://www.env.go.jp/content/000220884.pdf
2. **Nakayama, H.**, **Ishibashi, F.**, **Kuwamura, M.**, and **Seino, S.** (2022). *A Study on the Unit Input of Plastic Products in Fishing Vessel Fisheries.*

Journal of Japan Society of Civil Engineers, Ser. G (Environmental Research), 78(6), II_11–II_17.

3. **Government of Japan** (2024). *Japan National Statement under Agenda Item 4: The Fourth Session of the Intergovernmental Negotiating Committee to Develop an International Legally Binding Instrument on Plastic Pollution, Including in the Marine Environment.* Retrieved May 2, 2025, from https://resolutions.unep.org/incres/uploads/japan_national_statement_under_agenda_4_inc4final_0.pdf
4. **Ishibashi, F.**, **Nakayama, H.**, **Seino, S.**, and **Shimaoka, T.** (2024). *A Study on the Outflow of Plastic Fishing Gear from Fishing Vessel Fisheries. Proceedings of the 2024 JSCE Western Branch Conference*, pp. 811–812.
5. **Isobe, S.** (2009). *Current Situation and Issues of Seabed Litter Collection by Fishermen—Focusing on the Seto Inland Sea.* *Regional Fisheries Research,* 49(3), 49–65. (in Japanese)
6. **Sanyo Techno Marine Co., Ltd.** (2024). *Demonstration Project on Marine Litter Collection with the Cooperation of Fishermen.* Ministry of the Environment, Japan. Retrieved May 6, 2025, from https://www.env.go.jp/water/post_80.html
7. **Tsushima City, Nagasaki Prefecture.** (2015). *Tsushima City Action Plan for Promoting Coastal Debris Countermeasures.* Retrieved May 6, 2025, from https://www.city.tsushima.nagasaki.jp/material/files/group/14/hyoutyakubututaisaku_h27.pdf
8. **Gonda, K.** (2022). *Efforts of Fishermen in Munakata City to Collect Marine Litter.* *Journal of Fisheries Engineering,* 59(1), 57–60. (in Japanese)
9. **Tokai, T.**, **Sakurai, N.**, **Yamamoto, T.**, and **Kumazawa, Y.** (2022). *Symposium on Marine Plastic Issues and Measures in Fisheries (2021 Autumn Meeting of the Japanese Society of Fisheries Engineering).* *Journal of Coastal Zone Studies,* 59(1), 31–36. (in Japanese)
10. **Ministry of the Environment, Japan.** (2011). *Manual for Coastal Cleaning Projects: Reference Materials.* Retrieved May 6, 2025, from https://www.env.go.jp/water/marine_litter/model/seisou-manual/manual_mat.pdf
11. **Ministry of Agriculture, Forestry and Fisheries (MAFF).** (2024). *Fishery Management Statistics Survey.* Retrieved May 6, 2025, from https://www.maff.go.jp/j/tokei/kouhyou/gyokei/
12. **Min-Fang Tsai**, **Tony Phuah**, **Pierre-Alexandre Château**, and **Yang-Chi Chang** (2024). *A System Dynamics Model for Evaluating Circular Economy Strategies of Marine Debris Mitigation.* *Journal of Coastal Research,* 113(sp1), 105–109. https://doi.org/10.2112/JCR-SI113-021.1
13. **Mousavi, S.H.**, **Kavianpour, M.R.**, and **García Alcaraz, J.L.** (2023). *The Impacts of Dumping Sites on the Marine Environment: A System Dynamics Approach.* *Applied Water Science,* 13(109). https://doi.org/10.1007/s13201-023-01910-9
14. **Rafew, S.M.**, **Islam, M.R.**, and **Kraft, E.** (2023). *A System Dynamics Based Policy Simulation Approach to Reduce Plastic Waste Flow for Inland and Riverine Areas in Khulna City of Bangladesh.* *Research Square.* https://doi.org/10.21203/rs.3.rs-3205338/v1
15. **Japan NUS Co., Ltd., Tsushima CAPPA, and Tsushima Eco Service Co., Ltd.** (2025). *Monitoring Survey Report on Coastal Debris in Tsushima City.* Retrieved May 6, 2025, from https://tsushima-mltic.com/document/
16. **National Institute of Population and Social Security Research.** (2023). *Future Population Projections by Gender and Age (5-year intervals) for Prefectures, Cities, and Towns in Japan.* Retrieved May 6, 2025, from https://www.ipss.go.jp/pp-shicyoson/j/shicyoson23/t-page.asp
17. **Hayashi, H.** (2009). *A Basic Study on Factors Contributing to the Decline of Fishery Workers.* *Technical Research Institute for Fishing Ports, Grounds, and Villages Research Papers,* 20, 7–11. (in Japanese)
18. **Ministry of Agriculture, Forestry and Fisheries (MAFF).** (2025). *2023 Fishery Census Report.* Retrieved May 6, 2025, from https://www.maff.go.jp/j/tokei/census/fc/2023fc/2023fc.html
19. **Ministry of Agriculture, Forestry and Fisheries (MAFF).** (2021). *2018 Fishery Census.* Retrieved May 6, 2025, from https://www.maff.go.jp/j/tokei/census/fc/2018/2018fc.html
20. **Fisheries Agency, Port and Fishing Grounds Department, Planning Division.** (2024). *Overview of Fishing Port Statistics.* p.362. (in Japanese)

Optimization of Municipal Solid Waste Collection and Transportation Routes in Odawara City, JAPAN

Tohru SATOH[1], Keiichi IKI[1], Hirotaka NARIMO[1], Nanako OHNO[1]
1 Environmental Solutions Design & Engineering Dept., Kanadevia Corporation, Osaka, Japan

Introduction

In the field of municipal solid waste (MSW) collection and transportation, there is growing expectation for the use of IoT and AI technologies to improve operational efficiency and labor-saving. These technologies are considered promising tools for cost reduction as they can support vehicle dispatching, route planning, and data management.

However, when applying AI to vehicle dispatching and route planning, it is essential to incorporate the timing of deliveries to incineration facilities. Although this approach is effective, it requires detailed input of unique conditions—such as the volume of waste at each collection site—which makes it difficult to apply existing services directly.

In order to overcome this issue, we have developed a system that utilizes wearable sensors to estimate the number of garbage bags accumulated at each collection site[1)]. This system enables the acquisition, accumulation and analysis of data necessary for vehicle dispatching and route planning, thereby allowing for the optimization of collection routes and contributing to both operational efficiency and labor-saving.

In this paper, we verify the effectiveness of route optimization in MSW for business-sector collection operations. Then, we report the results of optimizing and verifying the collection and transportation routes for household MSW collection, which one route was removed from the original 14 routes, resulting in a reconfiguration to 13 optimized routes.

Waste Collection and Transportation in Japan

We explain the types and characteristics of waste collection and transportation in Japan. Waste collection is broadly divided into two categories: industrial waste collection and general waste collection. General waste collection is further classified into household and business-sector waste collection based on the waste generation process. Table 1 shows the characteristics of these types of waste collection.

Japanese household waste collection corresponds to the "Curbside Pick-Up" system[2)], where residents place their waste in front of their homes and municipalities or service providers collect it. Household waste collection has two main formats in Japan: door-to-door collection, where waste is collected individually from each household (e.g. in front of houses or apartment buildings), and station-based collection, where waste from multiple households is gathered at a single collection point (hereafter referred to as a “station”). Table 2 outlines the characteristics of these formats.

Business-sector waste collection typically involves fewer constraints regarding the number of collection points and road access, which has enabled various companies to develop and business-sector automated dispatch planning services. In contrast, household waste collection involves a large number of collection points and often requires roadside parking for collection vehicles. This necessitates constraints such as left-side parking and U-turn prohibitions. Additionally, dispatch planning that includes delivery to waste treatment facilities requires data on the amount of waste at each

Table 1: Characteristics of Business-sector and Household General Waste Collection

	Collection Format	Collection Sites	Roadside Parking	Waste Volume per Collection Site
Business-sector MSW Collection	-	Hundreds	Few	Often held by the business
Household MSW Collection	Curbside Pick-Up (Station-based)	Thousands	Many	Often not held by the service provider

Table 2: Characteristics of Household Waste Collection Formats

Collection Format	Installation Method	Distance Between Nearby Station
Station-based	1 station per ~10 households	Tens to hundreds of meters (wide)
Door-to-door	One station per detached house; one per apartment building	A few meters (narrow)

station, which is often not available to service providers, making route optimization difficult.
In addition, station-based collection often involves stations located tens to hundreds of meters apart, offering multiple route options and greater potential for reducing travel distances. Therefore, this development focuses on optimizing collection routes for general waste collection using the station-based format.

Process of optimization for collection routes

As shown in Figure 1, the workflow for optimizing collection and transportation routes consists of four major stages: preliminary interviews, data acquisition and accumulation, optimization of collection and transportation routes, and follow-up interviews. The system used in this process comprises the following components:
(a) a garbage bags detection system,
(b) a cloud server,
(c) a PC terminal, and
(d) an on-board equipment.
First, the information obtained during the preliminary interviews is used to create master data on the PC terminal (c), which is then managed on the cloud server (b). Next, during the data acquisition and accumulation, data collected via the garbage bags detection system (a) and the on-board equipment (d) is stored on the cloud server (b) and subsequently analyzed and organized on the PC terminal (c).
After that, optimization of collection and transportation routes using AI technologies are performed on the PC terminal (c) based on the data managed on the cloud server (b). The results are compiled into materials such as maps, routes and collection site lists for use in follow-up interviews.

This paper primarily discusses the verification results within the dashed box shown in Figure 1, which corresponds to the optimization of collection and transportation routes and validation phase.

Verification of the Effectiveness of Collection Route Optimization

In this section, we present the results of a study conducted to verify the effectiveness of optimizing collection and transportation routes for one route of business-sector municipal solid waste (MSW) collection in Odawara City.
For the optimization study, data including the location (latitude and longitude) of each collection site, the estimated volume of waste, and the collection time were obtained through data acquisition and interviews. These data were then used in the optimization calculations for the collection and transportation route.
Figure 3 compares the mileage and driving time between the conventional route and the optimized route. In the area enclosed by the dashed line in the figure, the conventional route required two round trips. However, by adjusting the collection sequence in consideration of the designated collection time, the optimized route significantly reduced the mileage by 17.3 km (31.9%) compared to the conventional route. This result confirmed the practical utility of the optimized route.
Furthermore, interviews with collection workers revealed positive feedback. They noted that such a reduction in mileage would have a substantial impact on fuel costs and expressed interest in applying route optimization to other collection and transportation routes as well.

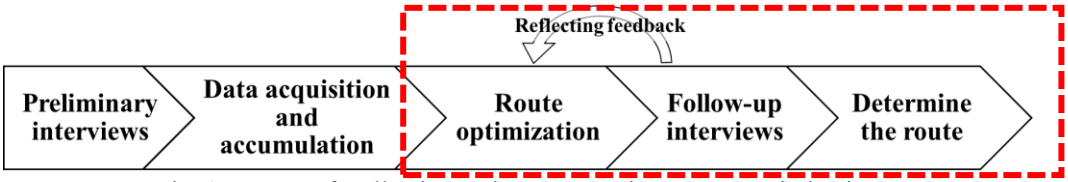

Fig. 1 Process of Collection and Transportation Route Optimization

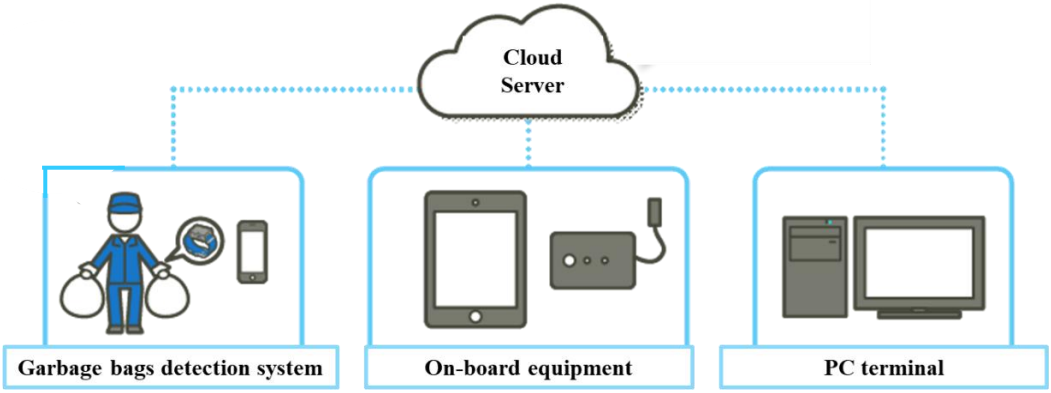

Fig.2 System Configuration

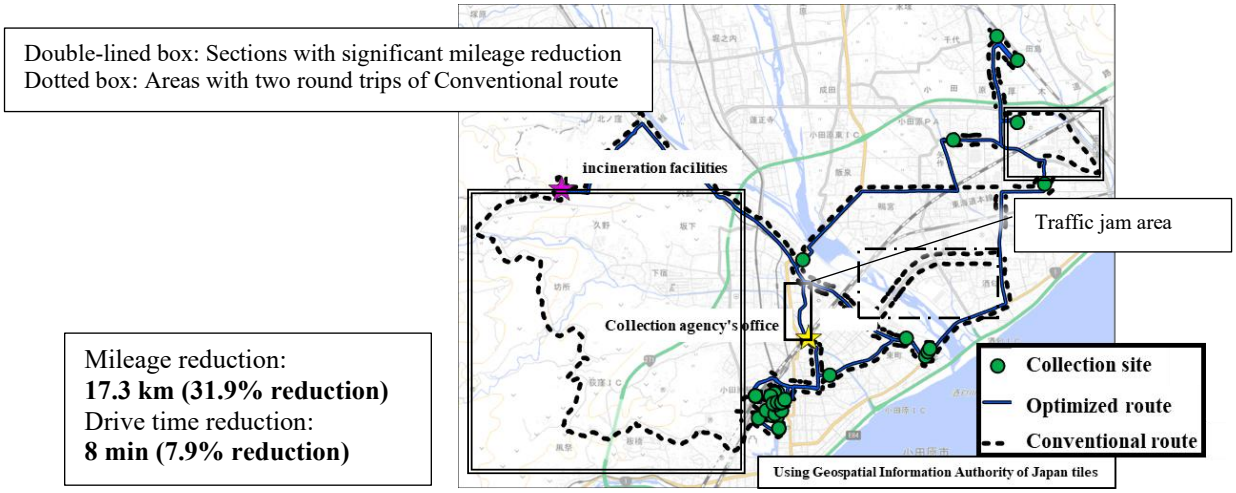

Fig. 3 Comparison of Conventional and Optimized Routes

Route Optimization for Household Municipal Solid Waste Collection and Transportation in Odawara City

Route Optimization Calculation

With the cooperation of a waste collection and transportation contractor in Odawara City, we conducted a route optimization process for the collection of household municipal solid waste (MSW), specifically focusing on combustible waste. It should be noted that Odawara City has adopted a station-based collection format.

In this study, the contractor originally collected waste from 1,685 stations using 14 routes (9 vehicles of 2-ton compactor trucks and 5 vehicles of 3-ton compactor trucks). The optimization aimed to reduce one 3-ton vehicle and reconfigure the collection into 13 routes—hereafter referred to as the "planned routes."

Figure 4 shows the coverage areas of the conventional routes and a representative example of the planned route. Because the optimization algorithm prioritizes collection while heading toward the waste treatment facility, the planned route became to span multiple conventional route areas. In addition to reducing one route, the planned route was reduced the total mileage by approximately 50 km (about 4.9%) compared to the conventional routes.

Field Verification and Evaluation

This section presents the results of a field verification that compares three types of household municipal solid waste (MSW) collection routes:

- The conventional route, which refers to the original routes used before optimization,
- The planned route, which was generated through optimization calculations, and
- The final route, which was further refined based on the experience and insights of collection workers.

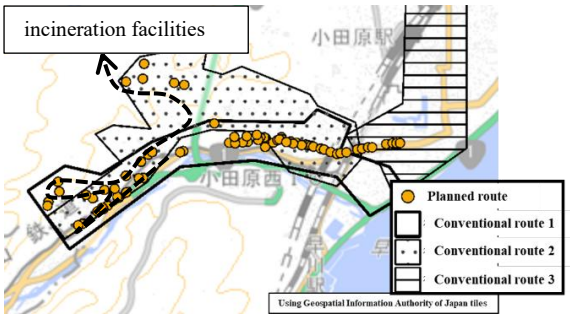

	Conventional route	Planned route
Number of Course	14	13
Total Waste Weight [kg]	92,525	92,525
Number of Total Delivery	53	52
Total Mileage [km]	1,026	976

Fig.4 Coverage Areas of Conventional and Planned Routes

The evaluation focuses on metrics such as total mileage, fuel consumption, and CO_2 emissions.

Table 3 summarizes the reduction achieved in each metric when switching from the conventional route to the planned and final routes. Additionally, interviews were conducted to gather feedback, requests, and impressions regarding the planned route (see Table 4).

Although the planned route was presented in detail during the verification, the actual driving order and path were left to the discretion of the collection workers. In the final route, adjustments were made based on worker experience, including the timing and order of deliveries

Table 3: Comparison of Field Verification Results

	Conventional Route	Planned Route (Verified)	Reduction from Conventional	Final Route (Verified)	Reduction from Conventional
Number of Course	14	13	1	13	1
Number of Vehicle	2-ton: 9 3-ton: 5	2-ton: 9 3-ton: 4	3-ton: 1	2-ton: 9 3-ton: 4	3-ton: 1
Number of Total Delivery	53	52	1	51	2
Total Waste Weight [kg]	92,525	82,435	-	83,695	-
Total Mileage [km]	1,026	976	50	953	73
Fuel Consumption [L]	245	233	12	227	18
CO_2 Emission [kg-CO_2]	610	579	31	564	46

Table 4: Feedback, Requests, and Impressions Regarding the Planned Route

Item	Contents
1	The route was unlike anything that could be conceived based on worker experience or intuition, which made it interesting.
2	It was appreciated that the route avoided left-side station approaches and U-turns, as some workers tend to force U-turns, which can be dangerous.
3	It is believed that incorporating worker experience into the AI-optimized route could result in even more efficient routing.

to the incineration facilities, pathway, and substitution of collection stations between routes.

As a result, the planned route achieved a reduction of 50 km (4.9%) in total mileage compared to the conventional route. Furthermore, the final route achieved a reduction of 73 km (7.1%) in total mileage.

Conclusion

This paper reported the results of route optimization and field verification for business-sector municipal solid waste (MSW) collection, confirming the effectiveness of these optimization efforts. It also presented the results of route optimization for household MSW collection.

- In business-sector MSW collection, the optimized route reduced mileage by 17.3 km (31.9%) compared to the conventional route, demonstrating the effectiveness of route optimization in reducing travel distance.
- In household MSW collection, the planned route achieved a reduction of 50 km in total mileage compared to the conventional route. Furthermore, by incorporating adjustments based on worker experience, the final route achieved a reduction of 73 km. Positive feedback was also received regarding the planned route.
- Route optimization using AI technology proved effective in reducing travel distance. Moreover, it was found that incorporating the experience and knowledge of collection workers could further enhance route efficiency.

Acknowledgments

The authors would like to express their sincere gratitude to the Odawara City Waste Collection and Transportation Contractor for their cooperation in data collection and field validation. We also thank our colleagues at Kanadevia Corporation for their valuable support and insights throughout the development and verification process.

References

1) Iki, Keiichi; Sato, Toru; Yamamoto, Noboru (n.d.). Demonstration of Efficiency Improvement in Collection and Transportation Operations for Municipal Solid Waste. Proceedings of the 44th National Urban Cleaning Research and Case Presentation Conference, II-1-53. (in Japanese)

2) Suzuki Kaoru, Garbage Collection Method, Nation Institute for Environmental Studies, Vol.39 No.4, p.11 – p.13. (in Japanese)

BIOGASIFICATION OF CELLULOSIC ETHANOL STILLAGE IN AN ANAEROBIC FLUIDIZED BED BIOREACTOR

Shunchang Yang[1,5*], Gayathri Ram Mohan[1], Na Wu[1,4], Clement Tseng[1], Lonnie Ingram[2], Keelnatham Shanmugam[2], Spyros Svoronos[3] and Pratap Pullammanappallil[1]

[1] Department of Agricultural and Biological Engineering

[2] Department of Microbiology and Cell Science

[3] Department of Chemical Engineering

University of Florida, Gainesville, FL 32611

[4] Department of Coatings and Polymeric Materials

North Dakota State University, Fargo, ND, 58102

[5]Future Environment Laboratory, Innovation Center of Yangtze River Delta, Zhejiang University, Jiaxing, China

*corresponding author Shunchang Yang

ABSTRACT

Thermophilic digestion of cellulosic ethanol stillage was investigated in an anaerobic fluidized bed reactor. Batches of coarsely separated (0.425 mm sieve) bagasse stillage (11.5 - 63 g sCOD/L) obtained from the biofuels pilot plant at the University of Florida was used as feed. The methane potential achieved was 12.9 L CH_4 (L Stillage)$^{-1}$ or 0.288 L CH_4 (g $sCOD_{loaded}$)$^{-1}$. The 5.5L digester was operated at a HRT of 7.3 days for a total period of 100 days at an organic loading rate of 6.54 g sCOD $L^{-1}d^{-1}$. The effluent COD at the end of the reactor operation was 3.5 g sCOD/L yielding a soluble organic matter removal efficiency of 93%. This translates to a methane yield of 0.311 L CH_4 (g $sCOD_{removed}$)$^{-1}$.Operation of the reactor at higher loading rates, i.e., 8.8 g sCOD $L^{-1}d^{-1}$ led to inhibition. The pH was maintained between 7.1 and 8.4 throughout the operational period.

INTRODUCTION

Due to global concerns about climate change and other environmental impacts of fossil fuels have accelerated efforts to commercialize and introduce biofuels into the transportation fuel supply chain. The Energy Independence and Security Act (EISA) passed by US Congress and Renewable Fuel Standards (RFS) administered by USEPA, mandates that biofuels should account for 36 billion gallons of the fuel mix used by the transportation sector by year 2022. Ethanol from corn-starch having been capped at 15 billion gallons, major fraction of the remaining mandate would be required to be sourced from cellulosic feedstocks like agricultural wastes, forestry residues and dedicated energy crops [1]. Ethanol from such feedstocks is referred to as 'cellulosic ethanol'. These biomass feedstocks are competitive in both low price and abundance with conventional feedstocks. To be classified as a cellulosic biofuel, in addition to the feedstock, the fuel must also generate 60% less lifecycle greenhouse gas emissions compared to the baseline emissions for gasoline or diesel in the year 2005. Due to recalcitrant structure of cellulosic biomass, inevitable pretreatment and enzyme saccharification process [2] have to be employed before the ethanol fermentation proceeding. This potentially raises the issue of energy intensive, special for large scale bioethanol plants. The whole fermentation broth was distilled to recover the ethanol, while the waste stream from the distillation step is referred to as 'stillage'. Large volumes of stillage are generated in an ethanol plant. Stillage generation will be 10 to 14 times the volume of ethanol of produced and is a highly polluting waste stream containing high content of organic carbon and other nutrients like nitrogen and phosphorus. Lignocellulosic ethanol stillage has a high COD content in the range of 11.5-63 g sCOD/L (Wilkie, Riedesel et al. 2000; Tian et al. 2013). Many options have been proposed for treatment and management of stillage. These treatments include dewatering and combustion of dewatered solids (Kazi et al., 2010; Steinwinder et al. 2011; Aden and Foust, 2009), recycling (Egg, et al. 1985), land application (Fuess adn Garcia, 2014; Gubicza, et al. 2016), composting (Klemes, et al. 2008), and processing as feed supplement (Sajbrt, et al. 2010). However, these techniques either recover low-value products from the stillage or generate more than 60% greenhouse gas emissions.

Anaerobic digestion (AD) of stillage is another option of managing stillage as it not only helps in reducing the organic carbon content (COD) into renewable energy (biogas) which can improve the energy efficiency of ethanol plant, but also is capable of reducing the industrial waste pollution and recovering high-value byproduct from the ethanol stillage (Tian 2011 ; Barta et al., 2010). Cconducted techno-economic evaluation of spruce to ethanol process

based on a SO_2-catalyzed steam pretreatment followed by simultaneous saccharification and fermentation trail using Aspen PlusTM. They also investigated the overall energy efficiency of the process by including various anaerobic digestion configurations and compared these with conventional evaporation of stillage. They reported that stillage yielded significantly higher overall energy efficiencies; 87-92%, (Energy Unit output= Ethanol energy + Lignin incineration energy; Total energy input = Raw material internal energy + Operation energy + equivalent of labor cost to Energy)； as opposed to the conventional evaporation of stillage that yielded 81% energy efficiency. Such increased energy efficiency of the ethanol production process may be attributed to production of biogas that can be used in a combined heat and power facility to produce energy or upgraded and sold as fuel. This helps offset the energy demanded in the process such as during steam generation for use in pretreatment and distillation.

The AD process can be implemented in many types of bioreactor designs. Various reactor configurations have been developed in the past for anaerobically digesting distillery wastewaters (Moletta 2005, References). These include continuous stirred tank reactors (CSTRs) (Tian 2011, References), upflow anaerobic sludge blanket (UASB) reactors (Vijayaraghavan and Ramanujam 2000; Moletta 2005); and downwards stationery fixed film reactors (Wolmarans and de Villiers 2002; Moletta 2005; Fernandez, Montalvo et al. 2008) and fluidized bed reactors (AFBR) (Callander, Clark et al. 1987; Bories, Raynal et al. 1988; Fernandez, Montalvo et al. 2008; Tian 2011). Choice of design is dependent on waste characteristics and can influence capital and operating costs as well as the footprint of the facility. There are only a couple of studies reported in the literature on the anaerobic treatment of cellulosic ethanol stillage due to the presence of inhibitory, slowly and poorly degradable organics such as phenolic compounds and furfural derivatives produced during the pretreatment and fermentation stages. Callander et al., (1987) carried out studies on laboratory scale mesophilic anaerobic digestion of wood ethanol stillage using a UASB reactor in the late 1980's. They investigated the amenability of anaerobically digesting cellulosic ethanol stillage that was 5 times as dilute as the feed used in the current study in a high rate treating system. However, since wood to ethanol stillage was nutrient deficient, N and P were externally added at 240 mg/L and 120 mg/L stillage, respectively (Callander, Clark et al. 1987). In another study by Tian (2011), a continuously fed stirred tank reactor which is a low rate technology was used for thermophilic digestion of lignocellulosic ethanol stillage. No external nutrients were added and 90% of methane yield as determined by the biochemical methane potential assay was produced within a 14 day retention time resulting in a residual COD of 7-8 g sCOD (L Effluent)$^{-1}$.

AFBR are characterized as high rate systems and have been applied to digest a variety of wastewaters. The organic loading rates (OLR) of AFBR range from 2 g COD/L/d to 35 g COD/L/d (Borja and Banks, 1995; Blanco et al., 1995; De Amorim et al., 2009; References). Use of a higher end design which is capable of handling higher OLR can be a more economical alternative management for stillage digestion. This work was based on digesting cellulosic ethanol stillage with AFBR design and demonstrated the strategy of maximizing the OLR by natural microbial acclimatization and the feasibility of scale-up operation based on techno-economic analysis. The elimination of inhibitors, COD removal efficiency, maximum OLR, minimum HRT and methane yield from anaerobic digestion of stillage and techno-economic analysis of integrating the AFBR to ethanol pilot-plant were also evaluated during long term operation of the AFBR.

MATERIALS AND METHODS

2.1 Cellulosic Ethanol Stillage

The cellulosic ethanol stillage used in this study was collected from the Stan Mayfield biorefinery pilot plant located at Perry, Fl, USA. In this biorefinery, cellulosic ethanol was produced from sugarcane bagasse using dilute phosphoric acid pretreatment and followed with recombinant E. coli fermentation by [Ingram, References]. The distilled downstream ethanol stillage was collected in 50-gallon drums and shipped directly to the bioprocessing lab at the University of Florida. The distilled stillage contained soluble sugar and undegradable suspended solids. [How the stillage was stored?] The stillage pH was around 6.5. The characteristics of the stillage feedstocks are analyzed by Analytical Services Laboratories (ANSERV Labs) as in Table 1.

Table 1. Characterization of cellulosic ethanol stillage

Property	Stillage
pH	
Total COD (mg/L)	
BOD5 (mg/L)	
Nitrogen (g/L)	65.8 ± 5.68
Ammonium-N (g/L)	23.6 ± 3.01
Nitrate-N (g kg-1)	33.6 ± 3.62
Total iron (g kg-1)	0.14 ± 0.02
Total aluminum (g kg-1)	0.09 ± 0.01
Total P (g kg-1)	35.2 ± 34.3

2.2 Anaerobic Fluidized Bed Reactor

Thermophilic anaerobic digestion of cellulosic ethanol stillage was carried out in an anaerobic fluidized bed reactor (AFBR) (Yang, 2019, 2020). This insulated reactor shown in figure 1 was constructed of a cylindrical vessel (pyrex glass column with dimensions: 84 cm in height and internal diameter of 28 cm) with a sealed lid on top and a conical bottom equipped with a heating tape wound around the cylindrical portion. The heating tape was controlled by modular data logger CR10 (CAMPBELL SCIENTIFIC, INC. UT, USA) through on-off protocol to maintain thermophilic temperature (55 ± 2°C).

The AFBR had a working volume of 5.5 L leaving a headspace of 1.5 L with 6 ports spaced 4" apart that were used for sample collection, feed input, recirculation and thermocouple access. A feed tank with a holding capacity of 4 L was refilled periodically with stillage and placed in a refrigerator and continuously stirred. A two headed peristaltic pump was calibrated and set on a timer to feed the digester and remove effluent simultaneously five to ten times a day.

Commercial prewashed activated carbon particles (0.5 mm in diameter) with expanded surface area were used as fluidization media in the AFBR. Fluidization was provided by recirculating the reactor liquid using a centrifugal pump at a flow rate of 2 L per minute. Use of such high flow rate ensured the fluidization of active carbon and good mixing of inocolumn in the reactor. In order to prevent clogging in the reactor due to draining of activated carbon particles into the recirculation line, a screen mesh was inserted between the bottom of the reactor and the PVC pipe. Biomass growth was observed on the surface of the activated carbon particles. This design was developed in collaboration with Southern Scientific Inc., located at Micanopy, FL (USA) and University of Florida's Agricultural and Biological Engineering machine shop. The particles kept fluidized by recirculating the reactor liquid using a high flow rate (2 L/min) peristaltic pump. Biofilm growth was observed on the surface of the activated carbon particles.

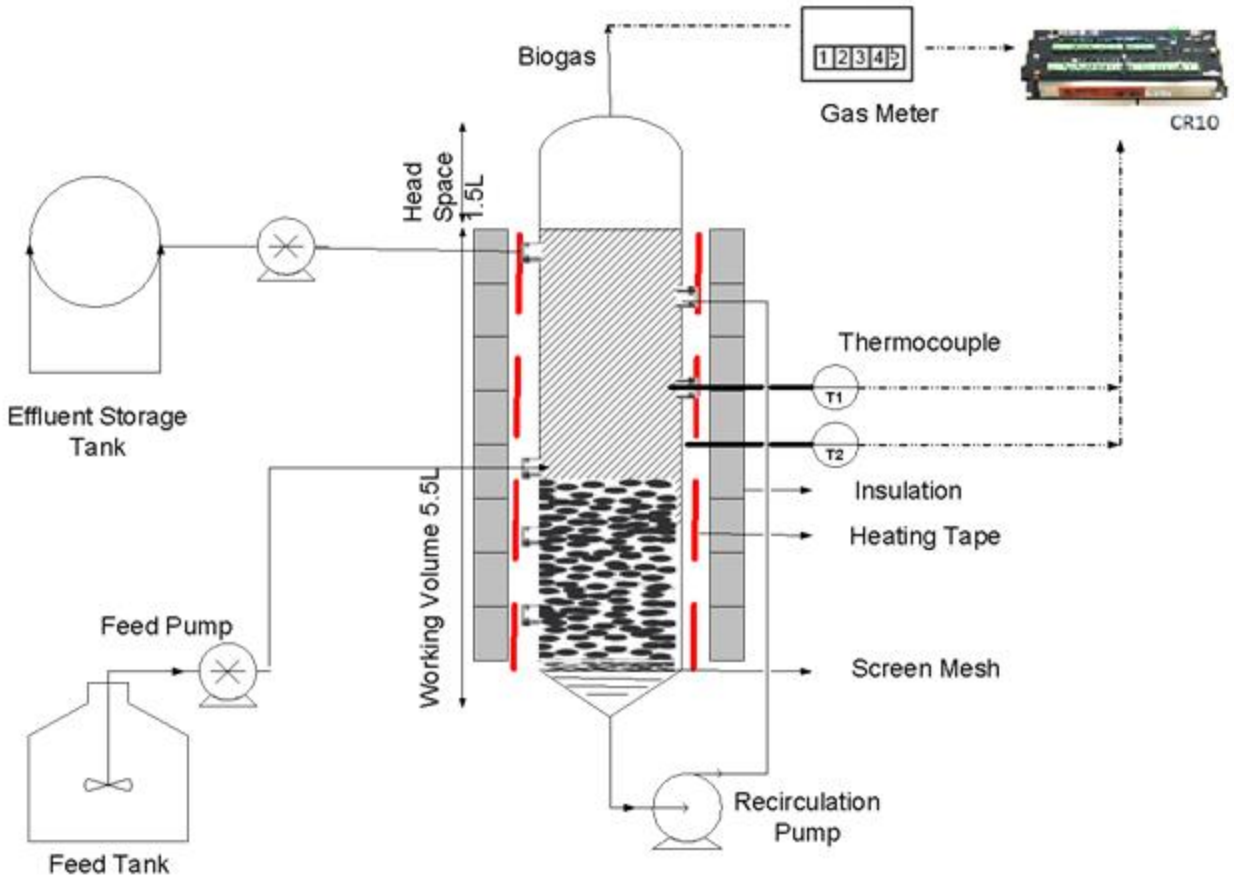

Figure 1. schematic diagram of reactor design for high rate stillage treatment.

2.3 AFBR Startup And Long-Term Acclimatization Operation

The AFBR was fed with cellulosic ethanol stillage. The acclimatization process lasted almost 1 year which included four phases. Phase 1: From day 1 to day 90, the organic loading rate was maintained XX g/l/d. anaerobic breakdown of stillage was initiated with seed inoculum broth from a continuous stirred tank reactor (CSTR) that was previously used to digest cellulosic ethanol stillage. A semi-continuous feeding method was applied to the AFBR with a two headed peristaltic pump and turn on and off with a timer set up. These two-pump head were calibrated to feed the digester and remove equivalent volume of effluent simultaneously for couple of times per day. The flow rate was determined by the operational time interval of feed pump, the varying feed rate was shown in figure 3. Phase 2. From day 91 to day 199, the organic loading rate had been increased from 150 ml/5500ml/day to 750 ml/5500ml/day by reducing the HRT from 5 to 7. The increment of loading rate was 150 ml/day stillage when a new steady state reached (based on total VFA and methane production). Use same method of loading. The duration is 109 days. With 10 days

starvation process, the phase 3 was initialized. Phase 3: From Day 209 day to day 276, the organic loading rate had been increased from 150 ml/5500ml/day to 1050 ml/5500ml/day by reducing the HRT from XXX to XXX. The increment of loading rate was 300 ml/day stillage. The duration is 67 days. With another 20 days starvation process, the phase 4 was initialized. Phase 4: From Day 296 day to day 362, the organic loading rate had been increased from 300 ml/5500ml/day to 1800 ml/5500ml/day by reducing the HRT from 2 to 3. The increment of loading rate was 300 ml/day stillage. The duration is 66 days. After the completion of startup and activation process, the anaerobic digester achieved with a high organic loading rate (1800 ml stillage/5500 ml inoculum/Day). During the operational phase, micronutrient for the microbial inoculum was not provided. The pH, tVFA, sCOD and methane content were monitored and recorded.

2.4 Biogas And Chemical Analyses (Parameters Monitored And Analyzed)

Daily biogas production rate (L/day) was measured by gas meter (designed by) copped with U-tube manometer. The gas meter was calibrated at 29 ml /click prior to start of the experiment and checked periodically. The CR10X (XXX) was also capable of recording the real-time biogas volume (Koppar and Pullammanappallil 2008). The methane content in the biogas was measured by gas chromatography (GOW-MAC, XXX) using thermal conductivity detector (TCD) and argon as carrier gas (References).

The chemical oxygen demand of both stillage and anaerobic fermented effluent were determined using HACH test kit (XXX). The volatile fatty acids were accessed by HPLC. Total volatile fatty acids were measured by titration method (Reference).

2.5 Techno-Economics Analyses

An ASPEN Plus (AspenTech, Cambridge MA) based process flow-sheeting model was developed for a lignocellulosic ethanol biorefinery (Na et al. 2019 Nashville conference). All sections of a biorefinery including pretreatment, saccharification, fermentation and ethanol recovery were modeled. The flowsheet was based on a bioethanol production model which was validated using operating data from the pre-commercial scale Stan Mayfield Biorefinery Pilot Plant of University of Florida (Gubicza et al., 2016). The AD system was integrated into the process. Detailed operating data for anaerobic digester and biogas yields was obtained from laboratory scale experiments mentioned in previous sections. The impact of introducing anaerobic digestion on the overall economics and energy balance were

investigated. The overall evaluation of the AD system was compared with other biotechnology integration scenarios and downstream management.

RESULTS AND DISCUSSIONS

3.1 Startup Activation

During phase (i) pH of the stillage was adjusted to 7 using 5N sodium hydroxide and buffered using 5 g/L of sodium bicarbonate before being fed to the digester. 300 ml of stillage was fed twice every week for the first week and then increased to 500 ml twice a week. Macro and micro nutrients used in conventional BMP assays were added to the reactor during the start-up phase (Owen, Stuckey et al., 1979). Reactor was fed daily once the inoculum was activated and acclimated to cellulosic ethanol stillage. This allowed the inoculum to be acclimated to the feedstock and to develop biofilm on the activated carbon carrier particles.

3.2 Long-Term Operational Acclimatization

Phase ii: The operational phase of the reactor can be further divided into three phases: (a) elevated loading, (b) normal operation and (c) inhibited phase. During the variable or elevated loading phase, the organic loading rates were gradually increased from 2.11 g sCOD $L^{-1}d^{-1}$ to 8.8 g sCOD $L^{-1}d^{-1}$ to test the organic handling capacity of the reactor. The digester was subjected to an increased organic loading rate of 8.8 g sCOD $L^{-1}d^{-1}$ for a period of 2 days by increasing the flow rate of the feed which in turn reduced the HRT.

After testing elevated organic loading rates, full fledged operation of the reactor was continued at a loading rate of 6.54 g $sCODL^{-1}$ d^{-1}.

Under normal operating conditions, 200 ml of stillage was fed daily at 11:30 AM using a timer. The timer was used to turn on a peristaltic pump for loading ethanol stillage. The methane measurements made over 23 days is reported here. During this period, to investigate the response of the on-line methane sensor to disturbances, the volume of feed was increased to 400 ml on days 1 and 2, 600 ml on day 3, returned to 200 ml for days 4 to 9, increased to 800 ml on day 10, further increased to 1200 ml from days 11-16 and brought back to the normal volume of 200 ml from day 17 [paper citing online paper]

REFERENCES

Belay, N., R. Boopathy, et al. (1997). "Anaerobic transformation of furfural by Methanococcus deltae Delta LH." Applied and Environmental Microbiology **63**(5): 2092-2094.

Bitton, G. (2005). Anaerobic Digestion Of Wastewater And Biosolids.

Bories, A., J. Raynal, et al. (1988). "Anaerobic-Digestion Of High-Strength Distillery Waste-Water (Cane Molasses Stillage) In A Fixed-Film Reactor " Biological Wastes **23**(4): 251-267.

Callander, I. J., T. A. Clark, et al. (1987). "Anaerobic-Digestion Of Wood Ethanol Stillage Using Upflow Anaerobic Sludge Blanket Reactor " Biotechnology and Bioengineering **30**(7): 896-908.

Callander, I. J., T. A. Clark, et al. (1987). "Anaerobic-Digestion Of Wood Ethanol Stillage Using Upflow Anaerobic Sludge Blanket Reactor

" Biotechnology and Bioengineering **30**(7): 896-908.

Callander, I. J., T. A. Clark, et al. (1986). "Anaerobic-Digestion Of Stillage From A Pilot Scale Wood-To-Ethanol Process .1. Stillage Characterization." Environmental Technology Letters **7**(6): 325-334.

Chen, Y., J. J. Cheng, et al. (2008). "Inhibition of anaerobic digestion process: A review." Bioresource Technology **99**(10): 4044-4064.

Fernandez, N., S. Montalvo, et al. (2008). "Performance evaluation of an anaerobic fluidized bed reactor with natural zeolite as support material when treating high-strength distillery wastewater." Renewable Energy **33**(11): 2458-2466.

Fuchs, W., H. Binder, et al. (2003). "Anaerobic treatment of wastewater with high organic content using a stirred tank reactor coupled with a membrane filtration unit." Water research **37**(4): 902-908.

Koppar, A. and P. Pullammanappallil (2008). "Single-stage, batch, leach-bed, thermophilic anaerobic digestion of spent sugar beet pulp." Bioresource Technology **99**(8): 2831-2839.

Lyberatos, G. and P. C. Pullammanappallil (2010). Anaerobic Digestion in Suspended Growth Bioreactors, Humana Press Inc, 999 Riverview Dr, Ste 208, Totowa, Nj 07512-1165 USA.

Mills, T. Y., N. R. Sandoval, et al. (2009). "Cellulosic hydrolysate toxicity and tolerance mechanisms in Escherichia coli." Biotechnology for Biofuels **2**.

Moletta, R. (2005). "Winery and distillery wastewater treatment by anaerobic digestion." Water Science and Technology **51**(1): 137-144.

Paramasivam, S., G. Z. Fortenberry, et al. (2008). "Evaluation of emission of greenhouse gases from soils amended with sewage sludge." Journal of Environmental Science and Health Part a-Toxic/Hazardous Substances & Environmental Engineering **43**(2): 178-185.

Polematidis, I., A. Koppar, et al. (2010). "Biogasification potential of desugarized molasses from sugarbeet processing plants." Journal of Sugar Beet Research **47**(3/4): 89-104.

Shrestha, J. N. (2001). Efficiency Measurement of Biogas, Kerosene and LPG Stoves. Lalitpur, Nepal, Tribhuvan University.

Tian, Z. (2011). Anaerobic Digestion Of Biofuel Production Residues. Agricultural and Biological Engineering. Gainesville, University of Florida. **Ph.D**.

Vijayaraghavan, K. and T. K. Ramanujam (2000). "Performance of anaerobic contact filter in series for treating distillery spentwash." Bioprocess Engineering **22**(2): 109-114.

Whittier, A. C. (1991). Investigations on the Estimation of Inorganic Phosphorous in Animal Tissues. The Journal of Industrial and Engineering Chemistry

American Chemical Society.

Wilkie, A. C., K. J. Riedesel, et al. (2000). "Stillage characterization and anaerobic treatment of ethanol stillage from conventional and cellulosic feedstocks." Biomass & Bioenergy **19**(2): 63-102.

Wolmarans, B. and G. H. de Villiers (2002). "Start-up of a UASB effluent treatment plant on distillery wastewater." Water Sa **28**(1): 63-68.

Tian, Z., Mohan, G. R., Ingram, L., & Pullammanappallil, P. (2013). Anaerobic digestion for treatment of stillage from cellulosic bioethanol production. Bioresource technology, 144, 387-395.

Borja, R., & Banks, C. J. (1995). Response of an anaerobic fluidized bed reactor treating ice-cream wastewater to organic, hydraulic, temperature and pH shocks. Journal of biotechnology, 39(3), 251-259.

De Amorim, E. L. C., Barros, A. R., Damianovic, M. H. R. Z., & Silva, E. L. (2009). Anaerobic fluidized bed reactor with expanded clay as support for hydrogen production through dark fermentation of glucose. International journal of hydrogen energy, 34(2), 783-790.

Blanco, V. D., Encina, P. G., & Fdz-Polanco, F. (1995). Effects of biofilm growth, gas and liquid velocities on the expansion of an anaerobic fluidized bed reactor (AFBR). Water Research, 29(7), 1649-1654.

Gubicza, K., Nieves, I. U., Sagues, W. J., Barta, Z., Shanmugam, K. T., & Ingram, L. O. (2016). Techno-economic analysis of ethanol production from sugarcane bagasse using a Liquefaction plus Simultaneous Saccharification and co-Fermentation process. Bioresource technology, 208, 42-48.

Optimization of Wet Alkali Hydrolysis Process for Treating Dead Livestock and Poultry

Hongzhi Ma[1,2*], Chengxuanyuan Liu[1,2], Yulian Wei[1,2], Fan Fei[1,2]
1 Department of Environmental Science and Engineering, University of Science and Technology Beijing 100083, China
2 Beijing Key Laboratory of Resource-oriented Treatment of Industrial Pollutants, Beijing 100083, China（E-mail: mahongzhi@ustb.edu.cn）

INTRODUCTION

This article systematically studies a wet process alkaline hydrolysis technology using calcium hydroxide as an alkaline catalyst, which is used to treat dead livestock and poultry and produce amino acid liquid fertilizer. By comparing the liquid-phase product characteristics of alkaline hydrolysis and traditional hydrothermal hydrolysis under different temperature conditions (140-220 ℃), the focus was on analyzing indicators such as amino acid nitrogen concentration, nitrogen conversion mechanism, organic composition, and biological toxicity. The results showed that the concentration of amino acid nitrogen was highest in alkaline hydrolysis at 200 ℃, reaching 3026.91 mg/L, significantly higher than the highest value of 642.27 mg/L in hydrothermal hydrolysis. After dilution or acid neutralization, the pH of the alkaline hydrolysis solution can reach 6.86, with a free amino acid content of 16.42 g/L and a moderate element calcium content of 14.02 g/L, which meets the NY 1429-2010 standard. Seed germination experiments and lettuce pot experiments have shown that alkaline hydrothermal solutions have good biological safety and significant growth promoting effects. This study provides a feasible technical path and theoretical basis for the high-value resource utilization of dead livestock and poultry.

MATERIALS AND METHODS

The experiment involved the utilisation of livestock and poultry, both healthy and deceased, supplied by a breeding base. Following mechanical grinding, the samples were thoroughly mixed and stored at -20°C for subsequent use.

Calcium hydroxide (analytical grade) was procured from Sinopharm Chemical Reagent Co., Ltd. The experimental water utilised in this study was deionised water. A miniature magnetic stirring reactor (model YSCLF-FL-250ml) from Shanghai Yusheng Instrument Co., Ltd. was employed to conduct the hydrothermal reaction under stirring conditions. The present study systematically investigated the optimal reaction conditions and mechanism of the alkaline-thermal hydrolysis process for diseased and deceased livestock and poultry. The study's primary objective was to analyse the effect of reaction temperature on the properties of hydrolysis products. A comparative analysis of the differences between alkaline-thermal and hydrothermal hydrolysis products was conducted to elucidate the merits of alkaline-thermal hydrolysis technology in the production of amino acid fertilisers. Concurrently, comprehensive evaluations of the hydrolysate's agricultural applicability were conducted through the following means: fertilizer index testing, safety assessments, seed germination experiments, and potted plant trials. The findings of the present study provide a theoretical foundation and technical support for the high-value utilisation of diseased and deceased livestock and poultry.

RESULT AND DISCUSSION

Temperature is a key factor affecting amino acid yield during thermal hydrolysis. As shown in Figure 1, the concentration of amino acid nitrogen in the alkaline hydrolysate first increases and then decreases with rising reaction temperature. When the temperature increased from 140°C to 200°C, the amino acid nitrogen concentration rose significantly from 1206.9 mg/L to 3026.91 mg/L, representing a 60.5% increase. However, when the temperature further increased to 220°C, the amino acid nitrogen concentration decreased to 2036.74 mg/L, representing a decrease of 32.7%. This phenomenon indicates that moderate temperature increases promote protein hydrolysis and amino acid formation, but excessively high temperatures induce thermal decomposition of amino acids, consistent with existing research findings (Cheng et al., 2022). In contrast, the amino nitrogen concentration in hydrothermal hydrolysate increased continuously with rising temperature, peaking at 642.27 mg/L at 220°C, yet remained significantly lower than that in alkaline hydrolysate. Notably, the amino acid nitrogen concentration in alkaline thermal hydrolysis at 140°C (1206.9 mg/L) already exceeded the maximum value of hydrothermal hydrolysis at 220°C, indicating that

alkaline thermal hydrolysis achieves more efficient protein hydrolysis at lower temperatures.

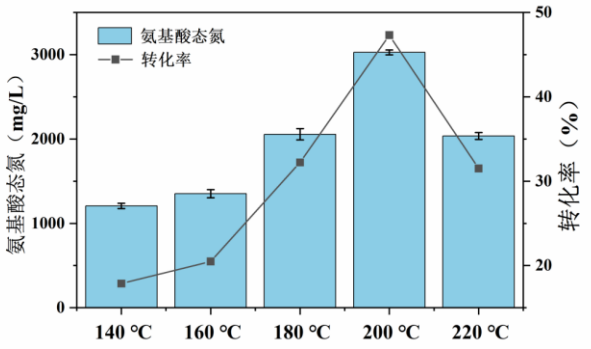

Fig.1. Concentration of amino acid nitrogen in liquid-phase products at different reaction temperatures

In order to meet the growth requirements of acidophilic plants, an acid neutralisation process was performed by adding a 0.1 mol/L HCl solution to the liquid-phase product at a temperature of 200°C. As demonstrated in Figure 2, the pH level exhibited a gradual decrease in conjunction with the increment of HCl addition. Upon attaining a HCl addition of 150 mL, the solution's pH level was found to be stabilised at 6.86, a reading that satisfied the growth requirements of the majority of acidophilic plant species.

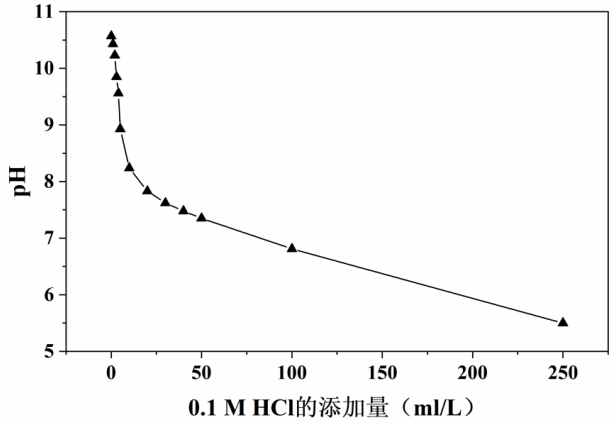

Fig.2. Relationship between the amount of HCl added during acid neutralization and pH change

It is evident that reaction temperature exerts a substantial influence on the migration and conversion patterns of nitrogen within the raw material. As demonstrated in Figure 3-3, amino acid nitrogen constitutes the primary nitrogen-containing component in the liquid-phase products, while soluble protein accounts for an extremely low proportion. At 200°C, the amino acid nitrogen conversion rate was observed to reach its maximum of 47.3%, with the total conversion rate of soluble protein, amino acid nitrogen, and $NH4^+N$ amounting to 66.21%. Under all temperature conditions, the amino acid nitrogen conversion rate was significantly higher than the $NH4^+$ -N conversion rate. This finding indicates that, under alkaline hydrothermal hydrolysis conditions, nitrogen-containing substances in the raw material tend to convert toward amino acid nitrogen. Conversely, hydrothermal hydrolysis exhibited a maximum total conversion rate of 40.29%, with a predominant conversion to $NH4^+$-N. This demonstrates that alkaline thermal hydrolysis not only enhances nitrogen recovery but also optimises its form, rendering it more suitable for use as an amino acid fertiliser.

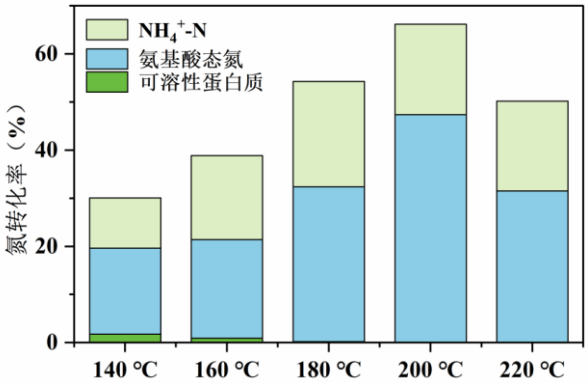

Fig.3.Mechanism of nitrogen conversion of liquid-phase products under different reaction temperatures.

The three-dimensional fluorescence spectral characteristics of the liquid-phase products were analysed at varying reaction temperatures, with the results illustrated in Figure 4. The spectra indicate that the fluorescence signal is predominantly concentrated in Region IV (protein-like peak), while the responses in other regions are comparatively weak. As the temperature increases, the fluorescence intensity in Region IV initially rises and then decreases, indicating that moderate heating promotes protein hydrolysis into protein-like substances (such as amino acids and soluble peptides), thereby increasing their concentration. However, elevated temperatures (for example, 220°C) have been observed to trigger amino acid degradation, resulting in a weakening of the protein-like peak. Concurrently, the intensity of Region V (the humic-like peak) increased in a continuous manner with rising temperature, primarily due to reactions forming humic-like substances under high-temperature conditions (Gao et al., 2020). The previously mentioned fluorescence characteristics are consistent with the variation pattern of amino acid nitrogen concentration, collectively demonstrating that 200°C is the optimal reaction temperature. Consequently, the yield of protein-like substances is maximised, while the excessive formation of byproducts, such as humic-like substances, is effectively suppressed.

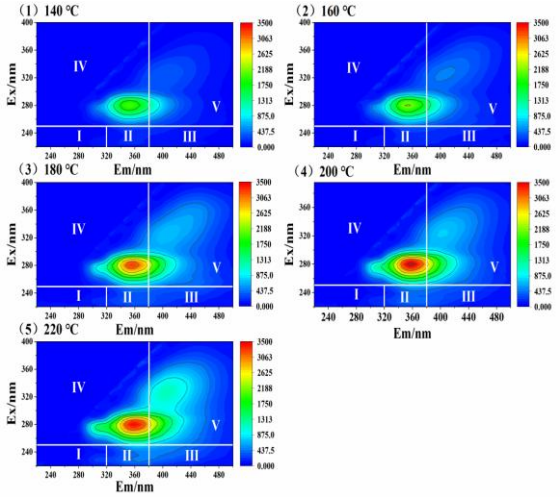

Fig.4. Three-dimensional fluorescence mapping of liquid-phase products under different reaction temperature conditions

The rates of seed germination are demonstrated in Figure 5(a). It is noteworthy that all treatment groups satisfied the fundamental non-toxicity criterion, with approximately 96% of groups attaining full compliance with non-toxicity requirements. A comprehensive analysis revealed that germination rates exhibited no substantial variations across a range of temperatures and dilution levels, consistently maintaining elevated levels. The germination rate at 220°C exhibited a slight decrease in comparison to other temperatures, a phenomenon that may be associated with the accumulation of toxic substances at elevated temperatures. However, it was demonstrated that all dilution gradients were still within the non-toxic standard. It is noteworthy that the alkali-thermal hydrolysis process enhanced the germination performance under elevated temperatures, primarily attributable to its inhibitory effect on the synthesis of inhibitory substances, including furfural and 5-hydroxymethylfurfural (5-HMF).

The alterations in primary root length are demonstrated in Figure 5(b). It should be noted that the analysis was conducted exclusively on experimental groups with GI ≥ 70%. The overall root length exhibited a U-shaped curve, with an initial increase followed by a subsequent decrease in response to rising temperature. The peak value was recorded at 200°C, where the root length reached 2.74 cm. This finding suggests that 200°C is the optimal temperature for optimal plant root and shoot development. At temperatures in excess of 220°C, a marked decline in root length was observed, with values ranging from 1.41 to 1.66 centimetres. This change demonstrated a positive correlation with the concentration of amino acid nitrogen in the liquid phase, with the highest recorded concentration occurring at 200°C. At 220°C, however, amino acid degradation and the accumulation of inhibitors such as furfural and 5-HMF collectively suppressed root growth. With regard to dilution ratios, low dilutions (100–300×) have been observed to inhibit root growth due to excessive organic matter concentration. At a dilution of 500×, the nutrient concentration is optimal, yielding the strongest growth promotion. Furthermore, an increase in dilution (700–1000×) has been shown to weaken the growth-promoting effect due to excessive dilution of nutrients.

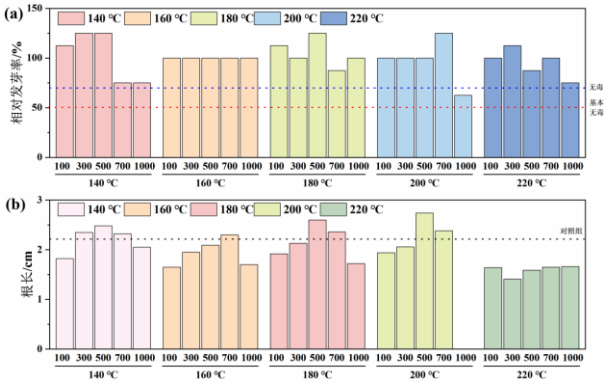

Fig.1 Effect of liquid-phase products on seed germination under different reaction temperature conditions

As demonstrated in Figure 6, the pH of hydrothermal hydrolysate exhibits a gradual increase with rising reaction temperature, while that of alkaline hydrothermal hydrolysate demonstrates a continuous decrease. It has been demonstrated that hydrothermal hydrolysate displays acidic characteristics at low temperatures, a phenomenon attributable to the accumulation of organic acids. As the temperature continues to rise, reactions such as the decomposition of organic acids and the deamination of amino acids cause a gradual shift towards alkalinity. Alkaline hydrothermal hydrolysate, which is initially strongly alkaline due to calcium hydroxide addition, continuously consumes its alkalinity under high-temperature conditions, resulting in a progressive pH decrease. It was observed that all hydrothermal hydrolysate pH values remained within the optimal range for plant growth (6.0–8.0). The alkaline hydrothermal hydrolysate required dilution adjustment; for instance, the 200°C product diluted 80-fold yielded a pH of 8.45, meeting the NY 1429-2010 standard for amino acid water-soluble fertilisers (pH 3.0–9.0). It is evident that further pH adjustment to crop-specific requirements can be achieved through acid neutralisation or analogous processes.

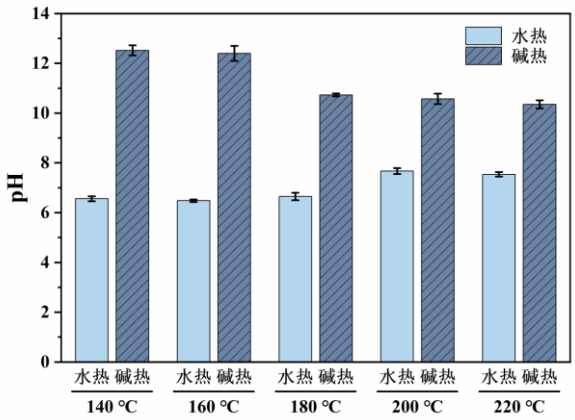

Fig.6 Comparative pH analysis of liquid-phase products

The pH value is a pivotal parameter in evaluating the feasibility of liquid-phase products for fertiliser applications, as its variation directly impacts nutrient bioavailability and crop growth safety. As demonstrated in Figure 6, the pH of hydrothermal hydrolysate gradually increases with rising reaction temperature, while the pH of alkalothermal hydrolysate continuously decreases. Hydrothermal hydrolysate has been shown to exhibit acidity at low temperatures due to the accumulation of organic acids (Zhang et al., 2023).

Struvite pyrolysate cycling technology assisted by thermal hydrolysis pretreatment has been demonstrated as a means of recovering ammonium nitrogen from composting leachate (Li et al., 2022). As the temperature is increased, reactions such as the decomposition of organic acids and the deamination of amino acids gradually shift the substance towards a state of alkalinity. The alkaline pyrolysate, which is initially strongly alkaline due to calcium hydroxide addition, continuously consumes its alkalinity under high-temperature conditions, causing a gradual decrease in pH. It was observed that all hydrothermal hydrolysate pH values remained within the optimal range for plant growth (6.0–8.0). The alkaline hydrothermal hydrolysate required dilution adjustment; for instance, the 200°C product diluted 80-fold yielded a pH of 8.45, meeting the NY 1429-2010 standard for amino acid water-soluble fertilisers (pH 3.0–9.0). It is evident that further pH adjustment to crop-specific requirements can be achieved through acid neutralisation or analogous processes.

CONCLUSION

Alkaline hydrothermal hydrolysis technology not only achieves harmless and reduced-volume treatment of diseased and dead livestock and poultry but also converts waste resources into high-value-added amino acid fertilizers, combining environmental benefits with agricultural application potential. This process significantly outperforms traditional hydrothermal hydrolysis in nitrogen recovery efficiency, product safety, and fertilizer functionality, providing a reliable technical pathway for the green circular utilization of livestock and poultry slaughter waste. Future research should focus on controlling phosphorus precipitation, optimizing recovery processes, and developing composite controlled-release fertilizers to further enhance the system's economic viability and practicality.

REFERENCE

1. Yan Y, Zhang Y, Gao J, et al. Intracellular and extracellular sources, transformation process and resource recovery value of proteins extracted from wastewater treatment sludge via alkaline thermal hydrolysis and enzymatic hydrolysis[J]. Science of The Total Environment, 2022, 852: 158512.

2. Cheng Shan ,Luo Rui ,Tian Hong , et al. Effect of hydrothermal carbonization temperature on transformation path of organic nitrogen in sludge[J]. CIESC Journal, 2022, 73(11): 5220-5229.

3. Wang Lixia ,Liu Yongxia ,Ding Zheli , et al. Influences of rhizosphere pH value on biomass and root growth of banana seedlings[J]. Jiangsu Agricultural Sciences, 2024, 52(22): 154-161.

4. GAO Yuan, HAN Yun, HAN Lu, et al. Effect of thermal hydrolysis treatment temperature on transformation and composition oforganic matter in high solid content sludge[J]. Chinese Journal of Environmental Engineering, 2020, 14(10): 2823-2830.

5. Zhang T, Wu X, Li H, et al. Struvite pyrolysate cycling technology assisted by thermal hydrolysis pretreatment to recover ammonium nitrogen from composting leachate[J]. Journal of Cleaner Production, 2020, 242: 118442.

6. Gao Limin, Guo Dongsen, Cui Lianming, et al. Effects of biodegradable amino acid fertilizer from feather on the growth and quality of pakchoi[J]. Soil and Fertilizer Sciences in China, 2023, (04): 178-183.

EVALUATION OF HEAVY-METAL LEACHING IN RETURNED AND CRUSHED CONCRETE AGGREGATES

Mitali Nag1, Hirofumi Sakanakura1

1 Material Cycles Assessment Research Section, Material Cycles Division, National Institute for Environmental Studies, 16-2 Onogawa, Tsukuba City, Ibaraki Prefecture, Japan

ABSTRACT

This study evaluated the heavy metal release of "returned concrete aggregates" (RCA) that is produced from returned fresh concrete, alongside simulated crushed concrete aggregates (CCA) representing early-stage hardened concrete. A JIS K 0058-1 leaching test assessed the impact of blade and container sizes on metal release, showing that larger blades yielded higher Cr concentrations over time. Cr levels in both RCA and CCA were <0.05 mg/L, far below cement's typical Cr content (5.6–9.3 mg/kg). Cr release from RCA and CCA ranged from 0.06–0.5 mg/kg and 0.07–0.3 mg/kg, respectively. The Cr leaching mechanism was identified as diffusion controlled. This study offers insights that may support future investigations of returned concrete from environmental, economic, technical, and managerial perspectives.

INTRODUCTION

Concrete, with more than 30 billion tons produced every year, is the most widely used material in the world [1]. This is due to its exceptional characteristics: wide availability, inexpensiveness, possibility to form any kind of geometric shapes in the fresh state and to harden in strong and durable structures. Nevertheless, the production of concrete implies several drawbacks related to the consumption of natural resources, carbon emissions and waste production.

One of the biggest problems in terms of waste is returned concrete. This is the residual unset concrete that, for different reasons, is not used at the jobsite and comes back to the ready-mixed concrete plant inside the truck mixer. One of the reasons for returned concrete is that an excess of concrete is necessary to avoid shortage during construction; in other cases, the fresh delivered concrete might not meet the quality specifications (consistency, temperature, time of delivery) and it is rejected by the customer. The amount of returned concrete in industrialized countries varies from 2 to 3% of the overall concrete production; this means that, every year, from 500 to 700 million tons of concrete are not used and come back to the ready-mix concrete plants with the truck mixers; in most cases, it becomes a waste, representing a serious environmental problem at the plant [2]. Japan generates hundreds of thousands of tons of returned plastic concrete annually. According to studies by the Japan Ready-Mixed Concrete Industrial Association (JRMIA), returned concrete accounts for around 2–5% of total concrete production — a large and persistent waste stream.

Only a fraction of all returned concrete may be reused as it is in concrete works, while for the most part, due to the lack of a viable possibility of using it again and transforming it, it must be disposed of, and it is by far the most abundant waste product at the concrete batching plants. Disposing of returned concrete in landfill sites has a heavy impact on the environment which may be expressed in terms of "equivalent" CO_2, the gas responsible for global warming. For concrete sustainability, it is crucial to recycle and recover both returning and hardened concrete. Fresh concrete can seriously burn human skin [3] and harm soil and water [4] due to its alkalinity, but hardened concrete is out of danger.

In Japan, the utilization of returned fresh concrete—often referred to as "residual concrete" or "zancon"—is an area of growing focus within the construction and environmental sectors. Approximately 3 to 5% of ready-mixed concrete produced annually is returned unused, leading to significant waste and environmental impact. Efforts are underway to recycle and repurpose this material, aiming to reduce CO_2 emissions and promote a circular economy. These initiatives reflect Japan's commitment to advancing concrete recycling technologies, promoting sustainability, and reducing environmental impact in the construction industry.

Despite these advancements, the widespread adoption of recycled concrete in Japan faces challenges. The use of recycled aggregates in new concrete is still limited, primarily due to conservative industry practices and stringent standards. However, ongoing research and development efforts, along with initiatives like the Osaka Expo 2025's "Zancon ZERO" project, aim to overcome these barriers and promote the sustainable use of returned concrete.

Promoting the use of recyclable resources supports a recycling-oriented society by reducing natural resource extraction, minimizing environmental impact, and preserving landfill capacity. Although recyclable construction materials are already widely utilized with minimal waste, their use should be further strengthened and trusted. Since these materials may contain environmentally concerning chemicals, both material quality and environmental safety quality must be reliably managed.

Recognizing that managing environmental safety quality is essential for all recyclable materials, this study applies JIS K 0058-1:2005—a Japanese Industrial Standard leaching test method for chemicals in slag and waste materials such as concrete and asphalt. This method assesses the chemical safety of waste-derived materials used in construction sites. In this research, the environmental safety quality of returned concrete aggregates and solidified crushed concrete aggregates was evaluated, along with the mechanisms of heavy metal leaching. We hope these findings will serve as a guide for establishing a social system that harmonizes a recycling-oriented society with low environmental risk.

MATERIALS AND METHODS

Materials

Two types of concrete samples were investigated in this research. The concrete remains after use in the construction site that returned in the ready-mixed concrete plant inside the truck mixer named as “Returned concrete aggregates (RCA)”, and the concrete prepared as simulated solidified concrete and later crushed it as a crushed concrete aggregate named as here “Crushed concrete aggregates (CCA)”. The CCA is prepared specially for experiments to investigate the initial/original state of crushed concrete aggregate. The RCA sample was collected from a local ready-mixed concrete plant in Tsukuba city, Japan. The samples were kept in closed containers and used for experiments.

Methods

The chemical compositions of each sample with different particle sizes have been examined by X-ray fluorescence (XRF) technique. Minerals of the different particle sizes have been investigated by X-ray diffraction (XRD) technique. Based on the JIS standard, we conducted a detailed study on the effects of propeller size, stirring intensity, and stirring time on the leaching of harmful substances. JIS is a propeller type leaching test method with specified regulations. In this study, the samples are used as their original state (no crushing). Two different diameter tanks were used (40 and 30 cm) for the leaching test. According to the JIS leaching test method for chemicals, amount of sample, amount of solvent and the body diameter of the tank are used as shown in **Table 1**. The samples were prepared on weight basis and mixed appropriately. Following mixing, the sample was placed uniformly on the bottom surface of the tank. Ultra-pure water was added to the sample slowly. The mixer is attached with the motor that capable of rotating a mixing blade in the range of 50 rpm to 500 rpm and a mixing blade. Three different sizes of propeller blades made of fluorocarbon resin without leaching and adsorbing of the objective component for measurement was used for maintaining the tank diameter/blade length (D/l) ratios of 2, 3 and 4. Attached the agitator to the tank and fix it so that the mixing blade becomes the middle between the upper surface of sample and the water surface. The conditions of slow, medium,

and fast mixing speed are investigated using three distinct blade sizes. The Liquid-solid ratio (L/S) was set as 10 and the agitation speed was maintained 200 rpm. To investigate the leaching concentration variation with time, samples were collected by using a syringe and a polytetrafluoroethylene (PTFE) membrane filter with a pore size of 0.45 µm at 10 minutes, 1, 2, 4, 6 and 24-hours of intervals. The pH and electrical conductivity (EC) of the filtrate were measured immediately after collection. Concentrations of Cl, F, and SO_4^{2-}, were determined by ion chromatography (Dionex ICS 2100, Thermo Fisher Scientific Inc., Waltham, MA, USA). Concentrations of Al, B, Ba, Cr, Ca, Na, Se, Si, and Zn were measured by ICP-OES (Model 720, Materials 2021, 14, 2534 7 of 15 Agilent Technologies Inc.) and ICP-MS (7500CX, Agilent Technologies Inc.), depending on their concentration level.

Table 1: Experimental condition

Sample	Tank Dia (cm)	L/S	L (L)	S (kg)	Blade length (cm) *(D/l)*	Agitation speed (rpm)	Time (h)
RCA	30	10	10	1	15, 10, 7.5 *(D/l=2, 3, 4)*	200	24
	40		30	3	20, 10 *(D/l=2, 4)*		
CCA	30	10	10	1	15, 10, 7.5 *(D/l=2, 3, 4)*		
	40		30	3	20, 10 *(D/l=2, 4)*		

Table 2: Bulk chemical composition

Compounds Mass (%)	**RCA**	**CCA**
Al_2O_3	10.4	10.2
SiO_2	46.9	51.6
CaO	30.2	25.7
Fe_2O_3	4.95	4.51
MgO	1.64	1.45
K_2O	2.23	2.17
SO_3	1.18	1.32
Na_2O	1.34	2.0
Trace elements (mg/Kg)		
Cr	80	110
Cl	490	470
Mn	730	920
Cu	150	100
Zn	320	190

RESULTS AND DISCUSSION

Physical and chemical characteristics

Samples were prepared for the experiment based on weight basis. The particle density of RCA and CCA samples are 2.58 ±0.008 and 2.60 ±0.002 g/cm^3, respectively, which are within the typical range of concrete (2.3-2.6 g/cm^3).

The XRD patterns of RCA and CCA samples in different size fractions and mixed states were investigated. It was observed that the quartz is the dominant mineral in both concrete and calcite peaks appeared as carbonation evidence. Portlandite disappeared from the CCA sample while being detected in the RCA sample. There is no significant variation in minerals with different particle sizes (data not shown). The chemical composition of RCA and CCA samples are presented in Table 2. It was observed that SiO_2 is the dominant in composition that ranges between 50 to 60% in both samples. CaO was the second abundant compound in both samples ranges between 20-30%. Al_2O_3 were about 10% and Fe_2O_3

were about 5% that found in both RCA and CCA samples. Na_2O, MgO, SO_3, Ke_2O compounds were also detected in both samples. Other trace elements such as Cr, Mn, Cu, and Zn were also detected in both samples**,** calculated by stoichiometric conversion.

Leaching characteristics

pH and EC

With three distinct D/l ratios, the pH and EC of the RCA and CCA samples are shown in Figure 1. Both samples had a high alkaline pH, with the RCA sample having a slightly higher pH than the CCA sample. Cement hydration forms calcium hydroxide, which makes concrete extremely alkaline. This high pH is necessary to prevent rust on embedded steel. At first, the pH increased steadily, but after four hours, it stabilized, and the RCA sample's pH readings were about 12.6 and the pH of the CCA samples were about 11.8 following a 24-hour leaching period. In the two different tank diameter (30 cm and 40 cm) leaching tests with the varying blade sizes (D/l ratios), no discernible pH changes were observed. In Figure (b), a higher EC in RCA indicates that concrete contains more salt or water than CCA. The EC values in the RCA sample were found to be almost four times greater than those in the CCA sample. In both types of concrete samples, larger blade sizes (smaller D/l ratios) exhibited higher EC than smaller blade sizes. EC values rose steadily over the leaching time in all cases.

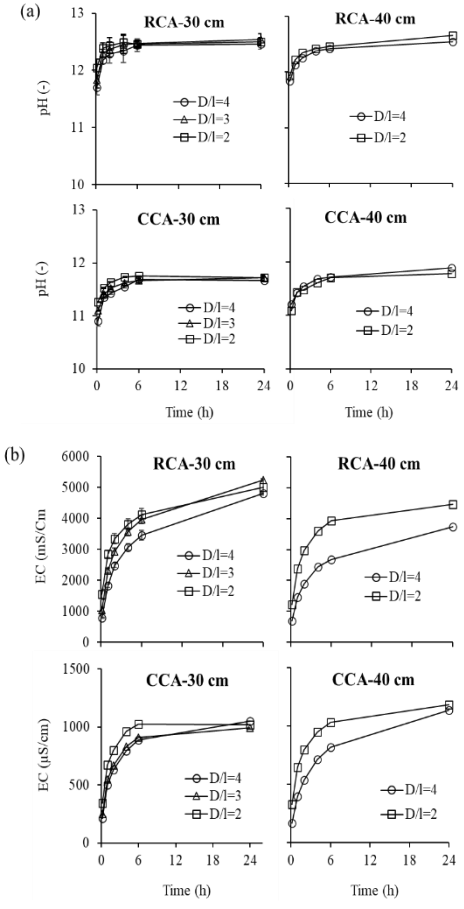

Fig. 1: pH and EC over time

Potential leaching of metals

In Figure 2 it is observed that the Cr concentrations in both samples increased over time, and the larger blade size insists higher concentrations than the small and medium size blades. Chromium (Cr), especially in its toxic hexavalent form (Cr(VI)), can leach out of concrete over time due to a combination of chemical, physical, and environmental factors. Chromium enters concrete primarily from cement and industrial additives like slag or fly ash. It is present as Cr(III) (trivalent) and Cr(VI) (hexavalent). Cr(III) is less soluble and less

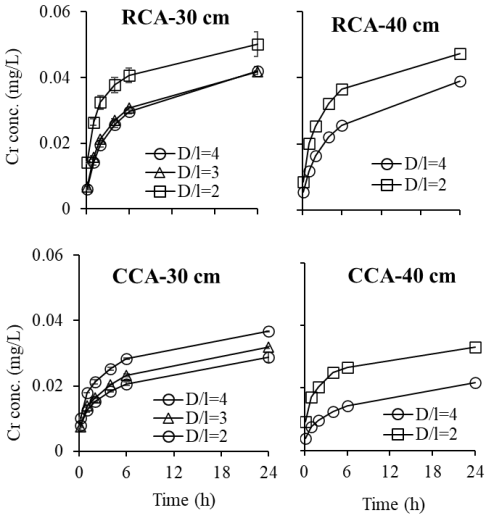

Fig. 2: Cr concentration over time

mobile. However, Cr(VI) is highly soluble, mobile, and toxic. High alkaline environment promotes Cr(VI) formation [5]. Fresh concrete has a high pH (~12.5–13.5) due to calcium hydroxide. This environment can oxidize Cr(III) to Cr(VI), especially in the presence of oxygen or oxidizing agents. Cr(VI) is highly water-soluble and easily leaches out when in contact with moisture or rainwater. Rain, groundwater, or surface water penetrates concrete pores. This water dissolves Cr(VI) and carries it to the surface or out of the concrete matrix. Cr(VI) is a known carcinogen, and leaching from concrete waste or structures can contaminate soil and groundwater. Regulations often limit Cr(VI) levels in cement and concrete products (e.g., EU limit: <2 mg/kg in cement). While Japan does not have a specific national standard for Cr(VI) content in cement, the Japanese soil environmental quality standard for Cr(VI) in leachate is 0.05 mg/L under L/S=10 L/kg. This standard is relevant when considering the potential leaching of Cr(VI) from cement products into the environment. It has been observed that the leaching concentrations of Cr in solidified crushed concrete of CCA sample were lower than the RCA sample. The solidified concrete can stabilize heavy metals, and this is a well-established method in environmental and waste management practices called Solidification/Stabilization (S/S). Solidification encases heavy metals in a solid concrete matrix, reducing their mobility.

In a leaching test, the goal is to understand how much of a substance (like Cr(VI)) could potentially leach out of a material (e.g. cement) into the environment (such as groundwater). While the concentration in the leachate (e.g. mg/L) tells you how much is present per unit volume of liquid, it doesn't fully represent the total amount of substance that might be released from a given mass of material. That's why we often convert concentration to amount, for better environmental risk assessment. Environmental regulations often specify limits in mg/kg of material, not just mg/L in water. It helps estimate total environmental impact — e.g. how much Cr(VI) would leach from 1 ton of cement over time. It allows for standardized comparisons between different materials or batches. For example, a cement that leaches 2 mg/kg Cr(VI) may be acceptable, but one leaching 30 mg/kg may not. Figure 3 shows the calculated Cr release quantity, which is between 0.06 and 0.5 mg/kg for the RCA sample and 0.07 and 0.3 mg/kg for the CCA sample. Concrete samples' Cr(VI) release amounts are significantly lower than the 5.6–9.3 mg/kg, Japanese cement regularity(https://www.taiheiyocement.co.jp/english/csr/fair_trade_fr.html). Discrepancy between the Cr(VI) content in cement (5.6–9.3 mg/kg) and the actual release (leaching) amounts from concrete samples, which are often much lower. Cr(VI) content in cement (e.g., 6.9–9.3 mg/kg) refers to the total water-soluble Cr(VI) present in dry cement powder, not the amount leached from hardened concrete. In hardened concrete, Cr(VI) is often chemically bound or reduced (e.g., by ferrous sulfate), encapsulated in hydration products, and less soluble due to pH buffering and physical barriers. Japanese environmental law does not regulate cement based on total Cr(VI) content. Instead, leaching Cr(VI) is regulated by the Soil Contamination Countermeasure Act by the limit of 0.05 mg/L.

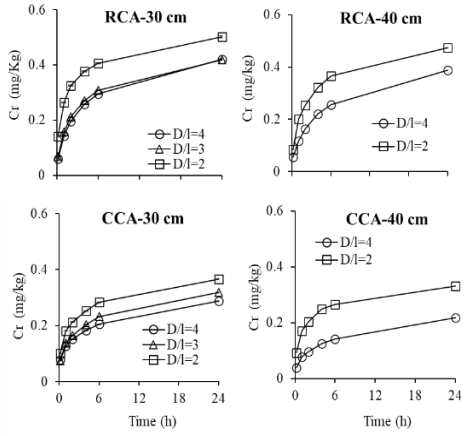

Fig. 3: Cr release amount over time

In the context of concrete and cement chemistry, both chromium and calcium (Ca) play important but different roles. Chromium is typically present as an impurity in cement, mainly from the raw materials or industrial byproducts (e.g., fly ash, slag). Calcium is a major component of cement and concrete, primarily in the form of calcium silicates (C_3S, C_2S) and calcium hydroxide ($Ca(OH)_2$). It contributes to setting, strength gain, and alkalinity. The high pH (alkaline environment) caused by calcium hydroxide in concrete can oxidize Cr(III) to Cr(VI). Cr(VI) is more mobile in high-Ca, high-pH environments, especially in early hydration stages. The calcium content and resulting pH affect how much chromium leaches, which is key in evaluating environmental risks of concrete waste.

It was found that the Ca concentrations were high in the RCA sample and lie between 123 to 481 mg/L shown in Figure 4. This is likely because returned concrete collected from the tank can mix with washing water, increasing the water-to-cement ratio and resulting in a more porous structure with higher void content. On the other hand, the Ca concentration in the CCA samples were lies between 8 to 68 mg/L, which is more than seven times lower than RCA sample. Solidified (hardened) concrete has lower calcium ion (Ca^{2+}) concentrations in its pore solution compared to fresh (plastic) concrete due to several key chemical and physical processes that occur during hydration. The reasons are calcium consumption during hydration where more calcium gets bound into solid phases, thus removing it from the pore solution, decreasing the free Ca^{2+} concentration over time. In fresh concrete, the pore solution is more fluid, and ions move freely. As concrete sets and hardens, the capillary pores become finer and more disconnected, which limits diffusion and mobility. This physical trapping further reduces the effective concentration of free Ca^{2+} in the accessible solution. The increase in Ca, Na, and Mg might indicate early dissolution of hydrated cement phases. Na and K concentrations were found gradually increased with time and range between 6-20 mg/L and 5-20 mg/L, respectively, in both RCA and CCA samples in both types of tanks. B and F^- concentrations were all found below the soil contamination standard limits.

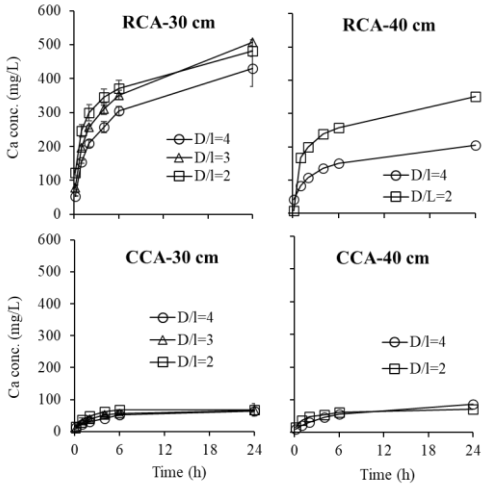

Fig. 4: Ca concentrations over time

MECHANISMS OF THE RELEASE OF METALS

Leaching is the dominant mechanism for heavy metal release, and it occurs due to contact with water (e.g., rain, groundwater, acidic water). Key factors are pH dependency since many metals are more soluble in low pH (acidic) conditions; carbonation that react with CO_2 lowers the pH of concrete, increasing metal solubility; dissolution of cement phases by decomposition of $Ca(OH)_2$ and C-S-H phases can release metals.

Diffusion is another important mechanism for heavy metal leaching. Heavy metals can slowly move through the concrete pore structure over time via diffusion [6]. This is often slow due to the low permeability of concrete but becomes significant over long durations.

In the leaching test, to investigate the diffusion mechanism, the specific surface area of particle was calculated by summing the particle size distribution across each diameter, as expressed in Eq. 1.

$$S = \sum \left[\frac{6.w_i}{\rho_i.d_i}\right] \quad (1)$$

Where S is the specific surface area (m^2kg^{-1}), w_i is each particle size fraction, ρ_i is the density of the material (kgm^{-3}) and d_i is the mean diameter of the particle each size range (cm). The concentration in the first fractions would be wash-off of soluble attached on the surface [7]. Figure 5 shows release flux of Cr as an example. The first two fractions were not plotted because of a high value caused by surface wash-off in some conditions. In each fraction, the mean value of the release flux between the sampling times is calculated from Eq. 2.

$$J_i = \frac{C_{out}V}{mS(t_i - t_{i-1})} \quad (2)$$

where $C_{out,i}$ is the released concentration of the component in fraction i (mgm^{-3}), V is the volume of the leachate (m^3), m is the total mass of the sample (kg), and t_i is the sampling time of the fraction. If the slope of the linear regression line between log J_i and log $\{(\sqrt{t_{i-1}} + \sqrt{t_i})^2/4\}$ is in the range -0.50 ± 0.15, then diffusion-controlled release is considered to occur. In that case the effective diffusion coefficient in each fraction $D_{e,i}$ ($m^2\ s^{-1}$) can be calculated by Eq. (3).

$$D_{ei} = \pi . \bar{t_i} . (\frac{J_i}{C_0})^2 \quad (3)$$

where C_0 (mg m^{-3}) is the internal concentration, such as total content and availability. As the availability value differs by its protocols, in this study we adopted total content value. The effective diffusion coefficient, D_e, is calculated from the average of -log $D_{e,i}$. Finally, the cumulative release M in a fixed time such as 100 years is estimated from Eq. 4.

$$M = 2C_0\sqrt{\frac{D_e t}{\pi}} \quad (4)$$

In Figure 5, RCA and CCA samples, every flux declined linearly. The correlation coefficient was in the range 0.998 ± 0.001 (mean ± SD) for all samples. Thus, flux can be adequately represented by two parameters: the slope and the interception of the linear regression lines. If a release occurs in the internal diffusion mechanism, the slope would ideally be shown as -0.50, or in the range -0.35 to -0.65.[8]. In Figure 5, the slopes obtained under the three different conditions fall within and nearly close in the typical diffusion range, indicating that the mechanism is diffusion-controlled. The effective diffusion coefficients of the RCA and CCA samples were determined to be 1 x 10^{-16} and 1 x 10^{-17} m^2 s^{-1}, respectively. The variation in blade size has little impact on the diffusion coefficients. The 100 years cumulative release in RCA and CCA samples were estimated as 95.4 and 64.8 mg/m^2, respectively, with D/l=2.

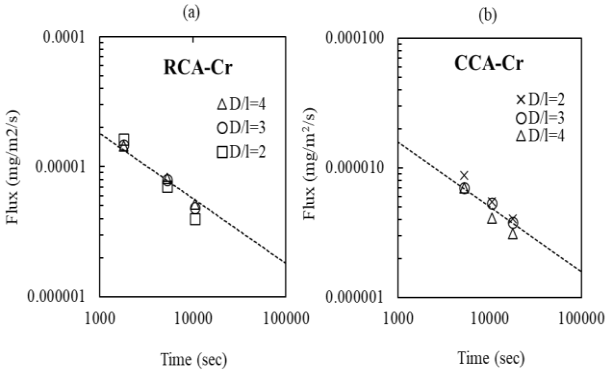

Fig. 5: Changes in the flux of Cr throughout the diffusion test. Dotted lines show a slope of -0.5.

CONCLUSIONS

This research has evaluated the returned concrete aggregates environmental risk by measuring the heavy metals leaching behavior and physical and chemical characteristics. Besides, a simulated crushed concrete aggregate has also been evaluated as a hardened concrete at initial stage in construction. In addition, according to JIS K 0058-1 leaching test the mixing of liquid and solid by using different blade sizes and different container sizes effects on heavy metal leaching has been investigated. The results evaluated that the larger blade size insists on releasing higher concentrations than medium and smaller blade size over time. This study confirmed that the leaching of Cr concentrations is below <0.05 mg/L in both returned and crushed concrete aggregate. Amount of Cr released from concrete in the returned concrete (RCA) and crushed concrete aggregates (CCA) samples in this investigation were ranged 0.06-0.5 mg/kg and 0.07-0.3 mg/kg, respectively. These amounts are considered low because the standard amount of Cr in cement in Japan is between 5.6 and 9.3 mg/kg. B and F^- ion were detected in lower concentrations than Japan soil standards. Most of the other toxic heavy metals were found below the detection limits. The leaching mechanism of Cr was identified as diffusion controlled. The 100-year cumulative releases of the RCA and CCA samples were calculated as 95.4 and 64.8 mg/m², respectively, based on the D/l = 2.

As a research implication, this study may help researchers who will investigate the returned concrete from the environmental, economic, technical, and managerial point of view. In terms of the practical implication, it may attract the attention of industrial practitioners to benefit from such waste. As a social implication, the selection of suitable methods of processing the returned concrete can save and enhance the sustainability of the overall environment and affect society positively.

REFERENCES

[1] Xiao J, Zou S. Cement at 200: towards net-zero fully recycled concrete. Nature. 2024 Jul;631(8022):740. doi: 10.1038/d41586-024-02395-5. PMID: 39043906.

[2] Ferrari Giorgio, Miyamoto Mitsuya, Ferrari Alberto, New sustainable technology for recycling returned concrete, Construction and Building Materials, Volume 67, Part C, 2014, Pages 353-359.
[3] W. Peters, Alkali burns from wet cement, Can. Med. Assoc. J. 130 (1984) 902-904.
[4] J.A.F. Papi, Recycling of fresh concrete exceeding and wash water in concrete mixing plants, Mater. Const. 64 (2014) 1-9.
[5] Frías, M.; Sánchez De Rojas, M.I. Total and soluble chromium, nickel and cobalt content in the main materials used in the manufacturing of Spanish commercial cements. Cem. Concr. Res. 2002, 32, 435–440).
[6] Huixia Lu, Fang Wei, Jingchun Tang, John P. Giesy,Leaching of metals from cement under simulated environmental conditions, Journal of Environmental Management, Volume 169,2016, Pages 319-327, ISSN 0301-4797, https://doi.org/10.1016/j.jenvman.2015.12.008.
[7] Hirofumi Sakanakura, Masahiro Osako, Akiko Kida. Effect of exposure test conditions on leaching behavior of inorganic contaminants from recycled materials for roadbeds. Waste Management, Volume 29, Issue 5, 2009, Pages 1658-1665.
[8] Sakanakura H, Mizutani S, Osako M, Kida A, Tasaki T, Sakai S. Evaluation of grains and mortars of waste molten slag by diffusion test. Proceeding of WASCON 2003, p 281–290.

Aeration-Enhanced Acid Leaching of Heavy Metals from Municipal Solid Waste Incineration Fly Ash

Pengfei Li[1*], Hirofumi Nakayama[1], Teppei Komiya[1], Takayuki Shimaoka[1, 2].

1 Department of Civil Engineering, Faculty of Engineering, Kyushu University, 744 Motooka, Nishi-ku, Fukuoka 8190395, Japan
2 Kyushu Environmental Evaluation Association, 1-10-1 Matsukadai, Higashi-ku, Fukuoka 813-0004, Japan

Keywords: Fly ash, acid leaching, heavy metals, aeration, metallic aluminum.

Abstract:

Municipal solid waste incineration (MSWI) is a prevalent method for waste disposal, leading to the generation of hazardous fly ash containing toxic heavy metals. The acid-leaching methods are used to recover heavy metals from fly ash. But the leaching rate of lead (Pb) and copper (Cu) are low. This study explores an aeration-enhanced acid leaching process to improve the leaching efficiency of these metals, with a focus on mitigating the challenges posed by metallic aluminum (Al^0) in the ash. Fly ash samples were subjected to both conventional and aeration-enhanced acid-leaching. Aeration was found to significantly increase the leaching efficiency of Pb and Cu, reaching leaching rates of approximately 85% and 90% respectively, in contrast to about 0% observed without aeration. Additionally, the reduction in chlorine content and the potential for using treated fly ash in cement production were evaluated. The findings demonstrate that aeration can effectively enhance the leaching process, offering a cost-effective alternative for the treatment and resource recovery from MSWI fly ash.

1. Introduction

In Japan, incineration is the most adopted method for municipal solid waste disposal due to its benefits, including energy recovery and reduction of MSW mass and volume (Hjelmar 1996). However, this process generates municipal solid waste incineration (MSWI) fly ash, which is classified as hazardous waste due to containing toxic elements, such as Pb, Cd, Cr and Hg, and trace amounts of persistent organic pollutants (Zhang et al. 2021; Shunda Lin et al. 2022). Most of the MSWI fly ash was landfilled after stabilization to decrease the potential leaching of the toxic elements (Zhang et al. 2021; Fan, Wang, and Zhang 2018). However, fly ash contains heavy metals, including zinc (Zn), lead (Pb), and copper (Cu), in significant concentrations, which can not be recovered and reused through landfilling (Quina et al. 2018; Tang et al. 2019; 2022; 2018).

In Europe, the acid-leaching methods are used to dispose of fly ash to recover heavy metals (Zn, Pb and Cu) (Quina et al. 2018; Karlfeldt Fedje and Andersson 2020; Zucha et al. 2020). In Switzerland, about 60% of the fly ash is treated by an acid-leaching process called FLUWA, in 2017 (Weibel et al. 2018). This method achieves mass reduction and resource recovery from fly ash. This approach has been established since 1995, involving the leaching of fly ash with hydrochloric acid collected from flue gas treatment systems (Weibel et al. 2021). Swiss fly ash contain up to 6.6 wt.% Zn, 1.9 wt.% Pb, 0.6 wt.% Cu, and 0.05 wt.% Cd make it suitable to be treated by this method and the fly ash samples in Japan, exhibited similar metal concentrations (Zucha et al. 2020; Li and Shimaoka 2023).

However, the presence of metallic aluminum

(Al^0) in fly ash leads to the formation of metallic copper (Cu^0) and metallic lead (Pb^0) in the acid-leaching process (Weibel et al. 2018; 2021; Zucha et al. 2020). Cu^0 does not react with hydrochloric acid; although Pb^0 can react, the reaction rate is slow. Consequently, using this method, the efficiency of leaching Cu and Pb from fly ash is relatively low. Weibel et al. employed hydrogen peroxide as an oxidizing agent, leading to a significant increase in the leaching efficiency of Cu and Pb from fly ash, with Cu leaching improving from 0% to 30% and Pb leaching from 11% to 66% (Weibel et al. 2021). Enhancing the efficient leaching of Cu and Pb from fly ash not only improves the resource recovery efficiency of the process but also mitigates the environmental impact of treated fly ash. However, this approach increases the cost of the treatment method. Therefore, there is a need to find a cheaper method to leach copper and lead from fly ash.

In this study, air was employed as an oxidizing agent to enhance the leaching of Pb and Cu from fly ash. The significance of this research lies in investigating the effect of aeration on the leaching efficiency of heavy metals from fly ash using the acid leaching method. Additionally, the impact of aeration on the speciation of heavy metals in the leached fly ash was examined. This study aims to lower the cost of fly ash leaching treatment and offer insights into the design of leaching reactors.

2. Materials and methods

2.1. Materials

The fly ash samples used in this study were collected from a stoker grate incineration facility in F City, Japan. Two batches of samples were taken, labeled as Fly ash A and Fly ash B. The fly ash samples were initially desiccated and preserved within an air-tight container following collection. In Japan, municipal solid waste management involves a categorization process aimed at facilitating resource retrieval and appropriate disposal practices. However, methodologies for classification exhibit regional disparities. In F City, municipal solid waste undergoes sorting into four distinct categories: combustible refuse, non-combustible refuse, glass and PET bottles, and bulky refuse. At this incineration plant, combustible refuse and combustibles separated from non-combustible, glass and PET bottles, and bulky refuse to constitute the primary waste inputs.

2.2. Leaching experiments

2.2.1. Acid leaching

Fly ash A was used in this part of the experiment. A 200 ml conical flask was filled with 20 g of fly ash and 100 ml of deionized water. The mixture was then heated to a specified temperature: room temperature (RT), 60℃, or 80℃. A magnetic stir bar was added to the conical flask to ensure proper mixing, and the contents were vigorously shaken. Subsequently, the conical flask was placed in a water bath heated to the specified temperature. The magnetic stir bar within the flask was set to rotate at a speed of 800 rpm, intensely stirring the ash slurry throughout the experiment. 36% hydrochloric acid (HCl) was added to achieve a pH of 2±0.05. The pH was maintained at this level for a duration ranging from 15 to 360 min. After the specified time had elapsed, the conical flask was removed from the water bath, and the ash slurry was transferred to a 250 ml centrifuge tube. The centrifuge tube containing the ash slurry was then centrifuged for 20 min at 3500 rpm. This process allowed for the separation of the leachate from the solid particles. The leachate was further filtered using a 0.45-μm filter membrane to remove any remaining solid particles. The solid phase obtained from the centrifugation was washed thrice with 20 ml of deionized water each time.

Following the washing step, the liquid phase obtained from the washing process was

combined with the previously filtered leachate. The leachate was allowed to cool to room temperature. The volume of the leachate was then adjusted to 250 ml using deionized water, ensuring a consistent book for subsequent analyses.

2.2.2. Aeration acid leaching

Fly ash B was used in this part of the experiment. Fly ash (140g) was added to a 1 L reaction vessel. Subsequently, 700 ml of deionized water and 80 ml of HCl (36%) were introduced. The pH was maintained at 2±0.01 using an automatic titrator (AT-700 KYOTO ELECTRONICS MFG.CO., L TD.) with 5 mol/L HCl while stirring at 400 rpm. Aeration of the fly ash slurry was conducted at airflow rates of 0 L/min and 8 L/min, with the reaction vessel sealed to prevent air ingress during the 0 L/min condition. The reaction proceeded for 2, 3, 4, 5, 6, and 7 h, during which dissolved oxygen concentrations in the slurry were measured and recorded. Upon completion of the reaction, centrifugation at 3000 rpm for 5 min was performed to separate the slurry. The leached fly ash was washed with 200 ml of water twice and dried at 105℃ for 24 hours. The volume of separated leachate was measured, and then leachate was diluted with HNO_3 (1%) before testing.

2.3. Determination of metallic aluminum content

The metallic aluminum content was determined by oxidizing Al^0 with H_2O under high pH conditions (Equation (1)) and measuring the generated gas using an Oxitop-C pressure testing instrument. The Al^0 content was calculated using the ideal gas law:

$$Al^0 + 3H_2O \rightarrow Al(OH)_3 + 1.5H_2 \quad (1)$$

Theoretically, all base metals can produce hydrogen upon contact with water. In a 1.114 L glass bottle, 25 g of fly ash and a magnetic stirrer were placed, and the atmosphere was rendered inert by flushing with N_2 gas for approximately 5 minutes. Subsequently, 100 ml of 1 M NaOH solution was added, and the bottle was immediately sealed with the Oxitop-C device manufactured by WTW (Xylem Analytics, Germany). The total volume of fly ash, magnetic stirrer, and NaOH solution was 112 ml. Pressure and temperature were monitored every hour using the Oxitop-C device and a thermometer, respectively, for at least 8 hours until equilibrium was achieved.

The metallic aluminum content is calculated using the following formula:

$$C = \left(\frac{P_1}{T_1} - \frac{P_0}{T_0}\right) \times \frac{V}{R} \times \frac{27}{1.5 \times 25} \times 100 \quad (2)$$

Where, C is the metallic aluminum content, expressed as mass percentage (%); P_0 and T_0 are the initial pressure and temperature, respectively, in pascals (Pa) and kelvin (K); P_1 and T_1 are the pressure and temperature after the reaction reaches equilibrium, respectively, in pascals (Pa) and kelvin (K); V is the volume of the gas in cubic meters (m^3); R is the ideal gas constant, in joules per mole per kelvin (J/(mol·K)). The content of hydrogen gas generated was tested using a Shimadzu GC-8A gas chromatograph.

2.4. Chemical analysis

The elemental composition of the fly ash samples was determined using the X-ray fluorescence technique (XRF, ZSX Primus II, Rigaku). The concentration of heavy metals in liquid samples was analyzed by ICP-OES (Agilent Technologies).

2.5. Mineral composition analysis

Fly ash B and Leached ash B samples, which had been leached for 5 hours, were used in this part of the experiment. For the elucidation of heavy metal speciation distributions, a modified three-step sequential BCR (European

Community Bureau of Reference) extraction procedure was employed. An adjustment was made to the first step of the BCR extraction to accommodate the high alkaline content of fly ash. Specifically, the acetic acid concentration was increased from 0.11 mol/L to 0.7 mol/L to ensure thorough leaching of heavy metals bound to carbonate fractions. The extracted fractions were classified into exchangeable/carbonate (F_1), reducible (F_2), oxidizable (F_3), and residual (F_4) fractions. Each extraction step involved centrifugation at 3000 rpm for 15 minutes, followed by filtration through a 0.45μm filter membrane.

Furthermore, an internal validation process was conducted to evaluate the reliability of the sequential extraction method. This involved calculating the recovery percentage by comparing the sum of the four fractions (F_1, F_2, F_3, and F_4) with the total concentrations of heavy metals obtained through pseudo-total digestion.

$$\text{Recovery rate}=\frac{F_1+F_2+F_3+F_4}{\text{Total concentration}}\times 100\ (\%) \qquad (1)$$

3. Result and discussion

3.1. Characterization of the raw fly ash samples

According to **Table 1**, Fly ash A contains 5.09% Zn, 1.11% Pb, 0.40% Cu, 5.28% Sb, and 5.28% K. Fly ash B contains 6.19% Zn, 1.83% Pb, 0.46% Cu, 6.40% Sb, and 6.40% K. Based on the Chinese geological and mineral industry standards, the Zn content in both Fly ash A and B meets the industrial grade range of 3.0-6.0% (DZ/T 0214-2020). The Pb content in Fly ash A exceeds the specified cut-off grade range of 0.5-1.0%, and the Pb content in Fly ash B meets the minimum industrial grade of 1.5-2.0% (DZ/T 0214-2020). Both Fly ash A and B meet the Sb cut-off grade range of 0.5-0.7% (DZ/T 0201-2020). The Cu content in both Fly ashes is close to the cut-off grade of 0.5% (DZ/T 0214-2020). Additionally, the K content in both Fly ashes reaches the minimum industrial grade of 2% (DZ/T 0212.2-2020).

The material with metal content greater than the cut-off grade is designated as ore because, under the existing economic situation, not only will this material pay for the cost of mining, processing, and refining, but also it will generate some profit (Asad, Qureshi, and Jang 2016; Thompson and Barr 2014; Hagni, Hagni, and Demars 1991). The minimum industrial grade of an ore refers to the minimum concentration or grade of valuable minerals or elements within the ore that is required to be economically feasible and suitable for industrial extraction and processing (Hagni, Hagni, and Demars 1991). An additional advantage of fly ash, compared to traditional ores, is that it eliminates the need for mining operations and long-distance transportation. These two fly ash samples are economically viable as raw materials for recovering valuable metals due to the combination of these factors.

The content of metallic aluminum in Fly ash A and B is 0.21% and 0.20%, respectively. The hydrogen gas content generated from Fly ash A and B is 8.53% and 7.62%, respectively. The presence of hydrogen gas indicates that metallic aluminum is indeed present in the fly ash.

3.2. Acid leaching

Tang et al.'s research demonstrates that HCl exhibits higher efficiency in leaching heavy metals, mainly Pb, from fly ash compared to HNO_3 and H_2SO_4 (Tang and Steenari 2016). This is attributed to the ability of Cl^- to form soluble complexes with Pb^{2+}, facilitating its leaching, while SO_4^{2-} tends to form a precipitate with Pb^{2+} (Weibel et al. 2018). Additionally, the study reveals that lower pH levels contribute to higher leaching efficiency, with pH 2 yielding excellent results (Tang and Steenari 2016). The solid-to-liquid ratio is also essential, significantly affecting lead leaching (Tang and

Steenari 2016). Under pH 2 and a solid-to-liquid ratio of 5, leaching for 72 h resulted in a nearly 100% leaching efficiency for Pb, whereas ratios of 20 and 40 achieved only 40% and 20% leaching, respectively (Tang and Steenari 2016). A lower solid-to-liquid ratio promotes a higher chloride ion concentration in the leachate, which enhances the leaching of Pb (Weibel et al. 2018). Therefore, pH 2 and a solid-to-liquid ratio of 5 were adopted in this study.

Table 1

The concentration of valuable metals in fly ash samples.

Sample	The concentration of valuable metals (wt. %)					
	Zn	Pb	Cu	Sb	K	Cl
Fly ash A	5.09	1.11	0.40	0.95	5.28	25.24
Fly ash B	6.19	1.83	0.46	0.98	6.40	27.66
Leached ash A (3h, 80°C)	1.35	0.30	0.055	2.31	0.52	0.41
Leached ash B (5h, non-aerated, RT)	4.14	5.44	1.89	2.99	0.40	0.31
Leached ash B (5h, aerated, RT)	5.09	0.64	0.14	3.12	0.45	0.48
Leached ash B (5h, aerated, 80°C)	1.28	0.52	0.078	2.76	0.38	0.52
Cut-off grade	1.5-2.0[a]	0.5-1.0[a]	0.5[a]	0.5-0.7[b]	0.5[c]	-
Minimum industrial grade	3.0-6.0[a]	1.5-2.0[a]	0.7[a]	1.0-1.5[b]	2.0[c]	-

[a]: DZ/T 0214-2020: Specifications for copper, lead, zinc, silver, nickel, and molybdenum mineral exploration.

[b]: DZ/T 0201-2020: Specifications for tungsten， tin， mercury, and antimony mineral exploration.

[c]: DZ/T 0212.2-2020: Specifications for salt mineral exploration—Part 2: Present saline lake mineral.

3.3. Acid leaching

Tang et al.'s research demonstrates that HCl exhibits higher efficiency in leaching heavy metals, mainly Pb, from fly ash compared to HNO_3 and H_2SO_4 (Tang and Steenari 2016). This is attributed to the ability of Cl^- to form soluble complexes with Pb^{2+}, facilitating its leaching, while SO_4^{2-} tends to form a precipitate with Pb^{2+} (Weibel et al. 2018). Additionally, the study reveals that lower pH levels contribute to higher leaching efficiency, with pH 2 yielding excellent results (Tang and Steenari 2016). The solid-to-liquid ratio is also essential, significantly affecting lead leaching (Tang and Steenari 2016). Under pH 2 and a solid-to-liquid ratio of 5, leaching for 72 h resulted in a nearly 100% leaching efficiency for Pb, whereas ratios of 20 and 40 achieved only 40% and 20% leaching, respectively (Tang and Steenari 2016). A lower solid-to-liquid ratio promotes a higher chloride ion concentration in the leachate, which enhances the leaching of Pb (Weibel et al. 2018). Therefore, pH 2 and a solid-to-liquid ratio of 5 were adopted in this study.

3.3.1. Impact of temperature on heavy metal leaching

As shown in **Fig. 1** (a), increasing the temperature significantly enhances the leaching rate of Zn. Furthermore, Zn in the fly ash achieves a relatively high leaching rate within a short period, and extending the leaching time does not markedly improve the leaching efficiency of Zn. As depicted in **Fig. 1** (b) and 1

(c), increasing the temperature significantly accelerates the leaching of Pb and Cu, although the maximum leaching rates of Pb and Cu are not significantly affected by temperature. **Fig. 1** (d) shows that temperature has little impact on the leaching efficiency and process of Cd.

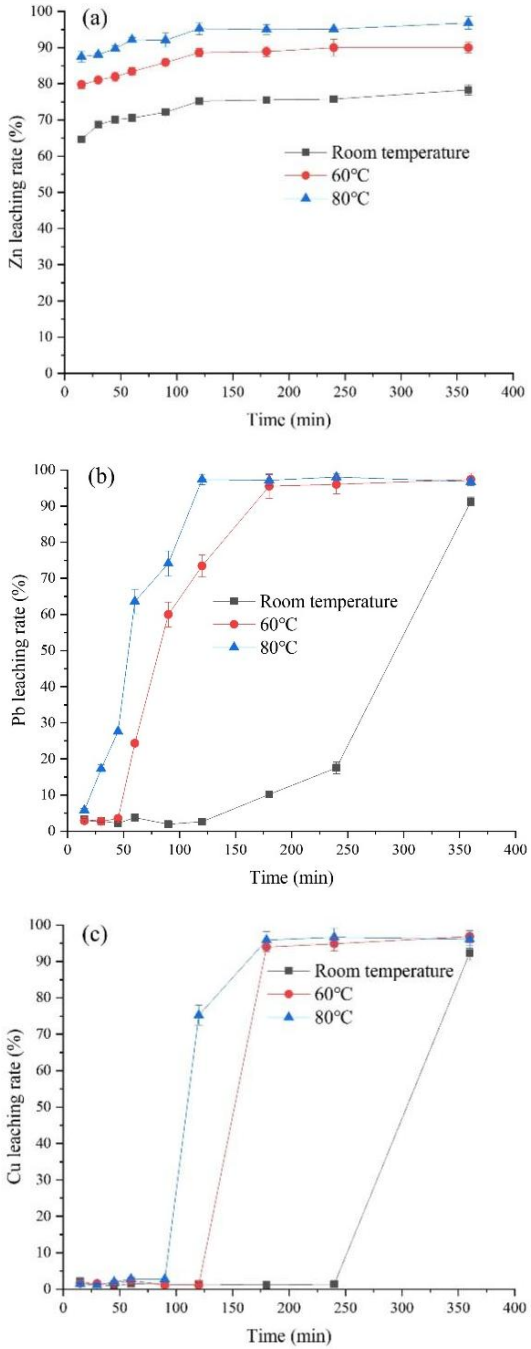

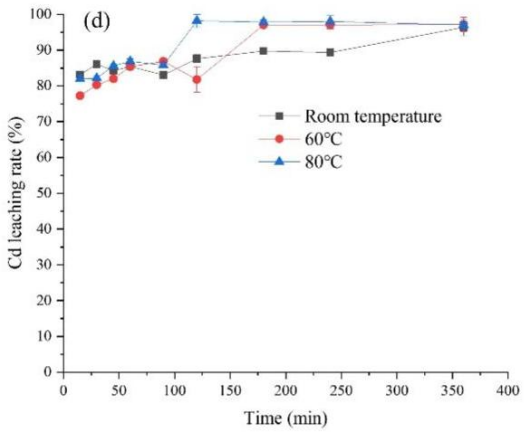

Fig. 1. The impact of temperature on the leaching rates of heavy metals from fly ash: (a) Zn; (b) Pb; (c) Cu; (d) Cd.

3.3.2. Sequential leaching phenomenon

Fig. 2 illustrates the leaching rates of Al, Pb, and Cu over time at different temperatures. It can be observed that the leaching of Al occurs earlier than that of Pb, and Pb leaches earlier than Cu, demonstrating a clear sequential leaching order for these metals. In **Fig. 2** (a), at room temperature, the leaching of Al peaks at 180 min, followed by a noticeable leaching of Pb. Before Pb reaches its peak leaching rate, Cu shows no significant leaching. In **Fig. 2** (b), at 60°C, the leaching of all three metals accelerates but still exhibits a clear sequential order. Al's leaching rate stabilizes at 60 min, followed by a noticeable leaching of Pb. Cu does not show significant leaching before Pb's leaching rate reaches its peak. In **Fig. 2** (c), at 80°C, the leaching rates of all three metals further increase but maintain a distinct sequential order. This phenomenon suggests that during the leaching process, Al^0 in the fly ash undergoes a displacement reaction with Pb and Cu, forming an Al-Pb-Cu alloy. Consequently, Al, Pb, and Cu leach into the solution in order of their activity.

Swiss researchers discovered the formation of such an alloy. However, in their study, the leaching efficiencies of Pb and Cu were very low without the addition of H_2O_2 (Weibel et al. 2018;

2021). This is because the reaction rate of Pb^0 with hydrochloric acid is very low, and Cu^0 cannot react with hydrochloric acid without an oxidizing agent. This study presents a stark contrast to the findings of the Swiss researchers. In this study, the leaching rates of Pb and Cu reached around 95%, a significant increase compared to the low leaching efficiencies reported by the Swiss researchers (Weibel et al. 2018; 2021). This discrepancy could be attributed to the unique conditions of our experiment, including the small reactor volume and vigorous stirring, which allowed oxygen to participate in the leaching reaction. To test this hypothesis, we designed an aeration leaching experiment.

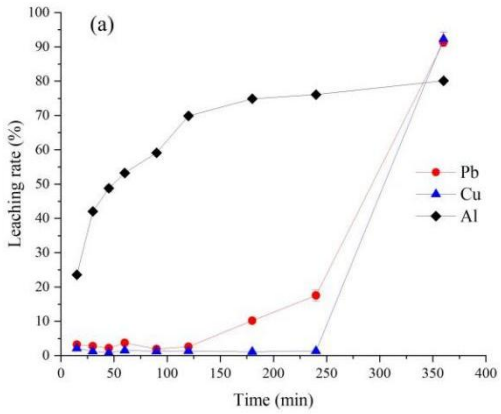

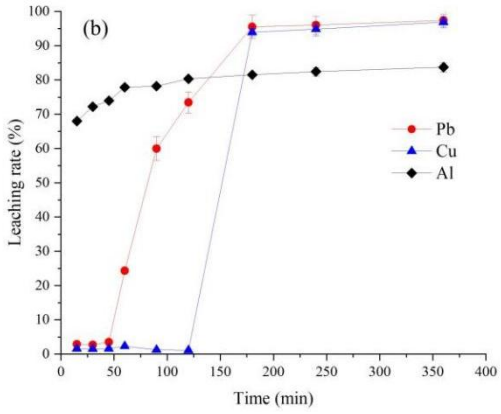

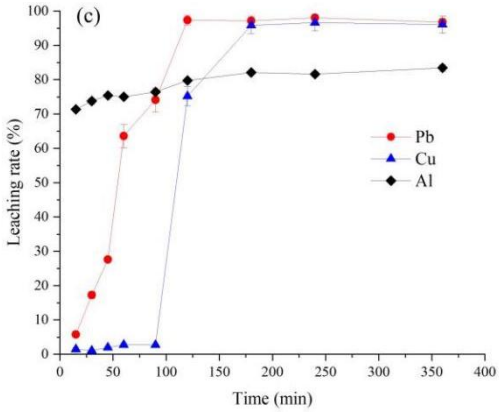

Fig. 2. Sequential leaching Behavior of Al, Pb, and Cu at Different Temperatures: (a) Room Temperature; (b) 60℃; (c) 80℃.

3.2.3. Impact of aeration on heavy metal leaching

Fig. 3 (a) depicts the aeration leaching reaction apparatus. When aeration is not applied, the reactor is sealed to minimize the influence of air on the leaching reaction. As shown in **Fig. 4** (a), when the aeration rate is 0 L/min, Cu is almost not leached, and the leaching rate of Pb is also very low. **Fig. 4** (b) shows that at an aeration rate of 8 L/min, both Pb and Cu can be effectively leached, exhibiting a sequential leaching phenomenon. Comparing **Fig. 4** (a) and 4 (b), it can be observed that the leaching of Zn is not affected by the aeration rate. Comparing **Fig. 3** (a) and 3 (b), it is evident that aeration significantly affects the color of the leachate. Under an aeration rate of 8 L/min, the leachate is light green, likely due to the leaching of copper. **Fig. 4** (c) illustrates the changes in the dissolved oxygen concentration in the slurry under different aeration rates. From **Fig. 4** (c), it is evident that at an aeration rate of 0 L/min, the dissolved oxygen in the slurry gradually decreases. At an aeration rate of 8 L/min, the dissolved oxygen in the slurry fluctuates between 1-2 ppm initially, then gradually increases around 5 hours, eventually stabilizing between 5-6 ppm. Comparing **Fig. 4** (b) and 4 (c), it can be noted that the rise in dissolved

oxygen coincides with the peak concentration of leached Cu. This further indicates that oxygen is involved in the leaching of Pb and Cu and is consumed during the process.

Oxygen can directly react with Pb^0 and Cu^0 to form the corresponding oxides. These oxides then react with hydrogen ions. However, due to the high concentration of chloride ions in the slurry, these chloride ions will form complexes with ferric ions (Fe^{3+}) and cuprous ions (Cu^+), causing these ions to dissolve in the liquid phase. Under aerated conditions, iron ions exist as ferric ions (Fe^{3+}). Ferric ions can react with Pb^0 and Cu^0 to produce ferrous ions (Fe^{2+}) and Pb and Cu ions. Ferrous ions can then be oxidized by oxygen to regenerate ferric ions (Fe^{3+}). Thus, iron ions act as a catalyst in the aeration leaching process of Pb and Cu. Similarly, cupric ions (Cu^{2+}) can react with Cu^0 to produce cuprous ions (Cu^+), which are then oxidized by oxygen back to cupric ions. Therefore, copper ions also play a catalytic role in the aeration leaching process of copper.

(b) (c)

Fig. 3. Aeration leaching reaction apparatus and leachate images: (a) Aeration leaching reaction apparatus; (b) leachate with 0 L/min aeration; (c) leachate with 8 L/min aeration.

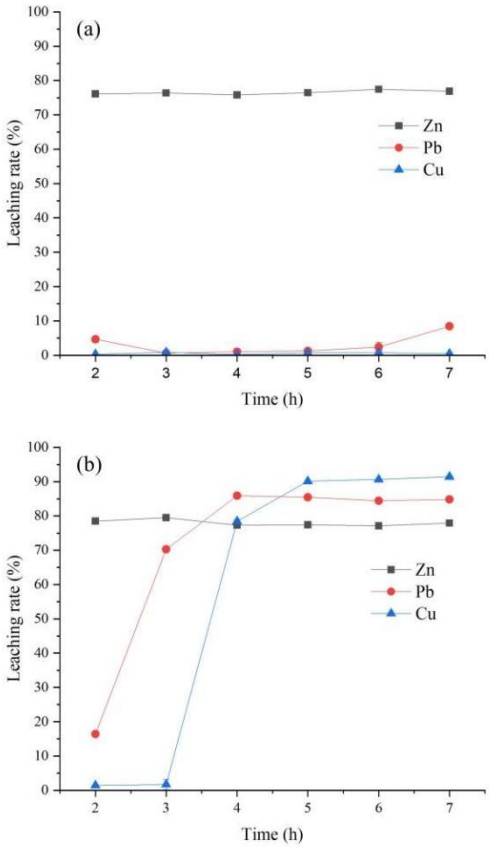

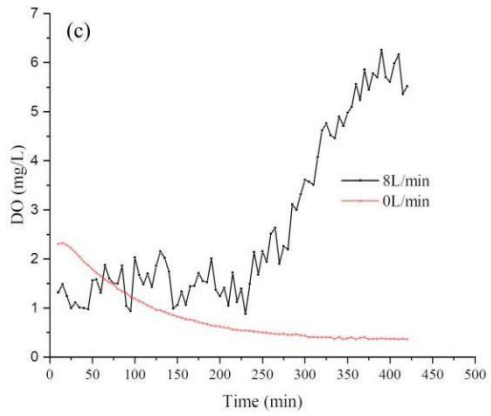

Fig. 4. The impact of aeration on the leaching rates of heavy metals from fly ash and changes in dissolved oxygen during leaching: (a) 0 L/min aeration; (b) 8 L/min aeration; (c) dissolved oxygen variation.

3.4. Characterization of the leached fly ash samples

3.4.1. Changes in chlorine content of leached fly ash

From **Table 1**, it can be seen that the chlorine content in the fly ash after leaching has significantly decreased, dropping from around 26% to 0.3-0.5%. This reduction makes the treated fly ash suitable for use as a raw material in cement production. Additionally, the content of heavy metals in the fly ash has significantly decreased after acid leaching, especially under heated conditions. However, the pollution characteristics of the metals in the fly ash are not only related to their concentration but also closely related to their forms of existence.

3.4.2. Modifications to the modified BCR method

In addition, this study employs the modified BCR method to analyze the speciation distribution of Zn, Cu, Pb, and Cd in both raw fly ash and leached fly ash. However, the modified BCR method was initially developed to determine heavy metals' speciation distribution in soils and sediments(Gabarrón et al. 2019; Gleyzes, Tellier, and Astruc 2002; Gabarrón et al. 2019; Soliman, El Zokm, and Okbah 2018). In the first step of the modified BCR, a 0.11 mol/l acetic acid solution is used to leach the samples, aiming to dissolve soluble salts, hydroxides, and carbonates of heavy metals. Nevertheless, fly ash exhibits a much higher acid-neutralizing capacity than soils and sediments. As shown in **Fig. 5** (a), when the acetic acid concentration is 0.11 mol/l, the pH of the leachate from both raw fly ash is about 5.7, making it ineffective in decomposing heavy metal carbonates(Tong et al. 2020). As depicted in **Fig. 5** (b), the concentrations of various heavy metals increase with the rise in acetic acid concentration. Additionally, it was observed that when the acetic acid concentration reaches 0.7 mol/L, further increasing the concentration does not significantly affect the metal concentrations in the leachate. Therefore, this study employs 0.7 mol/l acetic acid as the leaching agent for the first step of the modified BCR.

3.4.3. Distribution of heavy metal species in fly ash samples

From **Fig. 6** (a), it can be seen that zinc in the raw ash mainly exists in an exchangeable form or bound to carbonates. After leaching, the proportion of zinc in these forms significantly decreases, and under high-temperature aeration conditions, zinc mainly exists in the residual form. From **Fig. 6** (b), despite the fact that lead is almost not leached under non-aerated conditions, its form also transitions to more stable forms, primarily existing in oxidizable and residual forms. Compared to non-aerated conditions, the proportion of oxidizable forms significantly decreases under aerated conditions. Additionally, increasing the temperature facilitates the transformation of lead to more stable forms. From **Fig. 6** (c), it can be seen that the form of copper does not show significant

changes compared to the raw ash under non-aerated conditions. However, under aerated conditions, the proportions of copper in residual, oxidizable, and reducible forms significantly increase. Under heated conditions, the proportions of residual and oxidizable forms increase even more notably. From **Fig. 6** (d), it is observed that under non-aerated conditions, the proportions of cadmium in residual, oxidizable, and reducible forms significantly increase, but cadmium still mainly exists in an exchangeable form or bound to carbonates. Under aerated conditions, the proportions of cadmium in residual, oxidizable, and reducible forms significantly increase, and under heated conditions, the proportion of reducible forms increases more significantly. However, the exchangeable form or carbonate-bound form remains the primary existence form of cadmium.

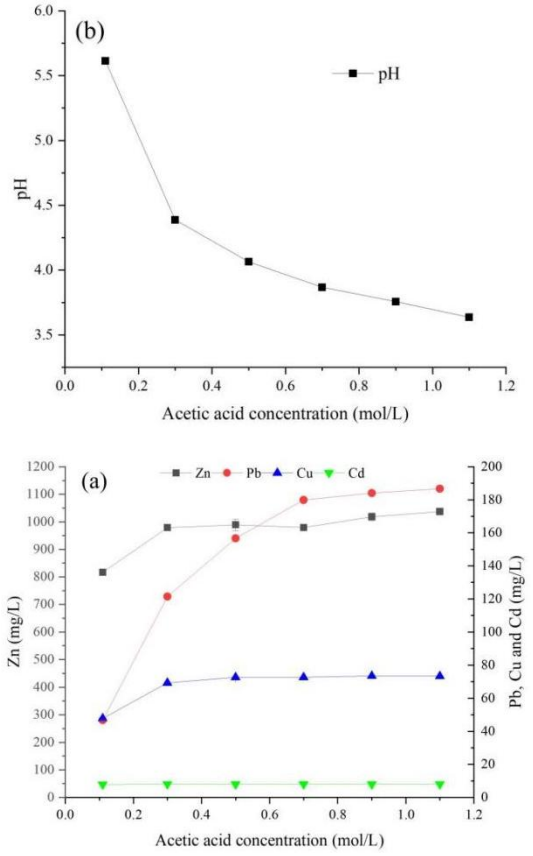

Fig. 5. (a) Relationship between acetic acid concentration and leachate pH;(b) relationship between metal concentrations in leachate of Fly ash B and acetic acid concentration.

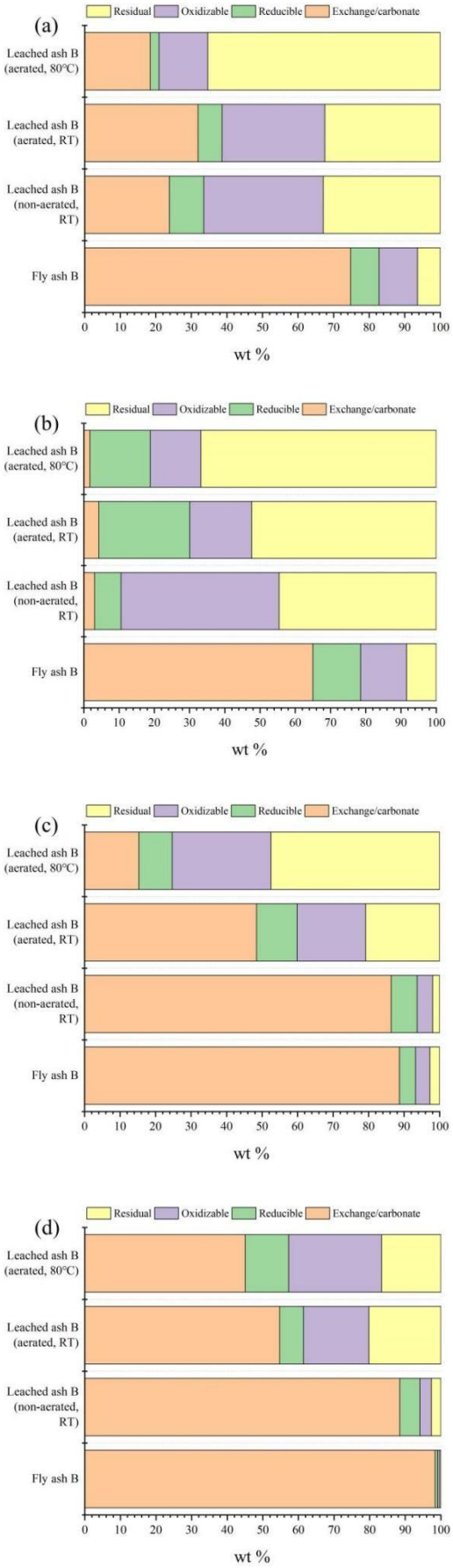

Fig. 6. Comparison of heavy metal speciation forms in Fly ash B and Leached ash B:(a) Zn; (b) Pb; (c) Cu; (d) Cd.

4. Conclusion

Increasing the temperature enhances the leaching rate of zinc. However, this increase does not have a significant impact on the leaching speed of zinc, indicating that temperature primarily affects the extent of leaching rather than the kinetics.

Higher temperatures can accelerate the leching of lead and copper significantly. Despite this, the maximum leaching rates of lead and copper remain largely unaffected by temperature changes. This suggests that while temperature accelerates the leaching process, the ultimate leachable quantities of lead and copper are not influenced by temperature.

During the acid leaching process, zero-valent aluminum in the fly ash forms alloys with lead and copper, which hinders the leaching of these metals. However, the introduction of aeration markedly improves the leaching efficiency of both lead and copper. This indicates that aeration plays a crucial role in overcoming the alloy formation barrier and enhancing metal recovery.

Acid leaching followed by water washing is highly effective in removing chlorine from the fly ash. The treated fly ash exhibits a significantly reduced chlorine content, rendering it suitable as a raw material for cement production. This highlights the dual benefit of acid leaching in both metal recovery and material repurposing.

Post-treatment, the heavy metals in the fly ash are present in more stable forms. Both aeration and heating contribute to further stabilization of these metals. This stabilization is crucial for minimizing the environmental impact of the treated fly ash, ensuring that heavy metals are less likely to leach out under environmental conditions.

These findings underscore the importance of temperature, aeration, and post-treatment processes in enhancing the leaching efficiency and environmental safety of treated fly ash, paving the way for its sustainable reuse in industrial applications.

Acknowledgment

We gratefully acknowledge the support provided by the Nishihara Cultural Foundation and JST SPRING (Grant Number JPMJSP2136). We would also like to express our appreciation to the operators of the MSWI plant for their provision of sample material. Additionally, we extend our sincere thanks to Yuki Kajino for his analytical support.

References

Asad, Mohammad Waqar Ali, Muhammad Asim Qureshi, and Hyongdoo Jang. 2016. “A Review of Cut-off Grade Policy Models for Open Pit Mining Operations.” Resources Policy 49 (September):142–52. https://doi.org/10.1016/j.resourpol.2016.05.005.

DZ/T 0201-2020: Specifications for Tungsten，Tin， Mercury, and Antimony Mineral Exploration.

DZ/T 0212.2-2020: Specifications for Salt Mineral exploration—Part 2: Present Saline Lake Mineral.

DZ/T 0214-2020: Specifications for Copper, Lead, Zinc, Silver, Nickel, and Molybdenum Mineral Exploration.

Fan, Chengcheng, Baomin Wang, and Tingting Zhang. 2018. “Review on Cement Stabilization/Solidification of Municipal Solid Waste Incineration Fly Ash.” Advances in Materials Science and Engineering 2018 (October):1–7. https://doi.org/10.1155/2018/5120649.

Gabarrón, María, Raúl Zornoza, Silvia

Martínez-Martínez, Viviana A. Muñoz, Ángel Faz, and Jose A. Acosta. 2019. "Effect of Land Use and Soil Properties in the Feasibility of Two Sequential Extraction Procedures for Metals Fractionation." Chemosphere 218 (March):266–72. https://doi.org/10.1016/j.chemosphere.2018.11.114.

Gleyzes, Christine, Sylvaine Tellier, and Michel Astruc. 2002. "Fractionation Studies of Trace Elements in Contaminated Soils and Sediments: A Review of Sequential Extraction Procedures." TrAC Trends in Analytical Chemistry 21 (6–7): 451–67. https://doi.org/10.1016/S0165-9936(02)00603-9.

Hagni, Ann M., Richard D. Hagni, and Christelle Demars. 1991. "Mineralogical Characteristics of Electric Arc Furnace Dusts." JOM 43 (4): 28–30. https://doi.org/10.1007/BF03220543.

Hjelmar, Ole. 1996. "Disposal Strategies for Municipal Solid Waste Incineration Residues." Journal of Hazardous Materials 47 (1–3): 345–68. https://doi.org/10.1016/0304-3894(95)00111-5.

Karlfeldt Fedje, Karin, and Sven Andersson. 2020. "Zinc Recovery from Waste-to-Energy Fly Ash – A Pilot Test Study." Waste Management 118 (December):90–98. https://doi.org/10.1016/j.wasman.2020.07.017.

Li, Pengfei, and Takayuki Shimaoka. 2023. "Assessing the Metal Recovery Value of Municipal Solid Waste Incineration Residues: Impact of Pretreatment on Fly Ash and Bottom Ash." Journal of Geoscience and Environment Protection 11 (10): 79–86. https://doi.org/10.4236/gep.2023.1110007.

Quina, Margarida J., Elza Bontempi, Anna Bogush, Stefan Schlumberger, Gisela Weibel, Roberto Braga, Valerio Funari, Jiri Hyks, Erik Rasmussen, and Jakob Lederer. 2018. "Technologies for the Management of MSW Incineration Ashes from Gas Cleaning: New Perspectives on Recovery of Secondary Raw Materials and Circular Economy." Science of The Total Environment 635 (September):526–42. https://doi.org/10.1016/j.scitotenv.2018.04.150.

Shunda Lin, Xuguang Jiang, Yimeng Zhao, and Jianhua Yan. 2022. "Disposal Technology and New Progress for Dioxins and Heavy Metals in Fly Ash from Municipal Solid Waste Incineration: A Critical Review." Environmental Pollution 311 (October):119878. https://doi.org/10.1016/j.envpol.2022.119878.

Soliman, Naglaa F., Gehan M. El Zokm, and Mohamed A. Okbah. 2018. "Risk Assessment and Chemical Fractionation of Selected Elements in Surface Sediments from Lake Qarun, Egypt Using Modified BCR Technique." Chemosphere 191 (January):262–71. https://doi.org/10.1016/j.chemosphere.2017.10.049.

Tang, Jinfeng, Shaobin Dong, Qian Feng, Minhua Su, Yongjun Wei, Jiawei Liang, Hongguo Zhang, et al. 2022. "Optimizing Critical Metals Recovery and Correlative Decontamination from MSWI Fly Ash: Evaluation of an Integrating Two-Step Leaching Hydrometallurgical Process." Journal of Cleaner Production 368 (September):133017. https://doi.org/10.1016/j.jclepro.2022.133017.

Tang, Jinfeng, and Britt-Marie Steenari. 2016. "Leaching Optimization of Municipal Solid Waste Incineration Ash for Resource Recovery: A Case Study of Cu, Zn, Pb and Cd." Waste Management 48

(February):315–22. https://doi.org/10.1016/j.wasman.2015.10.003.

Tang, Jinfeng, Minhua Su, Qihang Wu, Lezhang Wei, Nana Wang, Enzong Xiao, Hongguo Zhang, et al. 2019. “Highly Efficient Recovery and Clean-up of Four Heavy Metals from MSWI Fly Ash by Integrating Leaching, Selective Extraction and Adsorption.” Journal of Cleaner Production 234 (October):139–49. https://doi.org/10.1016/j.jclepro.2019.06.198.

Tang, Jinfeng, Minhua Su, Hongguo Zhang, Tangfu Xiao, Yu Liu, Yifan Liu, Lezhang Wei, Christian Ekberg, and Britt-Marie Steenari. 2018. “Assessment of Copper and Zinc Recovery from MSWI Fly Ash in Guangzhou Based on a Hydrometallurgical Process.” Waste Management 76 (June):225–33. https://doi.org/10.1016/j.wasman.2018.02.040.

Thompson, Matt, and Drew Barr. 2014. “Cut-off Grade: A Real Options Analysis.” Resources Policy 42 (December):83–92. https://doi.org/10.1016/j.resourpol.2014.10.003.

Tong, Lizhi, Jinyong He, Feng Wang, Yan Wang, Lei Wang, Daniel C.W. Tsang, Qing Hu, Bin Hu, and Yi Tang. 2020. “Evaluation of the BCR Sequential Extraction Scheme for Trace Metal Fractionation of Alkaline Municipal Solid Waste Incineration Fly Ash.” Chemosphere 249 (June):126115. https://doi.org/10.1016/j.chemosphere.2020.126115.

Weibel, Gisela, Urs Eggenberger, Dmitrii A. Kulik, Wolfgang Hummel, Stefan Schlumberger, Waldemar Klink, Martin Fisch, and Urs K. Mäder. 2018. “Extraction of Heavy Metals from MSWI Fly Ash Using Hydrochloric Acid and Sodium Chloride Solution.” Waste Management 76 (June):457–71. https://doi.org/10.1016/j.wasman.2018.03.022.

Weibel, Gisela, Anna Zappatini, Mirjam Wolffers, and Stefan Ringmann. 2021. “Optimization of Metal Recovery from MSWI Fly Ash by Acid Leaching: Findings from Laboratory- and Industrial-Scale Experiments.” Processes 9 (2): 352. https://doi.org/10.3390/pr9020352.

Zhang, Yuying, Lei Wang, Liang Chen, Bin Ma, Yike Zhang, Wen Ni, and Daniel C.W. Tsang. 2021. “Treatment of Municipal Solid Waste Incineration Fly Ash: State-of-the-Art Technologies and Future Perspectives.” Journal of Hazardous Materials 411 (June):125132. https://doi.org/10.1016/j.jhazmat.2021.125132.

Zucha, Wolfgang, Gisela Weibel, Mirjam Wolffers, and Urs Eggenberger. 2020. “Inventory of MSWI Fly Ash in Switzerland: Heavy Metal Recovery Potential and Their Properties for Acid Leaching.” Processes 8 (12): 1668. https://doi.org/10.3390/pr8121668.

Crystallization process enhanced by quaternary ammonium salt surfactant for dewaterability improvement of waste-activated sludge

1. Introduction

Waste activated sludge (WAS), an inevitable byproduct of biological wastewater treatment, presents considerable challenges in sustainable management due to its exceptionally high water content and complex colloidal structure.[1] Effective deep dewatering is therefore essential, as it significantly reduces sludge volume, facilitates subsequent handling and transportation, and lowers the overall operational costs.[2-4] Moreover, it diminishes potential environmental risks associated with sludge disposal, underscoring its critical role in the entire sludge treatment chain.[5]

The dewaterability of WAS is inherently limited by its stable colloidal structure, where extracellular polymeric substances (EPS) form a highly hydrated and porous matrix that encapsulates various forms of bound water.[6-8] Conventional conditioning techniques, such as chemical oxidation using hydroxyl or sulfate radicals[9], and physical methods including thermal, ultrasonic or microwave treatment, primarily aim to disrupt the floc structure and degrade hydrophilic constituents.[10, 11] However, these approaches often involve non selective destruction, require significant chemical or energy inputs, and risk altering the original sludge composition.[12-14]

Recently, hydrate-based conditioning has emerged as a novel approach that utilizes guest molecules (e.g., CO_2 or propane) to form clathrate hydrates under moderate pressure and low temperature without disrupting sludge flocs or using chemicals, thereby enabling targeted water extraction and solid-liquid separation in a more sustainable manner.[8, 15, 16] Despite its promise, the application of hydrate-

based dewatering is hindered by slow reaction kinetics. The formation of hydrates primarily occurs at gas-liquid interfaces and on the surface of sludge particles, where initially formed hydrate films act as a diffusion barrier, impeding further mass transfer of guest molecules into the aqueous phase and restricting continuous hydrate growth. This self-limiting mechanism is exacerbated in sludge systems due to the high water-binding capacity of EPS and the steric hindrance of porous floc structures, which collectively reduce the effective contact area between water and guest molecules and prolong the induction period. Consequently, the process requires extended reaction times and elevated energy input to achieve meaningful water conversion, posing a significant challenge for scaling and practical implementation.

To address these limitations, this study introduces a composite quaternary ammonium salt (QAS) surfactant, termed G-agent, as a promoter to improve hydrate-based dewatering in waste-activated sludge. Surfactants are widely recognized as kinetic promoters in gas hydrate formation due to their ability to reduce interfacial tension, facilitate the dissolution of guest molecules, and disrupt hydrogen bonding at gas–water interfaces.[17, 18] These properties collectively enhance nucleation site density and accelerate crystallization kinetics. Specifically, QAS possess amphiphilic characteristics that promote local water structuring and support hydrate crystal growth through electrostatic and hydrophobic interactions.

Expanding on this basis, the G-agent used herein is a polymer-integrated QAS complex that fulfills a dual role: it functions not only as a coagulant and flocculant, improving sludge concentration through charge neutralization and floc bridging, but also as a hydrate promoter. Previous studies, including work by Wang et al. (2023)[18], suggest that such composite agents can induce conformational changes in extracellular proteins, disrupt hydration shells around solid particles, and enhance

molecular ordering at interfaces. These mechanisms work together to facilitate more organized and rapid hydrate formation. This synergistic action enables simultaneous enhancement of solid–liquid separation and crystalline water entrapment, offering a new dewatering strategy that does not depend on cellular disruption.

To achieve the objectives of this study, a systematic investigation was conducted focusing on three main aspects: First, the feasibility of enhancing hydrate synthesis was evaluated by examining thermodynamic conditions, such as equilibrium pressure and temperature, along with kinetic parameters to quantify the promotion effect of the conditioning agent. Second, the dewatering performance was comprehensively assessed through capillary suction time (CST) analysis and integrated process evaluation, establishing an efficient treatment pathway. Third, the underlying mechanisms were elucidated from a multi-scale perspective: advanced surface analytical techniques were employed to reveal the mechanism of hydrate crystallization promotion, while changes in interfacial properties, water occurrence states, and three-dimensional pore structure were analyzed to clarify the enhancement of dewaterability. This work not only provides fundamental insights into the synergistic mechanisms between chemical conditioning and physical crystallization processes, but also provides theoretical support for the optimization and practical application of hydrate-based sludge dewatering technologies.

2. Materials and methods

2.1 Sludge samples and conditioning agents

The sludge samples used in this study were obtained from a municipal wastewater treatment plant with the capacity of 200,000 m^3/day located in Shanghai, China. The conditioning agents (G-agent) used to enhanced crystallization process

was provided by a research team from Fujian, China.

2.2 Instrument and procedure of thermodynamics experiment

In order to accurately control and monitor the temperature and gas pressure, a small-volume tube reactor (9 mm internal diameter, total volume 10 cm^3) with high precision chiller (JULABO, Co. Ltd., Germany) was used to conduct thermodynamics experiment. The estimated error of temperature measurement was ±0.01 K. Pressure value was recorded with a pressure transducer (OMEGA Engineering, Inc., USA) and the estimated error was ±5 kPa.

6 mL sludge was loaded into tube reactor and pressurized with CO_2 to 5 MPa for thermodynamics experiment. The experiment comprised heating and cooling phases. During the heating phase, the reactor was initially held in the 0.5 °C chiller for crystallization. After pressure stabilized, the temperature was raised to 3 °C to mark the onset of heating. Subsequently, the temperature was increased incrementally at 1 °C intervals until reaching 10 °C, while pressure and temperature were continuously monitored. The system was allowed to equilibrate at ambient temperature until the pressure stabilized after heating stage. For the cooling phase, the reactor was reintroduced into the 0.5 °C chiller, with pressure and temperature recorded through rapid cooling. All heating and cooling cycles were performed in triplicate to ensure reproducibility.

2.3 Analytical Methods

2.3.1 Dewaterability evaluation

Sludge dewaterability was evaluated by modeling capillary suction time (CST) using a CST instrument (type 304M, Triton Elec tronics Ltd., U.K.). Additionally, the water content of sludge cake after pressure filtration was also tested to characterize the sludge dewaterability. Specifically, 5g sludge cake was dried in an oven at 105 ℃

overnight, and then water content of dewatered sludge cake was calculated through the mass difference before and after drying.

2.3.2 Interfacial properties characterization

The interfacial properties of sludge samples were investigated through both macroscopic surface tension measurements and molecular-level spectroscopic analysis.

From the perspective of macroscopic surface tension measurements, surface tension properties testing was conducted. The surface tension properties evaluated in this study included gas–liquid surface tension and solid interfacial energy. Specifically, gas–liquid surface tension, indicative of gas diffusion efficiency within the sludge matrix, was directly determined using a tensiometer (DCAT21, Dataphysics, Germany). The interfacial energy of sludge solids, which correlates with dewaterability, was analysised based on the contact angle method described in the previous literature.[19]

Complementary to the macroscopic surface tension analyses, interfacial molecular characterization was performed using a commercial Sum Frequency Generation (SFG) spectrometer (Ekspla) with a picosecond Nd:YAG laser. The visible (532 nm) and tunable IR (1000–4000 cm^{-1}) beams were set at incident angles of 60° and 55°, respectively. Sludge samples was briefly air-dried after centrifugation, then redispersed in ultrapure water, and spin-coated onto a CaF_2 window. The sample was equilibrated for 10 minutes in a humidified chamber with controlled water vapor exposure before SFG measurement. Spatially and temporally overlapped visible and IR beams were directed at the interface, and the resulting sum frequency signal was collected through filters and a polarization analyzer.

2.3.3 Analysis of water occurrence states

The water occurrence states in sludge were characterized using Low-Field Nuclear Magnetic Resonance (Low-Field NMR) and Atomic Force Microscopy (AFM), providing complementary insights into both bulk water distribution and interfacial water layers.

T_2 relaxation time was measured using a Low-Field NMR analyzer (NMI20-030H-1, Niumag Electric Corporation, Shanghai, China) to evaluate the water occurrence states. The instrument parameters and data processing methods were adapted from our previous study to optimize signal quality.[19] The area under each peak of T_2 spectrum was determined by cumulative integration for the relative quantification of water molecule protons with different mobility.

A contact model AFM (MFP-3D, Oxford Instruments, UK) was used to measure the force curve of sludge samples to determine the thickness of vicinal water film.

2.3.4 Three-dimensional internal structure of sludge

The three-dimensional internal pore structure and spatial characteristics of sludge samples were investigated using in situ synchrotron X-ray computed microtomography (CMT). The high flux and coherence of synchrotron radiation enabled high-resolution, non-destructive visualization of micron-morphology of sludge.

Scanning was conducted at the Shanghai Synchrotron Radiation Facility with an incident beam energy of 15 keV. A series of 1800 projections were acquired over 180° rotation with an exposure time of 200 ms per projection. The effective voxel size was 0.325 μm, providing sufficient resolution to characterize pore networks and solid-phase architecture.

The acquired projections were converted to 8-bit grayscale and imported into Avizo 2022 (Thermo Fisher Scientific, USA) for image processing and three-

dimensional reconstruction. The internal structure parameters obtained from software analysis include segmentation of pores and solids based on grayscale thresholding, calculation of porosity, pore connectivity, tortuosity, etc. The pore network model (PNM) was extracted to analyze throats and nodes representing the fluid transport paths, enabling evaluation of sludge dewaterability enhancement.

2.3.5 Correlative analysis on solid pore structure and dewaterability of sludge

Statistical analysis was performed using OriginPro 9.0 64bit (OriginLab Corporation, USA). The pearson correlation coefficient (R_p) was employed to assess potential relationships between sludge dewaterability and internal pore structure parameters. The Pearson coefficient ranges from -1 to +1, where -1 indicates a perfect negative correlation, +1 indicates a perfect positive correlation, and 0 denotes no linear relationship. Correlations were considered statistically significant at a 95% confidence level ($p \leq 0.05$).

3. Results and discussion

3.1 Thermodynamics of CO_2 hydrate formation in WAS with QAS amendment

3.1.1 Equilibrium pressure curve

The equilibrium pressures for CO_2 hydrate formation in sludge samples, with and without G-agent amended, are presented in Fig.1. A significant promotive effect of G-agent on the thermodynamic feasibility of crystallization was observed.

As illustrated in Figure 1, the equilibrium partial pressure of the sludge system falls below the theoretical equilibrium pressure of CO_2 hydrate in pure water[20] starting from 5 °C. A more pronounced reduction is observed between 9 and 10 °C, where the G-agent amended sludge exhibits equilibrium partial pressures lower than those of the raw sludge by 0.16 MPa and 0.36 MPa, respectively. This represents a 5.3-10.9% decrease in the equilibrium pressure, indicating that the addition of G-

agent markedly lowers the energy barrier for hydrate nucleation and growth. The enhanced thermodynamic favorability implies a substantial reduction in energy consumption for the crystallization process, highlighting the potential of this conditioning strategy for improving the energy efficiency of sludge dewatering in practical applications.

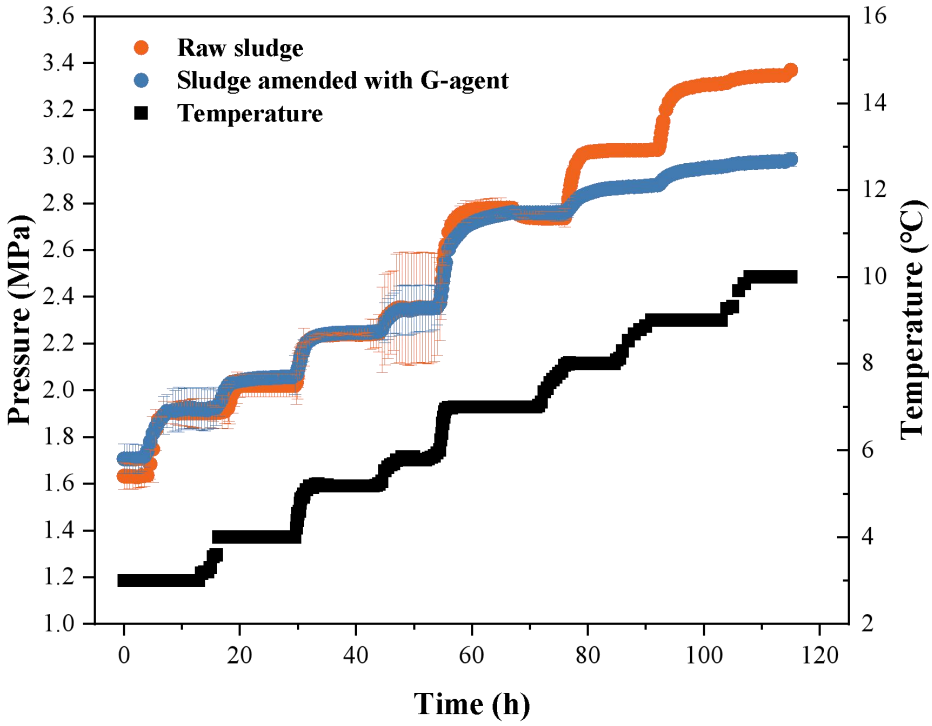

Figure 1. Equilibrium pressure curve of hydrate formation in WAS. Experimental conditions: 10 mL WAS with initial water content of 98.1 wt.%; the total volume of tubular reactor was 13 mL; the initial pressure of CO_2 was 4.5±0.1 MPa; the temperature increased step was 1 °C. Error bars represent standard deviation of duplicate experiments (too small if not shown).

3.1.2 Enthalpy of hydrate formation in WAS with QAS amendment

To quantitatively evaluate the thermodynamic promoting effect of G-agent on hydrate formation as described in section 3.1.1, the enthalpy of hydrate formation (ΔH) was determined using the Clausius-Clapeyron equation. Fig.2 shows the relationship between lnP and 1/T for both raw and G-agent amended sludge.

A strong linear correlation was observed for both systems (R^2=0.997 and 0.998,

respectively), validating the application of the Clausius-Clapeyron approach. As shown in fig.2, the calculated ΔH value for the raw sludge system was 52.38 kJ/mol, which falls within the typical range reported for carbon dioxide hydrates in pure water or complex aqueous systems. In contrast, the ΔH value for the G-agent amended system decreased markedly to 60.01 kJ/mol, representing a reduction of approximately 14.57%. This decrease in ΔH indicates that hydrate formation in the presence of G-agent is less exothermic, implying a lower energy barrier. The result corroborates the facilitated equilibrium conditions observed in Section 3.1.1—such as lower equilibrium pressure at given temperatures—and aligns with reported effects of thermodynamic promoters like R141b in mixed guest hydrate systems[17].

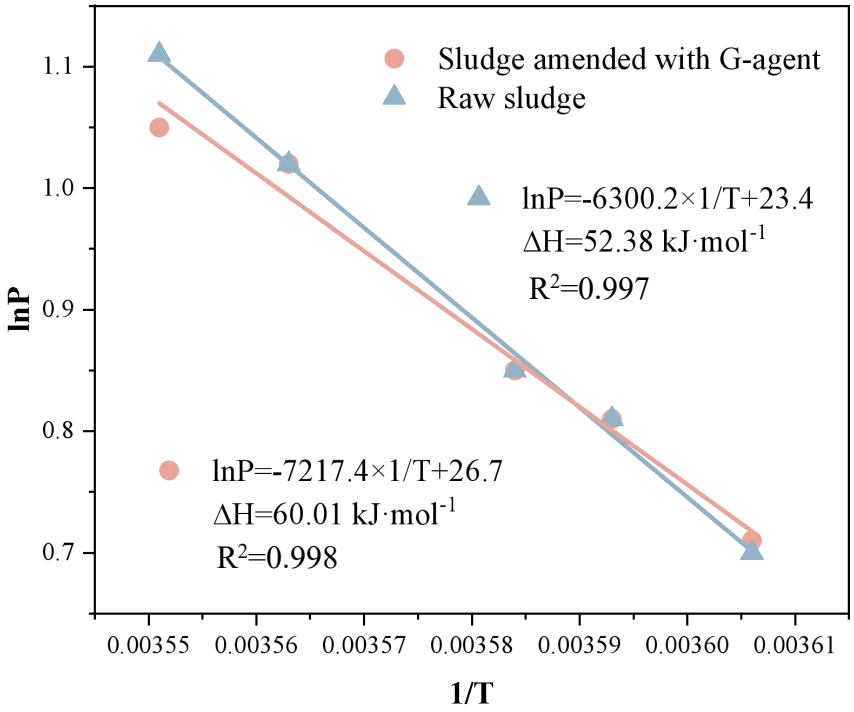

Figure 2. Clausius–Clapeyron plots based on the data of hydrate equilibrium. Experimental conditions: 10 mL WAS with initial water content of 98.1 wt.%; the total volume of tubular reactor was 13 mL; the initial pressure of CO_2 was 4.5±0.1 MPa; the temperature increased step was 1 °C. Error bars represent standard deviation of duplicate experiments (too small if not shown).

3.1.3 Kinetics of hydrate formation

Beyond the thermodynamic promotion established in Sections 3.1.1 and 3.1.2,

213 the kinetics of hydrate formation — governing the rate and efficiency of gas
214 conversion — is crucial for practical application. The kinetic profiles, including
215 induction time and growth rate, were analyzed from the temporal pressure and
216 temperature data (Fig. 3).

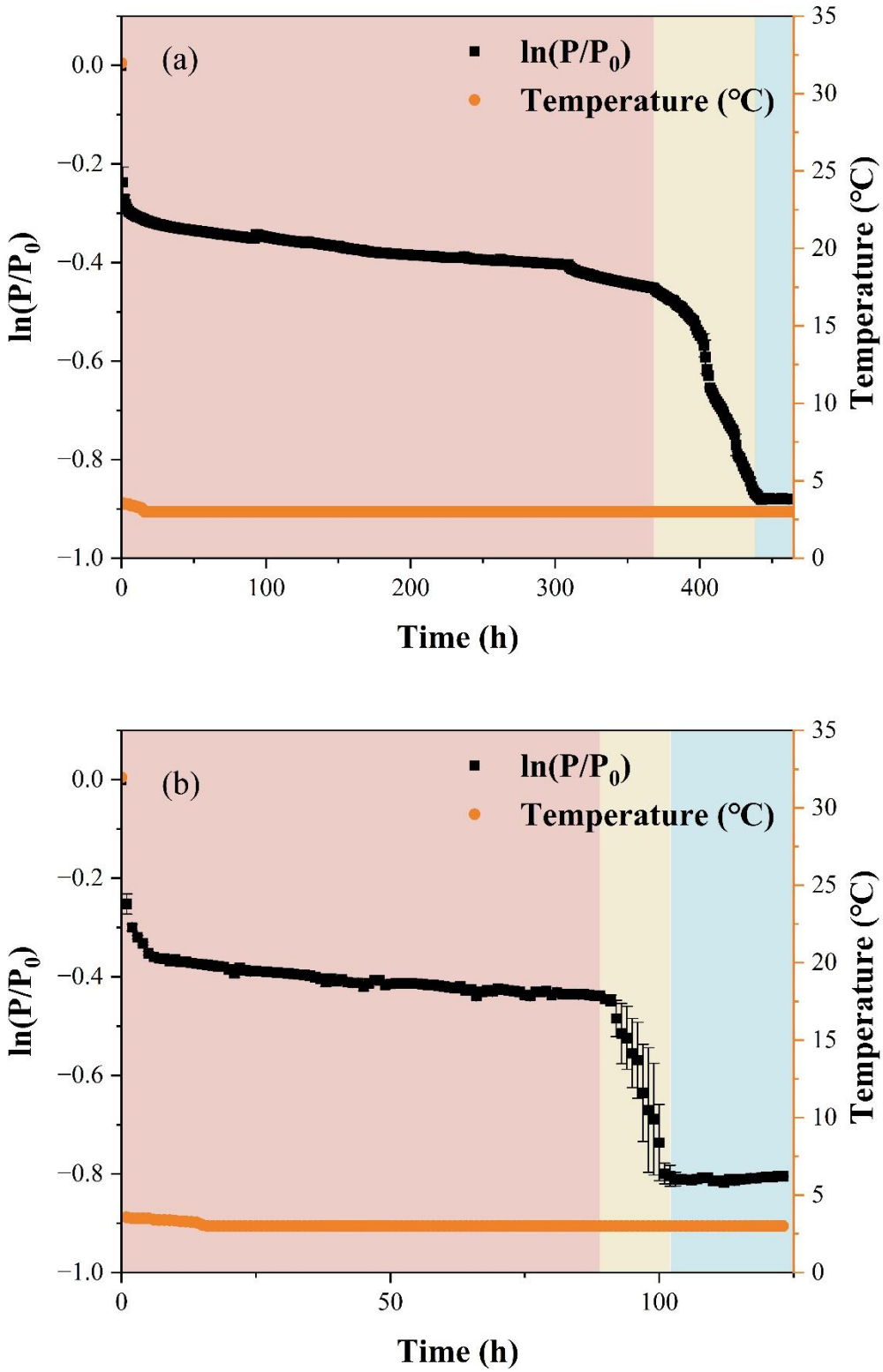

Figure 3. Dynamics characteristics of hydrate formation: a) raw sludge; b) sludge amended with 0.5 wt.% DM G-agent. Experimental conditions: 10 mL WAS with initial water content of 98.1 wt.%; the total volume of tubular reactor was 13 mL; the initial pressure of CO_2 was 4.5±0.1 MPa; the temperature was maintained at 1 °C. Error bars represent standard deviation of duplicate experiments (too small if not shown).

Comparative kinetic curves between raw and G-agent amended sludge reveal a

significant enhancement in formation kinetics. The induction time was notably shortened by G-agent addition. The raw sludge exhibited a prolonged induction time of 370 h, reflecting high nucleation stochasticity within the complex WAS matrix. In contrast, the modification of G-agent reduced it to 90 h, with a reduction rate of 75.7%, indicating its role as nucleation sites and alleviating the kinetic inhibition of organic components. The reaction rate, as indicated by the rate of pressure decline (dlnP/dt), further demonstrates the kinetic enhancement effect of G-agent. During the induction stage, the reaction rate increased from 0.000325 h^{-1} for the raw sludge to 0.000866 h^{-1} after G-agent amendment, representing an increase of 166.6%. In the rapid growth stage, the reaction rate rose markedly from 0.00743 h^{-1} to 0.0255 h^{-1}. This substantial improvement rate of 273.7% indicates that the hydrate growth rate was significantly accelerated following the addition of G-agent.

In summary, G-agent amendment significantly enhances hydrate formation kinetics by shortening induction time and accelerating growth. Coupled with thermodynamic facilitation, this highlights its potential as an effective promoter for advancing hydrate-based sludge treatment.

3.2 Dewaterability improvement of WAS through QAS-enhanced hydrate formation

The modification of WAS with G-agent has been demonstrated to significantly enhance hydrate formation thermodynamics (Section 3.1.1) and reduce the enthalpy of formation (Section 3.1.2). This section quantitatively evaluates the direct impact of G-agent amendment and subsequent hydrate formation on the dewaterability of WAS, primarily through the analysis of CST data. Concurrently, the CST data guided the selection of the optimal dosage for the G-agent addition and the most effective water

conversion ratio for hydrate formation. The experimental results are summarized in Fig.4.

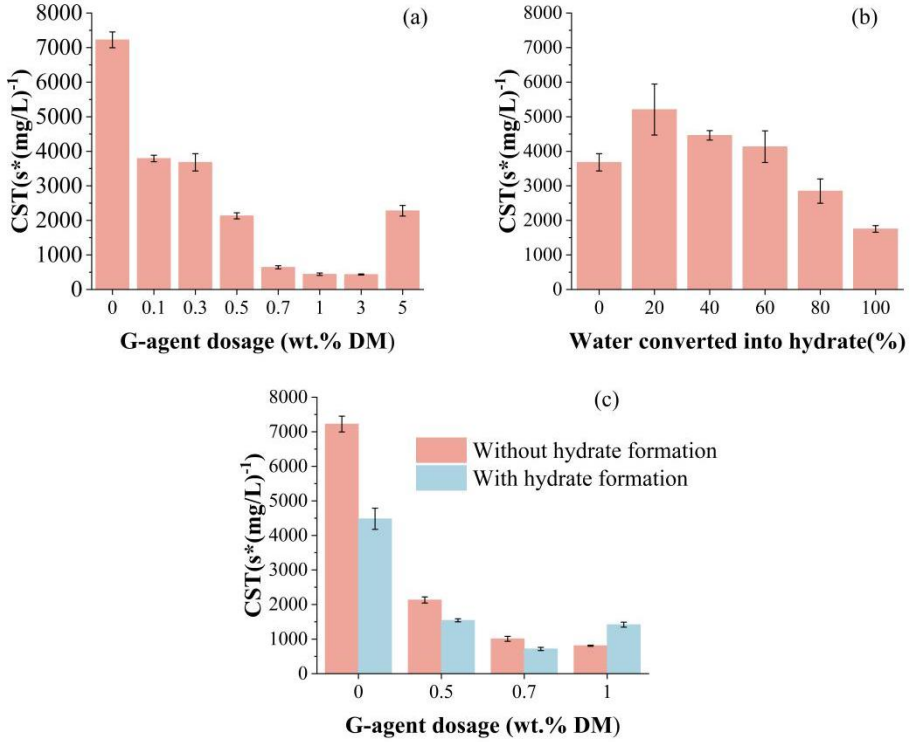

Figure 4. Normalized CST of a) WAS amended with G-agent of 0.1-5wt.% DM; b) WAS with 0.3% G-agent added, and water conversion percentage of 20%-100%; c) G-agent treated sludge with/without hydrate formation. Experimental conditions: 200 mL WAS with initial water content of 98.0 wt.%; the headspace for gas pressurization was 800 mL; the initial pressure of CO_2 was 5 MPa; the temperature for CO_2 hydrate formation was kept at around 1.5 °C.

As shown in Fig.4(a), the addition of G-agent alone, without inducing hydrate formation, already resulted in a measurable improvement in dewaterability. The CST decreased from approximately 7223.4±228.4 s*(mg/L) for raw sludge to 434.8±16.0 s*(mg/L) as the G-agent dosage increased from 0 to 3 wt.% DM dry matter. This represents a 94% reduction in CST at the optimal dosage. Further increase in G-agent dosage to 5 wt.% DM led to a slight rebound in CST to 2278.8±154.7 s*(mg/L), potentially due to particle re-stabilization.

Fig.4(b) illustrates the influence of varying hydrate formation ratios on the dewaterability of sludge amended with 0.3 wt.% DM G-agent. It was observed that

the CST exhibited an adverse trend within the 20–60% water conversion range. However, a notable improvement in dewaterability was achieved at higher conversion ratios, with CST values decreasing by 22.6% at 80% water conversion and by 52.4% at complete conversion, both of which were lower than that of the G-agent conditioned sludge without hydrate formation. These results clearly indicate that the optimal endpoint for the hydrate-based process is 100% water conversion, under which the best dewatering performance is attained.

In order to further optimize the dosage of the agent, the CST was measured with and without hydrate formation within a dosage range of 0.5-1.0 wt.% DM. This comparison aimed to evaluate the specific contribution of the hydrate reaction to sludge dewatering improvement and to identify an optimal balance between chemical consumption and dewatering performance. As shown in Fig.4(c), the lowest CST value of 716.7±45.9 s*(mg/L) was achieved with 0.7 wt.% DM G-agent addition followed by hydrate formation. This represents an 84% reduction compared to the CST value obtained from crystallization without G-agent amended, and a 29% reduction compared to the sample with only 0.7 wt.% DM G-agent addition and no crystallization.

In summary, the experimental data quantitatively confirms that the integration of G-agent amendment and hydrate formation technology creates a highly effective process for sludge dewatering. G-agent conditioning preliminarily improves sludge filterability, while the subsequent hydrate crystallization process is the primary driver for achieving extreme dewaterability, as unequivocally demonstrated by the drastic reduction in CST values.

3.3 Mechanism insights into QAS-enhanced hydrate crystallization

3.3.1 Effects of QAS on gas-liquid mass transfer

The formation of gas hydrates is an interfacial process initiated at the gas–liquid interface, where guest molecules dissolve into the aqueous phase and organize water molecules into clathrate cages. The efficiency of this process is strongly influenced by the physicochemical properties of the interface, particularly surface tension, which governs gas dissolution and mass transfer. This study investigates the effect of G-agent on the gas–liquid interfacial characteristics to elucidate its role in promoting hydrate crystallization in WAS.

Fig.5 demonstrated that G-agent amendment significantly reduced the surface tension of the sludge-water system. The value decreased from approximately 64.5±0.3 mJ/m^2 in raw sludge to below 62.3±0.6 mJ/m^2 after G-agent addition. This reduction is attributed to the amphiphilic structure of G-agent, comprising hydrophilic quaternary ammonium groups and hydrophobic alkyl chains. G-agent molecules preferentially adsorb at the gas–liquid interface, orienting with hydrophobic tails extending into the gas phase and hydrophilic heads immersed in the aqueous phase. This configuration effectively lowers interfacial energy, thereby facilitating CO_2 dissolution, which is a critical initial step for hydrate nucleation.

The decreased surface tension enhances CO_2 dissolution kinetics, leading to localized supersaturation near the interface, which in turn increases the driving force for hydrate nucleation. This observation aligns with Wu et al. (2023)[8], who reported that interfacial active agents accelerate hydrate formation by improving gas transfer rates.

In conclusion, QAS significantly enhances hydrate formation in WAS by reducing gas–liquid surface tension. These changes improve CO_2 dissolution and mass transfer, promote local supersaturation, and collectively enhance the kinetics and yield of hydrate formation.

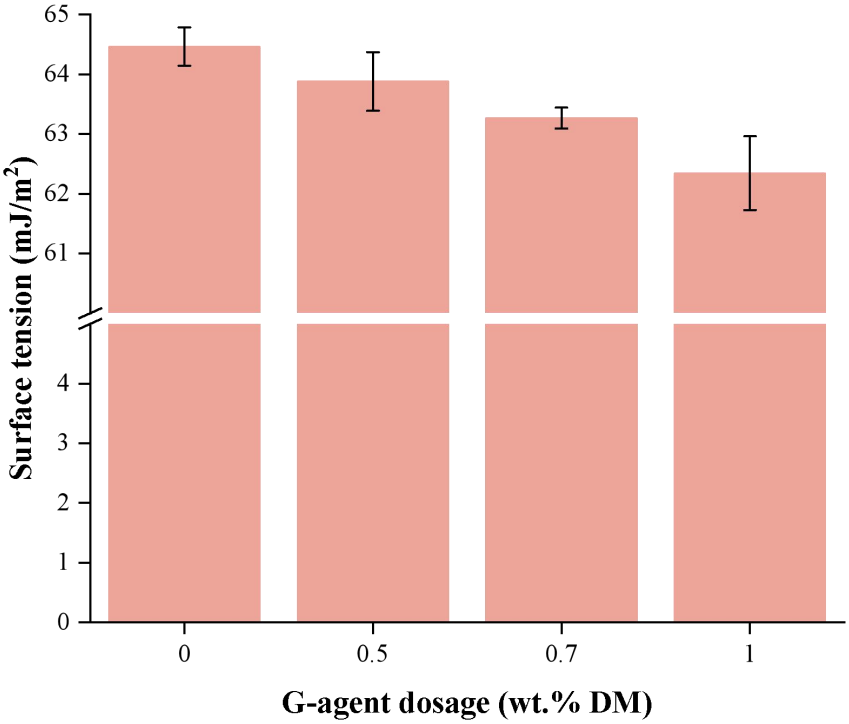

Figure 5. Surface tension of WAS amended with G-agent. Experimental conditions: WAS with water content of 98.0 wt.% was amended with 0.5-1 wt.%DM G-agent.

3.3.2 Effects of QAS on surface water conformation

The molecular structure and ordering of water at the interface are critical factors influencing the initial stages of gas hydrate formation. SFG spectroscopy was used to investigate how the G-agent modifies the conformation and organizational state of interfacial water molecules in WAS. The experimental results are shown in Fig.6.

The SFG vibrational spectra in the O–H stretching region provide direct evidence of changes in interfacial water ordering. The spectral data indicate that the addition of the G-agent induces a marked increase in the number of discernible resonance peaks within this region. This proliferation of spectral features signifies a substantial increase in the degree of order and structural heterogeneity of the water molecules at the interface.

In the raw sludge sample, the SFG spectrum exhibits a relatively broad and

featureless profile, indicative of a disordered water interface with a wide, random distribution of hydrogen-bonding environments. Upon incorporation of the G-agent, even at a dosage of 0.5 wt.% DM, a noticeable increase in spectral peaks emerges. This suggests that the surfactant molecules begin to assemble at the interface, imposing a templating effect that guides the adjacent water molecules into more defined and specific orientations.

This effect is most pronounced at the optimal dosage of 0.7 wt.% DM. The spectrum displays a significant increase in the number and sharpness of resonant peaks, clearly reflecting a highly structured and ordered interfacial water layer. The enhanced interfacial ordering is crucial for hydrate formation, as it effectively reduces the interfacial free energy. A more ordered interface provides a thermodynamically more stable template that facilitates the organization of water molecules into the nascent cage-like structures of hydrates, thereby lowering the nucleation energy barrier.

In summary, the SFG results demonstrate that G-agent addition significantly enhances the structural ordering of water at the interface. The increase in the number of resonant peaks directly correlates with a higher degree of interfacial organization, which reduces interfacial energy and provides an optimal template for hydrate nucleation. This molecular-level ordering effect is a key mechanism behind the macroscopic enhancement of hydrate formation kinetics and efficiency observed in the QAS-amended system.

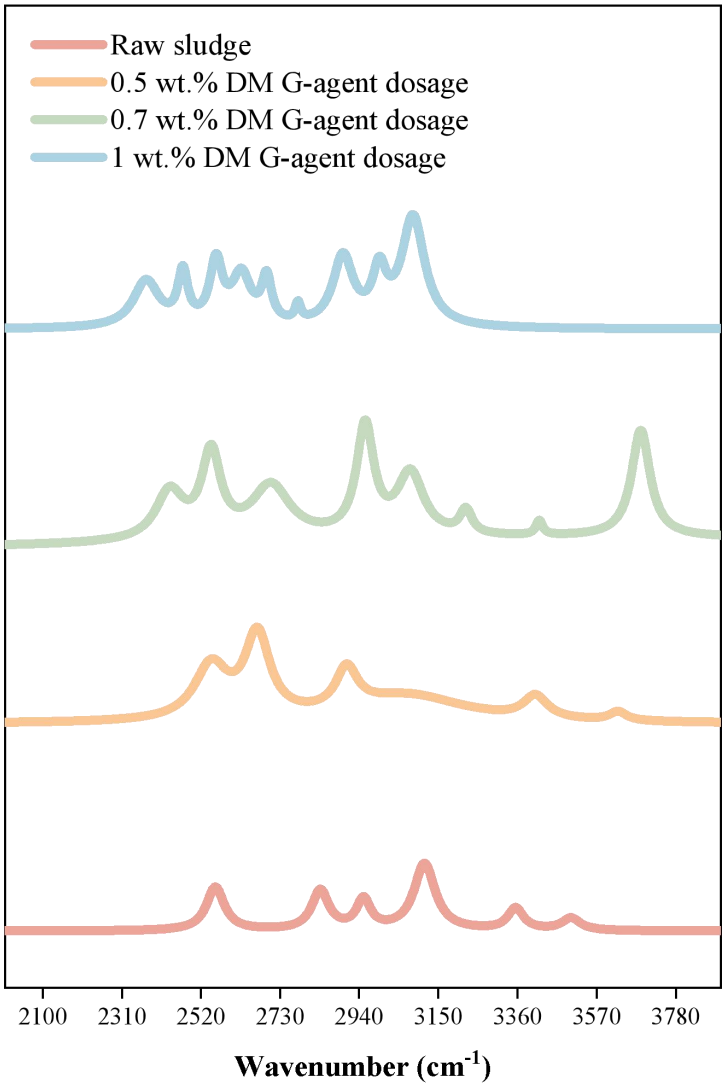

Figure 6. SFG spectra of WAS amended with G-agent. Experimental conditions: WAS with the initial water content of 98.0 wt.% was amended with 0.5-1 wt.%DM G-agent, and then dewatered to sludge cake with water content of 80 wt.% by vacuum filtration.

3.4 Mechanism insights into WAS dewaterability improvement accompanied by QAS-enhanced hydrate crystallization

3.4.1 Physiochemical properties of interface

The dewaterability of WAS is intrinsically linked to the interfacial free energy between sludge flocs and water, which governs the binding strength of water molecules. A reduction in this energy indicates increased hydrophobicity of the solid surface, thereby facilitating water release. To mechanistically elucidate the

remarkable dewaterability improvement achieved through QAS-enhanced hydrate crystallization (Section 3.2), the evolution of surface thermodynamic properties was quantitatively analyzed. The total interfacial free energy (ΔG_{SL}) and its Lifshitz-van der Waals (ΔG_{SL}^{LW}) and Lewis acid-base (ΔG_{SL}^{AB}) components for sludge are presented in Fig.7.

The results demonstrate a systematic and substantial reduction in ΔG_{SL} from -63.18±9.37 mJ/m^2 in the raw sludge to -68.37±3.30 mJ/m^2 after G-agent amendment, and further to a markedly lower value of -70.66±6.71 mJ/m^2 following hydrate formation. This progressive decline is predominantly driven by a drastic decrease in ΔG_{SL}^{AB}, which reflects the polar and hydrogen-bonding interactions between the sludge surface and water. The ΔG_{SL}^{AB} value plummeted from -58.24±8.90 mJ/m^2 to -65.11±6.83 mJ/m^2, indicating a severe weakening of the surface's affinity for water. In contrast, ΔG_{SL}^{LW} associated with non-polar interactions, remained relatively stable, slightly decreasing from -4.94±0.76 mJ/m^2 to -5.55±0.24 mJ/m^2.

The sharp reduction in ΔG_{SL} signifies a fundamental shift in sludge surface properties from hydrophilic to more hydrophobic. This transformation is initiated by the adsorption of G-agent onto the sludge flocs and EPS, where its hydrophobic alkyl chains reorient outward, shielding polar functional groups and reducing hydrogen bonding sites. The subsequent hydrate crystallization process powerfully amplifies this effect.

In conclusion, the synergistic combination of G-agent amendment and hydrate crystallization effectively lowers the interfacial free energy. This renders the sludge surface more hydrophobic, which is a core physicochemical mechanism responsible for the severe weakening of water-sludge interactions and the consequent enhancement of dewaterability.

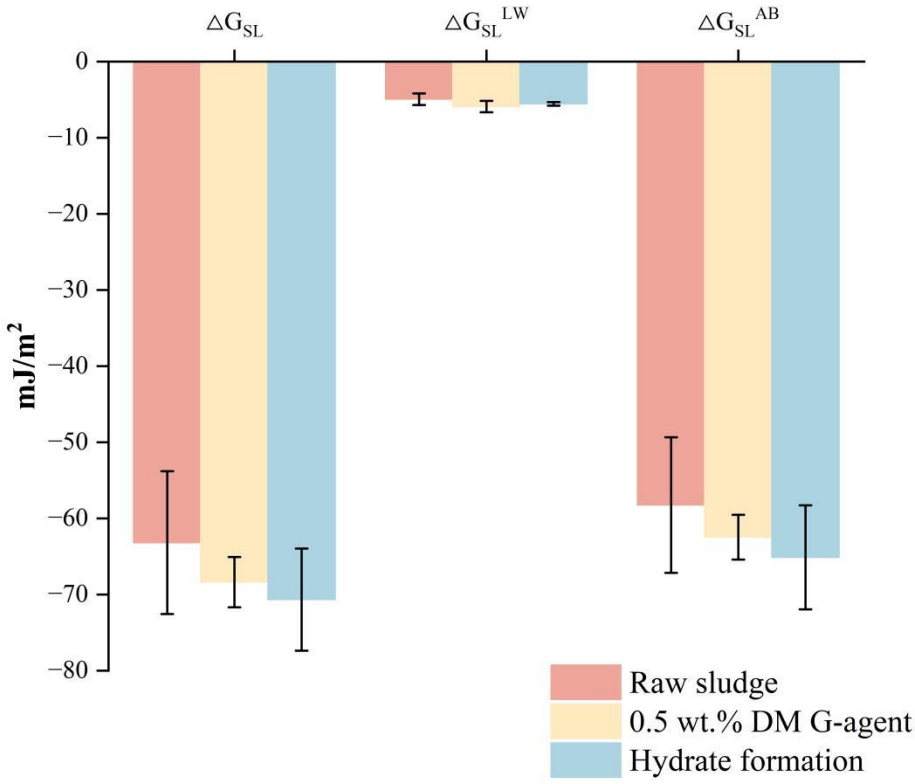

Figure 7. Surface tension of raw sludge, WAS amended with 0.5 wt.% DM G-agent and G-agent-treated sludge with hydrate formation. Experimental conditions: 200 mL WAS with initial water content of 98.0 wt.%; the headspace for gas pressurization was 800 mL; the initial pressure of CO_2 was 5 MPa; the temperature for CO_2 hydrate formation was kept at around 1.5 ℃; the water conversion percentage was 100%.

3.4.2 Water mobility states

The transformation of water occurrence states within the sludge matrix is a fundamental mechanism governing dewaterability. To quantitatively analyze this transformation induced by G-agent amendment and subsequent hydrate crystallization, the mobility of water molecules was investigated using Low-Field NMR and AFM.

The Low-Field NMR T_2 relaxation spectra provide a direct measurement of the mobility of water protons, which are constrained to varying degrees by their interactions with sludge solids. The T_2 spectra for all samples (Fig.8) were characterized by three primary peaks: the T_{21} peak (< 10 ms) is assigned to vicinal water strongly bound to organic surfaces via hydrogen bonding; the T_{22} peak (10–100

ms) represents interstitial water trapped within the pores of sludge flocs; and the T_{23} peak (> 100 ms) corresponds to free water with the highest mobility.

Quantitative analysis of the peak areas revealed a significant re-distribution of water states. The area proportion of the strongly bound T_{21} water increased from a negligible 0.002% in raw sludge to 0.43% and 0.42% after amendment with 0.5 and 0.7 wt.% DM G-agent, respectively. This initial increase suggests that G-agent addition may promote the association of water molecules with the newly formed organic-QAS complexes. However, following the hydrate formation process, the T_{21} area proportion rose further to 1.08%, but this was accompanied by a dramatic right-shift in its peak position from about 0.02 ms to 0.43 ms. This critical shift indicates that the remaining bound water fraction, though larger in proportion, possesses significantly higher mobility, reflecting a substantial weakening of the binding forces that constrain it.

Concurrently, the state of the predominant capillary water (T_{22}) was also altered. Its peak position shifted from 1.83 ms in raw sludge to 13.67 ms after the complete process, indicating a major enhancement in the mobility of water within the sludge pores. The area proportion of the T_{22} peak remained dominant, increasing from 96.52% to 97.67%. The state of free water (T_{23}) exhibited a more complex trend: its mobility initially decreased with higher G-agent dosage (peak position shifting from 310.79 ms to 252.354 ms at 0.7 wt.% DM dosage) but recovered significantly after hydrate formation (382.75 ms). At the same time, it was observed that when the drug was overdosed (5.0 wt.% DM), the T_{23} peak position shifted significantly toward shorter relaxation times. Although the corresponding peak area increased, this shift indicates a remarkable reduction in the mobility of free water, thereby adversely affecting dewaterability.

436 The Low-Field NMR results can be interpreted by following mechanism: The
437 cationic head of G-agent initially binds water, slightly increasing the T_{21} fraction.
438 However, it primarily acts by disrupting the original EPS hydration shell through
439 charge neutralization and adsorption. The subsequent growth and dissociation of
440 hydrate crystals provide a powerful physical restructuring force. This process is the
441 primary driver for the profound changes observed after hydrate formation: it liberates
442 bound water, converting it into a more mobile form, and simultaneously improves
443 pore connectivity and reduces flow resistance, thereby enhancing the mobility of both
444 capillary and free water.

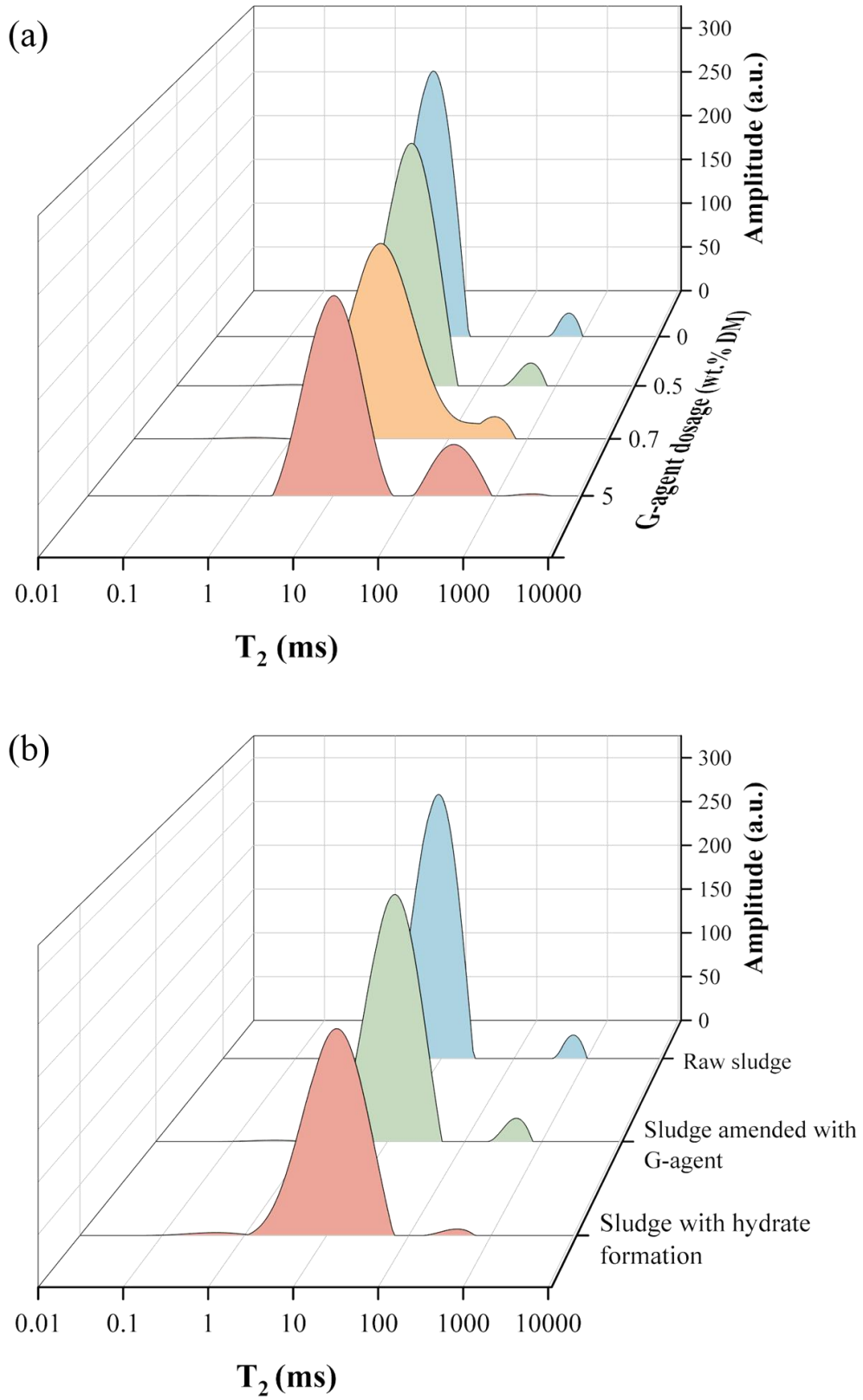

445
446 **Figure 8.** Water states characterized by T_2 distribution spectra. a) WAS amended with
447 0-5 wt.%DM G-agent, b) raw sludge, WAS amended with 0.5 wt.% DM G-agent and
448 G-agent treated sludge with hydrate formation. Experimental conditions: 200 mL
449 WAS with initial water content of 98.0 wt.%; the headspace for gas pressurization

was 800 mL; the initial pressure of CO_2 was 5 MPa; the temperature for CO_2 hydrate formation was kept at around 1.5 ℃; the water conversion percentage was 100%.

To further corroborate the Low-Field NMR findings and specifically probe the changes in the strongest bound water layer, the thickness of the vicinal water film was quantified using AFM force-distance measurements. The results, detailed in Fig.9(a), show that the vicinal water layer thickness decreased dramatically from 37.28±2.52 nm in raw sludge to 8.37±0.60 nm after amendment with 0.7 wt.% DM G-agent. This reduction of 78% in total aligns perfectly with the increase in mobility of the bound water fraction (right-shifted T_{21} peak) observed in Low-Field NMR.

The drastic thinning of the vicinal water layer has profound implications. This hydrated layer exerts a strong repulsive force between adjacent solid surfaces, preventing their aggregation. The G-agent treatment, followed by the intense phase change during hydrate crystallization, effectively reorganizes the water-solid interface. This process disrupts the structured vicinal water network, severely weakening the hydration repulsion. Consequently, solid particles with similar surface properties can aggregate more readily, facilitating the separation of the solid phase from the bulk water phase and ultimately enhancing dewaterability.

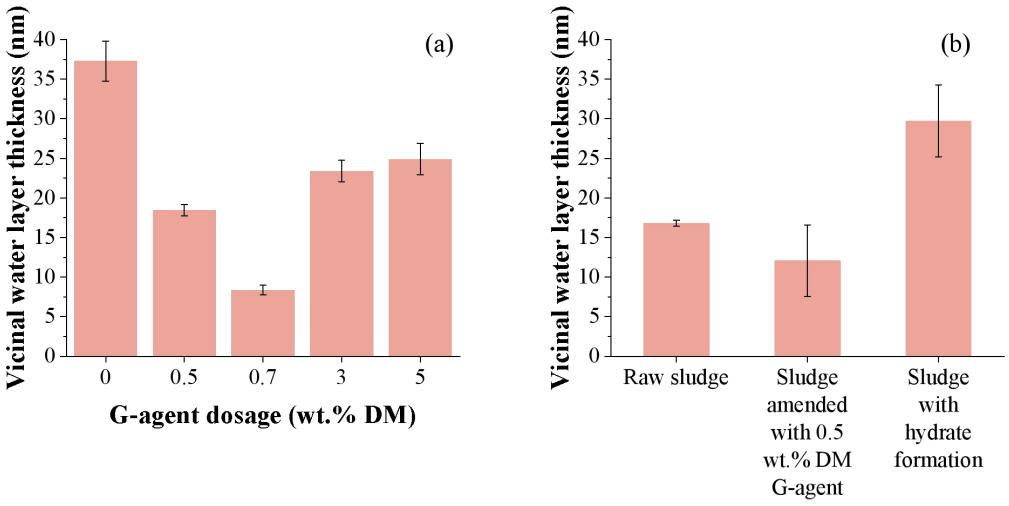

Figure 9. Vicinal water layer thickness of a) WAS amended with 0-5 wt.%DM G-agent; b) raw sludge, WAS amended with 0.5 wt.%DM G-agent and G-agent treated sludge with hydrate formation. Experimental conditions: 200 mL WAS with initial water content of 98.0 wt.%; the headspace for gas pressurization was 800 mL; the initial pressure of CO_2 was 5 MPa; the temperature for CO_2 hydrate formation was kept at around 1.5 ℃; the water conversion percentage was 100%.

In summary, the integration of Low-Field NMR and AFM results provides compelling evidence that the synergistic effect of G-agent and hydrate crystallization profoundly alters water mobility states. The treatment effectively strips the bound water layer from solid surfaces, converts it into more mobile water forms, and drastically reduces the thickness of the vicinal water film. This fundamental change at the molecular and micro-scale interface is a key mechanism behind the significant improvement in sludge dewaterability.

3.4.3 Solid porosity

Solid porosity of sludge obtained by the different dewatering steps

The structural architecture of pores within WAS, particularly their connectivity and morphology, is a critical factor governing mass transfer, hydration processes, and dewatering efficiency. Avizo 2022 was employed to quantitatively analyze the evolution of the porous structure in WAS subjected to different treatments, including centrifugation, hydrate formation, and dewatering.

A pronounced transformation in pore architecture was observed across treatments. The total porosity increased markedly from 0.1951 in raw sludge to 0.7836 after hydrate formation, indicating a substantial restructuring of the sludge matrix. Subsequent mechanical dewatering reduced the porosity to 0.6338, which nonetheless remained significantly higher than that of the raw sludge, suggesting a lasting modification of the microstructure.

The most striking change occurred in the isolated pore population. The number of isolated pores plummeted from 96,202 in raw sludge to just 2,561 after hydrate formation—a reduction of over 97%. Concurrently, their mean volume decreased from 0.539 μm^3 to 0.177 μm^3, and mean area from 2.283 μm^2 to 1.159 μm^2. This indicates that treatments, particularly hydrate formation, effectively eliminated a vast number of fine, isolated pores, which are known to hinder mass transfer by trapping water and impede efficient dewatering through steric effects.

Conversely, the volume of connected pores—the primary pathways for fluid flow—exhibited a substantial increase. The connected pore volume expanded from 785,225 μm^3 in raw sludge to 3,362,037 μm^3 after hydrate formation. Although dewatering reduced this volume to 2,719,230 μm^3, it remained 3.5 times larger than in the raw sludge. This signifies a dramatic enhancement in pore connectivity and the establishment of continuous, effective water-conduction channels.

Further analysis of the pore network model corroborates this structural enhancement. The mean coordination number, indicative of pore connectivity, rose from 5.087 in raw sludge to 12.085 after hydrate formation, confirming a more interconnected and continuous pore network. The average pore aperture nearly doubled from ~11.3 μm to ~18.6 μm, significantly reducing flow resistance. Furthermore, the average throat radius increased from 1.446 μm to 4.066 μm, and the throat number surged, collectively pointing to the formation of wider, less tortuous pathways for water and gas transport.

The mechanism behind this transformation can be attributed to the hydrate formation process. The crystallization and subsequent dissociation of gas hydrates within the sludge matrix likely disrupt the dense, gel-like structure of EPS and microbial aggregates. This disruption collapses fine, isolated pores and promotes the

coalescence of water into larger channels, thereby creating a more open and connected skeletal framework. This engineered microstructure is highly conducive to mass transfer during hydrate formation and drastically reduces the hydraulic resistance encountered during mechanical dewatering.

In conclusion, the treatments, especially hydrate formation, fundamentally remodel the WAS microstructure from a closed, impermeable system to an open, connected porous media. The drastic reduction in isolated pores and the concurrent development of a highly connected macro-pore network are identified as the key factors significantly enhancing both the thermodynamics/kinetics of hydrate formation and the efficiency of subsequent solid-liquid separation.

4. Conclusions

This study systematically investigated the enhancement of WAS dewaterability through a novel process integrating quaternary ammonium salt surfactant amendment and CO_2 hydrate crystallization. The G-agent acts not only as a flocculant that modifies interfacial properties and promotes particle aggregation but also as a hydrate formation promoter that facilitates water crystallization and pore restructuring. The key findings are summarized as follows:

The addition of G-agent significantly enhances CO_2 hydrate formation in waste-activated sludge, reducing the equilibrium pressure by up to 12% and the enthalpy of formation by approximately 14.57%, while also shortening the induction time by 78% and accelerating the growth rate by 273.7%. This dual role as both a thermodynamic promoter and kinetic enhancer leads to a drastic improvement in sludge dewaterability, with a maximum reduction of 94% in capillary suction time and a final cake water content of 53.83% after plate-frame filtration at the optimal dosage of 0.7 wt.% DM

under complete water conversion. The modification effects of the G-agent on the sludge interface were experimentally characterized. These include a reduction in gas–liquid surface tension to enhance CO_2 dissolution, induction of structural ordering in interfacial water molecules thus providing a templating effect that lowers nucleation energy barriers, and an improvement in surface hydrophobicity, ultimately optimizing dewatering performance. Furthermore, Low-Field NMR and AFM analyses demonstrate that the treatment converts strongly bound water into more mobile forms, reduces the vicinal water layer thickness by 78%, eliminates isolated pores, increases connected pore volume by over 3.5 times, and enhances pore coordination and throat dimensions, collectively reducing hydraulic resistance and significantly improving dewaterability.

In summary, the combination of G-agent and CO_2 hydrate crystallization offers a highly effective and energy-efficient strategy for improving WAS dewaterability. This process operates through multiple mechanisms, including interfacial modification, enhancement of water mobility, and microstructural transformation, all of which contribute synergistically to improved solid-liquid separation. This approach holds promising potential for application in advanced sludge treatment processes aimed at reducing energy consumption and improving operational efficiency, providing a sustainable pathway for sludge management with recyclable conditioning agents.

References

1. Wu, B., X. Dai, and X. Chai, *Critical review on dewatering of sewage sludge: Influential mechanism, conditioning technologies and implications to sludge re-utilizations.* Water Research, 2020. **180**: p. 115912.
2. Luo, Z., et al., *Dewatering of High Organic Sludge by Biochemical Conditioning Combined with Vertical Filter Press: a Case Analysis.* Water, Air, and Soil Pollution, 2023. **234**(4).
3. Ye, X., et al., *Research progress in the improvement of sludge dewatering by*

physical conditioning. Industrial Water Treatment, 2022. **42**(8): p. 51-59.
4. Yuan, H., et al., *Effects of different pretreatment methods on sludge dewatering performance.* Chinese Journal of Environmental Engineering, 2015. **9**(8): p. 4015-4020.
5. Wang, S., et al., *Life Cycle Assessment and Life Cycle Cost of Sludge Dewatering, Conditioned with Fe2+/H2O2, Fe2+/Ca(ClO)2, Fe2+/Na2S2O8, and Fe3+/CaO Based on Pilot-Scale Study Data.* ACS Sustainable Chemistry & Engineering, 2023. **11**(20): p. 7798-7808.
6. Gao, Y.-Y., et al., *Skeletal Structure-Based Conditioning for Improved Deep-Dewatering Efficiency of High-Salinity Food Waste Digestate.* ACS ES&T Engineering, 2025. **5**(3): p. 620-630.
7. Wang, Y., et al., *Unveiling the role of pore characteristics in sludge dewatering: Visualization by Nano-CT and micromodel study.* Water Research, 2024. **252**.
8. Wu, B., et al., *Crystallization-driven evolution of water occurrence states with implications on dewaterability improvement of waste-activated sludge.* Water Research, 2023. **244**.
9. Barati Rashvanlou, R., et al., *A combined ultrasonic and chemical conditioning process for upgrading the sludge dewaterability.* International Journal of Environmental Analytical Chemistry, 2020. **102**(7): p. 1613-1626.
10. Liu, Z., et al., *Physical conditioning methods for sludge deep dewatering: A critical review.* Journal of Environmental Management, 2024. **360**.
11. Wu, Y., et al., *Dewatering performance enhancement of waste activated sludge using FeCl3 and freeze-thaw synergistic co-conditioning method.* Journal of Water Process Engineering, 2024. **66**.
12. Cao, B., et al., *Enhanced technology based for sewage sludge deep dewatering: A critical review.* Water Research, 2021. **189**.
13. Chen, D., et al., *New insight on the combined effects of hydrothermal treatment and FeSO4/Ca(ClO)2 oxidation for sludge dewaterability improvement: From experimental to theoretical investigation.* Fuel Processing Technology, 2020. **197**.
14. Mahmoud, A., et al., *Advances in mechanical dewatering of wastewater sludge treatment*, in *Wastewater Reuse and Management*. 2013. p. 253-303.
15. Wu, B., et al., *Free-conditioning dewatering of sewage sludge through in situ propane hydrate formation.* Water Research, 2018. **145**: p. 464-472.
16. Sun, L., et al., *Advancement in Sewage Sludge Dewatering with Hydrate Crystal Phase Change: Unveiling the Micro-Moisture Migration and Dewaterability Mechanisms.* ACS Sustainable Chemistry and Engineering, 2023. **11**(32): p. 12075-12083.
17. Sun, L., *Study on a novel hydrate-based wastewater treatment method and thermal/kinetic regulation mechanism*. 2024, Dalian University of Technology. p. 126.
18. Zhang, H., et al., *A novel approach for sludge deep-dewatering via flowing-out enhancement but not relying on cell lysis and bound water release.* Water Research, 2024. **257**.
19. Wu, B., et al., *A quantitative theory integrating solid surface hydrophilicity and pore structure features for non-phase-change drying of sewage sludge through gradient increase of ultrahigh filtration pressure.* Water Research, 2023. **247**.

20. Zhang, J. and J.W. Lee, *Enhanced Kinetics of CO2 Hydrate Formation under Static Conditions.* Industrial & Engineering Chemistry Research, 2009. **48**(13): p. 5934-5942.

Low-Temperature, Ambient-Pressure and Rapid Mineralization of Per- and Polyfluoroalkyl Substances by Molten Alkali

Huan Zhang[a], Timothy J. Strathmann[b], Xiaoli Chai[a, c], Xiaohu Dai[a, c], Boran Wu[a, c, *]

[a]State Key Laboratory of Pollution Control and Resource Reuse, College of Environmental Science and Engineering, Tongji University, Shanghai 200092, China

[b]Department of Civil and Environmental Engineering, Colorado School of Mines, Golden, Colorado 80401, USA

[c]Shanghai Institute of Pollution Control and Ecological Security, Shanghai 200092, China

*Corresponding author: boranwu@tongji.edu.cn

Abstract

Per- and polyfluoroalkyl substances (PFASs) exhibit extreme environmental persistence due to the high strength of C-F bonds (~485 kJ/mol). This study presents an innovative NaOH-KOH binary eutectic molten system capable of achieving rapid and complete PFAS mineralization under mild conditions (NaOH:KOH = 3:7 molar ratio, 150 °C, ambient pressure), with consistent defluorination approaching 100%. For perfluorooctanesulfonate (PFOS), degradation followed pseudo-first-order kinetics ($-d[PFOS]/dt = k_{obs}[PFOS]$; k_{obs} = 0.0121±0.0009 min^{-1} – 0.5432±0.0129 min^{-1} at 150–300 °C), with defluorination activation energy (45.55±2.90 J/mol) lower than that of PFOS removal (51.94±1.51 J/mol), suggesting that the initial reaction step of degradation process of PFOS may require overcoming a greater energy barrier than the subsequent defluorination process. $^{13}C/^{19}F$ NMR analysis identified formate, carbonate, oxalate, and fluoride as major end products, while polyfluoroalkenes (CF_3-CF_2-CF_2-CF_2-CF_2-CF=CHF, C_7HF_{13}), 1H-perfluorohexane (CF_3-CF_2-CF_2-CF_2-CF_2-CHF_2, C_6HF_{13}), perfluoroenoic acid (CF_3-CF_2-CF_2-CF_2-CF_2-CF=CF-COOH, $C_8HF_{13}O_2$),

polyfluoroenol (CF_3-CF_2-CF_2-CF_2-CF_2-CF=CHOH, $C_7H_2F_{12}O$) were detected as transient intermediates by high-resolution Time-of-flight mass spectrometer (UPLC-ToF-MS), indicating that an initial OH^--catalyzed cleavage of the sulfonate head group may result in the formation of per- and poly- fluoroalkenes followed by sequential hydroxylation and decarboxylation reactions, ultimately leading to complete mineralization. This work provides a promising technology for treating PFASs-laden concentrates and solid wastes (e.g., spent activated carbon, industrial residues, sewage sludge), filling a critical gap in the PFASs destruction field.

Keywords: PFASs, PFOS, defluorination, molten alkali, fluorochemical

Synopsis: This study presents an innovative NaOH-KOH binary eutectic molten system capable of achieving rapid and complete destruction of refractory PFASs under low-temperature, ambient-pressure and solvent-free conditions.

Introduction

Per- and polyfluoroalkyl substances (PFASs) are a diverse class of anthropogenic chemicals that are extensively used in plastics, textiles, food wrapping materials, and fire-fighting foams. Widespread application of PFASs has led to significant environmental releases,[1-5] which raise serious public health concerns due to the toxicity and potential for bioaccumulation.[6] However, the efficient elimination of PFASs is difficult to realize by natural decomposition because of the high bond energy of C-F (~485 kJ/mol) and resulting long half-lives for natural attenuation (>100 years).

Many efforts have been devoted to mineralization of PFASs via UV photochemical and photocatalytic,[7,8] electrochemical,[9] sonochemical,[10] mechanochemical,[11] and thermal technologies.[12,13] However, the widely reported photochemical approaches are only applicable to transparent aqueous media and the efficiency is limited by the co-

existing oxyanion/oxidizing species that can scavenge hydrated electrons, e.g., oxygen, nitrate, and nitrite. The application of electrochemical, sonochemical and mechanochemical approaches generally requires complex devices that can be difficult to scale up. Thermal technologies, e.g., plasma incineration, are effective in complete mineralization of various PFASs, but the complex operating conditions, e.g., high temperature (1100 °C), present challenges for the wide-scale application.[14-16]

Since C-F bond is the highly polar covalent bond, partially positive carbon atoms are susceptible to attack by nucleophilic reagents (i.e., the species with negative charge or unbonded electron pairs), including OH^- associated with common alkali reagents. According to the previous reports, PFAS defluorination during the application of thermal treatment processes was enhanced by amendment with alkali or alkaline earth metal ions like calcium ion (Ca^{2+}). Wang et al.[17,18] investigated the effect of calcium hydroxide on mineralization behavior of perfluorooctanesulfonate (PFOS) under thermal conditions and the fate of PFOS during pyrolysis of lime-conditioned sewage sludge; it was found that the presence of $Ca(OH)_2$ in the mixture could facilitate PFOS decomposition at 350 °C, a lower temperature than required in unamended reactions (425 °C); however, even when the pyrolysis temperature was increased to 900 °C, the decomposition still remained in incomplete or slow PFOS transformation, which was accompanied by detection of shorter-chain fluorinated compounds that may still pose environmental risks.[17,18] Recently, PFAS degradation and defluorination was found to be mediated by sodium hydroxide (NaOH) at mild temperatures (80-120 °C) and pressures in dimethyl sulfoxide (DMSO):water mixtures, but the reaction required use of a flammable and toxic solvent and was limited to perfluorocarboxylic acids only.[19-21] NaOH has also been found to be an effective reagent for PFAS destruction and defluorination in aqueous media at near-critical temperatures and pressures (e.g.,

350 °C, 15 MPa, 1-5 mol/L NaOH).[22,23] This technology is proving to be practical for destruction of PFASs-containing wet concentrates (e.g., aqueous film-forming foams (AFFF) stockpiles, industrial waste, sorbent regenerate and membrane reject waste streams), but pressure-resistant reactor materials (e.g., high nickel alloys) are required to maintain alkali solutions as liquids at these reaction temperatures. Hence, there remains a critical need for technologies that can facilitate destruction of PFASs under the milder conditions, i.e., temperature of ~200 °C, ambient pressure and solvent-free.

Following the findings that alkali can induce the destruction of PFASs under thermal conditions, this study examined the direct application of molten alkali as a reaction medium for PFASs mineralization. Molten alkali, comprising a single alkali or mixture of multiple alkalis with a relatively low melting point, has a variety of applications in many sectors. Due to their excellent performance in high diffusivity, heat transfer, and thermal stability, molten alkalis should favor to provide the continuously renewing interface among reactants.[24] This dynamic environment facilitates chemical transformations that do not occur under typical conditions.[24] Consequently, the energy and solvent limitations of conventional methods may be overcome. Upon optimizing the mixture ratio of NaOH and KOH, we observed rapid and complete defluorination of several commonly identified perfluorosulfonic and perfluorocarboxylic acids at 150 °C and ambient pressure. Systematic experiments were then undertaken to quantify reaction kinetics and identify process parameters controlling the transformation of PFOS as a representative perfluorosulfonic acid. Furthermore, the insights into the controlling reaction mechanisms were provided by high-resolution mass spectrometry analysis of reaction mixtures. Findings of this study suggest an alternative technology for treatment of PFASs-contaminated solid wastes, e.g., industrial byproduct streams, PFASs-contaminated biosolids and PFAS-laden

adsorbents.

Materials and Methods

Chemicals and Reaction Process. A list of chemical reagents is provided in **Table S1 of Supporting Information**. The mixed alkali, composed of NaOH and KOH in a specific ratio, was synthesized via melt-crushing operation followed by cooling to the room temperature (**Text S1 of Supporting Information**).[25] Typically, 0.05 g PFAS was homogenized within 5 g synthesized mixed alkali through mechanical grinding.[26] The muffle furnace was preheated to the target reaction temperature (150–300 °C) and stabilized for 30 min to ensure thermal uniformity. Then, the nickel crucible containing the homogenized mixture of PFAS and alkali was rapidly transferred to the preheated muffle furnace, where the reaction proceeded at the specified temperature for a specified duration. Reactions were then quenched by transfer of the crucible to a dry ice-methanol bath (-78 °C) for 5 min. All experiments were conducted in duplicate to ensure reproducibility.

Analyte extraction. The reacted samples, as described above, were dissolved in 100 mL of 50% (v/v) methanol–water mixture, subjected to ultrasonication at 40 kHz and 200 W for 30 min until complete dissolution and clarification. Organic analytes were analyzed after dilution of the extracts with pure methanol, while inorganic components were detected after dilution of the extracts with deionized water.

PFAS and Fluoride Ion Quantification. Fluoride ion (F^-) concentrations were analyzed using ion chromatography (IC) after the liquid extract was diluted with ultrapure water to an appropriate concentration (**Text S2**). Concentrations of PFASs were quantified using the internal standard method (calibration curves: 1–1000 μg/L, R^2 >0.995; isotopically labeled ^{13}C-PFAS as internal standards) via ultra-high-performance liquid chromatography-triple quadrupole mass spectrometry (UPLC-

MS/MS, UltiMate 3000-TSQ Quantiva, Thermo Scientific, USA). Detailed UPLC-MS/MS analysis conditions are provided in **Table S2**.

Intermediate Product Analysis. The target PFAS (1wt.%) was processed in molten alkali (molar ratio of NaOH and KOH: 3:7) at 200 °C for 0–20 min. After reaction quenching, the residual reactants were extracted with methanol under sonication (40 kHz, 30 min). Non-targeted characterization of reaction intermediates was performed using a Waters ACQUITY UPLC-Bruker maXis II ETD high-resolution Time-of-flight mass spectrometer (TOF-MS) platform in full-scan mode (m/z 100–1200), with parameters provided in **Table S3**.

Potential volatile intermediates generated from PFOS-binary alkali mixture (1:1 w/w) were monitored in real-time using a CDS6200 pyrolyzer-Thermo ISQ7610 GC-MS system under programmed temperature pyrolysis (250 °C, 20 °C/min), with analytical conditions detailed in **Table S4**.

Final Product Analysis. ^{19}F NMR was used to analyze the conversion of PFAS organic fluorine to inorganic fluorine. PFAS (1 wt.%) in molten alkali was treated at 200 °C for a specified duration (0–60 min). The reactants were completely dissolved in a solvent mixture (v/v, 1:1) of deuterated dimethyl sulfoxide (DMSO-d_6) and deuterium oxide (D_2O). After vortexing until clear, 0.8 mL of the solution was transferred into a 5 mm NMR tube. ^{19}F NMR spectra were acquired on a Bruker ARX400 spectrometer (400 MHz) using parameters provided in **Table S5**.

^{13}C NMR analysis was used for structural validation and quantification of PFOS degradation carbon end-products. PFOS (5 wt.%) was treated in molten alkali at 200 °C for 30 min. The products were dissolved in 10 mL D_2O with sodium acetate (CH_3COONa) added as internal standard (δC 182.0 ppm, carboxyl carbon). The mixture was vortexed until homogeneous, and 0.8 mL was transferred into a 5 mm NMR tube.

^{13}C NMR spectra were recorded on a Bruker Avance NEO 500 MHz spectrometer equipped with a prodigy cryoprobe, following the parameters in **Table S5**. Quantitative analysis of carbon end-products was performed using sodium acetate as an internal standard. Fluoride, sulfate, formate, and oxalate were quantitatively analyzed using an ion chromatography system (IC; Dionex ICS-6000+, USA), as described in **Text S2 of Supporting Information**. The carbonate content was determined by diluting the reacted samples to an appropriate concentration, pre-adjusting the pH to neutrality (7), and then quantifying the CO_2 released through further acidification-purging by using a total organic carbon analyzer (Shimadzu, Japan); the carbonate content was then calculated based on stoichiometric relationships.[27]

Computational Methodology. Density functional theory (DFT) coupled with transition state theory (TST) was applied to evaluate the energetics of proposed reaction steps for PFOS destruction in molten alkali systems. DFT calculations were performed with the Gaussian 16 package.[28] All the geometry optimization, frequency calculation and transition state search were carried out with the 3-parameter hybrid functional B3LYP and a basis set consisting 6-31+G(d) for all atoms.[29-35] The single-point energy was performed with a basis set consisting 6-311+g(d,p).[35-37] The dispersion was described via Grimme's method.[36] The TS method was employed to search transition states. The frequency calculation was carried out under 473 K. All transition states were confirmed to have only one imaginary vibrational mode corresponding to movement along the reaction coordinate.

Results and Discussion

Performance of molten alkali system for PFAS destruction

Primarily, the feasibility of molten alkali in PFAS destruction was investigated. The eutectic temperature (T_e) variation across the compositional range of NaOH in

NaOH-KOH mixed alkali was calculated using FactSage 8.2 thermochemical software (Modified Quasichemical Model with the FTSalt database),[38,39] as shown in **Figure 1**. The lowest T_e of 145.6 °C was achieved at the molar ratio of NaOH and KOH of 3:7, corresponding to the reductions of 52.8% and 58.3% compared with the melting points of pure NaOH (318 °C) and KOH (360 °C), respectively. That is, by applying alkali in appropriate mixing ratios, molten alkali reaction matrices can be generated at much lower temperatures.[25] To assess the role of molten alkali in PFOS degradation, the PFOS destruction experiments were conducted in the mixed alkali with the varying ratio of NaOH and KOH but all at 180 °C for 120 min (**Figure 1**). Nearly complete PFOS degradation (~100% removal) was observed only when the mixed alkali had a predicted eutectic temperature <180 °C. Instead, the co-thermal process of PFOS and unmolten alkali (fraction of NaOH ranging from 80%-100%) only resulted in <15% PFOS degradation. This contrast indicated that the fully molten state of alkali was crucial for PFOS degradation. This may be attributed to the dissociation state of the NaOH-KOH binary system, which enhances the reactivity of OH^- with PFOS, and the superior dissolution capability of fully molten alkali, promoting thorough dispersion of reactants.[25] Given that the NaOH-KOH molar ratio of 3:7 exhibited the lowest eutectic temperature, this ratio was used for subsequent experiments.

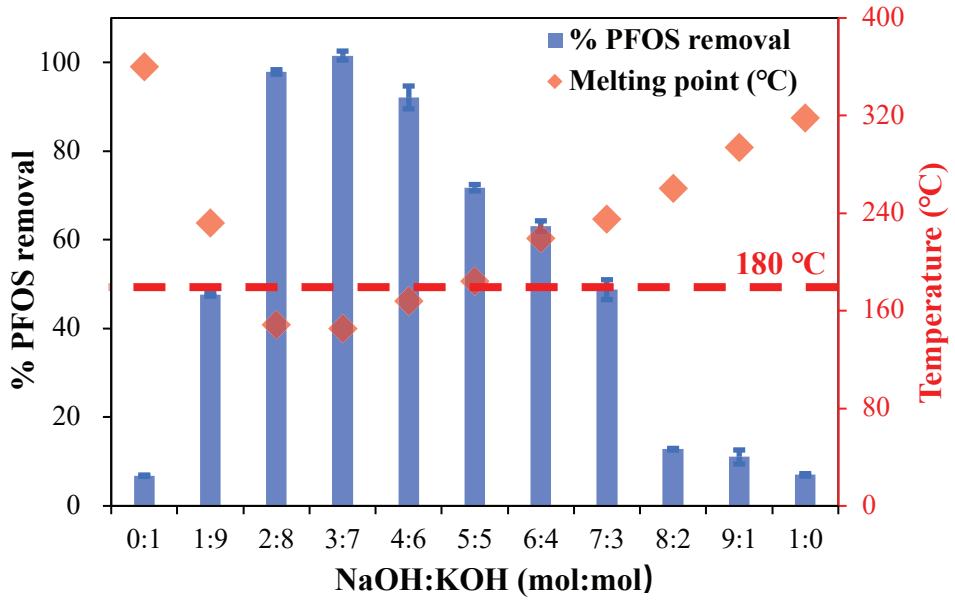

Figure 1. Role of molten alkali in destruction of PFOS. Symbols show the predicted melting point of NaOH:KOH alkali mixtures with different molar ratios, and bars show the measured extent of PFOS destruction. Reaction conditions: PFOS (1 wt.%) in alkali (5 g) at 180 °C for 120 min. Error bars represent the standard deviation observed for duplicate experiments (smaller than symbol if not shown).

Given the structural diversity of PFASs, the broad-spectrum efficacy of molten alkali treatment was further assessed for representative perfluoroalkyl sulfonic acids—PFOS, perfluorohexanesulfonic acid (PFHxS) and perfluorobutane sulfonic acid (PFBS)—as well as perfluoroalkyl carboxylic acids—perfluorooctanoic acid (PFOA), perfluorohexanoic acid (PFHxA), and perfluorobutanoic acid (PFBA)—spanning different carbon chain lengths. As shown in **Figure 2**, all the tested PFASs were degraded and defluorinated >95% within 60 min at 200 °C. The observed structural insensitivity implied that the molten alkali enabled the degradation of structurally different PFASs, irrespective of chain length and head group, in contrast to reactivity trends observed for most PFAS destruction technologies.[7,40,41] This applicability also reflected the great potential and practicality of molten alkali treatment for diverse PFAS mixtures.

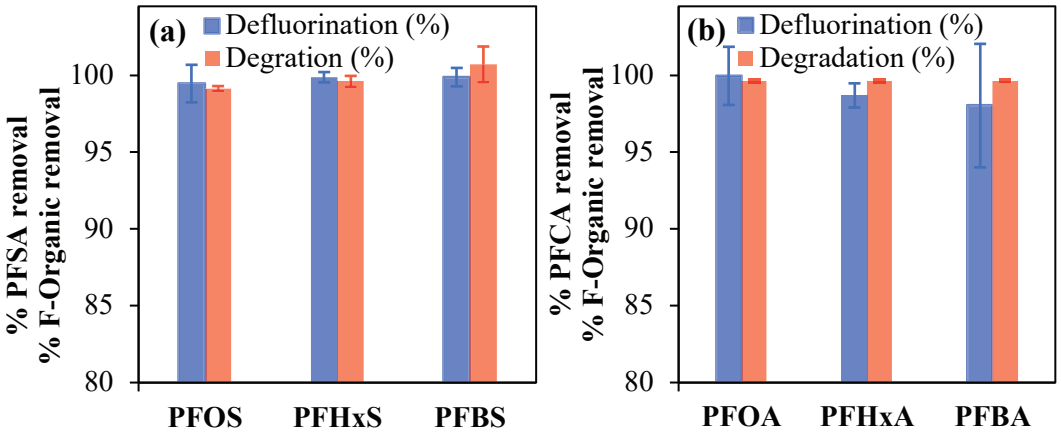

Figure 2. Molten alkali for destruction of representative perfluoroalkyl sulfonic acids (a) and perfluoroalkyl carboxylic acids (b). Reaction conditions: PFAS (1 wt.%) in molten alkali (5 g; molar ratio of NaOH and KOH: 3:7) at 200 °C for 60 min. Error bars represent the standard deviation observed for duplicate experiments (smaller than symbol if not shown).

^{19}F-NMR spectroscopy was also implemented to evaluate the efficiency of molten alkali in complete destruction of PFASs, since the conventional PFAS treatment approaches may generate by-products that are more toxic, harder to degrade, or more challenging to detect.[42-44] By monitoring the samples at various time points throughout the reaction process, it was observed that the complex spectral features associated with different C-F bonds in PFASs were progressively replaced by a single dominant peak corresponding to F^- after at least 40 min of reaction at 200 °C (**Figure S2**). Additionally, the spectral signals representing organic fluorine structures remained consistent with those of the initial PFAS, implying that no other major intermediate organic fluorinated compounds formed as stable reaction intermediates at this reaction temperature. Thus, according to the NMR data, the complete defluorination process appears to be accompanied by the degradation of the parent PFAS molecule at 200 °C.

Thermodynamics analysis on destruction of PFOS in molten alkali

The thermodynamic characteristics of PFOS destruction in molten alkali were systematically studied by varying the temperature between 150 °C and 300 °C, with an emphasis on clarifying the correlation between the degradation and defluorination

processes. The results revealed that PFOS removal during individual batch reactions followed pseudo-first-order kinetics (**Figure 3a**):

$$\frac{\mathrm{d[PFOS]}}{\mathrm{dt}} = -k_{\mathrm{obs}}[\mathrm{PFOS}] \quad (1)$$

The apparent rate constant (k_{obs}) increased significantly as the temperature rose, increasing from 0.0121±0.0009 min^{-1} (150 °C) to 0.5432±0.0129 min^{-1} (300 °C) Concurrently, **Figure 3b** illustrates that the defluorination rate of PFOS also exhibited a significant increase from 0.0098±0.0006 min^{-1} at 150 °C to 0.2840±0.0233 min^{-1} at 300 °C. Notably, both the removal and defluorination kinetics demonstrated highly consistent temperature dependence, suggesting a potential intrinsic relationship between these two processes. **Figure S3** compares the incremental extent of defluorination with PFOS degradation. Data collected at all four temperatures showed a general consistency between %PFOS degradation and %defluorination. This finding was in accordance with NMR analysis (**Figure S2**) that showed no evidence of stable fluorinated organic reaction intermediates. This further indicated that the molten alkali could effectively break the highly stable C-F bonds in PFAS molecules and promote their complete transformation into inorganic fluoride species.

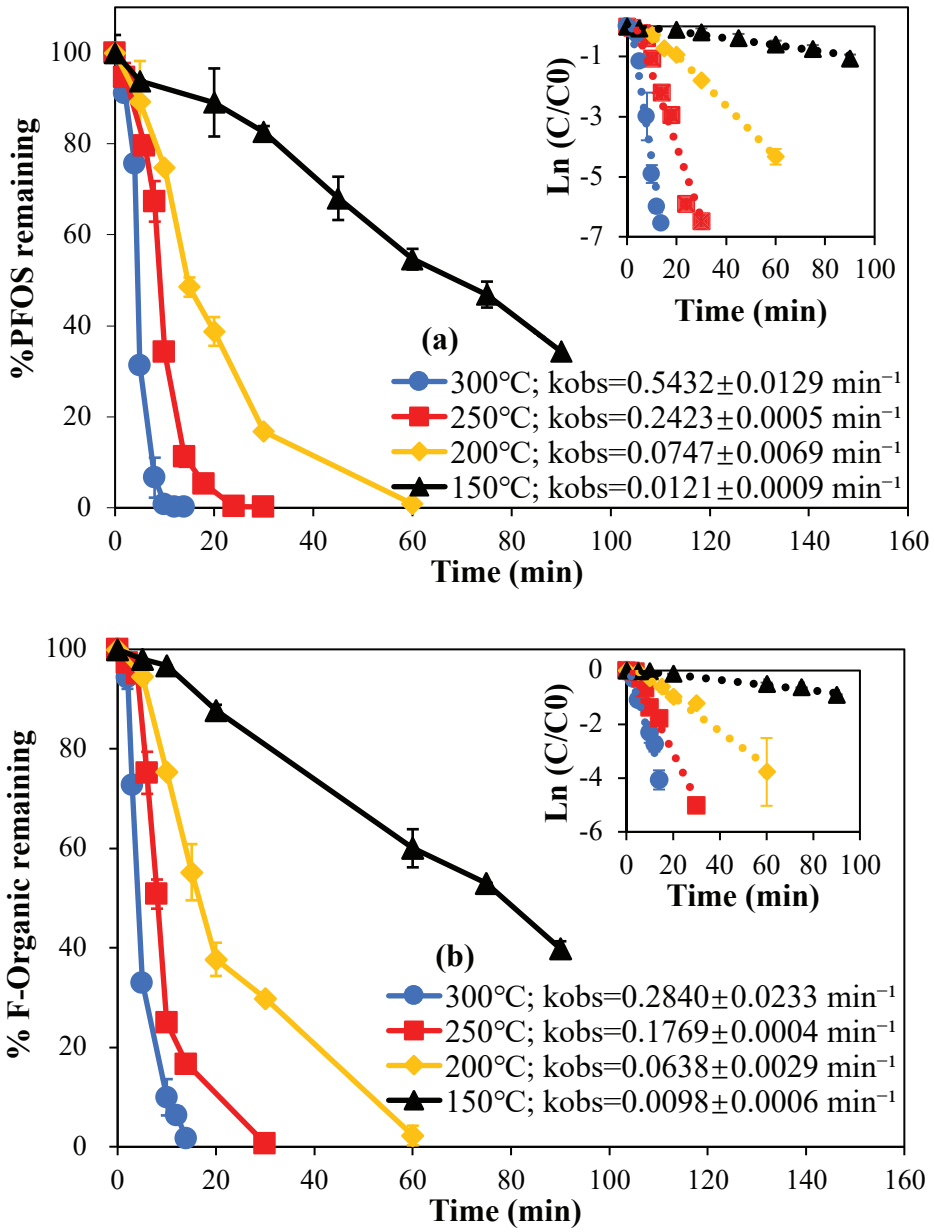

Figure 3. Kinetic analysis of PFOS destruction (a) and defluorination (b) as a function of reaction temperature. Reaction conditions: PFOS (1 wt.%) in molten alkali (5 g; molar ratio of NaOH and KOH: 3:7) at 150-300 °C for 0–90 min. Error bars represent the standard deviation observed for duplicate experiments (smaller than symbol if not shown). Inset in panel (a) and (b) shows linearized first-order model fits.

The activation energies of PFOS removal and defluorination processes were both calculated through fitting the apparent rate constant (k_{obs}) vs. temperature by Arrhenius equation as following:[45]

$$k_{obs} = Ae^{-\frac{Ea}{RT}} \quad (2)$$

or

$$lnk_{obs} = -\frac{E_a}{RT} + lnA \quad (3)$$

where k_{obs} is rate constant; E_a is activation energy; R is molar gas constant, 8.314 J/(mol·K); T is reaction temperature; A is pre-exponential factor. The fitting results based on equation (3) are shown in **Figure S4**. The activation energy refers to the energy required for a molecule to transition from its normal state to an active state that is more susceptible to chemical reactions.[45] The apparent activation energy for PFOS removal (51.94±1.51 J/mol) was higher than the activation energy for defluorination (45.55±2.90 J/mol), which reflected that the initial reaction step of degradation process may require overcoming a greater energy barrier than the subsequent defluorination process,[45] but the transformation rate of organic fluoride into F^- has the lower temperature sensitivity. Thus, raising the temperature didn't increase the defluorination rate to the same extent as the PFOS removal rate, and accordingly %defluorination slightly lagged behind %PFOS degraded at 300 ℃, particularly in samples where PFOS was nearly completely degraded (**Figure S3**). Furthermore, the first reaction step of PFOS degradation already led to the PFOS removal, but the complete defluorination of PFOS may contain multiple reaction steps. Especially, the small molecule fluorides probably generated by PFOS degradation are more difficult to completely mineralize.[18] Consequently, the complete defluorination process of PFOS could be influenced by several rate-limiting steps, leading to an apparent rate constant (k_{obs}) lower than that of PFOS removal.

Proposed destruction mechanism

Relationship between sulfonate group removal and defluorination

Under highly alkaline conditions, the removal of sulfonate group should correspond to the generation of sulfate ion (SO_4^{2-}).[46] Regarding the reaction pathways of PFOS destruction, the dynamic evolution of sulfate (SO_4^{2-}) and fluoride (F^-) ions

over time was primarily analyzed based on PFOS destruction reaction in molten alkali at 200 °C for 60 min (PFOS initial content: 1wt.%; molar ratio of NaOH and KOH: 3:7). As shown in **Figure 4a**, at 200 °C, the organic fluorine removal and sulfonate group removal exhibited a highly consistent upward trend over time, both approaching 100% at 60 min. This high consistency over time indicates that PFOS destruction in molten alkali likely initiated with the removal of the non-fluorinated group (sulfonate group), immediately followed by rapid and complete defluorination reaction steps. Instead, if PFOS degradation were to begin with partial defluorination, sulfonate group removal would likely lag behind the organic fluorine removal due to the formation of partially defluorinated intermediates containing sulfonate group.[47] However, as discussed in the above sections, the highly consistent extent of defluorination and degradation and NMR analysis results both indicated that no fluorinated intermediates were accumulated at 200 °C. On the other hand, the sulfonate removal followed by rapid defluorination also reflected that the rate-limiting step in PFOS degradation should be the cleavage of C-S bond.

As widely reported in the literature on alkaline PFAS destruction,[19,20,48] the departure of the sulfonic acid group destabilizes the electronic structure of the perfluorinated carbon chain, initiating the formation of highly reactive perfluorinated carbanion intermediates. These intermediates then undergo β-elimination, releasing fluoride ions (F^-) and forming an unsaturated structure, such as perfluorooctene-1 (**Figure 5a**). However, the defluorination proceeded extremely rapidly, it was difficult to monitor fluorinated intermediates due to their transient presence and low concentrations.[19,20,48] Therefore, to further investigate the degradation pathways of PFOS after sulfonate group removal, PFOS and perfluorooctene-1 (highly likely to be the product of PFOS after removing sulfonic acid group) were employed as the control

318 reactants.[19,20] Once perfluorooctene-1 (sulfonic acid-free) is generated from PFOS, it is
319 degraded rapidly. But directly using the high-concentration perfluorooctene-1 as the
320 starting reactant may provide more possibility to track intermediates of the
321 defluorination process.

322 In order to further substantiate the rationale for using perfluorooctene-1 as the
323 control group, the final carbon-containing products resulting from the degradation of
324 PFOS and perfluorooctene-1 in molten alkali were comparatively analyzed. As shown
325 in **Figure 4b**, regardless of the degradation ratio, the carbon end-product compositions
326 yielded from PFOS and perfluorooctene-1 degradation were nearly identical in terms
327 of their relative percentages to the initial reactant, e.g., formate (13.5% vs 12.5%),
328 oxalate (34.8% vs 32.8%), and carbonate (33.9% vs 28.3%) in the case of complete
329 degradation. These observations suggested that PFOS and perfluorooctene-1 likely
330 undergo the similar degradation mechanisms within molten alkali.[20] Accordingly, using
331 the high concentration perfluorooctene-1 as the starting reactant for PFOS degradation
332 pathway investigation could be acceptable.

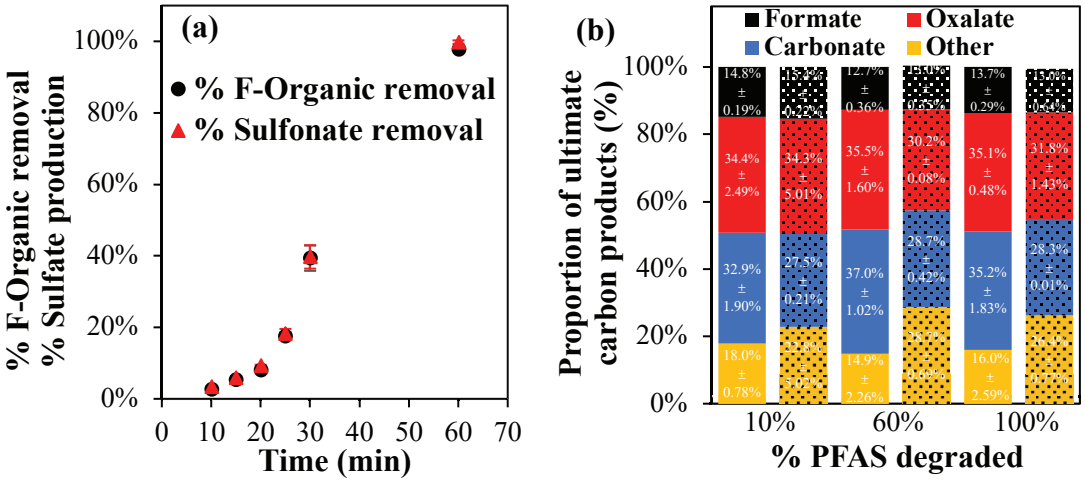

Figure 4. (a) Comparison between organic fluorine removal rate and sulfonate removal rate during PFOS degradation. (b) Comparison of the ultimate carbon fate of PFOS (solid fill) and perfluorooctene-1 (dotted). Conditions: PFOS (1wt.%) or perfluorooctene-1 (1wt.%) in molten alkali (molar ratio of NaOH and KOH: 3:7) at 200 ℃ for 0–60 min.

Proposed degradation pathway

As discussed above, rapid mineralization occurs once the initial pefluoroalkyl carbanion is formed by sulfonate group cleavage and undergoes β-elimination to form perfluorooctene-1. Therefore, perfluorooctene-1 was directly used as the model compound for controlled degradation at lower reaction temperatures and times (150 ℃ for 5 min) in an attempt to isolate fluorinated intermediates. Using UPLC-Q-TOF MS, the intermediates, i.e., CF_3-CF_2-CF_2-CF_2-CF_2-CF=CF-COOH ($C_8HF_{13}O_2$), CF_3-CF_2-CF_2-CF_2-CF_2-CF=CHF (C_7HF_{13}) and CF_3-CF_2-CF_2-CF_2-CF_2-CF=CHOH ($C_7H_2F_{12}O$), were identified, providing the experimental evidence for the defluorination mechanism of PFOS. As shown in **Figure 5a**, following the sulfonate group removal, an alkene intermediate is proposed to form via β-elimination (**Table S6**, Pathway A, RII).[19] Subsequent nucleophilic attack by OH^- induces substitution of fluorine and hydroxylation of alkene, forming an enol structure (CF_3-CF_2-CF_2-CF_2-CF_2-CF_2-CF=CFOH, **Table S6**, Pathway A, RIV-b). This intermediate further undergoes the γ-elimination to release F^- and produces an α, β-unsaturated acyl fluoride (CF_3-CF_2-CF_2-CF_2-CF_2-CF=CF-CF=O) through retro-conjugate addition (**Table S6**, Pathway B, RI),

liberating inorganic fluorine. The resulting unsaturated acyl fluoride (CF_3-CF_2-CF_2-CF_2-CF_2-CF=CF-CF=O) could further react with nucleophiles, perpetuating hydroxylation to form unsaturated carboxylic acid (CF_3-CF_2-CF_2-CF_2-CF_2-CF=CF-COOH, **Table S6**, Pathway B, RIII). The subsequent reaction decarboxylates the unsaturated carboxylic acid into unsaturated polyfluoroalkenes (CF_3-CF_2-CF_2-CF_2-CF_2-CF=CHF, **Table S6**, Pathway B, RV-VI), and also produces CO_2 that can be converted into carbonate (CO_3^{2-}) under alkaline conditions. The formation of carbonate (CO_3^{2-}) was confirmed as one of the final products according to the NMR analysis (**Figure 5c**). The following nucleophilic substitution converts unsaturated polyfluoroalkenes (CF_3-CF_2-CF_2-CF_2-CF_2-CF=CHF) into the enol structure again (CF_3-CF_2-CF_2-CF_2-CF_2-CF=CHOH, **Table S6**, Pathway B, RVIII). The following elimination steps progressively degrade the perfluorinated chain into free fluoride ions, formate and polyfluorohexene-1 (CF_3-CF_2-CF_2-CF_2-CF=CHF, **Table S6**, Pathway B, RXII), which could go through a series of elimination and substitution reactions shown in Pathway B, RIII-RVI steps again. As a result, an iterative cycle could be formed, achieving full mineralization of organic fluorine and generate formate.[19,49] Accordingly, the final product, formate, was also accumulated (**Figure 5c**). Theoretical calculations indicate that the steps following sulfonate group removal exhibit significantly reduced energy barriers, with near-barrierless steps for alkene hydroxylation and fluoride elimination, consistent with the rapid defluorination observed following sulfonate removal PFOS in molten alkali (**Figure S5**).

The degradation of PFOS in molten alkali may not be driven by a single pathway. When PFOS was used as the initial reactant, additional intermediates such as 1H-perfluorohexane (CF_3-CF_2-CF_2-CF_2-CF_2-CHF_2, C_6HF_{13}) and perfluorocyclopentane (CF_3-CF_2-CF_2-CF_2-CF_2-CHF_2, C_5F_{10}) were detected via Py-GC-MS. The

corresponding formation pathways of these intermediates are also proposed in **Figure 5a**. The C-S cleavage (**Table S6**, Pathway A, RI) results in the formation of carbon radicals,[49] which can further shorten the carbon chain by removing carbene or react with H_2O to form 1H-perfluorohexane (CF_3-CF_2-CF_2-CF_2-CF_2-CHF_2) (**Table S6**, Pathway C & D). H_2O can be produced through other intermediate reaction steps, such as self-dissociation reaction of OH^- in molten alkali ($2OH^- = O^{2-} + H_2O$)[50,51], as well as the decarboxylation/dehydroxylation reactions (Pathway B, RIV and RIX), as listed in **Table S6**. Under highly alkaline conditions, 1H-perfluoroalkane products are more likely to transform into reactive perfluoroanion, which can be further converted into perfluoroalkene and enters the cycles back to Pathway A followed by Pathway B for the complete mineralization.[19] Beyond formate and carbonate mentioned above, the analysis on the final carbon products (**Figure 5c**) further confirmed that the fluorinated organics intermediates can be broken down into oxalate salts as final products. That reflected the possible existence of other degradation pathways. For example, under highly alkaline conditions, the unsaturated carboxylic acid (CF_3-CF_2-CF_2-CF_2-CF_2-CF=CF-COOH) generated from RIII of Pathway B (**Table S6**) could also undergo the substitution reaction to form CF_3-CF_2-CF_2-CF_2-CF=CF-CFO^--COOH, which can readily split into oxalate ($C_2O_4^{2-}$), fluorine ion (F^-) and perfluoroanion by OH^-.[19]

As illustrated in **Figure 5a**, the degradation mechanism of perfluorooctane sulfonic acid (PFOS) in a molten alkali-driven deprotonation system can be generally summarized as two sequential processes: removal of non-fluorinated functional groups and defluorination. The chemical instability of PFOS originates from the charge localization effect in the deprotonated sulfonate group ($-SO_3^-$). The sulfur atom in sulfonate group exists in the +4-oxidation state, and its positive charge characteristic is amplified by the electron-withdrawing inductive effect of the perfluorocarbon chain

406 ($C_8F_{17}^-$), leading to a significant increase in charge density within the sulfonate group.
407 Limited delocalization capacity of sulfur's 3d orbitals and the rigid helical structure of
408 the perfluorocarbon chain collectively hinder charge dispersion via resonance or
409 conformational adjustments.[52] Consequently, the sulfonate group becomes highly
410 susceptible to the deprotonated agent, i.e., OH^-, in the strongly alkaline environment,
411 ultimately resulting in molecular framework collapse.[52] The terminal group elimination,
412 inferenced as the starting step of PFOS degradation, can be significantly enhanced
413 under the strong deprotonation conditions of molten alkali.

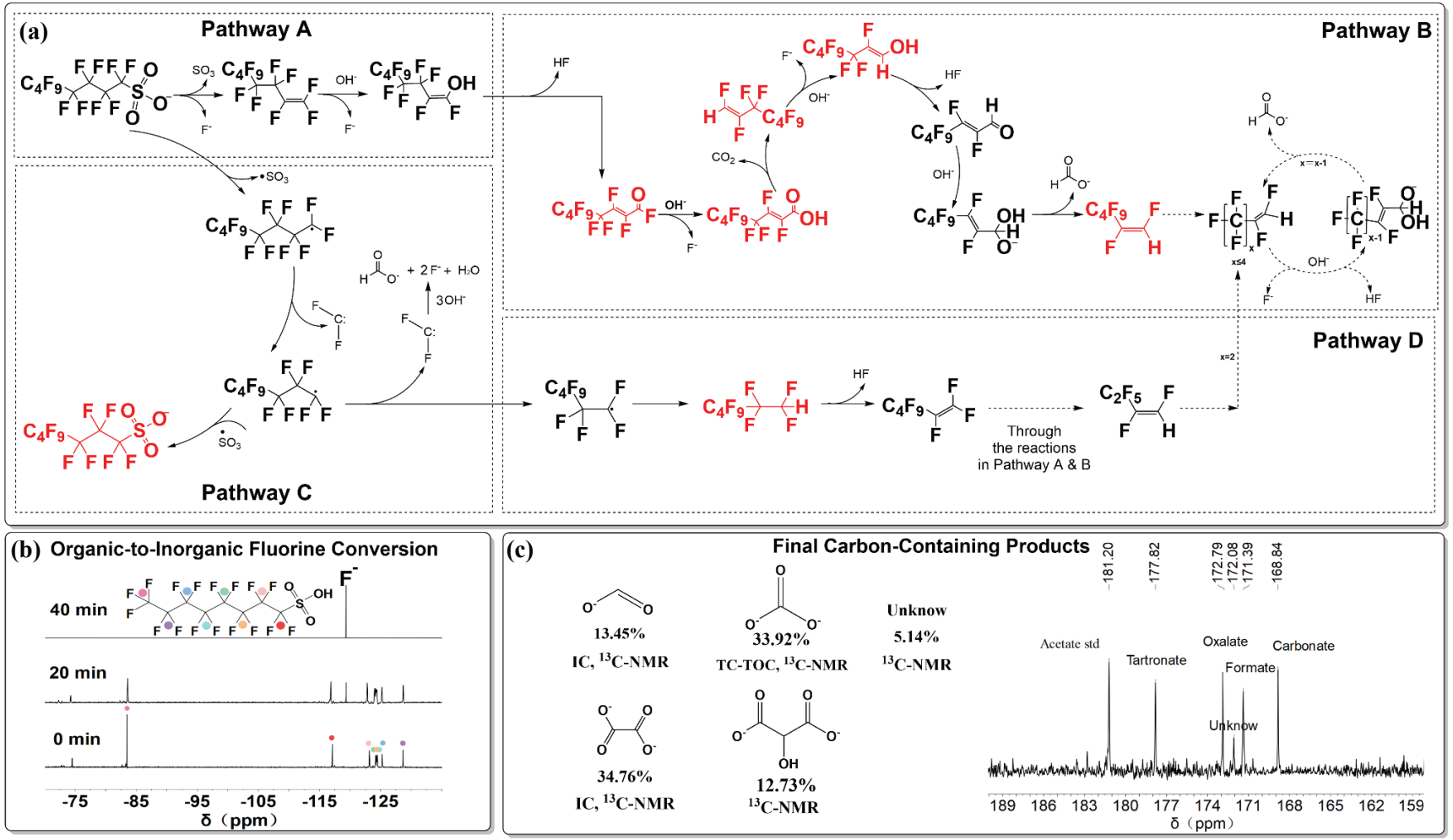

Figure 5. (a) Proposed destruction mechanism of PFOS in molten alkali. (b) Conversion of organic fluorine compounds during the reaction of PFOS (1wt.% in 5 g molten alkali (molar ratio of NaOH and KOH: 3:7), 200 °C, 0–40 min) in molten alkali. (c) Final carbon-containing products after the destruction of PFOS (5wt.% in 5 g molten alkali (molar ratio of NaOH and KOH: 3:7), 200 °C, 60 min) in molten alkali. The chemical formulas in red refer to the compounds detected by the intermediates' searching experiments.

Environmental implications

Per-and polyfluoroalkyl substances (PFAS) have emerged as global environmental contaminants due to their extensive industrial and consumer applications, environmental persistence and high toxicity. The extreme chemical stability of these compounds poses significant challenges to existing degradation technologies. Current PFAS degradation technologies primarily rely on advanced reduction and oxidation process (AOP/ARP), which degrade PFAS by breaking carbon-carbon (C-C) and carbon-fluorine (C-F) bonds. However, these methods face limitations such as low utilization efficiency of reactive species, incomplete mineralization, and inability to treat solid waste. The molten alkali-based strong deprotonation system developed in this study achieves complete PFAS mineralization through the following mechanism: efficient removal of non-fluorinated functional groups, followed by rapid conversion of organic fluorine to inorganic fluoride through nucleophilic substitution reactions. We think the molten alkali-based deprotonation system can achieve efficient destruction for various PFAS-contaminated solid wastes, including spent activated carbon, sewage sludge, contaminated soil (e.g., firefighting training grounds and fluorochemical legacy sites), and fluoropolymer waste (such as discarded waterproof textiles and non-stick coating residues). The solid waste can be placed in a mesh container and submerged into the molten alkali for PFAS defluorination. After treatment, the materials can be easily separated from the molten alkali by simply lifting the mesh container. The technology demonstrates significant techno-economic advantages: industrial-grade NaOH/KOH is used to construct the reaction system, with reagent recycling through alkali regeneration processes and mild reaction conditions (ambient pressure, 150–200 °C) to reduce long-term operational costs. All the findings here open up a novel

way for highly effective PFAS mineralization with potentials in engineering-scale application.

Supporting Information

Additional chemical information, analytical procedures, tables, and figures. This information is available free of charge on the ACS Publications website.

Acknowledgement

This study was financially supported by National Natural Science Foundation of China [Grant number 52270137].

References

1. Higgins, C. P.; Field, J. A.; Criddle, C. S.; Luthy, R. G., Quantitative determination of perfluorochemicals in sediments and domestic sludge. *Environ. Sci. Technol.* **2005,** *39* (11), 3946-3956.
2. Kim, S.-K.; Kannan, K., Perfluorinated acids in air, rain, snow, surface runoff, and lakes: relative importance of pathways to contamination of urban lakes. *Environ. Sci. Technol.* **2007,** *41* (24), 8328-8334.
3. Sun, H.; Li, F.; Zhang, T.; Zhang, X.; He, N.; Song, Q.; Zhao, L.; Sun, L.; Sun, T., Perfluorinated compounds in surface waters and WWTPs in Shenyang, China: mass flows and source analysis. *Water Res.* **2011,** *45* (15), 4483-4490.
4. Houtz, E. F.; Higgins, C. P.; Field, J. A.; Sedlak, D. L., Persistence of perfluoroalkyl acid precursors in AFFF-impacted groundwater and soil. *Environ. Sci. Technol.* **2013,** *47* (15), 8187-8195.
5. Kotthoff, M.; Müller, J.; Jürling, H.; Schlummer, M.; Fiedler, D., Perfluoroalkyl and polyfluoroalkyl substances in consumer products. *Environ. Sci. Pollut. Res.* **2015,** *22* (19), 14546-14559.
6. Wang, Z.; DeWitt, J. C.; Higgins, C. P.; Cousins, I. T., A never-ending story of per- and polyfluoroalkyl substances (PFASs)? *Environ. Sci. Technol.* **2017,** *51* (5), 2508-2518.
7. Bentel, M. J.; Yu, Y.; Xu, L.; Li, Z.; Wong, B. M.; Men, Y.; Liu, J., Defluorination of per-and polyfluoroalkyl substances (PFASs) with hydrated electrons: structural dependence and implications to PFAS remediation and management. *Environ. Sci. Technol.* **2019,** *53* (7), 3718-3728.
8. Sahu, S. P.; Qanbarzadeh, M.; Ateia, M.; Torkzadeh, H.; Maroli, A. S.; Cates, E. L., Rapid degradation and mineralization of perfluorooctanoic acid by a new petitjeanite Bi3O (OH)(PO4) 2 microparticle ultraviolet photocatalyst. *Environ. Sci. Technol. Lett.* **2018,** *5* (8), 533-538.
9. Schaefer, C. E.; Choyke, S.; Ferguson, P. L.; Andaya, C.; Burant, A.; Maizel, A.; Strathmann, T. J.; Higgins, C. P., Electrochemical transformations of perfluoroalkyl acid (PFAA) precursors and PFAAs in groundwater impacted with aqueous film forming foams. *Environ. Sci. Technol.* **2018,** *52* (18), 10689-10697.

10. Shende, T.; Andaluri, G.; Suri, R. P., Kinetic model for sonolytic degradation of non-volatile surfactants: Perfluoroalkyl substances. *Ultrason. Sonochem.* **2019,** *51*, 359-368.
11. Zhang, K.; Huang, J.; Yu, G.; Zhang, Q.; Deng, S.; Wang, B., Destruction of perfluorooctane sulfonate (PFOS) and perfluorooctanoic acid (PFOA) by ball milling. *Environ. Sci. Technol.* **2013,** *47* (12), 6471-6477.
12. Stratton, G. R.; Dai, F.; Bellona, C. L.; Holsen, T. M.; Dickenson, E. R.; Mededovic Thagard, S., Plasma-based water treatment: efficient transformation of perfluoroalkyl substances in prepared solutions and contaminated groundwater. *Environ. Sci. Technol.* **2017,** *51* (3), 1643-1648.
13. Singh, R. K.; Fernando, S.; Baygi, S. F.; Multari, N.; Thagard, S. M.; Holsen, T. M., Breakdown Products from Perfluorinated Alkyl Substances (PFAS) Degradation in a Plasma-Based Water Treatment Process. *Environ. Sci. Technol.* **2019,** *53* (5), 2731-2738.
14. Burdeniuc, J.; Jedicka, B.; Crabtree, R. H., Recent advances in C–F bond activation. *Chem. Ber.* **1997,** *130* (2), 145-154.
15. Watanabe, N.; Takata, M.; Takemine, S.; Yamamoto, K., Thermal mineralization behavior of PFOA, PFHxA, and PFOS during reactivation of granular activated carbon (GAC) in nitrogen atmosphere. *Environ. Sci. Pollut. Res.* **2018,** *25* (8), 7200-7205.
16. Wang, F.; Lu, X.; Li, X.-y.; Shih, K., Effectiveness and mechanisms of defluorination of perfluorinated alkyl substances by calcium compounds during waste thermal treatment. *Environ. Sci. Technol.* **2015,** *49* (9), 5672-5680.
17. Ochoa-Herrera, V.; Field, J. A.; Luna-Velasco, A.; Sierra-Alvarez, R., Microbial toxicity and biodegradability of perfluorooctane sulfonate (PFOS) and shorter chain perfluoroalkyl and polyfluoroalkyl substances (PFASs). *Environ. Sci.: Processes Impacts* **2016,** *18* (9), 1236-1246.
18. Brendel, S.; Fetter, É.; Staude, C.; Vierke, L.; Biegel-Engler, A., Short-chain perfluoroalkyl acids: environmental concerns and a regulatory strategy under REACH. *Environ. Sci. Eur.* **2018,** *30* (1), 9.
19. Trang, B.; Li, Y.; Xue, X.-S.; Ateia, M.; Houk, K.; Dichtel, W. R., Low-temperature mineralization of perfluorocarboxylic acids. *Science* **2022,** *377* (6608), 839-845.
20. Zhang, H.; Chen, J. X.; Qu, J. P.; Kang, Y. B., Photocatalytic low-temperature defluorination of PFASs. *Nature* **2024,** *635* (8039).
21. Trang, B.; Li, Y. L.; Xue, X. S.; Ateia, M.; Houk, K. N.; Dichtel, W. R., Low-temperature mineralization of perfluorocarboxylic acids. *Science* **2022,** *377* (6608), 839-+.
22. Wu, B.; Hao, S.; Choi, Y.; Higgins, C. P.; Deeb, R.; Strathmann, T. J., Rapid destruction and defluorination of perfluorooctanesulfonate by alkaline hydrothermal reaction. *Environmental Science & Technology Letters* **2019,** *6* (10), 630-636.
23. Hao, S.; Choi, Y.-J.; Wu, B.; Higgins, C. P.; Deeb, R.; Strathmann, T. J., Hydrothermal alkaline treatment for destruction of per-and polyfluoroalkyl substances in aqueous film-forming foam. *Environmental Science & Technology* **2021,** *55* (5), 3283-3295.
24. Nunes, V.; Queirós, C.; Lourenço, M.; Santos, F.; De Castro, C. N., Molten salts as engineering fluids–A review: Part I. Molten alkali nitrates. *Applied energy* **2016,** *183*, 603-611.

25. Dai, S. J.; Liu, L. B.; He, H. P.; Yang, B.; Wu, D. L.; Zhao, Y. C.; Niu, D. J., Highly-efficient molten NaOH-KOH for organochlorine destruction: Performance and mechanism. *Environmental Research* **2023,** *217*.
26. Zakiriyanova, I. D.; Khokhlov, V. A.; Kochedykov, V. A., Raman spectra and microdynamics of the hydroxide-ion in molten NaOH and NaCL-NaOH mixtures. *Journal of Molecular Liquids* **1999,** *83* (1-3), 153-162.
27. St-Jean, G., Automated quantitative and isotopic (13C) analysis of dissolved inorganic carbon and dissolved organic carbon in continuous-flow using a total organic carbon analyser. *Rapid Commun. Mass Spectrom.* **2003,** *17* (5), 419-428.
28. Frisch MJ, T. G., Schlegel HB, Gaussian 16, Revision A.03. In *Wallingford, CT: Gaussian, Inc.*, 2016.
29. Clark, T.; Chandrasekhar, J.; Spitznagel, G. W.; Schleyer, P. V., EFFICIENT DIFFUSE FUNCTION-AUGMENTED BASIS SETS FOR ANION CALCULATIONS. III. THE 3-21+G BASIS SET FOR FIRST-ROW ELEMENTS, LI-F. *Journal of Computational Chemistry* **1983,** *4* (3), 294-301.
30. Francl, M. M.; Pietro, W. J.; Hehre, W. J.; Binkley, J. S.; Gordon, M. S.; Defrees, D. J.; Pople, J. A., SELF-CONSISTENT MOLECULAR-ORBITAL METHODS .23. A POLARIZATION-TYPE BASIS SET FOR 2ND-ROW ELEMENTS. *Journal of Chemical Physics* **1982,** *77* (7), 3654-3665.
31. Gordon, M. S., Binkley, J. Stephen, Pople, John A., Pietro, William J., Hehre, Warren J, Self-consistent molecular-orbital methods. 22. Small split-valence basis sets for second-row elements. *J. Am. Chem. Soc* **1982,** *104, 2797-2803*.
32. Hariharan PC, P. J. A., The influence of polarization functions on molecular orbital hydrogenation energies. *Theor Chim Acta* **1973,** *28(3):213-222*.
33. Hehre, W. J.; Ditchfield, R.; Pople, J. A., Self—Consistent Molecular Orbital Methods. XII. Further Extensions of Gaussian—Type Basis Sets for Use in Molecular Orbital Studies of Organic Molecules. *Journal of Chemical Physics* **1972,** *56*, 2257-2261.
34. Spitznagel, G. W.; Clark, T.; Schleyer, P. V.; Hehre, W. J., EFFICIENT DIFFUSE FUNCTION-AUGMENTED BASIS-SETS FOR ANION CALCULATION .4. AN EVALUATION OF THE PERFORMANCE OF DIFFUSE FUNCTION-AUGMENTED BASIS-SETS FOR 2ND-ROW ELEMENTS, NA-CL. *Journal of Computational Chemistry* **1987,** *8* (8), 1109-1116.
35. Krishnan R, B. J., Seeger R, Pople JA, Self-consistent molecular orbital methods. XX. A basis set for correlated wave functions. *J Chem Phys* **1980,** *72(1):650-654*.
36. Grimme, S.; Antony, J.; Ehrlich, S.; Krieg, H., A consistent and accurate ab initio parametrization of density functional dispersion correction (DFT-D) for the 94 elements H-Pu. *J Chem Phys* **2010,** *132* (15), 154104.
37. McLean, A. D.; Chandler, G. S., Contracted Gaussian basis sets for molecular calculations. I. Second row atoms, Z=11–18. *Journal of Chemical Physics* **1980,** *72*, 5639-5648.
38. Bale, C. W.; Bélisle, E.; Chartrand, P.; Decterov, S. A.; Eriksson, G.; Gheribi, A. E.; Hack, K.; Jung, I. H.; Kang, Y. B.; Melançon, J.; Pelton, A. D.; Petersen, S.; Robelin, C.; Sangster, J.; Spencer, P.; Van Ende, M. A., FactSage thermochemical software and databases, 2010-2016. *Calphad-Computer Coupling of Phase Diagrams and Thermochemistry* **2016,** *54*, 35-53.

39. Jiang, Y. F.; Sun, Y. P.; Liu, M.; Bruno, F.; Li, S., Eutectic Na₂CO₃-NaCl salt: A new phase change material for high temperature thermal storage. *Solar Energy Materials and Solar Cells* **2016,** *152*, 155-160.
40. Park, H.; Vecitis, C. D.; Cheng, J.; Choi, W.; Mader, B. T.; Hoffmann, M. R., Reductive defluorination of aqueous perfluorinated alkyl surfactants: effects of ionic headgroup and chain length. *The Journal of Physical Chemistry A* **2009,** *113* (4), 690-696.
41. Bentel, M. J.; Liu, Z.; Yu, Y.; Gao, J.; Men, Y.; Liu, J., Enhanced degradation of perfluorocarboxylic acids (PFCAs) by UV/sulfite treatment: Reaction mechanisms and system efficiencies at pH 12. *Environmental Science & Technology Letters* **2020,** *7* (5), 351-357.
42. Li, J. N.; Austin, C.; Moore, S.; Pinkard, B. R.; Novosselov, I. V., PFOS destruction in a continuous supercritical water oxidation reactor. *Chemical Engineering Journal* **2023,** *451*.
43. Singh, R. K.; Fernando, S.; Baygi, S. F.; Multari, N.; Thagard, S. M.; Holsen, T., Breakdown products from perfluorinated alkyl substances (PFAS) degradation in a plasma-based water treatment process. *Abstracts of Papers of the American Chemical Society* **2019,** *258*.
44. Yang, M.; Du, Z. C.; Bao, H. J.; Zhang, X. L.; Liu, Q.; Guo, W. S.; Ngo, H. H.; Nghiem, L. D., Experimental and Theoretical Insight of Perfluorooctanoic Acid Destruction by Alkaline Hydrothermal Treatment Enhanced with Zero-Valent Iron in Biochar. *Acs Es&T Water* **2023,** *3* (5), 1286-1293.
45. Jensen, F., Activation energies and the Arrhenius equation. *Quality and Reliability Engineering International* **1985,** *1* (1), 13-17.
46. Yu, H.; Shan, C.; Li, J.; Hou, X.; Yang, L., Alkaline absorbents for SO2 and SO3 removal: A comprehensive review. *Journal of Environmental Management* **2024,** *366*, 121532.
47. Long, M.; Elias, W. C.; Heck, K. N.; Luo, Y.-H.; Lai, Y. S.; Jin, Y.; Gu, H.; Donoso, J.; Senftle, T. P.; Zhou, C., Hydrodefluorination of perfluorooctanoic acid in the H2-based membrane catalyst-film reactor with platinum group metal nanoparticles: pathways and optimal conditions. *Environmental Science & Technology* **2021,** *55* (24), 16699-16707.
48. Wang, J. L.; Chen, K. P.; Jin, B. S.; Woo, W.; Lum, M.; Canchola, A.; Zhu, Y. W.; Men, Y.; Liu, J. Y.; Lin, Y. H., Pyrolysis of Two Perfluoroalkanesulfonates (PFSAs) and PFSA-Laden Granular Activated Carbon (GAC): Decomposition Mechanisms and the Role of GAC. *Environmental Science & Technology* **2024,** *58* (49), 21850-21860.
49. Arnett, E.; Whitesell Jr, L.; Amarnath, K.; Cheng, J.; Marchot, E. In *Reactions of carbocations with carbanions through coordination and single electron transfer. Heterolysis and homolysis of carbon - carbon bonds*, Makromolekulare Chemie. Macromolecular Symposia, Wiley Online Library: 1988; pp 21-31.
50. Jin, W.; Du, H.; Zheng, S.; Xu, H.; Zhang, Y., Comparison of the oxygen reduction reaction between NaOH and KOH solutions on a Pt electrode: the electrolyte-dependent effect. *The Journal of Physical Chemistry B* **2010,** *114* (19), 6542-6548.
51. Castro, D. J.; Dragulin, S. M.; Manning, M.; Nathanson, G. M., Collisions and reactions of gaseous propanol with molten NaOH / KOH. *The Journal of Chemical Physics* **2006,** *125* (14).

52. Petersen, M. K.; Voth, G. A., Characterization of the solvation and transport of the hydrated proton in the perfluorosulfonic acid membrane nafion. *Journal of Physical Chemistry B* **2006,** *110* (37), 18594-18600.

Urban-Industrial Synergies in Sustainability: Evaluating the Co-Processing of MSWI Fly Ash in Industrial Kilns from Environmental and Economic Perspectives

Run Shi[1,2], Fan Fei[1,2], Xuguang Wang[3], Dawei Liu[4], Shuang Wu[4], Junwei Bai[3], Yan Zhang[3], Wei Su[1,2], Rongrong Lei[1,2], Hao Wang[1,2], Hongzhi Ma[1,2]*

1 School of Energy and Environmental Engineer, University of Science and Technology Beijing, 30 Xueyuan Road, Haidian District, Beijing 100083, China;
2 State Key Laboratory of Iron and Steel Industry Environmental Protection, University of Science and Technology Beijing, Beijing 100083, China
3 Changzhi Shougang biomass energy limited company, No.9 Guxian East Street, Luzhou District, Changzhi City, Shanxi Province, 046031
4 Shougang Environmental Industry Co., Ltd, Beijing 100043, China

INTRODUCTION

As rapid urbanization and improvements in living standards progressed, the generation of municipal solid waste (MSW) continuously increased. Currently, the global MSW production is estimated at 2.1 billion tons per year and is projected to reach 3.8 billion tons by 2050（Yang and Know et al.,2024; Liu, J. and L. Hu, et al. 2020 ）. Developing low-carbon and sustainable treatment technologies for MSWIFA is crucial for promoting sustainability in the global MSW management industry. Thermal treatment technology promoted chemical bonding, element substitution, and the formation of new crystalline phases through high-temperature reactions, which fixed the harmful components in MSWIFA within the high-temperature reaction products, achieving the goal of detoxification（Xiang, T. and R. Feng, et al. 2020）. The thermal treatment and resource utilization of MSWIFA were widely studied. To standardize MSWI-FA treatment technologies, a systematic evaluation of the environmental and economic impacts of these methods was considered essential. The Life Cycle Assessment (LCA) method was widely used to quantify environmental impacts and identify potential weaknesses in the product disposal process. It provided valuable insights for improving environmental assessments and allowed for multidimensional comparisons of MSWIFA management options（Xue, Y. and X. Liu2021; Fei, W. A. and X. B. Jian, et al. 2021; Kan, L. and R. Shi, et al. 2020）. This study applied Life Cycle Analysis (LCA) and Net Present Value (NPV) evaluation to assess three scenarios for the disposal or reuse of MSWIFA: 1) Landfilling after chelation solidification, 2) Co-disposal in a cement kiln followed by use in construction materials, 3) Co-disposal in a steel furnace sintering process. Life cycle inventories and cash flow lists for the three processes were established, and the distribution and migration efficiency of heavy metals during the disposal process were examined. The environmental impacts and economic benefits were compared, and the energy and resources used, as well as the emissions' impact on the environment, were quantified.

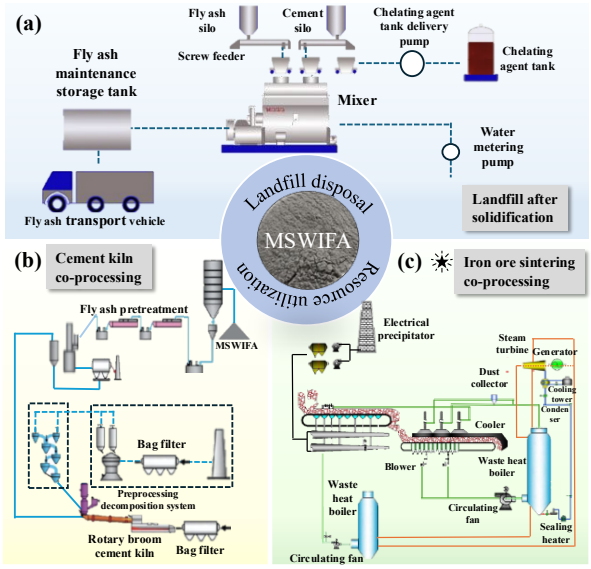

Fig.1. Non-hazardous landfill and industrial kiln collaborative processing processes for MSWIFA.

MATERIALS AND METHODS

The aim of this study was to assess and compare the environmental impacts and economic indicators of two MSWIFA treatment and disposal options, namely washing coupled with co-disposal in a cement kiln and co-disposal in a steel furnace sintering process. These two sintering disposal methods were compared with the

traditional chelation solidification and landfilling methods. In this study, the functional unit for LCA was defined as the treatment and disposal of 1000 kg of MSWIFA produced by a company in China. The system boundary was defined from the input of raw materials in the material production process to the output of the product, excluding the generation and transportation of fly ash, as well as the transportation and use of the product. Based on field surveys and preliminary calculations, the environmental impact of the transportation process was found to be relatively small. Therefore, in this study, the environmental impact of the transportation process was excluded from the life cycle analysis of the three resource utilization approaches. MSWIFA was considered as a waste that must be treated, and the environmental impact of its production process was disregarded.

The scope of the LCA study for the production process was from raw material extraction to finished product production. To comprehensively assess the three scenarios for MSWIFA disposal or reuse, including environmental impacts and economic benefits, three schemes and their corresponding system boundaries were proposed, as shown in Figure 2.

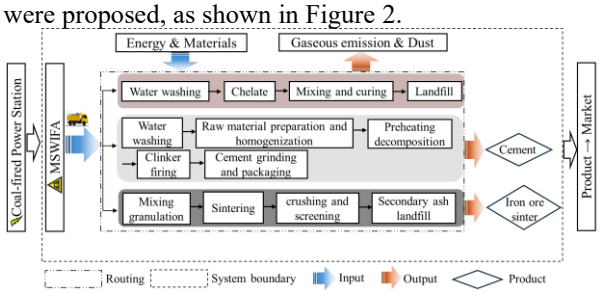

Fig.2. System Boundaries of Three MSWIFA Disposal or Reuse Scenarios

RESULT AND DISCUSSION

Based on the input and output data analysis of the life cycle inventory for the three processes, the material flow analysis and material flow diagrams of the entire process were shown in Figure 3. Based on the raw material input quantities and carbon emission factor data in Figure 2, it was calculated that 1 t of limestone decomposition produced 0.44 t of CO_2, the combustion of 1,636 kg of coal generated 4,538 kg of CO_2, limestone production emitted 577.4 kg of CO_2, and fly ash production emitted 81.5 kg of CO_2. The generation of exhaust gases and dust primarily originated from the clinker production process. Figure 3(a) showed that, in S2, 52.76% of material inputs ultimately flowed toward clinker preparation and cement production. The inventory data and Figure 4 showed that 83.46% of the material input in S3 ultimately flowed into the sinter product output, achieving a higher raw material utilization rate than the S2 process. Additionally, S3's carbon emissions accounted for 13.68%, compared to 33.04% in S2, indicating a better performance in carbon reduction. The CO_2 emissions in the cement industry were significantly higher than those of a single steel production enterprise.

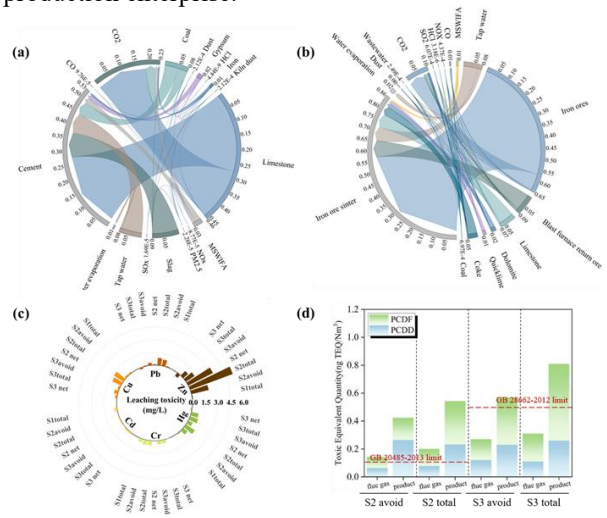

Fig.3. Material flow of （a）S2 and （b）S3

Based on the maximum emission values of the three treatment processes—chelation solidification and landfilling, water-washing pretreatment coupled with cement kiln co-processing, and iron and steel kiln sintering co-processing—a comparison was made of their emissions, reduction in emissions, and net emissions for the harmless treatment and resource utilization of MSWIFA. The goal was to support the exploration of sustainability in the harmless treatment and resource utilization processes of MSWIFA through a comprehensive analysis. Specific results were shown in Figure 4, indicating that when net emissions were included in the impact category analysis, the resource utilization of MSWIFA in industrial kilns outperformed traditional landfill methods.

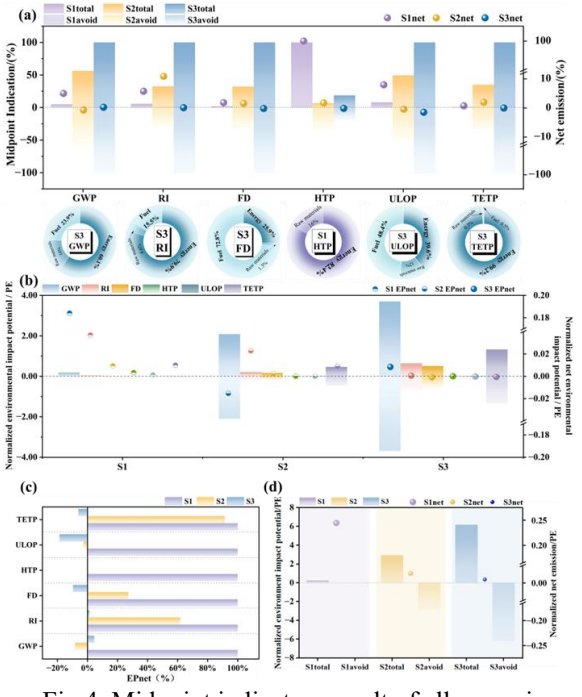

Fig.4. Midpoint indicators result of all scenarios.

The sensitivity analysis aimed to identify key factors in the Life Cycle Assessment (LCA) to evaluate the project's risk resilience and support emission reduction decisions. Results showed that under the S1 scenario, cement and diesel were the most sensitive parameters, with cement usage having a significant impact on global warming potential (GWP), among others. In the S2 and S3 scenarios, energy consumption parameters such as electricity and coal showed the highest sensitivity, particularly affecting toxicity-related indicators. Research indicated that using renewable energy sources like wind power could reduce environmental impacts by over 95%, while transportation contributed minimally to global warming. Co-processing MSWIFA in industrial kilns demonstrated clear environmental advantages over landfilling.

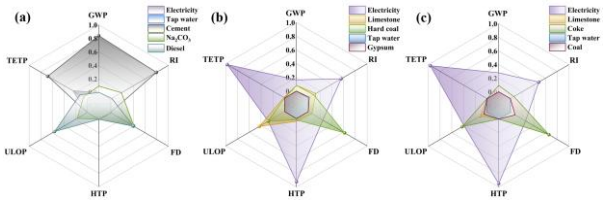

Fig.5. Sensitivity analysis of LCA results for the three-resource utilization process of MSWI fly ash.

To evaluate the socio-economic feasibility of producing materials from MSWIFA, a discounted cash flow (DCF) analysis was conducted based on material and energy flows. Scenario 3 (S3), which produces iron sinter, demonstrated the highest economic potential due to substantial raw material savings and higher product value—steel prices being approximately ten times that of cement. S3 achieved positive net present value (NPV) by the fifth year, indicating earlier commercial viability compared to S2 (ninth year) and S1 (landfilling). Operating cost analysis revealed that over 75% of S3's costs came from raw materials, while S2 incurred significant expenses in labor and resource consumption during water-washing. Improvements for S3 should focus on cost-effective raw material alternatives or low-cost pretreatment to increase MSWIFA substitution. Sensitivity analysis under varying subsidy assumptions showed S3 remains economically resilient with minimal policy dependence, whereas S1 relied heavily on subsidies. These results align with China's shift toward green finance and performance-based incentives, highlighting S3 as a sustainable and economically robust approach within industrial symbiosis frameworks.

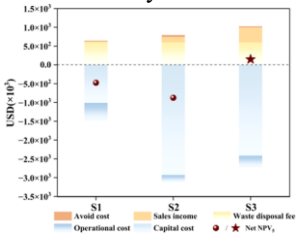

Fig.6. NPV_5 of MSWIFA treatment technologies by eLCC

CONCLUSION

This study evaluated the environmental and economic feasibility of treating MSWIFA through industrial kiln co-processing versus traditional stabilization/landfill using life cycle assessment (LCA). Results demonstrated that kiln co-processing effectively decomposes dioxins (at 700–1200°C) and immobilizes heavy metals, reducing human toxicity potential (HTP) while enabling resource recovery. Sensitivity analysis identified electricity consumption as a key environmental factor, suggesting renewable energy as an effective mitigation strategy. Steel sintering, with its advanced desulfurization and denitrification systems, minimized air pollution risks and achieved faster investment return, demonstrating superior environmental and economic performance. Overall, high-temperature co-processing in industrial kilns offers a sustainable MSWIFA management solution that balances waste reduction, resource utilization, and economic viability.

REFERENCE

1. Yang, D.K and Kow, K.W, et al.(2024). "Co-treatment of municipal solid waste incineration fly ash and alumina-/ silica-containing waste: A critical review. " Journal of Hazardous Materials **479:** 135677.

2. Liu, J. and L. Hu, et al. (2020). "Utilisation of Municipal Solid Waste Incinerator (MSWI) Fly Ash with Metakaolin for Preparation of Alkali-Activated Cementitious Material." Journal of Hazardous Materials 402(4): 123451.

3. Xiang, T. and R. Feng, et al. (2020). "Co-disposal of MSWI fly ash and spent caustic through alkaline-activation: Immobilization of heavy metals and organics - ScienceDirect." Cement and Concrete Composites 114.

4. Xue, Y. and X. Liu(2021). "Detoxification, solidification and recycling of municipal solid waste incineration fly ash: A review." Chemical Engineering Journal(11): 130349.

5. Fei, W. A. and X. B. Jian, et al. (2021). "Sustainable stabilization/solidification of the Pb, Zn, and Cd contaminated soil by red mud-derived binders." Environmental Pollution.

6. Kan, L. and R. Shi, et al. (2020). "Feasibility study on using incineration fly ash from municipal solid waste to develop high ductile alkali-activated composites." Journal of Cleaner Production 254: 120168.

Interpretable Machine Learning Framework for Optimization and Inverse Design of Catalytic Pyrolysis of Plastics

Zhengyu Wang[1], Linhai Ye[1], Tao Zhou[1] and Youcai Zhao[1]
1 The State Key Laboratory of Pollution Control and Resource Reuse, College of Environmental Science and Engineering, Tongji University, 1239 Siping Road, Shanghai 200092, China

ABSTRACT
The accurate prediction of catalytic pyrolysis products from plastics is crucial for advancing sustainable resource utilization of plastic waste. While machine learning (ML) can significantly improve experimental design efficiency, historical datasets are often plagued by substantial incompleteness. This study introduces a novel semi-supervised enhanced regression and denoising autoencoder (SERDA) model for robust imputation of missing product data, combined with ensemble learning techniques to optimize predictive models for methane yield. The SERDA model demonstrated superior performance over typical imputation methods, successfully reconstructing 70% continuous labels while preserving data distribution integrity. Support vector regression (SVR) achieved high coefficient of determination (R^2) for methane yield (testing R^2 = 0.88). Model interpretation further revealed that catalyst design parameters were pivotal for methane production. Guided by ML insights, catalytic pyrolysis of waste low-density polyethylene using computationally tailored Zn-ZSM-11 catalyst yielded 80.9 wt.% gaseous products, with methane and hydrogen accounting for 12.0 vol.% and 39.6 vol.%, respectively. This study establishes a comprehensive imputation-prediction-optimization framework that not only mitigates prediction inaccuracies caused by missing data but also enables inverse optimization of product yields. By integrating ML with experimental validation, this study enhances catalytic pyrolysis design efficiency and provides an intelligent framework for the sustainable plastic resource recycling.

INTRODUCTION
Plastics have become indispensable in modern life due to their low cost, durability, and versatility. However, global plastic production surpasses 400 million metric tons annually (Nayanathara and Ratnayake, 2024), with less than 30% of this waste being recycled (Pottinger et al., 2024). The widespread accumulation of plastic waste contaminates aquatic and terrestrial ecosystems, infiltrating water sources, soil, food chains, and even living organisms, where it poses significant toxicological risks (Gibb, 2019). Substantial research efforts have been directed toward developing efficient and scalable plastic recycling technologies (Al-Salem et al., 2009; Garcia and Robertson, 2017).
Thermochemical conversion has emerged as a leading approach for mitigating plastic pollution and enabling waste valorization, primarily due to its compatibility with existing petroleum refinery infrastructure for monomer and fuel production (Nanda and Berruti, 2021). Among these techniques, catalytic pyrolysis has demonstrated significant potential. This process, which involves heating plastics in the presence of a catalyst under an inert atmosphere, presents a cleaner alternative to conventional combustion and gasification methods (Shah et al., 2023). The catalytic approach can be precisely optimized to enhance the yield of high-value outputs, such as hydrogen and methane (Zhou et al., 2022). However, achieving directional conversion with high yield remains a critical challenge, hindering the reliable scale-up of pyrolysis technologies for industrial applications.
Currently, systematic methodologies for optimizing catalytic pyrolysis processes to maximize product yields are insufficiently developed. While traditional optimization relies on inefficient one-factor-at-a-time experimental approaches, emerging computational science methodologies are proving transformative for high-throughput screening and process optimization. Machine learning (ML) has emerged as a cost-effective computational approach that leverages historical data to predict pyrolysis outcomes (Mahesh and others, 2020).
Previous applications have demonstrated the potential of ML in predicting three-phase (gas, liquid, solid) product distributions and analyzing pyrolysis kinetics (Belden et al., 2023; Li et al., 2023). However, attempts to optimize monomer yields in catalytic pyrolysis remain limited, with existing models often exhibiting substantial prediction bias and failing to exceed experimental benchmarks (Li et al., 2025). This limitation arises from the exponential relationship between prediction accuracy and variable dimensionality, which demands large, high-quality datasets (Liu et al., 2022). A notable gap exists in the quantitative characterization of mixed product streams, resulting in inadequate data for robust model training. Recent advances in data imputation techniques offer promising solutions (Emmanuel et al., 2021), suggesting that a comprehensive optimization framework should incorporate (1) enhances datasets

through advanced imputation methods, (2) high-fidelity product distribution modeling, and (3) systematic process parameter optimization.

This study introduces an interpretable imputation-prediction-optimization framework to enhance plastic catalytic pyrolysis processes, aiming to maximize methane yield. Comprehensive historical datasets, encompassing plastic composition, catalyst properties, pyrolysis conditions, and product distributions, were systematically collected and preprocessed for ML model development. A novel "**S**emi-supervised **E**nhanced **R**egression and **D**enoising **A**utoencoder" (SERDA) model was developed to address data gaps in methane yield reporting from literature sources. Typical ML algorithm was rigorously evaluated to achieve high prediction accuracy. The framework integrates interpretability tools and optimization modules to guide experimental design toward maximizing target product yields. Validation through catalytic pyrolysis experiments confirmed the efficacy of this approach, providing critical insights for advancing plastic valorization through artificial intelligence (AI)-driven data refinement. This paradigm shift from conventional trial-and-error experimentation to data-driven AI solutions represents a significant advancement in process optimization efficiency.

METHODOLOGY

Data collection and preprocessing

A systematic literature review was conducted to compile experimental data from peer-reviewed publications spanning 2000 to 2024, sourced from Web of Science and Google Scholar. The search employed key terms such as "plastics", "plastic waste", "pyrolysis", "thermal cracking", "catalyst", and "catalytic cracking". After removing abnormal values, 329 sets of distinct experimental data were extracted, each containing comprehensive documentation of reaction conditions and product analyses. The dataset incorporates 27 potential predictor variables (**Table 1**), with methane yield serving as the response variable. To ensure robust model development and validation, the dataset was divided into training and testing subsets at an 8:2 ratio.

Table 1. Predictor variables and their characteristics in the plastic catalytic pyrolysis dataset.

Variables	Range
Low-density polyethylene (LDPE) High-density polyethylene (HDPE) Polypropylene (PP) Polystyrene (PS)	0-100 (wt.%)
Sample category	"Virgin", "Waste"
Particle size	0.1-50 (mm)
Catalyst type	"Carbon-based", "FCC", "Al-based", "Zeolite-based"
Molar ratio of Al	0-100 (%)
Electronegative	0-2
Ion radius	0-106 (pm)
Oxidation state	0-3
Weight percentage	0-40 (wt.%)
Acidity	"Non", "Lewis", "Bronsted", "Mixed"
Average pore diameter	0.1-20 (nm)
Total pore volume	0.01-1.5 (cm^3/g)
BET surface area	20-2200 (m^2/g)
Catalyst contact mode	"Solid", "Liquid", "Vapor", "Liquid and vapor"
Catalyst-to-polymer ratio	0-10 (w/w)
Operation mode	"Batch", "Semi-batch", "Continuous flow"
Reactor	"Tube reactor", "Fixed-bed reactor", "Microwave reactor", "Fluidized bed reactor", "Stirred reactor", "Autoclave reactor", "Conical spouted bed reactor", "Batch reactor".
Additives	"None", "Sand", "Organic waste"
Initial temperature	25-300 (°C)
Reaction temperature	300-800 (°C)
Heating rate	"Slow", "Fast", "Flash"
Carrier gas	"Nitrogen", "Air", "Reductive gas"
Gas flow rate	0-3500 (mL/min)
Hold time	0-80 (min)

Development of the SERDA model for data-imputation

The SERDA model developed in this study addresses a significant gap in methane yield reporting by reconstructing missing data from incomplete literature sources.

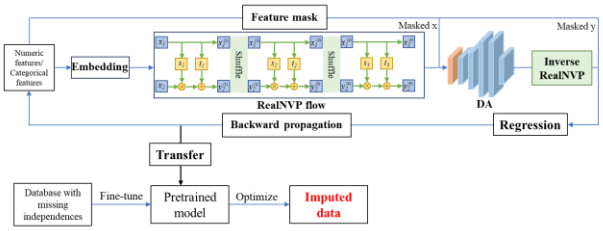

Figure 1. Architecture of the proposed SERDA model. Numeric and categorical features are transformed via RealNVP flow, encoded/denoised through neural networks, and optimized via regression for missing data imputation.

This innovative framework combines several key modules: (1) data embedding, (2) nonlinear feature transformation, (3) denoising autoencoding for robust feature extraction, (4) supervised regression modeling, and (5) transfer learning capabilities. These units form

an integrated pipeline capable of handling incomplete datasets and markedly enhances prediction accuracy (**Figure 1**).

The embedding process ensures optimal data preparation for the training of the SERDA model. The input feature space comprises numerical feature matrix (X_{num}), categorical feature indices (X_{cat_idx}), cardinality specifications for each categorical feature (*card*), and predetermined embedding dimensions (*emb*). Categorical features undergo transformation through embedding layers:

$$E_i = Embedding(card_i, emb_i)(X_{cat_idx}^{(i)})$$

Where E_i denotes the embedded representation of the *i*-th categorical feature, and $X_{cat_idx}^{(i)}$ represents the index value of the *i*-th categorical variable. All categorical features with numerical features are concatenated along the feature dimension:

$$X = [X_{num} \parallel E_i \parallel \cdots \parallel E_k]$$

Where $\parallel$ denotes feature-width concatenation. The preprocessed feature matrix X subsequently serves as input to RealNVP affine coupling layers for nonlinear feature transformation. The RealNVP architecture implements a bijective transformation that establishes an invertible mapping between the data distribution and latent space. The flow structure comprises three successive coupling layers, each utilizing feature masking and nonlinear transformations. The transformation is computed as:

$$y_b = x_b \odot \exp\big(s(x_a)\big) + t(x_a)$$

$$y = x_a + y_b$$

$$J = \frac{\partial y}{\partial x} = \begin{bmatrix} I & 0 \\ \dfrac{\partial y_b}{\partial x_a} & diag(\exp(s(x_a))) \end{bmatrix}$$

Where $s(\bullet)$ and $t(\bullet)$ represent scaling and shifting networks, implemented as fully-connected neural networks; $\odot$ is the Hadamard product. The Jacobian determinant J preserves both the data volume and probability mass during distribution mapping. This architecture design enables unobserved variables to directly inform the estimation of the underlying data distribution while ensuring computational tractability.

The denoising autoencoder (DA) component serves to eliminate irrelevant noise while retaining the primary distribution characteristics of the transformed data. Operating on the regularized latent space generated by the RealNVP flow, the DA architecture incorporates one dropout layer followed by five fully-connected layers, using LeakyReLU activation functions for both noise extraction and feature transformation (Farooq and Savaş, 2024). A masked reconstruction loss function is employed to effectively recover clean data representations from corrupted inputs.

The regression module implements a collaborative learning paradigm that jointly optimizes the tasks of data imputation and target prediction. The composite loss function combines:

$$\mathcal{L}_{total} = E \parallel x_{num}^{masked} - x_{rec} \parallel^2 + \beta \cdot E\, y_{obs} - y_{pred} \parallel^2$$

Where x_{num}^{masked} represents features with artificially introduced missing values, x_{rec} denotes the reconstructed features, and β controls the relative weighting between the imputation and prediction objectives. The reconstruction loss and regression loss ensure the continuous refinement of imputed values during training, thereby enhancing overall prediction accuracy.

The training protocol consists of pretraining phase and transfer learning phase. In the pretraining phase, the model is initially trained on complete gaseous product yield datasets, with 70% of target values masked to simulate missing data. Model performance is evaluated via five-fold cross-validation, with $\mathcal{L}_{total}$ serving as the primary optimization metric. In the transfer learning phase, the pretrained model is fine-tuned on the target dataset, leveraging observed variables and responses to adapt to new data distributions. This transfer learning approach facilitates the effective imputation of missing values while preserving prediction fidelity in the target domain.

Predictive model based on machine learning

The predictive model and the SERDA model were developed in Python 3.6 using scikit-learn (v0.24.2) within the PyCharm IDE (2022.2.2). Support vector regression (SVR) algorithm was employed to predict methane yield. Prior to model training, the dataset was normalized using Z-score standardization, transforming the features to a distribution with a mean of 0 and a standard deviation of 1 to mitigate potential prediction biases. The model was trained on a dedicated training set, while predictive performance was assessed using an independent testing set. Five-fold cross-validation was implemented to evaluate generalization capability and enhance the reproducibility of results. Model performance was quantified using the root mean squared error (RMSE) and R^2 on the testing set:

$$RMSE = \sqrt{\frac{1}{n}\sum_{i=1}^{n}(\hat{y}_i - y_i)^2}$$

$$R^2 = 1 - \frac{\sum(y - \hat{y})^2}{\sum(y - \bar{y})^2}$$

Where $\hat{y}$ represents the fitted y value, $\bar{y}$ is the average y value. After initial training and evaluation, the best-performing model was selected to inform subsequent experimental design.

Reverse design of catalytic pyrolysis process

To gain deeper insights into the variables influencing predictive performance, the Shapley Additive Explanation (SHAP) method was applied to the best-performing model to quantify the contribution of each input feature to the final predictions (https://github.com/shap). The SHAP values were

visualized through beeswarm and bar plots, enabling an interpretable assessment of how individual variables influenced the model outputs.

Building on these findings, the particle swarm optimization (PSO) algorithm was employed to simulate experimental conditions that maximize methane yields. The PSO-driven optimization focused on adjusting the top 20 most influential features identified by their SHAP values. Based on the model-derived optimization results, a catalytic pyrolysis experiment was conducted in a tube reactor (Hefei Kejing Material Technology Co., Ltd.). The catalyst, selected through the optimization process, was prepared by AOS Catalytic Material Co., Ltd. The feedstock plastic and catalyst were precisely weighed, mixed, and loaded into the reactor under controlled temperature, atmosphere, and reaction time conditions. The C_1-C_5 hydrocarbon quantification was conducted by gas chromatography with flame ionization detection (GC-FID; Trace 1300, Thermo Fisher Scientific, USA, equipped with an HP-Al_2O_3/KCl column, Agilent Technology, USA). Hydrogen was analyzed by GC with thermal conductivity detection (GC-TCD; Trace 1300, Thermo Fisher Scientific, USA, equipped with columns of 10301-U Hayesep Q, 20325 Porapak N and 13133-U MolSieve 5 A, Supelco, USA). Compound identification was achieved by matching retention times to certified standards, and quantification was performed using the external standard method.

RESULTS AND DISCUSSION

Description of plastic catalytic pyrolysis dataset

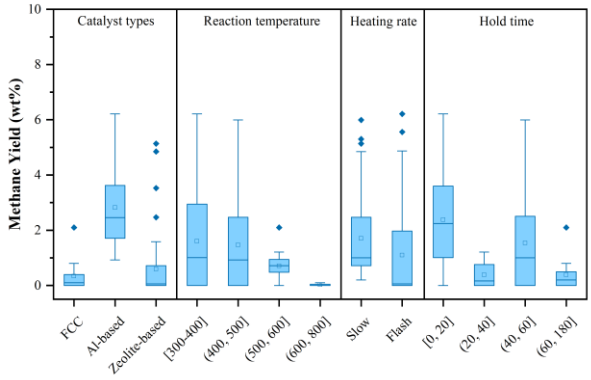

Figure 2. Yield distribution analysis of methane across experimental conditions, categorized by catalyst type, reaction temperature (°C), heating rate, and hold time (min).

The distribution of methane yields revealed a range of values from 0 to 6.2 wt.% (**Figure 2**). Prior to imputation, the methane data was relatively sparse (94 groups of data), but a discernible trend emerged: aluminum (Al)- and zeolite-based catalysts exhibited higher methane yields compared to FCC catalysts. High methane yields were predominantly observed between 300°C and 500°C, with different heating rates showing minimal effect on methane production. At the peak temperature, the hold time of 0-20 minutes or 40-60 minutes was primarily studied that associated with higher yields.

Imputation performance of SERDA model

Table 2. Frequency distribution of categorical variables in the gas and methane yield datasets.

Categorical variables	Counts	
	Gas yield	Methane yield
Batch	248	82
Semi-batch	73	4
Continuous flow	8	8
Carbon-based	57	-
FCC	46	12
Al-based	32	32
Zeolite-based	194	50
Slow	159	34
Fast	42	-
Flash	128	60
LDPE	99	21
HDPE	42	48
PP	66	8
PS	36	6
PE+PS	23	-
PP+PS	21	-
PE+PP+PS	42	11

According to statistics shown in **Table 2**, out of the 329 data groups collected, only 94 contained methane data. To enhance the robustness of methane prediction results, it is essential to impute methane production values into the entire set of 329 groups. Pretraining the imputation model on the gas yield dataset, as illustrated by the iteration process in **Figure 3 (a)-(c)**, shows that the regression loss converged at the 50th epoch, and the reconstruction loss converged after 200 epochs. This indicates that the model successfully captured the underlying distribution pattern of the independent data (Ma et al., 2023). Through the reconstruction of

source-domain data during fine-tuning, the model retained previously learned knowledge while adapting to new tasks, thus preventing overfitting to the limited target data (Laptev et al., 2018). The mean-square error (MSE), which is included as part of the regression loss, stabilized after the 50th epoch, suggesting that the DA structure significantly reduced noise within the dataset.

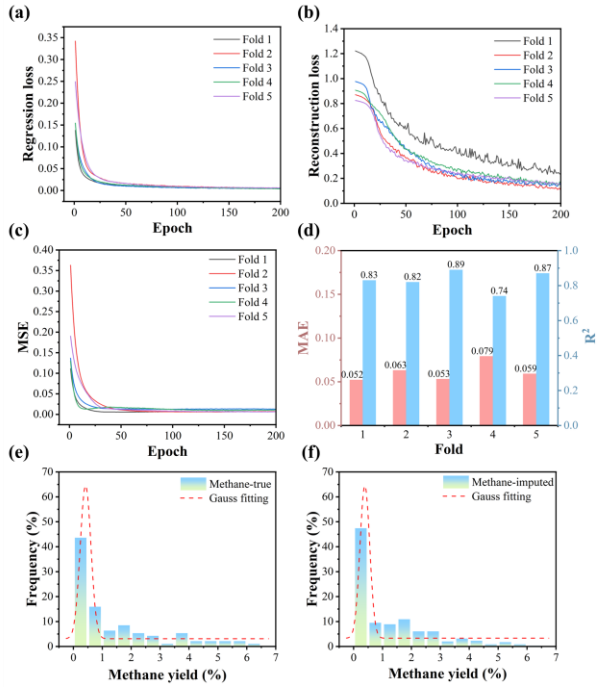

Figure 3. Performance evaluation of the SERDA model during pretraining and imputation phases. Training convergence metrics showing (a) regression loss, (b) reconstruction loss, and (c) MSE; (d) MAE and R^2 evaluation on masked gas yield data; Distribution comparison between (e) experimentally measured methane yields and (f) SERDA-imputed methane yields.

The results obtained from the SERDA model demonstrate the model's effectiveness in imputing missing data and its ability to preserve the underlying distribution of methane yields. Five-fold cross-validation yielded an R^2 between 0.74 and 0.89 and MAE between 0.052 and 0.079 (**Figure 3 (d)**). As shown in **Figure 3 (e)-(f)**, when predicting new instances, the imputed methane data followed a distribution where 40%-50% of the methane yield was concentrated between 0-0.5 wt.%. As the methane yield increased in both the real and imputed data, the frequency of the data decreased. Gaussian fitting revealed that the highest frequency of imputed and true methane yields occurred at 0.41 wt.% and 0.43 wt.%, respectively. These findings highlight the SERDA model's ability to capture complex data relationships and maintain distribution characteristics that are crucial for catalytic pyrolysis, aligning with the principles of high-dimensional data mapping which are central to the development of imputation models (Huang et al., 2024).

Product yield prediction and feature importance analysis

The prediction and visualization of methane yields, as shown in **Figure 4 (a)**, demonstrate that SVR algorithm achieved an R^2 of 0.8833 in predicting the methane yield based on the imputed dataset. Methane yield includes values near 0 in many studies. Regression models typically struggle with these near-zero values, frequently underestimating their distribution. Feature engineering preprocessing typically scales these zero values to a non-zero range, resulting in information loss (Alenazi, 2019). Consequently, predicting methane near zero becomes a critical factor affecting the accuracy of models.

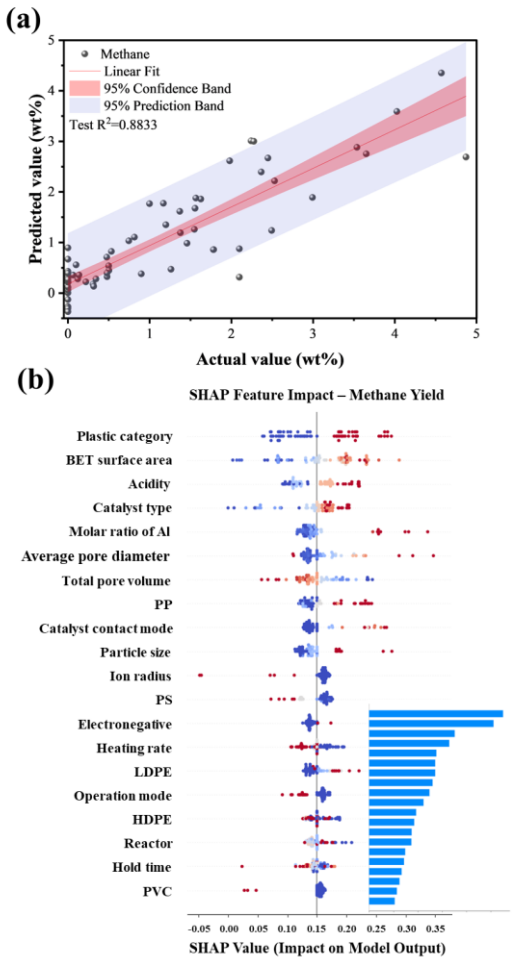

Figure 4. Model performance evaluation and interpretable machine learning analysis. (a) Linear fitting plots comparing experimental versus predicted methane yields; (b) SHAP summary plots showing

feature importance for methane yield prediction, ranked by mean absolute SHAP value.

Feature importance analysis, as summarized in **Figure 4 (b)**, revealed that plastic sample category was a significant factor influencing methane yield. Waste plastics were found to generate a higher proportion of methane than virgin plastics, potentially due to the presence of additives in the waste plastics or prior degradation by light, heat, and mechanical stress during usage, which makes them easier to emit greenhouse gas (Royer et al., 2018). Catalyst characteristics also played a pivotal role in methane generation. The red dots representing acidity, corresponding to Lewis and Bronsted acidity, showed high SHAP values, indicating a positive influence on methane yield (Zhou et al., 2022). Red dots for catalyst type identifies Al- and zeolite-based catalysts, and their usage at promoting methane yield is widely-accepted (Liu et al., 2024). Furthermore, higher BET surface area, a higher molar ratio of Al, a larger average pore diameter, and a smaller total pore volume were all found to be beneficial for methane yield.

Model-guided plastic catalytic pyrolysis design

Based on the developed feature analysis and ML-based framework, a global adjustment of variables was conducted. HDPE, LDPE, and PP were identified as suitable plastics for methane production based on SHAP analysis (**Figure 4 (b)**). The influence of the compositional ratio among these three plastics on methane yield (**Figure 5 (a)**) indicated that a higher proportion of LDPE, coupled with lower proportions of HDPE and PP, led to increased methane production. Specifically, feedstock containing >80 wt.% LDPE yielded higher methane. This enhanced methane production from LDPE can be attributed to its structural properties, including weak tertiary C–H bonds and a great propensity for radical formation, which facilitate methane generation (Marcilla et al., 2008).

Optimization of reaction conditions revealed that a reaction temperature range of 345-700°C and the hold time of 0-30 minutes were optimal for maximizing methane yield (**Figure 5 (b)**). For catalyst design, high methane production was favored by a mesopore distribution between 6-15 nm, a BET surface area below 700 m^2/g, and a pore volume ranging from 0.02 to 0.2 cm^3/g (**Figure 5 (c)**). These textural properties are critical, as they enable the adsorption of larger molecules, such as benzene and cyclohexane, which subsequently undergo further cracking into methane (Tao et al., 2003; Van Donk et al., 2003; Wu et al., 2023). Additionally, for Al-based and zeolite-based catalysts, the molar ratio of Al should be maintained below 70% (**Figure 5 (d)**). A lower Al ratio corresponds to an increased Si/Al or additive/Al ratio, which reduces apparent activation energies (Serrano et al., 2012). Following these optimizations, the highest predicted methane yield reached 6.7 wt.%.

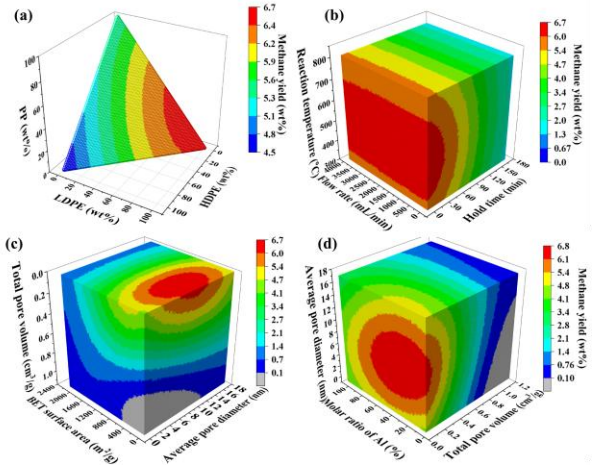

Figure 5. Process optimization for methane yield maximization from plastic catalytic pyrolysis. (a) Feedstock composition showing mass distribution of LDPE, HDPE, and PP; (b) Key reaction parameters: reaction temperature, carrier gas flow rate, and hold time; (c-d) Catalyst characterization: pore volume, pore size, BET surface area, and molar ratio of Al.

Guided by the optimized catalyst and reaction parameters derived from model-based experimental design, catalytic pyrolysis experiments of waste LDPE were performed using a tube reactor. The gas product fraction reached 89.08 wt.%. The actual methane yield was 5.57 wt.%, accompanied by 2.31 wt.% of hydrogen and 81.2 wt.% of other gaseous products. In terms of molar/volume ratio, hydrogen constituted the highest proportion (39.6 vol.%), followed by methane (12.0 vol.%). While hydrogen and methane were the primary gas-phase products, their relatively low molecular weights led to smaller contributions to the total mass balance.

CONCLUSION

Catalytic pyrolysis has emerged as a promising and widely studied approach for converting plastics into valuable chemical products. This study demonstrated that ML-based design strategies can effectively integrate historical data to optimize experimental parameters, thereby enhancing methane yield. To address the critical challenge of missing data that limits the accurate prediction of methane yield, a novel semi-supervised flow model, named SERDA, was developed. SERDA outperformed state-of-the-art imputation methods, successfully recovering approximately 70% of the missing methane data from prior studies.

Utilizing the supplemented dataset, the SVR model

achieved superior performance in methane yield prediction (testing R^2 = 0.88). Model interpretation revealed that catalyst design parameters—particularly aluminum ratio, BET surface area, and pore structure—were the most influential factors governing product distribution. Experimental validation of the ML-optimized pyrolysis of waste LDPE over a tailored catalyst yielded 80.9 wt.% of gaseous products, with methane and hydrogen at 12.0 vol% and 39.6 vol%, respectively.

This work develops a comprehensive and generalizable ML framework that integrates data imputation, robust prediction, catalyst insight, and optimization. This pipeline facilitates inverse design of catalysts and pyrolysis conditions, overcoming the data limitations commonly encountered in modern pyrolysis studies.

REFERENCES

Alenazi, A., 2019. Regression for compositional data with compositional data as predictor variables with or without zero values. Journal of Data Science 17, 219–237.

Al-Salem, S.M., Lettieri, P., Baeyens, J., 2009. Recycling and recovery routes of plastic solid waste (PSW): A review. Waste Management 29, 2625–2643. https://doi.org/10.1016/j.wasman.2009.06.004

Ascher, S., Watson, I., You, S., 2022. Machine learning methods for modelling the gasification and pyrolysis of biomass and waste. Renewable and Sustainable Energy Reviews 155, 111902.

Belden, E.R., Rando, M., Ferrara, O.G., Himebaugh, E.T., Skangos, C.A., Kazantzis, N.K., Paffenroth, R.C., Timko, M.T., 2023. Machine Learning Predictions of Oil Yields Obtained by Plastic Pyrolysis and Application to Thermodynamic Analysis. ACS Eng. Au 3, 91–101. https://doi.org/10.1021/acsengineeringau.2c00038

Emmanuel, T., Maupong, T., Mpoeleng, D., Semong, T., Mphago, B., Tabona, O., 2021. A survey on missing data in machine learning. Journal of Big data 8, 1–37.

Farooq, Y., Savaş, S., 2024. Noise Removal from the Image Using Convolutional Neural Networks-Based Denoising Auto Encoder. Journal of Emerging Computer Technologies 3, 21–28. https://doi.org/10.57020/ject.1390428

Garcia, J.M., Robertson, M.L., 2017. The future of plastics recycling. Science 358, 870–872. https://doi.org/10.1126/science.aaq0324

Gibb, B.C., 2019. Plastics are forever. Nature Chemistry 11, 394–395.

Huang, B., Zhu, Y., Usman, M., Chen, H., 2024. Semi-supervised learning with missing values imputation. Knowledge-Based Systems 284, 111171. https://doi.org/10.1016/j.knosys.2023.111171

Laptev, N., Yu, J., Rajagopal, R., 2018. Reconstruction and regression loss for time-series transfer learning, in: Proceedings of the Special Interest Group on Knowledge Discovery and Data Mining (SIGKDD) and the 4th Workshop on the Mining and LEarning from Time Series (MiLeTS), London, UK. pp. 1–8.

Li, J., Liu, T., Palansooriya, K.N., Yu, D., Wan, G., Sun, L., Chang, S.X., Wang, Y., 2025. Zeolite-catalytic pyrolysis of waste plastics: Machine learning prediction, interpretation, and optimization. Applied Energy 382, 125258. https://doi.org/10.1016/j.apenergy.2024.125258

Li, J., Yu, D., Pan, L., Xu, X., Wang, X., Wang, Y., 2023. Recent advances in plastic waste pyrolysis for liquid fuel production: Critical factors and machine learning applications. Applied Energy 346, 121350. https://doi.org/10.1016/j.apenergy.2023.121350

Liu, J., Jia, D., Xu, W., Chen, Z., Evrendilek, F., Cao, H., Zhong, S., Yang, Z., He, Y., Qi, J., 2024. Catalytic pyrolysis of FeAlOx and medical plastic waste: kinetic, slag conversion, and gas emission patterns. Journal of Environmental Chemical Engineering 12, 112605.

Liu, X., Lu, D., Zhang, A., Liu, Q., Jiang, G., 2022. Data-Driven Machine Learning in Environmental Pollution: Gains and Problems. Environ. Sci. Technol. 56, 2124–2133. https://doi.org/10.1021/acs.est.1c06157

Ma, S., Xu, Z.-S., Sun, T., 2023. Parallel generative adversarial imputation network for multivariate missing time-series reconstruction and its application to aeroengines. IEEE Transactions on Instrumentation and Measurement 72, 1–16.

Mahesh, B., others, 2020. Machine learning algorithms-a review. International Journal of Science and Research (IJSR).[Internet] 9, 381–386.

Marcilla, A., Beltrán, M.I., Navarro, R., 2008. Evolution of Products Generated during the Dynamic Pyrolysis of LDPE and HDPE over HZSM5. Energy Fuels 22, 2917–2924. https://doi.org/10.1021/ef800229d

Nanda, S., Berruti, F., 2021. Thermochemical conversion of plastic waste to fuels: a review. Environmental Chemistry Letters 19, 123–148.

Nayanathara, P.G.C., Ratnayake, A.S., 2024. The world of plastic waste: A review. Cleaner Materials 11, 100220. https://doi.org/10.1016/j.clema.2024.100220

Pottinger, A.S., Geyer, R., Biyani, N., Martinez, C.C., Nathan, N., Morse, M.R., Liu, C., Hu, S., De Bruyn, M., Boettiger, C., Baker, E., McCauley, D.J., 2024. Pathways to reduce global plastic waste mismanagement and greenhouse gas emissions by 2050. Science 386, 1168–1173. https://doi.org/10.1126/science.adr3837

Renzini, M.S., Sedran, U., Pierella, L.B., 2009. H-ZSM-11 and Zn-ZSM-11 zeolites and their applications in the catalytic transformation of LDPE. Journal of Analytical and Applied Pyrolysis 86, 215–220. https://doi.org/10.1016/j.jaap.2009.06.008

Royer, S.-J., Ferrón, S., Wilson, S.T., Karl, D.M., 2018. Production of methane and ethylene from plastic in the environment. PloS one 13, e0200574.

Serrano, D.P., Aguado, J., Escola, J.M., 2012. Developing Advanced Catalysts for the Conversion of Polyolefinic Waste Plastics into Fuels and Chemicals. ACS Catal. 2, 1924–1941. https://doi.org/10.1021/cs3003403

Shah, H.H., Amin, M., Iqbal, A., Nadeem, I., Kalin, M., Soomar, A.M., Galal, A.M., 2023. A review on gasification and pyrolysis of waste plastics. Frontiers in Chemistry 10, 960894.

Tao, Y., Kanoh, H., Kaneko, K., 2003. ZSM-5 Monolith of Uniform Mesoporous Channels. J. Am. Chem. Soc. 125, 6044–6045. https://doi.org/10.1021/ja0299405

Van Donk, S., Janssen, A.H., Bitter, J.H., de Jong, K.P., 2003. Generation, characterization, and impact of mesopores in zeolite catalysts. Catalysis Reviews 45, 297–319.

Wu, G., Hu, Y., Bao, Q., Zhang, J., Ge, J., 2023. Improved Catalytic Performances of the NaOH-Treated ZSM-22 Zeolite in the 1-Butene Skeletal Isomerization Reaction: Effect of External Acid Sites. ACS Omega 8, 14349–14364. https://doi.org/10.1021/acsomega.2c05478

Zhou, X.-L., He, P.-J., Peng, W., Lü, F., Shao, L.-M., Zhang, H., 2022. From plastics to methane and carbon spheres: The evolution of pyrolysis products during pyrolysis under autogenic atmosphere. Journal of Analytical and Applied Pyrolysis 161, 105421.

EFFECT OF LOADING ON TEMPERATURE MEASUREMENT USING OPTICAL FIBER SENSORS IN IMPERMEBLE LINER OF WASTE LANDFILLS

Yuto Yamakawa[1], Teppei Komiya[2], Hirofumi Nakayama[2], Takayuki Shimaoka[2,3]
1 Graduate school of Engineering, Kyushu University, 744 Motooka, Nishi-ku, Fukuoka, JAPAN
2 Faculty of Engineering, Kyushu University, 744 Motooka, Nishi-ku, Fukuoka, JAPAN
3 Kyushu Environmental Evaluation Association, 1-10-1 Matsukadai Higashi-ku, Fukuoka, JAPAN

1. INTRODUCTION

In Japan, the enactment of the Basic Act on the Promotion of a Recycling-Based Society spurred the recycling of waste, significantly reducing the volume of waste requiring final disposal. However, due to technical and economic constraints, the generation of waste that is difficult to recycle is unavoidable, making final disposal sites an indispensable social infrastructure going forward. For general waste final disposal sites and managed final disposal sites, eleven criteria are established for closure [1]. One of these is that "the interior of the landfill shall not exhibit abnormally high temperatures compared to the surrounding area." "Not exhibiting abnormally high temperatures" refers to a state where the temperature difference between the interior of the landfill and the surrounding ground is less than 20°C. The method for measuring and evaluating the temperature inside the landfill requires the use of vertical vent pipes or boreholes. Temperature measurements must be taken at intervals of 1 meter, from the surface to a depth of approximately 10 meters (a depth unaffected by air temperature), at least once every three months for a period of two years or more (totaling at least 8 measurements) [2]. Current temperature monitoring is limited to specific points. For waste landfills, which cover vast areas, have enormous landfill capacity, and exhibit internal heterogeneity, selecting representative points is difficult. Therefore, evaluating the internal landfill temperature over a broader area or in three dimensions is desirable.

Optical fiber sensors can measure various physical quantities such as strain, temperature, and voltage by detecting the intensity of reflected or scattered light within the fiber. They have the characteristic of using the optical fiber itself as the sensing element, enabling distribution measurements along the fiber's linear direction [3), 4)]. By installing optical fiber cables within the impermeable liner or capping at the base or slopes—which form the boundary between the landfill and the underlying foundation—it is possible to grasp the planar temperature distribution at the boundary. Using this boundary temperature distribution as boundary conditions in inverse analysis enables estimation of the three-dimensional temperature distribution within the landfill. This is expected to contribute to high-precision management of the landfill and its decommissioning assessment.

Komiya et al.[5)] demonstrated, using a slope model of a waste landfill with a double-layer impermeable sheet structure, that optical fiber cables installed within the impermeable liner enabled two-dimensional temperature distribution measurements via optical fiber sensors, indicating the applicability of optical fiber sensors for detecting leaks in the impermeable liner. Hamada et al.[6)] demonstrated that optical fiber cables can be installed within the capping layer constructed over the closed sections of a landfill, enabling two-dimensional temperature distribution measurements of the capping layer using optical fiber sensors. However, previous studies did not consider loads acting on the optical fiber cable in actual landfills, such as those from the landfill waste and overburden, loads from heavy machinery performing landfill and compaction operations, or the pulling of the impermeable liner due to settlement of the waste layer. It remains unclear whether temperature measurement using optical fiber sensors is possible under conditions where these loads are applied.

This study conducted experiments using a soil tank with a loading device simulating a landfill slope, aiming to clarify the effects of loads on temperature measurement, assuming the measurement of the surface temperature distribution of a liner system on a landfill slope using an optical fiber sensor.

2. EXPERIMENTAL METHOD

2.1 Optical Fiber and Measuring Instruments Used

Figure 1 shows the structure of the optical fiber cable used in this study. These cables enable distributed measurement and allow any position along the entire fiber length to function as a measurement point. Two types of multimode optical fiber cables with different coatings were used: M-PAC(14/18)1GI-R(5.0HDPE) (Sumitomo Electric Industries, Ltd.) and 0.9GI(PE-A1G)-NH (Sumitomo Electric Industries, Ltd.).

Hereafter, these are referred to as Cable I and Cable II, respectively. Cable I is a optical fiber cable with a PE-coated SUS tube embedded structure. It protects Φ0.25 mm bare strands (optical fibers (quartz glass) coated with UV-curable resin) within a stainless-steel tube coated with PE resin. Cable II is a non-halogen resin-coated optical fiber cable, consisting of a Φ0.9 mm optical fiber made of Φ0.25 mm strands coated with non-halogen resin.

In this study, two experiments were conducted using the same cables. The first experiment using Cable I is referred to as Experiment 1-I, and the second as Experiment 2-I. The first experiment using Cable II is referred to as Experiment 1-II, and the second as Experiment 2-II.

An optical fiber sensor was formed using the ROTDR method, which measures temperature from the intensity of Raman scattered light. This method involves measuring the optical intensity of anti-Stokes light and Stokes light, then determining the temperature from the ratio of their intensities. The spatial resolution of this measuring instrument was 150 cm, and the measurement interval was 25 cm. Here, the measurement interval refers to the spacing between temperature measurement points, while spatial resolution indicates the average temperature value over a length of m centered on the measurement point. The measurement error is specified in the catalog as a maximum of ±2.0°C. Measurement results using optical fiber cables immersed in constant-temperature water tank set to 20, 25, and 30°C showed the following measurement errors in this experimental system: a maximum of ±0.5°C in Experiment 1-I, a maximum of ±0.8°C in Experiment 1-II, and a maximum of ±0.5°C in Experiments 2-I and 2-II. The number of additions was set at 2^{22}, with each measurement taking approximately 3 minutes.

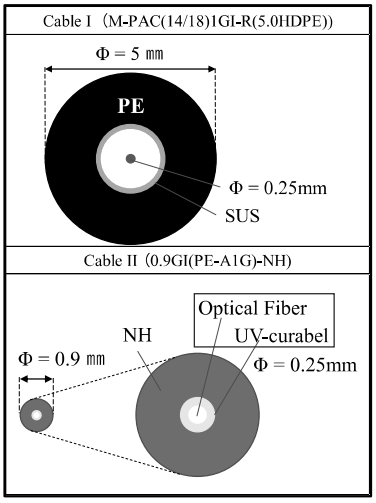

Fig.1 The used optical fiber cable

2.2 Soil Tank and Liner System

Figure 2 shows the internal structure of the soil tank. A foundation ground (slope 1:1.8 ratio) made of concrete panels was installed inside the soil tank (W1985 mm × D800 mm × H1135 mm). A liner system simulating a double-sheet configuration (three layers of nonwoven fabric (spunbond, Toyobo Co., Ltd.) and two layers of geomembrane liner (TPO-PP, Mitsuboshi Belt, Ltd.) laid alternately) where the flat surface of the embankment shoulder was fixed. Sand was filled over the liner system. manufactured by Mitsuboshi Belting, Ltd.) were alternately laid and fixed to the flat surface of the crest of the slope. Sand was filled on top of the liner system. Normally, a protective soil layer is placed on top of the liner system, followed by a waste layer, but since the main purpose of this study was to apply load, the waste layer was also replaced with sand. Greer was applied to the inside wall of the soil tank, and a rubber sheet was installed to eliminate friction between the filled sandy soil and the side wall.

Figure 3 shows the structure of the liner system. Optical fiber cables were laid on the nonwoven fabric in the center of the liner system. Cable I was secured with cable ties, and cable II was secured with wire.

Figure 4 shows the optical fiber cable routing and the installation locations of soil pressure gauges, and thermocouples for measuring true temperature to compare with the optical fiber sensor readings.

The optical fiber cable routing direction relative to the slope gradient was set parallel for Cable I and parallel or perpendicular for Cable II. Measurements with light incident in the direction of the arrows in the figure are termed positive direction temperature measurements; measurements with light incident in the opposite direction are termed negative direction temperature measurements. For temperature calibration of the optical fiber sensors, a 15 m optical fiber cable (Cable II) was spliced at two points: the start and end of the optical fiber sensor. This spliced cable was fixed within a constant-temperature water tank.

Soil pressure gauges were installed at three locations on the liner system of the slope. Specifically, they were placed on the upper non-woven fabric. Thermocouples were installed at a total of six locations adjacent to the optical fiber cable, positioned at the same height as the soil pressure gauges. The optical fiber measurement points near the thermocouples were named as shown in Figure 4. Starting from the closest to the toe, they were designated A, B, and C. For Experiment 1-I, corresponding points at the same height were named A', B', and C'. For Experiment 1-II, the points were named A', B', C', and additionally A″, B″, and C″. Although the ' (prime) and ″ (double prime) locations in the Cable II experiment are adjacent, they represent distinct points

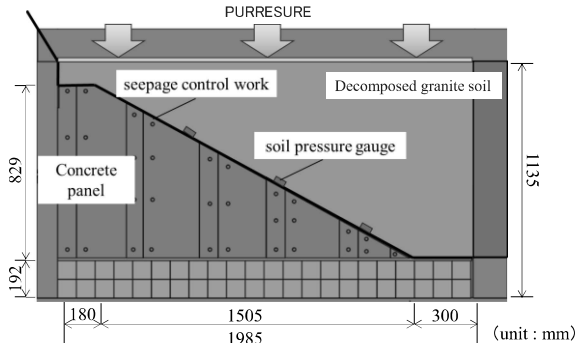

Fig.2 Internal Structure of the soil tank

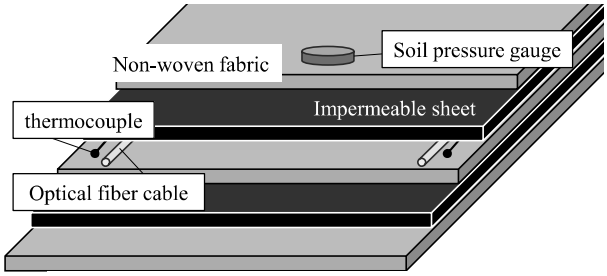

Fig.3 Seepage Control Work

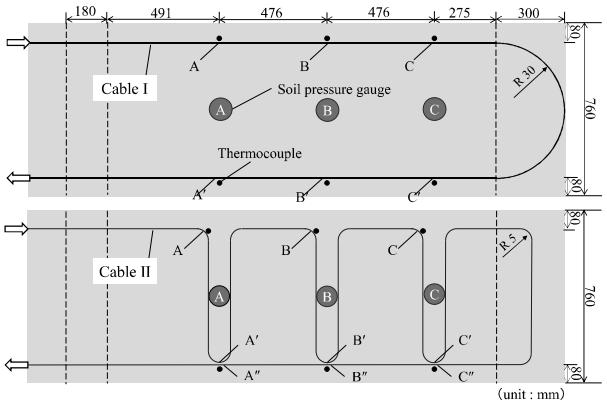

Fig.4 Optical fiber cable routing

Table 1 Experimental conditions

Item		Experiment name			
		1-I	1-II	2-I	2-II
Cable		Cable I	Cable II	Cable I	Cable II
Sand filling conditions	Water content (%)	4.0	8.2	11.2	
	Bulk density (g-dry/cm^3)	1.25	1.29	1.38	
	Compuction method	2-layer		5-layer	
Repeated	loading pressure (kPa)	23.6, 29.5, 35.4		5.9, 11.8, 17.7, 23.6, 29.5, 35.4	
	Number of cycles	3		2	
	Loading time (min)	3		3	
	Time required for measurement (min)	3		3	
Specific	loading pressure (kPa)	35.4		35.4	
	Loading time (min)	65		60	
	Number of temperture measurements	13 (positive)		9 (positive), 9 (negative)	
	Time required for measurement (min)	3		3	

for optical fiber sensor measurements.

To eliminate interference with the optical fiber cable, the strain gauges used in Experiments 2-I and 2-II were installed 5 cm closer to the soil pressure gauge from the thermocouple installation points.

2.3 Backfill and Loading Conditions

Three steel plates of equal size were laid on the top surface of the sandy soil layer. A loading plate attached to the Servo-system cylinder applied load to the steel plates, and the load was transmitted through the steel plates to the top surface of the sandy soil layer. Table 1 lists the experimental conditions.

For Experiments 1-I and 1-II, the loading condition simulated compaction by heavy machinery. A load equivalent to an internal pressure of 23.6 kPa was applied for 3 minutes, followed by unloading. This operation was repeated three times. Subsequently, loading was performed at 29.5 kPa and 35.4 kPa using the same procedure (hereinafter referred to as repeated loading). The number of temperature measurements using the optical fiber sensor during repeated loading matched the number of loading cycles. Following repeated loading, a load equivalent to the weight of compacted landfill waste was applied at 35.4 kPa for one hour (hereinafter referred to as constant loading). Note that 35.4 kPa corresponds to the weight of a 3.6 m thick waste layer assuming a wet density of 1.1 g/cm^3. During the constant loading, 13 temperature measurements were taken using the optical fiber sensor. Temperature measurements using the optical fiber sensor in Experiments 1-I and 1-II were performed in the positive direction.

For Experiments 2-I and 2-II, as the cyclic loading, the pressure increased in 5.9 kPa increments from 5.9 kPa to 35.4 kPa. At each loading pressure, a 3-minute loading and unloading cycle was repeated twice. During the loading phase at each pressure in the cyclic loading, one temperature measurement was taken using the optical fiber sensor in the positive direction. After the cyclic loading, a constant loading at 35.4 kPa was applied for 1 hour. During this constant loading, temperature measurements using the optical fiber sensor were performed nine times in the positive direction and nine times in the reverse direction.

The three steel plates installed on the top of the sandy loam layer—one near the toe, one on the slope top, and one near the toe—were designated No. 1, No. 2, and No. 3, respectively. In Experiment 2-II, settlement was measured at six locations on each steel plate, and the average value was taken as the settlement for that plate. Settlement measurements were performed once at the end of loading for each loading pressure during the repeated loading.

3. RESULT AND DISCUSSION

3.1 Temperature Difference Between Optical Fiber Sensor and Thermocouple Measurements

3.1.1 Effect of Cable Sheath Differences

No optical fiber breakage occurred due to loading in Experiments 1-I and 1-II. Figure 5 shows the difference (hereafter referred to as the temperature difference) between the temperature measured by the optical fiber sensor and the temperature measured by the thermocouple (considered the true value) at the thermocouple installation points for each experiment and loading condition. Each point represents the average value, and the upper and lower lines indicate the overall distribution range (minimum to maximum value).

The temperature difference in Experiment 1-I ranged from -0.4 to 1.5°C. While this falls within the maximum measurement error of ±2.0°C for the instruments used in this study, it was approximately 1.0°C larger than the measurement error of ±0.5°C for Cable I under no load. Overall, the temperatures measured by the optical fiber sensor tended to be slightly higher, showing a tendency for the temperature difference to be positive.

In Experiment 1-II, the temperature difference at points A, A′, B, B′, C, and C′ ranged from -1.0 to 0.4°C. While this falls within the maximum measurement error of ±2.0°C for the instruments used in this study, it was slightly larger than the ±0.8°C measurement error of Cable II under no-load conditions. Conversely, the temperature differences at points A″, B″, and C″ ranged from -6.1 to -1.0°C. Although points A′ and A″, B′ and B″, and C′ and C″ were nearly identical locations, the temperatures measured by the optical fiber sensors differed significantly. Locations A–C and A′–C′ were points where the front and rear optical fiber cables were laid perpendicular to the slope gradient direction. In contrast, locations A″–C″ were points where the optical fiber cables, including the front and rear sections, were laid parallel to the slope gradient direction.

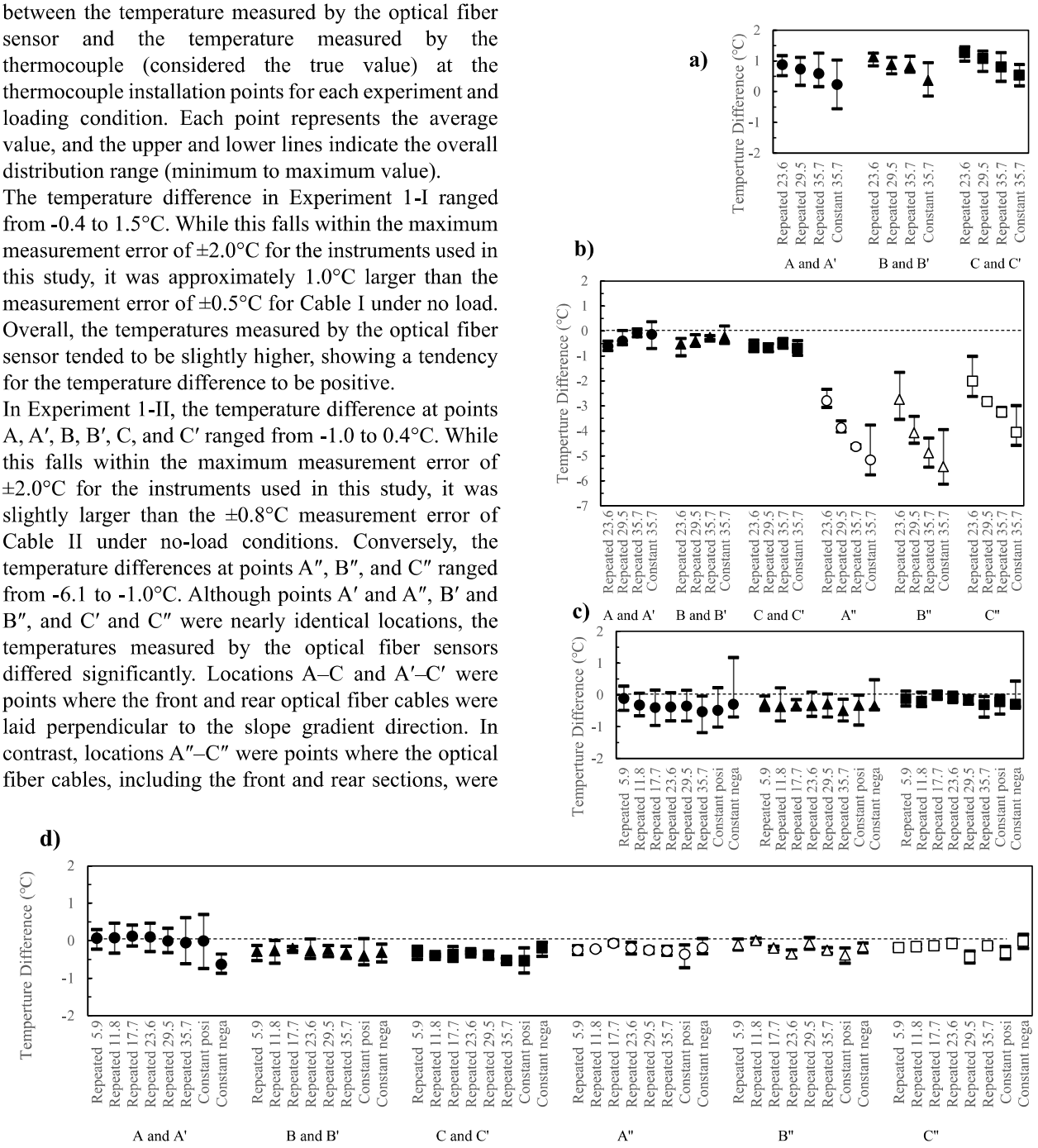

Fig.5 Temperature difference at each point under each loading condition
a) 1-I, b) 1-II, c) 2-I, d) 2-II

In Experiment 1-I using Cable I, the temperature difference fell within the instrument's maximum error range of ±2.0°C. The cable structure is cited as a reason for the small impact of loading on the measured temperature. As shown in Figure 1, Cable I incorporates a stainless-steel tube and features a structure where the optical fiber and sheath are not integrated. While the stainless-steel tube's excellent resistance to external pressure may be a factor, another contributing reason is likely the structure where the stress applied to the sheath

is less likely to be directly transmitted to the optical fiber because the sheath and optical fiber are not integrated.

On the other hand, Cable II has a structure where the sheath is integrated with optical fiber, making it easier for stress applied to the sheath to be transmitted to the optical fiber. Therefore, at locations where the cable was laid parallel to the slope gradient direction, As the sandy loam layer subsided, the topmost non-woven fabric layer of the liner system was pulled inward. Consequently, the upper geomembrane sheet was also pulled inward due to friction. This friction easily induced strain in the optical fiber in contact with the upper geomembrane sheet, resulting in the significant temperature difference observed in Experiment 1-II. To minimize temperature measurement errors in the optical fiber sensor using Cable II, it is considered necessary to avoid parallel wiring to the slope gradient direction as much as possible to reduce the stress acting on the optical fiber, and to provide protection preventing direct external forces from acting on the cable.

In Experiment 1-I, the average temperature difference decreased as the applied load pressure increased, showing a tendency to approach 0°C. In Experiment 1-II, the average temperature difference increased with increasing load pressure, showing a tendency to approach 0°C. This is thought to be caused by movement in the optical fiber due to immediate settlement accompanying the loading, which changed the optical intensity. While the settlement amount is large at the start of repeated loading, it is considered to decrease as loading pressure increases with repeated cycles. Consequently, the movement of the optical fiber decreased, leading to the temperature difference with the thermocouple approaching 0°C. Furthermore, measurements under constant loading showed a relatively larger range of temperature difference variation compared to those under repeated loading. This is likely because the number of measurements during repeated loading was 3, whereas the number during constant loading was 13; the greater number of measurements resulted in larger variation.

3.1.2 Effects of Different Loading Conditions

In Experiment 1-II, a significant temperature difference between the optical fiber cable and the thermocouple occurred simultaneously with the 23.6 kPa cyclic loading. To identify the load pressure causing this temperature difference, Experiment 2 changed the load pressure sequence from the three stages used in Experiment 1 (23.6→29.5→35.7 kPa) to six stages (5.9→11.8→17.7→23.6→29.5→35.7 kPa).

No optical fiber breakage occurred in Experiments 2-I and 2-II. Figure 5c) and d) show the temperature differences at each thermocouple installation point in Experiments 2-I and 2-II, categorized by loading condition. The temperature differences in Experiment 2-I ranged from -1.2 to 1.2°C. While this falls within the maximum measurement error of ±2.0°C for the instrument, it was 0.7°C larger than the measurement error of ±0.5°C observed for Cable I under unloaded conditions. In Experiment 2-II, the temperature difference during loading at all thermocouple locations was within ±0.9°C, and no large temperature differences like those in Experiment 1-II occurred. A possible reason for this is the difference in experimental conditions between Experiment 1-II and Experiment 2-II. First, the difference in loading conditions: Experiment 1-II applied three loading stages (23.6→29.5→35.7 kPa), whereas Experiment 2-II applied six loading stages (5.9→11.8→17.7→23.6→29.5→35.7 kPa). Second, the compaction method during sandy soil filling differed. Experiment 1-II involved filling in two layers, whereas Experiment 2-II involved filling in five layers, resulting in a higher filling density in Experiment 2-II. As mentioned earlier, the temperature difference observed in Experiment 1-II is thought to have been caused by strain on the optical fiber due to the pulling-in of the liner system. However, due to differences in loading conditions, the immediate settlement in Experiment 2-II was more gradual compared to Experiment 1-II. It is believed that loading without rapid settlement did not cause the pulling-in of the liner system that induces strain on the optical fiber.

3.2 Relationship between Soil Pressure and Temperature Difference

Figure 8 shows the relationship between the temperature difference at each location in Experiment 1-II, and the soil pressure measured by soil pressure gauges installed at the same depth on the slope. Like Section 3.2, results for other experiments where the temperature difference

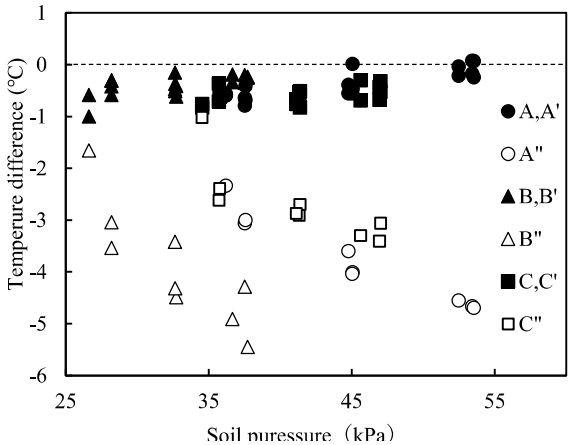

Fig.6 Relationship between temperature difference and soil pressure

was not greater than the measurement error of ±2.0°C are omitted. At locations A–C and A′–C′, no change in temperature difference was observed with increasing soil pressure. However, at locations A″–C″, the temperature difference clearly increased in the negative direction as soil pressure rose. It is considered that the influence of stress is perpendicular to the surface of the liner system, where the optical fiber cable is laid, on the temperature difference is small. The effect of external stress on temperature measurements by the optical fiber sensor is presumed not to be caused by compressive stress in the cross-sectional direction of the optical fiber cable.

4. CONCLUSION

1) Under all conditions in this study, the difference between temperature measurements from the optical fiber sensor and thermocouple was within ±1.5°C. Therefore, if a temperature difference of less than 18.5°C from the surrounding environment can be confirmed, temperature-based determination for decommissioning a landfill site is considered feasible.
2) In the experiment using non-halogen resin-coated cables, temperature differences measured in sections laid perpendicular to the slope gradient direction were considered measurable with an accuracy of approximately ±1.0°C. However, in sections wired parallel to the slope gradient direction, the measured temperature values from the thermocouple could differ from the true value by up to 6.1°C.
3) In the experiment using non-halogen resin-coated cables, for sections wired parallel to the slope gradient direction, under conditions where the applied pressure gradually increased, the error relative to the true value was within ±0.9°C. Therefore, when installing non-halogen resin-coated cables to measure temperature distribution in slope liner systems, it is recommended to primarily route them perpendicular to the slope gradient direction and minimize the length of sections routed parallel to the slope gradient.
4) The relationship between the measured temperature difference (absolute value) using the optical fiber sensor and thermocouple, and the soil pressure installed on the slope when using non-halogen resin-coated cables showed an increase in the measured temperature difference (absolute value) in sections parallel to the slope gradient direction. However, no proportional relationship was observed in sections perpendicular to the slope gradient direction. The cause of the temperature measurement anomaly was not considered to be the influence of pressure perpendicular to the surface of the impermeable liner where the optical fiber cable was laid.

Based on the above, temperature measurement using optical fiber sensors installed in liner system on actual landfill slopes is considered feasible under the conditions of this study when using PE-coated SUS pipe-embedded cables as the optical fiber cable. When using non-halogen resin-coated cables, cases of abnormal temperature measurements occurred at locations wired parallel to the slope gradient direction. When using non-halogen resin-coated cables, it is considered necessary to avoid parallel wiring to the slope gradient direction as much as possible and to provide protection preventing direct external forces acting on the cable.

A future task is to conditions that cause temperature measurement differences between the non-halogen resin-coated cable and thermocouples in experiments using the former. Furthermore, since the loading conditions used in this study were smaller than the actual loads acting on landfill sites, experiments under conditions with larger loads are also necessary. Since the strain values of the impermeable sheet vary, it is necessary to collect more accurate data, precisely understand the behavior of the impermeable sheet, and clarify the forces exerted on the optical fiber.

REFFERENCE

1) Ministry of the Environment: Overview of criteria for the closure of final disposal sites, https://www.env.go.jp/recycle/kosei_press/h980616a/h980616a-3.html (Date of viewing: April 5, 2025)
2) Japan Society of Waste Cycles and Waste Cycles Society (JCRSS): Landfill Disposal Study Group: Investigation and Evaluation Method for Waste Final Disposal Site Abolition Standards Revised Edition ~Research on Application and Evaluation of Standards~, p.87, 2025
3) Non-Profit Organization for the Promotion of Optical Fiber Sensing: Introduction to Optical Fiber Sensors, p.288, 2012
4) Teppei Komiya, Rion Hamada, Takayuki Shimaoka, Michio Imai, Kazuki Ozawa: Applicability of Optical Fiber Sensor on Temperature Distribution Estimation and Leakage Detection of Impermeable Liner in Solid Waste Landfills, Geosynthetics Journal, Vol.37, pp.113-118, 2022. https://doi.org/10.5030/jcigsjournal.37.113
5) Rion Hamada, Takayuki Shimaoka, Teppei Komiya: Measurement of the temperature distribution of the capping layer of a landfill using an optical fiber sensor, Proceedings of the 34th Annual Conference of the Japan Society of Material Cycles and Waste Management, pp.445-446, 2023. https://doi.org/10.14912/jsmcwm.34.0_445

Speciation Analysis and Extractability Potential of Rare Earth Elements in Landfill Humus Soil

Linhai Ye[1], Zhengyu Wang[1], Tao Zhou[1] and Youcai Zhao[1]
1 The State Key Laboratory of Pollution Control and Resource Reuse, College of Environmental Science and Engineering, Tongji University, 1239 Siping Road, Shanghai 200092, China

ABSTRACT
Long-term stabilization of landfills facilitates the migration of trace elements into landfill humus soil (LHS), a crucial component of landfill ecosystems. The historical disposal of industrial and electronic wastes has led to significant accumulation of rare earth elements (REEs) in LHS, challenging its traditional classification as a low-value material. This study investigates the REE speciation-extractability relationship in LHS, assessing recovery potential through tailored alkali hydrothermal treatment (HTT). Results show that light REEs (La-Nd) are predominant REE components and primarily exist as residual phases, immobilized in mineral phases such as apatite, quartz, and anorthite. HTT enriches REE content to 630 mg/kg by disrupting mineral structures and concentrating REEs into acid-soluble hydroxides, achieving near-quantitative recovery (~100%) at pH 0. This study highlights that LHS, once deemed economically marginal, holds substantial potential as an REE reservoir.

INTRODUCTION
Rare earth elements (REEs), comprising the lanthanide series and yttrium, have become strategically critical materials for clean energy technologies and advanced electronics due to their unique catalytic and magnetic properties (Goodenough et al., 2018). While China dominates > 60% of global REE production, emerging suppliers like Brazil and Vietnam are reshaping the geopolitical landscape of these essential resources (Dushyantha et al., 2020). The environmental costs of conventional mining (e.g., soil acidification and radioactive tailings), combined with supply chain vulnerabilities exposed during recent trade conflicts, have driven the shift toward urban mining of anthropogenic deposits (Burlakovs et al., 2013; Gao et al., 2024).

Landfills, particularly those operational prior to modern waste segregation practices, constitute substantial reservoirs of industrial and electronic wastes containing 200–1500 mg/kg REEs (Gaustad et al., 2021; Gerardo et al., 2022; Kayla Kilgo et al., 2022), which have a positive recycling revenue considering life cycle cost evaluation (Wu et al., 2024). Current landfill mining strategies face a critical knowledge gap: the spatial distribution of REEs remains obscured without intrusive excavation, while long-term stabilization processes (e.g., precipitation, biochemical transformations, and advective transport) drive elemental migration through waste strata (Li et al., 2023; Wang et al., 2021). Although groundwater monitoring indicates attenuated REE concentrations (~800 μg/L) due to adsorption and organic complexation with soil matrix (Bradl, 2004; Nigro et al., 2018), a pilot investigation revealed that topsoil and clay samples revealed pseudo-total REE contents ranging from 11.86 to 27.68 mg/kg (Barbieri et al., 2020). Another soil-like fraction in landfill, called landfill humus soil (LHS), was found containing <100 mg/kg REEs in domestic waste landfills and >200 mg/kg REEs in industrial/municipal waste mixing landfills (Gutiérrez-Gutiérrez et al., 2015; Valentim et al., 2019). Such disparities underscore LHS's potential as a diagnostic matrix for estimating in situ REE inventories, particularly given the pervasive lack of waste characterization data in improperly managed landfills (Long et al., 2024).

The speciation-leachability nexus in LHS demands advanced characterization. Conventional REE extraction relies on aggressive acid leaching (pH <1) (Cánovas et al., 2019), which requires excessive acid to disrupt mineral matrices. However, this approach is highly inefficient for complex materials like LHS, as the co-dissolution of acid-soluble impurities (e.g., Ca, Fe) generates contaminated REE solutions, necessitating costly purification (Goli et al., 2022). Pretreatment methods are thus critical to selectively liberate REEs while minimizing waste. Calcination, often mixed with acids or salts, improves extraction but demands energy-intensive temperatures (~1000°C) (Carrillo García et al., 2020; Demol et al., 2019). In contrast, hydrothermal treatment (HTT) offers a greener alternative by enabling alkaline digestion at moderate temperatures (<300°C) (Lin et al., 2018). HTT selectively converts REE-bearing phases (e.g., monazite) into stable acid-soluble hydroxides while transforming impurities into water-soluble compounds,

thereby reducing acid consumption, waste generation, and energy use compared to conventional methods (Dai et al., 2018; Su et al., 2024). This selectivity is particularly advantageous for LHS that mineral heterogeneity challenges traditional acid leaching and calcination.

This study provides a comprehensive investigation into REE speciation and recovery potential from LHS. Through integrated application of analytical techniques, the mineralogical controls and microstructural determinants of REE distribution in LHS matrices were systematically characterized. HTT pretreatment approach was evaluated before the recovery protocol. Mechanistic routine behind the leachability was clarified to discuss the applicability. These findings establish LHS as a technologically viable source of critical REEs while advancing sustainable landfill mining.

MATERIALS AND METHODS

Sample collection and pretreatment

LHS specimens were obtained from waste units at Shanghai Laogang Landfill (31.02°N, 121.52°E), a representative coastal municipal landfill operational since 1989 receiving approximately 12,000 tonnes/day of solid waste. 10 landfill units sealed for more than 20 years were sampled, in each 16 points were selected based on Kriging spatial interpolation method (Robinson and Metternicht, 2006). At each point, LHS at a depth of 8 m was extracted using SH-30A rotary drilling rig equipped with split-spoon samplers to minimize cross-contamination.

Following collection, raw materials underwent sequential granulometric separation through stainless steel sieves to isolate the <40 mm fraction. Sieved samples were immediately transferred to gas-tight polyethylene bags and stored at -20°C during transport to prevent organic matter degradation.

HTT process: Alkaline activation was performed in a Teflon beaker to avoid any possible reaction with the vessel. LHS was added to 5 M NaOH solution at a solid-to-liquid ratio of 1:3 (w/v). The mixture was heated in muffle furnace under static air at 10°C/min heating rate to 300°C, with dwell time of 30 min (Su et al., 2024). Post-treatment residues were subjected to triple rinsing cycles with deionized water followed by vacuum drying at 60°C for 24 h.

Mineralogical, microscopic, and spectroscopic analysis of LHS

XRD analysis was conducted (Bruker, D8 ADVANCE Diffractometer) with Cu Kα radiation at 40 kV and 40 mA, scanning 10°–70° 2θ range. XPS analysis (Thermo Scientific K-Alpha) was performed with binding energies calibrated against C 1s (284.8 eV) for samples that do not contain carbon. SEM (ZEISS Sigma 360) coupled with energy-dispersive X-ray spectroscopy (EDS, Oxford Xplore30) was conducted at 5 kV. Surface characterization was executed using time-of-flight secondary ion mass spectrometry (TOF-SIMS, PHI NanoTOFII system), which ensured ppm-level trace element detection. The analysis was carried out with Bi_3^{2+} primary ions at 30 keV in negative mode. Maps consisting of 100 × 100 pixels, covering a field of 100 μm × 100 μm, were collected with a pixel resolution of 1 μm in both the X and Y directions.

Leaching, chemical extraction and quantification of REEs in LHS

HCl (ACS grade, 36%–38% w/w) was selected as the representative lixiviant to evaluate pH-dependent REE mobilization. Batch leaching experiments employed a gradient of HCl concentrations (1 M to 0.0001 M, pH 0–4). For long-term ambient leaching, 50.0 ± 0.5 mg LHS aliquots were added into 20 mL of HCl solution and agitated at 25°C for 72 h. For accelerated hydrometallurgical leaching, 50.0 ± 0.5 mg LHS aliquots were added into 10 mL of 1 M HCl refluxed at 85 ± 2°C for 8 h. Post-leaching suspensions were vacuum-filtered through 0.22 μm cellulose membranes (Millipore) and diluted to 50.00 mL with 2% HNO_3.

The modified BCR sequential extraction protocol was employed to differentiate REEs into four operationally defined fractions: exchangeable/weak-acid-soluble phases (e.g., carbonates), reducible phases associated with Fe/Mn oxides, oxidizable phases bound to organic/sulfide components, and residual phases primarily comprising crystalline mineral structures (e.g., phosphates) (Rao et al., 2010). This multi-stage procedure involved sequential treatment with 0.11 M acetic acid (16 h, 25°C) for carbonate dissolution, followed by 0.5 M hydroxylamine hydrochloride (pH 1.5, 85°C) targeting Fe/Mn oxides. Subsequent oxidation using 8.8 M H_2O_2 (pH 2, 2 h), and 1 M ammonium acetate liberated organically-bound species. 0.25 g residual sample was subjected to total digestion with a mixture of 10 mL concentrated HNO_3 and 5 mL HF. The mixture was heated at 150°C to dissolve silicates, aluminates, and phosphates. 2 mL H_2SO_4 and 1 mL $HClO_4$ were added, and the temperature was raised to 180°C to dissolve REE fluorides. After removing acids at 300°C, the digestate was treated with 1.25 mL of HCl and 3.75 mL of HNO_3, then diluted to 50 mL with ultrapure water. All reagents used were in ACS grade.

REE concentrations were determined using ICP-MS (Agilent 7700) with 10 μg/L of indium as an internal standard. The REEs and their isotopes, counting to 25 elements (^{72}Y, ^{139}La, ^{140}Ce, ^{142}Ce, ^{141}Pr, ^{143}Nd, ^{145}Nd, ^{146}Nd, ^{147}Sm, ^{149}Sm, ^{151}Eu, ^{153}Eu, ^{155}Gd, ^{157}Gd, ^{158}Gd, ^{159}Tb, ^{161}Dy, ^{163}Dy, ^{165}Ho, ^{166}Er, ^{167}Er, ^{169}Tm, ^{172}Yb, ^{173}Yb, and ^{175}Lu), were measured simultaneously. Calibration standards (0, 5, 10, 50, 100 μg/L) of REEs

were measured every 20 samples. Blanks were processed identically to confirm no cross-contamination, and all the samples were prepared with two duplicates. Triplicate measurements per sample were conducted to afford standard deviations.

RESULTS AND DISCUSSION

Characterization of LHS

The X-ray diffraction analysis revealed three dominant crystalline phases in LHS: apatite ($Ca_5(PO_4)_3$ (F, Cl, OH)), anorthite ($Me_xO{\cdot}Al_2O_3{\cdot}SiO_2$) and quartz ($SiO_2$) (**Figure 1a**). Notably, apatite and anorthite phases sometimes demonstrate structural competence for REE accommodation through isomorphic substitution of Ca^{2+}, Al^{3+}, and Fe^{3+}, suggesting their potential as hosting phases for REE sequestration.

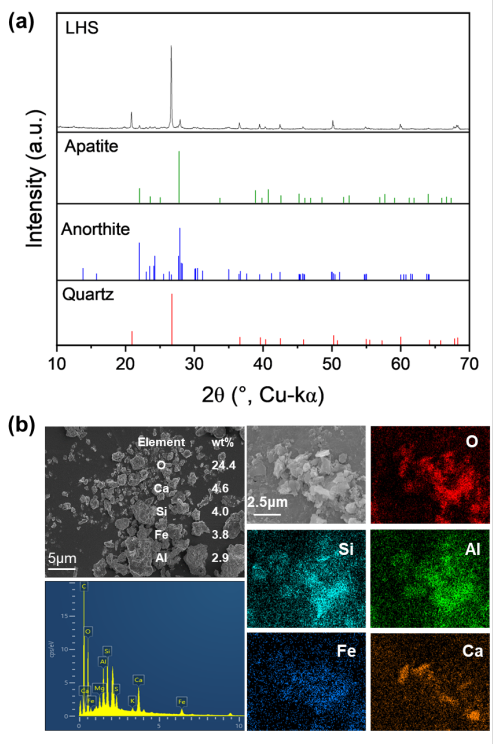

Figure 1. Multiscale characterization of LHS mineralogy and elemental distribution. (a) XRD patterns identifying three dominant crystalline phases: apatite, anorthite, and quartz; (b) SEM-EDS elemental mapping showing the spatial distribution of major elements (O, Ca, Si, Fe, Al) with corresponding weight percentage.

Spatially resolved elemental mapping in **Figure 1b** and TOF-SIMS analyses in **Figure 2** decoupled the phase-specific element distribution. The co-localization of Si-Al-O signatures in SEM-EDS confirmed anorthite domains, while TOF-SIMS molecular fragments ($AlSiO_4$, $AlSi_2O_6$) revealed submicron-scale mineral assemblages. Notably, the TOF-SIMS sputtering process induced in-situ recombination of sputtered species with ambient oxygen, generating transient ions that deviate from stoichiometric formulas but provide mechanistic insights into surface coordination environments, identified the distribution of positive ions ranging from O to Fe and negative ions such as CH to $AlSi_2O_6$ on soil particles. The Ca-P-Al matrix in LHS created a self-buffering system maintaining alkaline conditions favorable for REE complexation, serving as proxies for identifying REE-hosting microdomains

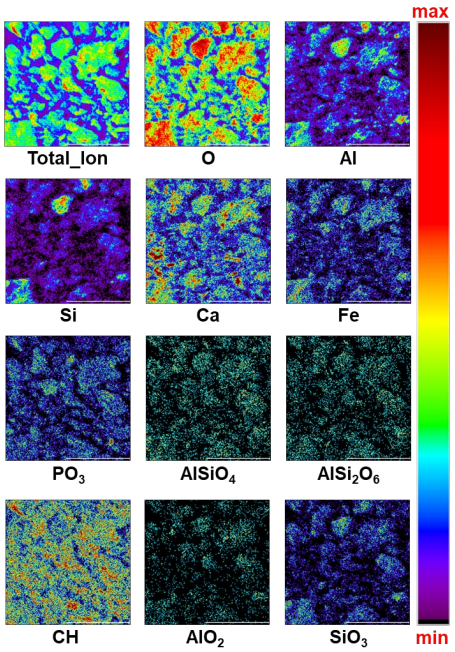

Figure 2. TOF-SIMS ion distribution maps acquired over a 100 × 100 μm² area. Positive ion maps show elemental distributions from O to Fe, while negative ion maps display molecular fragments from CH to $AlSi_2O_6$. Color scales represent ion intensity normalized to the maximum intensity (Max) observed within a 1 × 1 μm² region.

Distribution of REEs in LHS

A total REE inventory in LHS ranged from 176.2 to 465.3 mg/kg, with acid-extractable fractions measuring between 106.3 and 288.2 mg/kg, demonstrating a maximum leachability of 61% (**Figure 3a**). The REE enrichment in LHS is significantly higher than that observed in adjacent soils (185.6 mg/kg). This confirms anthropogenic accumulation pathways through landfilling. Light REEs (LREEs: La–Nd) dominated the elemental profile with mean concentrations >30 mg/kg (**Figure 3b**), while middle/heavy REEs (M/HREEs: Sm–Lu+Y) showed depleted levels (<30 mg/kg). Ce exhibited anomalous enrichment (46.1–246.0 mg/kg) with coefficient of variation >80%, suggesting localized geochemical hotspots. The HCl leachability of REEs

varied significantly across REE groups, ranging from 34.7% to 74.8%. La demonstrated the highest recovery (74.8 ± 5.1%), while Pr showed the lowest leachability (34.7 ± 2.0%). The large variability reflects the inherent heterogeneity of REEs in LHS, where microscale variations in host mineral phases and organic matter interactions govern their mobilization potential. Also, the waste matrix complexity introduces variability to exogenous REE inputs such as particle size, solubility, and binding strength (Xavier et al., 2023).

Sequential extraction through modified BCR protocol revealed that >50.0% ∑REE were dominated by the residual fraction (**Figure 3c**). Consistent with findings in CFA and red mud, this fraction has limited short-term diffusion risk to the surrounding ecosystem (Choudhary et al., 2024; Ilkhani et al., 2024). This observation suggests that the long-term stabilization process in landfills has transformed the extractable compounds into more stable and less bioavailable phases. Additionally, 2.4%–21.0% of REEs were classified as exchangeable/weak-acid-soluble (Step 1), 9.3%–36.7% as reducible fraction (Step 2), and 1.1%–9.4% as oxidizable fraction (Step 3). The alkaline buffering capacity, competitive sorption between organics and inorganics, and co-precipitation with Ca-P phases are critical mobility constraints emerged in LHS (Zhang and Shan, 2001).

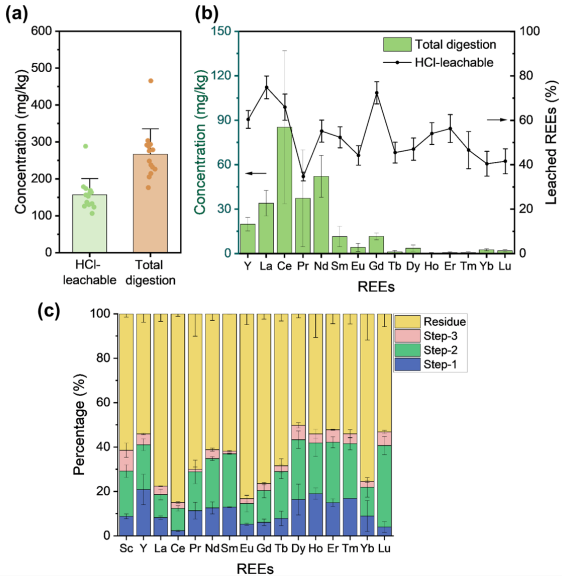

Figure 3. Geochemical speciation and spatial distribution of REEs in LHS. (a) Comparative REE inventory showing total concentrations and 1 M HCl-extractable fractions; (b) Element-specific leaching behavior displaying total and acid-extractable REE concentrations. LREEs (La–Nd) show higher enrichment over M/HREEs (Sm–Lu+Y); (c) Modified BCR sequential extraction results quantifying REE phase distribution into exchangeable/weak-acid-soluble (Step 1), reducible (Step 2), oxidizable (Step 3), and residual phases in LHS.

Microscale characterization via SEM-EDS (**Figure 4a**) and TOF-SIMS (**Figure 4b**) uncovered REE-Al-Si coordination domains, such as La-Ce clusters in Al-Si matrix. This finding indicates the interaction between REEs and aluminosilicate, especially in alkaline environment (Aide, 2012). The pH-dependent speciation suggests that acidification could remobilize fractions. Also, the co-occurrence of Y and P corresponded to discrete REE-phosphate precipitates (**Figure 4a**), further confirmed by TOF-SIMS identification of La, Ce, and phosphate-related ions analysis, such as PO_3, LaO_2, and CeO_2 (**Figure 4b**). Phosphate-mediated sequestration explains residual fraction dominance, reducing ecotoxicity risks (Liu and Byrne, 1997).

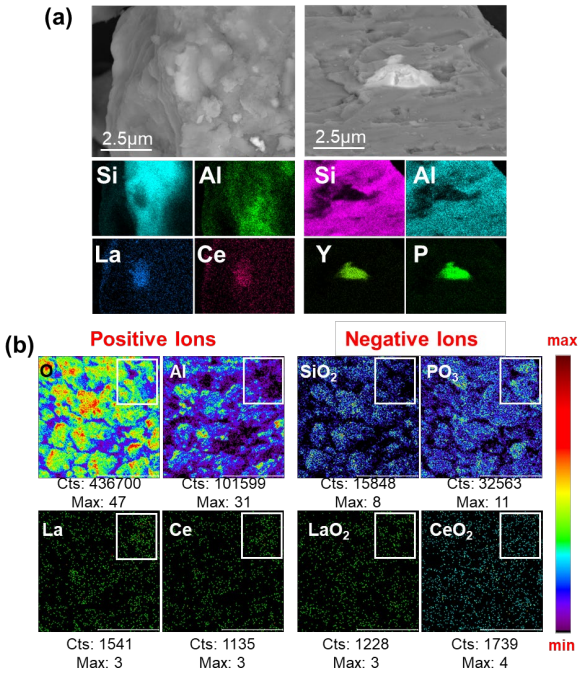

Figure 4. (a) SEM-EDS phase mapping revealing REE-Al-Si ternary associations and Y-P co-localization; (b) TOF-SIMS molecular mapping identifying positive Ce, La, Y ions, and negative PO_3, LaO_2, CeO_2 ions. White dashed boxes demarcate microdomains with simultaneous REE^+/PO_3^-, confirming rare earth phosphates crystallization.

Leachability of REE content in LHS after phase transition

The abundance of REEs in LHS increased following HTT processes. Prior to treatment, the raw LHS contained 398.5 mg/kg of REEs, with approximately 63.3% considered leachable. After HTT, the mean REE

content increased to 630.3 mg/kg, accompanied by a near-complete enhancement in leachability to nearly 100% (**Figure 5b**). These results highlight the structural modifications induced by HTT that the conversion of silicon oxides and aluminum oxides into soluble silicates and aluminates was facilitated, thereby enriching REEs previously dispersed within the mineral matrix. pH-dependent leaching tests further elucidated the dissolution dynamics of REE from LHS (**Figure 5c**). REE extraction commenced between pH 2 and 3. At pH 2, the leachability of REEs from HTT-treated samples was nearly negligible, whereas raw LHS released approximately 10% of REEs, consistent with the exchangeable/weak-acid-soluble fraction observed in **Figure 3c**. This reduction suggests that thermal processes redistributed REEs into more stable phases. For HTT-treated samples, REE phases dissolve rapidly at aggressive acidic environment, with 65.9% dissolved at pH 1 and 100% dissolved at pH 0 after three-days agitating, which significantly exceeded that of raw LHS samples.

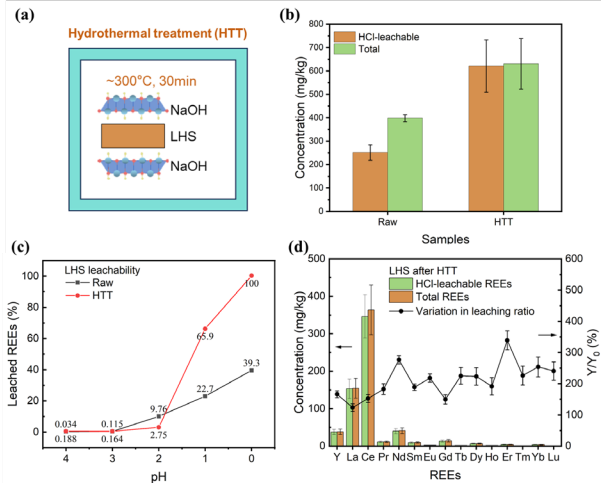

Figure 5. Effects of heat treatments on REE concentration and leachability in LHS. (a) Schematic diagrams illustrating the HTT method; (b) Total REE concentrations and HCl-extractable fractions in raw and treated LHS; (c) pH-dependent leaching profiles of REEs from LHS before and after treatment; (d) Post-HTT changes in individual REE concentrations and their corresponding acid-extractable fractions.

According to **Figure 5d**, individual REEs were differentially influenced. For instance, HTT substantially increased the mean concentrations of Y, La, and Ce to 38.2 mg/kg, 154.3 mg/kg, and 363.7 mg/kg, respectively. Here, Y_0 and Y (right vertical axis) denote leachability in HCl solution before and after treatment. At pH=0, acid leachability increased dramatically, with near-complete extraction of LREEs, MREEs and HREEs despite their inherent variability in raw LHS. These findings demonstrate that HTT substantially alters the concentration and leachability of REEs in LHS by modifying the mineral matrix and inducing phase transitions. However, the underlying mechanisms related to dissolution-recrystallization processes, changes in phosphate phases, or broader alterations in silicate structures remain partially unresolved. In the following section, thermodynamic analyses were employed to elucidate how each treatment pathway governs REE stability and solubility.

Mechanism behind REE extractability from LHS and after treatment

The mineral phases in raw LHS, primarily comprising phosphate and Al-Si oxides, were identified as the dominant host of REE. The interaction of these phases with NaOH at 300°C during HTT induced the transformation of Si, Al, and Fe oxides into soluble sodium silicates, aluminates, and ferrates (**Figure 6a**). Concurrently, REE phosphate reacted with NaOH to form REE hydroxides. Due to their insolubility in water, REE hydroxides can be readily separated from soluble mineral salts through rinsing.

Experimental validation of phase transitions was conducted using synthetic $CePO_4$ as model systems to simulate REE-hosted mineral interactions during HTT. This model system was necessary because the low REE concentration in raw LHS (<500 mg/kg) and its complex mineral matrix preclude direct detection of REE phases by XRD/XPS. As shown in **Figure 6b**, the formation of $Ce(OH)_4$ confirmed the hydrothermal reactions (Kramar et al., 2024). XPS analysis in **Figure 6b** revealed that the Ce 3d binding energies were located at 882.9 eV, 889.4 eV, 898.8 eV, 901.4 eV, 907.6 eV and 917.4 eV. These peaks correspond to the characteristic spin-orbit splitting of Ce 3d in Ce^{4+}-O (Rack et al., 1999).

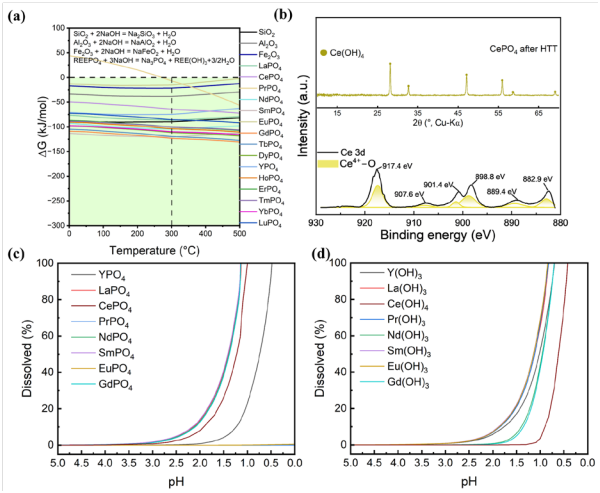

Figure 6. (a) Gibbs free energy changes (ΔG) for reactions occurring during HTT. The green shaded region indicates thermodynamically favorable conditions for reaction initiation, and the vertical

dashed line represents the operational temperature; (b) XRD patterns of $Ce(OH)_4$ after HTT, as well as XPS spectra of Ce compounds generated after HTT, highlighting Ce^{4+} oxidation state; Dissolution performance of (c) REE phosphates and (d) hydroxides (Y, La to Gd were listed, which are primary REEs in landfill humus soil), simulating 1 g sample in 100 mL HCl solution.

The dissolution of primary REE phosphates and hydroxides in 100 mL of HCl solution across pH 0–6 was stimulated using PHREEQC (**Figure 4c-d**). The results indicated that most REE phosphates exhibited high leachability at pH ~0, with the exception of $PrPO_4$ and $EuPO_4$, which were nearly insoluble at pH 0. These findings suggest that the dissolution of REE phosphates in diluted acid was thermodynamically favorable, excluding $PrPO_4$ and $EuPO_4$. The dissolution of REE phosphates is driven by the protonation of phosphate ions, which reduces the concentration of free phosphate ions in the solution. According to Le Chatelier's Principle, this shift in equilibrium promotes the forward dissolution reaction, leading to the release of additional REE and phosphate ions into the solution (Cheng et al., 2019; Liu and Byrne, 1997). However, in actual leaching experiments, dissolution of REE phosphates is slow due to precipitation on their surface, inhibiting the mass transfer capacity (Sevim et al., 2003; Wu et al., 2018).

REE hydroxides exhibit high solubility in acidic conditions. Complete dissolution of $REE(OH)_3$ and $Ce(OH)_4$ was achieved at pH > 0, including Pr and Eu species. Under mildly acidic conditions (pH 1–3), the calculated leaching ratios of REE hydroxides were slightly lower than those of phosphates. This difference arises because the dissolution of hydroxides consumes significantly more H^+ ions per unit compared to phosphates, and the H^+ concentration in moderately acidic solutions is insufficient to drive complete dissolution. Nevertheless, the dissolution kinetics of hydroxides are rapid, as surface atoms readily detach, exposing fresh reactive sites and facilitating continuous dissolution (Crundwell, 2014). Notably, the equilibrium state predicted by thermodynamic calculations closely aligns with the leaching behavior of HTT-treated LHS (**Figure 5c**), further demonstrating the effectiveness of HTT in activating the sample and overcoming mass transfer barriers.

CONCLUSION

Historically overlooked due to its perceived low economic value, LHS has emerged as a promising resource, particularly given its widespread presence in aged landfills. This study reveals that stabilized landfill units in the Shanghai Laogang Landfill contain 176.2-465.3 mg/kg of REEs in LHS, predominantly LREEs (La-Nd), which exceed regional soil background levels. Over 50% of these REEs are found as phosphate-bound species and trace mineral phases in the alkaline, organic-rich environment of LHS. These compounds exhibit minimal leaching potential (<1%) under landfill-relevant moderately acidic conditions (pH 3–6). Following alkali HTT at 300°C, REE concentrations in LHS exhibit a remarkable enrichment of approximately 160%, primarily in the form of hydroxides. This treatment effectively disrupts the mass transfer barrier, facilitating near-quantitative REE extraction efficiency. This functionality positions LHS as a strategic resource reserve, supporting circular economy principles and advancing sustainable waste-to-resource transitions.

REFERENCES

Goodenough, K.M., Wall, F., Merriman, D., 2018. The rare earth elements: demand, global resources, and challenges for resourcing future generations. Nat Resour Res 27, 201–216. https://doi.org/10.1007/s11053-017-9336-5

Dushyantha, N., Batapola, N., Ilankoon, I.M.S.K., Rohitha, S., Premasiri, R., Abeysinghe, B., Ratnayake, N., Dissanayake, K., 2020. The story of rare earth elements (REEs): Occurrences, global distribution, genesis, geology, mineralogy and global production. Ore Geology Reviews 122, 103521. https://doi.org/10.1016/j.oregeorev.2020.103521

Burlakovs, J., Kriipsalu, M., Arina, D., Kaczala, F., Shmarin, S., Denafas, G., Hogland, W., 2013. Former dump sites and the landfill mining perspectives in Baltic countries and Sweden: The status. Proceeding of International Multidisciplinary Scientific GeoConference Surveying Geology and Mining Ecology Management (SGEM 2013).

Gao, W., Zhang, Haizhen, Zhang, Hongwei, Yang, S., 2024. The role of G7 and BRICS country risks on critical metals: Evidence from time- and frequency-domain approach. Resources Policy 88, 104257. https://doi.org/10.1016/j.resourpol.2023.104257

Gaustad, G., Williams, E., Leader, A., 2021. Rare earth metals from secondary sources: Review of potential supply from waste and byproducts. Resources, Conservation and Recycling 167, 105213. https://doi.org/10.1016/j.resconrec.2020.105213

Gerardo, S., Davletshin, A.R., Loewy, S.L., Song, W., 2022. From Ashes to Riches: Microscale Phenomena Controlling Rare Earths Recovery from Coal Fly Ash. Environ. Sci. Technol. 56, 16200–16208. https://doi.org/10.1021/acs.est.2c04201

Kayla Kilgo, M., Anctil, A., Kennedy, M.S., Powell, B.A., 2022. Metal leaching from Lithium-ion and Nickel-metal hydride batteries and photovoltaic modules in simulated landfill leachates and municipal solid waste materials. Chemical Engineering Journal

431, 133825. https://doi.org/10.1016/j.cej.2021.133825
Wu, Y., Huang, G., Zhang, P., Yao, Y., Zhao, K., Shen, J., Feng, R., Chen, N., 2024. Synchrotron-aided exploration of REE recovery from coal fly ashes within a Canadian context. Chemosphere 367, 143562. https://doi.org/10.1016/j.chemosphere.2024.143562
Li, S., Zhao, M., Xu, Y., Huang, Q., Yao, G., Liu, Y., Zhao, Y., 2023. Pathway, flux and accumulation of pollutant emission from landfill receiving As- and Hg-containing hazardous waste. Journal of Cleaner Production 403, 136697. https://doi.org/10.1016/j.jclepro.2023.136697
Wang, Q., Ko, J.H., Liu, F., Xu, Q., 2021. Leaching characteristics of heavy metals in MSW and bottom ash co-disposal landfills. Journal of Hazardous Materials 416, 126042. https://doi.org/10.1016/j.jhazmat.2021.126042
Bradl, H.B., 2004. Adsorption of heavy metal ions on soils and soils constituents. Journal of Colloid and Interface Science 277, 1–18. https://doi.org/10.1016/j.jcis.2004.04.005
Nigro, A., Sappa, G., Barbieri, M., 2018. Boron isotopes and rare earth elements in the groundwater of a landfill site. Journal of Geochemical Exploration 190, 200–206. https://doi.org/10.1016/j.gexplo.2018.02.019
Barbieri, M., Andrei, F., Nigro, A., Vitale, S., Sappa, G., 2020. The relationship between the concentration of rare earth elements in landfill soil and their distribution in the parent material: A case study from Cerreto, Roccasecca, Central Italy. Journal of Geochemical Exploration 213, 106492. https://doi.org/10.1016/j.gexplo.2020.106492
Gutiérrez-Gutiérrez, S.C., Coulon, F., Jiang, Y., Wagland, S., 2015. Rare earth elements and critical metal content of extracted landfilled material and potential recovery opportunities. Waste Management 42, 128–136.
https://doi.org/10.1016/j.wasman.2015.04.024
Valentim, B., Abagiu, A.T., Anghelescu, L., Flores, D., French, D., Gonçalves, P., Guedes, A., Popescu, L.G., Predeanu, G., Ribeiro, J., Santos, A.C., Slăvescu, V., Ward, C.R., 2019. Assessment of bottom ash landfilled at Ceplea Valley (Romania) as a source of rare earth elements. International Journal of Coal Geology 201, 109–126. https://doi.org/10.1016/j.coal.2018.11.019
Long, Y.-Y., Pang, M., Guo, S., Li, X., Shen, D.-S., 2024. Grading characteristics of humus soil particle size in landfill and its pollution status assessment of heavy metals. Environmental Pollution & Control 45, 1677–1683.
Cánovas, C.R., Chapron, S., Arrachart, G., Pellet-Rostaing, S., 2019. Leaching of rare earth elements (REEs) and impurities from phosphogypsum: A preliminary insight for further recovery of critical raw materials. Journal of Cleaner Production 219, 225–235. https://doi.org/10.1016/j.jclepro.2019.02.104
Goli, V.S.N.S., Singh, P., Singh, D.N., Tak, L.K., 2022. Investigations on characteristics of landfill-mined-soil-like-fractions and their dependency on organic matter. Process Safety and Environmental Protection 162, 795–812. https://doi.org/10.1016/j.psep.2022.04.052
Carrillo García, A., Latifi, M., Samih, S., Chaouki, J., 2020. Production of rare earth oxides from raw ore in fluidized bed reactor. Journal of Industrial and Engineering Chemistry 85, 141–151. https://doi.org/10.1016/j.jiec.2020.01.034
Lin, R., Stuckman, M., Howard, B.H., Bank, T.L., Roth, E.A., Macala, M.K., Lopano, C., Soong, Y., Granite, E.J., 2018. Application of sequential extraction and hydrothermal treatment for characterization and enrichment of rare earth elements from coal fly ash. Fuel 232, 124–133. https://doi.org/10.1016/j.fuel.2018.05.141
Dai, S., Yan, X., Ward, C.R., Hower, J.C., Zhao, Lei, Wang, X., Zhao, Lixin, Ren, D., Finkelman, R.B., 2018. Valuable elements in Chinese coals: a review. International Geology Review 60, 590–620. https://doi.org/10.1080/00206814.2016.1197802
Su, B., Mochizuki, Y., Murao, R., Higuchi, K., Tsubouchi, N., 2024. Effects of Preheating and Alkaline Roasting on Gangue Removal During the Alkaline Hydrothermal Treatment of Low-Grade Iron Ores. Metall Mater Trans B 55, 5158–5174. https://doi.org/10.1007/s11663-024-03324-7
Robinson, T.P., Metternicht, G., 2006. Testing the performance of spatial interpolation techniques for mapping soil properties. Computers and Electronics in Agriculture 50, 97–108. https://doi.org/10.1016/j.compag.2005.07.003
Xavier, L.H., Ottoni, M., Abreu, L.P.P., 2023. A comprehensive review of urban mining and the value recovery from e-waste materials. Resources, Conservation and Recycling 190, 106840. https://doi.org/10.1016/j.resconrec.2022.106840
Choudhary, A.K.S., Kumar, S., Maity, S., 2024. A study on speciation and enrichment of rare earth elements (REE) by sequential extraction from a potential coal fly ash resource and its role in REE extractability. Hydrometallurgy 224, 106256. https://doi.org/10.1016/j.hydromet.2023.106256
Ilkhani, Z., Vakilchap, F., Sadeghi, N., Mohammad Mousavi, S., 2024. Base metals (Fe, Al, Ti) and rare earth elements (Ce, La, Pr) leaching from red mud through an efficient chemical-biological hybrid approach. Minerals Engineering 208, 108603. https://doi.org/10.1016/j.mineng.2024.108603
Zhang, S., Shan, X., 2001. Speciation of rare earth elements in soil and accumulation by wheat with rare earth fertilizer application. Environmental Pollution 112, 395–405.
https://doi.org/10.1016/S0269-7491(00)00143-3
Aide, M.T., Aide, C., 2012. Rare Earth Elements: Their Importance in Understanding Soil Genesis. ISRN Soil

Science 2012, 1–11. https://doi.org/10.5402/2012/783876
Liu, X., Byrne, R.H., 1997. Rare earth and yttrium phosphate solubilities in aqueous solution. Geochimica et Cosmochimica Acta 61, 1625–1633. https://doi.org/10.1016/S0016-7037(97)00037-9
Rack, P.D., O'Brien, T.A., Zerner, M.C., Holloway, P.H., 1999. Determination of the Ce+3 bonding in the Ca0.5Sr0.5Ga2S4:Ce phosphor via x-ray photoelectron spectroscopy. Journal of Applied Physics 86, 2377–2384. https://doi.org/10.1063/1.371063
Cheng, H., Cui, P., Wang, F., Ding, L., Wang, H., 2019. High Efficiency Electrochemical Nitrogen Fixation Achieved with a Lower Pressure Reaction System by Changing the Chemical Equilibrium. Angew Chem Int Ed 58, 15541–15547. https://doi.org/10.1002/anie.201910658
Sevim, F., Saraç, H., Kocakerim, M.M., Yartaşı, A., 2003. Dissolution Kinetics of Phosphate Ore in H2 SO4 Solutions. Ind. Eng. Chem. Res. 42, 2052–2057. https://doi.org/10.1021/ie020168o
S. Wu, L. Wang, L. Zhao, P. Zhang, H. El-Shall, B. Moudgil, X. Huang, L. Zhang, Recovery of rare earth elements from phosphate rock by hydrometallurgical processes – A critical review, Chemical Engineering Journal 335 (2018) 774–800. https://doi.org/10.1016/j.cej.2017.10.143.
Crundwell, F.K., 2014. The mechanism of dissolution of minerals in acidic and alkaline solutions: Part III. Application to oxide, hydroxide and sulfide minerals. Hydrometallurgy 149, 71–81. https://doi.org/10.1016/j.hydromet.2014.06.008

Poster

Title:

Risk assessment of long-term leaching of heavy metals during solidification/stabilization of MSWI fly ash landfill disposal under the coupling effect of freeze-thaw cycle and carbonation

Abstract:

Municipal solid waste incineration (MSWI) fly ash is a hazardous material rich in heavy metals and dioxins, requiring effective stabilization/solidification (S/S) before landfill disposal. This study systematically evaluates the long-term stability, transformation mechanisms, and environmental risks of S/S-treated fly ash under freeze-thaw (F-T) cycles and natural environmental conditions. Using sodium dimethyldithiocarbamate (SDD) as a chelating agent and ordinary Portland cement (OPC) as a solidifying binder, we employed an innovative polyvinyl alcohol (PVA) membrane coating to isolate CO_2 and decouple carbonation effects from physical F-T damage. An accelerated laboratory simulation based on the climatic conditions of a typical seasonal frozen region (Harbin, China) was conducted over 120 F-T cycles. The results reveal that F-T action primarily induces physical degradation through repeated ice expansion and melting, increasing pore connectivity and microcrack development, whereas natural exposure promotes chemical corrosion via carbonation, leading to alkaline consumption and pH decline. The combined use of OPC and SDD significantly enhanced the long-term structural integrity and immobilization efficiency, reducing the leaching concentrations of key heavy metals such as Cd and Pb. The PVA membrane effectively hindered CO_2 penetration, mitigating carbonation-induced metal mobilization. BCR sequential extraction and risk assessment models (RAC and OPTI) indicated higher environmental risks under natural conditions, with Cd exhibiting very high risk levels. Cement-based S/S samples demonstrated superior performance in suppressing heavy metals mobility under both environments. These findings provide valuable insights into the coupling mechanisms of freeze-thaw and carbonation in S/S fly ash aging, and offer practical strategies for the engineering application and environmental risk control of pretreated fly ash in cold regions.

FACILITATING ANAEROBIC DIGESTION OF KITCHEN WASTE THROUGH DIATOMITE-MEDIATED SPATIAL ECOLOGICAL NICHES CONSTRUCTION

Dong Li[1] and Xiaoli Chai[1, 2]
1 College of Environmental Science and Engineering, Tongji University
1239 Siping Road, Shanghai 200092, China
2 Shanghai Institute of Pollution Control and Ecological Security
1239 Siping Road, Shanghai 200092, China

ABSTRACT
Anaerobic digestion (AD) presents an effective strategy for sustainable management of kitchen waste (KW), yet its widespread application remains constrained by suboptimal organic conversion efficiency and process instability. This study elucidates the critical role of diatomite (DE)-mediated spatial ecological niches construction in enhancing AD performance through microbial community regulation. Experimental results revealed that DE supplementation with optimal dosage of 10 g/L significantly improved methane production by 11.76%, and maintained system stability through effective mitigation of volatile fatty acid accumulation and ammonia nitrogen inhibition. Further analysis demonstrated that DE served as an optimal surface for microbial attachment, enhancing biofilm formation and extracellular polymeric substance secretion, which in turn facilitated the selective enrichment and spatial organization of functional microbial communities. Microbial characterization showed that fermentative bacteria predominantly occupied the tightly-adsorbed community, while acetoclastic and hydrogenotrophic methanogens were enriched in the suspended community. Finally, the established ecological niches enhanced electron transfer and promoted syntrophic metabolism among methanogenesis-associated microorganisms. These findings provide mechanistic insights into material-mediated niche engineering strategies, establishing DE as an effective biofilm carrier for optimizing microbial resource utilization in AD systems.

KEYWORDS
Diatomite; Spatial ecological niches; Biofilm; Anaerobic digestion; Kitchen waste

1. INTRODUCTION

The global rise in kitchen waste (KW) presents escalating environmental threats, particularly through greenhouse gas emissions linked to inadequate disposal practices (Jin et al., 2021). Despite these concerns, KW represents a valuable organic resource rich in carbohydrates, proteins, and cellulose (Chew et al., 2021; Huang et al., 2024). Therefore, it is imperative to implement sustainable valorization strategies to reconcile ecological preservation with resource recover. Anaerobic digestion (AD) has emerged as a sustainable solution for converting organic material into biogas and digestate, thereby reducing greenhouse gas emissions and promoting a circular economy (Chen et al., 2022; Wang et al., 2018). Nonetheless, the inherent inefficiencies of AD such as slow fermentation rates, low organic matter conversion, and unstable operation remain major obstacles for widespread application (Cui et al., 2021; Wang et al., 2021).

To address the challenges associated with AD, various strategies have been explored to enhance the process, including improved hydrolysis (Zhu et al., 2022), facilitated electron transfer (Cui et al., 2021), and enhanced mass transfer (Li et al., 2022). Beyond these strategies, microbial ecological niche engineering has emerged as a transformative paradigm that optimizes microbial colonization, synergistic metabolism, and stress resilience by creating favorable microenvironments (Bu et al., 2022; Cayetano et al., 2022; Luo et al., 2015; Shah et al., 2014). In AD systems, microorganisms actively reconstruct the spatial distribution and functional dynamics of microbial ecosystems through biofilm assembly, extracellular polymeric substance (EPS) secretion, and microenvironment modulation (Fernández et al., 2008; Fulaz et al., 2019; Langer et al., 2014). These modulations contribute to enhancing nutrient accessibility, promoting syntrophic partnerships, and buffering inhibitory compounds (Bu et al., 2022).

While microbial self-organization enables niche construction, its spontaneous progression is inherently stochastic and time-intensive (Mainardis et al., 2020). This limitation has spurred interest in engineered solutions utilizing porous biofilm carriers to accelerate functional microbial stratification (Bu et al., 2021; Bu et al., 2022; Paritosh et al., 2020). These materials promote spatially organized microbial consortia through surface

adhesion and biofilm stabilization, thereby constructing the creation of ecological niches and enhancing microbial community interactions (Cayetano et al., 2022; Tang et al., 2023). Among various porous materials, diatomite (DE) stands out for its unique structure and cost-effectiveness (Erdem et al., 2005; Hao et al., 2020; Sari et al., 2010). DE, a naturally occurring porous sedimentary rock composed primarily of amorphous form of silica ($SiO_2 \cdot nH_2O$) and small amounts of mineral elements, exhibits high porosity, loose texture, low bulk density, and large specific surface area, contributing to the strong adsorption capacity and filtration properties (Eleftheriou et al., 2013; Hao et al., 2020). More importantly, DE has also garnered attention for its ability to enhance microbial activity and facilitate the microbial aggregation (Wang et al., 2023; Wang et al., 2024a; Wu et al., 2022), making it promising for modifying the spatial ecological niches of AD process. Despite previous reports on the potential benefits of DE in AD (Wei et al., 2021; Zhang et al., 2021), critical knowledge gaps persist regarding its mechanistic role in sculpting functional microbial niches and governing metabolic partitioning between suspended and biofilm-associated communities.

Therefore, this study aims to (1) evaluate methane yield and the stability of the AD process with DE addition, (2) verify the effect of DE on microbial aggregation and spatial distribution of dominant microorganisms, and (3) understand the regulation of ecological niches construction on specific metabolic functions. The novelty of our work lies in the comprehensive exploration of the role of DE in altering microbial ecological niches to improve AD performance in KW treatment. Through controlled experiments and detailed analyses, our work provides novel insights into the interplay between carrier materials and microbial community dynamics, offering practical strategies for improved KW management.

2. MATERIALS AND METHODS

2.1. FEEDSTOCK, INOCULUM, AND DIATOMITE

The KW used in this study primarily consists of fruit and vegetable waste, sourced from a community garbage collection station in Shanghai, China. Upon collection, KW was homogenized using an electric blender and then stored at 4 °C until use. The inoculum was obtained from a long-term operated mesophilic AD reactor.

The DE material used in this study was obtained from a diatomite deposit in Linjiang, Jilin, China, where it underwent preliminary treatments including crushing, screening, purification, milling, and grading. Prior to its introduction into the AD reactor, the DE sample was sieved to achieve a particle size of <100 μm and washed with distilled water to eliminate impurities. Subsequently, it was dried at 100°C for 24 hours to ensure uniformity and cleanliness for experimental use. Physicochemical characterization revealed that the DE material exhibited a porous, disk-like structure, with a contact angle of 20.1°, a zeta potential of -22.87 mV, a specific surface area of 23.02 m^2/g, a total pore volume of 0.04 cm^3/g, and an adsorption average pore diameter of 6.93 nm.

2.2. ANAEROBIC DIGESTION PROCESS

Batch biochemical methane potential assays were performed in 500 mL serum bottles as reactors, each with an effective working volume of 350 mL. The substrate and inoculum were introduced at a VS ratio of 1:2, with an organic loading rate of 6 g VS/L for the substrate. DE was added to the reactors at four concentrations: 0 g/L (Control), 1 g/L (DE1), 5 g/L (DE5), and 10 g/L (DE10). After adding the specified dose of DE to each reactor, the contents were thoroughly mixed. The initial pH of all reactors was adjusted to 7.5 using either NaOH or HCl, as necessary. Prior to the start of the AD process, the reactors were purged with pure nitrogen gas for 5 minutes to establish anaerobic conditions. Subsequently, the reactors were placed in a heated water bath shaker operating at 170 rpm and maintained at a mesophilic temperature of 37 ± 0.5 °C for a duration of 45 days. To ensure the reliability and reproducibility of the results, each experimental condition was performed in triplicate.

2.3. PHYSICOCHEMICAL ANALYSIS

The composition of biogas was quantified through a gas chromatograph (Agilent 7890B, USA) equipped with a thermal conductivity detector. To prepare samples for subsequent analyses, fermentation residues were centrifuged at 10000 rpm for 10 minutes at 4 °C. Volatile fatty acids (VFAs), encompassing acetate, propionate, iso-butyrate, n-butyrate, iso-valerate, and n-valerate, were detected using a gas chromatograph (Agilent 6890, USA) equipped with a flame ionization detector. The values of TS, VS, pH, ammonia nitrogen (NH_4^+-N), and alkalinity were determined according to the standard methods (APHA). Elemental compositions (C, H, N and O) were analyzed using an elemental analyzer (Vario ELIII, Germany). The crude protein, crude lipid, and carbohydrate were quantified in accordance with the previous study (Huang et al., 2024).

To investigate the morphological characteristics of DE and anaerobic sludge samples, scanning electron microscopy (SEM, Hitachi S4800, Japan) was employed. Moreover, the hydrophilicity of DE and sludge was measured by a contact angle measurement system (Powereach JC2000, China), while the surface area and pore structure of DE were determined via a specific surface area analyzer (Micromeritics ASAP2460, USA). In addition, the zeta potential of DE was measured using a nanoparticle size and zeta potential analyzer (Malvern Zetasizer Nano ZS90, UK) to evaluate its surface charge properties. To further characterize microbial viability and biofilm formation in anaerobic sludge, living and dead cells in anaerobic sludge were detected by a confocal laser scanning microscopy (CLSM, Leica

STELLARIS5, Germany). EPS were extracted using a thermal extraction method. The protein and carbohydrate concentrations of the EPS were determined using the Lowry method and the phenol-sulfuric acid method, respectively. Three-dimensional fluorescence excitation-emission matrix (3D-EEM) spectra were measured using a fluorescence spectrophotometer (Hitachi F-7000, Japan). To assess microbial electron transfer capabilities, bacterial electron transfer system (ETS) activity was determined following the methodology described in previous studies (Zhu et al., 2022). Additionally, cyclic voltammetry (CV) analysis was conducted using an electrochemical workstation (Chenhua CHI660E, China) in a single-chamber three-electrode electrolytic system, as described by Chen et al. (Chen et al., 2023). The electrochemical setup consisted of a glassy carbon working electrode, an Ag/AgCl reference electrode, and a platinum wire counter electrode. The working electrode was scanned within a voltage range of -1.4 V to 1.0 V at a scan rate of 100 mV/s to evaluate electron transfer properties.

2.4. MICROBIAL ANALYSIS

Microbial community stratification in control and diatomite (DE)-amended systems was analyzed through high-throughput sequencing, with spatial fractionation adapted from established protocols (Bu et al., 2022; Luo et al., 2015). The microorganisms were divided into three spatial communities: suspended (S), loosely-attached (L) and tightly-adsorbed (T). To obtain the "S" fraction, the sample mixture was vortexed for 1 minute and centrifuged at 700 × g for 5 minutes, with the supernatant containing the suspended microorganisms. The above sediment was then resuspended in phosphate buffered saline (PBS, 0.01 mol/L), vortexed for 30 seconds, again under the same conditions to separate the loosely-attached microbes. This procedure was repeated four times: twice using PBS with 0.1% Tween-80 and twice with PBS alone. The collected supernatants represented the “L” fraction, while the remaining microorganisms in the final sediment was considered the “T” fraction, which included microorganisms tightly adsorbed on the DE surface. The control group sludge underwent the same fractionation process to account for any potential impact of centrifugation on the microorganisms.

The DNA from the “S”, “L” and “T” fractions was extracted using the soil DNA kit (Omega, USA). Amplicon primers 515FmodF-806RmodR were selected to target the V4 region of the 16S rRNA gene for both bacteria and archaea. The amplified sequence was analyzed via Illumina MiSeq from Majorbio Bio-Pharm Technology Co., Ltd (Shanghai, China). Functional predictions of metabolic pathways and key enzymes were conducted using PICRUSt2, with functional annotation carried out through the Kyoto Encyclopedia of Genes and Genomes (KEGG) database.

3. RESULTS AND DISCUSSIONS

3.1. PERFORMANCE OF AD OPTIMIZED BY DE

3.1.1. METHANE PRODUCTION

The variations in daily and cumulative methane production were illustrated in Fig. 1. All groups exhibited an initial methane yield peak within the first three days, which can be attributed to the rapid degradation of readily available soluble organic substrates (Di et al., 2022; Li et al., 2019). Following this peak, the methane production rate declined sharply, entering a stagnation phase. The control group achieved peak daily methane output (58.18 ± 4.18 mL/g VS) at day 22, culminating in a final cumulative yield of 503.73 ± 5.43 mL/g VS.

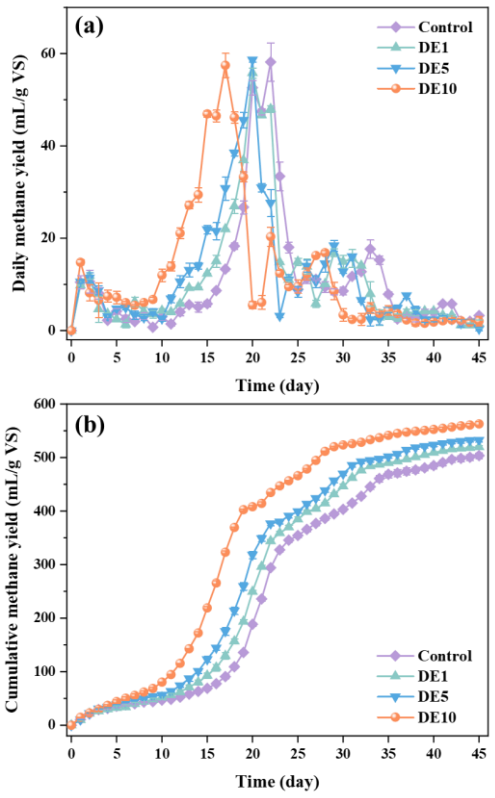

FIG. 1. (A) DAILY AND (B) CUMULATIVE METHANE PRODUCTION UNDER DIFFERENT DE DOSAGE.

DE supplementation significantly influenced methane production dynamics, with 10 g/L DE accelerating peak methane generation by five days, reaching its maximum on day 17 compared to the control group (Fig. 1a). Furthermore, the cumulative methane production values increased with the DE dosage and reached a maximum of 562.97 ± 3.90 mL/g VS in the DE10 group, which was 11.76% higher than that of the control group ($p < 0.05$) (Fig. 1b). This enhancement can be attributed to the unique porous structure of DE, which provides ample surface area for microbial colonization and growth (Tang et al., 2023; Wu et al., 2022). Consequently, DE facilitates the reconstruction of spatial ecological niches, optimizing the microenvironment for functional

microbial communities. Such microenvironmental improvements promote synergistic metabolic interactions among key microorganisms, thereby enhancing the conversion efficiency of methanogenic substrates (Chen et al., 2017).

The impact of DE on AD performance was further evaluated using a modified Gompertz model ($R^2 > 0.98$). Parameter analysis revealed that the lag phase (λ) in the DE10 system was significantly shortened to 7.94 days, compared to 12.79 days in the control group. These findings suggest that DE addition not only accelerates the startup phase of AD but also facilitates the rapid adaptation of methanogens to the reactor environment, thereby reducing the delay associated with methane production.

3.1.2. PROCESS STABILITY

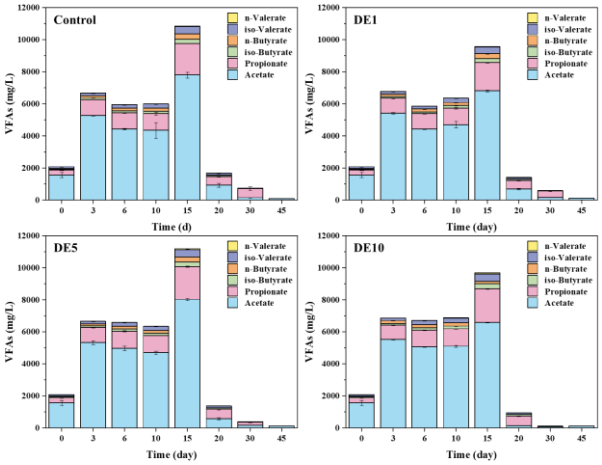

FIG. 2. VARIATIONS IN VFA COMPOSITION UNDER DIFFERENT DE DOSAGES.

The concentration and composition of VFAs serve as critical indicators for monitoring the methane production process. As illustrated in Fig. 2, the variations in VFAs across different experimental groups were analyzed during AD process. Initially, a rapid accumulation of VFAs was observed, peaking between 9571.67 ± 97.56 mg/L and 11188.82 ± 107.81 mg/L on day 15, primarily due to the accelerated hydrolysis of KW. This was followed by a progressive decline as VFAs were consumed by microbial communities. Notably, the DE group exhibited significantly lower VFAs concentrations than the control group ($p < 0.05$). On day 20, the total VFAs concentration in the DE10 group was 932.15 ± 55.43 mg/L, in contrast to 1676.43 ± 165.73 mg/L in the control group. This accelerated depletion of VFAs coincided with the peak methane production phase (days 17 to 20), indicating the efficient conversion of VFAs into methane. Furthermore, the marked reduction in acetate levels underscores the role of DE in promoting acetoclastic methanogenesis, which likely facilitated by the porous structure of DE that enhanced microbial access to the substrates.

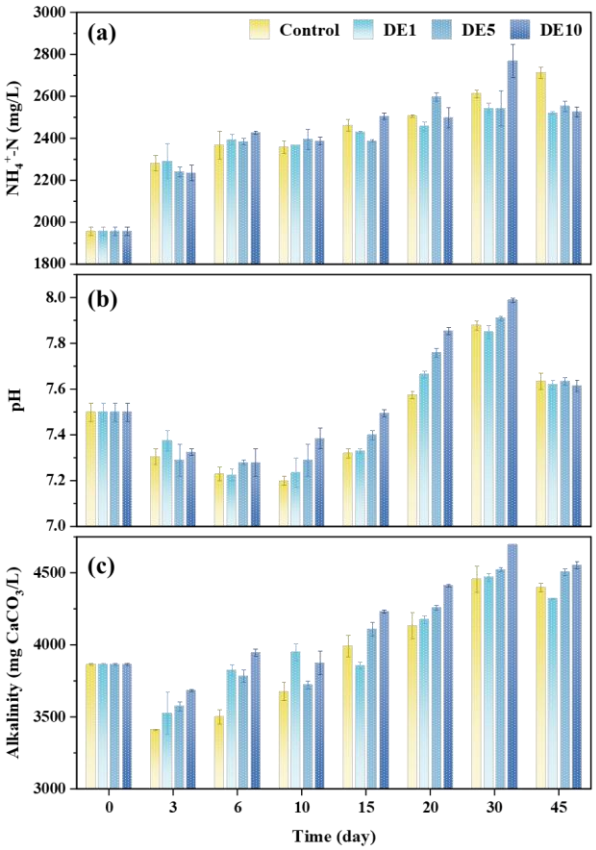

FIG. 3. VARIATIONS IN (A) NH_4^+-N, (B) PH VALUE AND (C) ALKALINITY.

NH_4^+-N can be used to assess the stability of AD systems. As shown in Fig. 3a, NH_4^+-N concentrations exhibited a rapid initial increase during the first 6 days, which was primarily attributed to proteolytic hydrolysis of protein in KW (Wang et al., 2022). Notably, the NH_4^+-N concentration in the DE10 group (2596.51 ± 23.32 mg/L) was lower than that of the control group (2713.98 ± 26.02 mg/L) ($p < 0.05$), suggesting that DE contributed to alleviating NH_4^+-N inhibition. This mitigation effect is likely attributed to the high specific surface area and porosity of DE, which facilitate NH_4^+-N adsorption (Wei et al., 2021). By reducing free NH_4^+-N levels, DE helps to maintain a more favorable environment for microbial activity, thereby enhancing system stability.

The trajectory of pH and alkalinity (Fig. 3b and 3c) reflects dynamic acid-base equilibrium regulation during AD. The initial decline in pH and alkalinity corresponded to the acidogenic phase, where buffering agents were consumed due to the accumulation of VFAs. However, as methanogenesis progressed, pH gradually recovered from 7.20 ± 0.02 to 7.89 ± 0.01, aligning with the conversion of VFAs into methane (Fig. 2). This stabilization ensured that conditions remained within the optimal pH range for methanogens (6.5 ~ 8.0) (Di et al., 2022). Furthermore, the inclusion of DE mineral materials provided trace elements (Zhang et al., 2021), as evidenced by the higher final alkalinity in the DE10

group (4556.04 ± 26.17 mg/L) compared to the control (4401.15 ± 27.88 mg/L, $p < 0.05$). This enhanced buffering capacity suggests that DE addition played a crucial role in stabilizing both pH and alkalinity, thereby improving overall process stability. Given the superior methanogenic performance observed in the DE10 group, subsequent mechanistic analyses focused on comparative assessments between the control group (referred to as Control) and the DE10 group (referred to as DE).

3.2. MICROBIAL SPATIAL ECOLOGICAL NICHES OF AD MEDIATED BY DE

3.2.1. MICROBIAL AGGREGATION CHARACTERISTICS

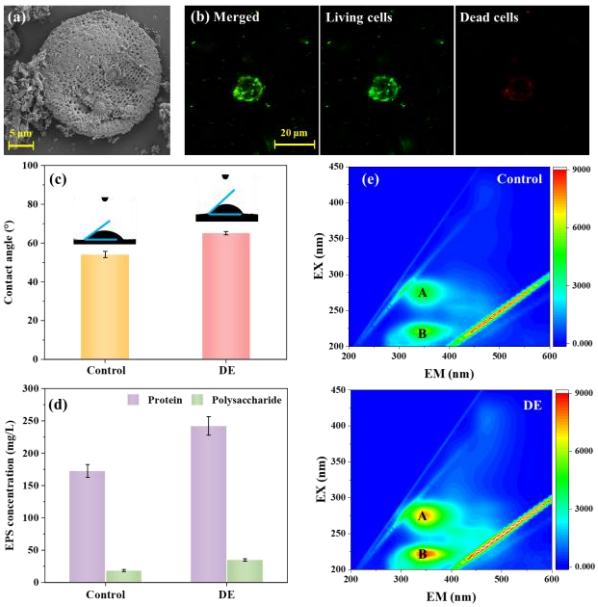

FIG. 4. ANAEROBIC SLUDGE PROPERTIES: (A) SEM AND (B) CLSM IMAGES OF BIOFILM-LOADED DE; (C) WATER CONTACT ANGLE OF ANAEROBIC SLUDGE, (D) EPS COMPOSITION AND CONTENT, AND (E) 3D-EEM SPECTRA OF EPS.

After AD process, SEM characterization of DE-mediated anaerobic sludge revealed extensive microbial aggregation and biofilm formation on the DE surface (Fig. 4a). CLSM imaging further confirmed this observation, showing a uniform distribution of viable microbial cells (green fluorescence) across the DE surface (Fig. 4b). The development and stabilization of biofilm can be attributed primarily to the large specific surface area of DE, which provides abundant attachment sites for microbial colonization. Additionally, the inherent hydrophilicity and porous structure of DE synergistically facilitate nutrient adsorption and retention, collectively creating a favorable microenvironment for microbial proliferation and biofilm stability throughout the digestion process (Al-Amshawee et al., 2021; Huang et al., 2022). Given that the hydrophobicity property of the sludge surface is a key factor in microbial aggregation (Wang et al., 2024b), the contact angle test was conducted to evaluate changes in sludge hydrophobicity upon DE addition (Fig. 4c). The results indicated an increase in the contact angle from 54.18 ± 1.63° to 65.19 ± 0.92°, which proved that microbial adhesion and aggregation were promoted.

Microbial adhesion to DE was accompanied by enhanced EPS production, further reinforcing biofilm development (Fulaz et al., 2019). EPS analysis revealed that DE significantly stimulated microbial secretion, particularly of proteins (Fig. 4d). Compared to the control group, DE supplementation notably increased the protein content from 172.81 ± 10.14 mg/L in the control group to 282.42 ± 14.35 mg/L in the DE group. Given the well-established correlation between the protein content in EPS and the hydrophobicity of sludge (Yin et al., 2015), this increase likely contributed to improved microbial aggregation. To identify the organic compounds in the EPS, 3D-EEM fluorescence spectroscopy was employed, revealing distinct differences in fluorescence intensity between the DE and control groups (Fig. 4e). The DE-injection groups exhibited notably stronger fluorescence intensities for soluble microbial products (peak A: Ex/Em = 250~310 nm/250~380 nm) and tryptophan-like protein substances (peak B: Ex/Em = 220~250 nm/330~380 nm) compared to the control. Since tryptophan-like substances belong to a class of hydrophobic amino acids (Wang et al., 2024b), their elevated presence in the DE group suggests that DE stimulated the production of hydrophobic biomolecules, further promoting biofilm formation.

Consequently, DE serves as an effective biofilm-supporting carrier to enhance microbial adhesion and aggregation in AD system, which effectively promotes the construction of ecological niches.

3.2.2. MICROBIAL COMMUNITY STRUCTURE

Microorganisms are crucial in the degradation and transformation of organics, with their abundance and community composition significantly influencing the AD performance of KW (Zhang et al., 2024). In addition, stratification structure would be formed in microbial particles mediated by carrier materials, which may be conducive to enhancing the activity and abundance of functional microorganisms (Wang et al., 2024b). To further understand the effect of DE on the spatial distribution of microbial communities, 16S rRNA high-throughput gene sequencing was conducted for taxonomic analysis of microbial species in the control group (C) and DE10 group (DE), and the results were shown in Fig. 5.

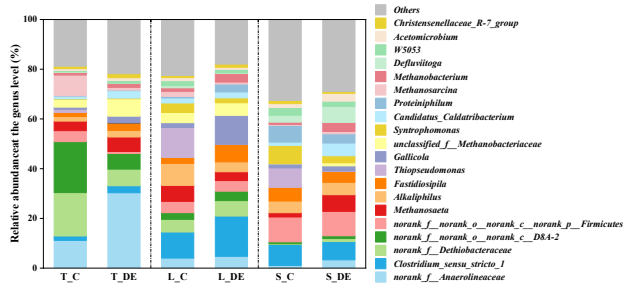

FIG. 5. EFFECTS OF DE ADDITION ON THE ABUNDANCE AND SPATIAL DISTRIBUTION OF THE TOP 20 MICROORGANISMS AT THE GENUS LEVEL. "T_C" AND "T_DE" MEANS TIGHTLY-ADSORBED COMMUNITIES IN CONTROL AND DE10 GROUPS; "L_C" AND "L_DE" MEANS LOOSELY-ATTACHED COMMUNITIES; "S_C" AND "S_DE" MEANS SUSPENDED COMMUNITIES.

The tightly-adsorbed layer refers to the community directly attached to the DE particles. The highly porous structure and large surface area of DE provided an optimal microenvironment for microbial colonization, thereby facilitating the formation of tightly-adsorbed biofilms. This layer played a crucial role in initiating the degradation of complex organic matter and establishing a foundation for subsequent microbial succession (Zhang et al., 2025). A notable shift in microbial composition was observed within this layer. Specifically, the relative abundance of norank_f__*Anaerolineaceae* (*Chloroflexi* phylum), a typical acetogenic bacterium capable of electron transfer to methanogens via conductive pili (Wang et al., 2019), significantly increased from 11.15% in the control group to 30.32% in the DE group. This enrichment of key functional microorganisms indicated that DE fostered a microenvironment conducive to the early-stage organic matter decomposition and efficient energy conversion. Similarly, among archaea, the total relative abundance of *Methanosaeta* and *Methanobacterium*, both of which facilitate direct interspecies electron transfer (DIET) (Liu et al., 2022; Ou et al., 2022), increased from 4.87% to 7.44%. This suggested that DE promoted the proliferation of electron-transferring microorganism essential for biofilm formation. The establishment of these conductive biofilms could enhance extracellular electron transfer (EET) and improve syntrophic interactions among diverse microbial communities.

The loosely-attached community consists of microorganisms associated with the DE surface but more readily detached compared to the tightly-adsorbed community. This transitional layer serves as a bridge between the tightly-adsorbed biofilms and the suspended microbial community, mediating the exchange of organic matter and nutrients (Luo et al., 2015). The microbial composition within this layer reflects its dual exposure to surface attachment and bulk liquid conditions, favoring species with metabolic flexibility to utilize diverse substrates and adapt to fluctuating environmental conditions. Consequently, the relative abundance of both bacteria and archaea within this community remained largely unchanged in response to DE supplementation.

The suspended community comprises free-floating microorganisms dispersed throughout the AD system. Compared to the tightly-adsorbed and loosely-attached communities, this fraction exhibited a relatively weaker response to DE addition (Bu et al., 2022). Nevertheless, it continues to play a critical role in maintaining the overall microbial balance. Notably, the relative abundance of acetoclastic methanogens (*Methanosaeta*), hydrogenotrophic methanogens (unclassified_f__*Methanobacteriaceae* and *Methanobacterium*), and mixotrophic methanogens (*Methanosarcina*) significantly increased in response to DE addition (De Vrieze et al., 2012; Zhang et al., 2020). This suggests that metabolic intermediates, such as acetate and H_2/CO_2, produced by microbial activity in the inner layers, were released into the suspended phase, where they were subsequently utilized by free-living methanogens.

Collectively, these findings highlight the distinct yet interconnected roles of the three microbial communities in response to DE amendment. As a result, the construction of ecological niches was achieved in response to DE induction, which ultimately affected the overall performance of AD systems.

3.3. METABOLIC FUNCTION LINKED WITH SPATIAL ECOLOGICAL NICHES MEDIATED BY DE

3.3.1 INTERSPECIES ELECTRON TRANSFER

Efficient electron transfer among microorganisms is essential for methane production during AD. To further elucidate the effect of the DE on intracellular electron transfer (INT) capacity and EET activity, ETS activity and CV curves were explored (Fig. 6).

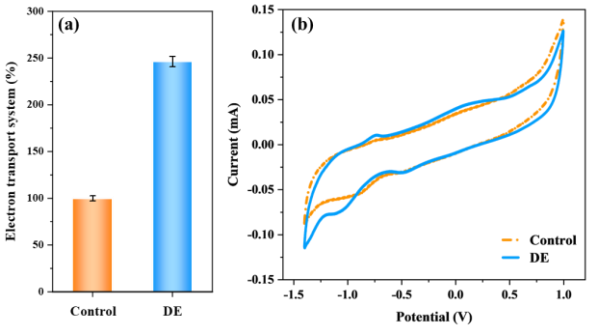

FIG. 6. COMPARATION OF (A) ETS ACTIVITY AND (B) CYCLIC VOLTAMMETRY CURVE.

As shown in Fig. 6a, ETS activity, an indicator of microbial INT capacity (Liu et al., 2022; Zhu et al., 2022), was significantly enhanced in the DE-supplemented reactor, which suggested that DE improves cellular respiration and contributes to more

efficient INT. Moreover, this enhancement likely contributes to improved EET efficiency, as the increased oxidation of electron donors may promote electron migration toward EET pathways (Liu et al., 2022). CV curve was measured using an electrochemical station to evaluate the EET capacity (Fig. 6b). Research findings suggested that the shape and potential of redox peaks correspond to the diversity of electroactive microbes and the presence of electrochemically active EPS, while the magnitude of the peak current reflects microbial population density (Cheng et al., 2020; Feng et al., 2018). A comparison of the CV curves revealed that the DE-mediated group exhibited a more pronounced contour, indicating an increased charge storage capacity in anaerobic sludge. Consequently, there is strong evidence supporting the notion that DE addition can enhance electron transfer within the AD system, in line with previous findings by Wei et al. (Wei et al., 2021) that natural DE increased the electron transfer efficiency during the conversion of waste activated sludge to methane.

It is worth noting that DE is primarily composed of non-conductive SiO_2 (Li et al., 2023), so its effect on electron transfer is not directly attributable to conductivity. Instead, the enhancement is likely due to improved biofilm formation, a recognized strategy for promoting electron transfer (Cayetano et al., 2022; Paritosh et al., 2020; Zhao et al., 2021). The porous structure of DE facilitated microbial attachment and biofilm formation, which triggered the secretion of EPS enriched with electroactive compounds. The favorable ecological niches selectively enriched electroactive microbial populations, leading to a tight distribution of clusters that reduced bioelectronic distances and fostered synergistic interactions. Consequently, electron migration from bacteria to archaea in the anaerobic sludge was greatly accelerated, enhancing overall extracellular electron transfer efficiency and methane production (Huang et al., 2022).

3.3.2. METHANOGENIC METABOLISM

The associated metabolic pathways were predicted using PICRUSt2 and annotated through the KEGG database. At the highest classification level (level 1), metabolism emerged as the dominant KEGG pathway, accounting for over 76.37% of the total. The secondary metabolic pathways included the global and overview maps (40.27%~41.46%), carbohydrate metabolism (8.78%~9.57%), amino acid metabolism (7.03%~7.36%), energy metabolism (4.47%~5.35%), and metabolism of cofactors and vitamins (4.01%~4.51%) (Fig. 7).

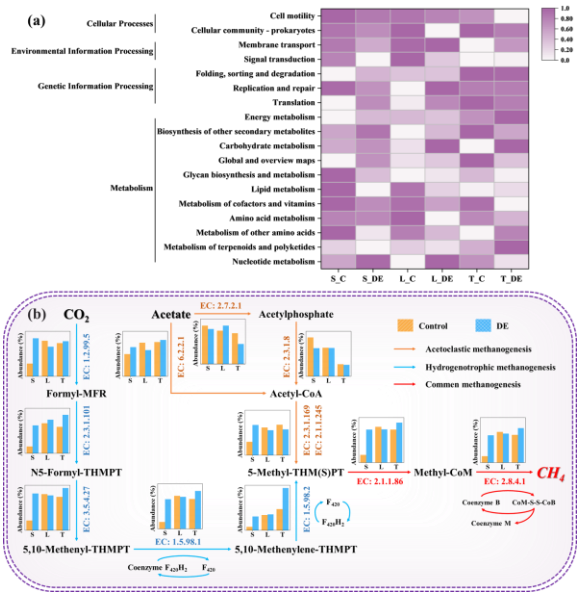

FIG. 7. (A) HEATMAP ANALYSIS OF THE ABUNDANCE OF KEGG PATHWAYS AT LEVEL 2, RELATIVE ABUNDANCE GREATER THAN 1% WAS COUNTED; (B) THE CHANGES OF KEY ENZYMES ABUNDANCES INVOLVING IN THE ACETOCLASTIC AND HYDROGENOTROPHIC METHANOGENESIS PATHWAYS.

The addition of DE particularly enhanced the carbohydrate metabolism and energy metabolism, both of which are associated with the organic matter decomposition and methane yield (Wang et al., 2022). These enhancements were most evident in the tightly-adsorbed community, where DE's porous structure promoted robust biofilm formation and enriched populations of functional microorganisms. In reactors supplemented with DE, there was an increased relative abundance of pathways involved in membrane transport and signal transduction, suggesting an improved capacity for organic substrate exchange across cell membranes that likely facilitates methanogen growth. In support of this, predicted metabolic pathway analysis at level 3 revealed a greater abundance of methane metabolism pathways in the DE-mediated group, along with a notable increase in quorum sensing, a mechanism critical for inter-microbial communication, EPS secretion, and biofilm development (Zhao et al., 2024).

Further insights were gained through functional module analysis via the KEGG database, which identified that methanogenic processes in our system were primarily carried out through acetoclastic (M00357), hydrogenotrophic (M00567) and methylotrophic (M00356 and M00563) methanogenesis pathways (Wang et al., 2022). Overall, the higher abundance of M00357 and M00567 modules in the DE group reflected the enhanced methanogenic activity. Taxonomic analysis showed that acetoclastic and hydrogenotrophic methanogens were dominant in our study, prompting a

deeper investigation using PICRUSt2 into the variations of key enzymes involved in converting acetate to methane and H_2/CO_2 to methane.

Hydrogenotrophic methanogenesis involved the stepwise reduction of CO_2 to formyl, methenyl, methylene, and methyl groups, culminating in methane generation (Huang et al., 2024). In this study, key enzymes essential for these reactions were more abundant in both the suspended and tightly-adsorbed layers of the DE group, a finding corroborated by the increased levels of unclassified_f__*Methanobacteriaceae* and *Methanobacterium* (Fig. 6b). Regarding acetoclastic methanogenesis, while the abundances of acetate kinase (EC: 2.7.2.1) and phosphate acetyltransferase (EC: 2.3.1.8) were lower in the DE group, the elevated abundance of acetyl-CoA synthetase (EC: 6.2.1.1) indicated that DE facilitated a more direct conversion of acetate to acetyl-CoA. Although there was a slight reduction in the overall enzyme abundance involved in converting acetate to 5-methyl-THM(S)PT in the tightly-adsorbed layer, the increased levels of the key enzymes in the final steps of methane formation (tetrahydromethanopterin methyltransferase (EC: 2.1.1.86) and methyl-CoM reductase (EC: 2.8.4.1)) indicated that the enhanced M00357 module abundance was primarily linked to the efficient conversion of intermediates to methane (Wang et al., 2022).

Previous studies have indicated that *Methanosaeta* (acetoclastic methanogens) can also function as an electroactive methanogen, which was capable for generating methane from CO_2 via the direct interspecies electron transfer (DIET) pathway (Liu et al., 2022). Therefore, the observed enrichment of *Methanosaeta* within the tightly-adsorbed layer supported the establishment of DIET with norank_f__*Anaerolineaceae*, thereby contributing to the hydrogenotrophic metabolism. Despite the potential inhibitory effects of NH_4^+-N adsorption by DE in the tightly-adsorbed layer, the overall increase in methane metabolism suggests that biofilm-mediated electron transfer effectively mitigated these challenges (Di et al., 2022). Additionally, DE stimulated the growth of fermentative bacteria such as norank_f__*Anaerolineaceae* in the tightly-adsorbed layer, allowing their metabolites (acetate and H_2/CO_2) to diffuse into the suspended layer and further strengthen methane metabolic pathways and associated enzyme activities. Consequently, the hydrogenotrophic methanogenesis pathway in the tightly-adsorbed layer was improved, both the acetoclastic and hydrogenotrophic methanogenesis pathways were enhanced in the suspended layer, with minimal changes observed in the loosely-attached layer.

Overall, the porous structure and high specific surface area of DE provided abundant attachment sites for microorganisms, facilitating microbial aggregation and stable biofilm formation. This biofilm-driven niche construction optimized the spatial organization of bacteria and methanogens, enhanced substrate degradation and electron transfer pathways, and promoted synergistic microbial metabolism, all of which played a critical role in improving AD efficiency. While this study underscores the potential of DE in ecological niche engineering for sustainable waste treatment, further research is needed to assess the long-term stability of DE-induced biofilms and their influence on microbial community dynamics. Future investigations should focus on refining DE application strategies, evaluating its role in digestate management across different feedstocks, and determining its feasibility for large-scale AD systems.

4. CONCLUSIONS

This study demonstrated that the construction of spatial ecological niches within AD systems is essential for enhancing methane metabolism from KW. The formation of biofilms on the DE surfaces established distinct microenvironments that optimized the spatial distribution of functional microorganisms. These constructed ecological niches improved substrate accessibility, facilitated efficient electrons transfer, and promoted synergistic interactions between bacteria and methanogens. Consequently, the conversion of substrates to methane was significantly enhanced, which increased methane yields, reduced lag phase, and improved system stability. Overall, these findings offer a theoretical basis for optimizing methanogenic pathways in AD and underscore the potential of DE-mediated ecological niche construction as an effective strategy to enhance methane yields in waste management.

REFERENCES

Al-Amshawee, S., Yunus, M.Y.B., Lynam, J.G., Lee, W.H., Dai, F., Dakhil, I.H., 2021. Roughness and wettability of biofilm carriers: A systematic review. Environ. Technol. Innov. 21, 101233. https://doi.org/10.1016/j.eti.2020.101233

Bu, J., Wei, H.L., Wang, Y.T., Cheng, J.R., Zhu, M.J., 2021. Biochar boosts dark fermentative H2 production from sugarcane bagasse by selective enrichment/colonization of functional bacteria and enhancing extracellular electron transfer. Water Res. 202, 117440. https://doi.org/10.1016/j.watres.2021.117440

Bu, J., Hu, B.B., Wu, H.Z., Zhu, M.J., 2022. Improved methane production with redox-active/conductive biochar amendment by establishing spatial ecological niche and mediating electron transfer. Bioresour. Technol. 351, 127072. https://doi.org/10.1016/j.biortech.2022.127072

Cayetano, R.D.A., Kim, G.B., Park, J., Yang, Y.H., Jeon, B.H., Jang, M., Kim, S.H., 2022. Biofilm formation as a method of improved treatment during anaerobic digestion of organic matter for biogas recovery.

Bioresour. Technol. 344, 126309. https://doi.org/10.1016/j.biortech.2021.126309
Chen, C.M., Liang, J.H., Yoza, B.A., Li, Q.X., Zhan, Y.L., Wang, Q.H., 2017. Evaluation of an up-flow anaerobic sludge bed (UASB) reactor containing diatomite and maifanite for the improved treatment of petroleum wastewater. Bioresour. Technol. 243, 620-627. https://doi.org/10.1016/j.biortech.2017.06.171
Chen, J.Q., Zhang, P.S., Zhang, J.X., He, Y.L., Tong, Y.W., 2022. Micro-nano magnetite-loaded biochar enhances interspecies electron transfer and viability of functional microorganisms in anaerobic digestion. ACS Sustain. Chem. Eng. 10(8), 2811-2821. https://doi.org/10.1021/acssuschemeng.1c08288
Chen, Y.D., Dai, X.H., Wang, H., Liu, X.G., Gu, L., 2023. Insights into the mitigative effects of microbial electrolysis cell on anaerobic digestion under high ammonia condition. Chem. Eng. J. 474. https://doi.org/10.1016/j.cej.2023.145760
Cheng, J., Hua, J.J., Kang, T., Meng, B., Yue, L.C., Dong, H.Q., Li, H., Zhou, J.H., 2020. Nanoscale zero-valent iron improved lactic acid degradation to produce methane through anaerobic digestion. Bioresour. Technol. 317, 124013. https://doi.org/10.1016/j.biortech.2020.124013
Chew, K.R., Leong, H.Y., Khoo, K.S., Vo, D.V.N., Anjum, H., Chang, C.K., Show, P.L., 2021. Effects of anaerobic digestion of food waste on biogas production and environmental impacts: a review. Environ. Chem. Lett. 19(4), 2921-2939. https://doi.org/10.1007/s10311-021-01220-z
Cui, Y.X., Mao, F.J., Zhang, J.X., He, Y.L., Tong, Y.W., Peng, Y.H., 2021. Biochar enhanced high-solid mesophilic anaerobic digestion of food waste: Cell viability and methanogenic pathways. Chemosphere. 272, 129863. https://doi.org/10.1016/j.chemosphere.2021.129863
De Vrieze, J., Hennebel, T., Boon, N., Verstraete, W., 2012. Methanosarcina: the rediscovered methanogen for heavy duty biomethanation. Bioresour. Technol. 112, 1-9. https://doi.org/10.1016/j.biortech.2012.02.079
Di, L., Zhang, Q.G., Wang, F., Wang, H., Liu, H.K., Yi, W.M., Zhang, Z.P., Zhang, D.L., 2022. Effect of nano-Fe3O4 biochar on anaerobic digestion of chicken manure under high ammonia nitrogen concentration. J. Clean. Prod. 375, 134107. https://doi.org/10.1016/j.jclepro.2022.134107
Eleftheriou, N.M., Ge, X., Kolesnik, J., Falconer, S.B., Harris, R.J., Khursigara, C., Brown, E.D., Brennan, J.D., 2013. Entrapment of Living Bacterial Cells in Low-Concentration Silica Materials Preserves Cell Division and Promoter Regulation. Chem. Mat. 25(23), 4798-4805. https://doi.org/10.1021/cm403198z
Erdem, E., Cölgeçen, G., Donat, R., 2005. The removal of textile dyes by diatomite earth. J. Colloid. Interf. Sci. 282(2), 314-319. https://doi.org/10.1016/j.jcis.2004.08.166
Feng, Q., Song, Y.C., Ahn, Y., 2018. Electroactive microorganisms in bulk solution contribute significantly to methane production in bioelectrochemical anaerobic reactor. Bioresour. Technol. 259, 119-127. https://doi.org/10.1016/j.biortech.2018.03.039
Fernández, N., Díaz, E.E., Amils, R., Sanz, J.L., 2008. Analysis of microbial community during biofilm development in an anaerobic wastewater treatment reactor. Microb. Ecol. 56(1), 121-132. https://doi.org/10.1007/s00248-007-9330-2
Fulaz, S., Vitale, S., Quinn, L., Casey, E., 2019. Nanoparticle-Biofilm Interactions: The Role of the EPS Matrix. Trends Microbiol. 27(11), 915-926. https://doi.org/10.1016/j.tim.2019.07.004
Hao, L.P., Gao, W.Y., Yan, S., Niu, M.H., Liu, G.S., Hao, H.S., 2020. Functionalized diatomite/oyster shell powder doped electrospun polyacrylonitrile submicron fiber as a high-efficiency adsorbent for removing methylene blue from aqueous solution: Thermodynamics, kinetics and isotherms. J. Mol. Liq. 298, 112022. https://doi.org/10.1016/j.molliq.2019.112022
Huang, T., Li, D., Chen, B., Wu, B.R., Chai, X.L., 2024. Utilization strategy for algal bloom waste through co-digestion with kitchen waste: Comprehensive kinetic and metagenomic analysis. Environ. Res. 255, 119194. https://doi.org/10.1016/j.envres.2024.119194
Huang, W., Zhou, J., Hu, Q., Qiu, B., Huang, M.N., Murugadoss, V., Guo, Z.H., 2022. Improved methanogenesis in anaerobic wastewater treatment by magnetite@polyaniline (Fe3O4@PANI) composites. Chemosphere. 296, 133953. https://doi.org/10.1016/j.chemosphere.2022.133953
Jin, C., Sun, S., Yang, D., Sheng, W., Ma, Y., He, W., Li, G., 2021. Anaerobic digestion: An alternative resource treatment option for food waste in China. Sci. Total Environ. 779, 146397. https://doi.org/10.1016/j.scitotenv.2021.146397
Langer, S., Schropp, D., Bengelsdorf, F.R., Othman, M., Kazda, M., 2014. Dynamics of biofilm formation during anaerobic digestion of organic waste. Anaerobe. 29, 44-51. https://doi.org/10.1016/j.anaerobe.2013.11.013
Li, B.W., Wang, T., Le, Q.J., Qin, R.Z., Zhang, Y.X., Zeng, H.C., 2023. Surface reconstruction, modification and functionalization of natural diatomites for miniaturization of shaped heterogeneous catalysts. Nano Mater. Sci. 5(3), 293-311. https://doi.org/10.1016/j.nanoms.2022.05.001
Li, J.H., Zhang, M., Ye, Z.Y., Yang, C.M., 2019. Effect of manganese oxide-modified biochar addition on methane production and heavy metal speciation during the anaerobic digestion of sewage sludge. J. Environ. Sci. 76, 267-277. https://doi.org/10.1016/j.jes.2018.05.009
Li, L.L., Wang, K., Sun, Z.J., Zhao, Q.L., Zhou, H.M., Gao, Q.W., Jiang, J.Q., Mei, W.Y., 2022. Effect of optimized intermittent mixing during high-solids anaerobic co-digestion of food waste and sewage sludge:

Simulation, performance, and mechanisms. Sci. Total Environ. 842, 156882. https://doi.org/10.1016/j.scitotenv.2022.156882
Liu, H.Y., Xu, Y., Li, L., Yuan, S.J., Geng, H., Tang, Y.F., Dai, X.H., 2022. A novel green composite conductive material enhancing anaerobic digestion of waste activated sludge via improving electron transfer and metabolic activity. Water Res. 220, 118687. https://doi.org/10.1016/j.watres.2022.118687
Luo, C.H., Lü, F., Shao, L.M., He, P.J., 2015. Application of eco-compatible biochar in anaerobic digestion to relieve acid stress and promote the selective colonization of functional microbes. Water Res. 68, 710-718. https://doi.org/10.1016/j.watres.2014.10.052
Mainardis, M., Buttazzoni, M., Goi, D., 2020. Up-flow anaerobic sludge blanket (UASB) technology for energy recovery: a review on state-of-the-art and recent technological advances. Bioengineering. 7(2), 43. https://doi.org/10.3390/bioengineering7020043
Ou, Y.F., Dong, H.P., McIlroy, S.J., Crowe, S.A., Hallam, S.J., Han, P., Kallmeyer, J., Simister, R.L., Vuillemin, A., Leu, A.O., Liu, Z.F., Zheng, Y.L., Sun, Q.L., Liu, M., Tyson, G.W., Hou, L.J., 2022. Expanding the phylogenetic distribution of cytochrome b-containing methanogenic archaea sheds light on the evolution of methanogenesis. Isme J. 16(10), 2373-2387. https://doi.org/10.1038/s41396-022-01281-0
Paritosh, K., Yadav, M., Chawade, A., Sahoo, D., Kesharwani, N., Pareek, N., Vivekanand, V., 2020. Additives as a support structure for specific biochemical activity boosts in anaerobic digestion: A review. Front. Energy Res. 8, 88. https://doi.org/10.3389/fenrg.2020.00088
Sari, A., Çitak, D., Tuzen, M., 2010. Equilibrium, thermodynamic and kinetic studies on adsorption of Sb(III) from aqueous solution using low-cost natural diatomite. Chem. Eng. J. 162(2), 521-527. https://doi.org/10.1016/j.cej.2010.05.054
Shah, F.A., Mahmood, Q., Shah, M.M., Pervez, A., Asad, S.A., 2014. Microbial ecology of anaerobic digesters: The key players of anaerobiosis. Sci. World J., 183752. https://doi.org/10.1155/2014/183752
Tang, C.C., Zhang, B.C., Yao, X.Y., Sangeetha, T., Zhou, A.J., Liu, W.Z., Ren, Y.X., Li, Z.H., Wang, A.J., He, Z.W., 2023. Natural zeolite enhances anaerobic digestion of waste activated sludge: Insights into the performance and the role of biofilm. J. Environ. Manage. 345, 118704. https://doi.org/10.1016/j.jenvman.2023.118704
Wang, C.Q., Qiao, W.L., Chen, H., Xu, X.Y., Zhu, L., 2019. A short-term stimulation of ethanol enhances the effect of magnetite on anaerobic digestion. Appl. Microbiol. Biotechnol. 103(3), 1511-1522. https://doi.org/10.1007/s00253-018-9531-2
Wang, C.X., Lu, B., Chen, H., Chen, H.Z., Li, T.T., Lu, W., Chai, X.L., 2023. Strengthen high-loading operation of wastewater treatment plants by composite micron powder carrier: Microscale control of carbon, nitrogen, and sulfur metabolic pathways. Sci. Total Environ. 904, 166593. https://doi.org/10.1016/j.scitotenv.2023.166593
Wang, C.X., Chai, X.L., Lu, B., Lu, W., Han, H.B., Mu, Y., Gu, Q., Wu, B.R., 2024a. Integrated control strategy for dual sludge ages in the high-concentration powder carrier bio-fluidized bed (HPB) technology: Enhancing municipal wastewater treatment efficiency. J. Environ. Manage. 351, 119890. https://doi.org/10.1016/j.jenvman.2023.119890
Wang, H., Chen, Y.D., Liu, X.G., Xu, H.L., Yang, D.H., Hua, Y., Dai, X.H., 2024b. Diatomite powder carrier improved nitrogen and phosphorus removal from real municipal wastewater: Insights into micro-granule formation and enhancement mechanism. Chem. Eng. J. 484, 149482. https://doi.org/10.1016/j.cej.2024.149482
Wang, J.F., Zhao, Z.Q., Zhang, Y.B., 2021. Enhancing anaerobic digestion of kitchen wastes with biochar: Link between different properties and critical mechanisms of promoting interspecies electron transfer. Renew. Energy. 167, 791-799. https://doi.org/10.1016/j.renene.2020.11.153
Wang, T., Zhang, D., Dai, L.L., Dong, B., Dai, X.H., 2018. Magnetite triggering enhanced direct interspecies electron transfer: A scavenger for the blockage of electron transfer in anaerobic digestion of high-solids sewage sludge. Environ. Sci. Technol. 52(12), 7160-7169. https://doi.org/10.1021/acs.est.8b00891
Wang, X.Z., Wang, P., Meng, X.Y., Ren, L.H., 2022. Performance and metagenomics analysis of anaerobic digestion of food waste with adding biochar supported nano zero-valent iron under mesophilic and thermophilic condition. Sci. Total Environ. 820, 153244. https://doi.org/10.1016/j.scitotenv.2022.153244
Wei, W., Chen, Z.J., Hao, D., Liu, X.Q., Ni, B.J., 2021. Natural diatomite mediated continuous anaerobic sludge digestion: Performance, modelling and mechanisms. J. Clean. Prod. 329, 129750. https://doi.org/10.1016/j.jclepro.2021.129750
Wu, B.R., Wang, X.Z., Wang, C.X., Lu, B., Yi, J., Dai, X.H., Chai, X.L., 2022. Novel micro-granular sludge process for highly efficient treatment of low-strength and low C/N ratio municipal wastewater. Chemosphere. 287, 132322. https://doi.org/10.1016/j.chemosphere.2021.132322
Yin, C.Q., Meng, F.G., Chen, G.H., 2015. Spectroscopic characterization of extracellular polymeric substances from a mixed culture dominated by ammonia-oxidizing bacteria. Water Res. 68, 740-749. https://doi.org/10.1016/j.watres.2014.10.046
Zhang, G.Y., Shi, Y.H., Zhao, Z.S., Wang, X.W., Dou, M., 2020. Enhanced two-phase anaerobic digestion of waste-activated sludge by combining magnetite and zero-valent iron. Bioresour. Technol. 306, 123122. https://doi.org/10.1016/j.biortech.2020.123122
Zhang, J., Liu, H., Wu, J.Y., Chen, C.J., Ding, Y., Liu, H.B., Zhou, Y., 2025. Rethinking the biochar impact on the anaerobic digestion of food waste in bench-scale

digester: Spatial distribution and biogas production. Bioresour. Technol. 420, 132115. https://doi.org/10.1016/j.biortech.2025.132115
Zhang, X.X., Wang, Y.W., Jiao, P.B., Zhang, M., Deng, Y., Jiang, C.Y., Liu, X.W., Lou, L.P., Li, Y.M., Zhang, X.X., Ma, L.P., 2024. Microbiome-functionality in anaerobic digesters: A critical review. Water Res. 249, 120891. https://doi.org/10.1016/j.watres.2023.120891
Zhang, Y.T., Wei, W., Wang, Y., Ni, B.J., 2021. Enhancing methane production from algae anaerobic digestion using diatomite. J. Clean. Prod. 315, 128138. https://doi.org/10.1016/j.jclepro.2021.128138
Zhao, J.T., Li, F., Cao, Y.X., Zhang, X.B., Chen, T., Song, H., Wang, Z.W., 2021. Microbial extracellular electron transfer and strategies for engineering electroactive microorganisms. Biotechnol. Adv. 53, 107682. https://doi.org/10.1016/j.biotechadv.2020.107682
Zhao, S.N., Zhu, S.Q., Liu, S., Song, G., Zhao, J., Liu, R.P., Liu, H.J., Qu, J.H., 2024. Quorum sensing enhances direct interspecies electron transfer in anaerobic methane production. Environ. Sci. Technol. 58(6), 2891-2901. https://doi.org/10.1021/acs.est.3c08503
Zhu, L.R., Wu, B.C., Liu, Y.L., Zhang, J.R., Deng, R., Gu, L., 2022. Strategy to enhance semi-continuous anaerobic digestion of food waste by combined use of calcium peroxide and magnetite. Water Res. 221, 118801. https://doi.org/10.1016/j.watres.2022.118801

DESTABILIZATION OF COLLOIDAL PARTICLES INDUCED BY IN-SITU CALCIUM CARBONATE CRYSTALLIZATION WITH IMPLICATIONS ON HIGHLY-EFFICIENT REMOVAL OF INSOLUBLE MATTER FROM ANAEROBIC DIGESTATE LIQUOR

Jieling Feng[1], Xiaoli Chai[1, 2], Xiaohu Dai[1, 2], Boran Wu[1, 2*]
1 State Key Laboratory of Pollution Control and Resource Reuse, College of Environmental Science and Engineering, Tongji University, 1239 Siping Road, Shanghai 200092, China
2 Shanghai Institute of Pollution Control and Ecological Security, Shanghai 200092, China

Background, Aims and Scope.
Anaerobic digestion (AD) is an effective method for organic waste treatment; however, its by-product, anaerobic digestate liquor (ADL), remains challenging to manage due to high concentrations of ammonia, phosphorus, and suspended solids (SS)[1, 2]. The anaerobic ammonia oxidation (ANAMMOX) process is a promising approach for ADL treatment, but excessive SS loading compromises reactor stability[3, 4]. Effective SS removal is crucial for enhancing ADL treatment efficiency and ensuring stable process performance. However, SS primarily exist as colloidal particles with highly hydrophilic surfaces, contributing to the stable suspension of the ADL colloidal system[5]. This study proposes an alternative SS removal method based on in-situ crystal formation via pH increase and calcium chloride ($CaCl_2$) addition, avoiding the limitations of conventional coagulation, such as ion interference and alkalinity loss. It is expected that in-situ crystals form through interactions between background ions and Ca^{2+}, subsequently facilitating co-precipitation with colloidal particles. The study evaluates SS removal efficiency, monitors the co-precipitation process, and examines the composition of co-precipitates and particle interactions. The findings are expected to provide insights into an efficient ADL pretreatment strategy, minimizing adverse effects on subsequent biological processes and contributing to more sustainable AD-based waste management.

Methods.
The study investigated SS removal through in-situ crystal formation by adjusting pH and adding $CaCl_2$. Tests were conducted to optimize pH and Ca^{2+} dosage to evaluate the SS removal efficiency of ADL supernatant after centrifugation. The co-precipitation process was monitored using Turbiscan multiple light scattering analysis to assess the destabilization of colloidal particles. The transformation of major elements and the composition of precipitates in $CaCl_2$-treated ADL were simulated using Visual MINTEQ, while the precipitate composition was verified by X-ray diffraction (XRD). Surface micromorphology and elemental composition were analyzed using scanning electron microscopy coupled with energy-dispersive spectrometry (SEM-EDS). These analyses aimed to identify the key precipitate components interacting with colloidal particles. The specific surface area and pore size distribution of freeze-dried precipitates were determined using a BET analyzer with nitrogen adsorption-desorption isotherms. Solid-liquid interface free energy was measured to characterize the hydrophilic and hydrophobic properties of different precipitate compositions. To evaluate the interactions among solid particles in ADL, the cohesion free energy of colloidal particles and the adhesion free energy between colloidal particles and in-situ crystals were calculated to reveal the fundamental mechanism underlying efficient SS removal via in-situ crystallization.

Results and Discussion.
Experiments demonstrated that SS removal efficiency increased with rising pH with a fixed $CaCl_2$ dosage of 1.0 wt.%, achieving 96.1% removal at initial pH of 13. SS removal improved significantly at $CaCl_2$ dosages above 1.0 wt.%, reaching a maximum removal efficiency of 96.8% at 2.0 wt.% $CaCl_2$ at a fixed initial pH of 13. The optimal conditions (1.0 wt.% $CaCl_2$ at an initial pH of 13) were selected for subsequent mechanistic studies.
The stability analysis was carried out based on the variation of transmitted signal, backscattering signal and Turbiscan Stability Index (TSI) by Turbiscan analyzer. Compared to raw ADL, $CaCl_2$-treated ADL exhibited notably destabilization phenomenon evidenced by obvious variations of light signal and TSI. Specific analysis indicated that $CaCl_2$ addition led to particle destabilization, coalescence, and sedimentation, resulting in increased clarification at the top and precipitate formation at the bottom. Dynamic calculation showed a particle diameter increase of ADL after $CaCl_2$ treatment. These findings suggested that the Ca-containing precipitates should promote the capture and co-precipitation of colloidal particles.

The study employed Visual MINTEQ simulations and XRD analysis to investigate Ca-containing crystal formation in ADL. Results indicate that $CaCO_3$ is the dominant precipitate at pH ≥ 10, primarily due to its low solubility compared to other Ca-containing species. The conversion of HCO_3^- to CO_3^{2-} in ADL was promoted by pH elevation, facilitating $CaCO_3$ precipitation. Increased $CaCl_2$ dosage enhanced $CaCO_3$ formation, contributing to SS removal. XRD confirmed calcite as the predominant phase, with minor $Ca(OH)_2$ presence (**Fig. 1**). SEM and EDS analyses revealed diverse morphologies and elemental distribution changes, highlighting the probable interaction between $CaCO_3$ and colloidal particles in ADL.

The study investigates the interactions between $CaCO_3$ crystals and colloidal particles in ADL through porosity analysis, interfacial free energy measurements, and extended DLVO theory. $CaCl_2$ treatment reduced porosity, indicating compact aggregation due to co-precipitation. BET analysis revealed decreased surface area and pore volume, likely caused by pore filling, pore merging, or crystal aggregation. The interfacial free energy shifted from negative to positive after $CaCl_2$ amendment, suggesting a transition from a hydrophobic to a hydrophilic state, likely due to $CaCO_3$ formation modifying the surface properties of precipitates. XDLVO analysis demonstrated that the adhesion between colloidal particles and $CaCO_3$ crystals was significantly stronger than the cohesion among colloidal particles, disrupting their stable repulsion and promoting co-precipitation (**Fig. 2**). This mechanism is essential for SS removal from $CaCl_2$-treated ADL.

Conclusion.

This study demonstrated that in-situ $CaCO_3$ crystallization induced by 1.0 wt.% $CaCl_2$ at pH 13 achieved up to 96.1% SS removal from ADL. The addition of $CaCl_2$ increased the mean particle size from 5.78 μm to 14.39 μm and significantly accelerated the downward migration rate, indicating effective destabilization of ADL colloidal particles. $CaCO_3$ was identified as the primary precipitate, exhibiting strong adhesion free energy to ADL organic matter, leading to the formation of tightly bound co-precipitates. This mechanism enhances solid-liquid separation, providing a novel strategy for efficient ADL pretreatment and improving sustainability in anaerobic digestate treatment.

Keywords: organic waste; anaerobic digestate liquor; solid-liquid separation; calcium carbonate

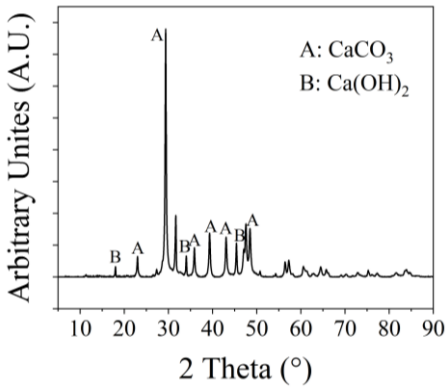

Fig. 1 XRD pattern of precipitates from ADL treated with 1.0 wt.% $CaCl_2$ at initial pH of 13.

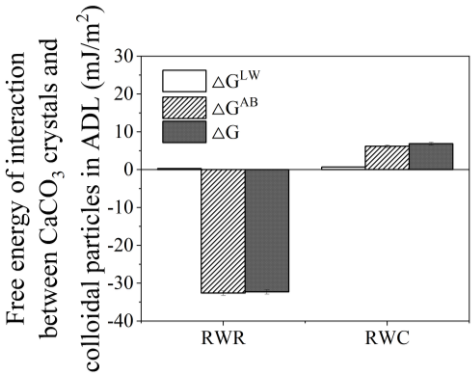

Fig. 2 Free energy of interaction between $CaCO_3$ crystals and ADL colloidal particles immersed in water.

References

[1] SELVARAJ P S, PERIASAMY K, SUGANYA K, et al. Novel resources recovery from anaerobic digestates: Current trends and future perspectives [J]. CRITICAL REVIEWS IN ENVIRONMENTAL SCIENCE AND TECHNOLOGY, 2022, 52(11): 1915-99.

[2] WEI C-Y, PAN S-Y, LIN Y-I, et al. Anaerobic swine digestate valorization via energy-efficient electrodialysis for nutrient recovery and water reclamation [J]. Water Research, 2022, 224: 119066.

[3] ZHANG Y, DENG J, XIAO X, et al. Insights on pretreatment technologies for partial nitrification/anammox processes: A critical review and future perspectives [J]. Bioresource Technology, 2023, 384: 129351.

[4] JIN R-C, YANG G-F, YU J-J, et al. The inhibition of the Anammox process: A review [J]. Chemical Engineering Journal, 2012, 197: 67-79.

[5] WANG Q, ZHANG W, YANG Z, et al. Enhancement of anaerobic digestion sludge dewatering performance using in-situ crystallization in combination with cationic organic polymers flocculation [J]. Water Research, 2018, 146: 19-29.

FUNDAMENTAL STUDY ON DRYING TREATMENT OF INCINERATION RESIDUES USING NON-POWER-GENERATING SOLAR ENERGY

Yosuke Tsuru[1], Teppei Komiya[2], Hirofumi Nakayama[2]
1 Dept. of Civil Engineering, Graduate School of Engineering, Kyushu University,
744 Motooka, Nishi-ku, Fukuoka, Japan
2 Dept. of Urban and Environmental Engineering, Faculty of Engineering, Kyushu University,
744 Motooka, Nishi-ku, Fukuoka, Japan

Abstract: Currently, the global community seeks to build sustainable societies, demanding the active utilization of renewable energy. Solar energy is one such renewable energy source. Utilizing solar energy directly as a heat source, without converting it to electricity, offers the potential for highly efficient solar energy utilization. This study conducted an annual thermal balance simulation of a solar-concentrated incineration residue drying system. The objective was to clarify the energy utilization efficiency and the required solar concentration area when using solar energy as a heat source without converting it to electricity, specifically targeting the drying treatment of incineration residues.

INTRODUCTION

Currently, there is a global desire to build sustainable societies. This includes creating a decarbonized society that does not rely on fossil fuels like oil and coal, which are considered causes of global warming, and utilizing sustainable energy. However, fossil fuels account for 83.5% (FY2022)[1)] of Japan's primary energy supply domestically. In power generation, fossil fuel-based thermal power accounts for 70% (FY2022)[2)], while renewable energy generation remains at only about 24% (FY2022)[2)]. This situation is far from achieving carbon neutrality by 2050. Among Japan's renewable energy sources, solar power generation holds the largest share at 10.6% (FY2022)[2)]. While solar power generation is the mainstream method for utilizing solar energy, its energy conversion efficiency, assumed to be 20%[3)], is not particularly high. Therefore, using solar energy directly as a heat source without converting it to electricity is expected to improve energy conversion efficiency.

Currently, solar thermal energy is primarily used in systems like water heating, heating, and cooling. Kodama et al.[4)] are conducting research on a technology that uses mirrors to concentrate sunlight into high temperatures. This intense solar heat is then used to decompose water, producing clean hydrogen energy. Hydrogen energy is anticipated as a next-generation energy source to replace fossil fuels, as it does not emit carbon dioxide—a major contributor to global warming—when used. However, the conventional method of producing hydrogen by reacting fossil fuels with water at high temperatures poses the challenge of carbon dioxide generation during the manufacturing process. Therefore, Kodama et al.[4)] have researched metal oxide catalysts and reactors that decompose water to generate hydrogen. They have developed technology to efficiently produce hydrogen at temperatures between 1200 and 1300°C, which can be collected using solar thermal energy and is below 1500°C. Furthermore, they have developed key technologies for utilizing the solar concentrator system installed at Miyazaki University and for practical implementation of solar-heated hydrogen production systems. Based on these efforts, it is suggested that utilizing solar energy directly as heat enables higher efficiency and more environmentally conscious energy use compared to electrical conversion.

This study conducted an annual heat balance simulation for a solar-concentrated incineration residue drying system. The objective was to clarify the energy utilization efficiency and required solar concentration area when using solar energy as a heat source without electrical conversion. The focus was on drying incineration residues, which offer advantages such as reduced transportation costs through lower moisture content and moisture adjustment during landfill pretreatment.

SOLAR CONCENTRATED INCINERATION RESIDUE DRYING SYSTEM

(1) Solar concentration method

Figure 1 shows the solar concentration method considered in this study. This type of device is called a beam-down solar concentrator. It features a large mirror called the central reflector (elliptical or hyperbolic surface) positioned at the top center. Directly below this is the receiver, surrounded by numerous mirrors called heliostats. The key feature of this system is that by adjusting the orientation of all heliostats so that sunlight

passes through the primary focus of the central reflector, high-density solar energy can be obtained at the receiver (the secondary focus of the central reflector).

(2) **Solar concentrated incineration residue drying system**

Figure 2 shows the solar-concentrated incineration residue drying system proposed in this study. This system consists of a solar concentrator, a drying furnace, two heat storage tanks, and a blower. In this study, the first heat storage tank (heat storage material: silica sand) was installed in the receiver section, corresponding to the position of the second focal point of the central reflector. Air supplied by the blower transports the heat required for the drying process from the first heat storage tank to the drying furnace. Excess heat is stored in the second heat storage tank. Furthermore, if the heat capacity of the first heat storage tank is insufficient, heat is transferred from the second heat storage tank to the first heat storage tank. The volume of the second heat storage tank was made variable according to the heat storage capacity. The temperatures of both the first and second heat storage tanks were maintained at 200°C, and the maximum temperature inside the drying furnace was assumed to be 200°C.

NUMERICAL SIMULATION OF ENERGY BALANCE IN SOLAR CONCENTRATED INCINERATION RESIDUE DRYING SYSTEM

(1) Assumption in drying process conditions

This study assumes that all incineration residues (moisture content 20%) delivered to the final disposal site will be dried to a completely dry state. With an incineration residue delivery volume of 50 t/day, delivery frequency of 5 times/day, delivery volume per trip of 10 t, and delivery times starting at 9:30 AM at hourly intervals, a system capable of drying 10 t of incineration residue per hour was envisioned to complete the drying process within the final disposal site's operating hours (9:00 AM to 4:00 PM).

(2) Heat balance equations

Equation 1 shows the heat balance equation for the first heat storage tank, Equation 2 for the second heat storage tank, and Equation 3 for the drying furnace.

$$C_1 m_1 \frac{dT_1}{dt} = Q_d Se - Q_{1\to2} - Q_{1\to f} - Q_{fhl,1} - Q_r \quad \cdots(1)$$

$$C_2 m_2 \frac{dT_2}{dt} = Q_{1\to2} - Q_{fhl,2} \quad \cdots(2)$$

$$C_f m_f \frac{dT_f}{dt} = Q_{1\to f} - Q_n \quad \cdots(3)$$

where, C [kJ/(ton·K)] is the specific heat capacity of the heat storage material or substance within the drying furnace, m [ton] is the mass of the heat storage material or substance within the drying furnace, T [K] is the temperature within the heat storage tank or drying

Figure 1. Solar Concentrator (Beam-Down System)

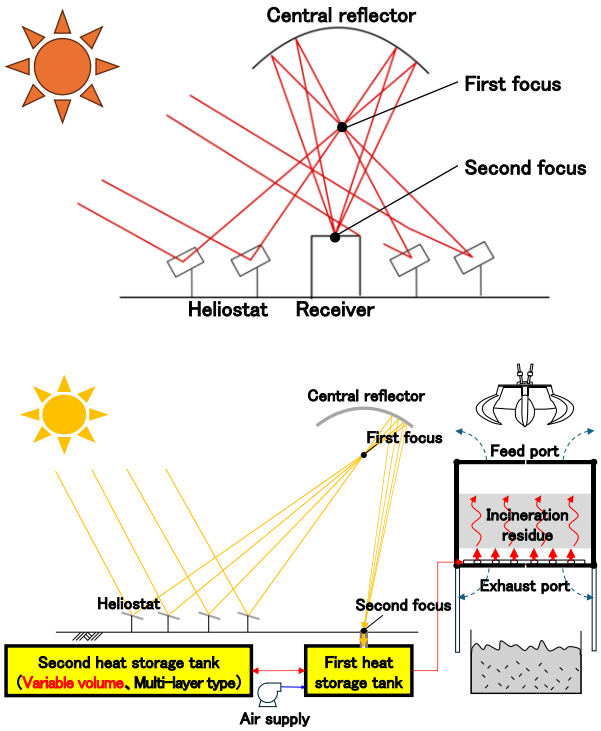

Figure 2. Solar-Powered Concentrated Incineration Residue Drying Furnace

furnace, t [h] is time, Q_d [kJ/(m²·h)] is the direct solar radiation[5], S [m²] is the solar collector area, e [-] is the solar energy conversion efficiency, $Q_{1\to2}$ [kJ/h] is the heat transfer rate from the first heat storage tank to the second heat storage tank, $Q_{1\to f}$ [kJ/h] is the heat transfer rate from the first heat storage tank to the drying furnace, Q_{fhl} [kJ/h] is the heat loss from the tank body of the heat storage tank or the furnace body of the drying furnace, Q_{egl} [kJ/h] is the exhaust gas heat, Q_n [kJ/h] is the required heat quantity for the drying furnace. Subscripts 1, 2, and f refer to the first heat storage tank, second heat storage tank, and drying furnace, respectively.

(3) Heat transfer quantity

Equation 4 shows the calculation formula for heat transfer from the first heat storage tank to the second heat storage tank, and Equation 5 shows the calculation formula for heat transfer from the first heat storage tank to the drying furnace.

$$Q_{1\to2} = Q_d Se - Q_{1\to f} - Q_{fhl,1} - Q_r \quad \cdots(4)$$

$$Q_{1\to f} = Q_n \quad \cdots(5)$$

(4) Heat losses

Equations 6 and 7 show the calculation formulas for the tank body heat loss of the heat storage tank, Equation 8 shows the calculation formula for the furnace body heat

loss of the drying furnace, and Equation 9 shows the calculation formula for the exhaust gas heat loss of the drying furnace.

$$Q_{fhl,1} = kA_1 \frac{T_1 - T_{amb}}{L} \quad \cdots(6)$$

$$Q_{fhl,2} = kA_2 \frac{T_2 - T_{amb}}{L} \quad \cdots(7)$$

$$Q_{fhl,f} = kA_f \frac{T_f - T_{amb}}{L} \quad \cdots(8)$$

$$Q_{egl,f} = VC_{air,s}T_s + m_{wv}C_{wv}T_s \quad \cdots(9)$$

where, k [kJ/(m·h·K)] is the thermal conductivity of the insulation, A [m²] is the heat transfer area of each storage tank, T_{amb} [K] is the ambient temperature, T_s [K] is the target furnace temperature (=378), L [m] is the insulation thickness, V [ton/h] is the air supply flow rate, m_{wv} [ton/h] is the water vapor mass flow rate, $C_{air,s}$ [kJ/(ton·K)] is the specific heat of air at the furnace target temperature, and C_{wv} [kJ/(ton·K)] is the specific heat of water vapor. Note that the heat transfer through the heat transfer pipe exposed to the outside air is assumed to be zero.

(5) Heat required for drying furnace

Equation 10 shows the heat required for the drying furnace. It consists of the heat required to raise the material inside the furnace to the set temperature, furnace body heat loss, and exhaust gas heat loss.

$$Q_n = VC_{air,h}T_h \quad \cdots(10)$$

where, $C_{air,h}$ [kJ/(ton·K)] is the specific heat of the heating air (200°C), and T_h [K] is the temperature of the heating air (=473) [K].

(6) Air heating heat quantity

Equation 11 shows the calculation formula for the heat quantity required to raise the ambient air temperature (=15°C) introduced into the first heat storage tank to the set temperature.

$$Q_r = Q_n - \frac{Q_n}{C_{air,s} \times T_s} \times C_{air,amb} \times T_{amb} \quad \cdots(11)$$

where, $C_{air,amb}$ [kJ/(ton·K)] is the specific heat of the ambient air.

(7) Calculation of solar concentration area

The solar concentration area was calculated as the area at which the annual heat balance of the thermal storage tank becomes zero and the minimum volume of the thermal storage tank becomes zero.

RESULTS AND DISCUSSION

Table 1 shows the effects of insulation materials and solar energy conversion efficiency on energy utilization efficiency. Note that this calculation assumes solar energy conversion efficiency ranges from 0.5 to 0.9. For the insulation materials and solar energy conversion efficiencies considered in this study, energy utilization efficiency was calculated to range from 33.8% to 64.3%. As mentioned in Section 1, the solar energy conversion efficiency assumed for photovoltaic power generation in this study is 20%. Therefore, even if the energy conversion efficiency from electricity generated by photovoltaics to heat were 100%, it was considered that a solar concentrator drying system would require a smaller necessary concentration area compared to drying using electricity generated by photovoltaics.

Table 2 shows the effects of insulation material and solar energy conversion efficiency on the solar collector area.

Table 1. Effects of Insulation Material and Solar Energy Conversion Efficiency on Energy Utilization Efficiency

Insulation material		Magnesia Brick	Calcium Silicate	Polystyrene Form
thermal conductivity [W/(m・K)]		0.400	0.066	0.034
Solar energy conversion efficiency[-]	0.5	33.8	35.5	35.7
	0.6	39.8	42.6	42.8
	0.7	46.3	49.7	50.0
	0.8	52.9	56.7	57.1
	0.9	59.6	63.8	64.3

Table 2. Effects of Insulation Material and Solar Energy Conversion Efficiency on Solar Energy Collection Area

Insulation material		Magnesia Brick	Calcium Silicate	Polystyrene Form
thermal conductivity [W/(m・K)]		0.400	0.066	0.034
Solar energy conversion efficiency[-]	0.5	7.72	7.20	7.15
	0.6	6.43	6.00	5.96
	0.7	5.51	5.14	5.11
	0.8	4.82	4.50	4.47
	0.9	4.29	4.00	3.97

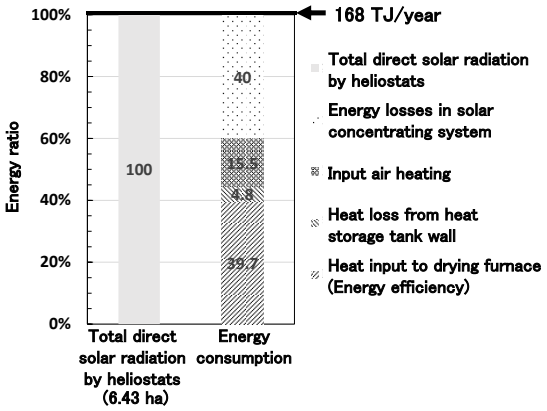

Figure 3. Example of Energy Balance (Solar Energy Conversion Efficiency: 0.6, Insulation Material: Magnesia Brick)

For the insulation materials and solar energy conversion efficiencies considered in this study, the required solar collector area was estimated to be 3.97 to 7.72 ha.

Figure 3 shows an example of the energy balance for a solar-concentrated drying system. Using the values from Tables 1 and 2, with a solar energy conversion efficiency of 0.6 and magnesia bricks as the insulation material for the heat storage tank, the solar concentration area required for drying incineration residues using solar energy as the direct heat source was 6.43 ha. Of the total direct solar radiation received by heliostat (168 TJ), the energy losses in solar concentrating system were 40%, the input air heating was 15.5%, and the heat loss from heat storage tank wall was 4.8%. As a result, the heat input to the drying furnace (energy efficiency) was 39.7%.

CONCLUSIONS

A heat balance simulation was conducted to clarify the energy efficiency and required solar collector area when using solar energy as a heat source for drying incineration residues without converting it to electricity.

The simulation assumed processing 10 tons of incineration residue with 20% moisture content to a completely dry state within one hour in a drying furnace. It was assumed that the inflowing air (15°C) was heated to 200°C in the heat storage tank, the heating air (200°C) in the drying furnace cooled to 105°C due to the heat consumption required for the drying process, and the heat loss through the heat transport pipes exposed to the outside air was zero.

The findings obtained are presented as follows.

1) The energy efficiency for the insulation materials and solar energy conversion efficiency studied in this research ranged from 33.1% to 64.3%, demonstrating higher efficiency than that of solar power generation (assumed to be 20% in this study).
2) The required solar collector area under the same conditions was estimated to be 3.97 to 7.72 ha.

Future challenges include verification through small-scale experiments and the evaluation of life-cycle costs.

REFERENCES

1) Agency for Natural Resources and Energy, Ministry of Economy, Trade and Industry (METI), Preliminary energy demand results for FY2022 [in Japanese]. [Online]. Available: https://www.meti.go.jp/press/2023/11/20231129003/20231129003-1.pdf [Accessed: Jan. 31, 2024].
2) Institute for Sustainable Energy Policies (ISEP), Share and deployment status of renewable electricity in Japan, FY2022 (preliminary) [in Japanese]. [Online]. Available: https://www.isep.or.jp/archives/library/14470 [Accessed: Jan. 31, 2024].
3) New Energy and Industrial Technology Development Organization (NEDO), Renewable Energy Technology White Paper, 2nd ed., ch. 2, p. 7, 2020.
4) T. Kodama et al., Development of a hydrogen production system using solar heat and water [in Japanese], Niigata University News, 2019. [Online]. Available: https://www.niigata-u.ac.jp/news/2019/58797/ [Accessed: Jan. 31, 2024].
5) New Energy and Industrial Technology Development Organization (NEDO), Solar Radiation Database Browsing System (METPV-20).

MICRO-GRANULAR SLUDGE DRIVEN BY POWDER CARRIER IN MEMBRANE BIOREACTOR: HIGHLY-EFFICIENT N & P REMOVAL AND MEMBRANE FOULING ALLEVIATION

Boran Wu[1,4], Junqian Zhong[1], Hao Chang[1], Dong Li[1], Chengxian Wang[2], Hongbo Han[3], Qun Gu[3], Yan Zhong[3], Xiaohu Dai[1,4], Xiaoli Chai[1,4]*

[1] State Key Laboratory of Water Pollution Control and Green Resource Recycling, College of Environmental Science and Engineering, Tongji University, Shanghai, China

[2] Qingdao Institute of Bioenergy and Bioprocess Technology, Chinese Academy of Sciences, Qingdao, China

[3] Hunan Sanyou Environmental Protection Co. Ltd., Changsha, China

[4] Shanghai Institute of Pollution Control and Ecological Security, Shanghai, China

Corresponding author: xlchai@tongji.edu.cn

Abstract: *Membrane bioreactors (MBRs) are widely recognized for their high effluent quality and compact footprint, yet remain constrained by membrane fouling, high operating costs, and limited phosphorus removal. This study introduces a novel strategy integrating micro-granular sludge (MGS), induced by powder carriers, with MBR technology (MGS-MBR). A pilot-scale system treating low-strength municipal wastewater achieved ultra-low effluent TN (<5 mg/L) and TP (<0.03 mg/L) under short hydraulic retention time (6 h) and low C/N ratio (~3.2). Powder carriers promoted MGS formation (~50 μm) and alleviated fouling, with transmembrane pressure (TMP) stabilized at ~8 kPa over 20+ days at 20 L/(m²·h). Microbial analyses revealed enrichment of denitrifiers (Pseudomonadota, Comamonadaceae) and phosphorus-accumulating organisms (Rhodocyclaceae, Bacteroidota), alongside suppressed quorum sensing (QS) activity, reducing EPS production. These findings demonstrate the strong compatibility of MGS with MBR operation, offering a sustainable pathway for enhanced nutrient removal and fouling mitigation.*

INTRODUCTION

Nutrient pollution, particularly nitrogen and phosphorus, poses significant threats to aquatic ecosystems. Although MBRs provide high-quality effluent and process stability, challenges such as fouling and poor phosphorus removal limit their large-scale application. Micro-granular sludge (MGS), induced by powder carriers, has shown potential to enhance biomass aggregation, facilitate microbial stratification, and improve pollutant removal under low-COD conditions. This study evaluates the integration of MGS with MBR in a pilot-scale system for low-strength municipal wastewater treatment.

METHODS

System setup

A pilot-scale MGS-MBR (A^2/O + membrane + hydrocyclone) was deployed in Shenzhen, China. Powder carriers (up to 4 g/L) induced MGS formation, with HRT reduced from 12 h to 6 h during operation.

Monitoring

COD, TN, TP, NH_4^+-N were measured daily; sludge properties (MLSS, EPS, PHA) and microbial communities were analyzed using kinetic tests, EEM spectroscopy, and metagenomics.

Comparisons

Performance was evaluated across three stages: blank (no carriers), start-up, and steady-state with carriers.

RESULTS AND DISCUSSION

Pollutant removal

1. Effluent COD <10 mg/L and NH_4^+-N <0.2 mg/L.
2. TN decreased to 4.35 mg/L, TP reached as low as 0.02 mg/L.
3. Intracellular PHA content increased ~30-fold, supporting EBPR under low C/N.

Membrane fouling control

1. TMP remained stable at ~8 kPa for >20 d at 20 L/(m^2·h), extending cleaning cycles compared to conventional MBRs.
2. 3D-EEM analysis revealed reduced LB-EPS (key fouling contributor), linked to weakened QS signaling.

Microbial community

1. Enrichment of denitrifiers (Pseudomonadota, Comamonadaceae) and PAO-related taxa (Rhodocyclaceae, Bacteroidota).
2. Functional genes for nitrification (amoA, amoB) and denitrification (nap, nir, nar) were upregulated.
3. Hydrocyclone operation facilitated selective PAO renewal and denitrifier retention, enhancing overall system stability.

CONCLUSION

The integration of powder-carrier-induced MGS with MBR significantly enhances nutrient removal and alleviates membrane fouling. The system achieved:

1. Ultra-low effluent TN (<5 mg/L) and TP (<0.03 mg/L) under low C/N and short HRT.
2. Extended membrane lifespan with reduced fouling pressure.
3. Microbial enrichment favoring denitrifiers and PAOs, supported by suppressed QS activity.

This study highlights MGS-MBR as a scalable, sustainable solution for advanced municipal wastewater treatment.

REFERENCES

[1]. Anderson, D.M., Glibert, P.M. and Burkholder, J.M. 2002. Harmful algal blooms and eutrophication: Nutrient sources, composition, and consequences. Estuaries 25(4b), 704-726.

[2]. APHA (2009) Standard Methods for the Examination of Water and Sewage, American Public Health Association, Washington, D.C.

[3]. Chen, W., Lu, Y., Jin, Q., Zhang, M. and Wu, J. 2020. A novel feedforward control strategy for simultaneous nitrification and denitrification (SND) in aerobic granular sludge sequential batch reactor (AGS-SBR). Journal of Environmental Management 260, 110103.

[4]. Chen, W., Westerhoff, P., Leenheer, J.A. and Booksh, K. 2003. Fluorescence excitation-emission matrix regional integration to quantify spectra for dissolved organic matter. Environmental Science & Technology 37(24), 5701-5710.

[5]. Coats, E.R., Brinkman, C.K. and Lee, S. 2017. Characterizing and contrasting the microbial ecology of laboratory and full-scale EBPR systems cultured on synthetic and real wastewaters. Water Research 108, 124-136.

[6]. Cui, Y., Zhang, L., Wang, H., Fan, X. and Peng, Y. 2025. Advanced nitrogen removal from extremely low carbon/nitrogen ratio municipal wastewater by optimizing multiple pathways based on step-feed and intermittent aeration. Bioresource Technology 421, 132202.

[7]. Döring, C. and Basen, M. 2024. Propionate production by Bacteroidia gut bacteria and its dependence on substrate concentrations differs among species. Biotechnology for Biofuels and Bioproducts 17(1), 95.

[8]. Du, R., Cao, S., Li, B., Niu, M., Wang, S. and Peng, Y. 2017. Performance and microbial community analysis of a novel DEAMOX based on partial-denitrification and anammox treating ammonia and nitrate wastewaters. Water Res. 108, 46-56.

Research on Material Flows of Agricultural Plastic Materials by Product Type and Region

Ryotaro Kawanishi[1] ・Hirofumi Nakayama[2] ・Takayuki Shimaoka[3]

[1] Department of Civil Engineering, Graduate School of Engineering, Kyushu University (744 Motooka, Nishi-ku, Fukuoka 819-0395, Japan)

[2] Department of Environment and Society, Graduate School of Engineering, Kyushu University (744 Motooka, Nishi-ku, Fukuoka 819-0395, Japan)

[3] Kyushu Environmental Management Association (1-10-1 Matsukadai, Higashi-ku, Fukuoka 813-0004, Japan)

In recent years, numerous studies have been conducted on the proper disposal of waste plastics generated in the agricultural sector. However, research focusing on detailed classification of plastic materials by specific agricultural product category to organize usage and disposal volumes remains insufficient. Therefore, this study estimated the usage and disposal volumes of plastics used by agricultural product category and region.

Introduction

In recent years, attention has focused on plastic resource circulation both domestically and internationally. The agricultural sector also uses and discharges large amounts of plastic materials. The estimated discharge of agricultural plastic waste[1)] in fiscal year 2020 was 101,312 tons nationwide, with 75,793 tons estimated to come from horticultural crops (vegetables, flowers, and fruit trees). However, it is difficult to discuss horticultural crops as a single category, as cultivation methods vary significantly by crop, and plastic usage and disposal volumes are also expected to differ. Previously, the authors conducted a questionnaire survey of agricultural workers affiliated with the Fukuoka City Agricultural Cooperative to investigate the usage and disposal volumes of agricultural plastics for each crop, broken down by material type[2)]. In this study, we conducted a questionnaire survey of agricultural extension centers within the Kyushu region to estimate the usage and emissions of agricultural plastic materials by region and crop type.

Research Methodology

(1) Questionnaires and Interviews

This study conducted a questionnaire survey of Agricultural Extension Centers. Agricultural Extension Centers are branch offices of prefectural governments staffed by agricultural specialists. The target area was Agricultural Extension Centers within the Kyushu region. The questionnaire was in Excel format and distributed via email. The survey period was one month, from August 2025 to the end of August of the same year. The target crops were horticultural crops grown in greenhouses, horticultural crops grown in open fields using mulch sheets, and fruit trees grown in greenhouses. Each

center surveyed all three types of crops. In this study, greenhouse-grown crops are designated as Horticultural Crop 1, and open-field crops using mulch sheets are designated as Horticultural Crop 2. Table 1 shows the crop names, crop classifications, response dates, and respondents surveyed to date. Questionnaires were distributed to 21 agricultural extension centers within the Kyushu region, yielding 9 valid responses. The valid response rate was approximately 43%. The plastic materials surveyed were limited to vinyl greenhouses, mulch sheets, tunnels, greenhouse shade nets, waterproof sheets, and weed control sheets, based on a previous survey in Fukuoka City, as these had high usage and disposal volumes. Limiting the target materials reduced respondent burden and aimed to improve the response rate.

Table 1: List of Agricultural Products Surveyed

Crops	Crop Classification	Date of Response	Respondent
Strawberry	Horticultural Products 1	2025/8/6	Fukuoka
Lettuce	Horticultural Products 2	2025/8/6	Fukuoka
Mandarin orange	fruit trees	2025/8/6	Fukuoka
Passion fruit	fruit trees	2025/8/21	Osumi, Kagoshima
Green onion	Horticultural Products 1	2025/8/26	Northern Oita
Potato	Horticultural Products 2	2025/8/26	Northern Oita
Grape	fruit trees	2025/8/26	Northern Oita
Leatherleaf fan	Horticultural Products 1	2025/8/28	Kumage, Kagoshima
Sweet potato	Horticultural Products 2	2025/8/28	Kumage, Kagoshima
Passion fruit	fruit trees	2025/8/28	Kumage, Kagoshima
Tomato	Horticultural Products 1	2025/8/28	Oshima, Kagoshima
Pumpkin	Horticultural Products 2	2025/8/28	Oshima, Kagoshima
Passion fruit	fruit trees	2025/8/28	Oshima, Kagoshima
Mango	fruit trees	2025/9/1	Nishimorokata, Miyazaki
Cucumber	Horticultural Products 1	2025/9/2	Central Miyazaki
Sweet potato	Horticultural Products 2	2025/9/2	Central Miyazaki
Mango	fruit trees	2025/9/2	Central Miyazaki
Mandarin orange	fruit trees	2025/9/4	Southern Oita
Strawberry	Horticultural Products 1	2025/9/4	Kitasatsuma, Kagoshima
Burdock	Horticultural Products 2	2025/9/4	Kitasatsuma, Kagoshima
Kumquat	fruit trees	2025/9/4	Kitasatsuma, Kagoshima

(2) Methods for Estimating The Use and Emission Intensity of Plastics of Agricultural Origin

The estimation method for unit consumption is shown in Figure 1. First, a questionnaire surveyed the cultivated area of the target items, the types and sizes of plastic materials used for cultivating them, the annual usage quantity, and the disposal interval (average usage period). Next, the annual usage quantity of plastic materials was calculated by multiplying the annual usage quantity by the weight unit consumption per unit usage quantity[3)4)], then summing this for each material to convert it to annual usage. Finally, dividing by the cropped area yielded the estimated unit consumption rate per cropped area for that crop. For the emission unit rate, the annual usage amount for each plastic material was divided by its respective disposal interval (years) to calculate the annual emissions. Summing the emissions for each material converted this to the annual emissions. Finally, dividing by the cropped area yielded the emission unit rate.

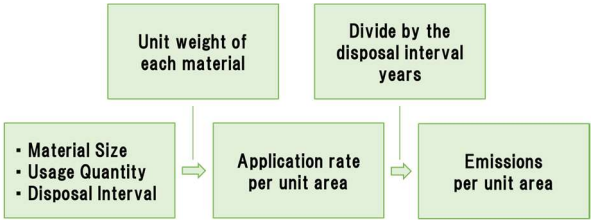

Figure 1: Flowchart for Estimating Base Units

3. Survey Results

(1) Usage Results

Figure 2 shows the unit consumption rates by agricultural product category obtained in this study. The highest consumption of agricultural

plastic materials was for green onions cultivated in the northern Oita region. This is largely due to the use of shading nets for greenhouses in addition to vinyl greenhouses. This characteristic was also observed for Kagoshima Kumage's leatherleaf fan, Kagoshima Oshima's passion fruit, Kagoshima Kita-Satsuma's kumquat, and Miyazaki Nishimorokata's mango, with plastic usage for these crops generally exceeding 200 g/m2. Outside of greenhouse cultivation, pumpkin in Kagoshima's Ōshima region showed high usage, largely due to tunnel cultivation. Tunnel use was also observed in lettuce cultivation in Fukuoka, where usage was relatively high. Conversely, sweet potatoes in Kagoshima's Kumage region, burdock in Kagoshima's Kita-Satsuma region, burdock in Miyazaki's Chūbu region, and potatoes in northern Ōita only used mulch sheets, showing significantly lower usage compared to other crops. Furthermore, polyolefin and polyvinyl chloride materials constitute the majority of the materials used. Based on the above, the materials that significantly impact the usage of agricultural plastic materials are vinyl greenhouses, greenhouse shading nets, and tunnels. Consequently, crops using these materials, such as green onions (Northern Oita) and pumpkins (Kagoshima Oshima), are estimated to have high usage levels.

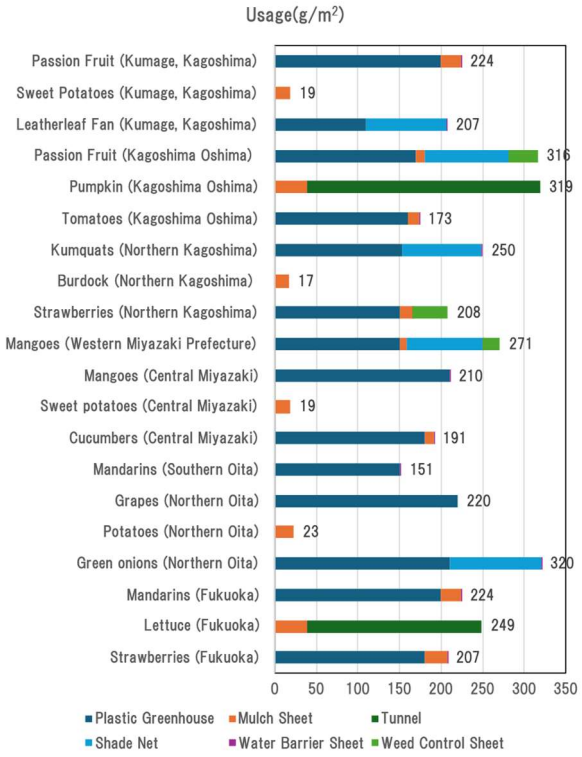

Figure 2: Unit Usage by Item

(2) Emissions Results

Figure 3 shows the emission intensity per unit of agricultural product obtained in this study. The largest emissions from agricultural plastic materials were for pumpkins grown on Kagoshima's Ōshima Island, at 319 g/m2. This is because, unlike other crops using tunnels, the tunnels are discarded once a year. The next highest was strawberries in Fukuoka, due to the vinyl greenhouses being discarded once a year. For other crops, higher emissions were estimated for those using vinyl greenhouses where the plastic covering is replaced every few years. However, for northern Oita's green onions, which had the highest estimated usage, emissions were estimated at 35 g/m2—

about one-tenth of the usage—due to the long disposal intervals for vinyl greenhouses and greenhouse shade nets. These results show that disposal intervals
vary for the same materials depending on the crop and region, and that disposal intervals significantly impact emissions.

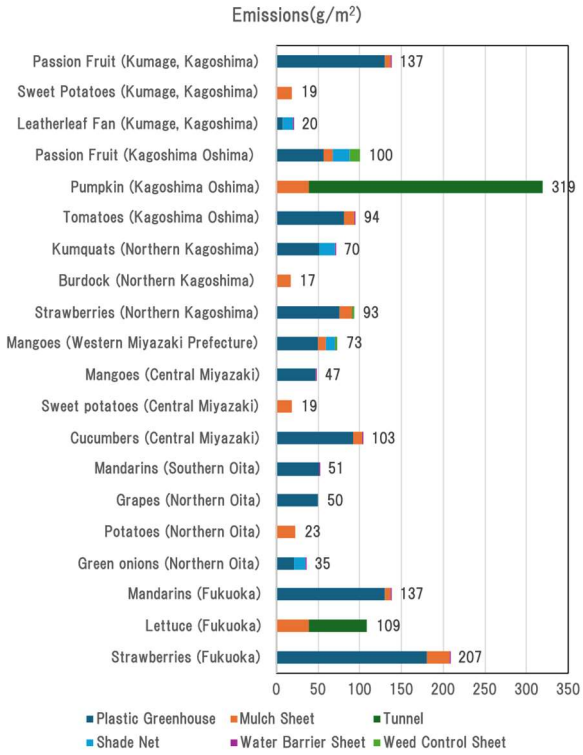

Figure 3: Unit Emission by Item

(3) Verification of the accuracy of survey results

To verify the accuracy of the emission factors obtained in this study, we compared the estimated agricultural plastic waste emissions in the horticultural sector (vegetables, flowers, and fruit trees) of the Kyushu region with the emissions published by the Ministry of Agriculture, Forestry and Fisheries (MAFF) for the same sector, thereby validating the consistency between the two. The MAFF published values are based on interviews with agricultural cooperatives. The total agricultural plastic waste emissions for the horticultural sector across Kyushu were calculated by multiplying the cropped area for each crop by its specific emission factor per cropped area, then summing these values. Cropped area data for each crop was taken from the “Kyushu Regional Agricultural Administration Bureau 70th Kyushu Agriculture, Forestry and Fisheries Statistical Yearbook[5]).” For crops not surveyed this time, specific emission factors were assumed based on previous surveys or the same crop classification.

Table 2 shows the results of the agricultural plastic waste emissions calculation for Fukuoka Prefecture from this study and the published value from the Ministry of Agriculture, Forestry and Fisheries (MAFF). For emissions from horticultural items (vegetables, flowers, and fruit trees), the estimated value from this study was 55,000 tons, approximately 2.5 times the MAFF published value (22,564 tons).

A factor contributing to this overestimation was the assumption of emission factors for unstudied crops based on values from studied crops within the same classification. Crops targeted in this survey were those using significant amounts of plastic materials such as vinyl greenhouses, mulch sheets, and tunnels; crops not using greenhouses or mulch sheets were not included. Consequently, the emission factors for the unstudied crops, which were set based on assumptions, may have been overestimated. This likely resulted in the overall estimated value exceeding the MAFF published value.

Moving forward, it is necessary to understand the actual use of plastic materials and the emission status for the crops not studied this time, and to set more accurate

emission factors.

	Survey Results	Ministry of Agriculture, Forestry and Fisheries (R.4 Published Values)
Vegetables	37,000	
Fruit Trees	16,000	
Floriculture	1,700	
Total	55,000	22,564

Table-2 Comparison of the Estimation Results from This Study with the Published Values from the Ministry of Agriculture, Forestry and Fisheries

4. Conclusion

This study revealed that the amount of agricultural plastic materials used and the resulting emissions vary considerably by crop type and region. Regarding usage, higher amounts were generally observed for crops grown in vinyl greenhouses, particularly those using shade nets attached to the greenhouse. For these crops, plastic usage exceeds 200 g/m^2. Additionally, high usage was observed for crops using tunnels instead of greenhouses. Regarding emissions, the disposal interval of materials significantly impacts estimates. For example, emissions from pumpkins on Kagoshima's Oshima Island are estimated to be high because tunnels are discarded annually. Conversely, emissions are low for crops using greenhouses or greenhouse shade nets long-term. Emissions for small green onions in northern Oita Prefecture, for instance, are only about one-tenth of the usage amount, at 35 g/m^2.

Acknowledgements

This research was conducted under Theme 2, Subtheme (1) “Establishment of an Evaluation System for the 3Rs Plus and Measures to Curb Marine Plastic Discharge” and the DEEP RECYCLE SYSTEM Study Group's “Environmental and Economic Evaluation of Resource Circulation Systems for the Efficient Utilization of Low-Grade Waste Plastics.” It is also based on the results of research conducted by the Fukuoka City Agricultural Cooperative Nishi Green Center, Fukuoka Prefecture Agriculture, Forestry and Fisheries Department, Kagoshima Prefecture Osumi Regional Promotion Bureau, Oita Prefecture Northern Promotion Bureau, Kagoshima Prefecture Kumage Branch Agriculture, Forestry and Fisheries Department, Kagoshima Prefecture Oshima Branch Agriculture, Forestry and Fisheries Department, Miyazaki Prefecture Nishimorokata Agriculture and Forestry Promotion Bureau, Miyazaki Prefecture Chubu Agriculture and Forestry Promotion Bureau, Oita Prefecture Southern Promotion Bureau, and Kagoshima Prefecture Hokusatsu Regional Promotion Bureau for their tremendous cooperation in the questionnaire survey for this research. We express our deep gratitude to all those involved.

REFERENCES.

1) Ministry of Agriculture, Forestry and Fisheries: Status of installation of horticultural facilities (R4), and status of discharge and disposal of agricultural waste plastics.
2) Ryotaro Kawanishi, Hirofumi Nakayama, Takayuki Shimaoka: Journal of Civil Engineering, Series G: A Study on Material Flows of Plastic Materials by Crop Type.
3) Agricultural Sheeting & Gardening Supplies

Specialist Agri Depot
https://agridepo.net/

4) Edge-Sealing PO/Waterproof Sheeting Edge-Sealing Materials Achilles Corporation https://www.achilles.jp/product/agriculture/horticulture/related-products/

5) Kyushu Agricultural Administration Bureau: The 70th Annual Report of Kyushu Agriculture, Forestry and Fisheries Statistics. No.4 Crops (R.4~R.5)

MOLECULAR TRANSFORMATION MECHANISMS OF HUMUS SOIL BIOMATERIAL IN ENHANCING HUMIFICATION PROCESS OF ANAEROBIC DIGESTATE COMPOSTING

Zhengliang Du [1], Boran Wu [1, 2], and Xiaoli Chai [1, 2]
1 College of Environmental Science and Engineering, Tongji University, Shanghai, Cina
2 Shanghai Institute of Pollution Control and Ecological Security, Shanghai, China

RESEARCH BACKGROUND

Background, Aims and Scope. Anaerobic digestate is an inevitable by-product from anaerobic digestion plants, which contains various hazardous components and plenty of unstable organic matter, posing a substantial threat to the environment. Composting is an effective biological approach for anaerobic digestate treatment, as it can remove hazardous substances and convert organic fractions into valuable humic substances. Nevertheless, the complex biopolymers in digestate show different decomposition sequences during composting due to their distinctive chemical structures, which result in the asynchronous production of humus precursors and thus hinders humus formation. The addition of supplementary materials to compost system can alter its physicochemical properties and enhance microbial activities and biopolymer decomposition, which has been regarded as effective in improving the humification process. Humus soil biomaterial (HSB) is rich in phenolic substances and porous volcanic rock, which makes it a potential compost ameliorant. This study aims to improve the humification process of digestate composting with humus soil biomaterial (HSB) as ameliorant, and unveils the underlying humification mechanisms. Through a systematic investigation, we propose a novel and rapid humification strategy for the resourceful treatment of anaerobic digestate.

ANALYTICAL METHODS

Anaerobic digestate served as the primary composting substrate, and maize straw was added as bulking agent to adjust the moisture content (60%) and C/N ratio (25). Three experimental groups were designed according to the addition of HSB and pumice stone: G0 (digestate + maize straw), G1 (digestate + maize straw + 1 wt.% pumice stone), and G2 (digestate + maize straw + 1 wt.% pumice stone + 25 wt.% HSB). G0 acted as the blank control, while G1 served as the mineral background control to investigate the effect of pumice stone fraction in HSB on the composting process. After thoroughly mixing the ingredients, the composting experiment was conducted in a lab-scale reactor equipped with a temperature control system, gas supply, and metering devices. Samples collected on days 0, 3, 7, 14, 21, 35, and 50 were freeze-dried and then soaked in ultrapure water for dissolved organic matter (DOM) extraction. The dynamic humification process of organic matters in G0-2 was monitored using excitation-emission matrix (EEM) fluorescence spectroscopy. Detailed DOM molecular composition was characterized using electrospray ionization coupled with Fourier-transform ion cyclotron resonance mass spectrometry (ESI FT-ICR M). The functional groups of freeze-dried DOM were analyzed with Fourier transform infrared (FTIR) and X-ray photoelectron spectroscopy (XPS), while two-dimensional FTIR correlation spectroscopy (2D-FTIR-COS) was employed to enhance the resolution of FTIR spectra to reveal the humification pathways during anaerobic digestate composting.

RESULTS AND DISCUSSION

The fluorescence regional integration (FRI) analysis of EEM spectra indicated that the FRI proportions representing humic substances in G2 inoculated with HSB increased rapidly from 28.9% to 52.4% within 21 days, which occurred much earlier than G0-1 achieving similar levels (53.9% and 53.1%, respectively) on day 35. Furthermore, G2 exhibited a greater humification index compared to G0 and G1, reflecting a higher humification degree. These results suggested that the addition of HSB effectively enhanced the transformation of organic matters into humic substances, which accelerated the accumulation of humus and shortened the maturation period of digestate composting. FT-ICR MS analysis identified the DOM molecular composition in G0-2 feedstocks, which consisted mainly of proteins/aliphatic, lipids, and lignin/carboxylic-rich alicyclic molecule (CRAM)-like substances. Notably, many aromatic DOM molecules detected exclusively in G2 feedstock were completely

removed after composting, implying that the phenolic substances in HSB participated in the composting humification process. As composting progressed, aliphatic compounds including proteins/aliphatic, lipids, and carbohydrates were converted into aromatic compounds such as lignin/CRAM-like, tannin, and condensed aromatic compounds, which contributed to an increase in both aromaticity and humification, particularly in G2. 2D-FTIR-COS analysis revealed the similar reaction sequences for organic matters in G0 and G1, where proteins (1578 and 1250 cm^{-1}) and polysaccharides (1020 cm−1) preferentially underwent hydrolysis reactions, followed by depolymerization and decomposition of lignin (1492 cm^{-1}) into phenolics (1415/1420 cm^{-1}), which were considered to be the aromatic core for the formation of humic substances. As for G2, the transformation sequence of phenolics (1409 cm^{-1}) occurred earlier than that of polysaccharides (1020 and 1170 cm^{-1}) and lignin (1492 cm^{-1}), except for proteins, suggesting that HSB modified the transformation pathway of organic matters during composting. Combined with the theory of humus formation, it can be inferred that the phenolic substances in HSB acted as an aromatic skeleton to participate in the assembly of humus macromolecules at the initial composting stage, thereby accelerating its humification process. XPS analysis suggested that pumice stone with porous structure facilitated the airflow throughout composting system and thus promoted the decomposition of proteins into amine-N precursors, which mitigated the adverse effects of lignin rate-limiting decomposition on humification process while reducing the mineralization of amine-N precursors.

CONCLUSION

This study provides insights into the humification mechanism of HSB in enhancing anaerobic digestate composting (Figure 1). Results demonstrated that HSB containing pumice stone and phenolics significantly enhanced the humification process of digestate composting and contributed to higher aromaticity and humification degree. Pumice stone material with porous structure improved the air permeability of the composting system, which promoted the decomposition of proteins into amine-N precursors. The additional phenolics in HSB acted as an aromatic skeleton to polymerize with amine-N to rapidly form humic substances, which mitigated the adverse effects of lignin rate-limiting decomposition on humification process while reducing mineralization of amine-N precursors.

Keywords: anaerobic digestate composting; biological humification; dissolved organic matter; humus soil biomaterial.

KEYWORDS

Anaerobic digestate Composting; Biological humification; Dissolved organic matter; Humus soil biomaterial

RESEARCH ON COORDINATED CONTROL OF DIOXINS IN FLUE GAS DURING WASTE INCINERATION FLY ASH DISPOSAL USING SINTERING MACHINES

Rongrong Lei[1], Panpan Guo[1]

1 School of Energy and Environmental Engineering, University of Science and Technology Beijing, Beijing, China

Abstract: As the volume of waste incinerated continues to increase, the dioxins produced have become a critical challenge in environmental pollution control. This paper focuses on the process of treating incineration fly ash using a sintering machine, employing activated coke adsorption technology as the core synergistic approach to investigate the synergistic control of dioxins in flue gas. By preparing ammonia-modified activated coke (NAC) and using o-dichlorobenzene as a dioxin analog, the physicochemical properties of NAC were comprehensively analyzed using characterization techniques. Using in situ infrared spectroscopy and computational modeling, we investigated the reaction mechanism between o-dichlorobenzene and NO on the surface of activated coke. The results indicate that ammonia modification can effectively introduce nitrogen-containing functional groups such as pyridine nitrogen and quaternary nitrogen onto the surface of activated coke, while significantly increasing the number of macropores. Nitrogen-containing functional groups not only provide adsorption sites for synergistic removal but also promote the reaction between NO and O_2 to form NO_2, thereby accelerating the ring-opening degradation of o-dichlorobenzene. This study provides a promising technical pathway for low-cost, high-efficiency synergistic control of multiple pollutants in flue gas.

1 INFLUENCE OF PHYSICAL AND CHEMICAL PROPERTIES OF ACTIVATED COKE

Unmodified activated carbon contains only pyrrole and quaternary nitrogen groups, while modified activated carbon exhibits an increase in pyrrole functional groups. The total nitrogen-containing functional group content exhibited an overall trend of first increasing, then decreasing, and finally increasing again following ammonia modification. During calcination at 600°C, the content increased from 0.42% to 0.76%. At 700°C, it decreased to 0.51%, but rebounded to 0.67% at 800°C. This indicates that ammonia modification can introduce more nitrogen-containing functional groups, though the effect is temperature-dependent. After calcination modification, pyridine nitrogen appears where none existed before, and its content gradually increases with rising temperature.

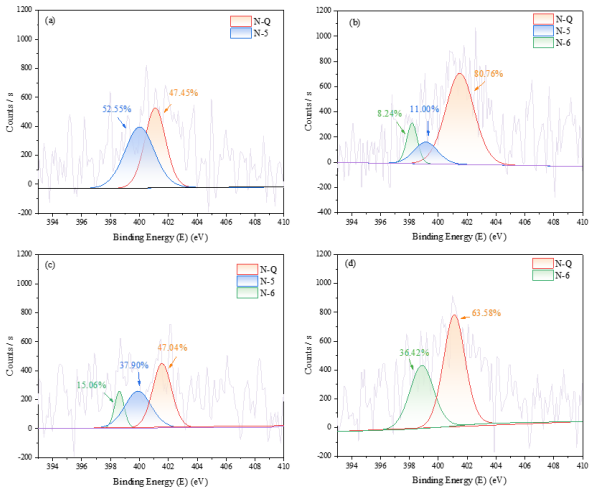

Figure.1 Deconvoluted N1s spectrum of YAC(a), 600NAC(b), 700NAC(c) and 800NAC(d).

The modified activated carbon exhibits enhanced removal efficiency for both o-dichlorobenzene and NO. This improvement stems from the increased macroporosity and nitrogen-containing functional groups in the modified activated carbon, which provide additional active sites for adsorbing o-dichlorobenzene and NO. Among them, 600NAC possesses the highest concentration of nitrogen-containing functional groups, thereby exhibiting the strongest capacity for pollutant removal. During the synergistic removal of o-

dichlorobenzene and NO, the removal efficiency of o-dichlorobenzene decreased on YAC, 700NAC, and 800NAC, while it increased on 600NAC. The NO adsorption capacity increased on both 600NAC and 800NAC, while it decreased on YAC and 700NAC. This is because o-dichlorobenzene and NO compete for adsorption on the pyrrole functional group. However, adsorption of o-dichlorobenzene on the pyridine functional group facilitates subsequent NO adsorption. Furthermore, on the quaternary nitrogen functional group, NO readily reacts with O_2 to form NO_2.

2 IMPACT OF POLLUTANT REMOVAL FROM THE ENVIRONMENT

The removal temperature has a negligible effect on the adsorption of o-dichlorobenzene, with removal efficiencies exceeding 96% across the range of 120°C to 240°C. As the temperature increased from 120°C to 240°C, the adsorption capacity of NO exhibited an overall trend of first rising and then decreasing, reaching a maximum adsorption capacity of 31.43 mg/g at 160°C. As the temperature rises from 120°C to 160°C, the thermal kinetic energy of NO molecules increases, enhancing their diffusion coefficient. This enables them to traverse mesoporous channels more rapidly, penetrate deeper into micropores, and adsorb onto active sites, thereby boosting adsorption capacity. The activated carbon adsorption process is exothermic, and high temperatures are detrimental to adsorption removal. Within the temperature range of 160°C to 240°C, the removal efficiency of activated carbon for NO decreases as the temperature increases.

The addition of 200 ppm SO_2 reduced the removal efficiency of o-dichlorobenzene from 97% to 92%. Adding 300 ppm SO_2 slightly improved the o-dichlorobenzene removal efficiency (94%), but it remained lower than the efficiency achieved without SO_2 addition. When 100 ppm of SO_2 is added, the NO adsorption capacity decreases to. When the added SO_2 concentration increases to 200 and 300 ppm, the NO adsorption capacity recovers. SO_2 competes with o-dichlorobenzene and NO for nitrogen-containing functional groups, thereby reducing the activated carbon's ability to remove o-dichlorobenzene and NO. SO_2 competes preferentially with NO for seasonal nitrogen adsorption sites, so as the concentration of added SO_2 increases, the adsorption capacity for NO decreases first. SO_2 adsorption following the pyridine functional group increases the adsorption energy of NO on pyridine, thereby restoring the adsorption capacity of NO. The recovery in o-dichlorobenzene removal efficiency is attributed to the formation of protonated sulfate salts on the activated carbon surface, which enhances Brønsted acid sites.

3 CONCLUSIONS

The synergistic removal of o-dichlorobenzene and NO involves two components: adsorption and degradation. O-dichlorobenzene and NO primarily adsorb onto nitrogen-containing functional groups via van der Waals forces. SO_2 competes with o-dichlorobenzene and NO for adsorption sites on quaternary nitrogen functional groups, thereby inhibiting their removal. Competitive adsorption occurs between o-dichlorobenzene and NO on pyrrole functional groups; however, o-dichlorobenzene adsorption on pyridine functional groups facilitates subsequent NO adsorption. Nitrogen-containing functional groups and NO promote the oxidative degradation of o-dichlorobenzene. This study presents a promising technical approach for the highly efficient synergistic control of multiple pollutants in flue gas.

Towards sustainable municipal solid waste treatment: Life cycle environmental-economic analysis under waste sorting

Rongxing Bian[1,2,*], Chenqi Gao[1,2], Yingjie Sun[1,*], Yating Niu[1], Xinran Du[1], Yanan Wang[1]

1 College of Environmental and Municipal Engineering, Qingdao University of technology, Qingdao, China

2 Key Lab of Industrial Fluid Energy Conservation and Pollution Control (Ministry of Education), Qingdao University of Technology, Qingdao, China

3 Solid Waste and Hazardous Chemical Center, Jinan, China

Abstract: Municipal solid waste (MSW) treatment is a significant contributor to greenhouse gas (GHG) emissions globally. The implementation of MSW classification policies is reshaping waste disposal strategies, particularly in China under the "Dual Carbon" targets. This study employed an integrated life cycle assessment and life cycle cost (LCC) framework to evaluate the environmental and economic performance of waste disposal under both current and idealized MSW sorting scenarios in Qingdao, China. Furthermore, scenario simulations were conducted to explore optimization pathways. The results indicate that MSW disposal under the baseline scenario (S0) resulted in net-negative carbon emissions (-159.18 kg CO_2-eq/t MSW) due to energy recovery, while also achieving substantial reductions in terrestrial ecotoxicity and human non-carcinogenic toxicity. The ideal waste sorting scenario (S1) offered significant environmental benefits, with GHG emissions reduced to -355.88 kg CO_2-eq/t MSW. However, its practical implementation remains constrained by capital investment and labor demands. Compared to S0, the optimized scenario (S2) improved environmental performance, reducing GHG emissions by 10.69 kg CO_2-eq/t MSW through better recyclables recycling, thermal energy use, and biogas upgrading. The weighted endpoint resource impact decreased from -5.61 Pt to -6.85 Pt. Moreover, the dynamic LCC evaluation revealed that S2 increased economic benefits by 85.36 % relative to S0. Our study provides insights into optimizing waste treatment pathways to reduce environmental impacts, enhance economic performance, and support low-carbon transition. It also offers quantitative evidence for sustainable management and practical strategies for MSW managers.

Key words:

Municipal solid waste incineration

Waste classification

Life cycle assessment

Life cycle costing

Environmental improvement

---

* Corresponding author. E-mail: bianrongxing@qut.edu.cn

1. Introduction

The greenhouse gas (GHG) emissions from municipal solid waste (MSW) treatment units are recognized as a critical issue contributing to climate change. It has been listed by the Intergovernmental Panel on Climate Change (IPCC) as one of the five most important emissions sources, accounting for about 3 % globally (Olivier and Peters, 2021). Currently, the global annual production of MSW is about 1.3 billion tons (Bt), and it is expected to reach 2.2 Bt by 2050 (Zhang et al., 2023). The MSW carbon emissions in 2020 were 24 million tons (Mt) CO_2 equivalent (CO_2-eq) worldwide, with recycling, incineration, and sanitary landfill being the primary MSW disposal methods (IEA, 2021; Liao et al., 2022). Owing to the substantial improvement in resident consumption levels in China, the quality of MSW has rapidly increased from 148.41 Mt in 2006 to 244.45 Mt in 2022 (NBSC, 2023). Subsequently, the GHG emissions in the MSW sector had grown from 55.38 in 2006 to 178.06 Mt in 2019 (Bian et al., 2022b). As the largest GHG emitter, China has introduced relevant policies successively to alleviate carbon emissions, such as “Dual Carbon” targets (to achieve “carbon neutrality” in 2030 and “carbon peak” in 2060), “Zero-Waste City” construction and MSW classification implementation.

The composition of MSW in China is characterized by high moisture content due to the large proportion of food waste (FW), while the low calorific value is influenced by both the proportion of recyclables and FW (Zhu et al., 2021). With the increasing complexity and quantity of MSW, traditional disposal methods such as landfilling and mixed incineration can no longer meet environmental sustainability requirements. The shift toward MSW classification has led to a transition from landfilling to incineration while promoting anaerobic digestion and composting for FW and facilitating the recycling of valuable materials (Zaikova et al., 2022). Prior studies have demonstrated that effective sorting of recyclables such as wastepaper, textiles, and plastics significantly reduces carbon emissions (Esteve-Turrillas and de la Guardia, 2017; Sun et al., 2023). For instance, packaging waste recycling alone has been reported to mitigate GHG emissions by 348.1 kg CO_2-eq/t MSW while yielding economic benefits of 376.7 €/t (Qiang et al., 2024). Similarly, FW anaerobic digestion and composting have been recognized as key measures for recovering energy through biodiesel and fertilizer production (Yu and Li, 2021). Moreover, Bian et al. (2022a) found that an optimized MSW management strategy combining FW anaerobic digestion, recyclables recycling, and incineration of residual waste could result in net-negative carbon emissions in Qingdao, China. However, MSW classification also presents new challenges, particularly for MSWI plants, where fluctuating waste composition may lead to increased

carbon intensity, overcapacity risks, and reduced energy recovery efficiency (Gao et al., 2025). Under China's "Zero-Waste City" initiative and "Dual Carbon" targets, low-carbon development pathways such as utilizing steam thermal energy for district heating, integrating clean energy sources, enhancing flue gas carbon capture, and promoting collaborative waste treatment have gained increasing attention (Xiao et al., 2023; Zhang et al., 2020, 2024).

Life Cycle Assessment (LCA) focuses on evaluating the environmental impacts of a product or activity throughout its entire life cycle, which includes material collection, transportation, production, use, recycling, and final disposal. It can evaluate the entire process of a product or service from cradle to grave (Christensen et al., 2020). In the field of waste management, it can help to understand and improve existing waste management systems, compare or develop technology performance, and make relevant policies (Christensen et al., 2020). Han et al. (2023) revealed the influence mechanism between the components of MSW and quarterly GHG emissions based on LCA methods, and they found that improving the efficiency of power generation could alleviate the carbon emissions in MSW incineration (MSWI) plants. Moreover, from the perspective of LCA, the source segregation of MSW could reduce the carbon emissions by nearly 160 kg CO_2-eq/t MSW (Liao et al., 2022). Bian et al. (2022a) and Chen et al. (2020) established several treatment modes for MSW by LCA and scenarios simulation to explore the characteristics of GHG emissions under MSW classification in Qingdao and Shanghai, respectively. Through comprehensive analyses, they provide feasible suggestions for MSW management, such as proper separation of FW and improvements of the garbage separation efficiency. Gao et al. (2025) using LCA and scenarios simulation methods, studied the GHG emissions from typical MSWI plants under waste classification in Qingdao city. Conversely, they found that the MSW classification could pose challenges for MSWI plants, such as high carbon emissions intensity and overcapacity. Therefore, further studies should focus on the variations in GHG emissions resulting from MSW separation. Although other methods such as input–output analysis (IOA), material flow analysis (MFA), the IPCC approach, the upstream–operation–downstream (UOD) model, and the Clean Development Mechanism (CDM) framework offer insights into macro-level emissions or specific carbon flows, they lack the process-level detail and multi-indicator scope required in this study. IOA and MFA are often used in combination with LCA (Amadei et al., 2025; Chen et al, 2023; Zhang et al., 2018). Therefore, LCA was chosen for its ability to provide a more comprehensive, process-level, and multi-indicator assessment compared to these alternative approaches.

Furthermore, life cycle cost (LCC) methods are usually integrated with LCA to evaluate the environmental and economic benefits in the field of waste disposal (Liu et al., 2022a). It has been widely used in the environmental and economic benefit evaluation of waste gasification, incineration and FW treatment (Liu et al., 2022a; Rodrigues et al., 2022).

MSW classification has introduced new requirements for waste disposal. However, most existing studies on waste management and its environmental impacts focus primarily on MSWI, while comprehensive environmental assessments encompassing the entire MSW disposal system—including incineration, FW anaerobic digestion, and recyclables recycling—remain limited. In particular, despite growing interest in waste treatment optimization, current research remains mainly focused on actual conditions, with insufficient attention paid to both the potential environmental benefits and challenges achievable under idealized waste sorting scenarios. Moreover, the influencing mechanism of MSW classification on the environmental and economic performance of waste disposal has not been sufficiently explored. The potential benefits and challenges associated with waste sorting for MSW disposal, such as changes in waste composition, variations in energy recovery efficiency, and economic cost fluctuations, also require further investigation.

To address these research gaps, this study systematically evaluates the environmental and economic performance of MSWI and FW treatment under waste classification. By integrating LCA and LCC, we aim to quantify the environmental performance and economic feasibility of different waste treatment scenarios. Scenario simulations are conducted to analyze variations in GHG emissions, resource consumption, and cost-effectiveness across different management strategies. Besides, environmental performance and challenges of ideal waste sorting were analyzed. The findings provide valuable insights into optimizing waste management pathways, minimizing environmental burdens, and enhancing economic sustainability. This study offers quantitative evidence to support policymakers and waste management practitioners in developing more effective and sustainable waste treatment strategies.

2. Materials and methods

2.1 Case study

Qingdao, a famous tourist megacity in China, generated 4.02 Mt of MSW in 2022 due to its large number of travelers and flourishing economy development (NBSC, 2023). Given its role as a national pilot city for waste classification, well-established treatment infrastructure, and the availability of detailed

local data, Qingdao was selected as the case study area for this research. To achieve the purpose of sustainable waste management, Qingdao has implemented the MSW classification since 2020, and the waste were separated into wet (FW), recyclables, hazardous, and others (dry waste). Since the implementation of garbage classification, the MSW in Qingdao has achieved a 100 % harmless disposal rate. In particular, MSWI plays a vital role in MSW treatment, accounting for 95.8 % (3.85 Mt) in 2022. In this study, FW refers to biodegradable residues from households and food services, such as leftovers, vegetable peels, and expired food. Due to its high moisture and organic content, it is typically treated by anaerobic digestion. In contrast, kitchen waste (KW), mainly from commercial kitchens and catering services, contains more fats and oils and is better suited for grease recovery via three-phase separation. In MSW management, only FW is generally considered domestic waste, while KW is usually excluded.

After waste classification, most of the MSW from the main urban districts of Qingdao was collected and mainly transferred to MSWI plants for incineration. Moreover, the FW were treated by anaerobic digestion in relevant plants, the recyclables were recovered (the proportion is small and has not yet been counted). For the purpose of future research, this study conducted field investigations at representative incineration plants and FW dry anaerobic digestion facilities in Qingdao, gathering relevant technical data. The information of MSW components in Qingdao city is shown in **Table 1**. The MSW disposal facilities information for Qingdao is presented in **Appendix A Table S1**.

Components	Food waste	Paper	Plastics and Rubber	Textile	Woods	Bricks	Glass	Metal	Others
Proportion (%)	67.20	10.32	13.55	1.93	1.67	1.23	2.27	0.94	0.89
Water content (%)	65.64	41.09	36.85	43.60	28.67	24.08	11.87	7.21	26.31

Table 1 Proportion and water content of MSW compositions in Qingdao city (wet base).

2.2 Goal and scope definition

This present study aims to assess the environmental and economic performance of various waste disposal methods throughout their life cycle under the implementation of Qingdao's garbage classification policy by developing a systematic evaluation framework. Besides, the potential for improvement based on domestic waste separation, technology upgrades, and integrated management for the MSWI plant was explored using scenarios simulation analysis. Functional unit is defined as one ton of MSW (Khandelwal et al., 2019).

In this work, the collection, transportation, and environmental benefits of recycling recyclables in MSW were not considered because we mainly focus on the final disposal of the waste. Meanwhile, the established

evaluation model boundary, including details on input materials, energy consumption, coproducts, and output emissions for each process, was based on the ISO 14040–14044 standards (ISO, 2006a, 2006b). The specific system boundary for the current waste disposal status is shown in **Fig. 1a**, while the ideal MSW treatment situation and the scenario simulation based on the current status are detailed in Section 2.3.

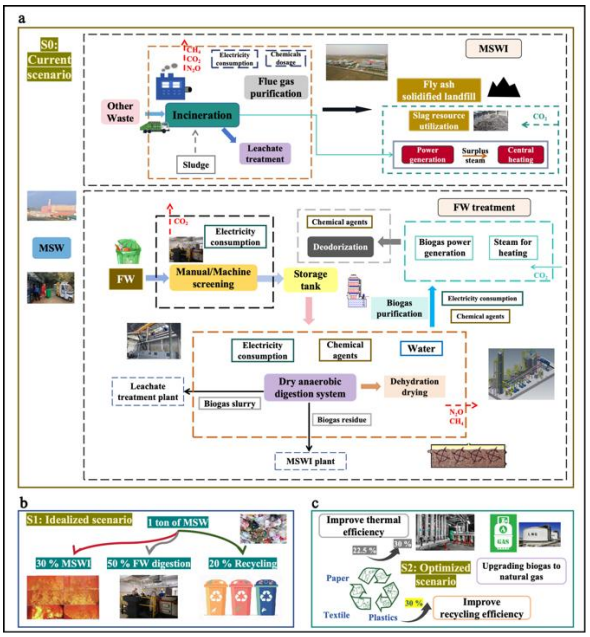

Fig. 1 Detailed system boundary of the current MSW disposal scenario in Qingdao city, (a) S0: Current scenario; (b) S1: Idealized scenario; and (c) S2: Optimized scenario. FW: food waste; MSW: municipal solid waste; MSWI: municipal solid waste incineration

2.3 Evaluation methodology

In this work, the SimaPro 9.4 software was used to evaluate the environmental performance of waste disposal based on its Ecoinvent database. In particular, the ReCiPe 2016 method was applied to clarify the Midpoint (Climate change, Human toxic effects, Ozone depletion, Acidification, Eutrophication, Photochemical ozone creation, etc.) and Endpoint (Human health, Ecosystems, and Resources surplus cost) impacts of the activities within the established system boundary (Huijbregts et al., 2017). The assessments of economic benefits were calculated using static LCC and dynamic LCC methods (Han et al., 2024). The unit of LCC was set as 1 ton of MSW/FW, and the formulas are as follows (Liu et al., 2022a):

$$Static\ LCC = C_0 - I_i + O_i + M_i + R \quad (1)$$

$$Dynamic\ LCC = C_0 - \sum_{t=0}^{T} I_i \times PV_{\mathrm{sum}} + \sum_{t=0}^{T} O_i \times PV_{\mathrm{sum}} + \sum_{t=0}^{T} M_i \times PV_{\mathrm{sum}} + \sum_{t=0}^{T} R_i \times PV_{\mathrm{sum}} - S \times PV \quad (2)$$

$$PV_{\mathrm{sum}} = \frac{(1+r)^t - 1}{r \times (1+r)^t} \quad (3)$$

$$PV = \frac{1}{(1+r)^t} \quad (4)$$

C_0 (Chinese yuan (CNY)) is capital cost; I (CNY) - operational income; O_i (CNY) represents operating cost; M (CNY) indicates maintenance cost; R (CNY) is management cost; i represents different disposal ways; S (CNY) - salvage value; T (year) is life cycle; PV_{sum} (CNY) - present value sum; PV represents discount factor; r (%) - discount rate.

Scenarios simulation is an important tool for developing improvement strategies for waste treatment and management pathways (Kosow and Gaßner, 2008). In this study, two new scenarios were developed by

integrating the current waste disposal status, local sorting policies, relevant literature (Fu et al., 2025; Gao et al., 2025; Liu et al., 2022b; Zhang et al., 2022), and the operational conditions of existing treatment facilities, in order to assess the environmental improvement potential of waste management under sorting conditions in Qingdao. (1) Scenario S0 represents the baseline condition without optimization measures (MSW composition is shown in **Table 1**. The thermal energy utilization efficiency is 22.05 %, and the biogas from FW anaerobic digestion is used for power generation). (2) Scenario S1 assumes ideal waste sorting, in which, for one ton of domestic waste, 50 % of MSW (FW) is diverted to anaerobic digestion, 20 % (recyclables) is fully recovered, and the remaining 30 % is incinerated (**Fig. 1b**). (3) Scenario S2 builds upon S0 with three key improvements: increasing the recycling efficiency of FW, plastics, textiles, and paper by 30 %; enhancing the thermal efficiency of the waste incineration plant to 30 %; and purifying excess biogas from the FW treatment plant into natural gas after meeting internal energy demands (**Fig. 1c**). These three scenarios provide a structured framework to evaluate the potential benefits of optimized waste sorting and resource recovery. They were designed to represent a typical baseline condition, a realistic disposal-technology-enhanced pathway, and an idealized sorting case, thereby allowing the exploration of environmental outcomes across different levels of implementation.

Life cycle inventory (LCI) can provide a detailed quantitative description of material and energy flow, which serves as the basis for subsequent life cycle impact assessments (Christensen et al., 2020). The LCI data in this work were compiled from primary annual data collected from local waste treatment facilities and secondary data sourced from Ecoinvent 3.8 and relevant literature, ensuring reliability. The detailed LCI data from investigations for the evaluation of various waste treatment processes is shown in **Appendix A Tables S2 and S3** (ideal scenario and simulated scenarios). Besides, the environmental emissions from the recycling process were estimated based on the assumption that recycled plastics and paper replace virgin materials in the production of polyethylene and pulp-based paper products, which are generally associated with higher environmental burdens. Moreover, in this study, negative values in environmental and economic indicators represent better performance.

3. Results and discussion

3.1 Evaluation of environmental performance in waste management

The environmental performance evaluation of waste disposal in this study showed that incineration

power generation from MSWI had a positive impact on the environment (**Fig. 2a**), particularly in terms of GW, terrestrial ecotoxicity (TE), and human non-carcinogenic toxicity (HNT). MSW treatment units are significant sources of global GHG emissions (Bian et al., 2022b). The generated CO_2 can induce the long-term greenhouse effect, thereby exerting a profound influence on climate change (Guo et al., 2023). Our results show that GHG emissions from energy use (electricity and steam), material consumption (water and chemicals), and fly ash disposal were major contributors to carbon emissions (120.92 kg CO_2-eq/t MSW). In contrast, carbon sinks from power generation and heat recovery at the MSWI and FW disposal (-280.10 kg CO_2-eq/t MSW) offset part of these emissions, resulting in a net reduction in GWP (-159.18 kg CO_2-eq/t MSW). HNT is typically assessed by quantifying the toxicity weights of various chemicals to evaluate their potential non-carcinogenic risks to human health. In this study, the total HNT was -120.20 kg 1,4-DCB/t MSW. If leachate is not properly treated, heavy metals and organic pollutants may remain, increasing HNT. To mitigate this toxic effect, most MSWI plants employ effective treatment technologies, such as membrane filtration and biological treatment, and strictly control discharge (Kundu et al., 2023). TE reflects the potential toxicity of chemicals to terrestrial ecosystems. Improper treatment of heavy metals and persistent organic pollutants (POPs) from leachate may lead to their discharge into soil and water systems, further increasing TE and HNT risks. In this study, TE was -279.92 kg 1,4-DCB/t MSW. MSWI power generation helped mitigate TE by reducing landfill volumes, degrading organics, and controlling heavy metals. However, inadequate flue gas treatment may cause secondary pollution (Zeng et al., 2024), highlighting the need to upgrade purification technologies for stricter emission control.

The endpoint values of the environmental assessment characterization for waste disposal are shown in **Fig. 2b**. Fly ash treatment had a negative impact on various environmental values, particularly on resources. Thus, resource-oriented disposal strategies integrating fly ash and slag should be actively explored to mitigate their environmental impacts (Huang et al., 2022). Moreover, waste heat utilization for heating and power generation through combustion could contribute to environmental improvement. Future efforts at incineration plants should prioritize the advancement and adoption of combined heat and power (CHP) technology (Yang et al., 2018). Additionally, adopting renewable energy sources, implementing advanced leachate and digestate treatment technologies, and enhancing ash management processes are essential strategies for sustainable FW treatment (Fei et al., 2021; Liu et al., 2022b). Compared to waste heat utilization, biodiesel production from high-grease FW-derived

grease provided greater environmental benefits, and extracting grease from FW was more challenging than from KW, highlighting the need for alternative recovery methods like anaerobic digestion or composting (Deena et al., 2022) based on waste characteristics. In the future, enhancing resource utilization from waste disposal, promoting anaerobic digestion technology, and supporting waste classification and diversified disposal strategies will be crucial to achieving improved environmental benefits and greater resource recovery efficiency.

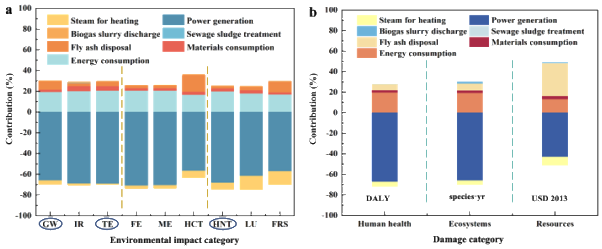

Fig. 2 Characterization results of the environmental impacts assessment of MSW disposal under S0. (a) Midpoint of waste treatment (Contribution); and (b) endpoint of waste treatment (Contribution). FE: Freshwater ecotoxicity; FRS: Fossil resource scarcity; GW: Global warming; HCT: Human carcinogenic toxicity; HNT: Human non-carcinogenic toxicity; IR: Ionizing radiation; LU: Land use; ME: Marine ecotoxicity; TE: Terrestrial ecotoxicity

3.2 Scenario analysis of waste disposal

Under the framework of MSW classification policies and the "Zero-Waste Cities" initiative in China, FW is separated for anaerobic digestion, recyclables is for recycling, and MSW incineration remains the primary method of disposal (Zhao et al., 2022). With the implementation of garbage classification, incineration plants face challenges such as overcapacity and high carbon emissions (Gao et al., 2025). In response, some MSW/FW disposal facilities are striving to enhance energy utilization efficiency to mitigate these pressures. In this section, we considered three key improvements (S2) and the ideal status (S1) to evaluate the environmental improvement potential of waste treatment.

3.2.1 Environmental impacts of MSW classification on waste disposal under ideal conditions

MSW classification policy in China would change the MSW composition, especially with significant impacts on the proportion of recyclables. Previous studies have primarily focused on the influence of domestic waste sorting on carbon emissions from MSW incineration (Bian et al., 2022a; Gao et al., 2025; Han et al., 2023). In addition to the GW, this study investigated the effects of changes in MSW composition on other environmental indicators of the MSW treatment.

Fig. 3 illustrates the midpoint and endpoint values associated with the reduction in environmental burden achieved through idealized MSW classification. Under the ideal waste sorting scenario, the recycling of recyclables, particularly plastic recycling, had a significant positive impact on the environment, leading to reductions in the total values of GW, TE and HNT by

123.56 %, 431.10 % and 367.40 %, respectively (**Fig. 3a**). In contrast, as a larger proportion of FW and recyclables were separated, the environmental benefits of waste incineration decreased. Similarly, in the endpoint value analysis (**Fig. 3b**), paper and plastic recycling made the most significant positive contribution to environmental performance under the S1 scenario, while anaerobic digestion of FW required further optimization to enhance its environmental benefits.

However, under the idealized MSW sorting, changes in waste composition posed significant challenges for both waste incineration and FW disposal. First, in the case of MSWI, the idealized garbage classification scenario led to a large amount of high-calorific value recyclables being recycled. As a result, the reduced calorific value of the remaining waste directly affected the heat recovery and power generation capacity of the incineration plant, while also increasing the energy consumption per unit of waste processed. Additionally, the incineration plant faced the issue of overcapacity. Under S1, the plant's designed processing capacity exceeded actual demand, leading to reduced energy utilization efficiency, excessive equipment investment, and resource waste, all of which undermined the environmental benefits of the incineration industry (Gao et al., 2025). Besides, overcapacity also raised the cost per unit of waste treated, thereby increasing the overall waste treatment expenditure. Regarding FW treatment, although 50 % of FW was directed to anaerobic digestion, which helped reduce waste and produce biogas, the complexity of FW (such as its high moisture content and diverse components) complicated the treatment process. High moisture and varying organic components led to unstable anaerobic digestion efficiency, especially in large-scale operations, requiring more advanced equipment and processes. Without timely optimization, this resulted in insufficient gas production or low biogas recovery efficiency, limiting resource utilization (Liu et al., 2022b). Additionally, FW may contain harmful substances, such as heavy metals or toxins, which could hinder the digestion process and affect biogas utilization. Therefore, it is crucial to advance the innovation and optimization of anaerobic digestion technology, particularly in the early stages of FW treatment. In conclusion, implementing ideal waste sorting requires significant governmental investment in infrastructure, regulatory frameworks, and public education, alongside high levels of public compliance and accurate waste segregation behavior. However, due to insufficient public participation and limited enforcement capacity, achieving this target remains challenging in the short term.

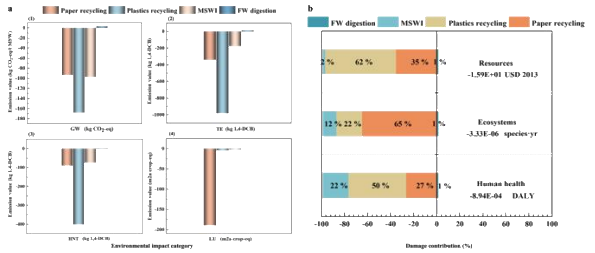

Fig. 3 Idealized environmental performance under MSW classification. (a) Mainly midpoint values of S1; and (b) mainly endpoint values of S1. FRS: Fossil resource scarcity; GW: Global warming; HNT: Human non-carcinogenic toxicity; LU: Land use; ME: Marine ecotoxicity; TE: Terrestrial ecotoxicity

3.2.2 Environmental performance of waste treatment under improved scenario

Fig. 4 illustrates the environmental benefits of MSW disposal following the implementation of S2. The results indicate that after waste sorting, the environmental benefits associated with GW improved by 10.69 kg CO_2-eq/t MSW. This can be attributed to two key factors: a reduction in the incineration of high fossil-carbon waste components and a corresponding decrease in the energy consumption required for waste incineration. Consistent with our previous study, MSW classification does not contribute to increased carbon storage from incineration power generation (Gao et al., 2025). Meanwhile, the environmental burdens of FE and ME decreased by 6.70 % and 7.00 %, respectively, demonstrating that the recycling of recoverable materials significantly reduces the release of toxic substances during waste incineration. Additionally, reductions in the environmental burdens of HCT and FRS highlight the role of waste recycling in decreasing the reliance of incineration on virgin resources. Notably, LU exhibited a substantial decline of 52.51 %, primarily due the efficient recycling of wastepaper. Overall, waste recycling proves to be highly effective in mitigating carbon emissions, minimizing water pollution, and reducing human health risks, reinforcing its essential role in sustainable waste management strategies.

This study also examined the environmental impact changes following an increase in the MSWI plant's thermal energy utilization efficiency to 30 %. The results indicate that enhancing heat recovery efficiency led to a 54.12 % increase in the environmental benefit of GW, aligning with previous findings by Yang et al. (2018) and Zafar et al. (2024), which highlight the role of waste-to-energy (WtE) in enhancing the carbon emission reduction potential of waste incineration. Furthermore, the environmental burdens associated with TE, HCT, and HNT decreased by 54.92 %, 66.62 %, and 45.26 %, respectively. These findings underscore that optimizing heat recovery in MSWI plants enhances the environmental benefits of incineration power generation while effectively mitigating overall environmental and ecological risks.

Furthermore, although the environmental benefits of upgrading biogas to natural gas were lower than those of biogas power generation, it helps reduce fossil fuel extraction and can lower the weighting of resource

scarcity in life cycle analysis. As China's electricity emission factor has been declining annually, the marginal emission reduction benefit of biogas power generation has also decreased, making biogas upgrading more aligned with future energy policies and the "Dual Carbon" strategy (Gao et al., 2025; Zueva et al., 2024). With increasing policy support for renewable natural gas, biogas is expected to have broad application prospects in transportation, industry, and other sectors. Therefore, from a long-term perspective, compared to biogas power generation, biogas upgrading offered greater advantages in future environmental benefits and market value. The FW/KW plants in Qingdao city are also considering the transition of biogas utilization, aligning with the objectives of clean development.

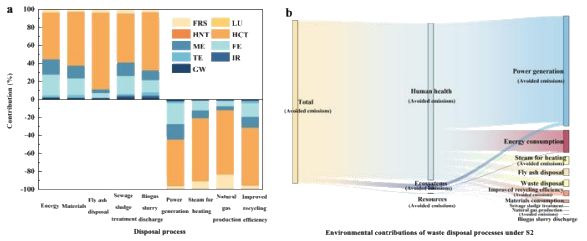

Fig. 4 Improved environmental performance of waste treatment based on S2 (Normalization and weighting results). (a) Midpoint of S2 (Normalization); and (b) endpoint of S2 (Weighting). FE: Freshwater ecotoxicity; FRS: Fossil resource scarcity; GW: Global warming; HCT: Human carcinogenic toxicity; HNT: Human non-carcinogenic toxicity; IR: Ionizing radiation; LU: Land use; ME: Marine ecotoxicity; TE: Terrestrial ecotoxicity

The comparison of midpoint and endpoint values of waste disposal based on S0, S1, and S2 is shown in **Fig. 5**. Totally, S1 exhibited greater environmental benefits from the respective of LCA, particularly in ME and TE, due to higher waste sorting efficiency. For S2, although its environmental benefits were not as significant as those of S1, its performance in terms of GW and FRS was significantly improved compared to S0 (**Fig. 5a**). For the endpoint, our research demonstrated strong environmental performance, with S1 and S2 achieving obvious enhancements, reflected in the weighted endpoint values of -15.92 Pt and -6.85 Pt, respectively (S0: -5.61 Pt, **Fig. 5b**). Specifically, human health impacts decreased by 9.47 and 1.18 Pt, ecosystem impacts were reduced by 0.74 and 0.04 Pt, and resource consumption showed a minor change (0.11 and 0.02 Pt), demonstrating effective mitigation of pollutant emissions and ecological degradation. In the future, MSWI plants should maximize environmental benefits by enhancing energy recovery, optimizing flue gas treatment, co-processing of waste, and developing carbon sequestration technologies (Ling and Chen, 2024; Lombardi et al., 2024). FW disposal plants should upgrade processing facilities and improve energy efficiency to address the potential challenges posed by MSW classification.

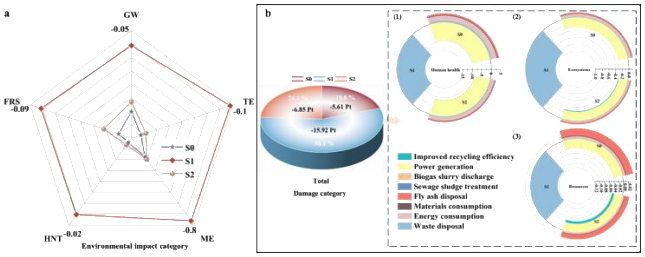

Fig. 5 Comparison of environmental benefits based on S0, S1, and S2 (Normalization and weighting results). (a) Midpoint (Normalization); and (b) endpoint (Weighting). FRS: Fossil resource scarcity; GW: Global warming; HNT: Human non-carcinogenic toxicity; ME: Marine ecotoxicity; TE: Terrestrial ecotoxicity

3.3 Analysis of economic cost fluctuations

Given that the ideal MSW classification scenario (S1) relies heavily on government investment in infrastructure and management systems and lacks a clear basis for cost estimation, this section focuses exclusively on the economic cost analysis of the current (S0) and feasible optimization (S2) scenarios for a typical MSWI plant and FW digestion facility. The economic variation after scenarios simulation is shown in **Fig. 6**. Positive values indicate economic costs, while negative values represent economic benefits. In S0, the MSWI plant's largest cost was the initial investment (2373.45 CNY/t MSW), followed by raw materials (45.48 CNY/t MSW) and maintenance costs (32.69 CNY/t MSW), primarily for pollution control. Its main revenue source was incineration power generation (241.61 CNY/t MSW), supplemented by garbage disposal fees (113.70 CNY/t MSW), with energy recovery as its key profit driver. In contrast, the FW treatment plant's highest cost was also its initial investment (181.98 CNY/t FW), but its revenue came mainly from the waste disposal fee (337.28 CNY/t FW), with only a small portion from biogas power generation (7.07 CNY/t FW). Overall, the incineration plant had a stable economic structure but faced high costs for pollution control, while the FW plant had limited income from energy recovery. Subsequent efforts should focus on improving biogas utilization to enhance both resource efficiency and economic performance.

The comprehensive LCC analysis showed that the S2 scenario significantly optimized the economic feasibility of both the MSWI plant and the FW treatment facility. At the MSWI plant, waste sorting and improved thermal energy utilization efficiency led to a 26.78 % reduction in energy consumption (from 7.1 to 5.6 CNY/t MSW) and a 10.33 % decrease in raw material costs (from 45.48 to 41.22 CNY/t MSW). Meanwhile, incineration power generation revenue increased by 27.05 % compared to S0 (from 241.61 to 306.98 CNY/t MSW), resulting in a substantial improvement in dynamic LCC outcomes (from -1020.18 to -1905.76 CNY/t MSW). For the FW treatment plant, although biogas upgrading to natural gas generated only a marginal increase of 0.012 CNY/t FW in direct revenue, it demonstrated considerable economic potential by increasing resource value, expanding energy utilization pathways, and aligning with future clean energy development trends. The optimization reduced the static LCC from 28.94 to 28.93 CNY/t FW and improved the dynamic LCC from -17.26 to -17.27 CNY/t FW. Overall, the S2 markedly improved the economic performance of

waste treatment by enhancing the efficiency of recyclables, optimizing energy recovery, and increasing resource utilization. Future improvements can incorporate carbon trading, district heating integration, and circular economy strategies to further maximize environmental and economic benefits, contributing to long-term sustainability (Magnanelli et al., 2021; Paiho et al., 2021).

The ideal classification implementation (S1) remains constrained by capital investment and labor demands. Li et al. (2023) conducted an integrated LCA–LCC analysis in Xi'an and found that source-separated collection systems incur high operational costs, with labor accounting for the largest share, and unit treatment costs reaching up to 628.93 CNY/t for residual waste. Similarly, Jiang et al. (2024) estimated the total LCC of Beijing's MSW system at 12.4 billion CNY per year, with incineration alone contributing over 80 % of total expenditures. These findings underscore that, although waste sorting offers environmental benefits, it also requires substantial capital and manpower, particularly for collection, transport, and treatment infrastructure.

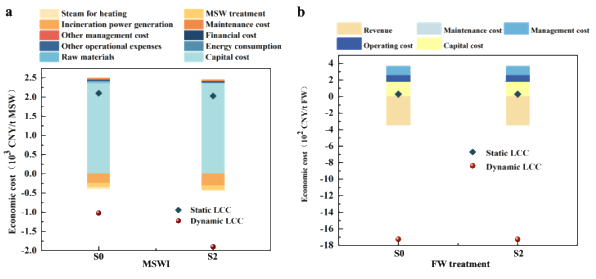

Fig. 6 Comparison of economic costs between S0 and S2 scenarios. (a) MSWI plant; and (b) FW plant. FW: food waste; LCC: life cycle cost; MSW: municipal solid waste; MSWI: municipal solid waste incineration

3.4 Limitations and uncertainty analysis

This study had certain limitations. First, although the S0 scenario data were based on actual emissions from 2023, certain parameters were not fully documented, such as the dosage of chemical agents in the FW treatment process. Second, in the scenario simulation, some parameters that were difficult to estimate were derived from macroscopic empirical values, which may have introduced uncertainties into the environmental assessment. Additionally, in the economic cost analysis, some data were unavailable or difficult to estimate due to confidentiality constraints, potentially affecting the accuracy of the results. Moreover, this study relied on emission factors from the SimaPro database, which contained inherent uncertainties due to variations in data sources, regional differences, and methodological assumptions.

Monte Carlo simulation was employed to propagate uncertainty, assessing how fluctuations in input parameters impacted the LCA results by allowing random variations within preset ranges. This method, widely applied in LCA research, effectively characterizes data uncertainty and enhances result reliability through model adjustments (Hung and Ma, 2009). This study conducted an uncertainty analysis on the environmental assessment across scenarios to

quantify potential error ranges. For instance, the uncertainty analysis results of waste treatment under S0 showed that its GW varied between -108 and -225 kg CO_2-eq, with a coefficient of variation (CV) of -17.8 %. Further results and detailed parameters related to the uncertainty analysis are provided in **Appendix A Table S4 and Fig. S2**, offering further insights into the variability and reliability of the LCA results.

3.5 Policy implication

The waste treatment sector has a large environmental improvement potential under waste classification. The implementation of domestic waste classification has enhanced the environmental benefits of waste disposal but also introduced certain challenges. MSWI plants should be wary of the risks of overcapacity and potential decrease in carbon emission reduction benefits in the future. Meanwhile, FW treatment facilities should explore innovative clean production methods to enhance energy efficiency and optimize resource utilization under MSW classification. In the future, waste treatment managers and government departments should actively collaborate to optimize waste management strategies. Special attention should be given to the rational co-incineration of sludge or industrial solid waste in MSWI plants and the integration of thermal district heating systems to enhance energy recovery. For FW treatment, the transition to a three-phase separation process should be carefully evaluated, particularly for high-grease FW, as it can enhance resource recovery efficiency and reduce environmental impacts. Additionally, to support energy-saving and emission-reduction initiatives, such as biogas purification for natural gas production, the government should establish a favorable financial and policy environment for related plants.

In addition to technical and institutional measures, social strategies play a critical role in ensuring the effective and sustainable implementation of MSW management. Strengthening public environmental awareness through educational initiatives and media campaigns can lay the foundation for behavioral change by highlighting both the environmental and economic benefits of waste separation and recycling. Furthermore, waste disposal parks should strengthen partnerships with research institutions to promote technological innovation and adopt effective public engagement strategies to mitigate the “NIMBY” (Not In My Backyard) effect, fostering greater societal acceptance. To reinforce public trust and sense of social responsibility, increasing the transparency of waste management outcomes is also essential. Open access to information on disposal processes and low-carbon outcomes can help reduce information gaps and improve the public credibility of waste treatment facilities. Besides, implementing MSW sorting incentive systems,

including rewards for communities with strong performance and penalties for non-compliance, can motivate active participation and support long-term behavioral change.

4. Conclusions

China's MSW classification policy has significantly influenced the environmental assessment of waste disposal systems, particularly in domestic waste incineration and FW treatment. This study examined waste disposal situations in Qingdao, employing an integrated LCA-LCC approach to systematically evaluate the environmental and economic performance of MSWI, FW digestion and recyclables recycling under both baseline and optimized scenarios. The key conclusions are as follows: (1) In the baseline scenario (S0), MSW disposal resulted in net-negative carbon emissions (−159.18 kg CO_2-eq/t MSW) due to energy recovery, and also led to reductions in TE and HNT, indicating favorable environmental performance. (2) Under the ideal waste classification scenario (S1), large amounts of recyclables such as paper, plastics, and textiles were recovered, resulting in notable environmental benefits. For instance, GW improved from -159.18 to -355.88 kg CO_2-eq/t MSW, and FRS from -36.85 to -81.93 kg oil eq. However, implementing such an ideal classification system remained challenging in practice. (3) The optimized scenario (S2), which integrated continuous waste sorting, improved thermal energy use, and biogas upgrading to natural gas, resulted in marked environmental improvements, including a 10.69 kg CO_2-eq/t MSW reduction in GHG emissions and a decrease in weighted resource impact from -5.61 Pt to -6.85 Pt. (4) Dynamic economic cost analysis showed that S2 significantly improved economic benefits (ranging from 1037.44 to 1923.03 CNY/t MSW), further confirming that waste sorting and energy efficiency enhancements effectively optimized both environmental and financial outcomes. (5) Finally, this study provides actionable recommendations for waste management authorities, emphasizing the need for proper waste sorting, improved resource utilization strategies, and policy support for low-carbon waste disposal pathways.

Declaration of competing interest

The authors declare that they have no known competing financial interests or personal relationships that could have appeared to influence the work reported in this paper.

Acknowledgements

This work was supported by the National Natural

Science Foundation of China (No. 52370139), China Postdoctoral Science Foundation (No. 2022M711747), the Youth Innovation Technology Project of Higher School in Shandong Province (No. 2023KJ117), the Open Fund of Key Lab of Industrial Fluid Energy Conservation and Pollution Control (Ministry of Education) (No. CK-2024-0032) and the Innovation and Entrepreneurship Plan Project of Shandong Province College Student (No. S202310429204).

Reference

Amadei, A.M., Rigamonti, L., Tosches, D., Sala, S., 2025. Combining MFA and LCA models to unveil the EU plastic value chain impacts. Resour. Conserv. Recycl. 219 (8), 108279.

Bian, R.X., Chen, J.H., Zhang, T.X., Gao, C.Q., Niu, Y.T., Sun, Y.J., et al., 2022a. Influence of the classification of municipal solid wastes on the reduction of greenhouse gas emissions: A case study of Qingdao city, China. J. Clean. Prod. 376 (47), 134275.

Bian, R.X., Zhang, T.X., Zhao, F.B., Chen, J.H., Liang, C.Y., Li, W.H., et al., 2022b. Greenhouse gas emissions from waste sectors in China during 2006-2019: Implications for carbon mitigation. Process Saf. Environ. Protect. 161 (5), 488-497.

Chen, J.H., 2023. Carbon footprint and emission reduction potential of different waste disposal modes under the background of waste classification: A case study of Qingdao city. Master thesis. Qingdao University of Technology, Qingdao, China.

Chen, S.S., Huang, J.L., Xiao, T.T., Gao, J., Bai, J.F., Luo, W., et al., 2020. Carbon emissions under different domestic waste treatment modes induced by garbage classification: Case study in pilot communities in Shanghai, China. Sci. Total Environ. 717 (20), 137193.

Christensen, T.H., Damgaard, A., Levis, J., Zhao, Y., Björklund, A., Arena, U., et al., 2020. Application of LCA modelling in integrated waste management. Waste Manag. 118 (18), 313–322.

Deena, S.R., Vickram, A.S., Manikandan, S., Subbaiya, R., Karmegam, N., Ravindran, B., et al., 2022. Enhanced biogas production from food waste and activated sludge using advanced techniques-A review. Bioresour. Technol. 355 (13), 127234.

Esteve-Turrillas, F.A., de la Guardia, M., 2017. Environmental impact of Recover cotton in textile industry. Resour. Conserv. Recycl. 116 (1), 107-115.

Fei, X., Jia, W., Chen, T., Ling, Y., 2021. Life-cycle assessment of two food waste disposal processes based on anaerobic digestion in China. J. Clean. Prod. 293 (16), 126113.

Fu, H., Chen, L., Fang, W., Gao, W.F., Hu, K., Zhang, P.Y., et al., 2025. Characteristics and life cycle carbon emission reduction potential of waste recycling after implementing new waste classification policy in China: From case study to national perspective. J. Environ. Sci. 155 (9), 645-657.

Gao, C., Bian, R., Li, P., Yin, C., Teng, X., Zhang, J.,

et al., 2025. Analysis of carbon reduction potential from typical municipal solid waste incineration plants under MSW classification. J. Environ. Manage. 373 (1), 123844.

Guo, J.B., Liu, L.Y., Zhang, G.R., Yue, R.W., Wang, T.Z., Zhang, X.J., et al., 2023. Temporal and spatial analysis of anthropogenic mercury and CO_2 emissions from municipal solid waste incineration in China: Implications for mercury and climate change mitigation. Environ. Int. 178 (8), 108068.

Han, Q.L., Zhao, H.L., Wei, G.X., Zhu, Y.W., Li, T., Xu, M., et al., 2024. Sustainable papermaking in China: Assessing provincial economic and environmental performance of pulping technologies. ACS Sustain. Chem. Eng. 12 (11), 4517-4529.

Han, X.Q., Chang, H.Z., Wang, C., Tai, J., Karellas, S., Yan, J.J., et al., 2023. Tracking the life-cycle greenhouse gas emissions of municipal solid waste incineration power plant: A case study in Shanghai. J. Clean. Prod. 398 (17), 136635.

Huang, B.B., Gan, M., Ji, Z.Y., Fan, X.H., Zhang, D., Chen, X.L., et al., 2022. Recent progress on the thermal treatment and resource utilization technologies of municipal waste incineration fly ash: A review. Process Saf. Environ. Protect. 159 (3), 547-565.

Huijbregts, M.A., Steinmann, Z.J., Elshout, P.M., Stam, G., Verones, F., Vieira, M., et al., 2017. ReCiPe2016: A harmonised life cycle impact assessment method at midpoint and endpoint level. Int. J. Life Cycle Assess. 22 (2), 138-147.

Hung, M.L., Ma, H.W., 2009. Quantifying system uncertainty of life cycle assessment based on Monte Carlo simulation. Int. J. Life Cycle Assess. 14 (1), 19-27.

IEA (International Energy Agency), 2022. Global energy review: CO_2 emissions in 2021. Paris, France: International Energy Agency. Available at: https://www.iea.org/reports/global-energy-review-co2-emissions-in-2021-2. Accessed March 20, 2025.

ISO (International Organization for Standardization), 2006a. ISO 14040: Environmental management – life cycle assessment – principles and framework. Geneva, Switzerland: International Organization for Standardization.

ISO (International Organization for Standardization), 2006b. ISO 14044: Environmental management – life cycle assessment – requirements and guidelines. Geneva, Switzerland: International Organization for

Standardization.

Jiang, Y.J., Leng, B.Y., Xi, J.X., 2024. Assessing the social cost of municipal solid waste management in Beijing: A systematic life cycle analysis. Waste Manage. 173 (1), 62-74.

Khandelwal, H., Dhar, H., Thalla, A.K., Kumar, S., 2019. Application of life cycle assessment in municipal solid waste management: A worldwide critical review. J. Clean. Prod. 209 (4), 630-654.

Kosow, H., Gaßner, R., 2008. Methods of future and scenario analysis: overview, assessment, and selection criteria. DEU. 39, 133.

Kundu, A., Reddy, C.V., Singh, R.K., Kalamdhad, A.S., 2023. Critical review with science mapping on the latest pre-treatment technologies of landfill leachate. J. Environ. Manage. 336 (12). 117727.

Li, H.M., Tian, Y., Li, Z.L., Wu, C., Liu, Y.L., 2023. Life-cycle economic and environmental impacts of municipal solid waste reverse logistics in residential areas. Waste Manage. 164 (10), 200-208.

Liao, N.L., Bolyard, S.C., Lü, F., Yang, N., Zhang, H., Shao, L.M., et al., 2022. Can waste management system be a greenhouse gas sink? Perspective from Shanghai, China. Resour. Conserv. Recycl. 180 (13), 106170.

Ling, J.L., Chen, X.J., 2024. Energy and economic analysis of a new combination cascade waste heat recovery system of a waste-to-energy plant. Energies 17 (20), 5196.

Liu, H.Q., Liu, T., Wei, G.X., Zhao, H.L., Li, T., Weng, F.K., et al., 2022a. Environmental and economic assessment of rural domestic waste gasification models in China. Waste Manage. 154 (18), 160-174.

Liu, M., Ogunmoroti, A., Liu, W., Li, M., Bi, M., Liu, W., et al., 2022b. Assessment and projection of environmental impacts of food waste treatment in China from life cycle perspectives. Sci. Total Environ. 807 (6), 150751.

Lombardi, L., Castaldi, M.J., Patel, A.K., 2024. Energy recovery from residual municipal solid waste: State of the at and perspectives within the challenge to climate change. Energies 17 (2), 395.

Magnanelli, E., Mosby, J., Becidan, M., 2021. Scenarios for carbon capture integration in a waste-to-energy plant. Energy 227 (14), 120407.

National Bureau of Statistics of China (NBSC), 2023. China Statistical Yearbook. Beijing, China: China Statistics Press. Available at: http://www.stats.gov.cn/tjsj/ndsj/. Accessed

March 20, 2025.

Olivier, J.G., Peters, J.A.H.W., 2021. Trends in global CO_2 and total greenhouse gas emissions: 2021 Report. PBL Netherlands Environmental Assessment Agency.

Paiho, S., Wessberg, N., Pippuri-Mäkeläinen, J., Mäki, E., Sokka, L., Parviainen, T., et al., 2021. Creating a circular city-An analysis of potential transportation, energy and food solutions in a case district. Sustain. Cities Soc. 64 (1), 102529.

Qiang, Z., Nan, Q., Chi, W., Qin, Y., Yang, S., Zhu, W., et al., 2024. Recycling packaging waste from residual waste reduces greenhouse gas emissions. J. Environ. Manag. 371 (23), 123028.

Rodrigues, L.F., dos Santos, I.F.S., dos Santos, T.I.S., Barros, R.M., Tiago, G.L., 2022. Energy and economic evaluation of MSW incineration and gasification in Brazil. Renew. Energ. 188 (8), 933-944.

Sun, Y.Q., Qian, Y.F., Chu, S.Q., 2023. The impact of waste classification on carbon emissions in the incineration process in Suzhou. Environmental Sanitation Engineering 31 (1), 104-111+118.

Xiao, W., Liu, T., Tong, X., 2023. Assessing the carbon reduction potential of municipal solid waste management transition: Effects of incineration, technology and sorting in Chinese cities. Resour. Conserv. Recycl. 188 (1), 106713.

Yang, Y., Wang, J., Chong, K., Bridgwater, A.V., 2018. A techno-economic analysis of energy recovery from organic fraction of municipal solid waste (MSW) by an integrated intermediate pyrolysis and combined heat and power (CHP) plant. Energy Convers. Manag. 174 (20), 406-416.

Yu, Q.Q., Li, H., 2021. Life cycle environmental performance of two restaurant food waste management strategies at Shenzhen, China. J. Mater. Cycles Waste Manag. 23 (2), 826-839.

Zaikova, A., Vinitskaia, N., Deviatkin, I., Havukainen, J., Horttanainen, M., 2022. Life cycle assessment of existing and alternative options for municipal solid waste management in Saint Petersburg and the Leningrad region, Russia. Recycling 7 (2), 19.

Zafar, A.M., Shahid, S., Nawaz, M.I., Mustafa, J., Iftekhar, S., Ahmed, I., et al., 2024. Waste to energy feasibility, challenges, and perspective in municipal solid waste incineration and implementation: A case study for Pakistan. Adv. Chem. Eng. 18 (2), 100595.

Zeng, J.C., Mustafa, A.B., Liu, M.W., Huang, G.R.,

Shang, N., Liu, X., et al., 2024. Environmental, energy, and techno-economic assessment of waste-to-energy incineration. Sustainability 16 (10), 4140.

Zhang, C.Y., Dong, H.J., Geng, Y., Song, X.Q., Zhang, T.Y., Zhuang, M.F., 2022. Carbon neutrality prediction of municipal solid waste treatment sector under the shared socioeconomic pathways. Resour. Conserv. Recycl. 186 (11), 106528.

Zhang, M., Wei, J.X., Li, H., Chen, Y., Liu, J.G., 2024. Comparing and optimizing municipal solid waste (MSW) management focused on air pollution reduction from MSW incineration in China. Sci. Total Environ. 907 (2), 167952.

Zhang Q.F., Fang K., Xu M., Liu Q.Y., 2018. Review of carbon footprint research based on input-output analysis. Journal of Natural Resources 33 (4): 696-708.

Zhang, T.X., Gao, S.D., Teng, X., Jiang, X.T., Chen, J.H., Gao, C.Q., et al., 2023. Spatio-temporal change in city-level greenhouse gas emissions from municipal solid waste sector in China during the last decade and its potential mitigation. Environmental Science 44 (11), 5946-5953.

Zhang, Y.D., Du, X.L., Yue, M., Yan, M.W., Shi, Y.T., 2020. Heat transfer and ash deposition performance of heat exchange surface in waste incineration flue gas. Int. J. Heat Mass Tran. 155 (10), 119691.

Zhao, F.B., Bian, R.X., Zhang, T.X., Fang, X., Chai, X.L., Xin, M.X., et al., 2022. Characteristics of polychlorinated dibenzodioxins/dibenzofurans from a full-scale municipal solid waste (MSW) incinerator in China by MSW classification. Process Saf. Environ. Protect. 161 (5), 50-57.

Zhu, Y.L., Zhang, Y.X., Luo, D.X., Chong, Z.Y., Li, E.Q., Kong, X.P., 2021. A review of municipal solid waste in China: characteristics, compositions, influential factors and treatment technologies. Environ. Dev. Sustain. 23 (5), 6603-6622.

Zueva, S., Ferella, F., Corradini, V., Vegliò, F., 2024. Review of organic waste-to-energy (OWtE) technologies as a part of a sustainable circular economy. Energies 17 (15), 3797.

IMPACT OF BIOCHAR ON GREENHOUSE GAS EMISSIONS: A LITERATURE REVIEW

Xiaona Wang[a], Enmiao Chen[a], Qunhui Wang[a], Dong Xu[c], Tianlong Zheng[b,*]

[a] Department of Environmental Engineering, School of Energy and Environmental Engineering, University of Science and Technology Beijing, 30 Xueyuan Road, Haidian District, Beijing 100083, PR China.

[b] State Key Laboratory of Environmental Aquatic Chemistry, Research Center for Eco-Environmental Sciences, Chinese Academy of Sciences, Beijing, 100085, PR China; University of Chinese Academy of Sciences, Beijing, 100049, PR China.

[c] Nanjing Institute of Environmental Sciences, Ministry of Ecology and Environment, Nanjing, 210042, PR China

ABSTRACT

Biochar, a product of biomass pyrolysis, can effectively reduce greenhouse gas (GHG) emissions. It has various economic benefits as a fuel and facilitates the zero-carbon production of biofuel. Furthermore it is an auxiliary fermentation material and, hence, can improve reaction conditions, increase the amount of methane generated during anaerobic digestion, and reduce GHG emissions during composting; the extent of GHG emission reduction varies across different fields. Previous studies have reviewed the characteristics, preparation, and application of biochar; however, only few have systematically described the specific contributions of biochar to the reduction of GHG emissions. This review aimed to synthesize recent advances in biochar application for the mitigation of greenhouse gas emissions. Our findings revealed that the effects of biochar on GHG are influenced by multiple factors, including the type of raw materials, pyrolysis conditions, and amount applied. Previous research on biochar predominantly focused primarily on its applications in the soil. Contradictory findings have been reported regarding the effects of biochar on soil carbon sinks. Future studies should focus on developing high-quality biochar production technologies, improving the recycling of aged biochar, and strengthening multi-scenario life cycle assessment to balance environmental benefits and economic costs and promote the sustainable application of biochar.

MECHANISM OF HEMICELLULOSE HYDROLYSIS BASED DFT AND MACHINE LEARNING

Sihao Li[1], Weiyun Wang[1]*, Can Zhou[1] , Chenrui Zhang[1] and Tianhua Yang[1]

(1 School of Energy and Environment, Shenyang Aerospace University, Shenyang, China))

ABSTRACT : Furfural, a byproduct of hemicellulose degradation, has emerged as a pivotal process in the conversion of low-value biomass into high-value chemicals, offering both economic and environmental advantages. This transformation has garnered significant attention within the domain of biomass chemistry, with intensive research efforts directed towards its optimization and commercialization. This study uses a combination of experimental methods and density functional theory (DFT) to examine the hydrolysis process that occurs during the alkali treatment of hemicellulose. It was determined that the cleavage of the covalent bond of hemicellulose constitutes a pivotal step in its hydrolysis, a phenomenon that has not been previously documented. The study utilized xylobiose as a model compound for hemicellulose, and the reactivity of the intermediates during hydrolysis, as well as their effects on the primary and secondary reactions, were elucidated by means of K-means clustering analysis in machine learning. Raman spectroscopy and X-ray photoelectron spectroscopy (XPS) analyses demonstrated that the glycosidic bonds within the reaction system underwent a gradual decrease with increasing temperature, thereby confirming the rupture of glycosidic bonds during the hydrolysis process.

KEYWORDS: hemicellulose hydrolysis, glycosidic bond cleavage, density functional theory, machine learning

1.Introduction

Fossil energy constitutes a significant component of the global energy landscape. However, the overexploitation of this resource has been shown to result in substantial greenhouse gas emissions[1]. Biomass energy, a crucial form of renewable energy, is imperative for the advancement of clean energy and the transition to a sustainable energy future.[2] Lignocellulose, a promising feedstock for the production of biobased fuels and chemicals, has emerged as a potential replacement for traditional fossil resources[3,4]. Lignocellulose is composed of three primary components: cellulose (35 - 45%), hemicellulose (15 - 30%), and lignin (20 - 30%)[5]. Hemicellulose is comprised of xylans, mannans, galactans, arabinoxylans, and other constituents[6]. Hemicellulose exhibits a high degree of versatility and can undergo hydrolysis to yield pentose or hexose sugars[7]. The latter can be converted into other value-added chemical products[8]. In particular, furfural, one of the end-products, has been recognized by the U.S. Department of Energy as one of the 12 most valuable platform compounds. Furfural's distinctive chemical structure suggests its potential for undergoing a series of chemical reactions, thereby yielding a multitude of chemical byproducts. This property is particularly significant in the domain of fine chemicals, where it serves as a notable example of converting and utilizing biomass resources[9]. The primary method of acquiring furfural involves the hydrolysis of hemicellulose, which is converted into xylose. Subsequent processing is then undertaken. However, this process is hindered by complex interactions between hemicellulose and cellulose in plant cell walls, which are achieved through hydrogen bonding, while hemicellulose is also connected to lignin through covalent bonds[10,11]. The complexity of these interactions impedes the efficient production and utilization of hemicellulose.

Hemicellulose, an amorphous polysaccharide polymer, exhibits limited processing and utilization efficiency, primarily due to the cross-linking structure between cell walls. By pre-treating to disrupt the chemical bonds between cell walls, intermolecular forces can be significantly reduced, while breaking the glycosidic bonds on the hemicellulose backbone lowers the degree of polymerization. This structural depolymerization effectively enhances the accessibility of polysaccharide chains, thereby increasing their reactivity in subsequent chemical conversions[12,13]. Hydrothermal treatment is used to preferentially extract hemicellulose from cellulose, hemicellulose, and lignin complexes[14]. The liquid resulting from hydrothermal treatment is predominantly composed of oligosaccharides and polysaccharides[15]. The solids that remain after pretreatment primarily contain cellulose

and lignin, which can undergo further conversion into valuable chemicals[16]. It is important to note that the observable processes of hemicellulose hydrolysis and xylose generation represent macroscopic manifestations of hemicellulosic glycosidic bond breakage. The study of hemicellulose covalent bond breaking is of great significance in revealing the mechanism of its hydrolysis.

Hemicellulose is a polysaccharide characterized by a structurally diverse and amorphous composition. Xylan has been identified as the predominant polysaccharide within the hemicellulose skeleton of diverse biomass types[17]. It is predominantly composed of xylose units that are linked by β-1,4 glycosidic bonds. Xylobiose, the cyclic structural unit of xylan, exhibits a multitude of chemical characteristics analogous to those observed in xylan-based hemicelluloses, including the presence of glycosidic bonds and adjacent xylose units. Therefore, xylobiose is frequently utilized as a model compound in lieu of hemicellulose for mechanistic analyses. This practice enables the comparison of the energy barriers of disparate initial reactions and facilitates the design of reaction pathways for pyrolysis processes in a more comprehensive manner.Ling et al[18] employed density functional quantum chemistry methods to simulate the conformation of wood polysaccharides using wood disaccharides and to compare their energy with that of fiber disaccharides. In a similar vein, Li et al[19]. employed xylobiose as a model compound for hemicellulose and investigated its pyrolysis behavior using a density-functional approach, in which the ring-opening of the xylobiose unit occurs at the initial stage of the reaction. However, extant theoretical studies have exclusively focused on the ring-opening reaction, neglecting to address the rupture of the glycosidic bond. However, it has been reported that the breaking of the glycosidic bond leads to the formation of a variety of important intermediate units that induce subsequent different reaction mechanisms and reaction pathways[20]. Li et al[21] therefore used xylobiose as a model compound for hemicellulose in order to study its pyrolysis pathway using a density-functional approach without discussing the specific role of the glycosidic bond therein. Bin et al[22] found that xylose and xylobiose were utilized as model compounds. A reaction network was constructed using a mechanically learned neural network potential. The study identified intermediates arising from glycosidic bond breaking. The inhibitory effect of glycosidic bonds on ring-opening reactions was revealed. Dehydration reactions were promoted, and the furfural formation pathways during pyrolysis of xylan were compared. However, it should be noted that the data were derived from machine simulations and were not combined with reality. Hu et al[23] combined the quantum chemical calculations and experiments to determine the pyrolysis characteristics and product distribution of hemicellulose by gas chromatography/mass spectrometry (Py-GC/MS). This approach revealed the mechanism of the rapid pyrolysis of xylobiose, xylobiose, and xyloglucan to yield 1,4-anhydro-d-xyloxypalmitoylglucose, furfural, and hydroxyglycolaldehyde. However, the investigation did not encompass an immersive discussion of the divergent reaction pathways within the process.Li et al[24] utilized xylobiose as a model compound and employed a density functional theory approach to theoretically investigate several pivotal reaction pathways in the pyrolysis of hemicellulose, including direct bond-breaking and inverse hydroxyaldol reaction, to systematically elucidate the effect of neighboring xylobiose on the pyrolysis mechanism of xylobiose. A notable absence in the extant literature pertains to the consideration of branched monosaccharides in xylan.

Conversely, Bin et al[25] conducted a thorough analysis of the similarities and differences in pyrolysis behaviors and mechanisms of the major branched monosaccharides in xylan, as influenced by variations in xylan structure. Pyrolysis, recognized as a highly effective decomposition method[26], has the capacity to convert a substantial quantity of biomass feedstocks into high-quality chemicals in the absence of oxygen[27]. Research conducted both domestically and internationally on the subject of hemicellulose pyrolysis has achieved a notable level of advancement. A number of hemicellulose pyrolysis mechanisms have been proposed, and the chemical pathways for the formation of the main products in the process of pyrolysis have been determined[28]. However, the pyrolysis products of hemicellulose are more numerous, and the yield of xylose is low. The products of hemicellulose hydrolysis are primarily concentrated in xylose[29]. Consequently, hydrolysis can enhance the utilization efficiency of hemicellulose in xylose production[30]. However, there have been no reported studies on the hydrolysis mechanism of hemicellulose during alkaline heat treatment.

This study investigates the reactivity of substances involved in in situ hydrolysis, focusing on the mechanistic pathways of hemicellulose hydrolysis during alkaline heat treatment. Xylodisaccharides serve as model compounds, with density functional theory (DFT) calculations employed to analyze reaction dynamics. Machine learning-assisted K-means clustering analysis further supported the exploration of transition states, intermediates, and reaction energy barriers in the xylose disaccharide hydrolysis process

under alkaline heat pretreatment conditions. Key functional groups and bond interactions in in situ hydrolysis are characterized, with experimental results exhibiting strong agreement with simulated data, thereby validating the theoretical framework.

2.Experimental Methods

The experimental corn stover was obtained from Dalian, Liaoning Province, China. The electronic analytical balance was procured from Sartorius Scientific Instruments (Beijing) Co. Ltd. The X-ray photoelectron spectrometer was obtained from Thermo Scientific K-Alpha, USA.

The experimental process is illustrated in Figure 1. Initially, the raw material, i.e., corn stover, was collected, subsequently ground, and then sieved through a 100-mesh sieve. Following this, the ground and sieved corn stover powder was baked and subsequently dried to room temperature. The dried corn stover powder (5 g) is introduced into the reactor, followed by deionized water (200 ml). Use NaOH to adjust the pH value to 8.The material and liquid are then thoroughly and evenly mixed using the balanced rotor. Subsequently, the reactor is secured and the exhaust valve is closed. The solid-liquid ratio of the dried corn stover powder to deionized water is 5 g/200 ml. The hydrolysis reaction should be set in the reactor to be processed at 150°C for 60 minutes, 120 minutes, 240 minutes, 300 minutes, 300 milliliters, and 150°C for 60 minutes, 120 minutes, 240 minutes, 300 minutes, and 300 minutes. The rotor should be set to 240 minutes, 300 minutes, 360 minutes, and the rotor should be set to "balanced" to ensure that the substances in the kettle are continuously and evenly mixed during the reaction. Subsequent to the completion of the reaction, the exhaust valve was opened, and the kettle was rapidly cooled to obtain the treated straw. The treated straw underwent a centrifugal process at a speed of 8,000 revolutions per minute for a duration of five minutes. Subsequent to this, a separation was conducted in which the bottom residue and liquid were disengaged from each other. Thereafter, the upper layer was filtered through a 0.45-micron organic filter membrane, resulting in the acquisition of the hydrolyzed upper layer.

3.Theoretical Calculation Methods

Materials Studio is a sophisticated molecular dynamics simulation software that boasts certain advantages in simulating the Newtonian motion of molecular systems. It is suitable for simulating a wide range of biological macromolecules and organic small molecules. Additionally, it is renowned for its highly accurate energy barrier calculations, which contributes to its predominance in the field of biomass mechanism simulation.

The K-means clustering algorithm of machine learning (ML) was used to analyze simulated data and determine the activity of different substances during in situ hydrolysis. The clustering results were analyzed to examine potential structural relationships between substances, revealing whether substances with different structures could continue to react and the type of reaction involved.It was implemented using the Eclipse software for Java programming. The global reactivity and single-point energy of all 126 substances were set as eigenvalues to construct the dataset, and it was iterated 100 times to convergence with the cluster setting of 3. The clustering results were then used to analyze the difficulty of continuing the reaction of the substances.

Quantum mechanical computational methods based on density-functional theory (DFT) are widely acknowledged as an effective means to elucidate the micro-mechanisms of reactions. At present, density functional theory (DFT) calculations are widely employed to elucidate the mechanisms of chemical reactions. However, there has been a decline in the number of DFT studies on hemicellulose hydrolysis in recent years.

In this paper, the primary focus is on the utilization of the DMol^3 module, which employs a linear combination of atomic orbitals to characterize the electronic states of a system. The most significant feature of DMol^3 that differentiates it from other methods is the utilization of numerical functions to describe the atomic orbitals.[31] This approach integrates computational accuracy and efficiency, and it can be employed for predicting the mechanism of a chemical reaction as well as solving the problems of catalyst design.[32] The electronic structure and transition states are analyzed computationally by means of its density-functional theory (DFT) based first principles.[33] Several studies have confirmed the feasibility of the DFT approach. The transition states are searched using TS Search. First principles are utilized to calculate and analyze the electronic structure and transition states.[34] The feasibility of the DFT method has been confirmed by several studies.[35] A transition state search was performed using TS Search. The reaction coordinates were determined based on the virtual frequency vibration modes derived from the initial path. The optimization method used was the synchronous transition state method (STQN) with convergence and validation criteria of 0.05 eV/Å and virtual frequency values <50 cm^{-1}, respectively. Hessian analysis was performed after each optimization step. The data and molecular models obtained from the calculations were analyzed and evaluated to eliminate interference terms in the virtual frequencies. This process yielded the correct transition state model and accurate energy barrier data.

In the molecular model optimization and computational simulation, corresponding adjustments are made according to the results of the software feedback. Ultimately, the appropriate optimization and computational parameters are obtained, and the target computational results are achieved. Basis set selection for molecular structure optimization:

Double Numerical + d-polarization (DND);functional selection: Generalized Gradient Approximation (GGA);gradient-corrected functional: PBE.Single-point energy and global reactivity are calculated using the generalized gradient approximation (GGA) at the theoretical level, with the basis set selected as Double Numerical + d/p-polarization (DNP).For transition state search calculations, the basis set is DNP (double numerical + d/p polarization), the functional is GGA, and the gradient-corrected functional is PBE,The SCF convergence standard is 1×10^{-5}Ha.The GGA-PBE functional strikes a good balance between computational cost and accuracy. For xylose (a large organic molecule) and hydrolysis reactions involving hydrogen bonding and proton transfer, PBE can accurately describe the electronic structure while maintaining low computational costs. This makes it suitable for medium-sized systems. PBE is a well-validated functional in condensed matter physics and chemistry. It is particularly suitable for solid-liquid interfaces, solution environments, and biomolecular systems. Its predicted reaction energy barriers and thermodynamic properties generally align with experimental trends. For reactions involving polar transition states, such as sugar hydrolysis, PBE can reasonably reflect changes in electronic structure along the reaction pathway.When performing a molecular reaction preview, set the maximum number of calculation points to 15 and the maximum number of cycles in electronic options to 50.

4.Results and Discussion

4.1.Machine Learning Clustering Analysis of Intermediate Reaction Activity in Hydrolysis Systems. Machine learning (ML) has demonstrated efficacy in the analysis of relationships between multidimensional data. [36-39] Consequently, ML can be utilized to study the classification of the activity of each intermediate in hemicellulose in situ hydrolysis systems. This allows for the determination of whether the different structural substances appearing during hydrolysis are able to continue the reaction and the type of reaction. The dataset was constructed by setting the global reactivity of intermediates such as oxonium ion intermediates, protonated post xylobiose, D-xylose, and xylobiose hydrate with single point energies as eigenvalues. The 126 intermediates(See the supplementary materials.) were subjected to 100 iterations to achieve convergence(At the 84th convergence), with a cluster setting of 3(Classified as easy, difficult, or extremely difficult to react). Cluster analysis employing machine learning methods was conducted to investigate the reactivity of these intermediates. Figure 2(a) presents the outcomes of K-means cluster analysis of 126 intermediates with global reactivity and single point energy (SPE) as feature vectors. In general, the closer the data point is to the upper left, indicating lower global reactivity and higher single point energy, the more probable the substance represented by that data point is to react. The results indicate that a mere fifteen intermediates are classified into the most reactive cluster 1, constituting a mere 12% of the total. The remaining intermediates demonstrate a comparatively lower propensity to persist in reacting. It is evident that the various positions of deprotonated xylobiose exhibited a reaction with 3-hydroxy-3-(2-((2,3,4,5-tetrahydroxypentyl)oxo)ethoxy)propionic acid (SR-1). The chemical compound, SR-2, is a 2,3-dihydroxy-3-(2-((2,3,4-trihydroxybutoxy)methoxy)ethoxy)propanal, and 2,3,4-trihydroxy-5-((4,5,6-trihydroxytetrahydro)). In Cluster 1, the most reactive substances are (4,5,6-trihydroxytetrahydro-(2hydro-pyran-3-yl)oxy)pentanal (SR-3).

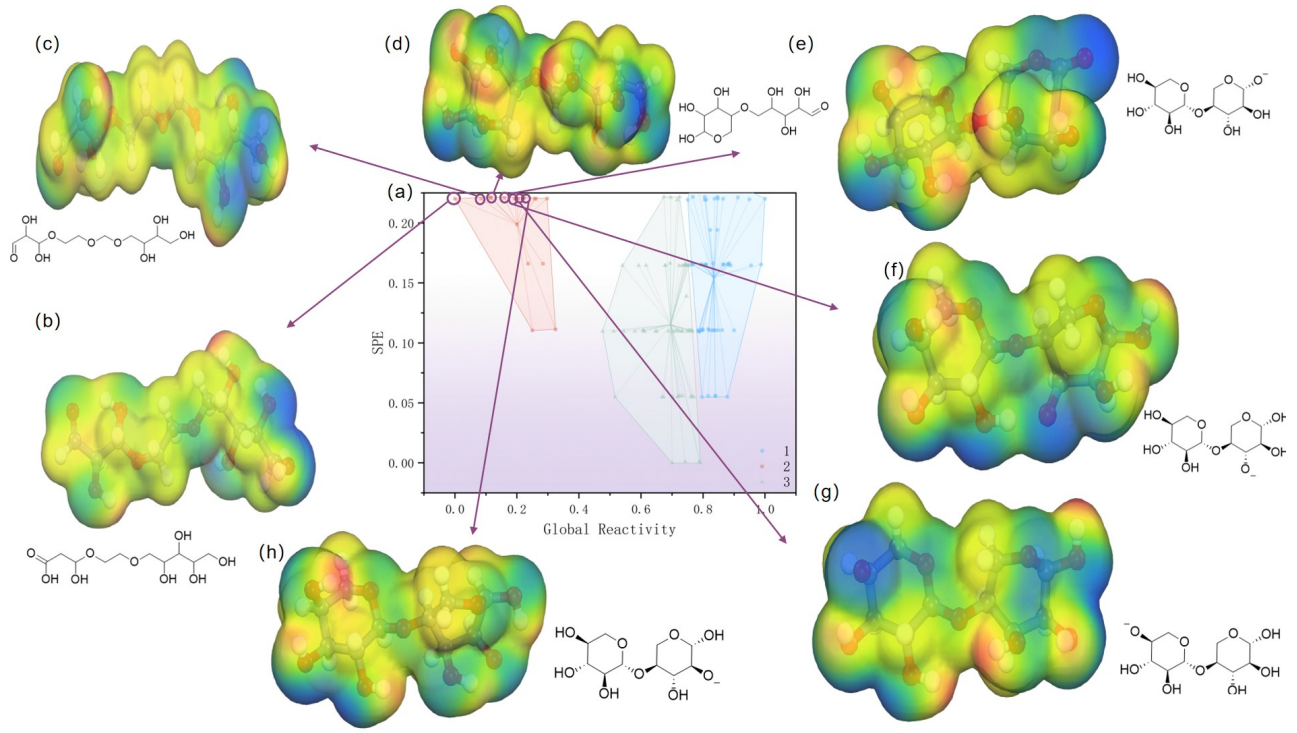

Figure 2. K-means cluster analysis and electrostatic potentials: (a) Clustering results of intermediates under the K-means algorithm; (b-h) electrostatic potentials of the seven most likely to continue reacting substances

The surface electrostatic potentials of deprotonated xylobioses at different positions (R-A, R-B, R-C, R-D) with respect to SR-1, SR-2, and SR-3 are depicted in Figure 2(b-h). The negatively charged regions of the deprotonated xylobiose, as depicted in Figure 2(e-h), are predominantly distributed in proximity to the deprotonated oxygen atoms when compared to SR-1, SR-2, and SR-3. This observation indicates that indirect deprotonation, resulting from the β-elimination reaction, leads to a modification in the local distribution of the electrostatic potential. This alteration leads to a redistribution of the electrostatic potential of the hydroxyl groups on the pyran ring, resulting in a substantial increase in the tendency to dissociate protons. In the un-deprotonated xylobiose, the electrostatic potential of O is relatively neutral and proton attack requires overcoming a higher energy barrier. Conversely, hydroxyl group deprotonation results in the transfer of negative charge through the molecular skeleton, leading to a significant decrease in the electrostatic potential around O. This decrease renders O more likely to attract protons, forming oxonium ions. The substantial accumulation of negative charges on the oxonium ions has been demonstrated to enhance the electron density of the glycosidic bonding oxygen atoms through an induced effect. This, in turn, has been shown to result in an increased polarity of the C-O bond, which is more prone to breakage. Consequently, deprotonated xylobiose exhibits a heightened negative electrostatic potential within the glycosidic bond region, thereby enabling the nucleophilic attack of reagents. Concurrently, the negative charge of the deprotonated hydroxyl group can stabilize the hydrolysis transition state through an intramolecular hydrogen bonding network. For instance, it can form a temporary hydrogen bond with the glycosidic bonding oxygen atoms, which assists in the hydrolysis of the oxonium ion intermediates in the charge off domain and reduces their energy, thereby facilitating the reaction. Conversely, it is evident that Fig. 2(e-h) represent single hydroxyl group deprotonations, while multiple hydroxyl group deprotonations of xylobiose are distributed in the less reactive clusters 2 and 3. This phenomenon can be attributed to the enhanced intramolecular electrostatic repulsion that occurs when multiple hydroxyl groups are deprotonated concurrently. This enhanced repulsion can result in the distortion of the sugar ring conformation. Furthermore, it can impede the approach of protons or water molecules, thereby reducing the hydrolysis efficiency.

Subsequently, the dissociation energies, global reactivities, and electron transfers for the continued reactions of the seven most reactive substances mentioned above were analyzed further, as illustrated in Figure 3. As illustrated in Figure 3(a), it is evident that only the dissociation energy of SR-2 is negative, while the remaining substances exhibit positive dissociation energies. This suggests that SR-2 is highly unstable in terms of dissociation energy, with the potential to spontaneously disrupt the chain. As illustrated in Figure 3(c), the electron transfer of the broken chain of SR-2 is evident. The electron transfer from the second hydroxyl group on the left to the ether bond in the middle is 0.0107. The electron transfer process results in the dissociation of the ether bond, leading to the dissociation of

SR-2 into an aldehyde and an alcohol. The two substances must undergo a ring-forming reaction to continue the reaction to produce xylose. This process requires a significant amount of energy; therefore, the dissociation reaction of SR-2 is treated as a side reaction that affects the whole. For SR-1, which has a relatively low dissociation energy, electrons are transferred from the third hydroxyl group on the right to the ether bond in the middle with an electron transfer of 0.1048, as shown in Figure 3(b). The electron transfer process results in the dissociation of the ether bond, leading to the formation of two carbon chains within SR-1. These carbon chains require significant energy to transform into a pyran ring structure, thereby classifying this reaction as a side reaction. Conversely, the electron transfer from the hydroxyl group on the pyran ring to the glycosidic bond of SR-3, which contains a pyran ring, resulted in the dissociation of SR-3 into a pyran ring with an aldehyde, accompanied by an electron transfer of 0.2151, as illustrated in Figure 3(d). The electron transfer process is the most significant, and elevated electron transfer is frequently accompanied by elevated activation energy. Consequently, the continuation of the reaction is impeded by SR-3. As illustrated in Figure 3(e-h), the electron transfer of four distinct positions of deprotonated xylobiose reflects the electron flow from the deprotonated hydroxyl oxygen to the glycosidic bond during glycosidic bond breaking. This electron enrichment leads to glycosidic bond breaking and the formation of a new C-O covalent bond between the broken C and O atoms.It is evident from Figure 3(a) that R-B exhibits the lowest dissociation energy and global reactivity, along with the least amount of electron transfer. In accordance with the theory that the magnitude of electron transfer directly correlates with the thermodynamic favorability of a reaction,[40] it was ascertained that the most optimal deprotonation site for the reaction is R-B. All of the aforementioned electron transfer scenarios are consistent with the electrostatic potential scenarios depicted in Figure 2(b-h). These scenarios are shifted from the deprotonated hydroxyl position, where negative charges are aggregated, to the glycosidic bond.

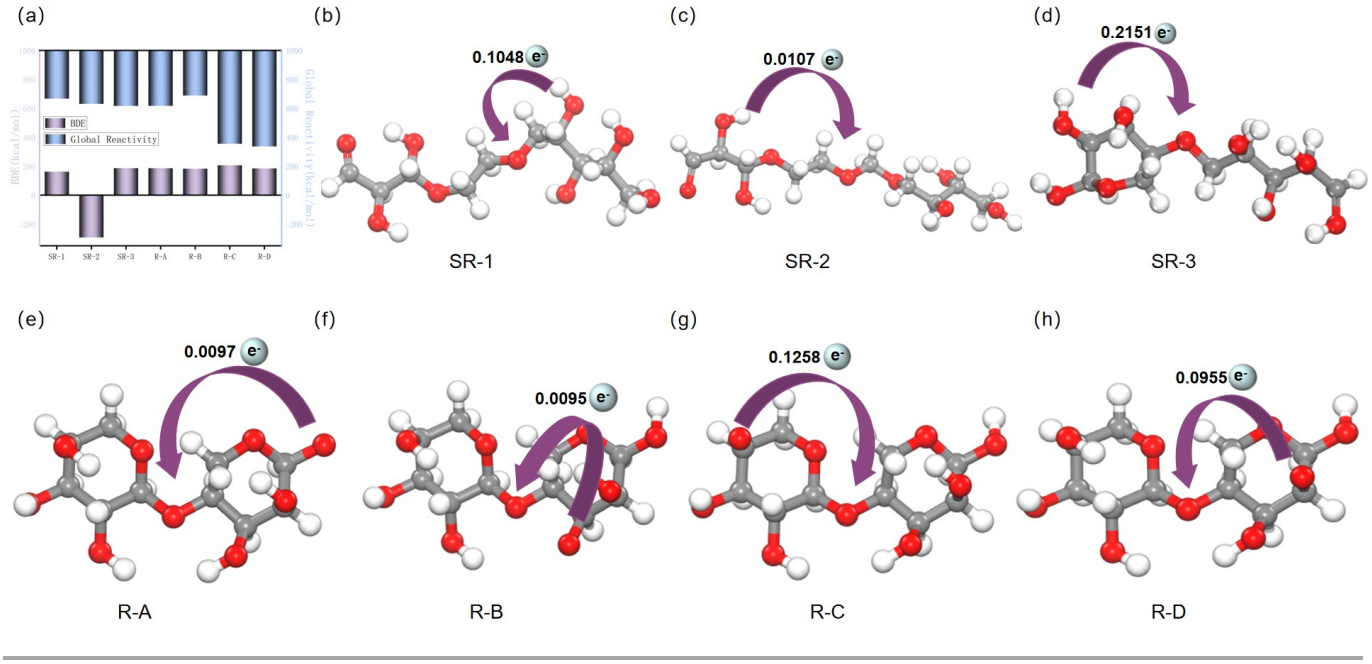

Figure 3. Dissociation energy versus global reactivity and electron transfer for different substances

4.2. Raman and XPS analysis of xylobiose hydrolysis during the hydrothermal pretreatment process. In order to ascertain the analog pathway for the conversion of xylobiose to xylose, X-ray photoelectron spectroscopy (XPS) analysis was conducted on the hydrolyzed products of xylobiose at the same temperature (423.15 K) for varying durations (60 min, 120 min, 240 min, 300 min, and 360 min).The XPS analyses are depicted in Figure 4. A characteristic peak indicative of C-O-C excitation manifested at approximately 286 electronvolts (eV). As the hydrolysis reaction time is extended, the characteristic peak formed by C-O-C gradually weakens, indicating a concomitant decrease in the content of C-O-C in the solution after the reaction. This peak only appears on the glycosidic bond in the structure of xylobiose. Therefore, it is congruent with the glycosidic bond found in xylobiose. As the hydrolysis reaction time was extended, the degree of hydrolysis increased gradually, resulting in the continuous breaking of the glycosidic bond. This, in turn, led to a gradual decrease in the characteristic peak area of C-O-C in the XPS plot. This demonstrated that the hydrolysis of xylobiose causes the breaking of glycosidic bonds, and thus the change path of hydrolysis of xylobiose to xylose was determined.

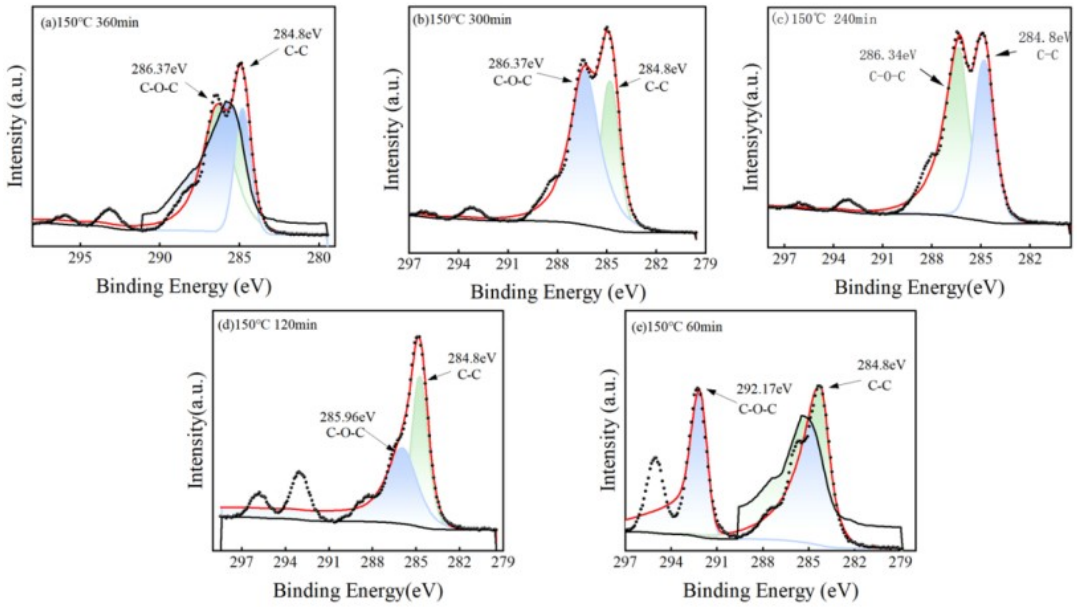

Figure 4. XPS photoelectron spectra of hydrothermal pretreatment of hemicellulose with different pretreatment times

Raman spectral analysis was carried out for different time periods (heating to 423.15 K, holding for 1h, holding for 2h, holding for 3h, holding for 4h, holding for 5h, holding for 6h) of the hydrolysis pretreatment of hemicellulose. The Raman spectral analysis is shown in Fig. 5. A large spectral band caused by glycosidic bond stretching vibration appeared near 1300 cm^{-1} . As the reaction proceeds, the vibrational peaks due to absorption tend to diminish, which indicates that the polymer is hydrolyzed. There is an absorption peak near 3400 cm-1 which may be the stretching vibrations of -CH_3, -CH_2 and -CH. As the holding time increases, the level of C-O-C group in the solution decreases, which corresponds to the glycosidic bond on the pyranose ring, and the vibrational peak tends to diminish due to the breakage of the glycosidic bond during the reaction, which is consistent with the X-ray photoelectron spectroscopy analysis above.

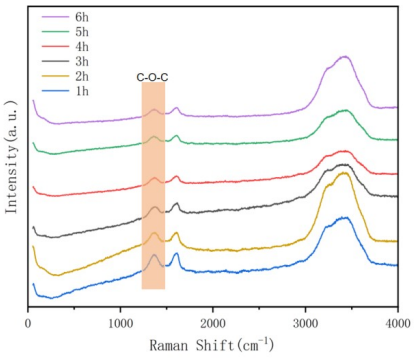

Figure 5. Raman spectra of hydrothermal pretreatment of hemicellulose with different pretreatment times

4.3.Construction of model compounds. In order to study the hydrolysis reaction mechanism of hemicellulose, it is necessary to obtain the conformation of hemicellulose. Xylobiose, a compound comprised of two pyran rings linked by a glycosidic bond[41], exhibits characteristics reminiscent of monosaccharides found in hemicellulose[42]. Additionally, it is noteworthy for its consideration of the interaction forces between monosaccharides[43], a feature that aligns it with the most reactive substance identified in the aforementioned machine learning model. Consequently, xylobiose was selected as the model compound for hemicellulose. The structural model of xylobiose was constructed in Materials Studio and calculated using DMol[3]. The most stable conformation of xylobiose was obtained after geometry optimization and frequency calculation. The molecular model of xylobiose, constructed and optimized, is displayed in Figure 6. The oxygen atoms are represented by red, the carbon atoms by gray, and the hydrogen atoms by white. This figure illustrates the stable molecular structure. The bond lengths have been enumerated and documented in Table 1.

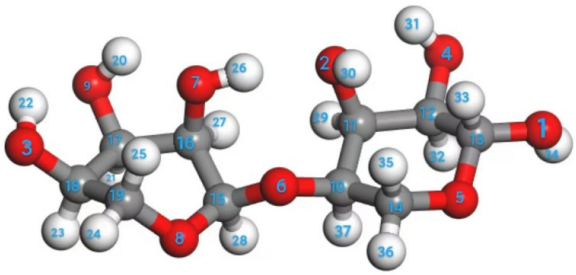

Figure 6. Optimized xylobiose molecules and their numbering

Table 1. Statistics on C-C and C-O bond lengths in the optimized structure of xylose

Bond	Length(Å)	Bond	Length(Å)
C10-C11	1.535	C13-O1	1.386
C11-C12	1.542	C11-O2	1.480
C12-C13	1.543	C12-O4	1.422
C10-C14	1.535	C13-O5	1.450
C15-C16	1.547	C14-O5	1.424
C16-C17	1.539	C10-O6	1.439
C17-C18	1.572	C15-O6	1.439
C18-C19	1.530	C18-O3	1.423
		C16-O7	1.435
		C15-O8	1.408
		C19-O8	1.443
		C17-O9	1.439

CONCLUSIONS

In summary, this thesis reveals the reactivity of intermediates and their effects on the primary and secondary reactions with the help of machine learning and employs a combination of experiments and density functional theory to reveal the mechanism of hemicellulose hydrolysis under hydrothermal pretreatment. K-means cluster analysis revealed that a mere 12% of the 126 intermediates were classified into the most reactive cluster (Cluster 1), in which deprotonated xylobiose (e.g., R-B) exhibited high reactivity. Electrostatic potential analysis demonstrated that the negative charge-enriched region of deprotonated hydroxyl groups facilitated the attack of nucleophilic reagents..

Corresponding Author

Weiyun Wang- College of Energy and Environment, Shenyang Aerospace University, Shenyang 110136, China; Key Laboratory of Clean Energy of Liaoning, Shenyang 110136, China

Email: cathywwy@sau.edu.cn

Acknowledgements

This work is supported by the National Natural ScienceFoundation of China (NSFC 52176195)

REFERENCES

(1) Koondhar, M. A.; Tan, Z.; Alam, G. M.; Khan, Z. A.; Wang, L.; Kong, R. Bioenergy Consumption, Carbon Emissions, and Agricultural Bioeconomic Growth: A Systematic Approach to Carbon Neutrality in China. *J. Environ. Manage.* **2021**, 296, 113242.

(2) Srirangan, K.; Akawi, L.; Moo-Young, M.; Chou, C. P. Towards Sustainable Production of Clean Energy Carriers from Biomass Resources. *Appl. Energy* **2012**, 100, 172–186.

(3) Paul, S.; Dutta, A. Challenges and Opportunities of Lignocellulosic Biomass for Anaerobic Digestion. *Resour. Conserv. Recycl.* **2018**, 130, 164–174.

(4) Zhang, L.; Li, Y.; Liu, X.; Ren, N.; Ding, J. Lignocellulosic Hydrogen Production Using Dark Fermentation by *Clostridium lentocellum* Strain Cel10 Newly Isolated from *Ailuropoda melanoleuca* Excrement. *RSC Adv.* **2019**, 9, 11179–11185.

(5) Zhou, M.; Tian, X. Development of Different Pretreatments and Related Technologies for Efficient Biomass Conversion of Lignocellulose. *Int. J. Biol. Macromol.* **2022**, 202, 256-268.

(6) Luo, Y.; Li, Z.; Li, X.; Liu, X.; Fan, J.; Clark, J. H.; Hu, C. The Production of Furfural Directly from Hemicellulose in Lignocellulosic Biomass: A Review. *Catal. Today* **2019**, 319, 14–24.

(7) Xiao, L.; Shi, Z.; Xu, F.; et al. Hydrothermal Treatment and Enzymatic Hydrolysis of *Tamarix ramosissima*: Evaluation of the Process as a Conversion Method in a Biorefinery Concept. *Bioresour. Technol.* **2013**, 135, 73–81.

(8) Huang, L.; Ma, M.; Ji, X.; Choi, S.; Si, C. Recent Developments and Applications of Hemicellulose from Wheat Straw: A Review. *Front. Bioeng. Biotechnol.* **2021**, 9, 1-14.

(9) Li, M.; Dong, X.; Zhang, N.; et al. Eco-Efficient Synthesis of 2-Quinaldic Acids from Furfural. *Green Chem.* **2019**, 21, 2234-2243.

(10) Mathews, S. L.; Pawlak, J.; Grunden, A. M. Bacterial Biodegradation and Bioconversion of Industrial Lignocellulosic Streams. *Appl. Microbiol. Biotechnol.* **2015**, 99, 2939–2954.

(11) Seidl, P. R.; Goulart, A. K. Pretreatment Processes for Lignocellulosic Biomass Conversion to Biofuels and Bioproducts. *Curr. Opin. Green Sustainable Chem.* **2016**, 2, 48–53.

(12) Periyasamy, S.; Karthik, V.; Senthil Kumar, P.; Isabel, J. B.; Temesgen, T.; Hunegnaw, B. M.; Melese, B. B.; Mohamed, B. A.; Vo, D.-V. N. Chemical, Physical and Biological Methods to Convert Lignocellulosic Waste into Value-Added Products. A Review. *Environ. Chem. Lett.* **2022**, 20, 1129–1152.

(13) Deng, W.; Feng, Y.; Fu, J.; Guo, H.; Guo, Y.; Han, B.; Jiang, Z.; Kong, L.; Li, C.; Liu, H.; et al. Catalytic Conversion of Lignocellulosic Biomass into Chemicals and Fuels. *Green Energy Environ.* **2023**, 8, 10–114.

(14) Gu, Y.; Zhang, X.; Deal, B.; et al. Correction: Advances in Energy Systems for Valorization of Aqueous Byproducts Generated from Hydrothermal Processing of Biomass and Systems Thinking. *Green Chem.* **2019**, 21, 1234–1245.

(15) Rivas, S.; Vila, C.; Santos, V.; et al. Furfural Production from Birch Hemicelluloses by Two-Step Processing: A Potential Technology for Biorefineries. *Holzforschung* **2016**, 70 (10), 901–910.

(16) Liu, L.; Chang, H.; Jameel, H.; et al. Furfural Production from Biomass Pretreatment Hydrolysate Using Vapor-Releasing Reactor System. *Bioresour. Technol.* **2018**, 252, 165–171.

(17) Wiederschain, G. Y. *Polysaccharides: Structural Diversity and Functional Versatility*. *Biochemistry (Mosc.)* **2007**, 72, 675–675.

(18) Ling, Z.; Edwards, J. V.; Nam, S.; Xu, F.; French, A. D. Conformational Analysis of Xylobiose by DFT Quantum Mechanics. *Cellulose* **2020**, 27 (3), 1207-1224.

(19) Li, Z.; Liu, C.; Xu, X.; Li, Q. A Theoretical Study on the Mechanism of Xylobiose During Pyrolysis Process. *Comput. Theor. Chem.* **2017**, 1117, 130–140.

(20) Zhou, X.; Li, W.; Mabon, R.; Broadbelt, L. J. A Critical Review on Hemicellulose Pyrolysis. *Energy Technol.* **2017**, 5, 52–79.

(21) Li, Z.; Liu, C.; Xu, X.; Li, Q. A Theoretical Study on the Mechanism of Xylobiose during Pyrolysis Process. *Comput. Theor. Chem.* **2017**, 1117, 130–140.

(22) Bin, H.; Wen-Ming, Z.; Xiao-Gang, W.; et al. The Formation Mechanism of Furfural in Xylan Pyrolysis: A Machine Learning Study Based on Neural Network Potential. *Fuel Process. Technol.* **2023**, 247, 107890.

(23) Hu, B.; Lu, Q.; Zhang, Z.; et al. Mechanism Insight into the Fast Pyrolysis of Xylose, Xylobiose and Xylan by Combined Theoretical and Experimental Approaches. *Combust. Flame* **2019**, 206, 177–188.

(24) Li, Z.; Liu, C.; Xu, X.; et al. A Theoretical Study on the Mechanism of Xylobiose during Pyrolysis Process. *Comput. Theor. Chem.* **2017**, 1117, 130-140.

(25) Bin, H.; Wen-Ming, Z.; Xue-Wen, G.; et al. Experimental and Computational Study on Xylan Pyrolysis: The Pyrolysis Mechanism of Main Branched Monosaccharides. *Fuel Process. Technol.* **2024**, 253, 107989.

(26) Tan, H.; Wang, S.-R.; Luo, Z.-Y.; Cen, K.-F. Pyrolysis Behavior of Cellulose, Xylan and Lignin. *Fuel Chem. Technol.* **2006**, 34, 61-65.

(27) Yin, C. Modelling of Heating and Evaporation of n-Heptane Droplets: Towards a Generic Model for Fuel Droplet/Particle Conversion. *Fuel* **2015**, 141, 64-73.

(28) Huang, J.; Liu, C.; Tong, H.; Li, W.; Wu, D. Theoretical Studies on Pyrolysis Mechanism of Xylopyranose. *J. Comput. Chem.* **2012**, 1001, 44–50.

(29) Periyasamy, S.; Karthik, V.; Senthil Kumar, P.; Isabel, J. B.; Temesgen, T.; Hunegnaw, B. M.; Melese, B. B.; Mohamed, B. A.; Vo, D.-V. N. Chemical, Physical and Biological Methods to Convert Lignocellulosic Waste into Value-Added Products. A Review. *Environ. Chem. Lett.* **2022**, 20, 1129–1152.

(30) Deng, W.; Feng, Y.; Fu, J.; Guo, H.; Guo, Y.; Han, B.; Jiang, Z.; Kong, L.; Li, C.; Liu, H.; et al. Catalytic Conversion of Lignocellulosic Biomass into Chemicals and Fuels. *Green Energy Environ.* **2023**, 8, 10–114.

(31) Zhang, Y.; Liu, C.; Chen, X. Unveiling the Initial Pyrolytic Mechanisms of Cellulose by DFT Study. *J. Anal. Appl. Pyrolysis* **2015**, 113, 621–629.

(32) Liu, C.; Zhang, Y.; Huang, X. Study of Guaiacol Pyrolysis Mechanism Based on Density Functional Theory. *Fuel Process. Technol.* **2014**, 123, 159-165.

(33) Zhang, Y.; Liu, C.; Xie, H. Mechanism Studies on β-D-Glucopyranose Pyrolysis by Density Functional Theory Methods. *J. Anal. Appl. Pyrolysis* **2014**, 105, 23-34.

(34) Zhang, Y.; Liu, C. A New Horizon on Effects of Alkali Metal Ions During Biomass Pyrolysis Based on Density

Functional Theory Study. *J. Anal. Appl. Pyrolysis* **2014**, 110, 297-304.

(35) Zhang, Y.; Liu, C.; Chen, X. Mechanism of Glucose Conversion in Supercritical Water by DFT Study. *J. Anal. Appl. Pyrolysis* **2016**, 119, 199-207.

(36) Ohyama, J.; Kinoshita, T.; Funada, E.; Yoshida, H.; Machida, M.; Nishimura, S.; Uno, T.; Fujima, J.; Miyazato, I.; Takahashi, L.; Takahashi, K. Direct Design of Active Catalysts for Low Temperature Oxidative Coupling of Methane via Machine Learning and Data Mining. *Catal. Sci. Technol.* **2021**, 11, 524-530.

(37) Sun, M.; Dougherty, A. W.; Huang, B.; Li, Y.; Yan, C. H. Accelerating Atomic Catalyst Discovery by Theoretical Calculations-Machine Learning Strategy. *Adv. Energy Mater.* **2020**, 10, 1903949.

(38) Artrith, N.; Lin, Z.; Chen, J. G. Predicting the Activity and Selectivity of Bimetallic Metal Catalysts for Ethanol Reforming Using Machine Learning. *ACS Catal.* **2020**, 10, 9438-9444.

(39) Zhong, M.; Tran, K.; Min, Y.; Wang, C.; Wang, Z.; Dinh, C.; De Luna, P.; Yu, Z.; Rasouli, A. S.; Brodersen, P.; Sun, S.; Voznyy, O.; Tan, C. S.; Askerka, M.; Che, F.; Liu, M.; Seifitokaldani, A.; Pang, Y.; Lo, S. C.; Ip, A.; Ulissi, Z.; Sargent, E. H. Accelerated Discovery of CO_2 Electrocatalysts Using Active Machine Learning. *Nature* **2020**, 581, 178–183.

(40) Koper, M. T. Thermodynamic Theory of Multi-Electron Transfer Reactions: Implications for Electrocatalysis. *J. Electroanal. Chem.* **2011**, 660, 254–260.

(41) Dai, Y.; Shao, C.; Piao, Y.; Hu, H.; Lu, K.; Zhang, T.; Zhang, X.; Jia, S.; Wang, M.; Man, S. The Mechanism for Cleavage of Three Typical Glucosidic Bonds Induced by Hydroxyl Free Radical. *Carbohydr. Polym.* **2017**, 178, 34–40.

(42) Yan, Z.; Lian, J.; Li, M.; Meng, L.; Zhang, Y.; Ge, C.; Lu, J. Deeper Insight into Hydrolysis Mechanisms of Polyester/Cotton Blended Fabrics for Separation by Explicit Solvent Models. *Int. J. Biol. Macromol.* **2020**, 154, 596–605.

(43) Loerbroks, C.; Rinaldi, R.; Thiel, W. The Electronic Nature of the 1,4-β-Glycosidic Bond and Its Chemical Environment: DFT Insights into Cellulose Chemistry. *Chem. Eur. J.* **2013**, 19, 16282–16294.

LIFE CYCLE ASSESSMENT OF THE EFFECTIVE UTILIZATION OF LOW-GRADE PLASTICS IN MELT SEPARATION SYSTEMS FOR MUNICIPAL SOLID WASTE INCINERATION AND NON-COMBUSTIBLE RESIDUES

Shuta Kawakami[1], Hirofumi Nakayama[2], Tohru Shibata[3], Shigenori Inoue[3] and Masahiro Osako[4]

1 Dept. of Civil Engineering, Graduate School of Engineering, Kyushu University,

744 Motooka, Nishi-ku, Fukuoka, Japan

2 Dept. of Urban and Environmental Engineering, Faculty of Engineering, Kyushu University,

744 Motooka, Nishi-ku, Fukuoka, Japan

3 Kubota Corporation, Water & Environment Research Institute, Water Environment R&D Department I, 1-1-1

Hama, Amagasaki, Hyogo 661-8567, Japan

4 National Institute for Environmental Studies, 16-2 Onogawa, Tsukuba, Ibaraki, Japan

Abstract: In the current waste management system, some low-grade plastics, characterized by material heterogeneity and contamination, are not being treated in an environmentally or economically optimal way. One promising method for utilizing these plastics is as a thermal input in the melt separation process for municipal solid waste incineration residues and non-combustible residues. In this study, we conducted a life cycle assessment (LCA) focused on Fukuoka Prefecture, designing a system in which low-grade plastics are used within the melt separation process. The assessment evaluated the system's impact on treatment costs, greenhouse gas emissions, and the volume of final disposal. The results showed that although CO_2 emissions increased by 38.2% compared to the current treatment system, the proposed system reduced treatment costs (by 34.5%) and final disposal volume (by 99.3%).

INTRODUCTION

The current plastic resource circulation system faces challenges, as a portion of low-grade plastics, those contaminated or composed of mixed materials, are not being treated in an environmentally or economically appropriate manner. In addition, although incineration residues and non-combustible residues from municipal solid waste contain valuable metals, many of these materials are still being disposed of in landfills. To address these challenges, attention was focused on the melt separation process as an effective method for recovering valuable metals from incineration and non-combustible residues while making effective use of low-grade plastics. In fact, there have been demonstration cases in which construction waste plastics were used as a substitute for heavy oil as the heat source in the melt separation process[1)].

In this study, a melt separation system was assumed for Fukuoka Prefecture, in which low-grade plastics are utilized as the thermal energy source to recover valuable metals from incineration and non-combustible residues.

The study then conducted a life cycle assessment (LCA) to evaluate the effects of introducing this system on treatment costs, CO_2 emissions, and the amount of final disposal.

MATERIALS AND METHODS

Collection and organization of information on low-grade plastics and melting target materials

In this study, as low-grade plastics for effective utilization, the following five types were selected.

(1) combustible residues generated from the crushing of municipal non-combustible and bulky waste (combustible residues)

(2) residues of separately collected container and packaging plastics as well as product plastics that are unsuitable for material recycling (separated plastic residues)

(3) combustible materials generated after the crushing and sorting of construction mixed waste (mixed construction residues)

(4) construction plastics primarily composed of PVC (construction PVC plastics)

(5) agricultural waste plastics used as mulching film and currently processed into fluff fuel (agricultural mulch plastics)

In addition, the following two types were selected as melting target materials.

(1) incineration residues from municipal solid waste (incineration residues)

(2) non-combustible residues generated from the crushing of municipal non-combustible and bulky waste (non-combustible residues)

For these seven types of waste, basic data necessary for the life cycle assessment (LCA) was collected and organized using the methods described below.

Collection of Statistical Data and Hearing Survey: Data on the annual generation and treatment flows of low-grade plastics and melting target materials were collected through a literature review and interviews with relevant business operators.

Characterization Analysis: For the sampled low-grade plastics and melting target materials, measurements of proximate composition, elemental composition, and higher heating value (HHV) were conducted. Based on these results, the lower heating value (LHV) was calculated. The results are presented in Figures 1–3 and Table 1.

For self-sustained melting in the surface melting furnace assumed in this study, the mixture fed into the furnace must have an LHV of at least 10 MJ/kg. Since all the investigated low-grade plastics exhibited LHVs exceeding 10 MJ/kg, they were considered suitable for use in the melt separation process.

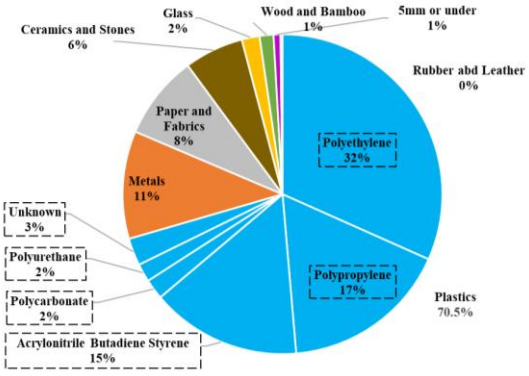

Figure 1. Composition of combustible residues

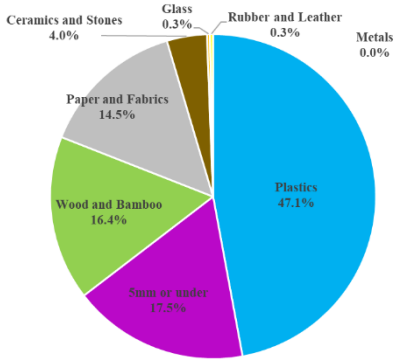

Figure 2. Composition of mixed construction residues

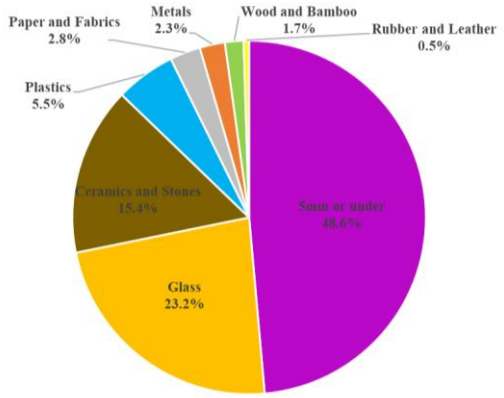

Figure 3. Composition of non-combustible residues

LCA of the effective utilization of low-grade plastics

Scenario settings for the LCA: The LCA target region is the entire Fukuoka Prefecture, and all incineration residues and non-combustible residues generated there are assumed to be processed by the melt separation system. Any surplus low-grade plastics beyond what the system can use are treated in the same manner as at present, even under the utilization scenario.

As functional units, three annual metrics within the scenario boundary for waste management were defined: life-cycle cost (LCC), life-cycle CO_2 (LC-CO_2), and the amount of final disposal. Figures 4 and 5 show the LCA scenarios and system boundaries. The LCA for this system refers to the methodology in Reference 2).

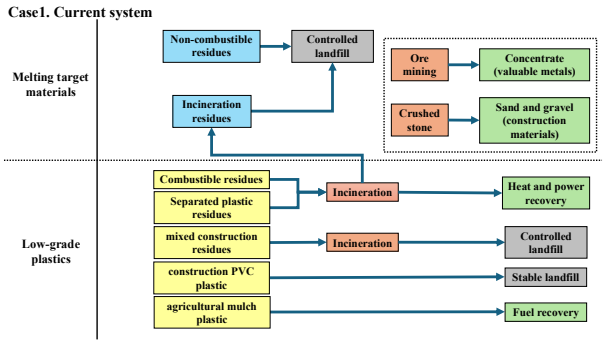

Figure 4. current system

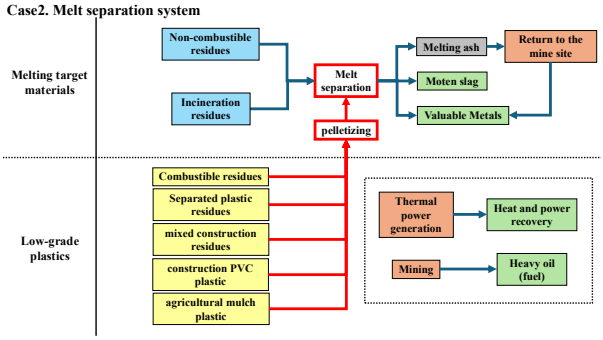

Figure 5. melt separation system

Results of the LCC Evaluation: Figure 6 shows the calculated LCC required for waste treatment within the scenario boundary. The results indicate that Scenario 1 (current system) amounts to 3,220 million JPY/year, whereas Scenario 2 amounts to 2,109 million JPY/year, representing a 34.5% reduction.

The main reason Scenario 2 became significantly more advantageous is that, although additional costs for the melt separation process and return to the mine site (4,307 million JPY/year) were incurred, cost reductions were achieved due to factors such as the substantial profits from the sale of recovered valuable metals (−3,368 million JPY/year) and the elimination of sanitary landfill disposal costs resulting from the volume reduction of incineration residues and other materials through melt separation (−2,684 million JPY/year).

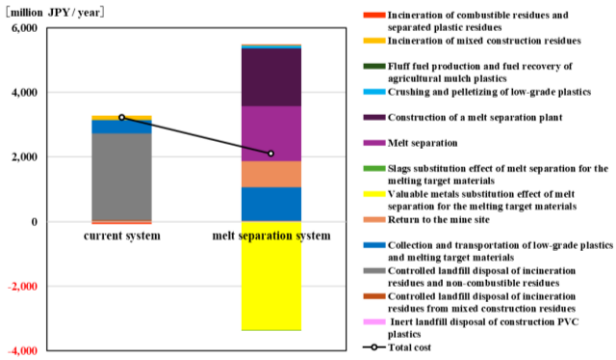

Figure 6. Results of the LCC calculation

Results of the LC-CO_2 Evaluation: Figure 7 shows the calculated LC-CO_2 for waste treatment within the scenario boundary. The results indicate that Scenario 1 (current system) is 1,308 hundred t-CO_2/year, whereas Scenario 2 is 1,809 hundred t-CO_2/year, representing a 38.2% increase. The increase in CO_2 emissions in Scenario 2 can be attributed to several factors, including the rise in direct CO_2 emissions from electricity consumption during the pelletizing of low-grade plastics and the melt separation process (124 hundred t-CO_2/year), the increase in indirect CO_2 emissions associated with the consumption of quicklime required to treat the chlorine content in PVC-dominated plastics (125 hundred t-CO_2/year), and the increase in indirect CO_2 emissions generated during the return to the mine site (97 hundred t-CO_2/year).

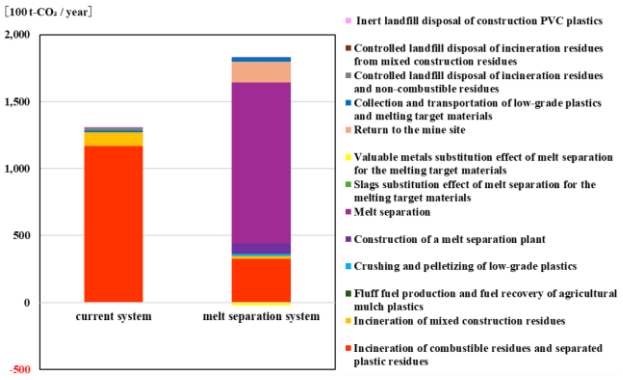

Figure 7. Results of the LC-CO_2 calculation

Results of Final Disposal Volume Evaluation: Figure 8 shows the final disposal volumes for the waste treatment system considered in this study. In Scenario 1, the final disposal volume is 134,257 t/year, whereas in Scenario 2 it is reduced to 1,003 t/year, representing a 99.3% reduction. In Scenario 2, the substantial decrease in disposal volume is due to the melt separation process, which converts most of the target materials into reusable slag or metals. This reduction is expected to provide significant social and environmental benefits, such as extending the lifespan of existing landfills and avoiding the construction of new disposal sites.

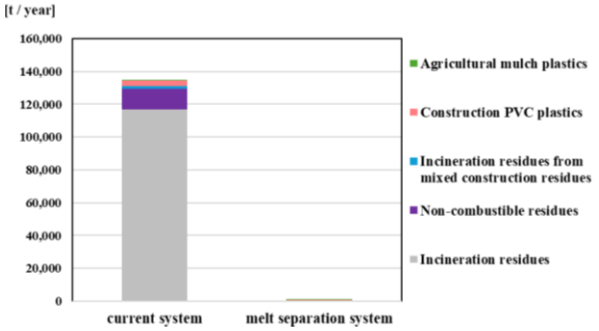

Figure 8. Results of the amount of final disposal calculation

Conclusion

・This system allows the effective use of previously hard-to-utilize low-grade plastics as a heat source in the melt separation process, avoiding extra CO_2 emissions from fossil fuels and enabling the recovery of valuable metals from incineration and non-combustible residues as urban mines.

・Although the annual CO_2 emissions increase by **38.2%**, the system can reduce treatment costs by **34.5%**. Furthermore, the annual final disposal volume can be reduced by **99.3%**, providing significant social and environmental benefits, such as extending the lifespan of landfills and avoiding the construction of new disposal sites. It should be noted, however, that the overall economic viability of the system is highly dependent on the valuable metal content in the incineration and non-combustible residues, as well as the market prices of these metals.

REFERENCES

1) Hosho, F. Inoue, S. Hirato, Y. and Sakamoto, M.: The Role of Melting and Separation Technology in Future Waste Management and Efforts Toward Its Implementation, Journal of Japan Waste Management Association, Vol.77, No.382, pp.618-628, 2024.
2) Matsuto, T.: Analysis, Planning, and Evaluation of Municipal Solid Waste Management Systems, *Gihodo*, 2005.

USING LARGE LANGUAGE MODELS AND MACHINE LEARNING TO ENABLE SUSTAINABLE ELECTROCHEMICAL CONVERSION OF BIOMASS-DERIVED HMF INTO VALUE-ADDED BHMF

Cheng Zeng[1], Zhichao Tan[1], Youcai Zhao[1,2,3*], Tao Zhou[1,2*]

1 The State Key Laboratory of Pollution Control and Resource Reuse, School of Environmental Science and Engineering, Tongji University, 1239 Siping Road, Shanghai 200092, PR China

2 Shanghai Institute of Pollution Control and Ecological Security, 1515 North Zhongshan Road (No. 2), Shanghai 200092, PR China

3 Tianfu Yongxing Laboratory, Chengdu 610213, PR China

Abstract

Electrochemical hydrogenation of 5-hydroxymethylfurfural (HMF) to 2,5-bis(hydroxymethyl)furan (BHMF) is a green route for biomass upgrading, but achieving high conversion with good selectivity is difficult. Here we present a computer-assisted workflow that combines large language models (LLMs), machine learning (ML), and Bayesian optimization to guide condition screening. Using GPT-4o, we extracted 248 reliable data points from over 300 published studies and built a dataset for model training. A neural network was then trained to predict HMF conversion and BHMF selectivity, reaching R^2 values of 0.824 and 0.927, respectively. SHAP analysis indicated that reaction kinetics strongly affected conversion, while electrode type dominated selectivity. With this model, Bayesian optimization proposed reaction conditions that balance conversion and selectivity. One validated experiment achieved 81.7% conversion and 52.1% selectivity, higher than reported results. This study highlights a practical human–machine approach to accelerate optimization of biomass-based electrochemical reactions.

Keywords

Biomass valorization; Sustainable electrosynthesis; Large language model (LLM); Machine learning (ML);

Biomass is a renewable alternative to fossil resources and a source of diverse platform molecules [1, 2]. Among them, 5-hydroxymethylfurfural (HMF) connects lignocellulosic sugars to valuable products. Its derivative, 2,5-bis(hydroxymethyl)furan (BHMF), is a versatile precursor for polymers and biofuels [3, 4]. Efficient and selective conversion of HMF to BHMF remains challenging [5].

Traditional hydrogenation uses high-pressure H_2 or chemical donors, often with safety risks and high cost [6, 7]. Electrocatalytic hydrogenation (ECH) provides a greener approach, using water as the hydrogen source under mild conditions [8]. owever, competing hydrogen evolution reaction (HER) lowers Faradaic efficiency, and strategies to suppress HER may reduce HMF conversion [15,16]. Optimizing both selectivity and conversion thus remains difficult [9].

Data-driven approaches can help. Machine learning (ML) captures complex variable interactions and supports reaction optimization [10, 11] [12]. Large language models (LLMs) can extract structured data from literature and combine with ML for condition discovery [13-15]. Integrating LLMs and ML has shown success in accelerating electrochemical reaction optimization [16].

Here, we develop an LLM–ML framework for HMF electroreduction to BHMF. Using structured prompts, experimental entries were extracted from over 300 publications. These data trained a neural network to predict conversion and selectivity, which was then combined with Bayesian optimization to identify promising conditions. One top-ranked condition was experimentally validated, demonstrating the framework's efficiency and mechanistic guidance.

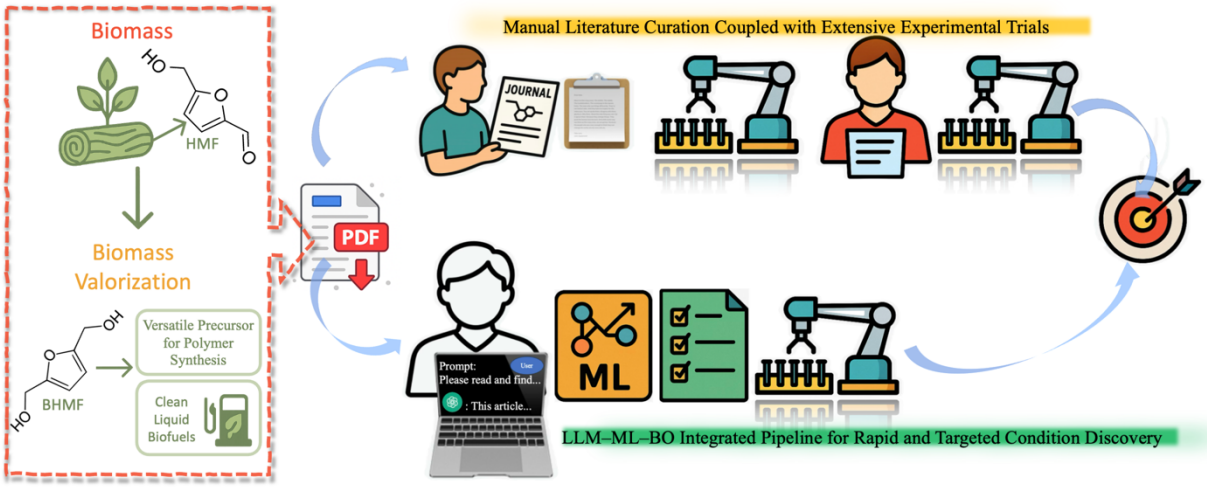

Figure 1. Overview

2. Results and Discussion

2.1 Literature Curation and Scope Definition

HMF electrochemical hydrogenation studies differ greatly in reporting style, figure conventions, experimental methods, and overall writing logic. Such variability makes automated extraction and LLM-based analysis difficult. This heterogeneity also complicates high-throughput literature mining with large language models (LLMs).

Recent LLMs, such as GPT-4o, can extract relevant chemical information from unstructured text, tables, and figures when guided by task-specific prompts. A key step is defining the reaction system clearly—here, HMF to BHMF. Many older studies report HMF and BHMF together under unclear conditions, while others focus on oxidation pathways (e.g., FDCA, FA, DFF) that are mechanistically unrelated. Including these studies would introduce noise and reduce model accuracy.

To ensure quality, we prioritized high-quality experimental studies from recent years and reputable journals (Figure S1, S2). We excluded reviews, non-electrochemical BHMF syntheses, and reports lacking sufficient experimental data. We also included two additional types of studies: (1) electrochemical hydrogenation of other biofuel intermediates where BHMF appears as a consistent side product, and (2) studies on electrode modifications with unmodified planar electrodes as controls. Eligible studies needed full reporting of electrochemical parameters, product distribution, HMF conversion, and BHMF quantification.

Using a two-stage prompting workflow with GPT-4o (Figure S4, S8), we extracted structured data from 378 publications. After filtering, normalization, and manual verification, we obtained 248 high-quality entries suitable for machine learning. Comparing prompt designs, the detailed prompt achieved an F1 score of 94.12%, outperforming a simple prompt at 57.14%, showing the importance of careful prompt engineering (Table S5, S6).

2.2 Model Performance Evaluation

The neural network was trained on 248 experimentally validated entries, split 80:20 for training and testing. Critical hyperparameters—including learning rate, batch size, and output loss weighting—were optimized via grid search. The best configuration used a learning rate of 0.01, batch size of 32, and a loss weight of 0.3 for HMF conversion and 0.7 for BHMF selectivity, emphasizing selectivity prediction.

On the held-out test set, the model showed strong predictive performance. Scatter plots of predicted versus experimental values were tightly clustered along the diagonal, indicating minimal bias (Figure 2a–b). The coefficients of determination reached 0.824 for HMF conversion and 0.927 for BHMF selectivity. These results confirm the model's ability to generalize across diverse electrochemical conditions and highlight the importance of weighted loss for prioritizing selectivity.

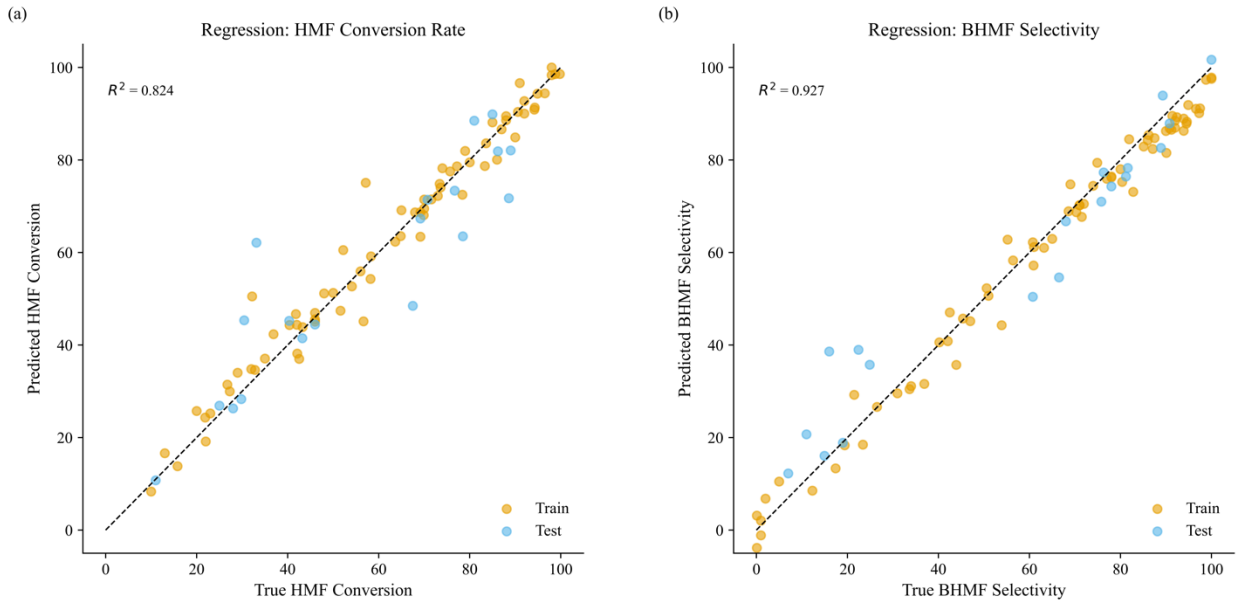

Figure 2. Regression parity plots of the neural network model for BHMF selectivity and HMF conversion. (a) Predicted versus true HMF conversion. (b) Predicted versus true selectivity for BHMF.

2.3 Model Interpretation

To understand the model's decision logic, SHAP (SHapley Additive exPlanations) analysis was performed using KernelExplainer. Summary plots for both outputs are shown in Figure 3a–b.

For HMF conversion (Figure 3a), applied potential was the most influential variable, with more negative voltages increasing SHAP values, suggesting stronger cathodic driving force enhances reduction. Reaction time and solution pH were also important, both positively affecting conversion. Electrode area and electrode identity had smaller contributions but still supported interfacial reaction efficiency.

For BHMF selectivity (Figure 3b), the control pattern differed. Applied potential remained important but within a narrower effective range, indicating milder reduction favors selectivity. Copper electrodes (WE_Cu) enhanced selectivity, likely by stabilizing intermediates. Other factors such as reaction time, pH, and initial HMF concentration also contributed, reflecting microenvironment effects and competing pathways.

Aggregating SHAP values by feature type revealed distinct trends. For conversion (Figure 3c), continuous operational variables dominated (65.1%), while electrolyte type and electrode identity contributed 19.4% and 15.5%, respectively. In contrast, for selectivity (Figure 3d), electrode identity contributed the largest share (44.3%), exceeding continuous variables (39.1%) and electrolyte composition (16.6%). This highlights that conversion is mainly controlled by tunable operational parameters, whereas selectivity is strongly influenced by catalyst properties and solution microenvironment.

Overall, SHAP analysis provides a mechanistic view of model behavior: conversion depends on electrochemical kinetics, while selectivity is more sensitive to electrode and microenvironment factors. These orthogonal dependencies emphasize the need for multi-objective optimization when designing HMF-to-BHMF electrochemical processes.

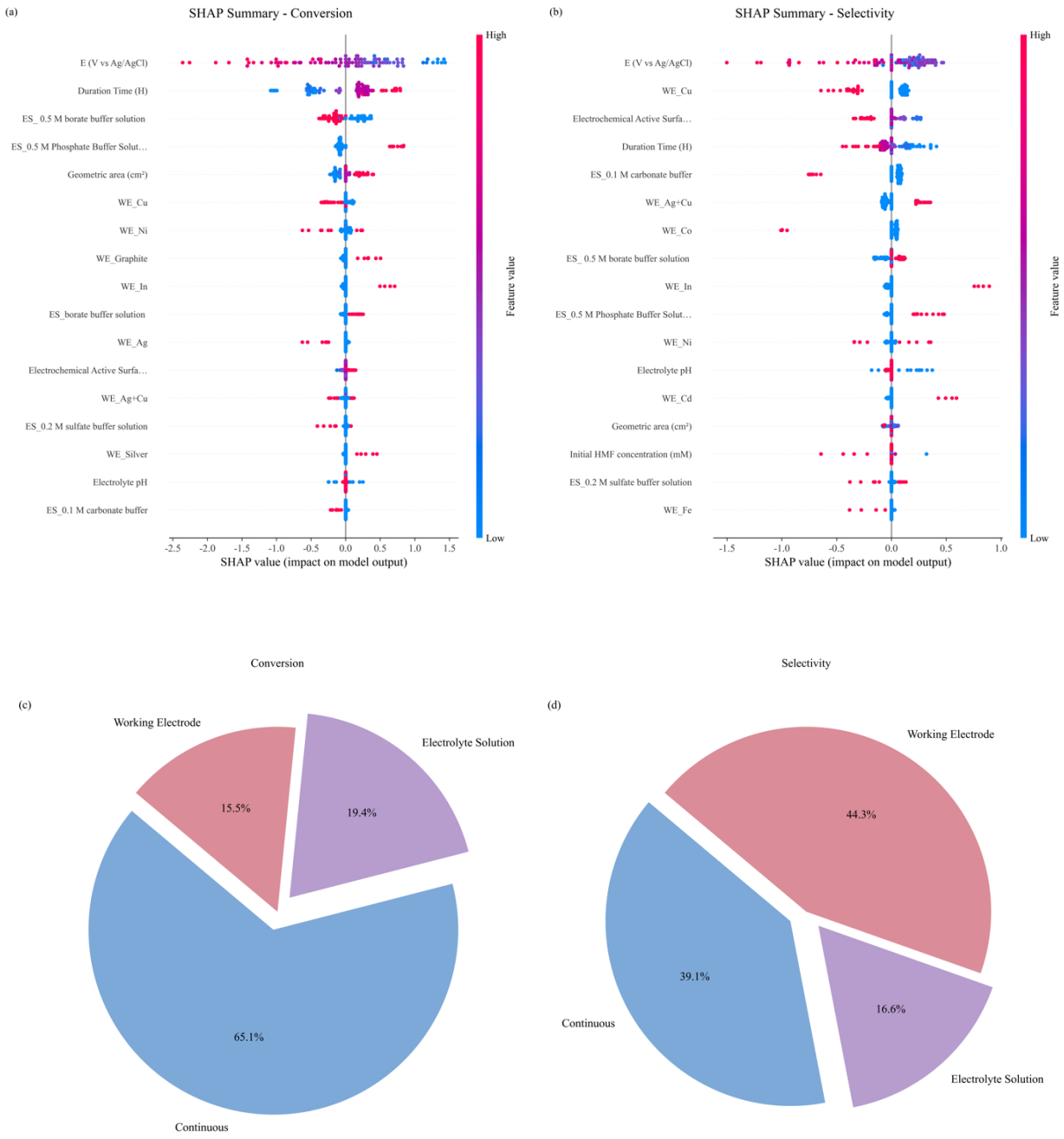

Figure 3. SHAP-based model interpretation for the prediction of HMF conversion and BHMF selectivity. (a, b) SHAP summary plots for conversion and selectivity prediction, respectively; (c, d) Grouped SHAP importance by feature category for conversion and selectivity models, respectively.

2.4 Model-Based Condition Recommendation and Optimization

To explore electrochemical conditions that optimize both HMF conversion and BHMF selectivity beyond the original experimental dataset, we leveraged the previously trained multi-output regression model as a predictive engine. Input features were processed using the same standardization and one-hot encoding procedures as during model training. Continuous variables were scaled according to the feature-wise normalization parameters from the training dataset, while categorical variables—such as electrode material and electrolyte identity—were transformed using one-hot encoding. Model outputs were inverse-transformed to the original units (%) for interpretability.

Condition screening was performed using Optuna in a global optimization framework. The search space was constrained to experimentally feasible ranges for all input variables (Figure S13). The objective function was defined as a weighted linear combination of conversion (0.7) and selectivity (0.3). At each trial, Optuna sampled a candidate condition, encoded it, and predicted the corresponding HMF conversion and BHMF selectivity. A total of 10,000 trials were executed, resulting in a comprehensive exploration of the multidimensional condition space. The top 10 configurations were archived (Table S7), from which a representative condition was selected for experimental validation.

The recommended configuration, Cu–Car, was absent from the original dataset and represented a balanced solution in terms of both conversion and selectivity. Experimental validation was conducted via a 4-hour electrochemical hydrogenation run, benchmarked against two reference systems, C-Car and Cu–Bo, selected for their chemical similarity and documented performance. All experiments employed identical setups and analytical protocols to minimize procedural variability (see Experimental Section). Complete experimental conditions are summarized in Table S8.

As shown in Figure 4, the Cu–Car configuration achieved a BHMF selectivity of 52.08% at 2 h, while HMF conversion reached 81.70% at 4 h. Although the conversion was slightly lower than C-Car (91.85%) and higher than Cu–Bo (33.67%), the Cu–Car configuration offered the most favorable balance between conversion and selectivity. In contrast, the benchmark systems showed only modest increases in selectivity, reaching 10.70% (In–Car) and 9.27% (Cu–Bo) at 4 h, indicating less favorable product specificity.

These results highlight the potential of machine learning-guided optimization to navigate complex, multivariable electrochemical systems. The model identified a compensated condition across electrode–electrolyte combinations that was not evident from the original training data. This data-driven approach accelerates electrosynthetic discovery by prioritizing experimental effort toward high-potential regions of the condition space and balancing intrinsic trade-offs between conversion efficiency and product selectivity.

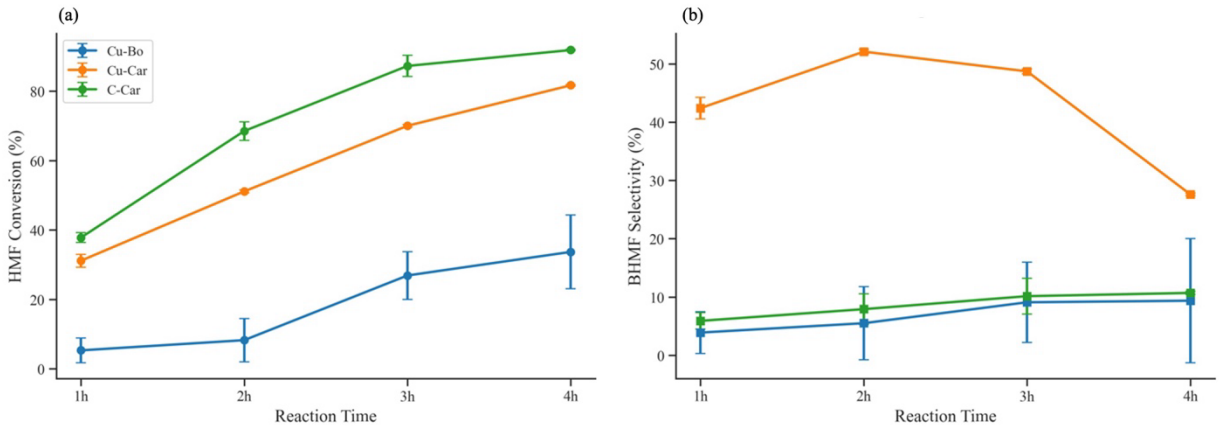

Figure 4. Time-dependent (a) HMF conversion and (b) BHMF selectivity over different catalysts for electrochemical hydrogenation.

3. Conclusions

We developed an integrated workflow combining large language models (LLMs) and interpretable machine learning (ML) to address the conversion–selectivity trade-off in the electrochemical hydrogenation of 5-hydroxymethylfurfural (HMF) to 2,5-bis(hydroxymethyl)furan (BHMF). A GPT-4o-driven pipeline curated 248 high-quality experimental entries from 378 publications, enabling robust training of a dual-output neural network with strong predictive performance (R^2 = 0.824 for HMF conversion; 0.927 for BHMF selectivity).

SHAP analysis elucidated orthogonal control mechanisms: conversion is mainly governed by applied potential, reaction time, and pH, reflecting electrochemical kinetics, while selectivity is more sensitive to electrode identity, solution composition, and microenvironmental factors, emphasizing interfacial effects. Response surface modeling revealed

multivariable compensation phenomena—including electrode area, buffering capacity, and substrate concentration—that mitigate the inherent trade-offs between conversion and selectivity.

Guided by these mechanistic insights, Bayesian optimization using Optuna identified a Cu–Car system predicted to achieve a favorable balance of conversion and selectivity. Experimental validation confirmed the model's predictive accuracy, with the selected condition showing superior BHMF selectivity (52.08%) at 2 hours and high HMF conversion (81.70% at 4 hours), outperforming benchmark systems (C-Car and Cu–Bo) in terms of product specificity without compromising conversion.

Collectively, this end-to-end framework—transforming heterogeneous literature data into mechanistically interpretable, experimentally validated recommendations—provides a scalable approach to accelerate selective electrosynthesis. Our study demonstrates a promising human–machine collaborative paradigm for efficient experimental optimization and advancement of sustainable electrosynthetic strategies for biomass valorization, with broad implications for environmental engineering.

References

[1] Z.-J. He, K. Chen, Z.-H. Liu, B.-Z. Li, Y.-J. Yuan, Valorizing renewable cellulose from lignocellulosic biomass toward functional products, Journal of Cleaner Production 414 (2023). https://doi.org/10.1016/j.jclepro.2023.137708.

[2] I.K.M. Yu, J. Fan, V.L. Budarin, F.P. Bouxin, J.H. Clark, D.C.W. Tsang, NaCl-promoted phase transition and glycosidic bond cleavage under microwave heating for energy-efficient biorefinery of rice starch, Green Chemistry 22(21) (2020) 7355-7365. https://doi.org/10.1039/d0gc01761b.

[3] I. Elsayed, M.A. Jackson, E.B. Hassan, Catalytic hydrogenation and etherification of 5-Hydroxymethylfurfural into 2-(alkoxymethyl)-5-methylfuran and 2,5-bis(alkoxymethyl)furan as potential biofuel additives, Fuel Processing Technology 213 (2021). https://doi.org/10.1016/j.fuproc.2020.106672.

[4] A. He, L. Hu, Y. Zhang, Y. Jiang, X. Wang, J. Xu, Z. Wu, High-Efficiency Catalytic Transfer Hydrogenation of Biomass-Based 5-Hydroxymethylfurfural to 2,5-Bis(hydroxymethyl)furan over a Zirconium–Carbon Coordination Catalyst, ACS Sustainable Chemistry & Engineering 9(46) (2021) 15557-15570. https://doi.org/10.1021/acssuschemeng.1c05618.

[5] X. Luo, C. Xie, Z. Zhao, M. Shi, H. Zheng, Optimization of Electrochemical Reduction of Biomass Derived 5-Hydroxymethylfurfural (HMF): A Volcano Plot and Bimetallic Catalysts, ChemSusChem 17(20) (2024) e202400723. https://doi.org/10.1002/cssc.202400723.

[6] W. Zhang, J. Liu, H. Gu, C. Pan, Y. Long, Q. Cheng, G. Fan, Transfer hydrogenation of 5-Hydroxymethylfurfural to 2,5-dihydroxymethylfuran by synergistic catalysis with a mixture of ZIF-8 and UiO-66-NH2, Renewable Energy 240 (2025). https://doi.org/10.1016/j.renene.2024.122148.
[7] H. Wang, C. Zhu, D. Li, Q. Liu, J. Tan, C. Wang, C. Cai, L. Ma, Recent advances in catalytic conversion of biomass to 5-hydroxymethylfurfural and 2, 5-dimethylfuran, Renewable and Sustainable Energy Reviews 103 (2019) 227-247. https://doi.org/10.1016/j.rser.2018.12.010.
[8] Q. Hou, X. Qi, M. Zhen, H. Qian, Y. Nie, C. Bai, S. Zhang, X. Bai, M. Ju, Biorefinery roadmap based on catalytic production and upgrading 5-hydroxymethylfurfural, Green Chemistry 23(1) (2021) 119-231. https://doi.org/10.1039/d0gc02770g.
[9] X.H. Chadderdon, D.J. Chadderdon, T. Pfennig, B.H. Shanks, W. Li, Paired electrocatalytic hydrogenation and oxidation of 5-(hydroxymethyl)furfural for efficient production of biomass-derived monomers, Green Chemistry 21(22) (2019) 6210-6219. https://doi.org/10.1039/c9gc02264c.
[10] X. Chen, W. Ma, F. Zheng, Z. Wang, C. Hua, Y. Li, J. Wu, B. Li, J. Jiang, C. Yan, T. Petaja, F. Bianchi, V.M. Kerminen, D.R. Worsnop, Y. Liu, M. Xia, M. Kulmala, Identifying Driving Factors of Atmospheric N(2)O(5) with Machine Learning, Environ Sci Technol 58(26) (2024) 11568-11577. https://doi.org/10.1021/acs.est.4c00651.
[11] Y. Pan, T.W. Hua, R.Z. Sun, Y.Y. Fu, Z.C. Xiao, J. Wang, H.Q. Yu, Machine Learning-Assisted Optimization of Mixed Carbon Source Compositions for High-Performance Denitrification, Environ Sci Technol 58(28) (2024) 12498-12508. https://doi.org/10.1021/acs.est.4c01743.
[12] Z. Zheng, Z. He, O. Khattab, N. Rampal, M.A. Zaharia, C. Borgs, J.T. Chayes, O.M. Yaghi, Image and data mining in reticular chemistry powered by GPT-4V, Digital Discovery 3(3) (2024) 491-501. https://doi.org/10.1039/d3dd00239j.
[13] D.A. Boiko, R. MacKnight, B. Kline, G. Gomes, Autonomous chemical research with large language models, Nature 624(7992) (2023) 570-578. https://doi.org/10.1038/s41586-023-06792-0.
[14] Z. Zheng, O. Zhang, C. Borgs, J.T. Chayes, O.M. Yaghi, ChatGPT Chemistry Assistant for Text Mining and the Prediction of MOF Synthesis, J Am Chem Soc 145(32) (2023) 18048-18062. https://doi.org/10.1021/jacs.3c05819.
[15] Y. Kang, W. Lee, T. Bae, S. Han, H. Jang, J. Kim, Harnessing Large Language Models to Collect and Analyze Metal-Organic Framework Property Data Set, J Am Chem Soc 147(5) (2025) 3943-3958. https://doi.org/10.1021/jacs.4c11085.
[16] Z. Zheng, F. Florit, B. Jin, H. Wu, S.C. Li, K.Y. Nandiwale, C.A. Salazar, J.G. Mustakis, W.H. Green, K.F. Jensen, Integrating Machine Learning and Large Language Models to Advance Exploration of Electrochemical Reactions, Angew Chem Int Ed Engl 64(6) (2025) e202418074. https://doi.org/10.1002/anie.202418074.

PREDICTION OF AIRBORNE BACTERIAL CONCENTRATIONS AND IDENTIFICATION OF CRITICAL FACTORS IN CONTAMINATED WASTE FACILITIES: INSIGHTS INTO INTERPRETABLE MACHINE LEARNING MODELS

Yanyan Guo[1], Tao Zhou[1] and Youcai Zhao[1]
[1] The State Key Laboratory of Pollution Control and Resource Reuse, School of Environmental Science and Engineering, Tongji University, 1239 Siping Road, Shanghai 200092, PR China

Abstract
The efficient prediction of airborne bacterial concentrations is crucial for better understanding and management of environmental sanitation risks in waste facilities. Traditional linear models have proven inadequate in capturing the complex relationships governing the formation of airborne microorganisms. This study developed four machine learning (ML) models to estimate airborne bacterial concentrations in waste facilities regarding the combined dataset as input features. The results revealed that integrating environmental factors, gaseous pollutants, and microbial datasets as input features yielded an improved testing R^2 of 0.7369, with a random forest (RF) model identified as the best-performing algorithm. The bacterial populations on the surfaces and handles of waste containers were identified as the most influential parameters in the RF model. The optimal ranges of temperature (32-36 °C) and relative humidity (62%-80%), the optimal concentrations of ammonia (< 0.15 mg/m^3) and particulate matter 2.5 (0.01-0.07 mg/m^3), and the effective disinfection measures of slightly acidic electrolyzed water were recommended for controlling airborne pollution in waste facilities. Overall, the research demonstrates that ML methods have the potential in the prediction of airborne bacterial concentrations in waste facilities. By identifying critical factors with the interpretability analysis, this study offers valuable insights for targeted airborne microorganisms' risk management strategies.

Keywords
Airborne bacteria; Waste facilities; Machine learning; Microbial dataset; Interpretability analysis

1. Introduction

The proliferation of various microorganisms in municipal solid waste (MSW) is mainly attributed to its rich organic matter and complex substrate composition, making it an important "microbial pool" (Guo et al., 2024). Recent studies indicate that MSW can serve as "hubs" for pathogens and act as carriers for pathogenic microorganisms (Lin et al., 2022; Zhang et al., 2024). During the waste recycling process, these microorganisms adhere to dust particles and are subsequently released into the atmospheric environment, contributing to the formation of bioaerosols. The resulting aerosols contain bacteria, fungi, and cell by-products, which have potential infectivity and sensitization (Tao et al., 2022). The inhalation of aerosols poses significant health risks to people with weakened immunity (Yu et al., 2021).

Kim et al. (2025) have demonstrated that airborne bacterial concentrations are affected by various environmental factors, which can provide conducive or inhibitory conditions for bacterial proliferation. Strategies for controlling airborne microbial contamination require a thorough understanding of how environmental factors impact their concentrations. Environmental variables such as temperature (T) and relative humidity (RH) were considered significant factors that impact the indoor bioaerosol concentrations (Lee et al., 2023). Wan et al. (2024) also revealed that air moisture had a direct positive impact on airborne bacterial concentrations in urban forests. Water plays a critical role in bacterial activity. Within a specific range, higher humidity levels can enhance bacterial growth.

However, few studies have explored the correlations between environmental factors and airborne microbial concentrations for predictive purposes (Jing et al., 2025; Mallik et al., 2025). Most previous studies relied on linear regression models to predict airborne microbial concentrations (Xu et al., 2022). However, comprehending the dynamics of airborne microorganisms in waste facilities is challenging because the airborne microbial concentrations vary both spatially and temporally. The simultaneous variations of multiple environmental parameters further complicate the identification of causal relationships (Hong et al., 2024). The linear assumption may not adequately capture the complex relationships governing the formation of airborne microorganisms.

Recently, machine learning (ML) models have gained prominence as effective tools for predicting microbial datasets (Yu et al., 2024). These models are particularly attractive for dissecting intricate nonlinear relationships. For example, Miao et al. (2022) indicated artificial neural network models performed excellently in predicting the concentrations of five enteric viruses in rivers based on physicochemical parameters as input features. Jiang et al. (2022) developed five ML models to predict the relative abundances of Vibrio spp. on

microplastics. The deep neural network model exhibited the highest predictive accuracy, achieving an average normalized root mean squared error (RMSE) of 12.16. Though ML methods have been increasingly utilized for microbial predictions, limited studies have attempted to predict airborne microbial concentrations in waste facilities based on involved environmental and microbial parameters.

To address this gap, we have developed four ML models that predict airborne bacterial concentrations using environmental factors, gaseous pollutants, and microbial factors as input features. Additionally, the Shapley additive explanation (SHAP) method and the partial correlation analysis have been utilized to elucidate the relationships between predictors and predictions, as well as to assess the contributions of various predictors to the model's outputs (Feng et al., 2024). We believe that the integration of ML models with interpretability analysis enhances the dependability of model predictions, while also offering valuable insights that contribute to airborne microorganisms' risk management in waste facilities.

2. Materials and methods

2.1 Sample collection

The study was carried out in six waste sorting rooms of residential communities in Shanghai, China, with three of these rooms implementing disinfection measures of spraying slightly acidic electrolyzed water (SAEW). The waste sorting rooms were equipped with a spraying system comprising a high-pressure nozzle sprayer and several 150 mm diameter nozzles for spraying SAEW. SAEW, containing an available chlorine concentration of 50-100 mg/L, was applied every 30 min for 1 min each time. The microbial samplings were conducted for six discontinuous days during the summer season. The microbial samplings of airborne and object surfaces of waste containers were determined at 9:00 a.m., 12:00 a.m., 5:00 p.m., 7:00 p.m., and 9:00 p.m. Meanwhile, the environmental factors and gaseous pollutants were also monitored during the microbial sample collection.

2.2 Analytical methods

Ammonia (NH_3, mg/m^3) was analyzed by an ultraviolet visible spectrophotometer (UVmini-1285, Shimadzu, Japan). $PM_{2.5}$ (mg/m^3) was determined using a dust concentration determinator (8532, TSI, USA). T (°C) and RH (%) were measured using a temperature and humidity instrument (625, Testo, Germany). Wind speed (WS, m/s) was assessed using a thermal anemometer (405-V1, Testo, Germany). Atmospheric pressure (P, kPa) was measured using an aneroid barometer (DYM3, Fengyun, China).

Airborne bacteria were collected using microbial samplers with an average flow rate of 28.3 L/min and a sampling time of 5 min. Microbial samples from the waste containers were collected using sterile saline for the non-disinfection group and phosphate-buffered saline (PBS) for the disinfection group. Following sample collection, the microbial samples were quickly transported to the lab for further analysis.

The airborne bacteria on nutrient agar plates were incubated at 37 °C for 48 h. The airborne bacterial concentrations are measured in colony-forming units (CFU)/m³. The swab suspensions were serially diluted using sterile saline or PBS. 1.0 mL of serial dilutions were inoculated onto plate count agar for total bacterial enumeration (48 h at 37 °C), which is presented as CFU/cm^2.

2.3 Dataset pretreatment

The environmental factors include T, RH, WS, and P. The gaseous pollutants include $PM_{2.5}$ and NH_3. Microbial datasets include disinfection conditions and bacterial populations of residual waste containers surfaces (RW-S), wet waste containers surfaces (WW-S), residual waste containers handles (RW-H), and wet waste containers handles (WW-H). The environmental factors, gaseous pollutants, and microbial factors were selected as input features, and the airborne bacterial concentration was the output feature. The dataset comprising 162 data points was collected and utilized for ML models.

The disinfection conditions consist of non-disinfection and disinfection. The data of disinfection conditions were transformed into binary format, with 0 representing non-disinfection and 1 indicating disinfection. The other features were normalized using Equation (1):

$$X_{new} = \frac{X - X_{min}}{X_{max} - X_{min}} \quad (1)$$

2.4 Machine learning algorithms selection and evaluation

To capture the multifaceted impacts of combined dataset on airborne bacterial concentrations, four widely-used ML algorithms were applied in this study, including Random Forest (RF), Light Gradient Boosting Machine (LGBM), K-Nearest Neighbors (KNN), and eXtreme Gradient Boosting (XGBoost), all of which have exhibited high precision in various regression tasks across different prediction fields (Ding et al., 2024). For each ML algorithm, the hyperparameters were optimized using the grid search technique.

The original dataset was randomly divided into training and test sets with proportions of 0.85 and 0.15, respectively. RMSE and R^2 were chosen to evaluate the accuracy of ML models, as shown in Equation (2) and Equation (3), respectively (Wu et al., 2025).

$$RMSE = \sqrt{\frac{1}{n}\sum_{i=1}^{n}(y_i - \hat{y}_i)^2} \quad (2)$$

$$R^2 = 1 - \frac{\sum_{i=1}^{n}(y_i - \hat{y}_i)^2}{\sum_{i=1}^{n}(y_i - \overline{y_i})^2} \quad (3)$$

2.5 Interpretability analysis methods

The SHAP method serves as a tool for elucidating the predicted output results from ML models (Jiang et al., 2024; Lv et al., 2024). The partial dependence plots (PDPs) are used to visualize the results of partial correlation analysis. It illustrates how a specific feature correlates with the predicted outcome, assuming other features remain constant (Xia et al., 2024). In combination, SHAP and PDP offer important perspectives into model interpretability by providing comprehensive explanations of feature importance and their impact on predictions (Liu et al., 2025). **Fig. 1** presents the workflow of this study.

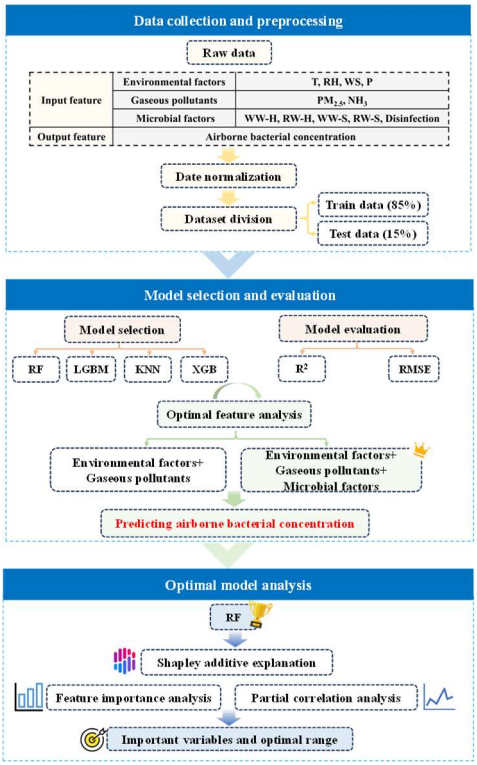

Fig. 1 The workflow of this study.

3. Results and discussion

3.1 Data descriptive statistics

The acquired data are presented in **Fig. 2**. The results showed the distributions of T, RH, WS, and P within the range of 25.4 °C to 40.2 °C (average = 31.6 °C), 48.4% to 95.6% (70.9%), 0.06 m/s to 1.48 m/s (0.43 m/s), and 100.2 kPa to 101.98 kPa (100.76 kPa), respectively. The average concentrations of $PM_{2.5}$ and NH_3 were 0.033 mg/m^3 and 0.16 mg/m^3, respectively. Regarding the microbial datasets, the average populations of bacteria on WW-S and WW-H were 6909 CFU/cm^2 and 25206 CFU/cm^2, respectively, on RW-S and RW-H were 8698 CFU/cm^2 and 24185 CFU/cm^2, respectively. And the average airborne bacterial concentration was 723 CFU/m^3.

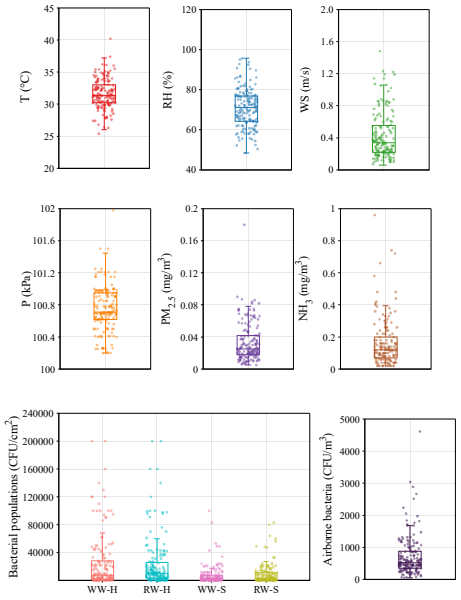

Fig. 2 Distributions of the parameters.

Fig. 3 shows the Pearson correlation coefficient matrix, which illustrates the correlation between the input and output variables. The absolute Pearson's correlation coefficient values ranged from 0 to 0.3, indicating no significant overlap between variables, which satisfied the ML model requirements (Bai et al., 2024; Wang et al., 2024a).

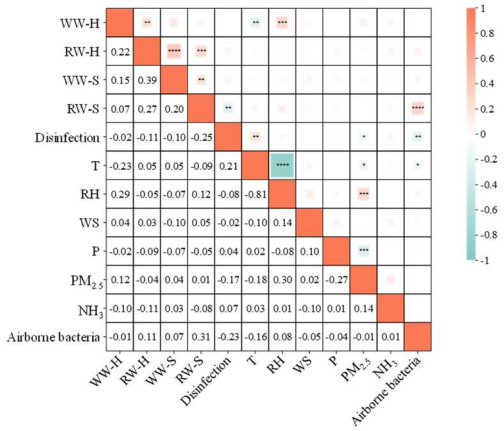

Fig. 3 Pearson correlation coefficient matrix between the parameters.

3.2 Prediction of airborne bacterial concentrations using environmental and gaseous dataset

In **Fig. 4**, the RF algorithm exhibited the best performance for the test dataset with R^2 of 0.6777 and RMSE of 186.7, but the KNN algorithm had the poorest accuracy (R^2 = 0.1085, RMSE = 590.2). It was observed that the R^2 for the training set was lower than that for the testing set in the KNN algorithm, suggesting the presence of an unusual overfitting issue. And the R^2 values of the LGBM (R^2 = 0.2087, RMSE = 326.9) and XGBoost (R^2 = 0.2862, RMSE = 398.2) algorithms were very close to each other.

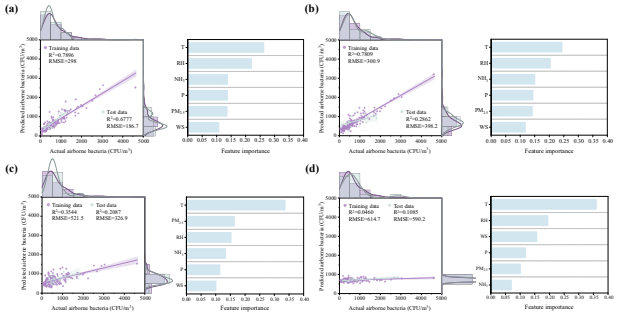

Fig. 4 ML model prediction results and feature importance analysis using environmental factors and gaseous pollutants as input features. (a) RF; (b) XGBoost; (c) LGBM; (d) KNN.

Additionally, each algorithm was used to evaluate the feature importance of various factors affecting airborne bacterial concentrations. In all four models, T and RH were consistently identified as the most crucial parameters with a weight of 24.37%-35.97% and 15.22%-21.98%, respectively. Cao et al. (2024b) found that T and RH were the key drivers influencing variations in microbial community structures of marine aerosols. Similarly, Núñez et al. (2021) reported that T and RH can impact the release, growth, and suspension of microorganisms, thereby affecting airborne microbial populations.

Overall, the ML algorithms using environmental and gaseous datasets resulted in relatively lower R^2 values. Guo et al. (2021) suggested that the object surfaces of waste containers in waste sorting rooms, due to frequent contact and organic matter accumulation, were prone to harboring large numbers of bacteria. These areas with high bacterial populations may be significant sources of airborne microbial contamination. The airborne bacterial concentrations in waste sorting rooms are not only influenced by external environmental factors but also directly affected by the dynamic changes in internal microbial reservoirs, such as the surfaces and handles of waste containers. Hence, the prediction accuracy was further evaluated by incorporating environmental factors and gaseous pollutants alongside microbial datasets as input features.

3.3 Prediction of airborne bacterial concentrations using combined dataset

As shown in **Fig. 5**, RF achieved the highest prediction accuracy (R^2 = 0.7369, RMSE = 304.2), followed by XGBoost (R^2 = 0.4202, RMSE = 236.6) and LGBM (R^2 = 0.4128, RMSE = 373.5). KNN had the worst performance, with testing R^2 of 0.1605 and RMSE of 469.9. This issue could stem from its constrained capacity to simulate complex interactions among various features and its high sensitivity to hyperparameter adjustments, making it potentially unsuitable for specific data variables and prediction tasks. RF algorithm is a typical and efficient ensemble learning technique. By aggregating the prediction results of numerous decision trees, RF typically yields higher accuracy compared to a single decision tree (Cao et al., 2024a). And RF avoids the risks of overfitting issues associated with a single decision tree and enhances model robustness through random features and samples selection during the training process. This approach improves generalization capability, making RF highly effective for complex and high-dimensional datasets (Zhao et al., 2024). Additionally, its robust feature selection mechanism helps reduce the impact of irrelevant or redundant variables, further enhancing predictive accuracy. RF exhibits strong predictive performance across diverse fields, such as environment species identification (Aviña-Hernández et al., 2023), biogas yield prediction in AD process (Long et al., 2021), and thermal desorption remediation efficiency prediction of contaminated soils (Chen et al., 2024). Overall, the optimal RF model has demonstrated reliable and accurate predictive capabilities for airborne bacterial concentrations, providing valuable insights for the management of airborne microorganisms' health risks in waste facilities.

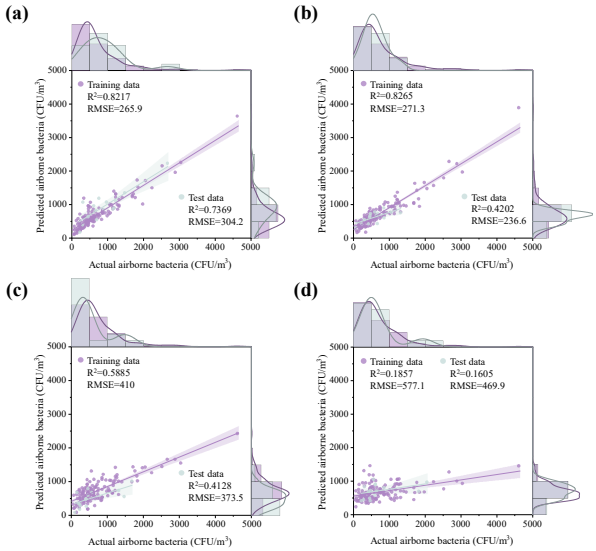

Fig. 5 The comparison graphs between the actual and predicted values of airborne bacterial concentrations from (a) RF; (b) XGBoost; (c) LGBM; (d) KNN.

The results also revealed that incorporating microbial datasets with environmental factors and gaseous pollutants led to superior prediction accuracy across all four models, outperforming the use of environmental and gaseous datasets alone (**Fig. 6**). Integrating additional levels of data knowledge improved the prediction performance of ML models.

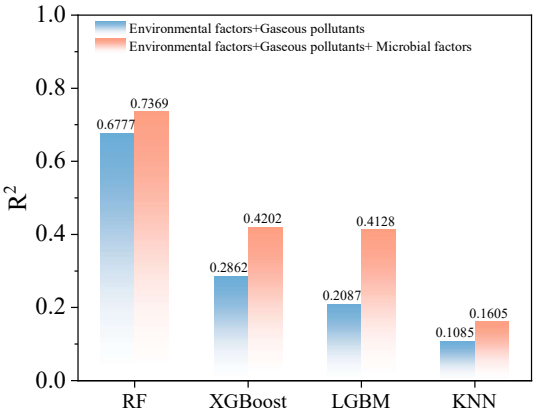

Fig. 6 Performance comparison of four models developed using different input features.

3.4 Interpretability analysis

Fig. 7a shows the SHAP features importance plot for the RF model, highlighting that microbial factors were the most influential category, contributing 53.4% of the impact on airborne bacterial concentrations, followed by environmental factors (31.5%) and gaseous pollutants (15.1%). The top four features affecting airborne bacterial concentrations were all from microbial datasets. The bacterial population of RW-S was the first critical variable for the prediction of airborne bacterial concentrations, followed by the WW-S, RW-H, and WW-H.

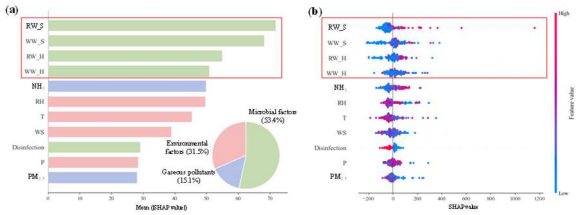

Fig. 7 (a) The SHAP features importance plot; (b) SHAP values summary plot based on the RF leader model.

Fig. 7b illustrates the SHAP values of features, where red points denote high feature values and blue points indicate low feature values. A positive SHAP value suggests that the corresponding feature positively impacts the output target. Specifically, a higher SHAP value indicates that the feature has a more significant influence (Aldrees et al., 2024). Additionally, the one-dimensional PDPs (**Fig. 8**) and two-dimensional PDPs (**Fig. 9**) were performed to reveal the specific impact of various input features on airborne bacterial concentrations.

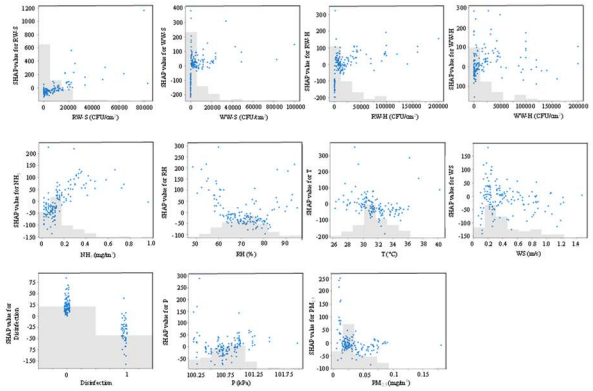

Fig. 8 Interpretability analysis of the RF model using one-dimensional PDPs.

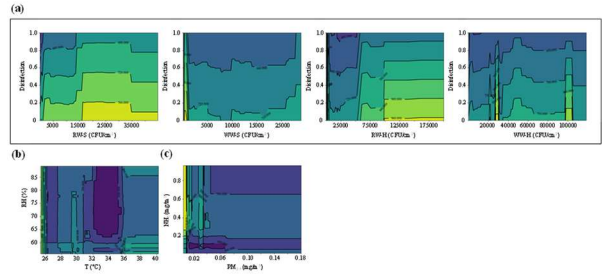

Fig. 9 Two-dimensional PDPs. (a) Disinfection conditions and bacterial populations of object surfaces; (b) RH and T; (c) NH_3 and $PM_{2.5}$.

As shown in **Fig. 7b**, high-intensity RW-S, WW-S, RW-H, and WW-H values (represented by blue points) were linked to the negative side, indicating a notable positive effect on airborne bacterial concentrations. Additionally, an upward trend in the SHAP values was observed with increasing bacterial populations on the surfaces and handles of waste containers, as depicted in **Fig. 8**. These findings demonstrated that accumulated bacterial populations of object surfaces had a favorable impact on the proliferation of airborne bacteria. According to **Fig. 7b** and **Fig. 8**, the SHAP values were negative in the disinfection group, whereas they were positive in the non-disinfection group. The results revealed that the airborne bacterial concentrations decreased if the disinfection equipment was installed in waste sorting rooms. From the interaction between disinfection conditions and bacterial populations of object surfaces in **Fig. 9a**, the effective disinfection efficiency of SAEW was also observed on object surfaces of waste containers. Guo et al. (2024) proved that SAEW as a novel disinfectant exhibited excellent effectiveness in controlling microbial contamination within waste sorting rooms. SAEW has the advantages of reducing equipment corrosion, limiting phototoxic side effects, and preventing human health and safety issues from Cl_2 off-gassing (Zhao et al., 2021).

The SHAP analysis indicated that T and RH had adverse effects on airborne bacterial concentrations, although these effects were less pronounced compared to microbial factors. As depicted in **Fig. 8**, the SHAP values

were negative when T ranged from 32 °C to 36 °C. These findings were in close agreement with the literature (Wang et al., 2024c), which indicated that high temperatures affected the metabolic activity of bioaerosols and decreased bioaerosol concentrations. Under such conditions, microorganisms may experience cell lysis and protein denaturation, further supporting the observed trends. When RH levels ranged from 62% to 80%, the SHAP values were initially negative but gradually became positive as RH increased. These findings suggested that excessively high RH levels positively influenced airborne bacteria. High humidity provides favorable conditions for microbial growth and metabolism. Furthermore, the optimal ranges of T (32-36 °C) and RH (62%-80%) for controlling airborne pollution in waste sorting rooms were also confirmed by the two-dimensional interaction analysis in **Fig. 9b**. The SHAP values distribution for the WS feature did not show a significant pattern, possibly due to similar ventilation occasions. Chen et al. (2025) reported that the ventilation condition was effective in lowering microbial concentrations within the environment. Specifically, ventilation can quickly eliminate microbial particles following the generation of aerosols, thereby improving air quality and reducing the potential for microbial exposure.

For gaseous pollutants features, the results showed significant differences in the SHAP values distribution. As can be seen from **Fig. 8**, the SHAP values were negative and positive when the concentrations of NH_3 were below 0.15 mg/m^3 and above 0.15 mg/m^3, respectively. NH_3 is a byproduct of the microbial decomposition of organic matter in the waste. Higher NH_3 concentrations (above 0.15 mg/m^3) indicate more active microbial decomposition processes, which could also foster the proliferation of specific microbial communities. At lower NH_3 concentrations (below 0.15 mg/m^3), microbial activity is less pronounced, leading to fewer bacteria being released into the air. In this case, the relationship between NH_3 and airborne bacteria may be negatively correlated. However, $PM_{2.5}$ caused a reduction in airborne bacterial concentrations when they exceeded 0.01 mg/m^3. $PM_{2.5}$ has the capacity to accumulate various pollutants and act as carriers for harmful components, potentially inhibiting bacterial growth (Wang et al., 2024b; Zhou et al., 2024). These particles may adsorb bacteria, leading to their sedimentation and consequently reducing airborne bacterial concentrations. As shown in **Fig. 9c**, the optimal concentrations of NH_3 and $PM_{2.5}$ for controlling microbial levels in contaminated waste facilities were suggested as below 0.15 mg/m^3 and within the range of 0.01 mg/m^3 to 0.07 mg/m^3, respectively.

3.5 Perspectives

This study developed four ML models with interpretability analysis for the prediction of airborne bacterial concentrations and identification of critical factors in contaminated waste facilities. The results revealed the correlations between airborne bacterial concentrations and key features, providing valuable insights for better understanding and management of environmental sanitation risks in waste facilities. Although this investigation contributes meaningful insights, it has certain limitations that future work could address. The accuracy of ML models mainly relies on the quantity and quality of data points, but the sample dataset used for this investigation was relatively small. To achieve improved prediction accuracy in future studies, it would be beneficial to utilize a more extensive dataset that encompasses a broader range of data points (Li et al., 2025). Another limitation is the restricted quantity of environmental variables incorporated as predictor variables, omitting several critical factors such as seasons, volatile organic compounds, and hydrogen sulfide, which could result in an incomplete grasp of the interactions between the input and output variables. Thus, future work should focus on analyzing a broader range of environmental variables and their combinations to better understand their impact on airborne bacterial concentrations in waste facilities and potentially enhance model prediction accuracy.

4. Conclusions

This study used ML methods for comprehensive microbial prediction analysis and targeted optimization of airborne microbial contamination in waste facilities. The results suggested that the integration of environmental and gaseous datasets with microbial datasets improved the prediction accuracy of airborne bacterial concentrations. The RF model had superior performance (R^2 = 0.7369, RMSE = 304.2) than those developed by LGBM, KNN, and XGBoost. The SHAP method revealed that the microbial factors were the most significant variables in the RF model. Additionally, the partial correlation analysis found that the optimal ranges of T (32-36 °C), RH (62%-80%), NH_3 (< 0.15 mg/m^3), $PM_{2.5}$ (0.01-0.07 mg/m^3), and the effective disinfectants of SAEW had greater potential for controlling contamination in waste facilities. Overall, this study offers a meaningful reference for making targeted airborne microorganisms' risk management strategies in waste facilities with the ML technique.

References

[1] Aldrees, A., Siddiq, B., Al-Rashed, W.S., Javed, M.F., Khan, M. 2024. Leveraging machine learning to model salinity and water flux for improved insights into forward osmosis membrane bioreactors. J. Water Process. Eng., 68, 106585.

[2] Aviña-Hernández, J., Ramírez-Vargas, M., Roque-Sosa, F., Martínez-Rincón, R.O. 2023. Predictive performance of random forest on the identification of mangrove species in arid environments. Ecol.

Inform., 75, 102040.
[3] Bai, B., Wang, L., Guan, F., Cui, Y., Bao, M., Gong, S. 2024. Prediction models for bioavailability of Cu and Zn during composting: Insights into machine learning. J. Hazard. Mater., 471, 134392.
[4] Cao, H., Li, Y., Chang, C., Zhang, X., Yang, A., Shen, W. 2024a. A Deep Learning Hybrid Framework Combining an Efficient Evolutionary Algorithm for Complex Many-Objective Optimization of Sustainable Triple CO2 Feed Methanol Production. ACS Sustain. Chem. Eng., 12(17), 6682-6696.
[5] Cao, Y., Xu, T., Yu, X., Hua, Z., Liu, H., Gu, W., Liu, H., Kang, H., Wei, Z., Xie, Z. 2024b. Fungal aerosols over the Northwest Pacific to Arctic Ocean: The influence of air mass and environmental factors. Atmos. Environ., 337, 120776.
[6] Chen, H., Cao, Y., Qin, W., Lin, K., Yang, Y., Liu, C., Ji, H. 2024. Machine learning models for predicting thermal desorption remediation of soils contaminated with polycyclic aromatic hydrocarbons. Sci. Total Environ., 927.
[7] Chen, Y., Lu, J., Li, Q., Hua, W., Zhang, W., Li, C., Liu, Y., Wang, Z. 2025. Influencing factors analysis of infectious SARS-CoV-2 aerosols sampling. J. Aerosol. Sci., 183, 106487.
[8] Ding, Y., Sun, Q., Lin, Y., Ping, Q., Peng, N., Wang, L., Li, Y. 2024. Application of artificial intelligence in (waste)water disinfection: Emphasizing the regulation of disinfection by-products formation and residues prediction. Water Res, 253, 121267.
[9] Feng, S., Karanth, S., Almuhaideb, E., Parveen, S., Pradhan, A.K. 2024. Machine learning to predict the relationship between Vibrio spp. concentrations in seawater and oysters and prevalent environmental conditions. Food Res. Int., 188, 114464.
[10] Guo, Y., Lin, K., Gao, X., Zheng, Q., Zhou, T., Zhao, Y. 2024. Disinfection efficacy of slightly acidic electrolyzed water on microorganisms: Application in contaminated waste sorting rooms across varied scenarios. J. Clean Prod., 467, 142938.
[11] Guo, Y., Zhu, Z., Zhao, Y., Zhou, T., Lan, B., Song, L. 2021. Simultaneous annihilation of microorganisms and volatile organic compounds from municipal solid waste storage rooms with slightly acidic electrolyzed water. J. Environ. Manage., 297, 113414.
[12] Hong, S.M., Morgan, B.J., Stocker, M.D., Smith, J.E., Kim, M.S., Cho, K.H., Pachepsky, Y.A. 2024. Using machine learning models to estimate Escherichia coli concentration in an irrigation pond from water quality and drone-based RGB imagery data. Water Res., 260, 121861.
[13] Jiang, J., Xiang, X., Zhou, Q., Zhou, L., Bi, X., Khanal, S.K., Wang, Z., Chen, G., Guo, G. 2024. Optimization of a Novel Engineered Ecosystem Integrating Carbon, Nitrogen, Phosphorus, and Sulfur Biotransformation for Saline Wastewater Treatment Using an Interpretable Machine Learning Approach. Environ Sci Technol, 58(29), 12989-12999.
[14] Jiang, J., Zhou, H., Zhang, T., Yao, C., Du, D., Zhao, L., Cai, W., Che, L., Cao, Z., Wu, X.E. 2022. Machine learning to predict dynamic changes of pathogenic Vibrio spp. abundance on microplastics in marine environment. Environ. Pollut., 305, 119257.
[15] Jing, Z., Zhang, Y., Liu, X., Li, Q., Hao, Y., Li, Y., Gao, H. 2025. Identifying human activities causing water pollution based on microbial community sequencing and source classifier machine learning. Environ. Int., 195, 109240.
[16] Kim, D., Shin, D., Kim, D., Kwon, B., Min, C., Geevarghese, G., Kim, S., Hwang, J., Seo, S. 2025. Revisiting joint effect of temperature and relative humidity on airborne mold and bacteria concentration in indoor environment: a machine learning approach. Build. Environ., 112548.
[17] Lee, J.Y.Y., Miao, Y., Chau, R.L.T., Hernandez, M., Lee, P.K.H. 2023. Artificial intelligence-based prediction of indoor bioaerosol concentrations from indoor air quality sensor data. Environ. Int., 174.
[18] Li, Y., Tao, C., Li, S., Chen, W., Fu, D., Jafvert, C.T., Zhu, T. 2025. Feasibility study of machine learning to explore relationships between antimicrobial resistance and microbial community structure in global wastewater treatment plant sludges. Bioresour. Technol., 417, 131878.
[19] Lin, W.-F., Guo, H.-Q., Zhu, L.-J., Yang, K., Li, H.-Z., Cui, L. 2022. Temporal variation of antibiotic resistome and pathogens in food waste during short-term storage. J. Hazard. Mater., 436, 129261.
[20] Liu, S., Long, Z., Liang, J., Zhang, J., Hu, D., Hou, P., Zhang, G. 2025. Interpretable causal machine learning optimization tool for improving efficiency of internal carbon source-biological denitrification. Bioresour. Technol., 416, 131787.
[21] Long, F., Wang, L., Cai, W., Lesnik, K., Liu, H. 2021. Predicting the performance of anaerobic digestion using machine learning algorithms and genomic data. Water Res., 199.
[22] Lv, J., Du, L., Lin, H., Wang, B., Yin, W., Song, Y., Chen, J., Yang, J., Wang, A., Wang, H. 2024. Enhancing effluent quality prediction in wastewater treatment plants through the integration of factor analysis and machine learning. Bioresour. Technol., 393, 130008.
[23] Mallik, S., Saha, B., Podder, K., Muthuraj, M., Mishra, U., Deb, S. 2025. Comprehensive assessment of E. coli dynamics in river water using

advanced machine learning and explainable AI. Process Saf. Environ. Protect., 195, 106816.
[24] Miao, J., Wei, Z., Zhou, S., Li, J., Shi, D., Yang, D., Jiang, G., Yin, J., Yang, Z.W., Li, J.W., Jin, M. 2022. Predicting the concentrations of enteric viruses in urban rivers running through the city center via an artificial neural network. J. Hazard. Mater., 438, 129506.
[25] Núñez, A., García, A.M., Moreno, D.A., Guantes, R. 2021. Seasonal changes dominate long-term variability of the urban air microbiome across space and time. Environ. Int., 150, 106423.
[26] Tao, J., Chen, Y., Wan, S., Wu, J. 2022. Abundance and diversity of ARGs in aerosol environments of waste recycling sites. J. Aerosol. Sci., 165, 106020.
[27] Wan, X., Yang, C., Qiu, S., Xu, W., Lian, J., Zhang, J., Xing, W., Yuan, Y. 2024. Natural volatile organic compounds (NVOCs) and airborne microorganisms in different stands of urban forests. Sci. Total Environ., 955, 176964.
[28] Wang, B., Zhang, P., Qi, X., Li, G., Zhang, J. 2024a. Predicting ammonia emissions and global warming potential in composting by machine learning. Bioresour. Technol., 411, 131335.
[29] Wang, S.-n., Shi, Y.-c., Lin, S., He, H.-f. 2024b. Particulate matter 2.5 accelerates aging: Exploring cellular senescence and age-related diseases. Ecotox. Environ. Safe., 284, 116920.
[30] Wang, Y., Li, L., Ma, J., Han, Y. 2024c. The response and factors of microbial aerosol emission from the sludge bio-drying process. Waste Manage., 175, 294-304.
[31] Wu, Y., Wang, Z., Yu, G., Zhao, Y., Chen, C., Xie, Y., Cao, H. 2025. Interpretable Machine Learning Models Delivering a New Perspective for the Reaction Mechanism between Organic Pollutants and Oxidative Radicals. Environ. Sci. Technol., 59(2), 1264-1273.
[32] Xia, L., Wu, B., Cui, X., Ran, T., Li, Q., Zhou, Y. 2024. Machine learning-based prediction of non-aeration linear alkylbenzene sulfonate mineralization in an oxygenic microalgal-bacteria biofilm. Bioresour Technol, 419, 132028.
[33] Xu, X., Rothrock, M.J., Reeves, J., Kumar, G.D., Mishra, A. 2022. Using E. coli population to predict foodborne pathogens in pastured poultry farms. Food Microbiol., 108, 104092.
[34] Yu, Y., Hossain, M.M., Sikder, R., Qi, Z., Huo, L., Chen, R., Dou, W., Shi, B., Ye, T. 2024. Exploring the potential of machine learning to understand the occurrence and health risks of haloacetic acids in a drinking water distribution system. Sci. Total Environ., 951, 175573.
[35] Yu, Y., Liang, Z., Liao, W., Ye, Z., Li, G., An, T. 2021. Contributions of meat waste decomposition to the abundance and diversity of pathogens and antibiotic-resistance genes in the atmosphere. Sci. Total Environ., 784, 147128.
[36] Zhang, L., Wang, B., Li, K., Su, Y., Wu, D., Zhan, M., Xie, B. 2024. The dynamics and assembly patterns of airborne pathogen communities in the municipal food waste treatment system and its risk implications. Environ. Int., 194, 109143.
[37] Zhao, L., Li, S., Yang, H. 2021. Recent advances on research of electrolyzed water and its applications. Curr. Opin. Food Sci., 41, 180-188.
[38] Zhao, Y., Zhang, L., Chen, Y. 2024. Water environment risk prediction method based on convolutional neural network-random forest. Mar. Pollut. Bull., 209, 117228.
[39] Zhou, Z., Yan, R., Liu, X., Xu, Z., Zhang, J., Yi, Q. 2024. Suspended particulate matter <2.5 μm (SPM2.5) in shallow lakes: Sedimentation resistance and bioavailable phosphorus enrichment after sediment resuspension. Sci. Total Environ., 912, 168780.

PROPER EVALUATION OF ENVIRONMENTALLY SAFE MUNICIPAL SOLID WASTE INCINERATION BOTTOM ASH AS MATERIAL OF ARTIFICIAL STONE

Koshiro Ikaruka[1], Teppei Komiya[2], Hirofumi Nakayama[2]
Takayuki Nuruyu[3], Keita Kudo[3], Daizo Fukuoka[3]
1 Dept. of Civil Engineering, Graduate School of Engineering, Kyushu University,
744 Motooka, Nishi-ku, Fukuoka, Japan
2 Dept. of Urban and Environmental Engineering, Faculty of Engineering, Kyushu University,
744 Motooka, Nishi-ku, Fukuoka, Japan
3 FKG Co., Ltd.,
262 Kogaide, Senchō-machi, Yatsushiro, Japan

Abstract: Although final disposal volume in Japan has been decreasing, landfill capacity remains limited, making the recycling of MSWI bottom ash important. However, it is hindered by heavy metals exceeding environmental quality standards for soil contamination. This study examined MSWI bottom ash without riddling ash, which typically contains fewer heavy metals. The results showed that the bottom ash without riddling ash met the environmental quality standards for heavy metal content in soil, and the artificial stone produced from it satisfied the environmental quality standards for heavy metal leaching from soil.

INTRODUCTION

In Japan, incineration is the predominant method for the intermediate treatment of municipal solid waste (MSW), and a substantial proportion of the resulting municipal solid waste incineration (MSWI) ash (hereafter referred to as MSWI ash) is ultimately disposed of in landfills. In municipalities where landfill capacity is severely constrained or where landfill facilities are unavailable[1], the recycling of incineration ash becomes an necessity. Potential applications for recycling include utilization as civil engineering materials, such as roadbed aggregates; however, the presence of heavy metals at concentrations exceeding the environmental quality standards for soil contamination poses a significant barrier to utilization.The present study seeks to evaluate the environmental safety of MSWI bottom ash (hereafter referred to as bottom ash), while explicitly excluding riddling ash[2], which is known to contain elevated concentrations of both precious and hazardous metals. Specifically, the concentrations and leaching behaviors of designated hazardous elements were determined for incineration ash and bottom ash by particle size, to assess their environmental compliance. Furthermore, artificial stones incorporating bottom ash at varying mix proportions were fabricated, and their environmental safety and optimal mix designs were systematically investigated.

MATERIALS AND METHODS

Materials

The samples used in this study were municipal solid waste incineration (MSWI) ash and bottom ash. Both were obtained from an MSWI facility T (two units of continuous stoker furnaces, 300 t/day each; hereafter referred to as Plant T). The samples were sieved to pass through a 37.5 mm mesh. Figure 1 shows the appearance of incineration ash, bottom ash, and artificial stone produced using bottom ash as raw material (hereafter referred to as the recycled form), which was prepared by crushing solidified bodies designed to simulate the particle size distribution of RC-40. For reference, the appearance of riddling ash discharged from another facility (two units of continuous stoker furnaces, 140 t/day each) is also presented.

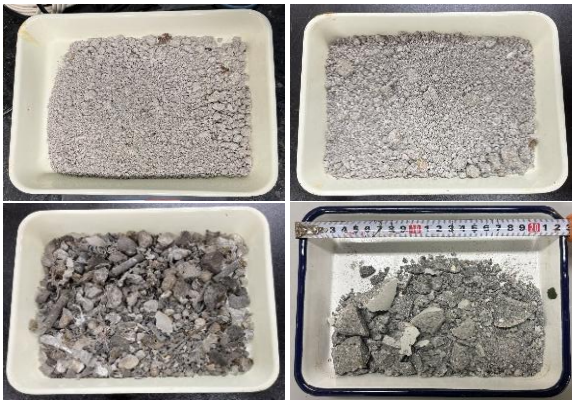

Figure 1. Appearance of the samples (upper left: incineration ash, upper right: bottom ash, lower left: falling dust ash, lower right: artificial stone (crushed solidified material simulating the particle size distribution of RC-40)))

Table 1. Mix proportions of the solidified bodies

No.		37.5 -C20	37.5 -C30	37.5 -C40	37.5 -C50
Particle size fraction of ash (mm)		<37.5 mm			
Cementitious binder content (%)		20	30	40	50
Mix proportion (g)	Ash	700	700	700	700
	Stabilizer	140	210	280	350
	Water	26.0	26.0	26.0	28.1
No.		4.75 -C20	4.75 -C30	4.75 -C40	4.75 -C50
Particle size fraction of ash (mm)		<4.75 mm			
Cementitious binder content (%)		20	30	40	50
Mix proportion(g)	Ash	700	700	700	700
	Stabilizer	140	210	280	350
	Water	26.0	27.6	27.7	30.1

Methods

Particle size classification: To obtain basic information on particle size distribution and to consider particle-size fractions suitable as raw materials for artificial stone—given that the content and leaching of hazardous elements vary with particle size—samples were classified into size fractions. After air-drying for approximately 24 h, the samples were sieved using ten sieves with openings of 0.075, 0.106, 0.25, 0.425, 0.85, 2, 4.75, 9.5, 19, and 26.5 mm, resulting in eleven particle-size fractions.

Content and leaching tests of hazardous elements: In accordance with the Notification No. 19 and No. 46 of the Ministry of the Environment, Japan, the contents and leaching concentrations of cadmium (Cd), total chromium (Cr), lead (Pb), and boron (B) were analyzed for each particle-size fraction. Based on these results, 95% confidence intervals of the population means were estimated. If the upper confidence limits were below the environmental quality standards for soil, the samples were evaluated as environmentally safe. With respect to hexavalent chromium (Cr(VI)), which is designated as a hazardous substance, it was assumed that if the total Cr content was below the soil environmental standard for Cr(VI), both the content and leaching concentration of Cr(VI) would also be below the standard.

Preparation of solidified bodies: Mixtures of bottom ash, cementitious binder, and water were compacted into cylindrical molds with lids (φ78 mm × H100 mm) and cured under sealed conditions for two weeks to obtain solidified bodies. As shown in Table 1, ten types of solidified bodies with different mix proportions were prepared, using two types of particle-size distributions of bottom ash and five levels of binder addition as parameters.

Content and leaching tests of hazardous elements in artificial stone: Solidified bodies were crushed and sieved to obtain fractions of less than 2 mm and those in the recycled form (utilization form). These were analyzed for hazardous element content and leaching concentration in the same manner as described in “Methods”. The target elements were Cd, Cr, Se, Pb, As, and B.

RESULTS AND DISCUSSION

Content of hazardous elements in incineration ash and bottom ash

For incineration ash, the upper confidence limits of Cd and B contents in all particle-size fractions were below the soil content standards. Figure 2 shows the contents of Cr and Pb in incineration ash and bottom ash. The plots represent sample means, the error bars represent 95% confidence intervals of the population means, and the dashed lines indicate the standards. The plot

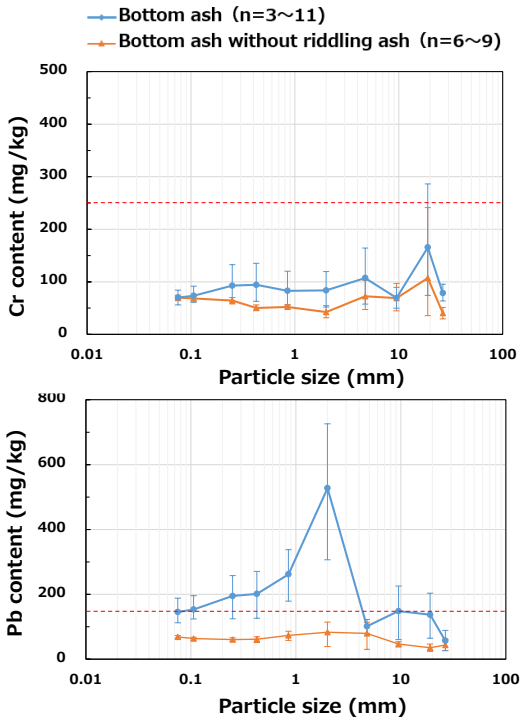

Figure 2. Concentrations of specified hazardous substances in incineration ash and bottom ash by particle size fraction (Top: Cr, Bottom: Pb)

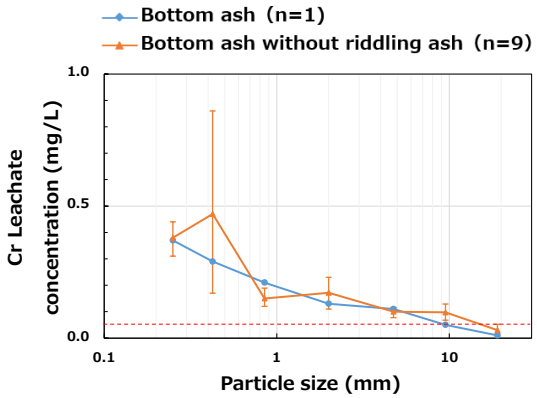

Figure 3. Leaching concentrations of specified hazardous substances from incineration ash and bottom ash (Cr)

positions correspond to the maximum particle size of each fraction. For incineration ash, the upper confidence limits of Pb content exceeded the standards in all fractions except 19–26.5 mm, and those of Cr content exceeded the standards in the 9.5–19 mm fraction. In contrast, the upper confidence limits of Pb content in bottom ash were below the standards in all fractions, indicating that the removal of riddling ash improved environmental safety.

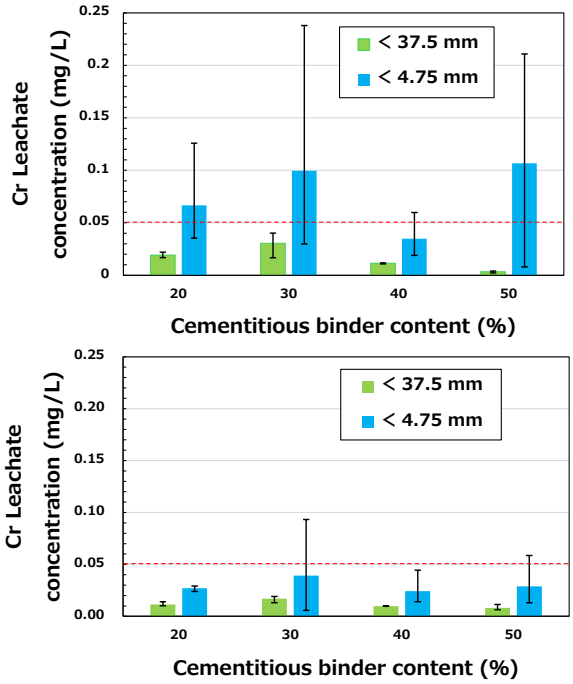

Figure 4. Leaching concentration of Cr from artificial stone (Top: < 2 mm, Bottom: as-is condition)

Leaching tests of hazardous elements

The leaching concentrations of Cd, Pb, and B in bottom ash met the soil leaching standards in almost all particle-size fractions, and the leaching concentrations of the entire sample were considered to be below the standards. Figure 3 shows the leaching concentrations of Cr in incineration ash and bottom ash. Except for the 9.5–19 mm fraction, the upper confidence limits exceeded the standards, and the leaching concentrations in the 0.106–0.425 mm fraction were higher than those in other fractions. Moreover, no reduction in Cr leaching was observed as a result of riddling ash removal.

Leaching tests of hazardous elements in artificial stone

For elements other than Cr, all solidified bodies met the soil leaching standards, except for the Pb leaching concentration in the recycled form of artificial stone pre pared using bottom ash with a maximum particle size less than 37.5 mm and a binder addition ratio of 20%. The exceedance of the standard for Pb was attributed to the low binder content. Figure 4 shows the mean, maximum, and minimum values of Cr leaching concentrations in artificial stone (crushed solidified bodies). For artificial stone produced from bottom ash

with a maximum particle size less than 37.5 mm, the maximum values of Cr leaching concentrations in both the <2 mm fraction and the recycled form were below the standards, confirming the effectiveness of solidification with cementitious binder in suppressing Cr leaching. In contrast, artificial stone produced from bottom ash with a maximum particle size of 4.75 mm, designed to prevent surface exposure of bottom ash, exhibited higher Cr leaching concentrations than those made from bottom ash with a maximum particle size of 37.5 mm, in both the <2 mm fraction and the recycled form. Even with a binder addition ratio of 50%, the maximum Cr leaching concentration in the <2 mm fraction substantially exceeded the standard. This was attributed to the fact that the bottom ash with a maximum particle size of 4.75 mm primarily consisted of finer fractions, which, as shown in Figure 3, exhibited Cr leaching concentrations far exceeding the standards. On the other hand, for artificial stone prepared from bottom ash with a maximum particle size less than 37.5 mm, the leaching concentrations of all elements could be maintained below the standards by setting the binder addition ratio at 30% or higher, demonstrating its high environmental safety.

CONCLUSIONS

For the samples examined in this study, the use of incineration ash as a raw material for artificial stone was found to be infeasible. However, it was demonstrated that environmentally safe artificial stone can be produced by using bottom ash, excluding riddling ash, as the raw material and by setting the cementitious binder addition ratio at approximately 30% or higher. Future issues include the investigation of additives for suppressing the leaching of hexavalent chromium and the evaluation of the engineering performance of artificial stone as a roadbed material, such as by the modified CBR test.

REFERENCES

1) Ministry of the Environment, Japan: Results of the Survey on the Actual Conditions of Municipal Solid Waste Management Projects (FY2023), 2025.] https://www.env.go.jp/recycle/waste_tech/ippan/r5/data/env_press.pdf (Accessed October 2, 2025)
2) Yamamoto, H. Yokoyama, T. Oshita, K. Takaoka, M. and Takeda, N.: The Study of Shifting of Valuable Metals to Riddling Ash in Municipal Solid Waste Incineration Process, The Journal of Material Cycles and Waste Management, Vol.18, Issue 5, pp. 314 324, 2007.

Design and Validation of a Novel Contraction–Expansion Array Conical Grit Remover for Grit Removal in Wastewater Sludge

Yi Xiong, Xiaoli Chai*
Tongji University, Shanghai, China
* Corresponding author, E-mail: xlchai@tongji.edu.cn

Abstract

Sludge discharged from secondary sedimentation tanks or membrane bioreactors (MBRs) in municipal wastewater treatment plants often contains fine grit, which causes pipeline abrasion, pump failures, sludge accumulation, and membrane fouling. In the high-concentration powder carrier bio-fluidized bed (HPB) process, existing carrier-recovery hydrocyclones may also mis-recover fine grit, further affecting system stability. To address these challenges, a novel conical grit remover with a contraction–expansion array structure was proposed and designed. Its performance was evaluated through CFD simulations and pilot-scale experiments. Simulation results indicated that the device effectively captured grit particles larger than 20 μm at low velocities, while only particles above 100 μm were consistently removed at higher velocities. Pilot-scale experiments under real sludge conditions confirmed the same trend, achieving measurable removal for particles larger than 40 μm. Although the absolute removal efficiencies were lower than predicted by simulations, the overall agreement demonstrated the feasibility of the device. The study highlights the potential of this grit remover to mitigate grit-related risks and support stable operation of secondary sedimentation and MBR systems, as well as optimization of HPB processes.

Keywords: Grit remover; contraction–expansion array; CFD simulation; Wastewater treatment

1. Introduction

Sludge discharged from secondary sedimentation tanks and membrane bioreactors (MBRs) in municipal wastewater treatment plants often contain fine grit. These particles cause pipeline abrasion, pump failures, sludge accumulation, and membrane fouling, increasing operation and maintenance costs. In the high concentration powder carrier bio-fluidized bed (HPB) process, existing carrier-recovery hydrocyclones may also mis-recover fine grit, further compromising process stability and efficiency. Therefore, there is a clear demand for a desanding device specifically designed for sludge systems. This study proposes and designs a novel conical grit remover with a contraction–expansion array structure, aiming to enhance grit removal efficiency by combining inertial separation with vortex entrapment. Its performance was evaluated and preliminarily validated through CFD simulations and pilot-scale experiments.

2. Methods

2.1 3D physical model

A 3D model of the contraction–expansion array conical grit remover was developed. Figure 1 illustrates the design of the grit remover, which consists of a 40-mm diameter inlet, two 60-mm diameter outlets (located at the top and bottom), and a swirling chamber with a diameter of 1.4 m, a cone angle of 150°, and a height of 20 mm. The inner wall is equipped with 24 grit traps, each measuring 20 mm × 20 mm, which lead into an annular chamber at the bottom with a height of 100 mm and a width of 20 mm.

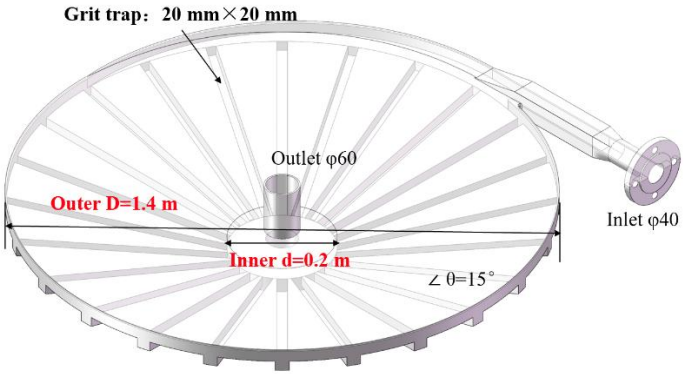

Figure 1 : Schematic of the device structure

2.2 CFD simulations

The flow inside the grit remover is turbulent and was simulated using the Reynolds Stress Model (RSM). The trajectories of grit particles were calculated using the Discrete Phase Model (DPM). The continuous phase was set as water, while sludge was represented as particles with a density of 1.1 g/cm³ and a size range of 1–100 μm, and grit was represented as particles with a density of 2.575 g/cm³ and a size range of 10–1000 μm.

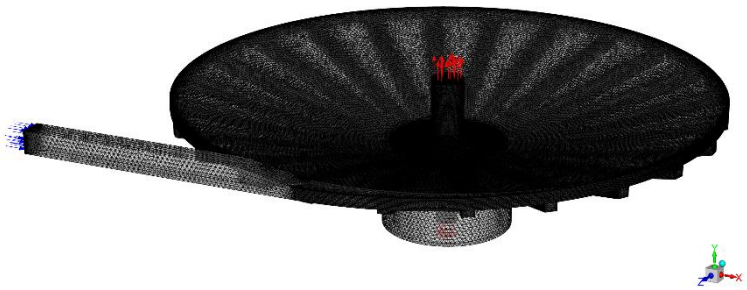

Figure 2: CFD mesh

2.3 Pilot-Scale Experiments

The pilot-scale grit remover was installed at a municipal wastewater treatment plant in Shenzhen and fabricated directly according to the dimensions of the CFD model. The mixed liquor withdrawn from the MBR of the pilot system was introduced into the grit removal device for testing under different operating conditions.

Figure 3: Pilot-scale grit remover

3. Results and discussion

3.1 Simulation Results

Figure 4 shows the flow field patterns inside the grit remover. A swirling flow can be observed in the swirling chamber, while elongated vortices are formed within the grit traps, which are favorable for particle entrapment. The flow velocity inside the bottom chamber is extremely low, ensuring that grit particles, once settled, are unlikely to be re-entrained.

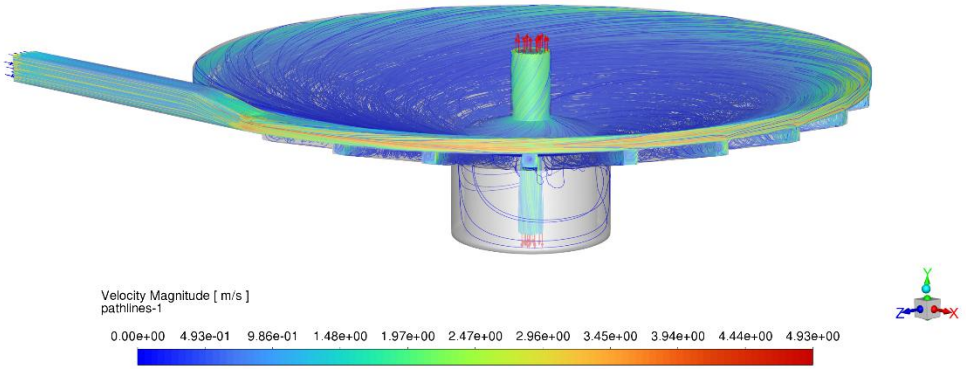

Figure 4: Flow field patterns inside the grit remover

Figure 5 shows the particle dynamics inside the grit remover at different time steps. Grit particles are represented in red and sludge particles in blue. It can be observed that grit particles are rapidly captured by the grit traps and transported into the bottom chamber, whereas most sludge particles follow the water flow and exit through the top and bottom outlets.

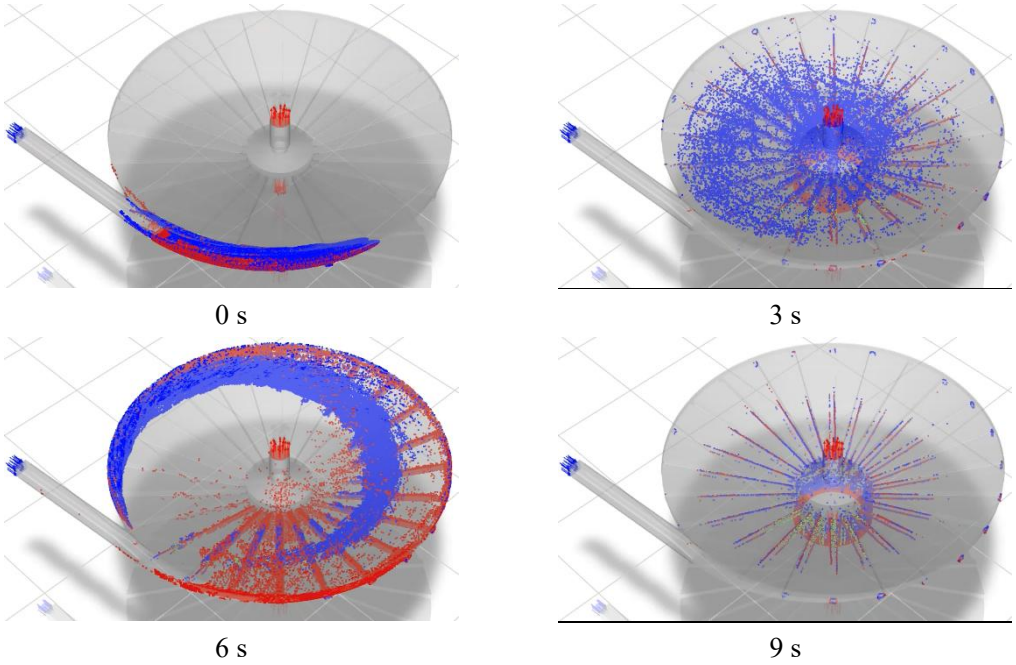

Figure 5: Particle dynamics inside the grit remover at different time steps

Figure 6 presents the simulation results under three flow velocities(3 m/s, 5 m/s, 10 m/s). It can be observed that with increasing velocity, the interception efficiency of the grit remover decreases for all particles. At 3 m/s, almost all grit particles larger than 20 μm are captured, whereas at 10 m/s, only particles larger than 100 μm can be fully captured. Sludge particles are even less likely to be captured.

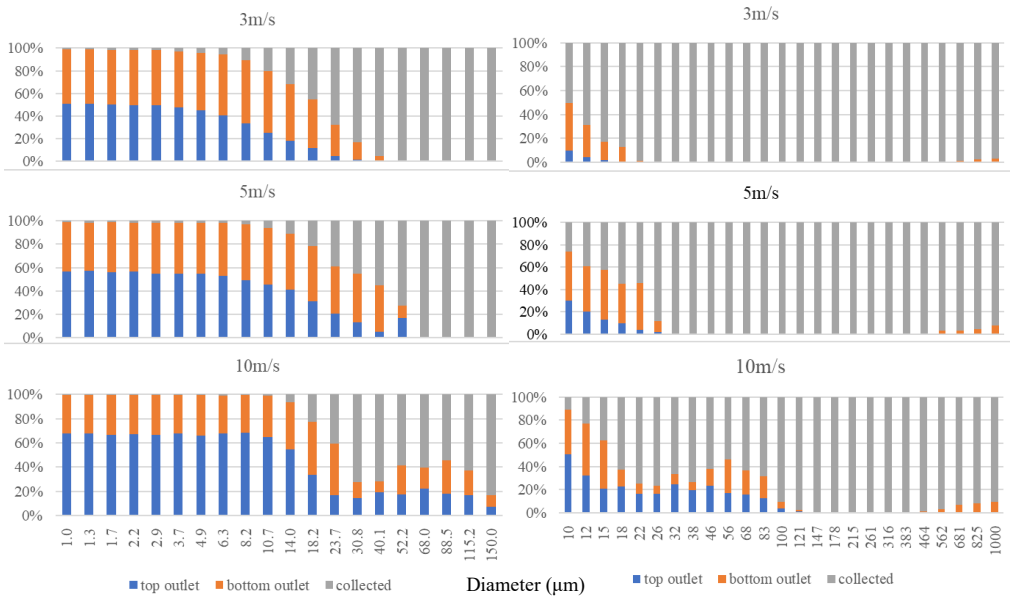

a b

Figure 6: Sludge(a) and grit(b) particle distribution under inlet velocity of 3m/s, 5 m/s and 10 m/s

3.2 Pilot-Scale Experiments

The pilot-scale experimental results further validated the CFD predictions. As shown in Figure 7, the removal efficiency of inorganic matter (representing grit) decreased from 7.94% at 1 m/s to 4.91% at 9 m/s. Figure 8 illustrates the particle size distributions in the influent and effluent under different velocities, indicating that the device achieved measurable removal for particles larger than 40 μm and pronounced removal for those exceeding 100 μm. Although the absolute removal efficiencies in real wastewater were significantly lower than the theoretical values predicted by simulation, the experimental results revealed the same overall trend, thereby highlighting both the performance gap and the potential of the system for scale-up validation.

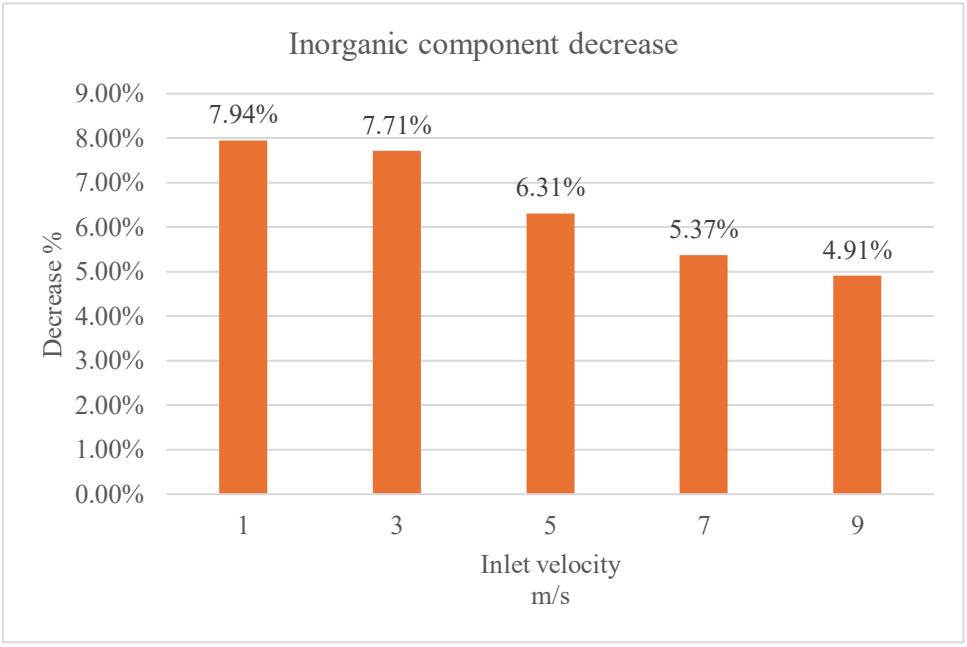

Figure 7: Inorganic component decrease

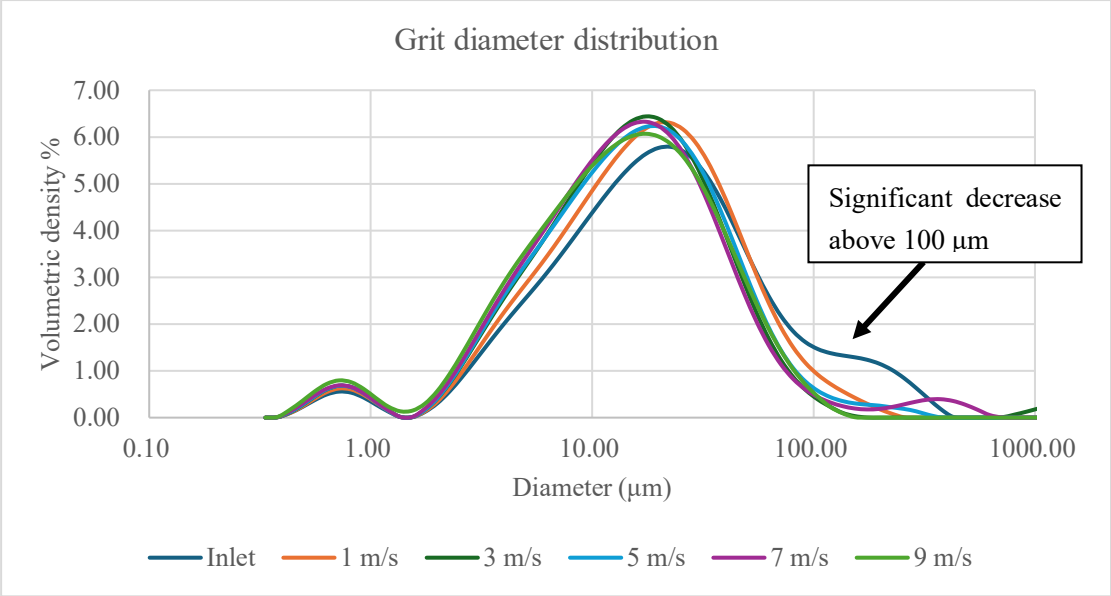

Figure 8: Grit diameter distribution

FROM BREWERY WASTEWATER TO BIO-OLEFINS: A COMPREHENSIVE TEA AND LCA

Na Wu[1,2], Yanran Cui[1], Yuanyuan Che[1], Shunchang Yang[3], and Zhenglong Li[1]
1 Institute of Zhejiang University - Quzhou, Quzhou, 324000, China
2 College of Chemical and Biological Engineering, Zhejiang University, Hangzhou, 310027, China
3 Future Environment Laboratory, Innovation Center of Yangtze River Delta, Zhejiang University, Jiaxing, China

ABSTRACT
This study conducts a Techno-Economic Analysis (TEA) and Life Cycle Assessment (LCA) of a novel process for recovering alcohols from brewing wastewater via steam stripping and catalytically converting them into olefins. The TEA, modeled in ASPEN Plus, reveals that the energy-intensive alcohol concentration step is the major cost contributor within the operational expenditure. The LCA shows the integrated system offers potential greenhouse gas reductions compared to conventional treatment and fossil-based olefin production, though process energy use remains a significant environmental hotspot. Sensitivity analysis identifies alcohol recovery rate, olefin selectivity, catalyst lifetime, and energy source as critical parameters influencing both economic viability and environmental performance. The combined TEA-LEA results demonstrate the feasibility of this valorization pathway while underscoring the need for optimizing energy efficiency to improve its overall economic competitiveness and environmental sustainability, supporting a circular economy approach for the brewing industry.

INTRODUCTION
The brewing industry generates substantial wastewater, characterized by high organic strength and elevated levels of nitrogen and phosphorus. A significant component of this waste stream is pit bottom water, a by-product of the fermentation process in Chinese liquor production. Traditional treatment methods, such as the activated sludge process, are often energy-intensive, produce large volumes of sludge, and represent a missed opportunity for resource recovery, as this wastewater contains valuable organic compounds, notably alcohols like ethanol.

Globally, there is a growing impetus to transition from fossil-based feedstocks to sustainable alternatives for chemical production. Bioethanol-derived olefins, particularly C4+ hydrocarbons like butadiene, are high-value platform chemicals used in synthetic rubber, plastics, and fuels. Concurrently, the treatment of brewing wastewater poses a significant environmental challenge, especially in ecologically sensitive regions like the Yangtze River Economic Belt.

This study, part of the larger research project "Technology Research and Application Demonstration for the Construction Mode of Small and Medium-Sized Green Watersheds in the Yangtze River", addresses these twin challenges of waste management and sustainable chemical production. It investigates an integrated technological pathway for the valorization of brewing wastewater. The core innovation involves a two-step process: firstly, the recovery of mixed alcohols from pit bottom water using an optimized steam stripping process, and secondly, the catalytic conversion of these alcohols into olefins over a newly developed multifunctional catalyst.

A critical gap in assessing such innovative pathways is a holistic understanding of their practical feasibility and sustainability. Therefore, this research combines experimental development with comprehensive Techno-Economic Analysis (TEA) and Life Cycle Assessment (LCA). The TEA evaluates the economic viability, identifying key cost drivers and sensitivities, while the LCA quantifies the environmental impacts from a cradle-to-gate perspective, benchmarking the technology against conventional methods. This integrated approach aims to provide a robust scientific foundation for evaluating the potential of brewing wastewater as a renewable resource within a circular economy framework, ultimately contributing to greener industrial practices in the Yangtze River region.

TECHNO-ECONOMIC ANALYSIS

Objective and Scope
The primary objective of the Techno-Economic Analysis (TEA) was to evaluate the economic feasibility and identify the key cost drivers of the integrated process for recovering alcohols from brewing wastewater and converting them into olefins. The analysis adopted a cradle-to-gate scope, encompassing the costs from wastewater intake through to the production of a crude olefin product stream. The assessment was based on the experimental data obtained from the steam stripping trials and catalytic conversion tests detailed in previous sections.

Methodology and Modeling Framework
A process model was developed using ASPEN Plus® simulation software to establish mass and energy balances for the integrated system, which includes filtration, a two-stage steam stripping process for alcohol concentration, and a catalytic reactor for olefin production. Two design scenarios were rigorously analyzed:

Scenario 1: The bottom stream from the first stripping column undergoes a second stripping pass. The combined overhead streams (approx. 80 wt% alcohol, 63% recovery rate) are sent for catalytic conversion.

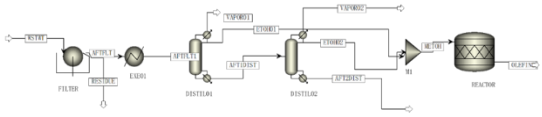

Figure 1: PFD of Scenario 1

Scenario 2: The overhead stream from the first (roughing) column (approx. 40 wt% alcohol) is fed to a second (refining) column to achieve a higher concentration (approx. 80 wt% alcohol, 80% recovery rate) before catalytic conversion.

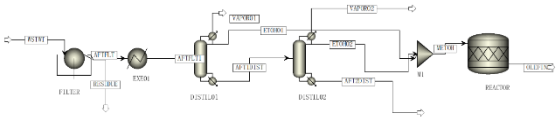

Figure 2: PFD of Scenario 2

The resulting mass and energy flow data were exported to ASPEN Process Economic Analyzer® to estimate capital expenditure (CAPEX) and operational expenditure (OPEX). The economic model was based on a plant with a 20-year operational lifetime, an 8% discount rate, and 330 operating days per year. Key cost assumptions included industrial electricity at ¥0.58/kWh, steam at ¥200/ton, and cooling water at ¥0.2/ton.

Key Economic Findings

The TEA revealed that the production cost is highly sensitive to the efficiency of the alcohol recovery step. Scenario 2, with its higher overall alcohol recovery rate (80%), demonstrated superior economics compared to Scenario 1, primarily due to increased olefin output.

Capital Expenditure (CAPEX): The major capital costs were associated with the distillation columns (reboilers, condensers) and the catalytic reactor system.

Operational Expenditure (OPEX): OPEX constituted approximately 77% of the total annualized cost. A detailed breakdown identified energy consumption as the dominant OPEX factor, accounting for ~43% of the total costs. Within the energy budget, the second stripping column was the most energy-intensive unit, responsible for over 51% of the total energy cost.

Olefin Production Cost: The analysis indicated that the cost of concentrating alcohol from the dilute wastewater stream is the primary economic bottleneck. The estimated production cost for the integrated process was significantly higher than a theoretical baseline cost that considered only the catalytic conversion step (¥1,800/ton olefin), underscoring the critical impact of the recovery stage.

Sensitivity Analysis

A sensitivity analysis was performed to identify parameters with the greatest influence on economic viability. The results highlighted that the following factors are crucial for improving process economics:

Alcohol Recovery Efficiency: A higher recovery rate directly increases product yield and revenue.

Energy Consumption: The price of steam and electricity and the thermal efficiency of the stripping process are major cost drivers.

Catalyst Performance: Longer catalyst lifetime and higher olefin selectivity reduce operational and raw material costs.

Plant Scale: Economies of scale are expected to significantly improve viability at higher treatment capacities.

LIFE CYCLE ASSESSMENT

This Life Cycle Assessment (LCA) aims to quantitatively evaluate the comprehensive environmental impacts of the proposed integrated technology for valorizing brewing wastewater into olefins. The assessment adopts a cradle-to-gate scope, encompassing all processes from raw material extraction and energy production for utilities (electricity, steam) through to the production of the final olefin product. The goal is to compare the environmental footprint of this novel pathway against two benchmark scenarios: (1) Conventional Treatment (e.g., activated sludge process) and (2) Fossil-based Production of olefins from naphtha cracking.

Methodology and Framework

The LCA was conducted according to standardized ISO 14040/14044 guidelines. The life cycle inventory (LCI) was built upon the mass and energy balances derived from the ASPEN Plus process model, which integrated data from experimental steam stripping and catalytic conversion trials. Key data inputs included the consumption of electricity, steam, and cooling water, as well as the production and consumption of catalysts and chemicals.

The environmental impact assessment focused primarily on:

Global Warming Potential (GWP): Calculated using the IPCC 2013 method to quantify greenhouse gas emissions (in kg CO_2-equivalent).

Other relevant impact categories, such as freshwater eutrophication (from effluent discharge) and resource depletion, were also considered.

Key Environmental Findings

Preliminary LCA results indicate a mixed environmental profile for the integrated technology:

Comparative Advantage vs. Fossil Route: The proposed system demonstrates a significant potential for reducing greenhouse gas emissions compared to the traditional fossil-based pathway for olefin production. This avoidance of fossil-derived carbon is a major environmental benefit.

Comparative Advantage vs. Conventional Treatment: When compared to standard wastewater treatment (activated sludge), the technology offers the dual benefit of producing a valuable product while avoiding the methane (a potent GHG) emissions typically associated with the anaerobic degradation of high-organic-content wastewater.

Identification of Environmental Hotspots: The LCA identified several critical environmental hotspots within the proposed system:

Energy Consumption: The steam stripping process for alcohol concentration was identified as the single largest contributor to the environmental footprint, due to the high energy input required for distillation. The associated emissions from steam and electricity generation dominate the GWP impact.

Catalyst Production: The manufacturing of catalysts, particularly those involving precious or energy-intensive metals (e.g., Ag, Pd, Zr), contributes to the overall resource consumption and environmental burden.

Waste Streams: The disposal of spent catalysts and concentrated process residues presents additional environmental challenges that must be accounted for.

Sensitivity and Scenario Analysis

A sensitivity analysis was integrated to explore pathways for enhancing environmental performance:

Energy Source: The analysis shows that the carbon footprint of the process is highly sensitive to the source of electricity and steam. Integrating renewable energy (e.g., solar, biogas from other waste streams) would dramatically reduce the GWP, potentially making the technology carbon-neutral or even negative compared to the BAU case.

Process Efficiency: Improvements in alcohol recovery rate and catalytic selectivity for olefins directly improve the resource efficiency of the entire system, thereby reducing the environmental impact per ton of olefin produced.

CONCLUSIONS

The TEA confirms the technical feasibility of the proposed valorization pathway but highlights its current economic challenges, primarily due to the high energy demand for alcohol concentration. The economic competitiveness of this technology is therefore contingent upon optimizing the steam stripping process to maximize recovery and minimize energy use. Furthermore, scaling the technology to handle larger wastewater volumes and integrating it with renewable energy sources to offset operational energy costs are identified as essential strategies for achieving economic viability. This analysis provides a clear roadmap for future research and development efforts aimed at transforming brewing wastewater from a treatment liability into a sustainable economic resource.

The LCA reveals that while the technology holds great promise for reducing reliance on fossil fuels and mitigating climate change compared to incumbent systems, its overall environmental sustainability is currently constrained by high energy demands. The environmental hotspots align directly with the economic bottlenecks identified in the TEA, underscoring that energy efficiency is the critical lever for simultaneous economic and environmental optimization.

To realize its full potential, future development must focus on:

Process Intensification: Optimizing the steam stripping process to minimize energy use.

Renewable Integration: Powering the plant with renewable electricity and employing biogas or solar thermal for steam generation.

Catalyst Innovation: Developing longer-lasting, more selective catalysts to reduce the environmental burden of catalyst manufacturing per unit of product.

This synergistic TEA-LCA approach provides a robust foundation for guiding the sustainable development of this innovative technology within a circular economy framework for the brewing industry.

REFERENCE

[1] Pu, L., Zhang, H., Wang, T., & Li, Y. "Utilization of pit bottom water from Luzhou-flavor liquor production for Ganoderma lucidum mycelia culture." Journal of Brewing Science, Vol. 45, No. 3, pp. 112-118, 2021.

[2] Li, X., Chen, R., Wu, Z., & Zhang, K. "Cultivation of artificial pit mud using pit bottom water to significantly improve its flavor." Journal of Industrial Microbiology & Biotechnology, Vol. 48, No. 5-6, pp. kuab033, 2021.

[3] Wang, G., Liu, Y., Zhao, M., & Sun, B. "Extraction of aroma and flavor compounds from brewing by-products using supercritical CO_2 technology." Separation and Purification Technology, Vol. 276, p. 119342, 2021.

[4] Li, A., Wang, J., Xu, Y., & Feng, L. "Systematic study on the influence of extraction conditions on the yield of flavor substances from pit bottom water." Food Chemistry, Vol. 362, p. 130192, 2021.

[5] Zhu, D., & Liu, Y. "Optimization of extractive distillation process for anhydrous ethanol production using ethylene glycol." Chemical Engineering and Processing: Process Intensification, Vol. 167, p. 108517, 2021.

[6] Bai, P., Li, S., Zhang, H., & Wang, X. "Solvent recovery study in batch extractive distillation for ethanol dehydration." Industrial & Engineering Chemistry Research, Vol. 60, No. 25, pp. 9175-9184, 2021.

[7] Shanghai Environment and Energy Exchange (SEEE). "National Carbon Market Trading Data." 2023.

[8] Ministry of Ecology and Environment of the People's Republic of China (MEE). "Annual Report of the National Carbon Emissions Trading Market (2023)." 2024.

[9] IPCC. Climate Change 2013: The Physical Science Basis. Contribution of Working Group I to the Fifth Assessment Report of the Intergovernmental Panel on Climate Change. Cambridge University Press, 2013.

[10] Aspen Technology, Inc. Aspen Plus® User Guide. Version 11.0, 2022.

[11] Aspen Technology, Inc. Aspen Process Economic Analyzer® User Guide. Version 11.0, 2022.

[12] International Organization for Standardization (ISO). ISO 14040:2006 Environmental management — Life cycle assessment — Principles and framework. 2006.

[13] International Organization for Standardization

(ISO). ISO 14044:2006 Environmental management — Life cycle assessment — Requirements and guidelines. 2006.

Resource Utilization Potential of Waste Glass in a typical city of China and Its Carbon Reduction and Economic Benefits Evaluation

Jiajun Lin[1], Yanyan Li[1], Xinmei Lin[1], Hongguo Zhang[1], Minhua Su[1], Jinfeng Tang[1,2*]

[1]*Linköping University - Guangzhou University Research Center on Urban Sustainable Development, School of Environmental Science and Engineering, Guangzhou University, Guangzhou 510006, China*

[2]*Nuclear Chemistry and Industrial Material Recycling, Department of Chemistry and Chemical Engineering, Chalmers University of Technology, 412 96, Gothenburg, Sweden*

Abstract: The resource utilization of recyclables in household waste plays a vital role in promoting urban green and low-carbon transformation. Under the national "dual carbon" goals, improving the recovery efficiency of household-source recyclables is essential for reducing the burden on waste management and advancing the circular economy. However, in many cities, waste generation is still estimated based on collection volume, which often underestimates the actual quantity produced. This discrepancy arises because high-value recyclables are frequently diverted before formal collection through informal channels such as community cleaners, scavengers, or direct reuse by residents.

This study focuses on waste glass as a key recyclable in a typical city in China. Through surveys of 448 households across its districts, front-end data on household waste generation and recycling behavior were collected. Monte Carlo simulation estimated household waste glass generation in 2023 at 251,000 tons, while the XGBoost model predicted total municipal generation at 618,300 tons, with 247,200 tons from households, closely aligning with observed data. The estimated carbon reduction potential was 44,700–150,900 tons CO_2, and the economic benefit ranged from -4.6 million to 28 million USD. Results highlight the significant environmental and economic value of glass recycling. The proposed modeling framework is scientifically sound and practically applicable, offering a replicable method for assessing other recyclables and supporting urban solid waste management under China's dual carbon goals.

Keywords: Household-source recyclables; Waste glass resource recovery; Monte Carlo simulation; XGBoost model; Carbon reduction and economic benefits

1. Introduction

Under the guidance of the "dual carbon" strategic goals, the construction of an efficient resource recycling system has become an important pathway for China to promote green and low-carbon transformation. In recent years, the country has introduced several policies, such as the "Guiding Opinions on Accelerating the Transformation and Upgrading of Traditional Manufacturing Industries" and the "Opinions on Accelerating the Establishment of a Waste Recycling System," which clearly call for the acceleration of the development of the recycling industry for renewable resources and the promotion of waste reduction, resource recovery, and harmless treatment[1,2]. With the acceleration of urbanization, the amount of municipal solid waste in Chinese cities has continued to rise. In 2023, the nationwide harmless treatment of urban solid waste reached 259 million tons[3]. Issues such as the complexity of waste composition and low recycling efficiency remain prominent, and a large amount of recyclable resources are not effectively utilized [4,5]. Household-origin municipal waste contains a considerable amount of low-value recyclables, and their recycling plays a significant role in improving

resource utilization efficiency, reducing carbon emissions, and advancing the construction of "zero waste cities" [6,7].

Although the recycling value of recyclable materials has increasingly attracted attention, most current studies focus on macro-level statistics or industrial data, lacking systematic evaluations at the urban household source level. Significant research gaps still exist in areas such as recycling behavior, data acquisition, estimation accuracy, and uncertainty, making it difficult to provide precise support for local policies.

This paper focuses on waste glass in a certain city in China. Based on household survey data, it constructs a composite evaluation system integrating Monte Carlo simulation and the XGBoost model to develop a scientific and applicable model for calculating the number of recyclables generated at the urban household source level. The study also further assesses carbon reduction and economic benefits. The goal of this research is to explore a data-driven evaluation path with scalability [8], providing a theoretical foundation and quantitative basis for the resource utilization of low-value recyclables in cities, thereby contributing to the optimization and upgrading of "dual carbon" policies for municipal solid waste management and resource utilization [9].

2. Experimental and Methodology

The technical approach of this study is presented as follow, first, household waste generation data from 448 households across all administrative districts of the city are collected through door-to-door tracking and questionnaires, and the annual generation of household-origin waste glass is calculated using the Monte Carlo simulation method. Based on this, multi-source statistical and structural variables are integrated, and an XGBoost-based prediction model for waste glass generation from household sources is developed and validated against the survey data. Next, two scenario paths—native and recycling paths — are set up to conduct carbon emission reduction and economic benefit assessments. Finally, based on population growth and economic development trends, the future ten-year waste glass generation and its resource recycling potential are predicted to support policy-making. In this study, "household source" specifically refers to the waste glass data obtained from residents' households through the door-to-door survey, which is the main data collection scope of this research; whereas "life source" is a broader term referring to urban waste sources, including households, shopping malls, institutions, restaurants, and other entities.

2.1 Data collection

This study conducted a two-month door-to-door tracking survey of urban household waste in the fourth quarter of 2023. The survey used one week as the basic time unit, with each household as the smallest unit of investigation, covering all administrative districts of the city, and a total of 551 households were sampled. To ensure the data's representativeness and statistical validity, the sample design was based on the city's population distribution and statistical sampling principles. The sample size was determined using the simple random sampling method, and the calculation formula is as follows:

$$n = \frac{N*Z^2*p(1-p)}{E^2*(N-1)+Z^2*p(1-p)} \qquad (1\text{-}1)$$

Where:

n: Sample size,

N: Total number of households in the city (approximately 7,185,023) [10],
Z: Confidence coefficient (1.96 for a 95% confidence level),
P: Estimated proportion (0.5),
E: Allowable margin of error (5%).

Based on the above parameters, the theoretical minimum sample size is 384 households. Considering sample loss and invalid questionnaires, the final survey sample size was set at 551 households [11]. The survey was conducted using a combination of "short-term and long-term" methods, where each household continuously recorded their waste generation over a two-month period. Specially designed garbage bags and electronic data sheets were provided to guide residents in weighing and recording waste classification data, including waste generated outside the home. Professional surveyors conducted regular follow-ups to ensure the accuracy and completeness of the data. Ultimately, 448 out of the 551 households surveyed fully participated in both rounds of the survey, completing waste classification and weighing records in two different months, resulting in a total of 896 valid continuous observation data points.

In addition to the door-to-door survey, the study also included field visits, literature reviews, questionnaire surveys, and expert interviews. Multi-source data from the National Bureau of Statistics, provincial and municipal statistical bureaus, and relevant authorities were integrated to provide the data foundation for the subsequent construction of the XGBoost-based prediction model, supporting the assessment of resource utilization potential.

2.2 Monte-Carlo Simulation

Monte Carlo Simulation is a random simulation method based on probability statistics, suitable for handling problems with complex structures and uncertainty characteristics. Its core lies in constructing a probabilistic model and performing large-scale random sampling on key variables according to predefined distributions to generate simulated samples. Through statistical analysis, the true solution of the problem is approximated, achieving uncertainty quantification and result visualization [12].

This study is based on the Central Limit Theorem (CLT). Under the condition that the sample size is sufficiently large, even if the original data does not follow a normal distribution, the distribution of the sample mean can be approximated as normal, thereby supporting statistical inference and simulation modeling based on the normality assumption [13, 14]. Its mathematical expression is as follows:

$$X_n \sim \mathcal{N}(\mu_n, \sigma^2{}_n) \qquad (1\text{-}2)$$

In the implementation of the model, the mean and standard deviation of the daily waste glass recycling amount per household are set based on the door-to-door survey data, and 50,000 random samples are taken to estimate the annual generation and its fluctuation range, constructing the probability distribution. To measure the relative dispersion of the data, the Coefficient of Variation (CV) is introduced as a dimensionless indicator, which is suitable for comparing data of different scales and conducting stability analysis [15].

2.3 Development and Construction of the XGBoost Model and Data Visualization

XGBoost (eXtreme Gradient Boosting) is an ensemble learning algorithm based on Gradient Boosting Tree (GBT), which iteratively trains weak classifiers and accumulates residuals to continuously improve the predictive performance of the overall model [16]. The algorithm excels in handling high-dimensional data, nonlinear relationships, and interactions between variables, making it well-suited to

the complex data structure required in this study [17].

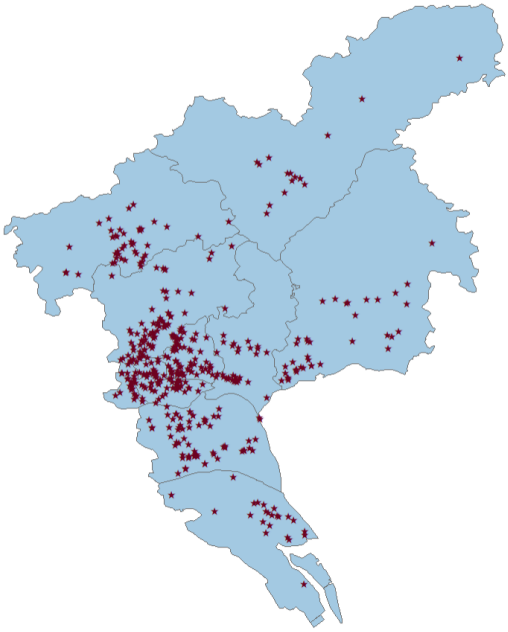

Figure 1 Spatial Distribution of Household Survey Samples in this city, 2023.

In addition, to explore the relationship between waste glass generation and multiple factors, a correlation heatmap was constructed, and the Pearson Correlation Coefficient (PCC) was used to quantify the linear relationships between variables. The PCC is calculated based on the covariance between variables, with a range from −1 to 1. The closer the absolute value is to 1, the stronger the correlation, while the sign indicates the direction of the correlation (positive/negative). The PCC expression is as follows:

$$R_{xy} = \frac{\sum_{i=1}^{n}(x_i-\bar{x})(y_i-\bar{y})}{\sqrt{\sum_{i=1}^{n}(x_i-\bar{x})^2 \sum_{i=1}^{n}(y_i-\bar{y})^2}} \qquad (1\text{-}3)$$

By calculating the PCC values between input variables and the target variable, the main factors influencing waste glass generation are identified, providing support for model construction and policy development [18, 19].

This study is based on relevant data published by the national and municipal governments from 2015 to 2023, collecting and organizing information related to waste glass generation. The data was standardized and missing values were filled, and an analysis variable set was constructed. As shown in Table 2-1, nine key variables were selected, including national glass production and recycling amounts, the city's resident population, per capita GDP, per capita disposable income, as well as factors such as policies, the pandemic, the catering industry, and consumer behavior [20,21].

3. Experimental and Methodology Results and discussion

3.1 Calculation of the Resource Utilization Potential of Household-Origin Waste Glass in a Certain City

According to the survey data, the annual generation of household-origin waste glass in the city reached 251,800 tons in 2023, showing significant regional disparities. As seen in the spatial

distribution map (**Figure 2**), District E ranks first with an absolute amount of 56,600 tons, accounting for 22.51% of the city's total. District H (37,300 tons) and District D (34,500 tons) rank second and third, accounting for 14.83% and 13.73%, respectively, which correlates positively with regional population density [22]. District E, being the city's largest area, with a dense population and frequent commercial activities, generates more waste glass than other areas. Districts D and H, as economically developed areas with dense commercial and residential properties, also have higher waste glass generation. On the other hand, Districts J and I, with lower population density and relatively fewer commercial activities, have lower waste glass generation.

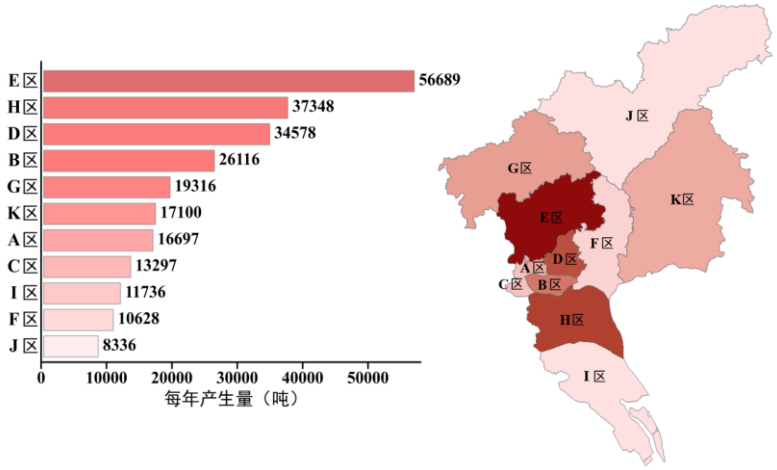

Figure 2 Annual Generation and Spatial Distribution of Household-Derived Waste Glass in this city.

As the core analysis method, Monte Carlo simulation can address the input parameter uncertainty and system complexity commonly found in waste glass generation prediction. It has significant advantages in the field of environmental system uncertainty quantification. Based on rigorous calibration of probability distribution parameters and control of simulation convergence, the system executed 50,000 simulations to ensure statistical significance. The final results provide the probability distribution characteristics of the annual household-origin waste glass generation in the city for 2023, with a mean value and 95% confidence interval of 238,600 to 264,900 tons. The error rate compared to the earlier field survey of 251,800 tons is less than 2.7%, indicating that the waste glass generation from household sources in the city is relatively stable, with a standard deviation of 6,700 tons.

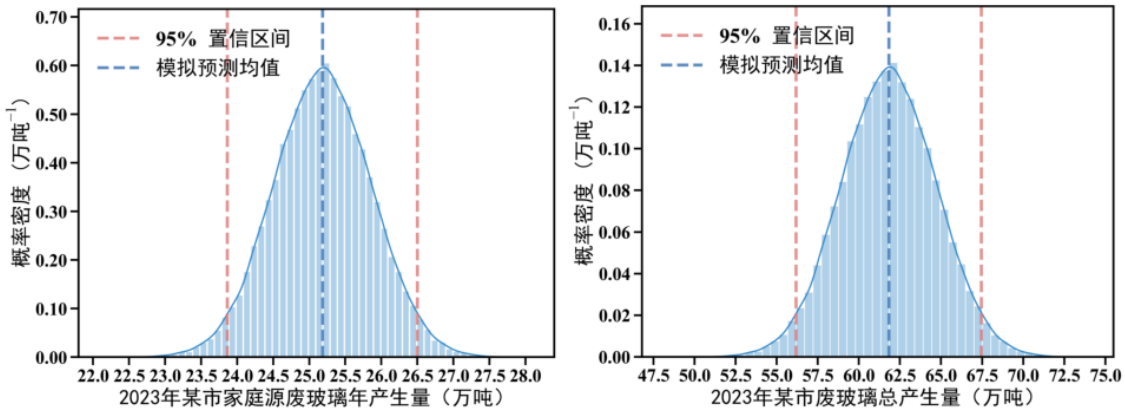

Figure 3 Probability distribution of 2023 a) household-source waste glass b) total wate glass generation in a city in China based on 50,000 Monte Carlo simulation.

After considering various influencing factors and their intensities, the model results show that the total

waste glass generation in the city reached 618,300 tons in 2023. Additionally, prediction residuals were calculated on the calibration set, and the 95% confidence interval deviation was determined, with the range varying from 561,700 to 674,700 tons. The contribution from household sources accounted for approximately 35% to 40% of the total, amounting to 216,300 to 247,200 tons, which aligns with the results from the Monte Carlo simulation. Furthermore, the heatmap in Figure 4 shows a high correlation between population density, per capita GDP, and per capita disposable income. With the added influence of policy, these can be considered as key influencing parameters and treated as noise interference for the next step in prediction.

Based on the 95% confidence interval of the annual household-origin waste glass generation (238,600 to 264,900 tons), the reduction benefits between the native and recycling pathways were evaluated through 50,000 Monte Carlo simulations. As shown in Table 2-2, carbon emissions come from various sources, including fossil fuel combustion, process emissions, and electricity and thermal energy consumption. In the recycling pathway, 100% recycling of waste glass is assumed. Combined with the carbon emission coefficients from various stages in the literature, the carbon emission per ton of virgin glass production is set at 0.802 to 0.975 tons of CO_2, while the carbon emission per ton of recycled waste glass is 0.456 to 0.765 tons of CO_2 [23,24]. According to the simulation results, the possible distribution range of carbon emission reduction from household-origin waste glass recycling in 2023 is between 2.99 and 17.14 tons, with an average reduction of 9.76 tons and a standard deviation of 2.91 tons. Within the 95% confidence interval, the carbon reduction potential ranges from 4.47 to 15.09 tons. Through 50,000 Monte Carlo simulations, the probability cumulative distribution of the economic cost differences between the native and recycling pathways was obtained, as shown in Figure 5. The estimated distribution range of economic benefits from household-origin waste glass is between -4.6 million and 28 million USD, with an average cost reduction of approximately 11.7 million USD and a standard deviation of 4.6 million USD. Within the 95% confidence interval, the cost difference ranges from 2.5 million to 20.7 million USD.

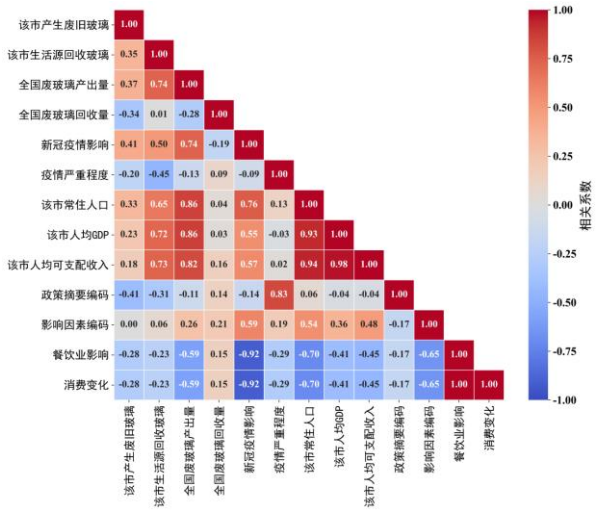

Figure 4 Correlation Heatmap of Variables in the Structural Model of Waste Glass Generation.

The economic benefit distribution range corresponding to the city's annual waste glass generation is between -11.9 million and 72.7 million USD, with an average cost reduction of 30.3 million USD and a standard deviation of 11.3 million USD. The coefficients of variation for the two simulation groups are 39% and 37%, respectively, reflecting some volatility in the economic benefits, but overall stability. The probability cumulative distribution results show that in the vast majority of simulation scenarios,

the benefits are positive, with the probability of negative benefits being less than 1% (0.62%), indicating strong feasibility and robustness, and the ability to effectively reduce expenditure uncertainty.

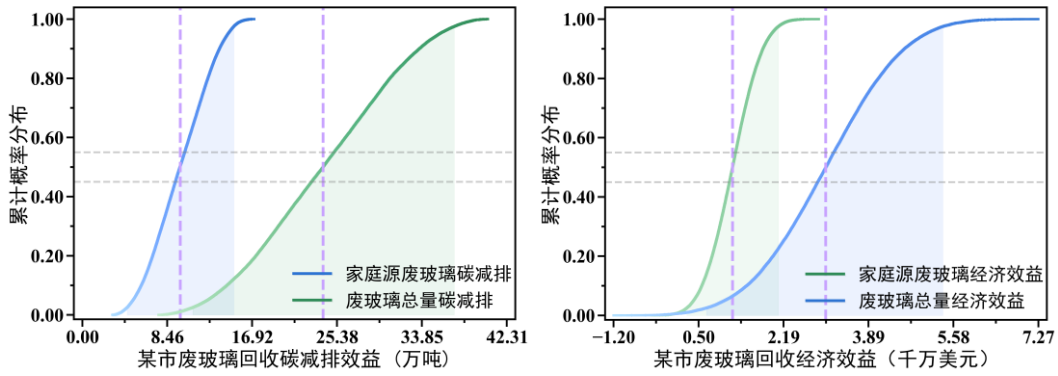

Figure 5 Cumulative probability distribution curve of a) potential carbon emission reduction, b) potential economic benefits from waste glass recycling in this city, based on 50,000 Monte Carlo.

4. Conclusion

This study focuses on the recyclable materials from household waste in a typical city in China, and develops a systematic accounting method covering generation estimation, resource utilization potential assessment, and carbon emission reduction benefit analysis. It accurately reveals the resource utilization potential and environmental-economic benefits of low-value recyclables such as waste glass. The findings provide scientific support for local governments to optimize waste sorting systems and improve resource recovery efficiency. Additionally, they offer data support and a reference path for the transformation of the urban management model of "from source control to resource utilization" of municipal solid waste.

Future research can build a dynamic database covering multiple types of recyclables by expanding the sample scope and monitoring period, with a focus on increasing data collection for low-value and low-frequency recyclables and systematically tracking the actual flow of resources. At the same time, spatial-temporal heterogeneity analysis can be incorporated to further enhance the comprehensiveness and effectiveness of waste resource utilization assessments. Furthermore, future studies could consider extending the existing model to other low-value recyclables, exploring their resource utilization potential and recycling pathways, and providing more comprehensive decision-making support for policymakers.

Acknowledgments

This work was supported by the National Natural Science Foundation of China (No. 22076034), the Natural Science Foundation of Guangdong Province, China (No. 2023A0505050143), Guangzhou Science and Technology Program, China (202206010054).

References

[1] Ministry of Industry and Information Technology et al. Guiding opinions on accelerating the transformation and upgrading of traditional manufacturing industries [J]. Resource Recycling, 2024, (01): 40–43.

[2] General Office of the State Council. Opinions on accelerating the establishment of a waste recycling system [J]. Renewable Resources and Circular Economy, 2024, 17(03): 2–4.

[3] Yang B W. System thinking, economic logic and scientific path for achieving carbon peak and neutrality under Xi Jinping's new development philosophy [J]. Economist, 2021, (09): 5–12.

[4] Wang Y M. Green and low-carbon transformation under China's carbon peak and neutrality goals: strategies and pathways [J]. Globalization, 2021, (06): 5–18+133.

[5] Su J, Liang Y B, Ding L, et al. Strategic discussion on China's energy development under the carbon neutrality target [J]. Bulletin of Chinese Academy of Sciences, 2021, 36(09): 1001–1009.

[6] Vyas S, Prajapati P, Shah A V, et al. Municipal solid waste management: Dynamics, risk assessment, ecological influence, advancements, constraints and perspectives [J]. Science of the Total Environment, 2022, 814.

[7] Zhang X, Liu C, Chen Y, et al. Source separation, transportation, pretreatment, and valorization of municipal solid waste: a critical review [J]. Environment Development and Sustainability, 2022, 24(10): 11471-513.

[8] Zeng ZQ. Simulation of residents' classification behavior and resource-based carbon reduction scenarios for low-value recyclables [D]. East China Normal University, 2024.

[9] Li ZH. Haizhu District Binjiang Subdistrict, Guangzhou: "Small fulcrum" leverages "great transformation," innovation in waste classification through the "Recyclable Materials+" model [J]. Urban and Rural Construction, 2025, (01): 66-67.

[10] Guangzhou Bureau of Statistics. Guangzhou Statistical Yearbook 2023 [M]. China Statistics Press, 2024.

[11] Wu Tianyu. Research on the Influence Path of Environmental Education on Tourists' Pro-environmental Behavior in Wuyishan National Park [D], 2023.

[12] Yin Zengqian, Guan Jingfeng, Zhang Xiaohong, et al. Monte Carlo Methods and Their Applications [J]. Physics and Engineering, 2002, (03): 45-49.

[13] Wang Wei, Xiang Hanlin, Gong Wenli, et al. Sample Size Requirements for the Central Limit Theorem in Common Distributions [J]. Journal of Science for Higher Education Institutions, 2021, 41(07): 20-25.

[14] HEYDE C. Central limit theorem [J]. Wiley StatsRef: Statistics Reference Online, 2014.

[15] ARACHCHIGE C N, PRENDERGAST L A, STAUDTE R G. Robust analogs to the coefficient of variation [J]. Journal of Applied Statistics, 2022, 49(2): 268-90.

[16] Li Zhanshan, Liu Zhaogeng. Feature Selection Algorithm Based on XGBoost [J]. Journal of Communications, 2019, 40(10): 101-108.

[17] Li Z. Extracting spatial effects from machine learning model using local interpretation method: An example of SHAP and XGBoost [J]. Computers Environment and Urban Systems, 2022, 96

[18] ISHFAQ K, SANA M, ASHRAF W M. Artificial intelligence–built analysis framework for the manufacturing sector: performance optimization of wire electric discharge machining system [J]. The International Journal of Advanced Manufacturing Technology, 2023, 128(11): 5025-39.

[19] Lu Yuchen, Lin Li. Design of a Campus Environmental Monitoring System Based on Android [J]. Information & Computer (Theoretical Edition), 2023, 35(23): 19-22.

[20] NIJMAN S W, LEEUWENBERG A, BEEKERS I, et al. Missing data is poorly handled and reported in prediction model studies using machine learning: a literature review [J]. Journal of clinical epidemiology, 2022, 142: 218-29.

[21] BUDACH L, FEUERPFEIL M, IHDE N, et al. The effects of data quality on machine learning performance [J]. arXiv preprint arXiv:220714529, 2022.

[22] LANDAU D, BINDER K. A guide to Monte Carlo simulations in statistical physics [M]. Cambridge university press, 2021.

[23] ZHANG Q, WANG R, SHEN Y, et al. An ignored potential microplastic contamination of a typical waste glass recycling base [J]. Journal of Hazardous Materials, 2022, 422: 126854.

[24] Ning B K, Zhang J X, Meng J, et al. Experimental study on the strength of waste glass powder–tailings sand concrete [J]. Comprehensive Utilization of Mineral Resources, 2015

RESEARCH ON THE CHARACTERISTICS AND KINETICS OF CO-PYROLYSIS OF SLUDGE AND BIOGAS RESIDUE

Zhengrui Chen[1], Jun Zhang[1]

1 School of Environment, Harbin Institute of Technology, Harbin 150090, Heilongjiang, China

Abstract

This study investigates the co-pyrolysis behavior and kinetics of sludge and biogas residue, both promising bioenergy sources. Through elemental and industrial analyses, 11 different mixing ratios were tested under pyrolysis at 1000°C. The results showed that when the biogas residue content exceeded 30%, a synergistic effect occurred, enhancing volatile matter release and devolatilization. Kinetic analysis using the Coats-Redfern model revealed that increasing the biogas residue ratio reduced both the activation energy (from 44.25 kJ/mol to 34.12 kJ/mol) and the reaction order (from 4 to 2.5), indicating a lower energy requirement and faster reaction rate. These findings highlight the potential for efficient pyrolysis and resource utilization of sludge and biogas residue.

Sludge and biogas residue, as two types of biomass with high utilization value, can be used as alternative energy sources and produce products with high byproducts through pyrolysis. This study is dedicated to the co-pyrolysis behavior and kinetic characteristics of sludge and biogas residue with bioenergy potential. The characterization of sludge and biogas residue is obtained through elemental analysis and industrial analysis. 11 kinds of sludge and biogas residue with different mixing ratios (1:0, 9:1, 8:2, 7:3, 6:4, 5:5, 4:6, 3:7, 2:8, 1:9, 0:1) were heated to 1000 ℃ at 10 ℃/min using a thermogravimetric analyzer. As shown in Figure 1, theoretical and actual co-pyrolysis characteristic indexes were calculated. When the mixing ratio of biogas residue was more than 30%, co-pyrolysis showed a synergistic effect and the concentration of volatile matter released from pyrolysis of the blend was increased and the devolatilization effect of pyrolysis was enhanced[1-3].

The kinetic parameters of co-pyrolysis were studied through Coats-Redfern integral model[4, 5]. The kinetic parameters fitted in the experiment are shown in Figure 2 and Table 1.It was found that with the increase of biogas residue mixing ratio from 0 % to 100 %, the activation energy and order of reaction in the volatilization analysis stage (main reaction stage) continuously decreased, the activation energy decreased

from 44.25 kJ/mol to 34.12 kJ/mol, and the order of reaction changed from 4 to 2.5, which reduced the energy required for the co-pyrolysis reaction and increased the reaction rate[6, 7]. At the same mixing ratio, the order of reaction and activation energy of co-pyrolysis were lower than the theoretical activation energy and order of reaction, and the co-pyrolysis of sludge and biogas residue showed obvious synergistic effect (Fig. 3、Fig. 4)[8-12]. This study will provide new ideas for the efficient pyrolysis and resource utilization of sludge and biomass.

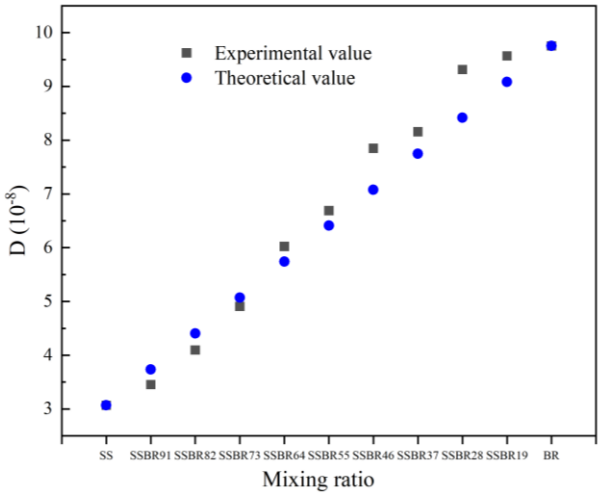

Fig.1 Co-pyrolysis characteristics index of sludge and biogas residue under different proportions

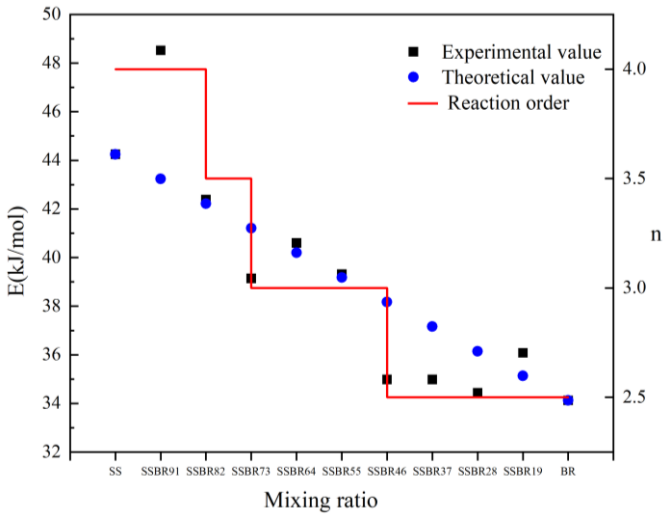

Fig. 2 Activation energy and order of reaction of co-pyrolysis of sludge and biogas residue under different mixing ratios

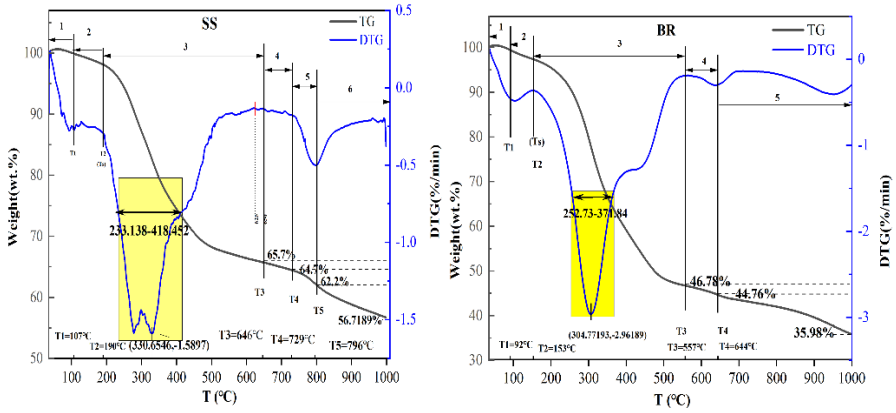

Fig. 3 TG-DTG curves of sludge and biogas residue during separate pyrolysis

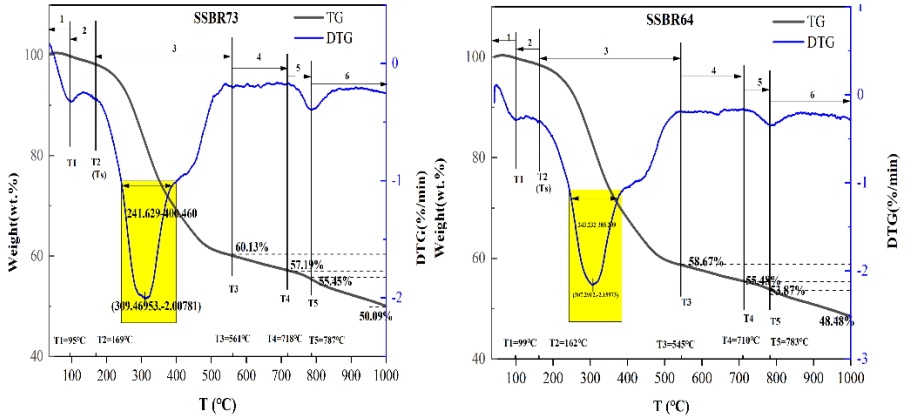

Fig. 4 TG-DTG curves of SSBR73 and SSBR64 for thermal degradation

Table 1 Kinetic parameters of co pyrolysis of sludge and biogas residue in the main reaction stage under different mixing ratios

Mixing ratio	Fitting equation	R^2	E(kJ/mol)	Reaction order
1:0	Y=-0.53219X-3.75225	0.9827	44.25	4
9:1	Y=-0.5836X-2.80329	0.9918	48.52	4
8:2	Y=-0.50984X-4.24102	0.9905	42.39	3.5
7:3	Y=-0.47081X-5.01822	0.9903	39.14	3
6:4	Y=-0.48836X-4.70244	0.9911	40.60	3
5:5	Y=-0.47289X-4.92583	0.9873	39.32	3
4:6	Y=-0.42081X-5.97501	0.9874	34.98	2.5
3:7	Y=-0.42081X-6.00962	0.9886	34.98	2.5
2:8	Y=-0.41424X-6.03907	0.9847	34.43	2.5
1:9	Y=-0.43399X-5.72429	0.9891	36.08	2.5
0:1	Y=-0.41045X-6.09332	0.9828	34.12	2.5

References

1. Lin, Y.; Liao, Y.; Yu, Z.; Fang, S.; Lin, Y.; Fan, Y.; Peng, X.; Ma, X., Co-pyrolysis kinetics of sewage sludge and oil shale thermal decomposition using TGA–FTIR analysis. *Energy Conversion and Management* **2016**.
2. Vikraman, V. K.; Kumar, D. P.; Boopathi, G.; Subramanian, P., Kinetic and thermodynamic study of finger millet straw pyrolysis through thermogravimetric analysis. *Bioresource Technol* **2021,** *342*, 125992.
3. Kumar, A.; Fouad, S. S.; El-Bana, M. S.; Mehta, N., Thermal analysis of cadmium addition on the glass transition and crystallization kinetics of Se-Te-Sn glassy network. *JOURNAL OF THERMAL ANALYSIS AND CALORIMETRY* **2018,** *131*, (3), 2491-2501.
4. Shao, Z.; Ma, Y.; Wang, B.; He, L.; Zhang, Z.; Yue, C., Study of pyrolysis and combustion kinetics of oil sludge. *Energy Sources, Part A: Recovery, Utilization, and Environmental Effects* **2021**, 1-15.
5. Li, D. Z., *Molecular Dynamics Simulations: Analysis for characterizing simulated atomic-scale defects in crystal, and Kinetic Analysis of Ethylene-Propylene Diene-Terpolymer(EPDM) pyrolysis using ReaxFF*. 2017.
6. Chaudhary, R. G.; Ali, P.; Gandhare, N. V.; Tanna, J. A.; Juneja, H. D., Thermal decomposition kinetics of some transition metal coordination polymers of fumaroyl bis (paramethoxyphenylcarbamide) using DTG/DTA techniques. *ARABIAN JOURNAL OF CHEMISTRY* **2019,** *12*, (7), 1070-1082.
7. Gou, X.; Zhao, X.; Singh, S.; Qiao, D., Tri-pyrolysis: A thermo-kinetic characterisation of polyethylene, cornstalk, and anthracite coal using TGA-FTIR analysis. *FUEL* **2019,** *252*, 393-402.
8. Zhang, X.; Lei, H.; Zhu, L.; Zhu, X.; Qian, M.; Yadavalli, G.; Wu, J.; Chen, S., Thermal behavior and kinetic study for catalytic co-pyrolysis of biomass with plastics. *BIORESOURCE TECHNOLOGY* **2016,** *220*, 233-238.
9. Chen, C.; Wu, H., Thermogravimetric kinetics of Chlorella pyrenoidosa and textile dyeing sludge blends during co-pyrolysis. *ENERGY SOURCES PART A-RECOVERY UTILIZATION AND ENVIRONMENTAL EFFECTS* **2017,** *39*, (14), 1469-1477.
10. Haque, M. A.; Chaudhary, R. G.; Paliwal, L. J., Synthesis, structural, morphological, and thermal decomposition kinetics of Iron (II) coordination polymer of sebacoyl bis (isonicotinoylhydrazone). *INORGANICA CHIMICA ACTA* **2017,** *462*, 298-307.
11. Xu, Z.-X.; Zhang, C.-X.; He, Z.-X.; Wang, Q., Pyrolysis Characteristic and kinetics of Polyvinylidene fluoride with and without Pine Sawdust. *JOURNAL OF ANALYTICAL AND APPLIED PYROLYSIS* **2017,** *123*, 402-408.
12. Yang, Z.; Gao, M.; Bai, Y.; Li, F., Model establishment for the kinetic evaluation of synergistic effect on the coal char gasification with H_2O and CO_2 mixtures. *APPLIED THERMAL ENGINEERING* **2017,** *118*, 682-690.

ANTI-FOULING APPLICATION FOR AIR-COOLED CONDENSERS TO IMPROVE POWER EFFICIENCY AT WASTE-TO-ENERGY PLANT

Ryo Nakajima, Kunihiro Takahashi, Hirotaka Fujiwara
Resource Circulation Technology Department Circular Economy Business Development Group
KURITA WATER INDUSTRIES LTD., Kurita Innovation Hub 1-4-1, Daikanyama, Akishima-shi, Tokyo, Japan

1.INTRODUCTION

In waste-to-energy plants, utilizing the heat energy produced by incineration is important. The air-cooled condenser is one component that contributes to the use of heat energy and affects power generation efficiency.

On the other hand, when dust adheres to the heat transfer tube surfaces of air-cooled condensers, cooling performance deteriorates. This causes the turbine exhaust pressure to rise and power generation output to decrease, particularly during the summer when outside air temperatures are high. Some facilities address this issue with regular cleaning, but periodic repairs and washing alone often fail to keep the area dust-free and may not fully resolve the problem.

To reduce dust-related performance issues, the authors applied an anti-fouling agent to the heat transfer tubes of the air-cooled condenser. This helped maintain airflow, reduce turbine exhaust pressure and cooling fan power, and stabilize power generation. The results are presented below.

2.MATERIALS AND METHOD

2.1 Overview of the evaluation facility

The evaluation test was conducted at the incineration facility shown in Table 1.

Table 1 Overview of Incineration Facilities

Waste type	Industrial waste
Years of operation	Over 10 years
Incineration capacity	60 t/day
Power generation output	2000 kW
Cooling fan specifications	55 kW × 2 units
Cleaning frequency	Twice a year (spring and summer)

At this facility, from spring to summer when the outside air temperature rises, the turbine exhaust pressure increases and the power output decreases. As a result of the investigation, it was found that the cause of the increase in turbine exhaust pressure was the adhesion of dirt such as soil dust, insects, and dust to the air-cooled condenser. The facility regularly cleans the air-cooled condenser, which involves a workload.

2.2 Chemicals

Table 2 shows the properties of the anti-fouling agent used in this evaluation test. The hydrophilic microparticles contained in the chemical form a film on the surface of the heat transfer tubes. This film is expected to provide anti-fouling properties by reducing the adhesion strength of hydrophobic dust.

Table 2 Characteristics of antifouling agents

Product name	KURITA KT
Main component	Hydrophilic fine particles
pH range	9.0～10.0

2.3 Application process

As shown in Fig.1 and 2, after high-pressure cleaning the surface of the heat transfer tubes of the air-cooled condenser, the anti-fouling agent was applied using the same procedure.

Fig.1Cleaning and Spraying Process (front side)

Fig.2 Cleaning and Spraying Process (back side)

2.4 Evaluation method

A comparative evaluation between untreated and anti-fouling agent coated cases was conducted based on the airflow volume outside the surface of the air-cooled condenser, cooling fan power, and power generation heat rate*. For the measurement of the air flow volume, the anemometer was used.

*As an indicator related to power generation efficiency, the power generation heat rate was used: the amount of power generation per unit steam (kW/t-main steam flow rate).

3.RESULTS AND DISCUSSION

3.1 Comparison of air flow volume

Table 3 shows the wind speed measurement results at the outlet of the heat transfer tube surface of the air-cooled condenser using an anemometer. Using the immediate post-cleaning state as a baseline, the airflow volume decreased by 27% after seven months without the application of anti-fouling agents. On the other hand, under the conditions where the agent was applied, the decrease was limited to 9%. Because the airflow volume

was maintained, the regular cleaning schedule, which had traditionally been twice a year (spring and summer), was able to be reduced to once a year (summer).

Table 3 Comparison of the wind speed measurements

State	immediate after cleaning (base line)	seven months after cleaning	Reduction rate %
No anti-fouling agent	7.5	5.5	27
With anti-fouling agent	7.5	6.8	9

* Measurement under cooling fan output condition of 97±3%

3.2 Comparison of Cooling fan output

When dust adheres to the heat transfer tubes of the air-cooled condenser, it leads to a decrease in heat exchange efficiency with the outside air and a decline in condensation efficiency, causing an increase in turbine exhaust pressure. Therefore, at this facility, cooling fans were controlled using turbine exhaust pressure as a control index. Table 4 shows the output results of the cooling fans for each outside air temperature with and without the anti-fouling agent. Conditions were compared in 5°C increments. Under conditions with outside air temperatures below 20°C, it was confirmed that turbine exhaust pressure did not increase, and improvement in heat exchange efficiency influenced the cooling fan output. When the anti-fouling agent was applied, the cooling fan output was confirmed to be reduced by about 10%.

On the other hand, under conditions where the outside air temperature is 20°C or higher, the turbine exhaust pressure tends to rise regardless of maintaining heat exchange efficiency by preventing dust adhesion, so the cooling fan operates at a value close to its maximum output, and a reduction in cooling fan output due to the application of anti-fouling agents was not observed.

Table 4 Comparison of cooling fan output by outside air temperature

Outside air temperature (°C)	0 to 5 °C	5 to 10 °C	10 to 15 °C	15 to 20 °C	20 °C<
No anti-fouling agent	50.9	56.6	64.3	74.6	88.9
With anti-fouling agent	- *	49.3	55.4	68.7	89.2
Comparison rate (%)	-	*87%*	*86%*	*92%*	*0*

* Data not obtained due to malfunction of the cooling fan instrument

3.3 Comparison of Power generation

When dust adheres to the heat transfer tubes of the air-cooled condenser, the heat exchange efficiency with the outside air decreases, resulting in an increase in turbine exhaust pressure. The rise in turbine exhaust pressure reduces the energy drop between the turbine inlet and outlet, which leads to a decrease in power generation. Table 5 shows a comparison of the power generation unit consumption with and without anti-fouling agents. The evaluation of power generation efficiency was conducted based on the amount of power generated per ton of steam (i.e., power generation unit consumption). As mentioned in "3.2 Trends in Cooling Fan Output," when the outside air temperature is 20°C or higher, the cooling fan operates near its maximum output. Therefore, if the cooling fan cannot maintain heat exchange efficiency under these conditions, the power generation unit consumption decreases. When the outside air temperature is below 20°C, the cooling fan can maintain heat exchange efficiency, so the power generation unit consumption does not decrease. When anti-fouling agents were applied, a suppression of 1.3 kWh/t–main steam flow reduction in the power generation unit consumption was confirmed at outside air temperatures of 20°C or higher, where heat exchange efficiency could not be maintained due to fluctuations in cooling fan output. This corresponds to approximately a 1% increase in power generation.

Table 5 Comparison of Power Generation Unit Values (kWh/t - Main Steam Quantity)

Outside Air Temperature (°C)	Below 20°C	Above 20°C
Cleaning Only	131.1	132.0
Cleaning + Antifouling Agent	131.2	133.3
Difference	*0.1*	*1.3*

4. SUMMARY AND FUTURE DEVELOPMENT

Table 6 shows the effects obtained by applying the anti-fouling agent "KURITA KT". Compared to conventional methods, the suppression of dust adhesion over time helped maintain heat exchange efficiency and airflow, resulting in a reduction in fan power consumption. Additionally, the frequency of cleaning operations decreased from twice a year to once a year, alleviating the workload of on-site workers. When converted to annual electricity consumption, the cooling fan's power improved by 66 MWh/year and the power generation intensity by 48 MWh/year, which also contributed to an increase in the facility's electricity sales revenue.

Table 6 Comparison of cooling fan output by outside air temperature

	cleaning frequency (time/year)	wind speed reduction rate* (%)	cooling fan output (<20°C) (%)	power generation unit consumption (kWh/t - Main Steam Quantity)
No anti-fouling agent	2	27	68.2	132.0
With anti-fouling agent	1	9	60.7	133.3

*seven months later

As a result of this initiative, it has been confirmed that applying anti-fouling agents to air-cooled condensers maintains condensation performance and contributes to the effective utilization of thermal energy. Based on the achievements discussed in this paper, we aim to develop more anti-fouling agents with higher effectiveness and improve the accuracy of diagnostic techniques, thereby supporting facilities facing challenges related to the effective use of thermal energy and onsite operational workloads.

References

1)Michiaki Hirose et al.: Recovery of Power Generation Terminal Efficiency by Cleaning Turbine Exhaust Condenser Fins at Toshima Incineration Plant, Cleaning Techniques No. 18, 2018

Recycling Li from Spent $LiFePO_4$ Batteries Through an Economical and Highly Efficient Strategy

Minhua Su[1]*, Jinfeng Tang[2], Junhua Xu[3], Diyun Chen[1]*

[1] *School of Environmental Science and Engineering, Guangzhou University, Guangzhou 510006, China*
[2] *Linköping University - Guangzhou University Research Center on Urban Sustainable Development, School of Environmental Science and Engineering, Guangzhou University, Guangzhou 510006, China*
[3] *Nuclear Chemistry & Separation and Purification Technology Laboratory, Fujian Institute of Research on the Structure of Matter, Chinese Academy of Sciences, Fuzhou 350002, Fujian, China*

Lithium (Li) recycling from spent Li-ion batteries remains a challenge primarily due to the many inherent complexities associated with conventional recycling processes. Herein, a low-cost and highly selective Li recovery strategy was innovatively assembled by employing a stoichiometric H_2SO_4–H_2O_2 system for the highly efficient recovery of metal Li from spent lithium iron phosphate ($LiFePO_4$, LFP) power batteries. The LFP cathode material was detached well from the aluminum plate under ambient conditions by using water as a stripping agent. Then, through a well-designed selective leaching process that consumed only very few amounts of acid, Li could be preferably extracted. At the same time, most iron (Fe) and phosphorus (P) were retained within the leaching residue in the form of $FePO_4$. The leaching rates for Li, Fe, and P varied remarkably, accounting for approximately 99, 0.02, and 1.5%, respectively, indicating that a highly selective strategy was achieved. Li ions present within the leaching solution were successfully precipitated as Li_2CO_3 by introducing Na_2CO_3 as a precipitant. Simultaneously, the leaching residue was converted directly to FePO4 via calcination at 600 °C for 4 h to eliminate residual organic impurities. The novel stripping method, combined with the optimized H_2SO_4–H_2O_2 selective leaching system, demonstrates significant potential for industrial application. The efficacy of this recovery process for spent $LiFePO_4$ ion batteries constitutes a significant advancement toward environmentally sustainable and economically feasible lithium recycling.

Keywords: Spent lithium-ion batteries, $LiFePO_4$, stripping, leaching, precipitation, recycling

Recovery of Valuable Metals from Incineration Ash as Non-Ferrous Refining Materials Using Melting Technology

Motohiro Sakamoto[1], Yuto Onuma[1], Shigenori Inoue[1]
1 Water and Environment R&D Dept.I, Kubota Corporation,
1-1, Hama 1-chome, Amagasaki, Hyogo ,661-8567 Japan

ABSTRACT

Incineration ash derived from municipal solid waste and industrial waste contains valuable metals, such as gold and copper, originating from small electronic devices, circuit boards, and wiring, and is anticipated to be utilized as an urban mine. However, the concentration of these metals in incineration ash is relatively low, resulting in a significant portion remaining unrecovered. The development of technology aimed at achieving both resource recovery from incineration ash and the extraction of valuable metals is currently being advanced by Kubota Corporation. This technology combines the Kubota Surface Melting Furnace (KSMF) with a uniquely developed metal separator which is wet specific gravity separator, thereby contributing to the establishment of a recycling-oriented society. In the melting furnace, valuable metals within the incineration ash alloy with iron to form metal particles, which can subsequently be recovered by separating them from the slag discharged from the furnace. This paper presents the results of a performance evaluation test of the metal separator, detailing the quantity of recoverable valuable metals and their assessed value from the slag produced by five Kubota Surface Melting Furnaces (KSMF) installed at waste treatment plants.

1. INTRODUCTION

The development of a resource recycling system centered on the Kubota Surface Melting Furnace (KSMF) is currently underway (shown in Fig. 1). To promote this system, efforts have focused on the practical application of technology aimed at effectively utilizing waste plastics containing vinyl chloride, which are challenging to recycle, as alternative fuel for KSMF [1-3]. Additionally, technology has been developed to concentrate, separate, and recover valuable metals present in low concentrations within incineration ash destined for landfill.

In KSMF, harmful heavy metals can be volatilized and removed by melting incineration ash in a furnace maintained at temperatures around 1,300°C using a fuel burner and/or waste plastics. This process results in the production of harmless molten slag (hereinafter referred to as "slag") through water cooling and vitrification of the melt. Valuable metals contained in low concentrations within the incineration ash are alloyed with iron and copper, forming molten metal with a diameter of several millimeters (hereinafter referred to as "metal"). The concentration of valuable metals in the recovered metals reaches levels tens of times greater than that of natural ores, indicating potential for utilization as an urban mine.

Previous investigations have demonstrated that slag from municipal solid waste and industrial waste disposal site contains a significant amount of valuable metals, which can also be marketed to non-ferrous metal refining manufacturers.[4-6]

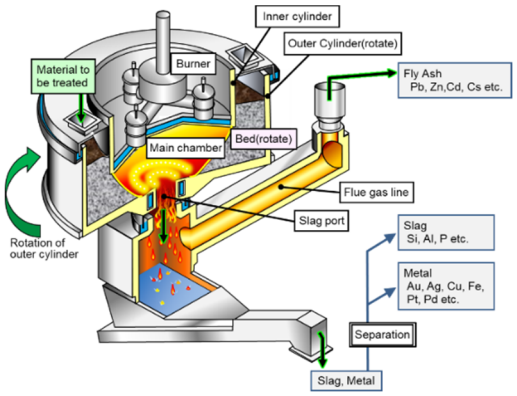

Fig. 1 Schematic Diagram of Kubota Surface Melting Furnace (KSMF)

In response to this finding, our company is advancing the development of a metal separator designed to efficiently extract and recover metal fractions containing valuable metals from these slags. This study involved the construction of a demonstration test facility of the metal separator currently under development, and its performance and recovery rate through long-term testing has been evaluated.

Furthermore, to evaluate the quantity of valuable metals that can be recovered from these slags by this metal separator and their respective value, an assessment of the molten slag was performed by inputting it into the metal separator from an actual waste treatment plants.

2. EXPERIMETAL METHOD

2.1. Development of Metal Recovery System

2.1.1. Outline

The metal separator is a wet specific gravity separator that can separate and recover materials based on differences in specific gravity.

Figure 2 shows the flow diagram of the metal

separation and recovery technology. A slag containing metal is transported to a metal separator body by conveyor from a slag hopper. The transported slag and water are supplied from the top of the rotating metal separator body. Additionally, another water is introduced from the bottom of the metal separator body, allowing metal with a high specific gravity (specific gravity 7–8) to be collected at the lower heavyweight side against the flow. Conversely, the slag with a lower specific gravity (specific gravity 2–3) is discharged from the top of the separator body to the slag discharge conveyor along with water. The water supplied to the metal separator is recycled from the slag discharge conveyor.

Figure 3 displays photos of the input slag introduced to the metal separator, recovered heavyweight materials and lightweight materials from the metal separator. The intentionally yellow-colored metal particles are observed to be recovered on the heavyweight side.

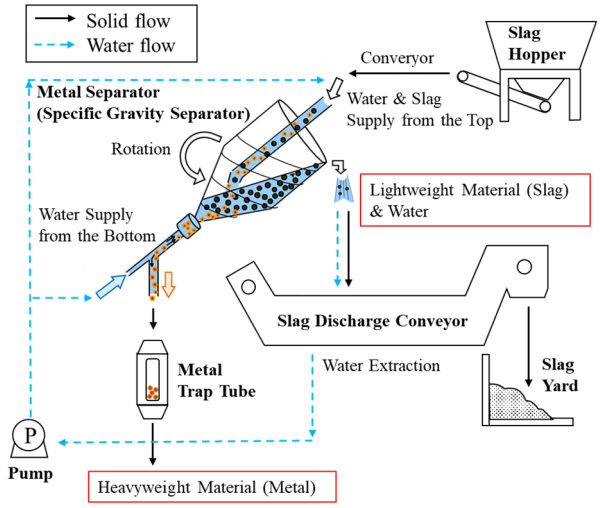

Fig. 2 Flow Diagram of the Metal Recovery System

Input Slag | Heavyweight Materials (Metal Particle) | Lightweight Materials (Slag)

Fig. 3 Input Slag, Recovered Heavyweight and Lightweight Materials from the Metal Separator

2.1.2. Evaluation of the metal recovery rate of this system

The slag samples used in this demonstration test, consisting of approximately 200 tons discharged from KSMF over several months, were collected. The metal ratio (defined as the amount of metal in the slag) is known to vary depending on the disposal site and region. Therefore, two types of slag with differing metal ratios (0.3% and 5.0%) were prepared for this test.

To investigate the effect of the slag feeding rate on the metal recovery rate, continuous tests were conducted for 5 to 7 hours under three conditions: slag feeding rates of 0.5 t/h, 2.0 t/h, and 3.5 t/h at a constant metal ratio of 0.3%, respectively.

In addition, to investigate the effect of the metal ratio of slag on the metal recovery rate, the similar continuous tests were conducted under two conditions: metal ratio of 0.3% and 5.0% at a constant feed rate of 3.5 t/h , respectively.

2.1.3. Evaluation Method

The performance of the metal separator was evaluated based on the metal recovery rate under each condition. The metal recovery rate was calculated by dividing the amount of metal recovered by the metal separator by the amount of metal contained in the slag prior to separation. The amount of metal before separation was determined from the quantity of metal recoverable by the metal separator and the amount of metal in the slag discharged into the slag discharge conveyor.

2.2. Evaluation on the Value of Metal Recovered from Actual Molten Slags

To evaluate the amount and the value of valuable metals recoverable from actual slag discharged from operational or previously operated melting furnaces, molten slag was sampled from municipal solid waste and industrial waste plants. The sampled slag was processed using the metal separator mentioned above to recover metals.

The concentrations of valuable metals (gold, silver, copper, platinum, palladium) in the recovered heavyweight materials (hereinafter call as metal) were determined by chemical analysis using inductively coupled plasma mass spectrometry (ICP-MS). Based on the concentrations of valuable metals in the heavyweight material and their current market prices, the recoverable value was assessed.

3. RESULUTS AND DISSCUSSIONS

3.1. Evaluation of Metal Recovery System

3.1.1. Metal Recovery Rates by Slag Feed Rate

The metal recovery rate, defined by a constant metal ratio, was evaluated as the slag feed rate to the metal separator varied, as illustrated in Fig. 4. Fluctuations between 80% and 90% or higher were observed during the experimental period; however, it was determined that

a high metal recovery rate consistently exceeded 80%. The average metal recovery rates were recorded at 92% for a feed rate of 0.5 t/h, 89% for 2.0 t/h, and 87% for 3.5 t/h, indicating a robust recovery rate above 85%. It was confirmed that a high recovery rate was maintained despite variations in the slag feed rate.

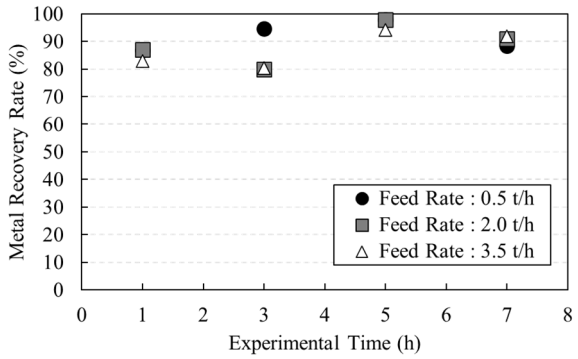

Fig. 4 Time Dependence of Metal Recovery Rates at Different Feed Rates with a Constant Metal Ratio

3.1.2. Metal Recovery Rates by Metal Ratio

The metal recovery rate of 0.3% and 5.0% at a constant slag feed rate of 3.5 t/h is shown in Fig.5. The average metal recovery rate was 87% when the metal percentage was 0.3%, and 89% when the metal percentage was 5.0%, and there was no significant difference. From this, it was found that even if the metal ratio changed, the metal recovery rate of 80% or more was maintained stably.

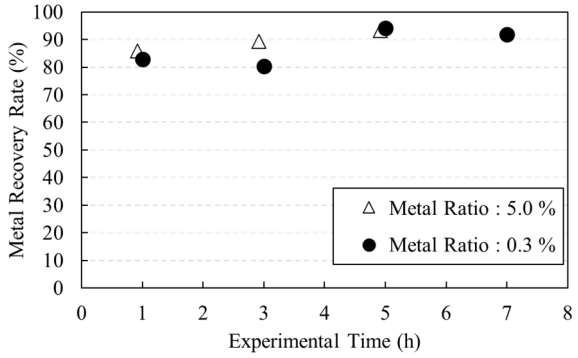

Fig. 5 Time Dependence of Metal Recovery Rates at Different Metal Ratios with a Constant Feed Rate

3.2. Value of Metals Recovered from Actual Slags

3.2.1. Amount of Metal in Actual Molten Slag

Metal separation tests were conducted on five (written in here as A to E plants) waste treatment plants. The results are shown in Fig. 6. 1 to 6 mass% of metals, that is heavyweight materials, could be recovered from the actual slag. The difference in the amount of metal seems to come from the kinds of waste and the region.

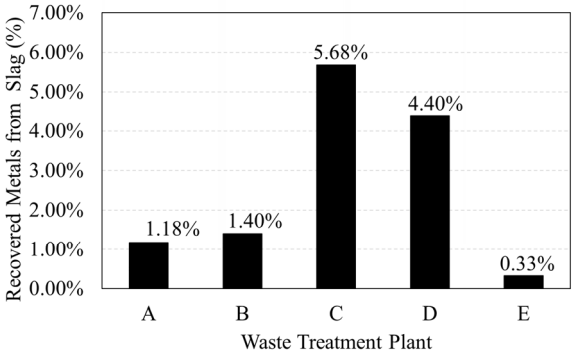

Fig. 6 Amount of Metal in the Actual Molten Slag

3.2.2. Average Composition of the Recovered Metal Amount in Each Molten Slag

Table 1 shows the average composition of the valuable metal in recovered metals of five plants.

High concentrations of valuable metals, including gold, silver, copper, platinum, and palladium, were found in the recovered metal from all waste treatment plants. In particular, the concentration of valuable metals recovered from the slag of plants A, B and E is confirmed to be high.

For example, a gold (Au) concentration of the recovered metal from all five treatment plants surpassed the average gold ore grade (around 4 mg/kg), allowing for sale as raw materials for non-ferrous smelting manufacturers. This suggests that low-concentration valuable metals present in incineration ash, which were previously underutilized, can be effectively recycled as raw materials for non-ferrous smelting by integrating a melting furnace with a separator.

Table 1 Average Composition of Metals Recovered by the Metal Separator

Plants	Gold	Silver	Copper	Platinum	Palladium
	Au	Ag	Cu	Pt	Pd
	mg/kg	mg/kg	mass%	mg/kg	mg/kg
A	211	1278	36	38	51
B	293	1786	59	64	82
C	44	167	9	54	65
D	32	402	24	8	10
E	561	2521	74	58.5	197

3.2.3. Value of Molten Slag and Recovered Metals

The value of the valuable metals in recovered metal was estimated based on the metal ratio of slag, their average composition, and the metal market prices as of September 2025 (Fig. 7). The estimated value of the recovered weight per ton of molten slag ranged from ¥42,000 to ¥100,000. Among the recovered metals, gold has the highest value at all treatment plants, followed by copper, palladium, and platinum.

Therefore, it is posited that the integration of a melting furnace and a metal separator could facilitate the

recovery of valuable metals from previously untapped low-concentration waste incineration ash, thereby completing the resource circulation loop and enhancing the profitability of treatment plants through the sale of recovered valuable metals.

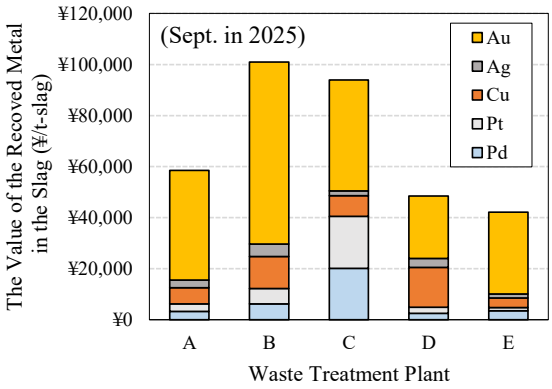

Fig. 7 Value of Valuable Metals in Actual Slags from Various Waste Treatment Plants

4. CONCLUSIONS

To establish a resource recycling system with zero landfill disposal centered on Kubota Surface Melting Furnace (KSMF), a demonstration test facility for metal separation and recovery technology was constructed. Tests were conducted under various operating and raw material conditions. Furthermore, the value of recovered metal from the slags of the five actual waste treatment plants was investigated by using the metal separator, leading to the following findings:

1) It was observed that, regardless of variations in the slag feeding rate and the metal ratio, defined as the amount of metal in the slag, in the slag, the average metal recovery rate exceeded 85%. Even considering operational variations, a high recovery rate of over 80% was consistently maintained.

2) The recovered heavy material from all five treatment plants surpassed the average gold ore grade and can be marketed as raw materials for non-ferrous smelting. This demonstrates that the low concentration of valuable metals in previously uncollected incineration ash can be effectively recycled as raw materials for non-ferrous smelting through the integration of a melting furnace and a separator.

3) The value of the recovered metal ranged from ¥42,000 to ¥100,000 per ton of molten slag, indicating that the sale of the recovered valuable metal has the potential to enhance the profitability of the treatment plant.

ACKNOWLEDGMENTS

We would like to express my sincere gratitude to the following companies for their invaluable support and cooperation in conducting this research: Greater Nagano Region Union, Chikuma Environmental Service, and Takasawa-Sangyo Co., Ltd. Your contributions have been instrumental in the success of this study.

REFERENCES

[1] Y.Hirato, F.Hosho, S.Inoue, E.Tsuji, “Development of energy-saving technology for a melting furnace using RPF as a combustion improver.” *Proceedings of the 34th Annual Meeting of the Japan Society of Waste Cycles*, pp373-374, 2023

[2] Y.Hirato, Y.Onuma, M.Sakamoto, F.Hosho, S.Inoue, E.Tsuji, “Development of Melting Furnace to Achieve Resource Circulation”, *Proceedings of the 14th China-Japan Joint Conference on Material Recycling and Waste Management,* 2023

[3] K.Fujiwara, Y.Hirato, K.Akasaka, S.Otaki, S.Okaichi, F.Hosho, S.Inoue “Development of the Surface Melting Furnace Technology by Using Fuel Made from Waste Plastics Difficult to Recycle as Materials” *Proceedings of the 35th Annual Meeting of the Japan Society of Waste Cycles,* pp.365-366, 2024

[4] N.Yamaguchi, T.Matsuto, Y.Tojo, A.Nakamine, “Assessment of the metallic resource potential of molten metal generated from municipal solid waste waste gasification and melting facilities”, ippan haikibutsu gasu-ka yōyū oyobi hai yōyū shisetsu de seisei sareru yōyū metaru no kinzoku shigen-sei hyōka(in Japanse), *Japanese Journal of JSC*. vol78, No.1, pp1-8, 2020

[5] M.Sakamoto, K.Akasaka, Y.Onuma, S.Okaichi, F.Hosho, S.Inoue, D.Higashi, F.Watanabe, K.Hoshiyama, “Development of Technology for Recycling Thermal Energy and Valuable Metals from Industrial Waste by Using the Surface Melting Furnace” *The 33rd Environmental Technology Symposium of JSME*, 2023

[6] M.Sakamoto, Y.Onuma, S.Inoue, “Recovering valuable metal from waste using a rotating surface melting furnace” *Proceedings of the 35th Annual Meeting of the Japan Society of Waste Cycles,* pp.321-322, 2024

Bioaerosol contamination binds to $PM_{2.5}$ during leachate treatment: Occurrence characteristics of human pathogens, virulence factor genes and antibiotic resistance genes

Ya-nan Wang, Wenyu Yang, Wenyu Wang, Yifan Zheng, Huawei Wang*, Yingjie Sun, Bingpeng Wang, Xiongbo Cui, Ying Gao**

School of Environmental and Municipal Engineering, Qingdao University of Technology

777 Jialingjiang East Road, Huangdao District,, Qingdao, China

The binding of bioaerosol contamination to $PM_{2.5}$ leads to significant ecological and public health concerns, but studies on the binding of bioaerosols to $PM_{2.5}$ during leachate treatment are rare. This study comprehensively investigated the behavior of bioaerosols bound to $PM_{2.5}$ and the potential pathogenicity that subsequently occurs during leachate treatment. The results revealed that the mass concentration of $PM_{2.5}$ was the lowest in the evaporation treatment workshop (ETW) and the highest in the biochemical treatment workshop (BTW). *Burkholderia* and *Aureobasidium* were the dominant strains in $PM_{2.5}$. The SO_4^{2-} content in $PM_{2.5}$ was significantly positively correlated with the *Burkholderia* and *Aquabacterium* abundances, whereas the Cl^-, NO_3^- and NO_2^- contents were negatively correlated with the *Burkholderia* and *Ralstonia* abundances. *Burkholderia cepacia, Ralstonia pickettii* and *Stenotrophomonas maltophilia* were the dominant bacterial pathogens. Hundreds of virulence factor genes (VFGs) and subtypes of antibiotic resistance genes (ARGs) were detected during leachate treatment, especially in the advanced membrane treatment of leachate and the evaporation treatment of concentrated leachate. VFGs and ARGs cooccur widely in $PM_{2.5}$-associated microbes, especially in *Burkholderia* and *Pseudomonas*. This study helps increase the understanding of the pollution behavior and potential disease risk of aerosol particles during landfill leachate treatment.

Keywords: Bioaerosol contamination; $PM_{2.5}$; Human pathogens; Virulence factor genes; Antibiotic resistance genes

INTRODUCTION

In recent years, epidemic respiratory diseases that are caused by bioaerosol pollution have become a popular research topic in the field of global public health (Wang et al., 2021). Bioaerosols, which are composed of airborne particles of biological origin, such as bacteria, fungi, viruses, and their genetic components, pose significant risks to public health and the environment, particularly in environments with high organic waste-processing activities (Han et al., 2020). The increase in antibiotic resistance worldwide and the increasing reports of pathogen-carrying bioaerosols have highlighted the role of bioaerosols as key routes of transmission for infectious diseases and antibiotic resistance genes (ARGs) (Chen et al., 2022a).

Landfill leachate, which is a complex wastewater that contains high concentrations of organic matter, heavy metals, and microorganisms, requires complicated treatment processes, such as aeration, agitation, and spraying (Yang et al., 2024). These activities inevitably generate bioaerosols, dispersing microbial contaminants into the surrounding environment (Wang et al., 2018). Inhalation of bioaerosols has been associated with respiratory diseases, allergic reactions, and even outbreaks of infectious illnesses. Mechanical operations (stirring, aeration, sludge dewatering, etc.) during leachate treatment can

aerosolize microbial contaminants, including ARGs and virulence factor genes (VFGs), which may bind to airborne fine particulate matter ($PM_{2.5}$) and be dispersed over long distances (Li et al., 2024). In addition, advanced oxidation processes (i.e., Fenton reactions and ozone oxidation) can effectively degrade recalcitrant organic compounds in leachate, which may inadvertently produce toxic intermediates that alter microbial communities and increase bioaerosol pathogenicity (Wang et al., 2022). However, previous studies have focused mainly on chemical pollutants in leachate, and bioaerosol emission during leachate treatment remains poorly characterized.

The association between bioaerosols and $PM_{2.5}$ introduces synergistic health risks, as $PM_{2.5}$ can penetrate deep into the alveolar regions of the human respiratory system and act as a vector for pathogenic invasion by facilitating the transport of human pathogens and genetic substances related to virulence and resistance (Zuo et al., 2024). Zhang et al. (2021a) sampled and analyzed aerosols in the air environment of a municipal sewage treatment plant, and they found that the aerosols contained 14 kinds of human pathogens, which carried 530 ARG subtypes. Additionally, Yang et al. (2023a) studied the ARGs of bioaerosols in sewage treatment plants; they detected 23 kinds of ARGs in 10 collected samples, consisting of 523 subtypes, and Proteobacteria and Actinobacteria were the most abundant ARG-related phyla in all the samples. Moreover, Zhou et al. (2024) analyzed the seasonal variation of VFGs in aerosol particles in Beijing and reported that *SigA* and *rpoV* (encoding regulatory factors), *sugC* (encoding nutritional and metabolic factors), and *groEL2* (encoding adhesion factors) were the most abundant VFGs across all seasons and that *Azospirillum* plays a key role in carrying VFGs. Bioaerosols from waste treatment facilities often harbor diverse human pathogens, such as *Acinetobacter*, *Pseudomonas*, and *Enterobacter*, as well as a wide array of VFGs and ARGs (Wang et al., 2024a). These microbial contaminants can persist in the air and exhibit enhanced resistance to environmental stressors when bound to $PM_{2.5}$ (Wu et al., 2022). At present, research on VFG and ARG transmission by bioaerosols has focused mainly on specific environments, such as waste disposal sites (Zhang et al., 2021a; Wang et al., 2024a). However, research on the binding bioaerosols to $PM_{2.5}$ in leachate treatment environments remains rare, limiting our understanding of their health implications.

Therefore, this study systematically investigated the behavior of bioaerosols bound $PM_{2.5}$ and the potential pathogenicity that occurred during leachate treatment. The aims of this study were (1) to study the differences in microbial composition between $PM_{2.5}$-associated and inhalable culturable bioaerosols; (2) to evaluate the relationship between the physicochemical properties of $PM_{2.5}$ and its microbial community; (3) to determine the main potential pathogens and their diversity and abundance in $PM_{2.5}$ during leachate treatment; and (4) to identify the occurrence and coexistence characteristics of human bacterial pathogens (HBPs), VFGs and ARGs in $PM_{2.5}$. This study will increasing the understanding of bioaerosol contamination behavior and potential disease risks in the leachate treatment process.

MATERIALS AND METHODS

Sampling points

A leachate treatment plant located at 120°09 '23 "E and 36°16' 51" N in Qingdao, Shandong Province, was selected as the study object. The leachate treatment plant mainly treats leachate that is produced by landfills, food waste plants and incineration plants, with a treatment capacity of 1700 t/d. The leachate treatment process mainly includes the following: a preprocessing system (regulating tank + preliminary sedimentation tank), a biochemical treatment system (two levels of anoxic-aerobic + membrane bioreactor), and a membrane deep treatment system (disc tube reverse osmosis membrane, DTRO). The concentrated leachate that is generated by the DTRO

system is treated by a mechanical vapor recompression (MVR) evaporation system.

Mechanical disturbance is a key factor in the formation of bioaerosols. For example, mechanical operations such as aeration and stirring in biochemical tanks, backwashing in membrane workshops, sludge pressure filtration, and evaporation treatment promote the aerosolization of microorganisms during the leachate treatment process. Therefore, a biochemical treatment workshop (BTW), a membrane deep treatment workshop (MDW), an evaporation treatment workshop (ETW) and a sludge dewatering workshop (SDW) were selected for the collection of culturable bioaerosols and $PM_{2.5}$. The specific sampling points are shown in **Fig. 1**.

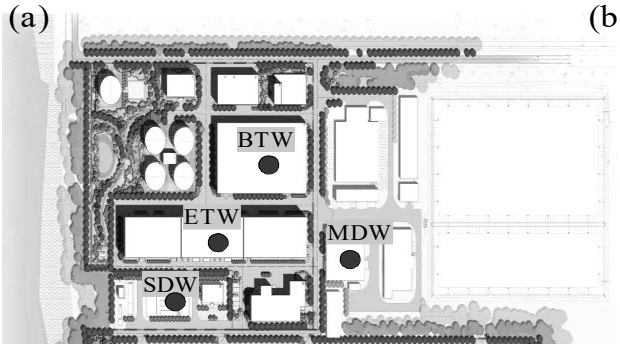

(b)

Sampling point		Function / Process
BTW	Biochemical treatment workshop	A/O-A/O process
MDW	Membrane deep treatment workshop	Disc tube reverse osmosis process (DTRO)
ETW	Evaporation treatment workshop	MVR evaporation process for concentrate leachate treatment
SDW	Sludge dewatering workshop	Sludge dewatering treatment

Fig. 1 The sampling points of culturable bioaerosols and $PM_{2.5}$ during the leachate treatment process

Sample collection

An Andersen six-level air microbial sampler (FA-1, Zhengzhou, China) was used to collect culturable bioaerosols (including bacterial and fungal aerosols). The sampling time for culturable bioaerosols was from September 22nd to 23rd, 2023. During the sampling period, the ambient temperature ranged from 23.6 to 24.8 °C. Sampling was conducted indoors at all points (the workshop was mainly sealed). All the samples were collected in parallel. The procedures for the collection and cultivation of culturable bioaerosols were described by Wang et al. (2024a).

The fine particulate matter ($PM_{2.5}$) in the workshops was sampled by a high-flow air-suspended particulate matter sampler equipped with a $PM_{2.5}$ cutter (Laoying 2031, Qingdao, China). The $PM_{2.5}$ sampling period was from September 22nd to 26th, 2023, and the ambient temperature during the sampling period was 23.6~25.3 °C. The sampling membrane was a polycarbonate membrane with a size of 30 cm×21 cm and a pore diameter of 0.22 μm. The gas flow rate during sampling was set to 1100 L/min, and the sampling time was 22 hours. Two sets of parallel samples were collected from each sampling point. The collected samples were stored at -80 ℃ for further analysis of the microbial genome and physicochemical properties of the particulate matter.

Sample analysis

Physicochemical properties of particulate matter: A sampling filter membrane with an area of 144 cm^2 was cut into fragments and placed in a sterile centrifuge tube containing 50 mL of ultrapure water. This membrane was subjected to extraction in an ultrasonic ice water bath for 60 minutes, followed by mechanical oscillation for 60 minutes, and then the supernatant was collected through filtration. Finally, the physicochemical properties of the collected $PM_{2.5}$ were analyzed.

The physicochemical properties of $PM_{2.5}$ include pH, electrical conductivity (EC), oxidation–reduction potential (ORP), total organic carbon (TOC), total nitrogen (TN) and water-soluble inorganic anions.

The pH, EC and ORP were determined through the electrode method with a pHS-3C meter, DDS-307 conductivity meter and Thermo-snK15317 ORP tester, respectively. The TOC and TN contents were analyzed using a TOC analyzer (MultiN/C2100, Jena, Germany). The concentrations of inorganic anions (i.e., F^-, Cl^-, SO_4^{2-}, NO_2^-, and NO_3^-) were analyzed by ion chromatography (Aquion, Thermo Fisher, America).

A sampling filter membrane with an area of 33 cm^2 was digested in a graphene digestion instrument. After digestion, the contents of heavy metals (Cu, Zn, Ni, Pb, Cr, and As) were determined by inductively coupled plasma–mass spectrometry (iCAP RQplus ICP–MS, Thermo Fisher, America).

Microbial community structure of bioaerosols：The samples of culturable bioaerosols and $PM_{2.5}$ on the filter membrane were subjected to DNA extraction using a soil microbial DNA extraction kit (Qiagen, America) according to the manufacturer's instructions. After extraction, the concentration and purity of the DNA were determined by a microspectrophotometer (NanoDrop, Thermo Fisher, America). The high-quality DNA samples were sent to Sangon Biotech (Shanghai) Co., Ltd., for high-throughput sequencing.

Metagenomic analysis：DNA samples from the $PM_{2.5}$ were subjected to metagenomic sequencing on the Illumina NovaSeq 6000 platform. The raw data were evaluated and filtered by Fastp, the contaminated sequences were removed, and the contigs were spliced using Megahit and SPAdes. Metawrap was used to complete bin sorting, quantification, reassembly and identification and screen for single bacterial genomes with high integrity and low contamination. Prodigal was used to predict ORFs (≥ 100 bp), and CD-HIT was used to eliminate redundancy and generate nonredundant gene sets. Salmon (version 1.5.0) was used to quantify gene abundance (Wang et al., 2024b).

The gene set protein sequences were compared with the Pathogen Host Interactions Database (PHI-base), the Virulence Factor Database and the Antibiotic Resistance Genes Database for blastp homology using DIAMOND to obtain functional annotations, homologous species information and gene information. The filter conditions were as follows: E value < 1e-5 and score > 60. Based on the results of the analyses, HBPs were identified, and the abundance of ARGs and VFGs in each sample was determined.

Statistical analysis

All the charts in this work were generated using Origin 2021. The correlations between the microbial community and the physicochemical properties of $PM_{2.5}$ were analyzed by SPSS Statistics 22. The microbial co-occurrence network was analyzed by using Gephi software.

RESUITS AND DISCUSSION

Differences in microbial composition between $PM_{2.5}$-associated and inhalable culturable bioaerosols

Composition of the microbial community bound to $PM_{2.5}$：The composition of the microbial community bound to $PM_{2.5}$ is shown in **Fig. 2**. *Burkholderia* was the dominant bacterial genus, accounting for 13.4%, 62.9%, 30.8%, and 27.1% of the samples from the BTW, MDW, ETW and SDW, respectively. *Burkholderia* has strong environmental adaptability and stress resistance because its cell membrane contains a high proportion of hydrophobic lipids, which can resist dryness and ultraviolet radiation and allow the microbe to survive for a long time in airborne particulate matter (Ghosh et al., 2023). *Burkholderia* is a genus within the β-*Proteobacteriaceae* that contains numerous opportunistic pathogens (such as *Burkholderia cenocepacia* and *Burkholderia*), which can be found in diverse environments and can infect the lungs of humans (Butt and Thomas, 2017). A high proportion

of *Ralstonia* was detected in the ETW sample, with a relative abundance of 59.5%. *Ralstonia* (such as *Ralstonia pickettii*) can survive and grow in extreme environments (such as high temperature and high humidity) and are emerging pathogens in the hospital setting that are increasingly associated with opportunistic infections (Rajni et al., 2023). *Aureobasidium* was the most dominant fungal genus, accounting for 67.6%, 82.1%, 74.4% and 34.2% of the samples from the BTW, MDW, ETW and SDW, respectively. A high abundance of *Alternaria* was detected in the SDW samples, accounting for 49.2%. *Alternaria* is one of the most common genera of allergic fungi and is considered one of the main sources of air allergens (Abel-Fernández et al., 2023). Compared with those in the MDW and ETW samples, the diversity and richness of the microbial communities in the BTW and SDW samples were greater **(Fig. 3)**. The BTW is the key area for the biological treatment of leachate, and the abundant organic matter and nutrients provide rich resources for the growth and reproduction of microorganisms; thus, the microbial community on $PM_{2.5}$ from the BTW exhibited high abundance and diversity. Sludge is rich in microorganisms, and the dewatering process causes many microorganisms to be discharged into the air, resulting in high abundance and diversity of the $PM_{2.5}$ microbial community in the SDW. In the MDW and ETW, biodegradable organic matter was scarce, resulting in simpler and less abundant microbial communities.

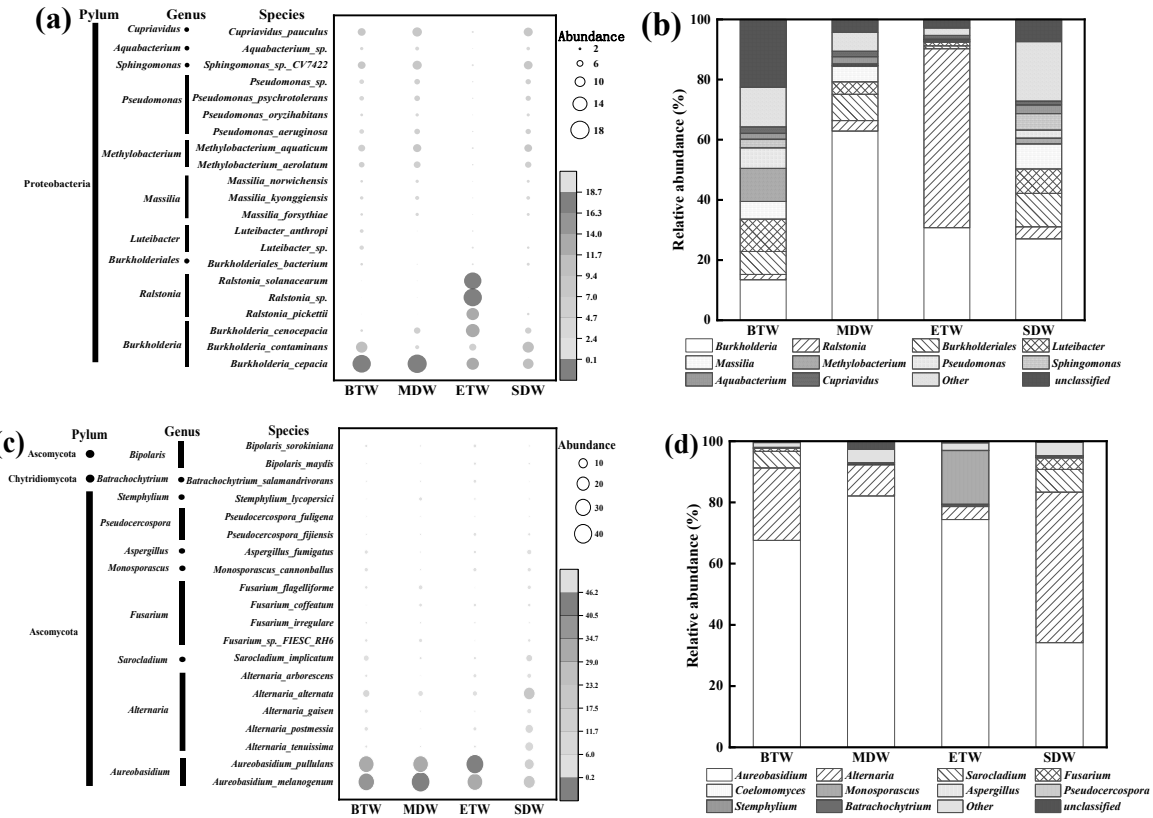

Fig. 2 The bacterial (a, b) and fungal (c, d) community composition in $PM_{2.5}$ during the leachate treatment process.

Differences in microbial community composition between $PM_{2.5}$-associated and inhalable culturable bioaerosols：The differences in bacterial and fungal community compositions between $PM_{2.5}$-associated and inhalable culturable bioaerosols (particle sizes of 0.65~2.1 μm) at the genus level are shown in **Fig. 4.**

Among the bacteria, *Bacillus*, *Staphylococcus* and *Kocuria* were the dominant genera in the inhalable culturable bioaerosol samples, indicating that these genera are more likely to accumulate and reproduce in nutrient-rich environments (Sutthiwong et al., 2023). *Bacillus* showed an absolute abundance advantage in each workshop, suggesting that *Bacillus* has a strong ability to become aerosolized during leachate treatment. *Bacillus* may cause respiratory tract infections or allergic reactions in occupationally exposed personnel; for example, some *B. cereus* strains can cause localized wound and eye infections as well as systemic disease (Ehling-Schulz et al., 2019). *Burkholderia* and *Ralstonia* were the dominant $PM_{2.5}$-associated genera in each sample, but they were not the main genera in the inhalable culturable bioaerosols.

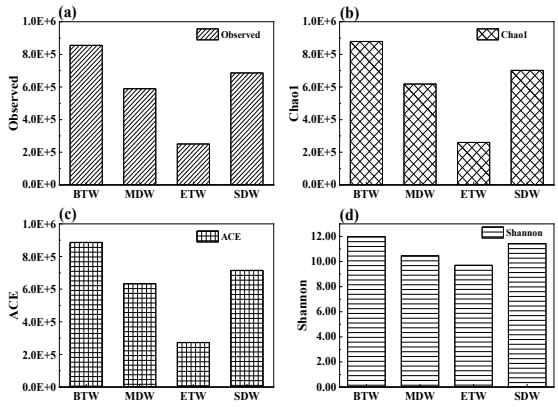

Fig. 3 Gene diversity index of each workshop (a) Observed, (b) Chao1, (c) ACE, and (d) Shannon culturable bioaerosol (a) bacteria and (b) fungi.

Alternaria and *Penicillium* were the dominant fungal genera in the inhalable culturable aerosol samples, whereas *Aureobasidium* and *Alternaria* were the dominant $PM_{2.5}$-associated genera. The relative abundance of *Alternaria* in culturable and $PM_{2.5}$-associated microorganisms in each workshop was relatively high because of its strong environmental adaptability and transmission ability (Filali et al., 2015). *Alternaria* is a strong allergen that can increase the risk of allergic rhinitis, asthma and chronic respiratory diseases with long-term exposure.

The microbes that bind to $PM_{2.5}$ include culturable and unculturable microorganisms that can efficiently utilize existing resources or adopt special survival strategies to survive under nutrient-deficient conditions, whereas the dominant microbes on inhalable culturable aerosols can more effectively obtain resources and resist competition from other microorganisms on the same culture medium (Xu et al., 2019). Therefore, the dominant microbes on $PM_{2.5}$-associated and inhalable culturable bioaerosols significantly differed.

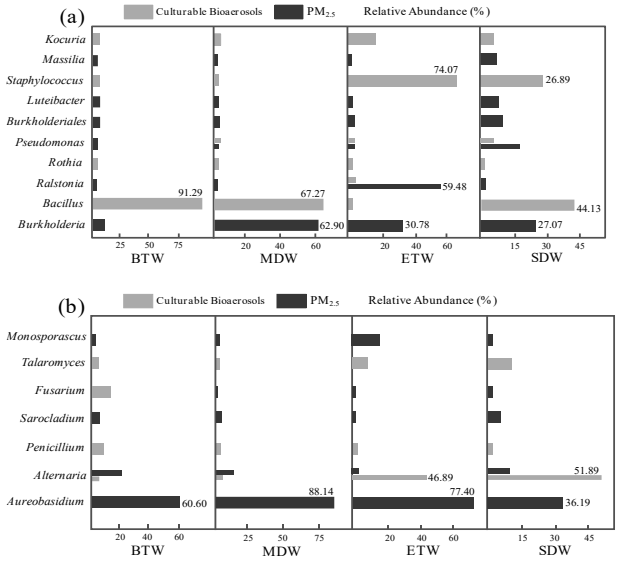

Fig. 4 Differences in microbial community composition between $PM_{2.5}$-associated and inhalable

Effects of the physicochemical properties of $PM_{2.5}$ on the composition of bound microbes

Physicochemical properties of $PM_{2.5}$:The physicochemical properties of $PM_{2.5}$ in the leachate treatment process are shown in **Fig. 5**. The mass concentration of $PM_{2.5}$ was lowest in the ETW but highest in the BTW. The TOC content in $PM_{2.5}$ ranged from 38.8 to 63.7 mg/g, and the TN content in $PM_{2.5}$ ranged from 43.4 to 67.3 mg/g. The BTW had the highest contents of TOC and TN, mainly because the decomposition of organic matter by microorganisms in the biochemical treatment process produces metabolic byproducts such as volatile fatty acids and organic acids, and these organic matters attached to

$PM_{2.5}$ to form bioaerosols after mechanical disturbances. The $PM_{2.5}$ samples that were collected in this study were weakly acidic overall, and the EC of the MDW and SDW samples was significantly greater than that of the ETW and BTW samples, indicating that the $PM_{2.5}$ was rich in acidic inorganic salts.

The water-soluble ions are important components of $PM_{2.5}$, which can account for 40% to 70% of the mass of particulate matter in the atmosphere (Yang et al., 2023b). The main water-soluble ions in the $PM_{2.5}$ in each workshop were NO_3^-, SO_4^{2-} and Cl^-. The high concentrations of SO_4^{2-} and Cl^- in the $PM_{2.5}$ were related mainly to their high concentrations in the leachate. The NO_3^- content of the BTW samples was significantly greater than that of samples from the other workshops, which was associated with the anoxic-aerobic biological treatment process for ammonia nitrogen removal in BTW. The concentrations of heavy metals in $PM_{2.5}$ followed the order of Zn> Pb > As >Ni > Cr > Cu. Among them, the concentration of Zn, which had the highest concentration, was approximately 70 times greater than that of Cu. The differences in heavy metal concentrations of Ni, Cr and As among the different workshops were small. There is a close relationship between $PM_{2.5}$ pollution (such as via the heavy metals adsorbed on $PM_{2.5}$) and human health, and the contaminant content directly affects the level of $PM_{2.5}$ toxicity (Kelly et al., 2017).

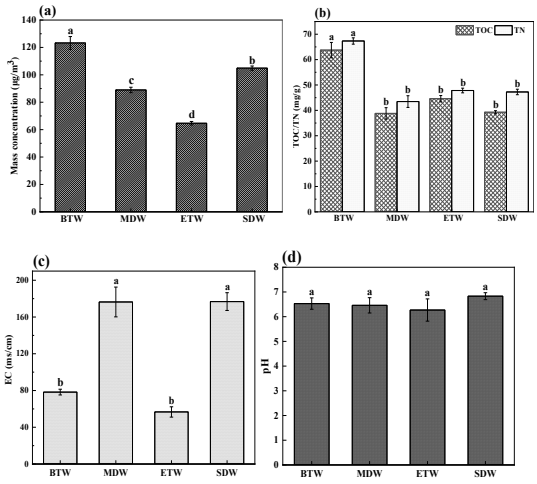

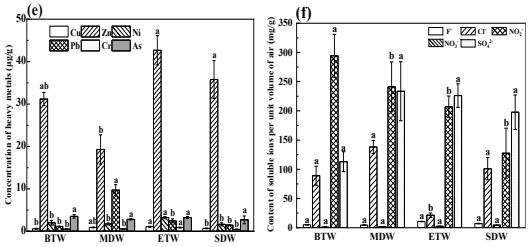

Fig. 5 The physicochemical properties of $PM_{2.5}$ (a) mass concentration, (b) total carbon (TOC) and total organic nitrogen (TN), (c) EC, (d) pH, (e) heavy metals, and (f) water-soluble ions

Relationships between the physicochemical properties of $PM_{2.5}$ and the community of bound microbes

The correlations between the top ten dominant bacterial and fungal genera in $PM_{2.5}$ and the water-soluble inorganic ions are shown in **Fig. 6 (a) and (b)**. Among the bacteria, F^- concentrations were significantly positively associated with the abundances of *Aquabacterium* and *Ralstonia*, and SO_4^{2-} concentrations were significantly positively associated with the abundances of *Burkholderia, Burkholderiales*, and *Aquabacterium*. Leachate contains a large amount of SO_4^{2-}, and thus, $PM_{2.5}$ carries a relatively high concentration of SO_4^{2-} (Gen et al., 2019). *Burkholderia*, *Burkholderiales*, and *Aquabacterium* are able to use SO_4^{2-} as an electron acceptor to participate in the sulfur cycle by converting it into organic sulfur compounds or amino acids to gain a growth advantage (Carrión et al., 2018). *Aquabacterium* and *Ralstonia*, which are environmentally adaptable bacteria, may have a specific mechanism for adapting to the environmental F^- pressure. However, Cl^-, NO_3^- and NO_2^- concentrations were negatively correlated with *Burkholderia* and *Ralstonia* abundances. The NO_3^- content was relatively high in the BTW, but the abundance of *Burkholderia* and *Ralstonia* was lower in the BTW than in the other workshops, possibly because these genera are more sensitive to high contents of NO_3^- and NO_2^- due to the inhibitory effects of these ions on the microbial redox state

(Mangalea et al., 2017). In addition, a high concentration of Cl^- had adverse effects on the normal function of the cell membrane (Li et al., 2022), resulting in strong negative relationships with these dominant genera. Among the fungi, F^- and SO_4^{2-} concentrations were positively correlated with the abundances of *Sarocladium* and *Fusarium*. The abundance of *Aureobasidium* was positively correlated with the concentrations of most of the water-soluble ions (except for NO_2^-).

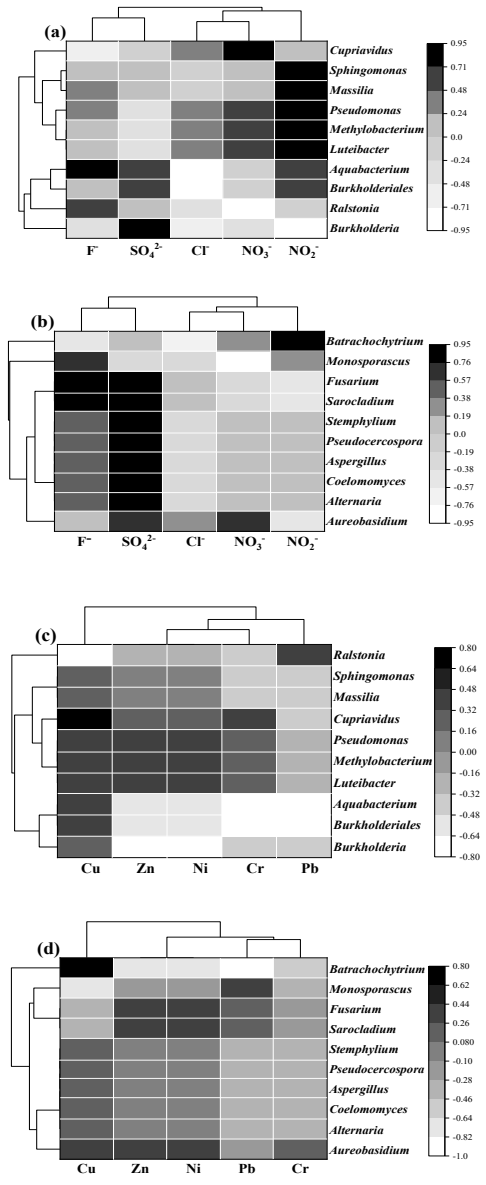

Fig. 6 Correlation between water-soluble ions and heavy metals and dominant microbial in $PM_{2.5}$ (a)(c) bacteria (b)(d) fungi.

Fig. 6 ((c) and (d)) shows the correlations between the top ten dominant bacterial and fungal genera in $PM_{2.5}$ and the heavy metal content. Low concentrations of Cu were negatively associated with the abundance of *Ralstonia* but positively associated with the abundance of other dominant bacterial genera. The abundances of most of the dominant fungal genera, except for *Monosporascus*, *Sarocladium*, and *Fusarium*, were positively correlated with the levels of Cu. The concentrations of the heavy metals Pb and Cr were negatively correlated with the abundances of most microorganisms, while Zn and Ni were positively correlated with the abundances of most microorganisms. Pb and Cr can interfere with the growth and reproduction of bacteria and fungi, causing cytotoxicity or oxidative damage (Chen et al., 2022b). During the growth process of microorganisms, some heavy metals (i.e., Zn and Ni) are considered to be essential trace elements that promote microorganism metabolism (Rathored et al., 2025).

Occurrence characteristics of human pathogens in $PM_{2.5}$

$PM_{2.5}$ exposed to the air during leachate treatment often carries many pathogenic bacteria. The proportion of bacterial pathogens accounting for the total bacterial abundance in the BTW, MDW, ETW and SDW samples was 12.6%, 39.4%, 47.6%, and 22.5%, respectively. The proportion of fungal pathogens accounting for the total fungal abundance in the four samples greatly differed, with highest proportion in the SDW (36.7%) and the lowest in the ETW (4.0%) **(Fig. 7)**.

Fig. 8 (a) shows the major species and relative abundances of bacterial pathogens during leachate treatment. *Burkholderia cepacia*, *Ralstonia pickettii* and *Stenotrophomonas maltophilia* were the dominant bacterial pathogens in the samples. *B. cepacia* had the highest relative abundance in the MDW, with a value of 35.6%; *R. pickettii* had the highest relative abundance in the ETW, with a value of 42.8%; and *S.*

maltophilia had the highest relative abundance in the BTW, with a value of 1.9%. *B. cepacia* has natural or acquired resistance to many common antibiotics, including aminoglycosides, beta-lactams, and quinolones, among others, and secretes a variety of toxins (e.g., exotoxins and proteases) that destroy host cells, activate inflammatory responses, and exacerbate tissue damage. *R. pickettii* possesses multiple virulence factors, such as the capacity for biofilm formation, efflux pumping systems, lipopolysaccharides, and invasiveness factors, which together help the bacteria survive in the host, evade immune surveillance, and thus cause severe infections (Krone et al., 2024). *S. maltophilia* is widespread in the human respiratory and intestinal tracts, is a major pathogen in infections of medical origin, and it is naturally resistant to most clinically used antibiotics (Wang et al., 2025).

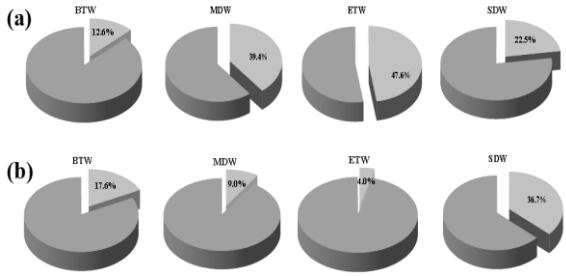

Fig. 7 The proportion of human pathogens in each workshop (a) bacteria, (b) fungi.

Two dominant fungal pathogens, namely, *Alternaria alternata* and *Alternaria tenuissima*, were detected in the samples **(Fig. 8 (b))**. *A. alternata* and *A. tenuissima* are common allergens that can cause allergic diseases. *A. alternata* can produce a variety of toxins that have strong cytotoxicity and can damage host cells, induce inflammation and lead to tissue damage (Kustrzeba-wójcicka et al., 2014). Overall, these dominant pathogens in $PM_{2.5}$ may pose an occupational health risk to workers in leachate treatment plants.

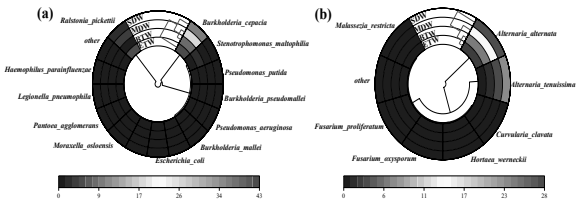

Fig. 8 The relative abundance of dominant pathogens in $PM_{2.5}$ during the leachate treatment process (a) bacteria (b) fungi.

Occurrence characteristics of VFGs in $PM_{2.5}$

Species and abundance of VFGs:A total of 151 kinds of VFGs were detected, with the BTW sample containing the highest number of VFG tpyes. The top ten VFGs in terms of relative abundance in each sample are shown in **Fig. 9 (a)**. Among the bioaerosols generated by leachate treatment, *wcbR* was the most abundant VFG carried by the hosts, accounting for 7.2% of the total VFGs, followed by *wcbT* (4.1%) and *cdpA* (4.0%). The abundance of these genes in the ETW samples was significantly greater than that in the BTW samples, suggesting that the potential risk of pathogenicity generated during the concentrated leachate evaporation treatment stage was greater than that during the leachate biological treatment stage. The VFs that were detected in each sample can be categorized into six classes, as shown in **Fig. 9 (b)**. Invasive VFs were the most abundant VFs, and antiphagocytic VFs also accounted for a high proportion, especially in the ETW and MDW samples, which further suggested that the pathogenic bacteria in the ETW and MDW have strong invasiveness.

Song et al. (2022) reported that tracking the bacterial hosts of VFGs is crucial for understanding the potential for pathogenicity in microbial ecosystems, as hosts are essential for determining their risks to human and ecosystem health. The relationships among the VFGs of the dominant hosts are shown in **Fig. 9 (c)**. The dominant VFGs were related mainly to putative hosts of *Burkholderia* (*wcbR*, *wcbT, cheB*, *cdpA*, *flgG*, *flgI*, *flhA*, *fliA*, *fliM*, and *motA*), *Pantoea* (*cheB*, *flgG*, *flgI*, *flhA*, *fliA*, *fliM*, and *motA*), and

Pseudomonas (*cheB*, *flgG*, *flgI*, *flhA*, *fliA*, *fliM*, and *motA*). Similarly, Kang et al. (2023) reported that *Burkholderia gladioli* was the most common host of VFGs in the biowaste transformation environment. *Burkholderia* contains a variety of highly abundant VFGs, among which *wcbR* and *wcbT* are the dominant VFGs. *wcbR* and *wcbT* are capsular polysaccharide biosynthesis fatty acid synthase genes, and they prevent phagocyte recognition and phagocytosis by facilitating capsule formation (Price et al., 2013). *flgG*, *flgI*, *flhA*, *fliA*, *fliM*, and *motA* are flagellar assembly- and operation-related genes (Han et al., 2023). Flagella endow bacteria with increased motility to evade being captured by phagocytes (Lewis et al., 2019). The *cheB* gene is a key gene in the chemotactic signaling pathway that can help bacteria migrate directionally to the eutrophic regions of the host (Garvis et al., 2009). These VFGs enable bacteria to produce flagella, which facilitate their movement through host tissues and thus their colonization, invasion, and spread to critical sites of infection.

Collinearity analysis of VFGs and HBPs:**Fig. 9 (d)** shows the co-occurrence patterns of pathogens and VFGs at each workshop. The network structure mainly analyzes the frequency relationship of the interaction between the dominant host cell and VFGs rather than the relationship between the host cell and the abundance of VFGs. The BTW, MDW, ETW and SDW samples had 18, 18, 15 and 22 nodes, respectively, and these nodes mainly interacted with the key VFGs by 8, 8, 5 and 12 pathogens, respectively. *Burkholderia*, *Pseudomonas*, and *Pantoea* were present in all four samples, suggesting that they are prevalent in these environments. The VFGs of *fliA*, *flgI*, *flgG*, and *motA* appeared with high frequency in each sample, and these genes were associated mainly with flagellum formation, suggesting that genera are closely related to the VF of invasion.

The presence of *Pseudomonas* and *Pantoea* in the BTW samples suggests that the workshop may be more favorable for the growth of these bacteria, which may be related to the characterization of the microbial community in the anoxic-aerobic biochemical treatment. The more complex connectivity of VFGs with strong relationships to multiple pathogens in the MDW suggests that this workshop may be at greater risk of VFG transmission in various pathogens. These results indicate that many pathogenic genes are retained in the concentrated leachate after deep membrane treatment. *Burkholderia* in the ETW samples was associated with multiple VFGs, suggesting that this workshop may be an area of enrichment for these pathogens. The diversity of pathogens in the SDW samples was greater than that in the ETW and MDW samples, which was attributed mainly to the fact that the sludge contains a rich variety of microorganisms. Moreover, *Burkholderia* showed complex relationships with multiple VFGs in the MDW, ETW and SDW samples, indicating that *Burkholderia* is prone to accumulating in bioaerosols resulting from concentrated leachate and sludge treatment and that it carries many VFGs, thus aggravating the spread of pathogenic factors through gene transfer.

.

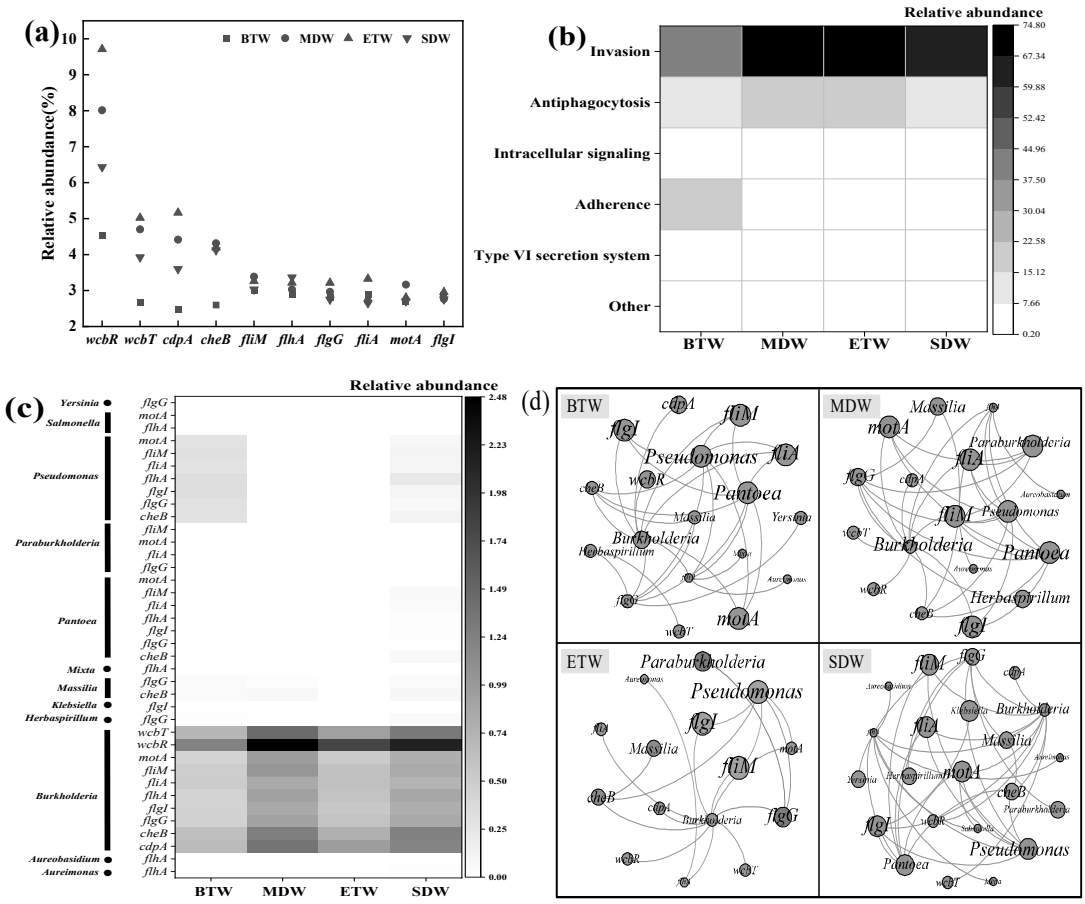

Fig. 9 Relative abundance of VFGs in samples from different workshops (a), the top ten VFGs in terms of relative abundance predominant types of VFs (b), the major VFGs and corresponding hosts (c) and network correlation of dominant VFGs with HBPs (d).

Occurrence characteristics of ARGs in $PM_{2.5}$

Species and abundance of ARGs:In addition to the virulence factors of human pathogens themselves, ARGs that are carried by microorganisms can increase the resistance of pathogens to antibiotics, making it more difficult to cure patients that are infected by these human pathogens (Barathe et al., 2024). As shown in **Fig. 10 (a)**, the number of ARG subtypes contained in the BTW, MDW, ETW, and SDW samples was 209, 163, 105 and 223, respectively. The distribution of ARG gene abundance revealed that the ARG abundance in the ETW samples was highest, with an abundance of 1.40 copies/cell, whereas the ARG abundance in samples from the other three workshops was relatively uniform, with an abundance of 0.57~0.77 copies/cell.

Fig. 10 (b) shows the relative abundance of various types of ARGs in each workshop. Multidrug, β-lactam and bacitracin antibiotic resistance genes were the most abundant ARGs in the samples. Previous studies have shown that ARGs are widely detected in leachate samples and these ARGs can be released into the air by bioaerosol microorganisms (Wang et al., 2022).

Multidrug resistance genes, such as *mecA* and *acrA,* are currently the main types of ARGs. The main reasons for the occurrence of multidrug resistance are the prevalence of multiple antibiotic screening pressures and multiple drug resistance efflux pumps in prokaryotes (Nishino et al., 2021). Yang et al. (2018) reported that multidrug resistance genes were dominant in samples of total suspended particulate

matter from urban atmospheres and sewage treatment plants. The emergence and spread of multidrug resistance genes are major challenges in the prevention and treatment of infectious diseases (Teng et al., 2023). Bacitracin antibiotic resistance genes (*VanA*, *VanB*, etc.) are common resistance genes, especially in gram-positive bacteria. The emergence of these genes is closely related to the selection pressure of bacitracin antibiotics, and the mechanism by which they mediate drug resistance is closely related to changes in the synthesis of bacterial cell walls (Chalker et al., 2000). Beta-lactam antibiotics function mainly by inhibiting the synthesis of bacterial cell walls, and bacteria develop drug resistance by producing beta-lactam enzymes or altering the targets of antibiotics (Santosaningsih et al., 2023). The abundance of multidrug, β-lactam and bacitracin ARGs was much greater in the MDW and ETW samples than in the BTW and SDW samples, similar to the results for VFGs. These results indicate that the bioaerosols that are generated during the advanced membrane treatment of leachate and the evaporation treatment of concentrated leachate carried a high abundance of ARGs and VFGs, which would pose a relatively high health risk to workers.

The host relationships of the major resistance genes in the bioaerosol particle samples are shown in **Fig. 10** samples, indicating that the microorganisms in the aerosols of these two workshops have greater **(c)**. The dominant ARGs were related mainly to putative hosts of *Burkholderia* (*ceoB*, *amrB*, *opcM*, *patA*, *axyY*, and *adeF*), *Ralstonia* (*ceoB*, *OXA-574*, *OXA-571*, and *OXA-898*), and *Pseudomonas* (*MexF*, *CpxR*, *MexW*, *MexK*, *MexD*, etc.). *Ralstonia* contains a variety of highly abundant ARGs, among which *OXA-574*, *OXA-571* and *OXA-898* are the dominant ARGs; these ARGs belong to the OXA beta-lactam class and can hydrolyze beta-lactam antibiotics (Steyaert et al., 2024). *ceoB* is a gene that encodes the transmembrane protein of the efflux pump system, which reduces the intracellular drug concentration through efflux antibiotics and increases resistance to a variety of antibiotics (such as tetracycline, chloramphenicol, and quinolones). *Pseudomonas* also contains a variety of drug resistance genes, but their abundance is not high. Among these genes, *MexF*, *MexW*, *MexK*, *MexD*, *AbaF*, *MexB*, and *mdtB* encode efflux pump proteins that enable bacteria to expel antibiotics through active transport and increase drug resistance (Avakh et al., 2023). *CpxR* and *rsmA* are genes that regulate the expression of efflux pump and drug resistance-related genes by encoding transcription regulatory factors (Zhang et al., 2021b). Regarding the main hosts of ARGs, the abundance of ARGs was greater in the ETW and MDW samples than in the BTW and SDW

antibiotic resistance.

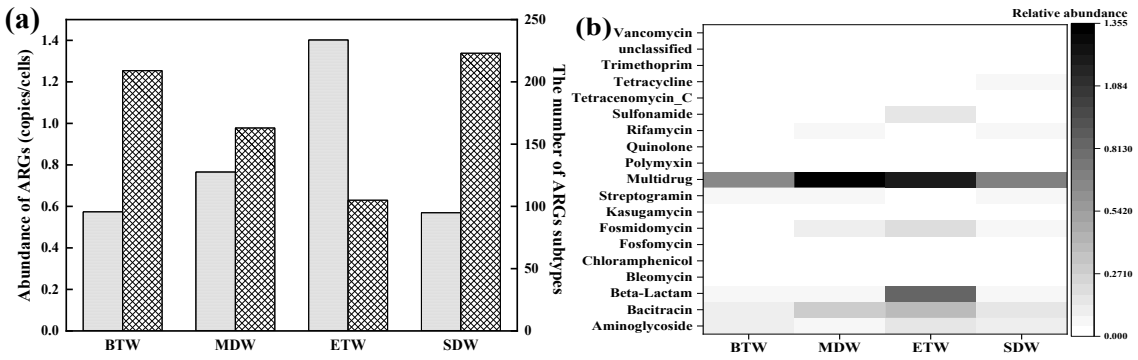

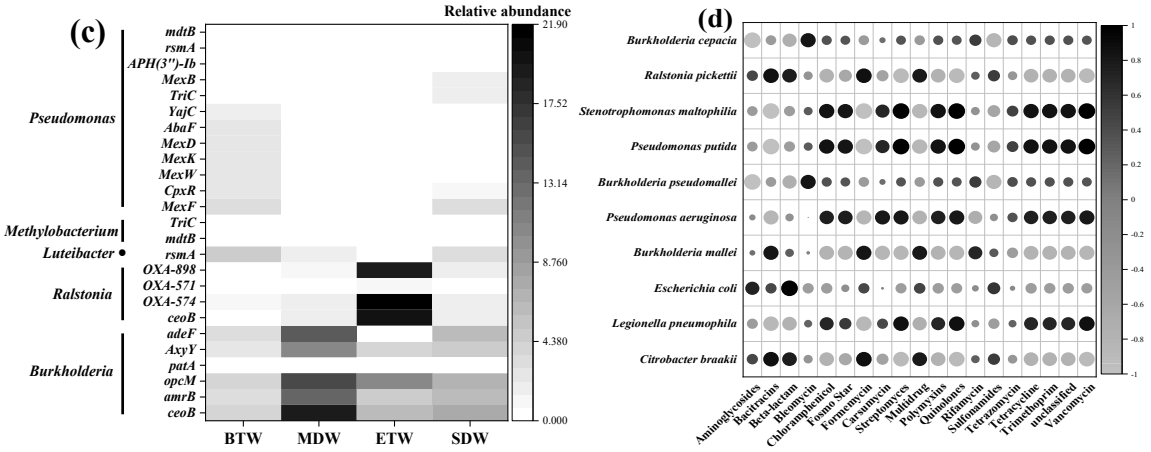

Fig. 10 Abundance and subtype number of ARGs in samples at different workshops (a), relative abundance of ARGs dominant type (b), major resistance gene corresponding hosts (c) and the correlation between ARGs and dominant pathogenic bacteria at the genus level (d).

The correlations between ARGs and dominant pathogenic bacteria at the genus level are shown in **Fig. 10 (d)**. The abundance of *Burkholderia cepacia* was significantly positively correlated with resistance to bleomycin. Moreover, the abundance of *Ralstonia pickettii* was significantly positively correlated with resistance to bacitracin, beta-lactams, formycin and multidrugs. Furthermore, the abundance of *Pseudomonas putida* was also significantly positively correlated with resistance to quinolones and vancomycin antibiotics, as was *Escherichia coli* with resistance to beta-lactam antibiotics. These correlations indicate that the abovementioned bacterial species may have strong resistance to the corresponding antibiotic categories (Jiang et al., 2022).

Notably, *Burkholderia* and *Pseudomonas* carried not only many VFGs but also many ARGs. Therefore, these two types of pathogenic bacteria need to be taken seriously and prevented from entering the atmospheric environment of leachate treatment plants, especially in the leachate advanced membrane treatment and concentrated leachate evaporation treatment stages.

CONCLUSIONS

The microbial community differed greatly between $PM_{2.5}$-associated and inhalable culturable bioaerosols. *Burkholderia* and *Aureobasidium* were the dominant bacterial and fungal genera in $PM_{2.5}$, whereas *Bacillus* and *Alternaria* were the dominant genera in the inhalable culturable bioaerosols. The SO_4^{2-} content in $PM_{2.5}$ was significantly positively correlated with the *Burkholderia* and *Aquabacterium* abundances, whereas the Cl^-, NO_3^- and NO_2^- contents were negatively correlated with the *Burkholderia* and *Ralstonia* abundances. Moreover, the Cu content was positively correlated with the abundance of most of the dominant bacterial and fungal genera, but the Pb and Cr contents were negatively correlated with the abundances of most microorganisms in $PM_{2.5}$. *B. cepacia*, *R. pickettii* and *S. maltophilia* were the dominant bacterial pathogens in the samples. *A. alternata* and *A. tenuissima* were the two dominant fungal pathogens. Hundreds of VFGs and subtypes of ARGs were detected in each workshop. *wcbR* and *wcbT* were the most abundant VFGs, and multidrug, bacitracin and sulfonamide ARGs were the main types of ARGs. VFGs and ARGs widely coexisted in *Burkholderia* and *Pseudomonas*, especially in the leachate advanced membrane treatment and concentrated leachate evaporation treatment stages. These two types of pathogens need to be taken seriously and prevented from entering the atmospheric environment of leachate treatment plants.

REFERENCES

Abel-Fernández, E., Martínez, M. J., Galán, T., et al. Going over Fungal Allergy: *Alternaria alternata* and Its Allergens[J]. Journal of Fungi, 2023; 9(5): 582-587.

Avakh, A., Grant, G. D., Cheesman, M. J., et al. The Art of War with *Pseudomonas aeruginosa*: Targeting Mex Efflux Pumps Directly to Strategically Enhance Antipseudomonal Drug Efficacy[J]. Antibiotics, 2023, 12(8): 1304-1360.

Barathe, P., Kaur, K., Reddy, S., et al. Antibiotic pollution and associated antimicrobial resistance in the environment[J]. Journal of Hazardous Materials Letters, 2024, 5: 100105.

Butt, A. T., Thomas, M. S. Iron Acquisition Mechanisms and Their Role in the Virulence of *Burkholderia* Species[J]. Front Cell Infect Microbiol, 2017, 7: 460-481.

Carrión, V. J., Cordovez, V., Tyc, O., et al. Involvement of *Burkholderiaceae* and Sulfurous Volatiles in Disease-Suppressive Soils[J]. The ISME Journal, 2018, 12(9): 2307-2321.

Chalker, A. F., Ingraham, K. A., Lunsford, R. D., et al. The *bacA* Gene, Which Determines Bacitracin Susceptibility in *Streptococcus pneumoniae* and *Staphylococcus aureus*, Is Also Required for Virulence[J]. Microbiology, 2000, 146(7): 1547-1556.

Chen, P., Guo, X. Y., Li, F. X., et al. Antibiotic resistance genes in bioaerosols: Emerging, non-ignorable and pernicious pollutants[J]. Journal of Cleaner Production, 2022a, 348: 131094.

Chen, X. M., Du, Z., Guo, T., et al. Effects of Heavy Metals Stress on Chicken Manures Composting via the Perspective of Microbial Community Feedback[J]. Environmental Pollution, 2022b, 294: 118624.

Ehling-Schulz, M., Lereclus, D., Koehler, T. M. The *Bacillus cereus* Group: *Bacillus* Species with Pathogenic Potential[J]. Microbiology Spectrum, 2019, 7(3): 1-35.

Filali, B. S. F., Bouziane, H., Trigo, M. M., et al. Airborne fungal spores of *Alternaria*, meteorological parameters and predicting variables[J]. International Journal of Biometeorology, 2015, 59: 339-346.

Kelly, J. F, Fussell, J. C. Role of oxidative stress in cardiovascular disease outcomes following exposure to ambient air pollution[J]. Free Radical Biology and Medicine, 2017, 345-367.

Garvis, S., Munder, A., Ball, G., et al. Caenorhabditis elegans Semi-Automated Liquid Screen Reveals a Specialized Role for the Chemotaxis Gene *cheB2* in *Pseudomonas aeruginosa* Virulence[J]. PLoS Pathogens, 2009, 5(8): e1000540.

Gen, M. S, Zhang, R. F, Huang, D. D., et al. Heterogeneous SO_2 Oxidation in Sulfate Formation by Photolysis of Particulate Nitrate[J]. Environmental Science & Technology Letters, 2019, 6 (2): 86-91.

Ghosh, D., Seth, M., Mondal, P., et al. Biocontrol of biofilm forming *Burkholderia cepacia* using a quorum quenching crude lactonase enzyme extract from a marine Chromohalobacter sp. strain D23[J]. Archives of Microbiology, 2023, 205: 374-388.

Han, Q., Wang, S. F., Qian, X. X., et al. Flagellar brake protein *YcgR* interacts with motor proteins *MotA* and *FliG* to regulate the flagellar rotation speed and direction[J]. Frontiers in Microbiology, 2023, 14: 1159974.

Han, Y. P., Li, L., Wang, Y., et al. Composition, dispersion, and health risks of bioaerosols in wastewater treatment plants: A review[J]. Frontiers of Environmental Science & Engineering, 2020, 15(3): 38-54.

Jiang, Q., Feng, M. B., Ye, C. S., et al. Effects and relevant mechanisms of non-antibiotic factors on the horizontal transfer of antibiotic resistance genes in water environments: A review[J]. Science of The Total Environment, 2022, 806: 150568.

Kang, X.Y., Lü, F., Wang, Y., et al. Metagenomic

Analysis of Microbiological Risk in Bioaerosols During Biowaste Valorization Using Musca Domestica[J]. Environmental Pollution, 2023, 320: 121118.

Krone, M., Rauschenberger, V., Blaschke, V., et al. *Ralstonia pickettii* bloodstream infections with potential genomic link to internationally distributed contaminated saline solution, Germany, October 2023[J]. Eurosurveillance, 2024, 29(3): 2400010.

Kustrzeba-wójcicka, I., Siwak, E., Terlecki, G., et al. *Alternaria alternata* and Its Allergens: a Comprehensive Review[J]. Clinical Reviews in Allergy & Immunology, 2014, 47: 354-365.

Lewis, K. A., Baker, A. E., Chen, A. I., et al. Ethanol Decreases Pseudomonas aeruginosa Flagellar Motility through the Regulation of Flagellar Stators[J]. Journal of Bacteriology, 2019, 201:1-17.

Li, G. N., Zheng, X., Zhu, Y., et al. In-depth insights into the disruption of the microbiota-gut-blood barrier of model organism (Bombyx mori) by fluoride[J]. Science of The Total Environment, 2022, 838: 156220.

Li, P. Y., Wang, C., Li, L., et al. Bioaerosols and VOC emissions from landfill leachate treatment processes: Regional differences and health risks[J]. Journal of Hazardous Materials, 2024, 480: 136232.

Liu, J. Y., Xiang, Y. H., Zhang, Y. Stenotrophomonas maltophilia: An Urgent Threat with Increasing Antibiotic Resistance[J]. Current Microbiology, 2023, 81(1): 6-20.

Mangalea, M. R., Plumley, B. A., Borlee, B. R. Nitrate Sensing and Metabolism Inhibit Biofilm Formation in *Burkholderia pseudomallei* by Reducing Intracellular c-di-GMP[J]. Frontiers in Microbiology, 2017, 8: 1353-1369.

Nishino, K., Yamasaki, S., Nakashima, R., et al. Function and Inhibitory Mechanisms of Multidrug Efflux Pumps[J]. Frontiers in Microbiology, 2021, 12: 737288.

Price, E., Sarovich, D.S., Mayo, M., et al., Within-Host Evolution of *Burkholderia pseudomallei* over a Twelve-Year Chronic Carriage Infection[J]. mBio, 2013; 4(2): e00388-13.

Rajni, E., Goel, P., Sarna, M. K., et al. The genus *Ralstonia*: The new kid on the block[J]. Journal of the Royal College of Physicians of Edinburgh, 2023, 53(1): 44 - 52.

Rathored, J., Malode, U., Shende, S., et al. Toxic Effect of Heavy Metal Poisoning on Living Organisms in Water and Health Risk: A Central India Study[J]. Geomicrobiology Journal, 2025, 42(1): 1-9.

Santosaningsih, D., Fadriyana, A. P., David, N. I., et al. Prevalence and Abundance of Beta-Lactam Resistance Genes in Hospital Wastewater and Enterobacterales Wastewater Isolates[J]. Tropical Medicine and Infectious Disease, 2023, 8: 193-207.

Song, R., Sun, Y., Li, X., et al. Biodegradable microplastics induced the dissemination of antibiotic resistance genes and virulence factors in soil: a metagenomic perspective[J]. Science of The Total Environment, 2022, 828: 154596

Steyaert, S., Peeters, C., Wieme, A. D., et al. Novel Ralstonia species from human infections: improved matrix-assisted laser desorption/ionization time-of-flight mass spectrometry-based identification and analysis of antimicrobial resistance patterns[J]. Microbiology Spectrum, 2024, 12: e04021-23.

Sutthiwong, N., Lekavat, S., Dufossé , L. Involvement of versatile bacteria belonging to the genus *Arthrobacter* in milk and dairy products[J]. Foods, 2023, 12: 1270-1288.

Teng, J. Y., Imani, S., Zhou, A. P., et al. Combatting resistance: Understanding multi-drug resistant pathogens in intensive care units[J]. Biomedicine & Pharmacotherapy, 2023, 167: 115564.

Wang, C., Prather, K. A., Sznitman, J., et al. Airborne transmission of respiratory viruses[J]. Science,

2021, 373: eabd9149.

Wang, Y., Lan, H., Li, L., et al. Chemicals and microbes in bioaerosols from reaction tanks of six wastewater treatment plants: survival factors, generation sources, and mechanisms[J]. Science Report, 2018, 8: 9362-9374.

Wang, H. L., Li, S. R., Ji, H. Y., et al. Epidemiology and Antimicrobial Resistance of Stenotrophomonas maltophilia in China, 2014-2021[J]. Infectious Diseases and Therapy, 2025, 14(1): 261-274.

Wang, H. W., Zhang, C., Wang, Y. N., et al. Simultaneous degradation of refractory organics, antibiotics and antibiotic resistance genes from landfill leachate concentrate by GAC/O_3[J]. Journal of Cleaner Production, 2022, 380: 135016.

Wang, J. T., Hu, W., Xue, Z. Z., et al. Mapping multi-omics characteristics related to short-term $PM_{2.5}$ trajectory and their impact on type 2 diabetes in middle-aged and elderly adults in Southern China[J]. Journal of Hazardous Materials, 2024b, 468: 133784.

Wang, Y. N., Wang, Q. Z., Li, Y. H., et al. Insights into bioaerosol contamination in the process of mineralized refuse mining: Microbial aerosolization behavior and potential pathogenicity[J]. Journal of Hazardous Materials, 2024a, 480: 136142.

Wu, D., Jin, L., Xie, J., et al. Inhalable antibiotic resistomes emitted from hospitals: metagenomic insights into bacterial hosts, clinical relevance, and environmental risks[J]. Microbiome, 2022, 10: 19-35.

Xu, Q. C., Wang, S. X., Jiang, J. K., et al. Nitrate dominates the chemical composition of $PM_{2.5}$ during haze event in Beijing, China[J]. Science of The Total Environment, 2019, 689: 1293-1303.

Yang, M., Zeng, H. X., Wang, X. F., et al. Sources, chemical components, and toxicological responses of size segregated urban air PM samples in high air pollution season in Guangzhou, China[J]. Science of The Total Environment, 2023b, 865: 161092.

Yang, T., Wang, X. Y., Hui, X. L., et al. Antibiotic resistome associated with inhalable bioaerosols from wastewater to atmosphere: Mobility, bacterial hosts, source contributions and resistome risk[J]. Water Research, 2023a, 243: 120403.

Yang, Y., Zhou, R. J., Chen, B. W., et al. Characterization of airborne antibiotic resistance genes from typical bioaerosol emission sources in the urban environment using metagenomic approach[J]. Chemosphere, 2018, 213: 463-471.

Yang, Y. Z., Zhang, Y., Zhan, Y., et al. Synergistic enhancement of UASB reactor for leachate treatment using Fe_2O_3 nanomodified pumice and ozone oxidation[J]. Chemical Engineering Journal, 2024, 497: 154891.

Zhang, H. P., Zhang, Z. H., Song, J. J., et al. Foam shares antibiotic resistomes and bacterial pathogens with activated sludge in wastewater treatment plants[J]. Journal of Hazardous Materials, 2021a, 408: 124855.

Zhang, M. K., Zhang, M. Y., Liu, S. B., et al. Double deletion of *cpxR* and *tolC* significantly increases the susceptibility of *Salmonella* enterica serovar Typhimurium to colistin[J]. Journal of Antimicrobial Chemotherapy, 2021b, 76(12): 3168-3174.

Zhou, Z. Z., Zhu, J., Yin, Y., et al. Seasonal variations of profiles of antibiotic resistance genes and virulence factor genes in household dust from Beijing, China revealed by the metagenomics[J]. Science of The Total Environment, 2024, 928: 172542.

Zuo, Z., Pan, Y. Y., Huang, X. Y., et al. Seasonal Distribution of Human-to-Human Pathogens in Airborne $PM_{2.5}$ and Their Potential High-Risk ARGs[J]. Frontiers in Microbiology, 2024, 15: 1422637.

MECHANISM OF IRON RELEASE FROM STEEL SLAG INDUCED BY DENITRIFYING MICROORGANISMS AND OPTIMIZATION OF ITS PHOSPHORUS REMOVAL PERFORMANCE IN WASTEWATER

Yan Guo[1], Huafang Yu[2], Hongzhi Ma[1], Qunhui Wang[1]

1 School of Energy and Environmental Engineering, University of Science and Technology Beijing, Beijing, 100083, PR China

2 State Key Laboratory of Advanced Metallurgy, University of Science and Technology Beijing, Beijing, 100083, PR China

Abstract

Adding iron salts is an efficient and stable method for phosphorus removal in wastewater; however, the cost of iron salts remains relatively high. China generates an enormous amount of low-alkalinity steel slag annually. If the iron contained in steel slag can be released and utilized for phosphorus removal in wastewater, it will not only reduce wastewater treatment costs and address the issue of steel slag disposal but also improve the utilization rate of iron ore resources, thereby achieving multiple objectives including resource conservation and energy consumption reduction.

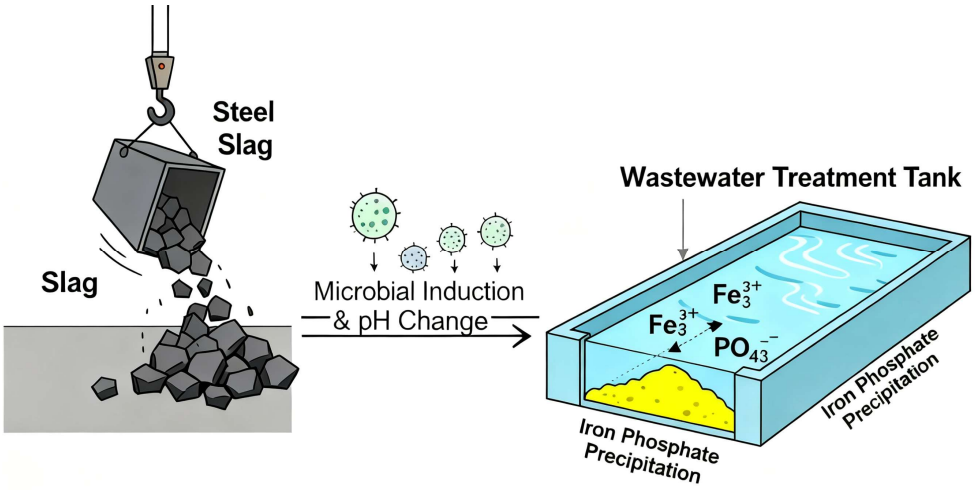

Fig.1 The combination of steel slag disposal and wastewater phosphorus removal

The metabolic processes of microbial aggregates can induce changes in pE-pH at local sites, which provides insights into biologically induced iron release from steel slag. Therefore, in this project, steel slag is employed in

a biological nitrogen removal reactor as a carrier for the attachment of ammonium-oxidizing microorganisms. Through steel slag modification and nitritation-driven biological induction, iron release from steel slag is achieved, followed by the crystallization of iron phosphate—ultimately enabling simultaneous nitrogen and phosphorus removal in wastewater, as shown in Fig.1.

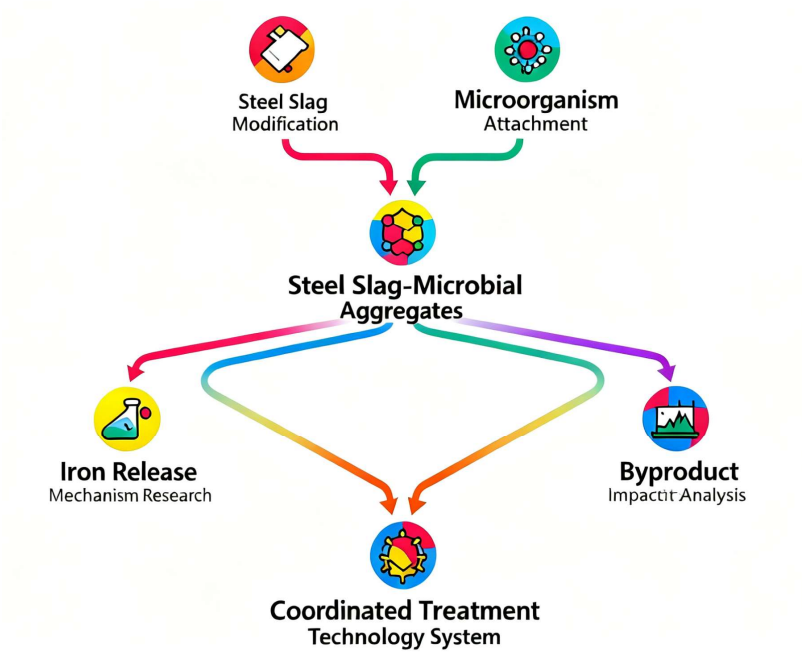

Fig.2 the critically research points

This project will investigate the effects of steel slag modification on the distribution of iron elements and its biocompatibility, clarify the mechanism of iron release from steel slag-microbial aggregates under microbial induction, and determine the influence of secondary released substances on microbial metabolic activities. Eventually, it will establish the technical theory for using steel slag in wastewater phosphorus removal and develop a theoretical and technological system for the coordinated development of steel slag disposal and wastewater treatment, , as shown in Fig.2.

This project realizes the synergistic treatment of industrial solid waste and wastewater, yielding significant social and economic benefits, and holds important practical significance for advancing China's "dual carbon" goals.

Keywords

Steel slag, iron release, microbe induction, wastewater treatment, phosphorus removal.

Reference

Yan Guo, Yu-You Li. Hydroxyapatite crystallization-based phosphorus recovery coupling with the nitrogen removal through partial nitritation anammox in a single reactor. Water Research. Volume 187, 15 December 2020, 116444.

Bioremediation of coking contaminated soil: MnOB boost the degradation of high-molecular-weight PAHs

Xueqin Wang, Huawei Wang*, Ya-nan Wang, Yingjie Sun, Jianwei Zhao

School of Environmental and Municipal Engineering, Qingdao University of Technology, Qingdao 266520, China

Abstract

The Mn(II) oxidizing bacteria (MnOB) process plays an important role in persistent organic pollutant remediation, but its performance in high-molecular-weight polycyclic aromatic hydrocarbons (PAHs) degradation remains unclear. In this study, the key role of MnOB under various nitrogen conditions in enhancing the degradation of high-molecular-weight PAHs in contaminated soil after pre-oxidation was investigated. The results indicated that the combination of MnOB and potassium nitrate stimulation with a C/N ratio of 100:15 was effective at degrading high-molecular-weight PAHs, and 80.59% of the total PAHs and 83.77% of benzo[a]pyrene (BaP) were degraded. The analysis of the Mn species revealed that MnOB can effectively utilize available Mn(II) to form biogenic Mn oxides, and the amorphous Mn oxides generated by MnOB were primarily responsible for high-molecular-weight PAH degradation. The relative abundance of some MnOB, including *Caulobacter*, *Domibacillus*, *Pseudomonas*, *Brevibacillus* increased during the MnOB process, contributing to the formation of biogenic Mn oxides. Nitrogen stimulation can effectively promote the expression of Mn(II) oxidation functional genes, and the *pht3*, *pcaH*, and *pcaG* genes are involved mainly in the microbial degradation of PAHs and the intermediate metabolites. This study provides a feasible method for promoting the remediation efficiency of high-molecular-weight PAHs in coking contaminated soil.

Keywords

Polycyclic aromatic hydrocarbons (PAHs); Mn(II)-oxidizing bacteria (MnOB); Coking soil; Nitrogen stimulation

1. Introduction

The environmental pollution caused by the coking industry has received global attention. Polycyclic aromatic hydrocarbons (PAHs) are typical pollutants present at contaminated coking sites (Gou et al., 2019; Zhang et al., 2021a). Sixteen typical PAH species have been listed as priority control pollutants by the USEPA due to their toxicity (Han and Currell, 2017). Among the sixteen PAHs, high-molecular-weight PAHs (i.e., benzo[a]pyrene), which are characterized by strong hydrophobicity, poor volatility and easy accumulation in the environment, pose a serious threat to the local environment (Li et al., 2023). There is an urgent need for cost-effective remediation strategies targeting high-molecular-weight PAHs in coke-polluted soils (Dai et al., 2024).

The main remediation technologies for PAH-contaminated sediments include washing (Bianco et al., 2022), thermal desorption (Zhao et al., 2019), chemical oxidation (Usman et al., 2018) and microbial remediation (Lü et al., 2024). Chemical oxidation technology is the most widely used remediation method at contaminated coking sites (Liao et al., 2019). $KMnO_4$, a strong oxidizing agent (E^0=1.7 V), is capable of decomposing organic compounds with C=C bonds, aldehydes, and hydroxyl groups and is also frequently employed in PAH degradation (Chen et al., 2024). However, permanganate has difficulty efficiently oxidizing and degrading some recalcitrant organics with

stable structures, such as high-molecular-weight PAHs. During the process of oxidizing organic pollutants with permanganate, a reduction occurs to generate soluble divalent Mn(II) ions, causing secondary pollution of groundwater (Wang et al., 2023). Moreover, permanganate is a nonselective oxidant, and excessive addition of permanganate causes a sharp decrease in organic matter, nutrients and soil microorganisms, leading to the loss of soil function (Dai et al., 2022).

Microbial-mediated remediation has received widespread interest owing to its mild reaction conditions, low energy requirements, and lack of secondary pollution (Zeng et al., 2024). Native soil microorganisms can adapt to elevated PAH contents at contaminated coking sites, and the microbial number can be restored after chemical oxidation (Gou et al., 2020; Gou et al., 2022). Nevertheless, microbial remediation by native soil microorganisms may not be applicable in all cases because it has a restricted content scope of PAHs, the timescales involved are relatively long, and the residual PAHs are at unacceptable levels. For example, low- and middle-molecular-weight PAHs, such as naphthalene (36.17%), fluorene (26.96%), and benzo(a)anthracene (11.61%), can be partially degraded in contaminated soil, but biodegradation of high-molecular-weight PAHs has not been observed after 250 days of incubation with indigenous microorganisms (Gou et al., 2024). To address this challenge, the technology of integrating preoxidation by permanganate and *in situ* biogenic stabilization by Mn(II)-oxidizing bacteria (MnOB) provides a unique method for enhancing soil remediation effectiveness and restoring soil functions.

Mn(II)-oxidizing bacteria (MnOB) can be used *in situ* to form biogenic manganese oxides (BMOs) and simultaneously achieve the adsorption immobilization of heavy metals and the degradation and mineralization of organic pollutants. MnOB are a class of microorganisms that can oxidize Mn(II) to generate biogenic Mn oxides (Wang et al., 2020). They are ubiquitous in soil, water, and sediment environments and even in highly saline environments. Some MnOB genera, such as *Pseudomonas putida* sp. MnB1 (Li et al., 2024a), *Pseudomonas* sp. KW-2 (Wang et al., 2024), and *Comamonas* sp. RM6 (Zhao et al., 2022), have been widely acknowledged for their contributions to environmental remediation. Compared with chemically synthesized MnO_2, the products of BMO during the biogenic Mn(II) oxidation process exhibit lower crystallization, higher Mn oxidation states, increased octahedral vacancies, and larger specific surface areas (Wang et al., 2020); this results in enhanced reactivity and greater oxidation capacity toward pollutants such as endocrine disruptors, fungicides, and pharmaceuticals (Tran et al., 2018). MnOB facilitate the reoxidation of dissolved Mn(II) to BMO, reducing Mn(II) release after $KMnO_4$ oxidation and providing new reactive sites for pollutant degradation. Furthermore, the production of transient reactive intermediates (i.e., superoxide and hydrogen peroxide) during the biogenic Mn(II) oxidation process also plays a vital role in the degradation and transformation of organic pollutants (He et al., 2023). Despite the fact that MnOB can convert Mn(II) to BMO and generate active intermediates such as superoxide and hydrogen peroxide to enhance the breakdown of organic pollutants, the process of manganese oxidation inevitably results in changes to environmental nutrients, notably nitrogen (Yi et al., 2022). Mn(II) can supply electrons for reducing the NO_3-N generated from the ammonification and NH_4-N oxidation processes (Zhang et al., 2021b). However, enhanced degradation of high-molecular-weight PAHs by MnOB in contaminated coking soil, with the addition of an extra nitrogen source, after preoxidation by potassium permanganate has not yet been reported.

Therefore, in this study, an enriched

complex MnOB consortium with strong biogenic Mn(II) ability was fabricated, and its performance in the degradation of high-molecular-weight PAHs in coking-contaminated soil after preoxidation by $KMnO_4$ was investigated. The effects of different nitrogen levels on PAH degradation during the biogenic Mn(II) oxidation process were investigated. The microbiological mechanism of PAH degradation was explored via Q–PCR, high-throughput sequencing and metagenomic sequencing. The aim of this study was to develop an alternative remediation strategy for practical engineering applications in coking soils contaminated with high-molecular-weight PAHs.

2. Materials and methods

2.1 Coking-contaminated soils

The coking soil samples were collected from a contaminated site of an abandoned coking plant in Hefei city of Anhui Province, China. After removing stones, weeds, and other impurities, the soils were air-dried, homogenized and passed through a 60 mesh nylon sieve. The physicochemical properties of the soil samples were as follows: 82.5 g/kg organic matter (OM), 4.2 g/kg total nitrogen, 581.2 mg/kg total Mn and a pH of 8.4. The contents of the 16 PAHs in the raw soil and soil preoxidized with $KMnO_4$ are presented in **Table 1**. The coking-contaminated soil is mainly composed of high-ring PAHs, among which benzo[a]anthracene (BaA), benzo[b]fluoranthene (BbF), benzo[a]pyrene (BaP), dibenzo[a, h]anthracene (DahA), and indeno[1,2,3-c, d]pyrene (IndP) are 1.97, 2.89, 18.07, 3.63, and 1.23 times the standard limit values, respectively.

The purpose of preoxidation is to degrade a portion of PAHs, promote the decomposition of high-ring PAHs into low-ring PAHs, increase the bioavailability of PAHs, and thereby facilitate the subsequent bioretention process. The preoxidation of soil by $KMnO_4$ was performed as follows: A 400.00 g soil sample was weighed and placed into a glass beaker. $KMnO_4$ was added at the optimal concentration of 0.15 mmol/g dry soil (the addition amount was based on the PAH content in the dry soil). After the reaction, the soil was pH 8.5. Then, deionized water was added to achieve a moisture content of 30%. The treated soil was incubated at 25 °C and 40% relative humidity for 24 h. After the reaction, the contents of PAHs in the soil were determined.

Table 1 Contents of the sixteen species PAHs in the contaminated soil

Compound name	Abbreviation	Rings	Standard * (mg/kg)	Raw soil (mg/kg)	Pre-oxidized soil (mg/kg)
Naphthalene	NAP	2	70	2.98 ± 0.31	N.D.
Acenaphthylene	ANY	3	/	3.53 ± 0.35	0.65 ± 0.02
Acenaphthene	ANA	3	/	2.70 ± 0.30	0.31 ± 0.01
Fluorene	FLU	3	/	2.94 ± 0.29	1.40 ± 0.04
Phenanthrene	PHE	3	/	23.74 ±2.36	6.42 ± 0.16
Anthracene	ANT	3	/	5.03 ± 0.51	4.69 ± 0.16
Fluoranthene	FLA	4	/	40.80 ± 4.05	13.02 ± 0.43
Pyrene	PYR	4	/	23.40 ± 2.32	8.15 ± 0.24
Benzo[a]anthracene	BaA	4	15	29.49 ± 2.96	9.64 ± 0.13
Chrysene	CHR	4	1293	40.39 ± 4.03	11.22 ± 0.24
Benzo[b]fluoranthene	BbF	5	15	43.44 ± 4.35	22.92 ± 0.57
Benzo[k]fluoranthene	BkF	5	151	13.60 ± 1.36	6.81 ± 0.19

Compound name	Abbreviation	Rings	Standard * (mg/kg)	Raw soil (mg/kg)	Pre-oxidized soil (mg/kg)
Benzo[a]pyrene	BaP	5	1.5	27.11 ± 2.68	7.42 ± 0.21
Dibenzo[a, h]anthracene	DahA	6	1.5	5.45 ± 0.55	3.05 ± 0.11
Benzo[g, h, i]pyrene	BghiP	6	/	17.11 ± 1.75	5.07 ± 0.17
Indeno[1,2,3-c, d]pyrene	IndP	6	15	18.46 ± 1.90	7.66 ± 0.14
Σ16 PAHs	/	/	/	300.15 ± 30.35	108.41 ± 6.45

*Note: The risk screening values for soil contamination of development land class II in soil environmental quality risk control standard for soil contamination of development land (GB 36600-2018).

2.2 Chemicals

High-performance liquid chromatography (HPLC)-grade dichloromethane, hexane, acetonitrile, and methanol were purchased from Merck Chemical Technology Co., Ltd. (Shanghai). Other chemicals used in this study, such as potassium permanganate ($KMnO_4$) and potassium nitrate (KNO_3), were of analytical purity and were obtained from Sinopharm Chemical Reagent Co., Ltd.

2.3 Incubation of MnOB

In this work, a complex MnOB consortium was enriched from a rust sample from a water pipe (Wang et al., 2024). Briefly, a 2.00 g rust sample was mixed with 50 mL sterile water and shaken at 150 rpm (30 °C) for 3 hours. Five milliliters of the rust-water mixture was added to 200 mL of nutrient broth (NB) medium containing 100 mg/L Mn(II) and incubated for 5 days at 150 rpm (30 °C). Bacterial domestication was carried out for five cycles, with each cycle lasting 5 days. The cultured MnOB colonies exhibited strong Mn(II) oxidation ability after leucobroimine blue I (LBB) tests turned blue **(Fig. S1)**. MnOB cultures were harvested at the exponential growth phase for subsequent experiments. The results of the bacterial community structure analysis revealed that the MnOB were mainly *Bacillus*, *Clostridium* and *Pseudomonas*.

2.4 Degradation of PAHs in preoxidized coking soil during the biogenic Mn(II) oxidation process

The degradation efficiency of PAHs in preoxidized soil was evaluated via batch experiments. The preoxidized soil was inoculated with MnOB, and various doses of potassium nitrate were added to the soil to regulate the C/N ratio, with C/N values of 100:10, 100:15 and 100:20. The experimental treatments were designed as follows 1) the addition of MnOB (denoted as M); 2) the addition of potassium nitrate to adjust the C/N ratio to 100:10, 100:15 and 100:20 (denoted as N10, N15, and N20); and 3) the combined addition of MnOB and potassium nitrate (denoted as MN10, MN15, and MN20) **(Table S1)**. The plants without the addition of MnOB or a nitrogen source were used as the control (denoted as CK). Four parallel samples were subjected to each experimental treatment. For each treatment, 40.00 g of preoxidized soil samples were mixed with deionized water, MnOB (3 mL/g, ~4.5×10^7 cells/mL) and/or three doses of potassium nitrate. A solid-to-solution ratio of 1:1 (w/w) was used for each treatment. After being thoroughly mixed, the samples were placed into glass petri dish and placed in an incubator (temperature, 25 °C; humidity, 40%). At time points within 7 days and 14 days, the soil was sampled from each treatment for PAH content and physicochemical property analyses (e.g., pH, OM and enzymatic activity).

2.5 Analytical methods

The content of PAHs in the soil samples was determined via high-performance liquid chromatography. The soil samples were first extracted with dichloromethane-acetone and then monitored by using an LC5090 HPLC instrument (Zhejiang Fuli Analytical Instruments Inc., China). The available Mn(II) in the soil was extracted via DTPA solution at a ratio of 1:5 (Huang et al., 2022). The free Mn oxides in the soil were extracted with 0.3 M sodium citrate and 1 M sodium bicarbonate. The amorphous Mn oxides in the soil were extracted with 0.2 M ammonium oxalate. The concentrations of Mn(II) and Mn oxides in solution were then analyzed via the former spectrophotometric method. Additionally, the contents of soil pH, EC, OM, urease and catalase activity were determined according to methods carried out previously (Liu and Ma, 2012).

The soil samples from the different treatments were collected for microbiological analysis. The primers used for amplification of the *phe* gene were pheF (CTGCTGACSAAYCTGYTGTTC) and pheR (GGCCAGAACCAYTTRTC) (Peng et al., 2015). The details are given in the supplementary materials.

2.6 Statistical analysis

The MnOB community structure was analyzed via Mothur software. The relationships between PAH degradation and soil physicochemical properties were determined via redundancy analysis (RDA). The types of Mn(II) oxidation-related genes and nitrogen metabolism pathways were predicted based on the FAPROTAX database.

3. Results and discussion

3.1 Degradation of typical PAHs during the biogenic Mn(II) oxidation process

The changes in the contents of total PAHs and the five high-molecular-weight PAHs with different treatments are shown in **Fig. 1**. During the $KMnO_4$ preoxidation period, the removal efficiency of total PAHs was 63.88% after reacting for 24 h **(Table 1)**. Similar results were reported by Gou et al. (2019), who reported that the removal efficiency of total PAHs in soil was 61.7% when PAHs were preoxidized with H_2O_2. For high-molecular-weight PAHs (i.e., BaA, IndP, BaP, BbF, and DahA), the removal efficiencies of BaA and IndP were 43.57% and 58.51%, respectively, by $KMnO_4$, and their contents were below the standard limit of class II in GB 36600. The removal efficiencies of BaP, BbF, and DahA were very limited, and their contents were still 4.95, 1.53 and 2.03 times higher than the standard limits of class II in GB 36600, respectively **(Table 1)**. Therefore, the removal of these five typical high-molecular-weight PAHs by MnOB in the subsequent biological treatment was a particular focus.

During the biological treatment period, after 7 days of incubation, the total PAH content in CK was close to that in CK pretreated with $KMnO_4$, with a value of 107.61 mg/kg. The total PAH content in the N and M treatments was nearly 100 mg/kg, while the total PAH content in the MN treatments decreased significantly, especially in the MN15 treatment, with a value of 70.76 mg/kg **(Fig. 1a)**. Compared with those in the other treatments, the contents of the five high-molecular-weight PAHs in the MN15 treatment were the lowest, and the BaP content in the MN15 treatment decreased from 27.11 mg/kg in the raw soil to 4.54 mg/kg **(Fig. 1b)**. After incubation for 14 days, the total PAH content in CK clearly decreased, with a value of 78.56 mg/kg. This might be because some high-toxicity PAHs were transformed into low-toxicity PAHs after preoxidation treatment, and the native PAH-degrading bacteria in the soil gradually regained their biological activity, which could further degrade low-toxicity PAHs. The contents of total PAHs in the MN treatments also continued to decrease to values of approximately 60 mg/kg, and the values were much lower than those in the N and CK

treatments **(Fig. 1c)**. The contents of the five high-molecular-weight PAHs in the MN treatments were also lower than those in the CK and N treatments, while the degradation efficiency of BaP in the MN15 treatment did not improve further **(Fig. 1d)**, possibly because the microbes mainly degrade low-toxicity PAHs. These results demonstrated that the combination of MnOB and exogenous nitrogen nutrients during the biogenic Mn(II) oxidation process was effective in promoting the degradation of PAHs in contaminated soil.

The nitrogen source is the basic nutrient element in microbial growth and the energy source for heterotrophic bacteria. Yang et al. (2018) reported that the addition of nitrogen enhanced the anoxic biodegradation of PAHs in soil; after 300 days of anoxic incubation, the removal efficiencies of 3-ring and 4-ring PAHs ranged from 45%~73% and 32%~63%, respectively. Yu et al. (2024) reported that the application of exogenous nitrogen with a C/N ratio of 100/2 facilitated the degradation of petroleum hydrocarbons in oil-contaminated soils. However, in our study, the elevated degradation of PAHs in the three N treatments was very limited, which was attributed mainly to the fact that permanganate treatment resulted in a notable decrease in indigenous microorganisms (Chang et al., 2022). Moreover, our experiments confirmed that the addition of exogenous nitrogen was necessary to increase the degradation of PAHs by MnOB. Notably, different nutrient conditions can affect the microbial metabolism of MnOB (Gonzalez and Aranda, 2023). Qi et al. (2025) suggested that a change in nutrient conditions led to a shift in the mechanism of microbial manganese oxidation. These authors reported that, under nutrient-rich conditions, multicopper oxidase predominantly drives manganese oxidation, whereas under nutrient-poor conditions, the extracellular superoxide radical produced by bacteria is the main factor leading to incomplete Mn(II) oxidation. In addition, Qi et al. (2024) reported that nutrients released from *Microcystis* sp. FACHB-905 promote the bacterial oxidation of Mn(II) via accelerated extracellular superoxide production.

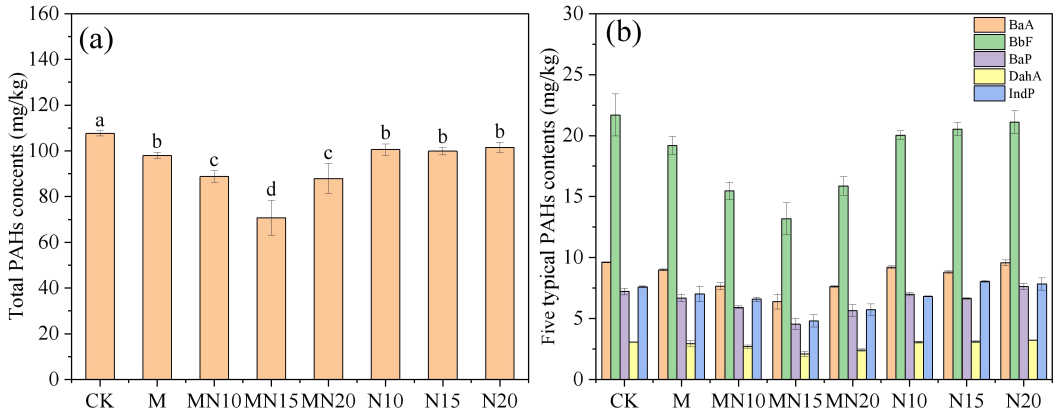

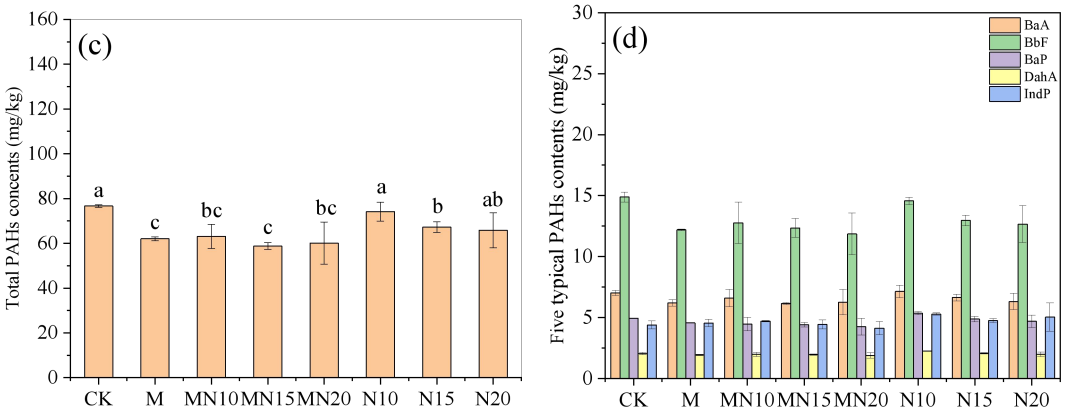

Fig. 1 Changes of total PAHs and the five high-molecular-weight PAHs contents after treated for 7 days (a, b) and 14 days (c, d).

The remediation effects of commonly used chemical oxidation coupled with biological enhancement on PAH degradation in contaminated soil were compared, as shown in **Table 2**. The results indicated that the combination of potassium permanganate oxidation and MnOB had good effects on PAH degradation. The total content of PAHs decreased from 300.15 mg/kg to 58.28 mg/kg, and its degradation efficiency reached 80.59%. The coupling of $KMnO_4$ and MnOB for PAH degradation was better than the corresponding results reported previously, such as H_2O_2 and indigenous microorganisms. Moreover, the MnOB system shortened the remediation period from several months to 14 days.

Table 2 Comparison of various chemical oxidation combined with microbial remediation on PAHs

Type of soil	Method	Dose	Initial PAHs content (mg/kg)	Treated PAHs content (mg/kg)	Efficiency	Ref.
PAHs contaminated subsurface soil	Sodium persulfate + indigenous microorganism	10 mL 1% (wt/wt) + Anoxic incubation for 80 days	142.2	≈93.18	34.47%	(Gou et al., 2020)
Creosote contaminated soil	O_3 + indigenous microorganism	1.0 L/min 1.00±0.02 mg/L + Aerobic incubation for 56 days	2370.5	≈592.63	75%	(Kulik et al., 2006)
PAHs contaminated soil	H_2O_2 + indigenous microorganism	150 ml 10% (v/v) + Anoxic incubation for 180 days	350.07	≈154.35	55.9%	(Gou et al., 2019)
Coking contaminated soil	$KMnO_4$ + ISBS@MnOB	0.15 mmol/g + MnOB aerobic incubation for 14 days	300.15	58.28	80.59%	This study

3.2 Changes in Mn species during the biogenic Mn(II) oxidation process

Microbial Mn(II) oxidation plays an important role in organic pollutant degradation (Yang et al., 2022). During the biogenic Mn(II) oxidation process, MnOB can convert available Mn(II) to unstable Mn(III) and then transform Mn(III) to insoluble Mn(IV), which mainly exists as amorphous Mn oxides (BMOs). The changes in Mn species during the biogenic Mn(II) oxidation process under different treatments are shown in **Fig. 2a-c**. After 7 days of incubation, the contents of available Mn(II) in the MN (172.00~185.22 mg/kg) and M (223.58 mg/kg) treatments were lower than those in the CK treatment (243.22 mg/kg), whereas the contents of amorphous Mn oxides in the M and MN treatments were slightly greater than those in the CK treatment. These results indicated that the available Mn(II) was transformed to amorphous Mn oxides during the biogenic Mn(II) oxidation process. After 14 days of incubation, the contents of available Mn(II) sharply declined in the M and MN treatments, with values decreasing from 438.08 mg/kg in the CK treatment to 30.02 mg/kg in the M treatment and 29.87~43.08 mg/kg in the MN treatment. Moreover, elevated contents of amorphous Mn oxides were observed in the M and MN treatments. The contents of amorphous Mn oxides increased from 36.14 mg/kg in the CK treatment to 612.93 mg/kg in the M treatment and 462.47~573.77 mg/kg in the MN treatment. Similarly, small increases in the contents of free Mn oxides in M and part of the MN treatment (MN10 and MN15) were detected.

These results indicated that MnOB can effectively utilize the available Mn(II) to form tetravalent Mn oxides, especially in the form of amorphous Mn oxides (BMOs). Previous studies have shown that the initial crystal morphology of microbial Mn(II) oxidation products is layered phyllomanganate Mn oxides with poorly or amorphous crystallinity and primary Mn(IV) as the structural Mn (Wang et al., 2020). For example, BMO generated by *Pseudomonas putida* strain MnB1 is a poorly crystalline layer-type Mn(IV) mineral with a high average oxidation state (3.9) and a moderately high surface area (98 m^2/g), which is most similar to δ-MnO_2 (Villalobos et al., 2003). BMO promotes the degradation of a wide array of organic pollutants, including bisphenol A, phenols, atrazine, glyphosate and diclofenac (Qiao et al., 2024). It can be inferred that in our study, the amorphous Mn oxides generated *in situ* by MnOB were primarily responsible for PAH degradation in the coking soils.

The Pearson correlation coefficient suggested that the degradation of PAHs was strongly negatively correlated with the available Mn(II) content and highly positively correlated with the amorphous Mn oxide content **(Fig. 2d)**. For example, the correlation coefficients of total PAHs and BaP with available Mn(II) were -0.96 and -0.89, respectively, whereas the correlation coefficients of total PAHs and BaP with amorphous Mn oxides were 0.81 and 0.84, respectively. These results further confirmed that biogenic Mn(II) oxidation by MnOB plays an important role in PAH degradation. Moreover, the degradation of PAHs was highly positively correlated with urease and catalase activities **(Fig. S2)**, with correlation coefficients of 0.91 and 0.82, respectively. Urease and catalase play vital roles in the biogenic Mn(II) oxidation process. Andeer et al. (2015) reported that urease can increase the efficiency of Mn(II) oxidation and promote the formation of Mn oxides by adjusting the pH and nitrogen source supply and that an increase in catalase activity accelerates the decomposition of H_2O_2, thereby promoting the conversion of Mn(III) ions to Mn(IV).

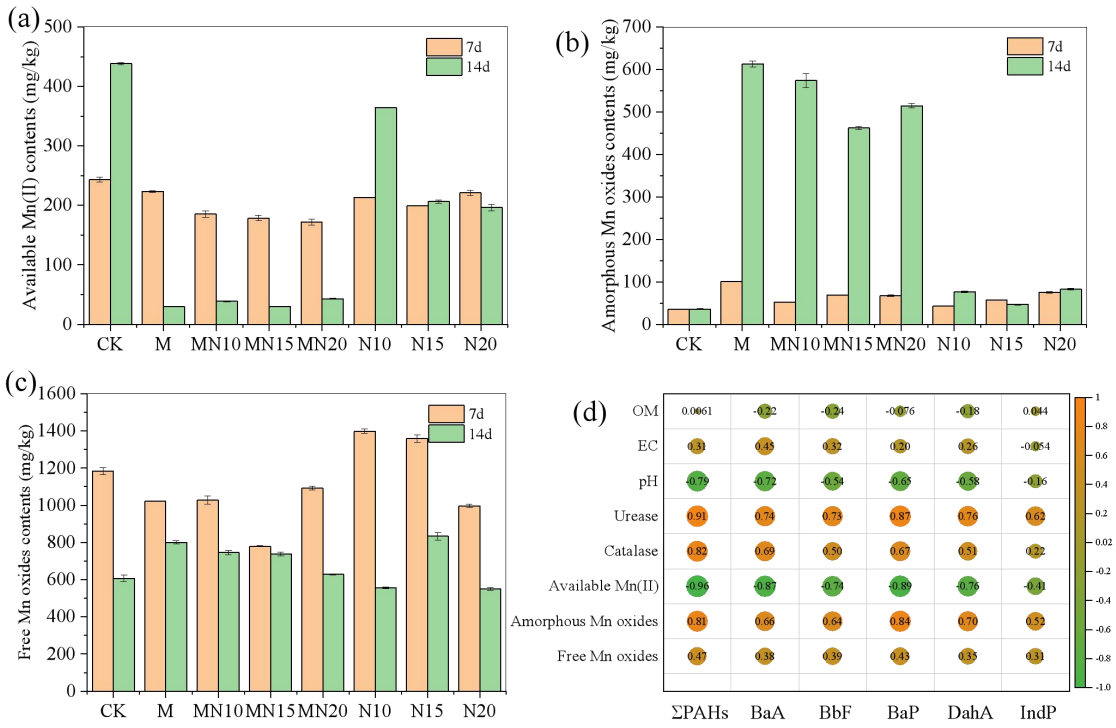

Fig. 2 Changes of the contents of available Mn(II) (a), amorphous Mn oxides (b) and free Mn oxides (c), and the relationships between PAHs degradation and the physical-chemical properties of soils (d).

3.3 Changes in bacterial number and phe gene abundance during the biogenic Mn(II) oxidation process

The changes in bacterial number during the biogenic Mn(II) oxidation process during different treatments are shown in **Fig. 3a**. After 7 days of incubation, the bacterial number in all the treatments was 10^6 copies/g, and the bacterial number did not increase significantly in the short period of time in the treatment groups with the addition of MnOB and exogenous nitrogen, which might be due to the inhibitory effect of residual $KMnO_4$ in the soils. After 14 days of incubation, the number of bacteria in all the treatment groups increased significantly. With the weakening of the inhibitory effect of $KMnO_4$ in the soil, the activity of microorganisms gradually recovered, and the highly toxic PAHs continuously decomposed into low-toxicity PAHs, which could provide a bioavailable carbon source for the growth of microorganisms; therefore, the bacterial number significantly increased after 14 days of incubation. The bacterial number in the CK treatment was 1.50×10^8 copies/g, while the bacterial number greatly increased in the M treatment (1.48×10^9 copies/g) and slightly increased in the MN10 (8.43×10^8 copies/g) and MN15 (4.97×10^8 copies/g) treatments. These results suggested that the addition of exogenous MnOB and certain levels of nitrogen nutrients (C/N=10-15) positively contributed to the increase in the number of soil microorganisms. It is generally believed that the application of exogenous nitrogen by adjusting the C/N ratio from 100/10-100/15 enhances the activities of indigenous microorganisms and promotes the degradation of organic pollutants (Liu et al., 2021; Zhang et al., 2023).

The *phe* gene, which is involved in the metabolism of PAHs, plays an important role in catalyzing the hydroxylation of aromatic compounds. The *Phe* gene acts as a rate-limiting component in the biodegradation of PAHs, so it is usually used as an indicator gene in the microbial degradation of PAHs (Lu et al., 2019). The abundance of the *phe* gene under the different treatments is shown in **Fig. 3b**. After 7

days of incubation, the *phe* gene abundance was 1.78×10^3 copies/g in the CK treatment, but it increased to $6.64\times103\sim1.96\times10^4$ copies/g in the MN treatment group and to $1.48\times104\sim4.69\times10^4$ copies/g in the N treatment group, which was much greater than that in the CK treatment group, suggesting that the addition of exogenous nitrogen significantly promoted the activity of indigenous PAH-degrading bacteria in the soil. After 14 days of reaction, an increase in *phe* gene abundance was observed in the M (2.18×10^4 copies/g) and MN10 (4.46×10^4 copies/g) treatments, whereas it decreased in the N treatments. The increase in bacterial number corresponded with the decrease in PAHs, which demonstrated that the biogenic Mn(II) oxidation process promoted the growth and reproduction of PAH-degrading bacteria in soil and increased the abundance of the *phe* gene, thereby promoting the degradation of PAHs.

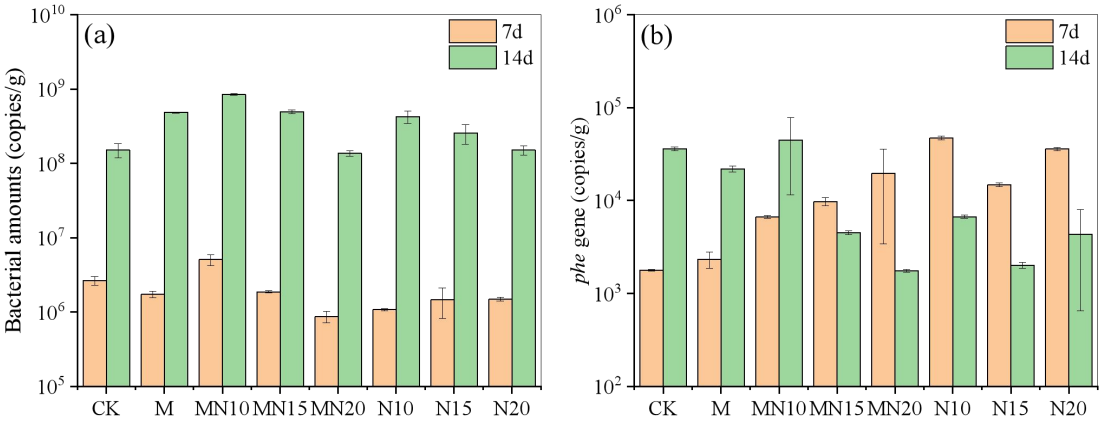

Fig. 3 The contents of bacterial amounts (a) and *phe* gene (b) in different treatments.

3.4 Changes in bacterial community structure during the biogenic Mn(II) oxidation process

The changes in bacterial structure at the phylum level after cultivation for 14 days are shown in **Fig. 4a**. Proteobacteria and Firmicutes had the highest relative abundances in all the treatments, and these microorganisms often exist in contaminated soils (Phulpoto et al., 2024). Compared with that in the CK treatment, the relative abundance of Firmicutes increased significantly, with 52.88%, 27.88% and 37.41% for MN10, MN15 and MN20, respectively. The results showed that the addition of MnOB and exogenous nitrogen effectively increased the abundance of Firmicutes. Yuan et al. (2023) reported that the addition of nitrate increased the abundance of Firmicutesand upregulated the expression of functional genes related to PAH degradation and denitrification. Moreover, Du et al. (2022) reported that the metabolic activity, such as the metabolic activity of nitrate consumption and organic matter mineralization, of Firmicutes may increase with increasing nitrogen levels in the environment.

The changes in the bacterial microbial community at the genus level after cultivation for 14 days are shown in **Fig. 4b**. Compared with those in the CK treatment, the relative abundances of *Domibacillus*, *Brevundimonas* and *Bosea* increased in the M treatment, but the abundances of *Agrobacterium* and *Sphingopyxis* decreased. The genera *Pseudomonas and Agrobacterium* were the dominant genera in the N10 and N15 treatments, with *Pseudomonas* relative abundances of 46.71% and 36.89%, respectively, and *Agrobacterium relative abundances* of 11.43% and 60.87%, respectively. The genera *Domibacillus* (69.81%) and *Alkalihalobacillus* (18.03%) predominated in the N20 treatment group. However, the diversity and composition of bacteria in the MN treatments were significantly different from those in the other treatments. *Agrobacterium* was the dominant genus in the MN treatments, with a relative abundance of 15.82%~33.16%, and the relative abundance of *Domibacillus* greatly

decreased in the MN10 and MN20 treatments, whereas *unclassified* genera accounted for high proportions, especially in the MN10 treatment.

The bacterial community structure of MnOB mainly consists of *Bacillus*, *Clostridium* and *Pseudomonas* **(Fig. 4c)**. However, the proportions of these genera were not significantly greater in the M and MN treatments than in the CK treatment, which indicated that the addition of MnOB did not lead to the formation of a dominant bacterial community in the soils. Conversely, well-known PAH degraders, such as *Agrobacterium* and *Sphingopyxis,* were still the dominant genera in all the treatments. The relative abundances of *Agrobacterium bacteria* and total bacteria in the MN15 treatment were greater than those in the CK treatment, and the removal efficiency of PAHs in MN15 was the highest, indicating that the synergistic effect of MnOB and exogenous nitrogen was conducive to the growth and proliferation of PAH-degrading bacteria in the soil. Moreover, the M treatment also had a high PAH degradation efficiency, while the relative abundance of *Agrobacterium* and *phe* genes was lower than that in the CK treatment, suggesting that the degradation of PAHs was mainly attributed to the formation of BMO during the biogenic Mn(II) oxidation process rather than to the MnOB bacteria.

The correlations between major microorganisms and environmental factors are shown in **Fig. 4d**. *Paenibacillus* was significantly positively correlated with amorphous manganese oxide, with a correlation coefficient of 0.73, but significantly negatively correlated with pH, with a correlation coefficient of -0.69. The abundance of Brevundimonas was also consistently correlated with the pH, with correlation coefficients of -0.58 and -0.54, respectively. *Sphingobacter* was significantly positively correlated with free manganese oxide and urease activity, with correlation coefficients of 0.79 and 0.60, respectively. The BMOs formed by *Pseudomonas* facilitate the degradation of tetracycline (Bai et al., 2020) and 17α-ethynylestradiol (Tran et al., 2018). *Pseudoxanthomonas* and *Agrobacterium* have been shown to contribute to the degradation of PAHs in soil (Kuppusamy et al., 2016). *Bacillus* has been found to eliminate 99% of phenanthrene, benzo[a]fluoranthene and pyrene from contaminated coking soil (Nan et al., 2022). Overall, the addition of nutrients and MnOB can not only increase the degradation of PAHs but also alter the structure of the soil microbial community.

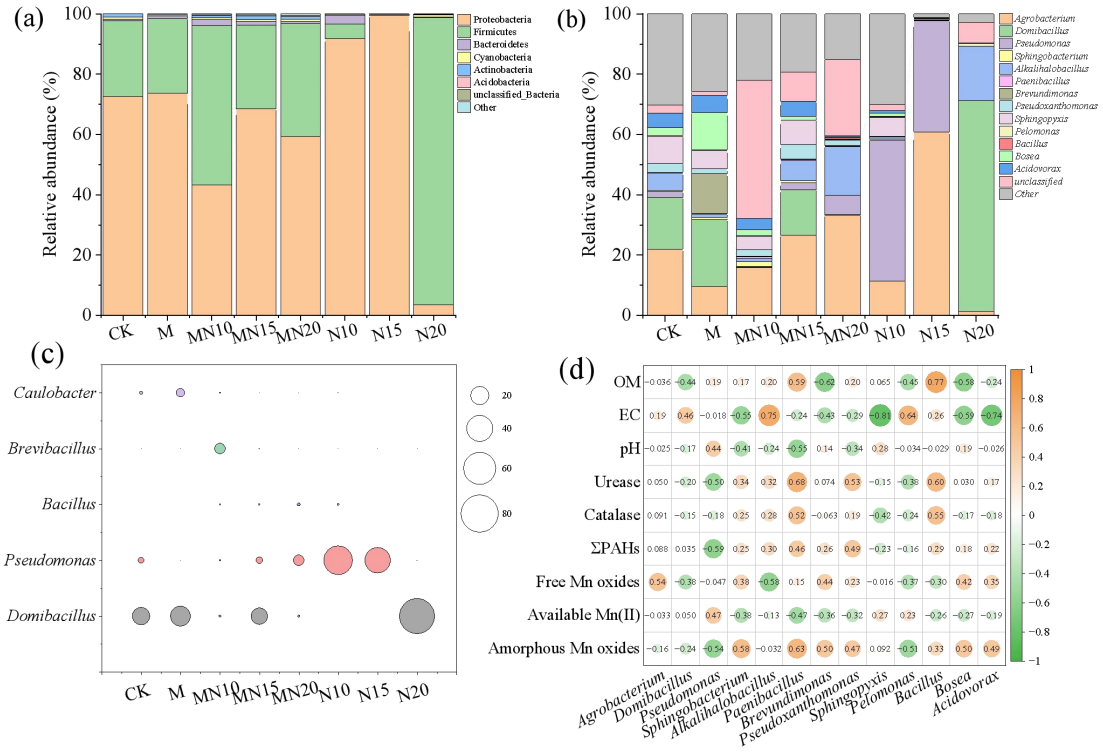

Fig. 4 Changes of the relative abundance (%) of bacteria at phylum level (a) and genus level (b) in different treatments; the relative abundance of potential MnOB in different treatments (c); The correlation relationships between major microorganisms and environmental factors (d).

3.5 Changes in bacterial metabolic function during the biogenic Mn(II) oxidation process

Based on the microbial metabolic pathways of KEGG categories (level 3), the relative abundance of pathways related to polycyclic aromatic hydrocarbon (PAHs) degradation, nitrogen cycle and manganese oxidation is analyzed **(Fig. S3a-c)**. Following the inoculation of manganese-oxidizing bacteria and/or nitrogen, there was a notable elevation in the abundance of ABC transporters, polycyclic aromatic hydrocarbon degradation, benzoate degradation, lipopolysaccharide biosynthesis, glycolysis/gluconeogenesis, drug metabolism-cytochrome P450, alanine, aspartate, and glutamate metabolism, and two-component system. The correlation coefficients demonstrate significant relationships between the two-component system and ABC transporters with polycyclic aromatic hydrocarbon degradation, fluorobenzoate degradation, benzoate degradation, lipopolysaccharide biosynthesis, butanoate metabolism, as well as glycolysis/gluconeogenesis, and pyruvate metabolism **(Fig. S3d)**. ABC transporters are crucial for maintaining the homeostasis of essential transition metals like manganese and iron, as well as for regulating the active uptake of nitrate (Li et al., 2024). The two-component system, as the central signaling pathway in bacteria, regulates various physiological processes including growth, reproduction, stress response, environmental adaptation, and pathogenicity. Benzoate degradation represents an essential downstream pathway for the degradation of numerous PAHs, including phenanthrene, pyrene, and fluorene, thereby emerging as one of the predominant pathways within the heterologous biodegradation metabolic network. Pyruvate metabolism in glycolysis/gluconeogenesis yields energy and substrates for the tricarboxylic acid (TCA) cycle or fermentation, producing essential precursors like ATP and pyruvate. The simultaneous

addition of MnOB and nitrogen markedly elevated the abundance of the Alanine, aspartate, and glutamate metabolic pathways. Alanine, aspartate, and glutamate metabolism can directly contribute to the energy supply of microorganisms by providing intermediates for energy metabolism (Tang et al., 2025). Moreover, the relative abundance of cytochrome P450 in MN15 exceeded that in both M and CK. PAHs undergo oxidation by cytochrome P450 monooxygenase to form catechol, which is subsequently metabolized into inert compounds by catechol dioxygenase, eventually entering the microbial TCA cycle (Silva et al., 2023).

3.6 Changes in genes related to biogenic Mn(II) oxidation and PAH degradation

Based on KEGG gene function annotation, the pathways and genes related to Mn(II) oxidation, the nitrogen cycle, PAH degradation and cell metabolism were determined, as shown in **Fig. 5a**. The presence of MnOB and nitrogen led to a notable rise in the abundance of the *mntABC* gene. The *mntA*, *mntB*, and *mntC* genes encode the ATP-binding protein of the manganese transport system, the permease protein of the manganese transport system, and the substrate-binding protein of the manganese transport system, respectively. This enhancement implies a more effective manganese uptake mechanism, which could enhance cellular functions and metabolic processes related to manganese utilization. Compared with the CK treatment, the M treatment had a greater abundance of the *ccmC* gene, which was mainly attributed to the high bacterial number in the M treatment. The *ccmC* gene is involved mainly in the correct folding and maturation of cytochrome c family proteins and is crucial for electron transport in the bacterial respiratory chain, especially aerobic or microaerobic metabolism (Li et al., 2024b). Compared with CK, the addition of nitrogen and MnOB sources increased the abundance of PAH degradation genes, including the *pht3*, *pcaG* and *pcaH* genes, which was in accordance with the degradation efficiency of PAHs in these treatments.

A total of ten types of manganese oxidation-related proteins were analyzed based on GO gene functional annotation, and their abundance changes are depicted in **Fig. 5b.** These Mn(II) oxidation-related proteins are involved primarily in processes such as copper ion binding, oxidoreductase activity, the periplasmic space, the cell membrane, calcium ion binding, heme binding, peroxidase activity, the oxidative stress response, the extracellular space, and manganese ion binding. The presence of MnOB and nitrogen led to a rise in oxidoreductase activity levels. Most of these manganese-oxidizing proteins are associated with oxidoreductase activity and the cell membrane, indicating that biogenic oxidation is central to the soil system and that redox reactions occur on the cell membrane.

Correlation analysis revealed significant associations between the expression of manganese transformation genes (*petc*, *opuBD*, *fumC*), a nitrogen cycle gene (*nirD*), and genes involved in PAH degradation (*pht3*, *pcaG*, *pcaH*). The *ccmC* gene exhibited a significant correlation with the *nosZ* and *nirA* genes **(Fig. 5c)**. In the M treatment, the abundances of the *nirA*, *napA*, *norB* and *nosZ* genes were slightly greater than those in the CK, whereas in the MN15 treatment, the abundances of the *norB* and *napA* genes were greater than those in the CK. Compared with that in CK, the abundance of the *napA* gene in M and MN15 was greater than that in CK, which indicated that the reduction of nitrate to nitrite was greater after the addition of MnOB. In addition, the abundances of the *norB* and *nosZ* genes were also greater in the M treatment, which also indicated that the addition of MnOB increased the degree of denitrification **(Fig. 5d)**. Overall, the addition of MnOB and nitrogen sources to pretreated soil can increase the abundance of manganese transformation-related genes,

nitrogen cycle-related genes, and PAH degradation-related genes and thus increase the degradation efficiency of PAHs in soils.

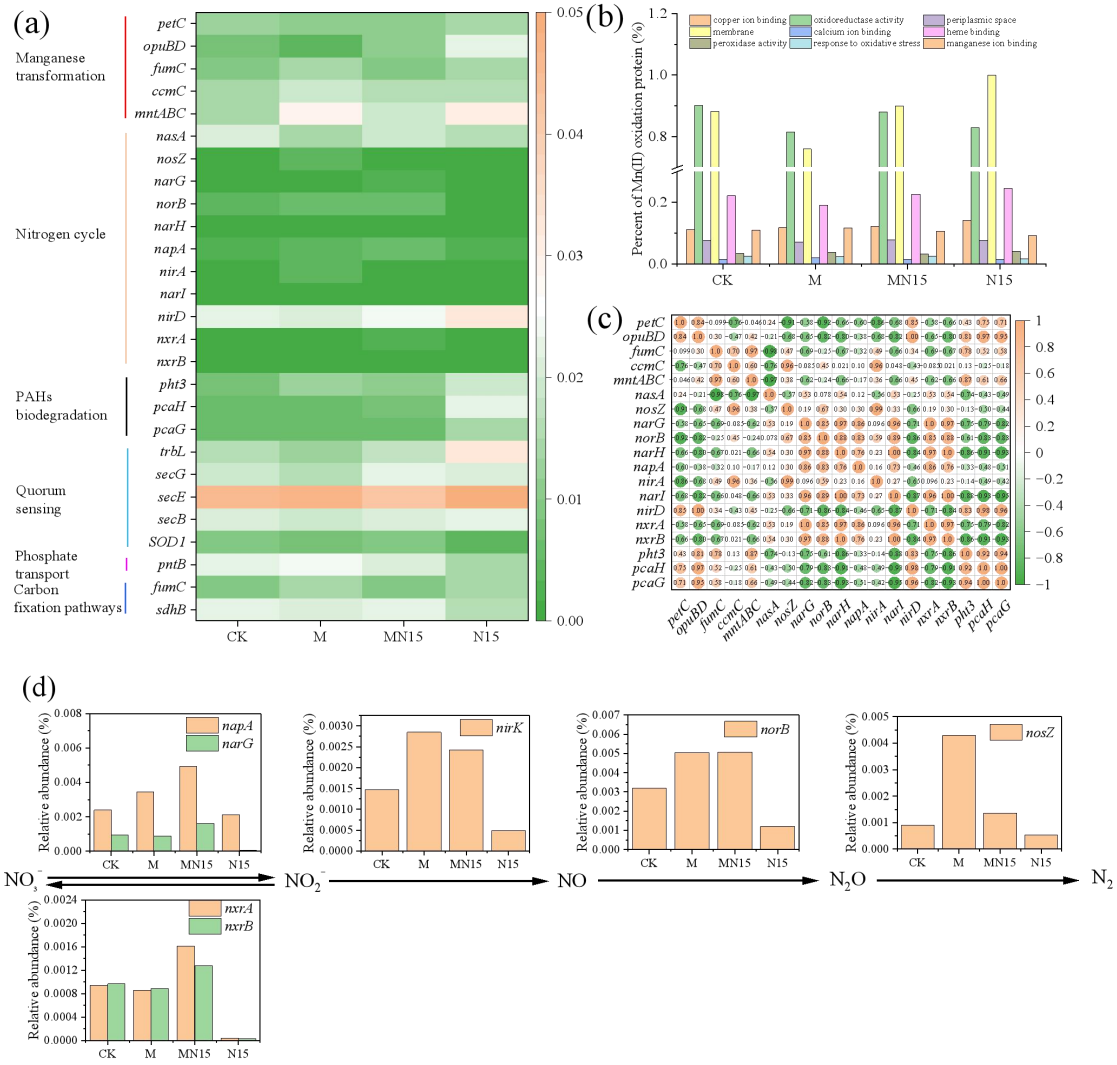

Fig. 5 Relative abundance of the genes related to PAHs degradation (a), Mn(II) oxidizing protein (b) and nitrogen metabolism genes (d) in different treatments; The correlation analysis of key genes associated with manganese transformation, nitrogen cycling, and PAH degradation(c).

3.7 Degradation mechanism of PAHs during the biogenic Mn(II) oxidation process with the addition of nitrogen

Based on the above results, the degradation mechanism of PAHs during the biogenic Mn(II) oxidation process was proposed, as shown in **Fig. 6**. First, after reacting with $KMnO_4$, BaP (a representative high-molecular-weight PAH) was oxidized and partially degraded into some intermediates, including phenanthrene (PHE) and benzo [a] pyrene 4,5-dione. Moreover, Mn(VII) was reduced to Mn(II) during the degradation of BaP. These available Mn(II) ions can be used as important Mn(II) sources for MnOB. MnOB can adsorb a large amount of bioavailable Mn(II) onto the surface of bacterial cells and then oxidize it into Mn(III) through enzymatic reactions (e.g., multicopper oxidase). Furthermore, Mn(III) was converted into Mn(IV) through a disproportionated reaction (Andeer et al., 2015; Learman et al., 2011). During the biogenic Mn(II) oxidation process, BaP is oxidized and degraded to produce benzo [a] pyrene 4,5-dione, which is further oxidized and converted into 1,2-dihydroxyanthraquinone and finally completes the mineralization of CO_2 and H_2O (Wang et al., 2022). The Mn(II) produced after BMO oxidation of BaP can be

reused by MnOB, providing new active sites for BaP degradation (Wang et al., 2024). In addition, highly active intermediates, including $\cdot O_2^-$ and H_2O_2, may also participate in the BaP degradation process (Qi et al., 2024). During the following biological treatment period, the low-toxicity PAHs were further degraded by the PAH-degrading bacterium, with the dominant PAH-degrading genes *pht3*, *pacH* and *pacG*. Overall, $KMnO_4$ preoxidation reduces the content and toxicity of PAHs and provides available Mn(II) for MnOB. Subsequently, MnOB utilize Mn(II) to induce BMO and further promote the oxidative degradation of PAHs as well as the biodegradation of PAHs during the biogenic Mn(II) oxidation process.

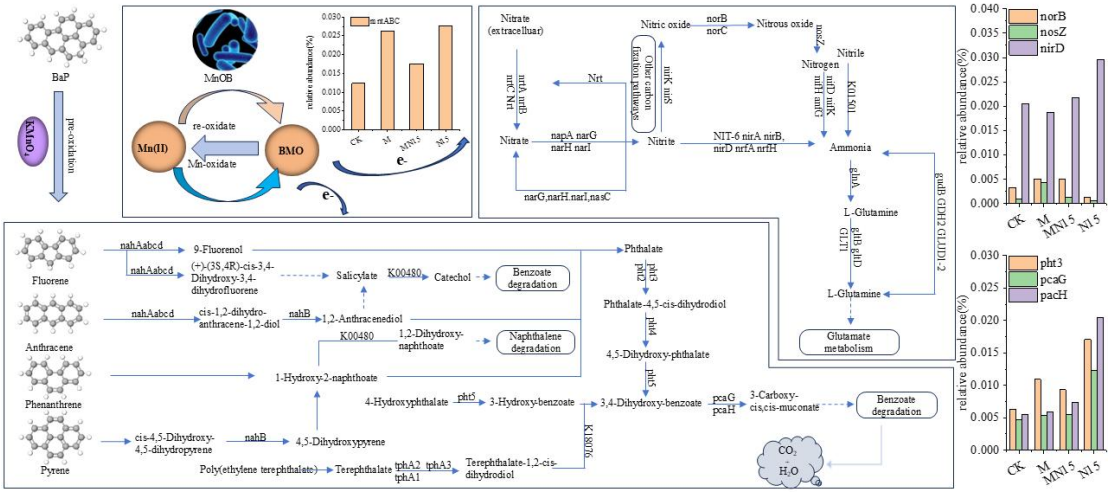

Fig. 6 The degradation mechanism of PAHs during the biogenic Mn(II) oxidation process

4. Conclusions

MnOB under various nitrogen conditions enhanced the degradation of high-molecular-weight PAHs in coking-contaminated soil. A high percentage of total PAHs and BaP were degraded when the combination of MnOB and potassium nitrate was stimulated with a C/N ratio of 100:15. MnOB can effectively utilize available Mn(II) to form biogenic Mn oxides, and the amorphous Mn oxides generated by MnOB are primarily responsible for the degradation of high-molecular-weight PAHs. Nitrogen stimulation can effectively promote the expression of Mn(II) oxidation functional genes, and the *pht3*, *pcaH*, and *pcaG* genes are involved mainly in the microbial degradation of PAHs and the intermediate metabolites.

Acknowledgments

This work was supported by the National Natural Science Foundation of China (52370173), Taishan Scholars Project Special Fund Shandong Province of China (tsqn202408218), and the Natural Science Foundation in Shandong Province of China (ZR2023ME042).

References

Andeer, P.F., Learman, D.R., McIlvin, M., Dunn, J.A., Hansel, C.M., 2015. Extracellular haem peroxidases mediate Mn(II) oxidation in a marine Roseobacter bacterium via superoxide production. Environ Microbiol 17, 3925-3936.

Bai, Y., Su, J., Wen, Q., Li, G., Xue, L., Huang, T., 2020. Removal of tetracycline by denitrifying Mn(II)-oxidizing bacterium *Pseudomonas* sp. H117 and biomaterials (BMO and MBMO): Efficiency and mechanisms. Bioresour Technol 312, 123565.

Bianco, F., Race, M., Papirio, S., Esposito, G., 2022. Phenanthrene biodegradation in a fed – batch reactor treating a spent sediment washing solution: Techno – economic implications for the recovery of ethanol as

extracting agent. Chemosphere 286, 131361.

Chang, Y.-C., Peng, Y.-P., Chen, K.-F., Chen, T.-Y., Tang, C.-T., 2022. The effect of different in situ chemical oxidation (ISCO) technologies on the survival of indigenous microbes and the remediation of petroleum hydrocarbon-contaminated soil. Process Saf Environ Prot 163, 105–115.

Chen, X., Li, Z., Fu, S., Liang, L., Liu, X., Hu, F., Zhang, W., Bi, Y., Jiao, Y., Gu, S., Li, Q., 2024. Sequential oxidation procedures with $KMnO_4$: Component characteristics of labile reducing capacity fractions in anaerobic sediments. Sci Total Environ 955, 177126.

Dai, C., Han, Y., Duan, Y., Lai, X., Fu, R., Liu, S., Leong, K.H., Tu, Y., Zhou, L., 2022. Review on the contamination and remediation of polycyclic aromatic hydrocarbons (PAHs) in coastal soil and sediments. Environ Res 205, 112423.

Dai, S., Zhou, Q., Yang, Y., Zhang, Y., Zhang, S., Yao, Y., 2024. Removal of polycyclic aromatic hydrocarbons (PAHs) and the response of indigenous bacteria in highly contaminated aged soil after persulfate oxidation. J Environ Manage 368, 122268.

Du, J., Liu, J., Jia, T., Chai, B., 2022. The relationships between soil physicochemical properties, bacterial communities and polycyclic aromatic hydrocarbon concentrations in soils proximal to coking plants. Environ Pollut 298, 118823.

Gonzalez, J.M., Aranda, B., 2023. Microbial Growth under Limiting Conditions-Future Perspectives. Microorganisms 11, 1641.

Gou, Y., Song, Y., Li, P., Wei, W., Luo, N., Wang, H., 2024. Study on the accelerated biodegradation of PAHs in subsurface soil via coupled low-temperature thermally treatment and electron acceptor stimulation based on metagenomic sequencing. J Hazard Mater 465, 133265.

Gou, Y., Song, Y., Yang, S., Yang, Y., Cheng, Y., Li, J., Zhang, T., Cheng, Y., Wang, H., 2022. Polycyclic aromatic hydrocarbon removal from subsurface soil mediated by bacteria and archaea under methanogenic conditions: Performance and mechanisms. Environ Pollut 313, 120023.

Gou, Y., Yang, S., Cheng, Y., Song, Y., Qiao, P., Li, P., Ma, J., 2019. Enhanced anoxic biodegradation of polycyclic aromatic hydrocarbons (PAHs) in aged soil pretreated by hydrogen peroxide. Chem Eng J 356, 524–533.

Gou, Y., Zhao, Q., Yang, S., Qiao, P., Cheng, Y., Song, Y., Sun, Z., Zhang, T., Wang, L., Liu, Z., 2020. Enhanced degradation of polycyclic aromatic hydrocarbons in aged subsurface soil using integrated persulfate oxidation and anoxic biodegradation. Chem Eng J 394, 125040.

Han, D., Currell, M.J., 2017. Persistent organic pollutants in China's surface water systems. Sci Total Environ 580, 602–625.

He, Z., Li, Q., Xu, Y., Zhang, D., Pan, X., 2023. Production of extracellular superoxide radical in microorganisms and its environmental implications: A review. Environ Pollut 338, 122563.

Huang, Q., Wang, Y., Qin, X., Zhao, L., Liang, X., Sun, Y., Xu, Y., 2022. Soil application of manganese sulfate effectively reduces Cd bioavailability in Cd-contaminated soil and Cd translocation and accumulation in wheat. Sci Total Environ 814, 152765.

Kulik, N., Goi, A., Trapido, M., Tuhkanen, T., 2006. Degradation of polycyclic aromatic hydrocarbons by combined chemical pre-oxidation and bioremediation in creosote contaminated soil. J Environ Manage 78, 382–391.

Kuppusamy, S., Thavamani, P., Megharaj, M., Lee, Y.B., Naidu, R., 2016. Isolation and characterization of polycyclic aromatic hydrocarbons (PAHs) degrading, pH

tolerant, N-fixing and P-solubilizing novel bacteria from manufactured gas plant (MGP) site soils. Environ Technol Innov 6, 204 – 219.

Learman, D.R., Voelker, B.M., Vazquez-Rodriguez, A.I., Hansel, C.M., 2011. Formation of manganese oxides by bacterially generated superoxide. Nat Geosci 4, 95–98.

Li, B., Wang, X., Li, Q., Xu, D., Li, J., Hou, W., Chen, Y., Jiang, Y., Zhou, C., 2024b. Allosteric regulation of nitrate transporter NRT via the signaling protein PII. PNAS 121, 2318320121-2318320121.

Li, Q., Shi, M., Liao, Q., Li, K., Huang, X., Sun, Z., Yang, W., Si, M., Yang, Z., 2024a. Molecular response to the influences of Cu(II) and Fe(III) on forming biogenic manganese oxides by *Pseudomonas putida* MnB1. J Hazard Mater 477, 135298.

Li, W., Wang, H., Yang, Y., Li, S., Liu, Y., Meng, X., Sun, Y., Liu, P., Wang, Y., 2023. Insights into the effects of hydrogen peroxide and Fenton oxidation on PAHs removal and indigenous microorganisms in a coking-contaminated soil. Environ Technol Innov 31, 103235.

Liao, X., Wu, Z., Li, Y., Cao, H., Su, C., 2019. Effect of various chemical oxidation reagents on soil indigenous microbial diversity in remediation of soil contaminated by PAHs. Chemosphere 226, 483–491.

Liu, F., Ma, J., 2012. Handbook of Soil Monitoring and Analysis. Chemical Industry Press, Beijing.

Liu, H., Wu, M., Gao, H., Yi, N., Duan, X., 2021. Hydrocarbon transformation pathways and soil organic carbon stability in the biostimulation of oil-contaminated soil: Implications of ^{13}C natural abundance. Sci Total Environ 788, 147580.

Lu, C., Hong, Y., Liu, J., Gao, Y., Ma, Z., Yang, B., Ling, W., Waigi, M.G., 2019. A PAH-degrading bacterial community enriched with contaminated agricultural soil and its utility for microbial bioremediation. Environ Pollut 251, 773–782.

Lü, H., Wei, J.-L., Tang, G.-X., Chen, Y.-S., Huang, Y.-H., Hu, R., Mo, C.-H., Zhao, H.-M., Xiang, L., Li, Y.-W., Cai, Q.-Y., Li, Q.X., 2024. Microbial consortium degrading of organic pollutants: Source, degradation efficiency, pathway, mechanism and application. J Clean Prod 451, 141913.

Nan, Z., Haijiao, G., Qingxin, L., Zuotao, Z., Jiao, S., Hui, W., 2022. Bioaugmentation of polycyclic aromatic hydrocarbon (PAH)-contaminated soil with the nitrate-reducing bacterium PheN7 under anaerobic condition. J Hazard Mater 439, 129643–129643.

Peng, A., Liu, J., Ling, W., Chen, Z., Gao, Y., 2015. Diversity and distribution of 16S rRNA and phenol monooxygenase genes in the rhizosphere and endophytic bacteria isolated from PAH-contaminated sites. Sci Rep 5, 12173.

Phulpoto, I.A., Qi, Z., Qazi, M.A., Yu, Z., 2024. Biosurfactants-based mixed polycyclic aromatic hydrocarbon degradation: From microbial community structure toward non-targeted metabolomic profile determination. Environ Int 184, 108448.

Qi, J., Lin, Z., Wang, X., Koju, R., Zhao, Y., Yu, H., Ma, B., Hu, C., Qu, J., 2025. Nutrient Condition-Induced Mechanism Shift of Microbial Manganese Oxidation: Significance of Catalase. ACS EST Water 5, 1907–1915.

Qi, J., Wang, X., Lin, Z., Zhao, J., Hu, C., Qu, J., 2024. Algae promotes the biogenic oxidation of Mn(II) by accelerated extracellular superoxide production. Water Res 261, 122063.

Qiao, A., Pan, H., Zang, J., Zhang, Y., Yi, X., Liu, Y., Zhan, J., Yang, X., Zhao, X., Li, A.,

Zhou, H., 2024. Can xenobiotics support the growth of Mn(II)-oxidizing bacteria (MnOB)? A case of phenol-utilizing bacteria Pseudomonas sp. AN-1. J Hazard Mater 469, 134095.

Silva, N.M., Romagnoli, C.L., Santiago, C.R.D.N., Lacerda, J.P.A.D. De, Leão, S.C., Digiampietri, L.A., Viana-Niero, C., 2023. Multi-Approach Characterization of Novel Pyrene-Degrading Mycolicibacterium austroafricanum Isolates Lacking nid Genes. Microorganisms 11, 1413.

Tang, C., Fan, Y., Wang, T.,Wang, J., Xiao, M., He, M., Chang, X., Li, Y., Li, X., 2025. Integrated Amino Acid Profiling and 4D-DIA Proteomics Reveal Protein Quality Divergence and Metabolic Adaptation in Cordyceps Species. J Fungi 11, 365-365.

Tran, T.N., Kim, D.-G., Ko, S.-O., 2018. Synergistic effects of biogenic manganese oxide and Mn(II)-oxidizing bacterium Pseudomonas putida strain MnB1 on the degradation of 17 α -ethinylestradiol. J Hazard Mater 344, 350–359.

Usman, M., Hanna, K., Faure, P., 2018. Remediation of oil-contaminated harbor sediments by chemical oxidation. Sci Total Environ 634, 1100–1107.

Villalobos, M., Toner, B., Bargar, J., Sposito, G., 2003. Characterization of the manganese oxide produced by *pseudomonas putida* strain MnB1. Geochim Cosmochim Acta 67, 2649–2662.

Wang, F., Dong, W., Zhao, Z., Wang, H., Li, W., Zhang, L., Ouyang, H., Huang, X., Li, J., 2022. Mechanistic insights into Fe(II)-citric acid complex catalyzed CaO_2 Fenton-like process for enhanced benzo[a]pyrene removal from black-odor sediment at circumneutral pH. Water Res 226, 119233.

Wang, H., Zou, R., Jiang, X., Wang, Y., Wang, X., Sun, Y., Li, S., Wang, Y., 2024. Isolation of halotolerant *Pseudomonas* sp. KW-2 for the effective degradation p-arsanilic acid and immobilization its released inorganic arsenic. Process Saf Environ Prot 192, 1271-1282.

Wang, Y., Qiu, W., Lu, X., Zhou, X., Zhang, H., Gong, X., Gong, B., Ma, J., 2023. Nitrilotriacetic acid-assisted Mn(II) activated periodate for rapid and long-lasting degradation of carbamazepine: The importance of Mn(IV)-oxo species. Water Res 241, 120156.

Wang, Y., Tsang, Y.F., Wang, H., Sun, Y., Song, Y., Pan, X., Luo, S., 2020. Effective stabilization of arsenic in contaminated soils with biogenic manganese oxide (BMO) materials. Environ Pollut 258, 113481.

Yang, S., Gou, Y., Song, Y., Li, P., 2018. Enhanced anoxic biodegradation of polycyclic aromatic hydrocarbons (PAHs) in a highly contaminated aged soil using nitrate and soil microbes. Environ Earth Sci 77, 432.

Yang, Y., Ali, A., Su, J., Chang, Q., Xu, L., Su, L., Qi, Z., 2022. Phenol and 17β-estradiol removal by Zoogloea sp. MFQ7 and in-situ generated biogenic manganese oxides: Performance, kinetics and mechanism. J Hazard Mater 429, 128281.

Yi, L., Sheng, R., Wei, W., Zhu, B., Zhang, W., 2022. Differential contributions of electron donors to denitrification in the flooding-drying process of a paddy soil. Appl Soil Ecol 177, 104527.

Yu, Y., Ou, Y., Wu, M., Zhang, X., Liu, Z., 2024. A comprehensive evaluation of bioremediation effects of oil-contaminated soils using various dosages of exogenous nitrogen supplementation: TPH removal, ecological toxicity, and microecological response. J Environ Chem Eng 12, 114835–114835.

Yuan, S., Han, X., Yin, X., Su, P., Zhang, Y., Liu, Y., Zhang, J., Zhang, D., 2023. Nitrogen transformation promotes the anaerobic degradation of PAHs in water level

fluctuation zone of the Three Gorges Reservoir in Yangtze River, China: Evidences derived from in-situ experiment. Sci Total Environ 864, 161034-161034.

Zeng, K., Huang, X., Guo, J., Dai, C., He, C., Chen, H., Xin, G., 2024. Microbial-driven mechanisms for the effects of heavy metals on soil organic carbon storage: A global analysis. Environ Int 184, 108467.

Zhang, Q., Meng, J., Su, G., Liu, Z., Shi, B., Wang, T., 2021(a). Source apportionment and risk assessment for polycyclic aromatic hydrocarbons in soils at a typical coking plant. Ecotoxicol Environ Saf 222, 112509.

Zhang, N., Li, C., Xie, H., Yang, Y., Hu, Z., Gao, M., Liang, S., Feng, K., 2021(b). Mn oxides changed nitrogen removal process in constructed wetlands with a microbial electrolysis cell. Sci Total Environ 770, 144761-144761.

Zhang, S., Zhang, M., Han, F., Liu, Z., Zhao, C., Lei, J., Zhou, W., 2023. Enhanced degradation of petroleum in saline soil by nitrogen stimulation and halophilic emulsifying bacteria *Bacillus* sp. Z-13. J Hazard Mater 459, 132102.

Zhao, C., Dong, Y., Feng, Y., Li, Y., Dong, Y., 2019. Thermal desorption for remediation of contaminated soil: A review. Chemosphere 221, 841–855.

Zhao, X., Xie, Z., Li, Y., Liu, T., Liu, D., 2022. Synergy of Fe and biogenic Mn oxide components mediated by a newly isolated indigenous bacterium to enhance As(III/V) immobilization in groundwater. Appl Geochem 140, 105266.

EFFICIENCY OPTTIMIZATION AND MECHANISTIC INSIGHTS INTO MICROBIAL ELECTROSYNTHESIS OF METHANE FROM CO2 UNDER HIGH CURRENT DENSITY CONDITIONS

Peng H Wang[1], Yan Dang[1], Zhi D Sun[2], Bin Qiu[3]

1.College of Environmental Science and Engineering, Beijing Forestry University, China, Beijing

2.College of Environmental Science and Engineering, Beijing Forestry University, China, Beijing

3.College of Environmental Science and Engineering, Beijing Forestry University, China, Beijing

4.College of Environmental Science and Engineering, Beijing Forestry University, China, Beijing

ASTRACT:

Microbial electrolysis cells (MECs) represents a promising technology for carbon dioxide utilization and renewable electricity storage. The practical application of MEC requires high current density and scalable reactor design. Herein, we report a 20 L MEC reactor for methane production. The MEC was constructed by inserting a tubular anode chamber into the cathode compartment. Under sequentially increased current conditions ranging from 0.5 to 6 A, the maximum methane production rate reached 15.2 L/d, with an average Coulombic efficiency of approximately 98%. The methane content in the generated gas reached up to 96%. The performance of this reactor surpasses most reported MEC systems. These results demonstrate the significant potential of MEC for scaling and practical application under high-current conditions.

1. Introduction

Fossil fuels, serving as the primary source of energy, satisfy 88% of global energy demand [1]. Carbon dioxide (CO_2), accounting for 76% of greenhouse gas emissions, plays a significant role in modulating the global climate system[2]. Increasing consumption of fossil fuels—driven by population growth, industrialization, and economic development—has resulted in substantial greenhouse gas (GHG) emissions and their rapid accumulation. According to an IEA report, in 2024, total energy-related CO_2 emissions increased by 0.8%, reaching a historic high of 37.8 billion tonnes. This rise contributed to atmospheric CO_2 concentrations reaching a record 422.5 ppm in 2024, approximately 3 ppm higher than in 2023 and 50% above pre-industrial levels (IEA, 2024)[3]. Elevated GHG emissions in the Earth's atmosphere contribute to rising global average temperatures, posing potentially severe consequences for the environment, as well as for human and animal health. The energy challenge and excessive carbon emissions have become driving forces behind efforts to reduce and reuse CO_2.

CO_2 is a highly stable compound, and the challenge in converting it into formic acid, acetic acid, or other chemicals lies in breaking the C=O bond. Therefore, facilitating the conversion of CO_2 inevitably requires additional, substantial energy input. Electochemical methods, which convert electrical energy into chemical energy, can serve as a strong driving force to achieve this transformation. Microbial electrosynthesis (MES) is an emerging technology that utilizes microorganisms as biocatalysts on the cathode to electrochemically reduce CO_2 into biofuels and

biochemicals[4]. The products of MES include methane, acetate, ethanol, butyrate, among others[5]. Compared to abiotic CO_2 reduction catalysts, microorganisms offer advantages such as lower overpotential, higher product selectivity, long-term operational stability, mild operating conditions, and the ability to produce long-chain organic compounds[6]. As a result, MES is regarded as one of the most promising technologies for CO_2 utilization and renewable energy storage, providing not only an alternative energy source but also contributing to the mitigation of the greenhouse effect.

CH_4 is a renewable energy source, and electricity-driven microbial methane production represents a promising technology for renewable energy storage and CO_2 utilization[7]. Microbial electrolysis cells (MECs), a category of microbial electrochemical systems, enable the generation of CH_4 via electromethanogenesis of CO_2 at the biocathode[8]. This process, known as electromethanogenesis, can occur through either direct or indirect mechanisms[8]. In direct electromethanogenesis, the biocathode serves as the electron source for methanogenic archaea, which directly uptake electrons from the electrode to reduce CO_2 into CH_4. In contrast, indirect electromethanogenesis involves mediators such as biologically or electrochemically generated hydrogen[9], or microbially produced formate or acetate[4, 10]. Cheng et al.[10] first reported the electrocatalytic conversion of CO_2 to CH_4 using a dual-chamber MEC reactor equipped with a carbon cloth-based biocathode coated with a carbon layer. Their study demonstrated that a cathodic biofilm could directly accept electrons from the electrode to reduce CO_2 to CH_4. Recognizing the advantages of CO_2 electromethanogenesis, extensive research has since been conducted on this strategy. Most studies to date have focused on electromethanogenesis systems where hydrogenotrophic methanogens are the dominant archaea enriched on the cathode[7, 11, 12].

In conventional microbial electrolysis cells (MECs), the initiation and progression of electrochemical reactions rely heavily on the biofilm attached to the cathode surface. The current density is directly determined by both the microbial density and metabolic activity within the biofilm, which in turn governs the overall reaction efficiency and treatment capacity of the MEC system. Therefore, over the past decade, significant research efforts have been devoted to elucidating the mechanisms of extracellular electron transfer (EET) in electromethanogenesis and enhancing EET efficiency[12-15]. These strategies include modifying electrode materials and structures, screening microorganisms with high electromethanogenic activity, and optimizing MEC reactor configurations[16-19]. Existing studies suggest that future developments in electromethanogenesis should focus on indirect mechanisms mediated by H_2[12]. Theoretically, if H_2 is employed as an electron mediator, the presence of a biofilm is no longer essential. Without the limitations imposed by biofilm formation, higher current densities can be applied to the cathode. Consequently, researchers have recently developed MEC reactors that utilize suspended microorganisms and in situ electrochemically generated H_2 for CO_2 conversion[20, 21]. Guo et al. reported an electrolytic H_2-fed bubble column reactor for methane production. The reactor consists of an electrochemical cell at the bottom and a bubble column on top. The extended retention time of electrolytically produced H_2 within the column enabled a maximum methane production rate of 1.42 $L \cdot L^{-1} \cdot d^{-1}$ in a 4.5 L reactor, with a coulombic efficiency close to 100%[22]. Additionally, a novel 20 L electrochemical continuous stirred-tank reactor (E-CSTR) was developed for electrochemical CO_2 reduction to methane. The E-CSTR was constructed by integrating a tubular electrochemical cell into a conventional CSTR. At a current of 4 A (119.94 $A \cdot m^{-2}$), the average and maximum methane production rates reached 317.84 $L \cdot m^{-2} \cdot d^{-1}$ (0.53 $L \cdot L^{-1} \cdot d^{-1}$) and 407.8 $L \cdot m^{-2} \cdot d^{-1}$ (0.68 $L \cdot L^{-1} \cdot d^{-1}$), respectively, with an average coulombic efficiency of approximately 98%[23]. The performance of this reactor surpasses that of most reported MEC systems. These results demonstrate that electromethanogenesis driven by in situ H_2 feeding and suspended microorganisms is feasible and can simultaneously achieve high current density and high coulombic efficiency. However, current studies on MEC reactors have paid limited attention to biomethane purity and practical applicability. To advance this

technology toward real-world application, it is essential not only to enhance CO_2 reduction capacity under high current conditions but also to achieve high biomethane purity. Furthermore, more efforts are needed to develop simple, efficient, and scalable reactor designs.

In this study, a 20-liter microbial electrolysis cell (MEC) reactor was constructed, utilizing CO_2 as the sole carbon source in the reaction system. A constant current was applied to both the anode and cathode to enable methanogens to utilize electrolytically produced H_2 for CO_2 fixation and methane generation. The current was gradually increased to acclimatize the microbial consortium, enhancing its capability for rapid CO_2 reduction to CH_4 under high current conditions. The objectives of this work were to progressively adapt the microbial community to overcome limitations at elevated current densities, achieve efficient electrochemical CO_2-to-CH_4 conversion, and obtain high-purity methane. The influence of current density on reactor performance was systematically investigated, along with the long-term operational stability of the system. Furthermore, shifts in microbial community structure and gene expression profiles under different current conditions were analyzed. This study provides important insights into the direct energy and resource recovery from CO_2, supporting the development of scalable bioelectrochemical technologies for carbon utilization.

2. MATERIALS AND METHODS

2.1 MEC Reactor Design

A dual-layer cylindrical MEC reactor with a working volume of approximately 20 L (Φ240 mm × 500 mm) was operated at 37 ± 1°C. The outer layer served as a water-jacketed circulation zone, while the inner chamber functioned as the cathodic compartment. The anode chamber was constructed by bonding a cation exchange membrane (270 mm × 140 mm, CMI-7000, Membranes International Inc., USA) with epoxy adhesive over a rectangular window (250 mm × 110 mm) on a PVC tube (outer diameter: 35 mm, length: 370 mm). The bottom of the PVC tube was sealed with a PVC cap (inner diameter: 35 mm, height: 20 mm). The effective membrane area of the tubular electrochemical cell was 275 cm² (250 mm × 110 mm). An IrO_2-coated titanium mesh (25 cm × 2.8 cm, Baoji Zhiming Special Metal Co., Ltd., China) was installed as the anode inside the anode chamber. The cathode consisted of a 304 stainless steel woven mesh (250 mm × 170 mm, 20 mesh, thickness: 0.1 mm, Anguo Chengli Metal Co., Ltd., China), which was folded into a tubular configuration along the membrane, providing an effective surface area of 425 cm². The reactor top was equipped with a custom-designed lid featuring four ports: a central opening for the impeller shaft, and three peripheral openings for the tubular anode, pH probe, and gas outlet. A recirculating water bath (SC-5A, Ningbo Kezi Biotechnology Co., Ltd., China) was connected to the external jacket to maintain temperature. CO_2 flow rate was regulated using a mass flow controller (D08-1, Beijing Sevenstar Flow Co., Ltd., China). A regulated DC power supply (MS-3010D, MAISHENG, China) was connected to the anode and cathode to provide constant current. The volumes of anolyte and catholyte were 0.3 L and 20 L, respectively.

2.2 Reactor Startup and Operation

Approximately 2 L of anaerobic sludge collected from an operational anaerobic digester at a municipal wastewater treatment plant in Beijing was used as the inoculum for the MEC reactor. The ratio of volatile suspended solids (VSS) to total suspended solids (TSS) in the anaerobic sludge was 0.70. The TSS concentration of the inoculum was approximately 13 g/kg. Carbon dioxide (CO_2) was supplied as the sole carbon source to the cathode chamber.The catholyte used in this study was a synthetic medium containing the following components per liter of deionized water:Na_2HPO_4, 5.5 g; KH_2PO_4, 7.2 g; NH_4Cl, 0.54 g; NaCl, 1 g; $MgCl_2 \cdot 6H_2O$, 0.2 g; $CaCl_2$, 14.6 mg; 10 mL of trace element solution; and 10 mL of vitamin solution.The anolyte consisted of a phosphate buffer solution (5.5 $g \cdot L^{-1}$ Na_2HPO_4 and 7.2 $g \cdot L^{-1}$ KH_2PO_4).A total of 20 L of catholyte was added to the cathode chamber, and 0.3 L

of anolyte was introduced into the anode chamber. The catholyte was purged with N_2 gas at a flow rate of 180 $mL \cdot min^{-1}$ for 60 minutes to remove dissolved oxygen. The temperature was maintained at 37 ± 1°C using a recirculating water bath, and the initial impeller speed was set to 210 rpm. A constant current ranging from 0.5 to 6 A was applied to the electrochemical cell. The current was increased stepwise only after gas production and methane concentration had stabilized under the previous current condition.Abiotic electrolysis tests confirmed that the electron-to-hydrogen conversion efficiency at the cathode was nearly 100%. Thus, the resulting H_2/CO_2 ratio in the reactor was maintained at 3.9:1. Compared to the stoichiometric H_2/CO_2 ratio required for methanation (4:1), CO_2 was supplied in slight excess. This ratio was selected to ensure maximum hydrogen utilization efficiency.Gas produced in the cathode chamber was sampled daily to monitor the concentrations of CO_2, H_2, and CH_4. Additionally, 50 mL of catholyte was collected daily for volatile fatty acid (VFA) analysis and microbial community profiling, with an equal volume of fresh catholyte replenished after each sampling. Fresh anolyte was periodically added to the anode chamber to compensate for water loss. Table 1 summarizes the operational conditions of the MEC.

2.3 Analytical Methods

The catholyte was centrifuged at 10,000 rpm for 5 minutes, and the supernatant was filtered through a 0.22 μm membrane for volatile fatty acid (VFA) analysis. Formate, acetate, propionate, butyrate, valerate, and caproate were quantified using high-performance liquid chromatography (HPLC; Bio-Rad, Hercules, California, USA) with 5 mM H_2SO_4 as the mobile phase[24]. pH was measured using a pH meter (HACH, USA).Gas samples were collected and stored in aluminum foil gas bags (Haide Technology, Dalian, China). Gas volumes were measured using glass syringes of 50 mL, 100 mL, or 500 mL capacities. The concentrations of gas components (CH_4, CO_2, and H_2) were analyzed by gas chromatography (GC7900, China) equipped with a thermal conductivity detector (TCD), following the manufacturer's operational manual[24].To determine the biomass concentration in the reactor, microbial samples were collected from the catholyte on the final day of each current stage. Biomass quantity was measured using the dry cell weight (DCW) method[25].

2.4 DNA Extraction and Microbial Community Analysis

To assess microbial community dynamics in the MEC reactor, sludge samples were collected during stable operation at each applied current stage (0.5 A, 1 A, 2 A, 3 A, 4 A, 5 A, and 6 A). DNA was extracted using the RNeasy PowerSoil DNA Elution Kit (QIAGEN) according to the manufacturer's instructions. The concentration and purity of DNA from each sample were determined using a NanoDrop UV spectrophotometer (Thermo Fisher Scientific, Delaware, USA).Bacterial and archaeal 16S rRNA gene fragments were amplified via polymerase chain reaction (PCR) using primer sets 338F/806R and Arch524F/Arch958R, respectively[26]. The amplified sequences were sequenced on the Illumina HiSeq 2000 platform (Illumina, San Diego, USA) by Majorbio Bio-Pharm Technology Co., Ltd. (Shanghai, China).

2.5 RNA Extraction and Metatranscriptomic Analysis

Total RNA was extracted from sludge samples collected at different operational stages using the RNeasy PowerSoil Total RNA Kit (QIAGEN). Following the manufacturer's instructions, the extracted RNA was treated with DNase I (Ambion) to remove genomic DNA contamination. To confirm the absence of DNA, RNA samples without reverse transcription were subjected to polymerase chain reaction (PCR) amplification using primers targeting the 16S rRNA gene. No amplification products were observed, confirming that the RNA samples were free from DNA contamination.Complementary DNA (cDNA) was synthesized from all RNA samples using the TRUESCRIPT First Strand cDNA Synthesis Kit (Aidlab BioTechnologies Co., Ltd.), as previously described[27]. Sequencing was performed by Majorbio Bio-Pharm Technology Co., Ltd. (Shanghai, China) on the Illumina MiSeq platform.Functional annotation and metabolic pathway analysis of the sequenced genes were conducted using the

BLASTP program (E-value cutoff of 10^{-5}) against the non-redundant protein database (NR), the Clusters of Orthologous Groups (COG) database, and the Kyoto Encyclopedia of Genes and Genomes (KEGG) database.

2.6 Calculations

In the MEC, the oxygen evolution reaction (OER) occurs at the anode (Eq. (1)), while the hydrogen evolution reaction (HER) takes place at the cathode (Eq. (2)). Together with the injected CO_2, the in situ produced H_2 is primarily converted to methane by methanogens in the cathode chamber (Eq. (3)). Other organic compounds, including biomass, can also be produced from hydrogen and carbon dioxide. Thus, the inputs to the MEC are electricity (i.e., electrons) and CO_2, and the outputs include CH_4, H_2, CO_2, and other organic compounds.

Anode reaction: $2H_2O - 4e^- = 4H^+ + O_2$ (1)

Cathode reaction : $2H^+ + 2e^- = H_2$ (2)

Reaction in the catholyte: $4H_2 + CO_2 = CH_4 + 2H_2O$ (3)

Electron balance was calculated based on the input current and the output flow rates of CH_4 and H_2. One mole of CH_4 requires eight moles of electrons, while one mole of H_2 requires two moles of electrons. The remaining electrons were attributed to other organic compounds to achieve approximate electron balance.Carbon balance was calculated from the input CO_2 flow rate and the output flow rates of CH_4 and CO_2. Other forms of carbon in the catholyte were categorized as “others” to approximate carbon balance.The Coulombic efficiency (CE) was defined as the fraction of electrons recovered as methane:

$$CE = \frac{n_{CH_4} \cdot F \cdot N}{\int_{t=0}^{t} I\,dt} \quad (4)$$

where F is the Faraday constant (96,485 C/mol e^-), 8 is the number of moles of electrons required per mole of methane, i is the current (A), t is time (s), and nCH4 is the methane production rate (mol).The energy efficiency (η_{energy}) represents the fraction of external electrical energy converted into methane, calculated based on the Gibbs free energy of methane combustion and the electrical energy input to the E-CSTR:

$$\eta_{energy} = \frac{-\Delta G_{CH_4} \cdot n_{CH_4}}{I \cdot \int_{t=0}^{t} E_{cell}\,dt} \quad (5)$$

where n_{CH4} is the methane production rate (mol), ΔG_{CH4} is the Gibbs free energy of methane oxidation, E_{cell} is the electrochemical cell voltage (V), i is the current (A), and t is time (s).

Table 1

Operational parameters of MEC

	Time/d	Current/A	j/A·m^{-2}	CO_2flowrate/mL·min^{-1}	Gascirculationrate/L·min^{-1}
Stage1	0-8	0.5	11.21	1	0
Stage2	9-18	1	22.62	2	0
Stage3	19-33	2	45.25	3.8	0.5
Stage4	34-61	3	67.87	5.8	1.5
Stage5	62-87	4	90.49	8.2	2
Stage6	88-106	5	113.12	9.9	2
Stage7	107-122	6	135.74	11.7	2

3. RESULTS AND DISCUSSION

3.1 Effect of Current on Methane Production Rate and Reactor Stability

The methane production and methane content in the biogas over time are shown in Fig. 1. At currents of 0.5 A and 1 A, hydrogen produced by cathodic electrolysis of water was almost completely utilized by methanogens. Methane production gradually stabilized, and the proportion of methane in the biogas increased steadily. At 1 A, the methane content exceeded 80%, reaching 86.18% on day 13.When the current was increased to 2 A, hydrogen accumulation occurred, leading to a decrease in methane content. After a period of operation, the methane content stabilized at around 80%, with hydrogen accounting for approximately 8%. To improve hydrogen utilization, a gas recirculation device was introduced at the end of day 22, operating at a flow rate of 0.5 L/min. After implementing gas recirculation, the hydrogen content decreased to about 1%, and the methane content reached 90%.Upon increasing the current to 3 A without gas recirculation, hydrogen accumulation gradually increased, and the methane content decreased to 60%. After 4 days of operation, gas recirculation was reinstated on day 36, resulting in a significant increase in methane content to approximately 80%. However, the reactor performance became unstable during subsequent experiments due to gas leakage through the recirculation tubing, which affected methane production between days 40 and 60. This issue was resolved by replacing the tubing with high-sealability tubing, leading to a noticeable improvement.At a recirculation rate of 0.5 L/min, the methane content stabilized at around 80%. When the recirculation rate was increased to 1 L/min, the methane content stabilized at approximately 85%. On day 73, the recirculation rate was further increased to 1.5 L/min, resulting in a methane content exceeding 90%, with a maximum of 95%.When the current was increased to 4 A with a recirculation rate of 1.5 L/min, the methane content stabilized at around 87% during steady operation, with hydrogen accounting for 3–5%. To further improve hydrogen utilization, the electrical stimulation time was reduced by 1 hour starting on day 99, with the remaining 1 hour dedicated solely to gas recirculation. This adjustment reduced the hydrogen content to about 1%, while the methane content stabilized at >93%, reaching a maximum of 96.2%.Under these conditions, the current was increased to 5 A. Initially, the methane content decreased to approximately 85%, but after an adaptation period, it steadily increased and eventually stabilized at >93%, with a maximum of 95.9%, while hydrogen content remained around 1%.When the current was further increased to 6 A, the electrical stimulation time was reduced by an additional 1 hour, resulting in 22 hours of electrical stimulation and 2 hours of gas recirculation per day. After one week of operation at 6 A, the reactor performance stabilized, with methane content exceeding 92% (reaching a maximum of 96.77%) and hydrogen content consistently around 1%.

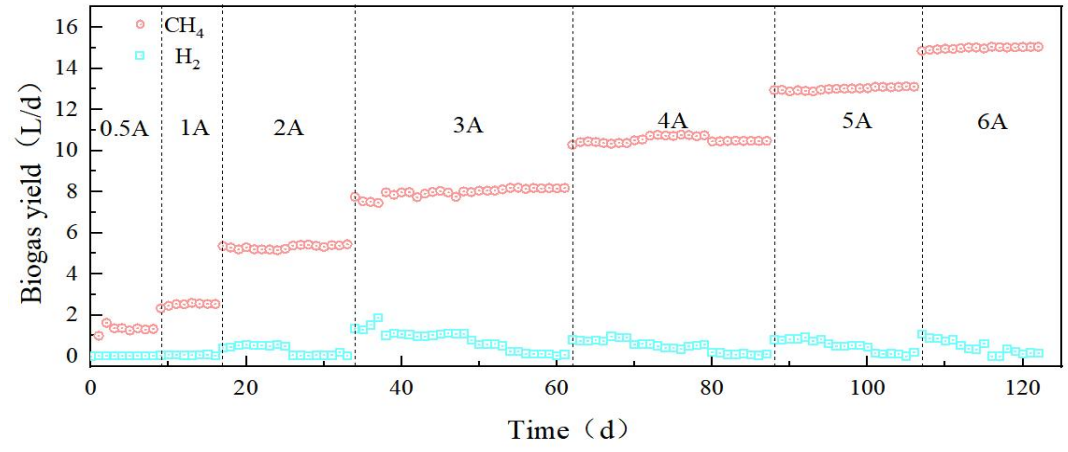

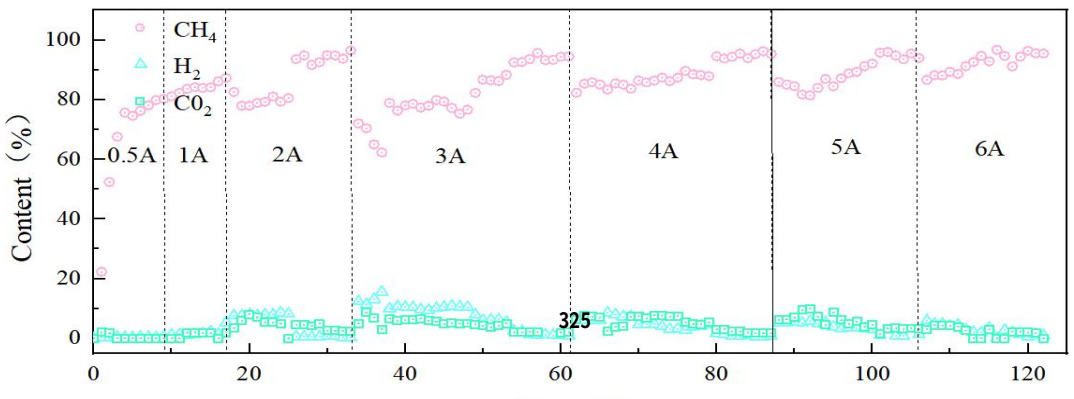

Fig. 1. Gas Production and Composition in the Microbial Electrolysis Cell

As shown in Fig. 2, the reactor was operated at currents ranging from 0.5 to 6 A. Under all current conditions, the hydrogen utilization efficiency exceeded 95%. When the system reached a stable state at each current level, both hydrogen and carbon dioxide utilization efficiencies were consistently greater than 99% and 90%, respectively, indicating that over 90% of the CO_2 was reduced and converted into methane under steady-state operation.Volatile fatty acid (VFA) analysis confirmed no accumulation of VFAs in the catholyte. Additionally, it was observed that the liquid level in the cathode compartment increased during operation, with an average daily volume increase of approximately 100 mL under 6 A current. This suggests that a certain amount of H_2 and CO_2 was converted into biomass or intracellular products.Due to reactor limitations, when the current was increased to 7 A, the applied voltage between the anode and cathode rose significantly. The resulting excessive power input caused a substantial temperature increase in the anolyte. Simultaneously, the temperature of the catholyte rose to 39 °C in the absence of active water-jacket cooling. Therefore, further investigation of microbial electrochemical CO_2 reduction to methane at higher currents would require a larger reactor system with enhanced temperature control.

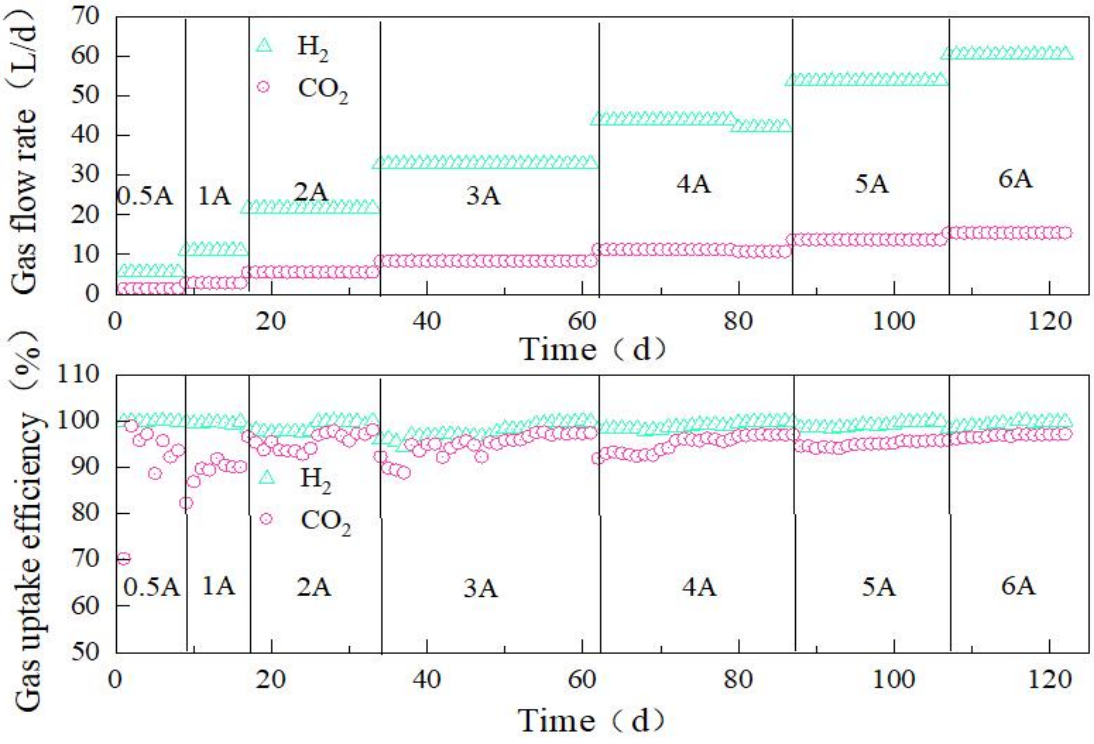

Fig. 2. Gas Utilization in the Microbial Electrolysis Cell

3.2 Electron and Carbon Balances

Electrons supplied to the reactor were consumed for the production of CH_4, H_2, and other organic compounds. The Coulombic efficiency for methane production is shown in Fig. 3. At a current of 0.5 A, the Coulombic efficiency

for methane was approximately 98%. On the second day, the value reached 118%, likely due to methane production from the anaerobic digestion of endogenous organic matter present in the inoculated sludge. This hypothesis was supported by volatile fatty acid (VFA) measurements, which detected certain VFAs during the initial days of operation, while almost no VFAs were observed in the catholyte in later phases.When the current was increased to 1 A, repair work was conducted on the reactor due to operational issues. After the repair, the Coulombic efficiency for methane temporarily decreased, but eventually stabilized at around 94%. At 2 A, the Coulombic efficiency gradually stabilized near 95%. However, after the introduction of the gas recirculation system, which improved hydrogen utilization, the Coulombic efficiency increased and remained stable at approximately 99%.Under a current of 3 A, the Coulombic efficiency experienced some fluctuations before stabilizing around 99%. When the current was further increased to 4–6 A, the methane production performance of the reactor became stable, and the Coulombic efficiency consistently reached 99% under steady-state conditions.

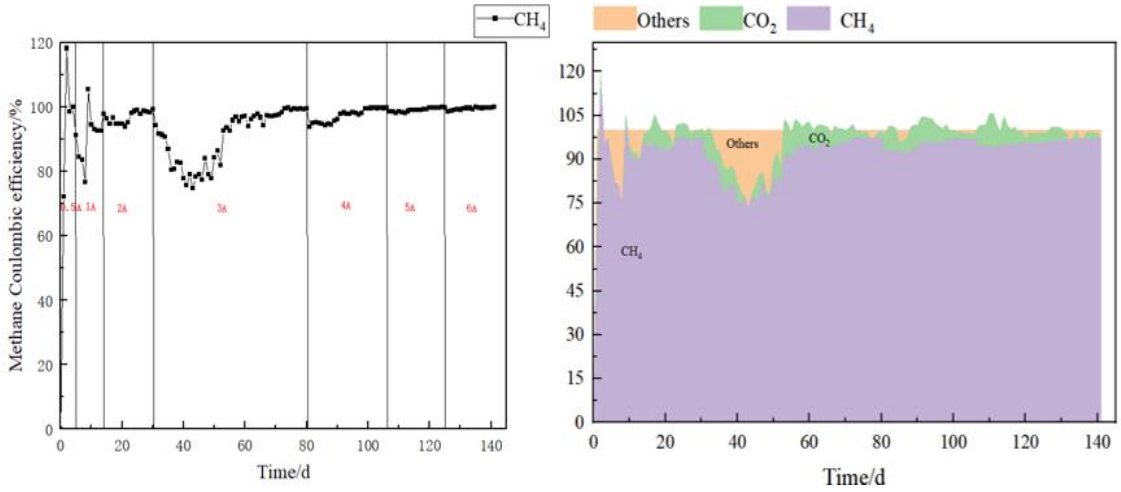

Fig. 3. Coulombic Efficiency and Carbon Balance in Methane Production via Microbial Electrolysis Cell

3.3 Energy Efficiency and pH Stability

The energy conversion efficiency of the system depends on both the cell voltage and the Coulombic efficiency. At a current of 0.5 A, the voltage applied between the anode and cathode was approximately 2.9 V, and the energy efficiency for electromethanogenesis reached around 40%, with a maximum of 47%. As the current increased, the circuit voltage rose, leading to a decrease in energy efficiency. At currents of 1 A and 2 A, the energy efficiencies were approximately 30% and 24%, respectively. Under a current of 3 A, the energy efficiency was about 20%, while at 4 A, it stabilized near 17%. At currents of 5 A and 6 A, the energy efficiency remained stable at approximately 13%.The theoretical water-splitting voltage is 1.23 V; however, the actual system voltage significantly exceeded this value across all currents from 0.5 A to 6 A. The high cell voltage was primarily attributed to the low conductivity of the electrolyte (i.e., high internal resistance) and high overpotentials at the electrode surfaces. Most of the excess electrical energy was dissipated as heat into the environment. At currents of 5–6 A, the heat generated from the electrodes was sufficient to maintain the optimal reaction temperature without requiring external water-jacket circulation.

Under a current of 0.5 A, the pH of the catholyte remained stable between 6.8 and 6.85. When the current was increased to 1 A, the pH gradually rose, reaching 6.99 by day 13. After switching to 2 A, the pH decreased, dropping to 6.86 by day 17. This fluctuation may have been caused by excessive current density, severe acidification of the

anolyte, and rapid transmembrane migration of protons generated at the anode.When the anolyte was periodically replaced under a current of 3 A, the catholyte pH stabilized between 6.9 and 7.2, while the anolyte pH continued to decrease, stabilizing around 0.8. At a steady-state current of 4 A, the catholyte pH remained between 7.0 and 7.3, and the anolyte pH stabilized in the range of 1.1–1.3. Under currents of 5–6 A, the anolyte pH was maintained at 1.3–1.45, and the catholyte pH remained between 7.1 and 7.5. These results indicate that, even under high-current conditions with a H_2/CO_2 feeding ratio of 3.9:1, the MEC reactor consistently provided suitable growth conditions for suspended methanogens in the cathode chamber without the need for additional acid or alkali to regulate pH.

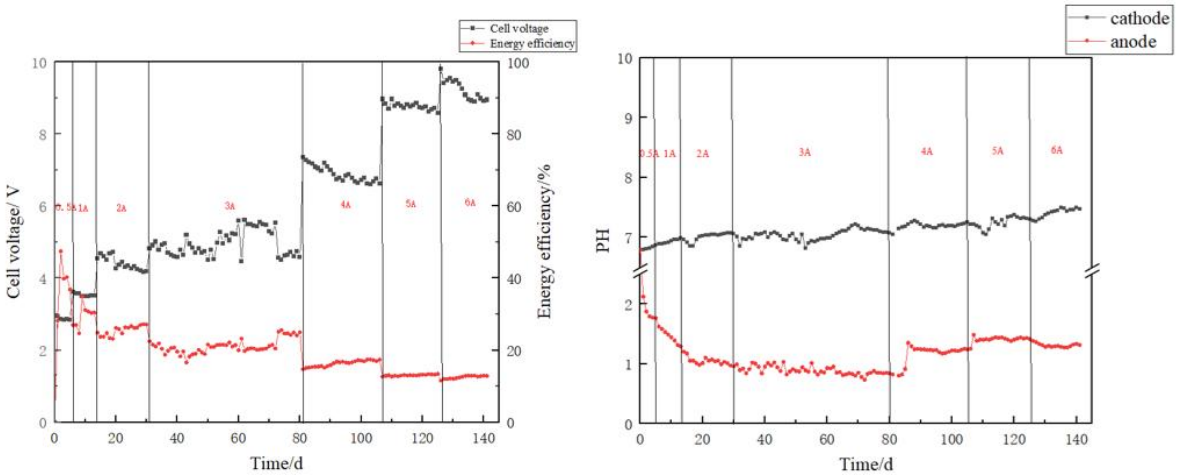

Fig. 4. Cell voltage, energy efficiency, and pH evolution of anolyte and catholyte in the Microbial Electrolysis Cell

3.4 Biomass Concentration and Microbial Community Evolution

To investigate temporal changes in microbial community structure and biomass concentration, biomass samples were collected from both the bulk solution and the carrier materials for community analysis and dry cell weight (DCW) measurement. The biomass concentration in the catholyte exhibited fluctuations corresponding to variations in applied current. As illustrated in Fig. 5, the biomass concentration in the reactor showed dynamic changes over time. Since the reactor was inoculated with anaerobic activated sludge, rapid microbial proliferation occurred during the initial phase, leading to a continuous increase in biomass.Under currents ranging from 0.5 to 2 A, the biomass concentration in the catholyte demonstrated an upward trend, rising from an initial value of 4.2 $g \cdot L^{-1}$ to 8.5 $g \cdot L^{-1}$. However, as a result of microbial community succession under currents of 3 to 6 A, the biomass concentration gradually decreased, declining to 1.3 $g \cdot L^{-1}$ by the end of the experiment.

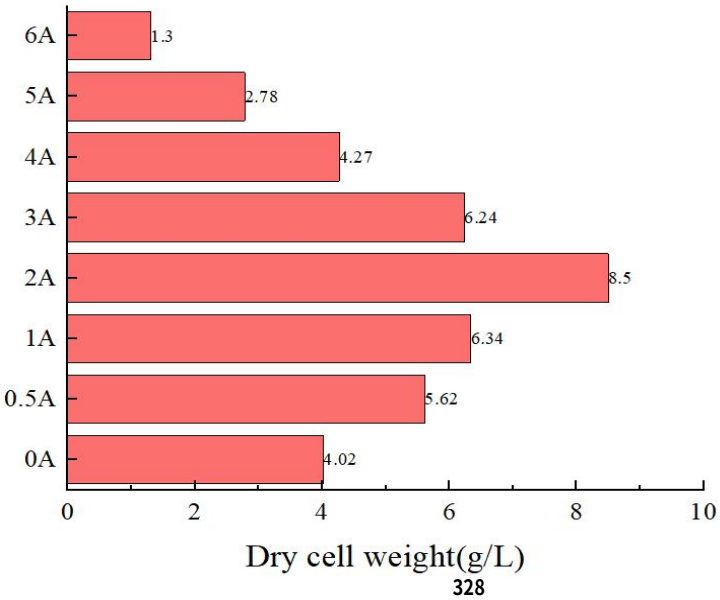

Fig. 5. Biomass Concentration in the Catholyte of the Microbial Electrolysis Cell

Microbial community succession at the genus level is shown in Fig. 6. Regardless of the applied current, *Methanobacterium* was the dominant archaeal genus. In the inoculated anaerobic sludge, Methanobacterium accounted for 50.55% of the total archaea, while *Methanothrix* represented approximately 40%. *Methanospirillum*, *Methanofastidiosum*, *Methanomassiliicoccus*, and *Methanobrevibacter* each constituted about 1.5%.Under currents of 0.5 A to 1 A, the microbial community structure remained relatively stable. As the current increased, the relative abundance of *Methanobacterium* continued to rise, reaching 85% at the end of the 3 A phase, 98.5% after 4 A, and exceeding 99% under 5–6 A. In contrast, the abundance of *Methanothrix* gradually decreased, dropping to 6.7% at 3 A and falling below 1% in the catholyte under 4–6 A conditions.*Methanospirillum* experienced a transient increase from 1.55% to 4.85% during the 0.5–2 A phases, but its abundance declined steadily with further current increases and became undetectable in the catholyte at 5–6 A.*Methanobacterium* and *Methanospirillum* are typical hydrogenotrophic methanogens, whereas *Methanothrix* is an acetoclastic methanogen. These results indicate that hydrogenotrophic and acetoclastic methanogens initially coexisted in the system, but hydrogenotrophic methanogens (specifically *Methanobacterium*) were selectively enriched over time.

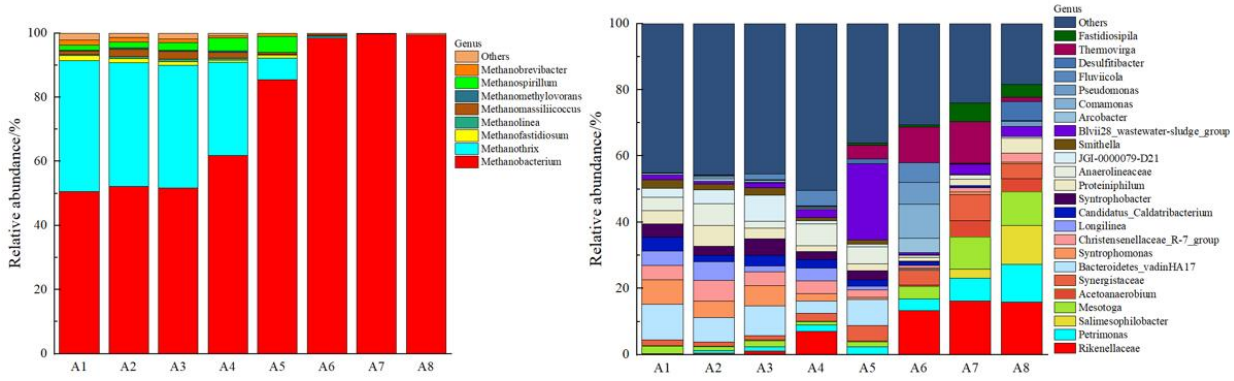

Fig. 6.Composition of Archaeal and Bacterial Communities in the Catholyte of the Microbial Electrolysis Cell

3.5 Microbial Gene Transcription in the Catholyte

To investigate the methanogenesis process, a genome-centric analysis was performed focusing on methane metabolism. Figure S2 shows the relative abundance of functional COG categories across four samples. "Energy production and conversion" (C) and "Coenzyme transport and metabolism" (H) were the dominant functional categories, accounting for more than 23% and 19%, respectively, which may be related to enhanced synthesis of coenzyme M and coenzyme B. As the current increased, the "General function prediction only" (R) category increased from 7% to 10%. Under high current conditions, the "Function unknown" (S) category also showed relatively high abundances of 9.8% and 9.9%.A more detailed analysis of methanogenesis was conducted using the KEGG database. Methane metabolism (ko00680), which is correlated with methanogenic activity, was the second most abundant pathway. The KEGG modules detected in the samples included M00567 (CO_2 to methane), M00357 (acetate to methane), M00356 (methanol to methane), and M00563 (methylated compounds to CH_4). However,

methyltransferases (e.g., K14083, K16176, K14082, K16178, and K16179) were present at low abundances. Nevertheless, the expression levels of genes related to methyltransferases increased with higher current intensity, suggesting that a portion of methane was produced via the methylotrophic methanogenesis pathway under high current conditions. Compared to the CO_2-reduction and acetoclastic pathways, this metabolic route appeared to be less dominant in the MEC system. Thus, acetoclastic and CO_2-reduction reactions remained the primary methanogenesis modes.Figure 7(a) illustrates differences in the relative abundance of major functional genes and pathways across the four samples. In the acetoclastic pathway, the relative abundance of acs-related genes gradually increased with current intensity, indicating that under high current conditions, some CO_2 was converted to acetate, which was subsequently transformed into methane (Fig. 7(B)). In the CO_2-reduction pathway, the abundance of nearly all relevant genes increased significantly with rising current intensity, consistent with enhanced expression required for reducing more CO_2 to methane. Accordingly, the CO_2-reduction pathway was strengthened.The mtrA gene (encoding a subunit of methyl-coenzyme M methyltransferase), essential for the common methanogenesis pathway, showed increased expression with higher current intensity. In the heatmap, genes within the mtrBCDEFGH operon exhibited varying degrees of upregulation. The gene encoding methyl-coenzyme M reductase (mcrG) was enriched at 3 A. Under 6 A conditions, the expression of genes involved in coenzyme M synthase (comABCD) was the highest (Fig. 7(a)). Therefore, as the current intensity increased, methane was predominantly produced via the CO_2-reduction pathway (Fig. 7(B)).

(a)

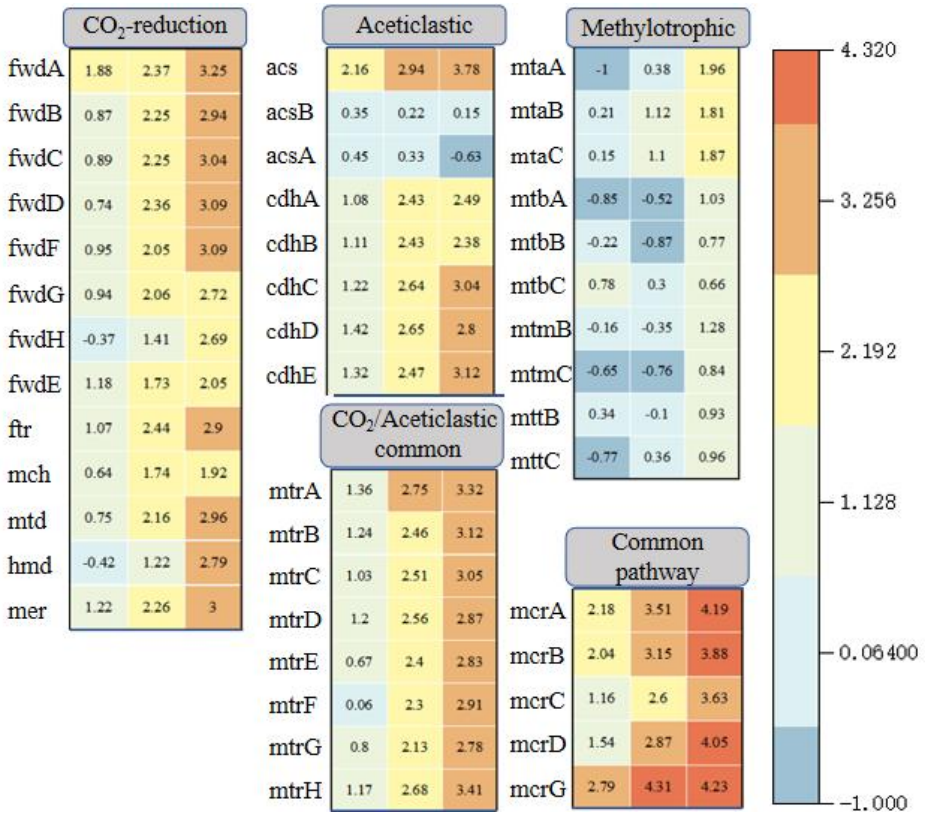

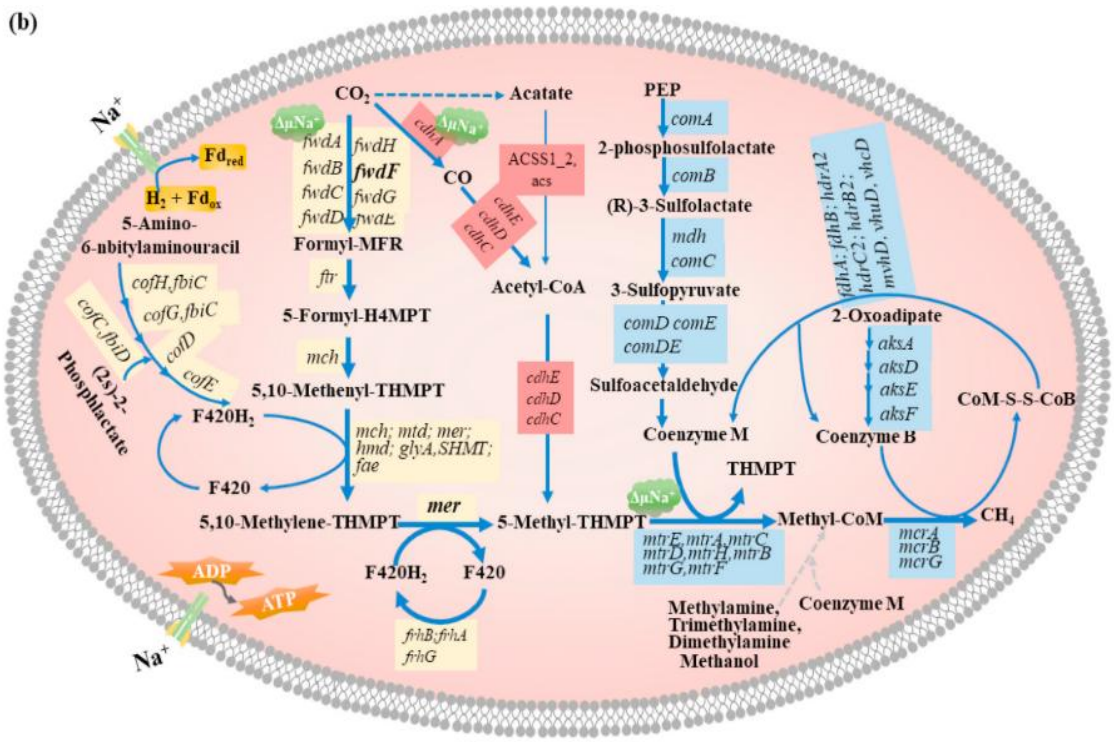

Fig. 7. Heatmap of the relative abundances of major functional genes and pathways (a) and dominant metabolic pathways (b).

4. CONCLUSION

In this study, a microbial electrolysis cell (MEC) was operated at elevated current intensities for the microbial electrosynthesis of methane from CO_2. This simple and scalable reactor design demonstrated superior performance in methane production rate, Coulombic efficiency (CE), and long-term stability compared to most previously reported systems. Under a constant current of 6 A, a stable methane production rate of 15 L/d was achieved with a CE of 99%. Future research should focus on further increasing current density. Additional efforts are needed to reduce internal resistance in order to decrease energy input and improve overall energy efficiency.

REFERENCES

[1] Saratale G D, Banu J R, Nastro R A, et al. Bioelectrochemical systems in aid of sustainable biorefineries for the production of value-added products and resource recovery from wastewater: A critical review and future perspectives[J]. Bioresource Technology, 2022, 359.

[2] Van Eerten-Jansen M C A A, Ter Heijne A, Buisman C J N, et al. Microbial electrolysis cells for production of methane from CO2: long-term performance and perspectives[J]. International Journal of Energy Research, 2012, 36(6): 809-819.

[3] IEA. CO2 emissions in 2024[Z]. GENCY I E A. 2025

[4] Rabaey K, Rozendal R A. Microbial electrosynthesis - revisiting the electrical route for microbial production[J]. Nature Reviews Microbiology, 2010, 8(10): 706-716.

[5] Daniell J, Nagaraju S, Burton F, et al. Low-Carbon Fuel and Chemical Production by Anaerobic Gas Fermentation[M]. HATTIKAUL R, MAMO G, MATTIASSON B. Anaerobes in Biotechnology. 2016: 293-321.

[6] Hidalgo D, Martin-Marroquin J M. Power-to-methane, coupling CO₂ capture with fuel

production: An overview[J]. Renewable & Sustainable Energy Reviews, 2020, 132.

[7] Blasco-Gomez R, Batlle-Vilanova P, Villano M, et al. On the Edge of Research and Technological Application: A Critical Review of Electromethanogenesis[J]. International Journal of Molecular Sciences, 2017, 18(4).

[8] Villano M, Aulenta F, Ciucci C, et al. Bioelectrochemical reduction of CO₂ to CH₄ via direct and indirect extracellular electron transfer by a hydrogenophilic methanogenic culture[J]. Bioresource Technology, 2010, 101(9): 3085-3090.

[9] Ishii S i, Imachi H, Kawano K, et al. Bioelectrochemical Stimulation of Electromethanogenesis at a Seawater-Based Subsurface Aquifer in a Natural Gas Field[J]. Frontiers in Energy Research, 2019, 6.

[10] Cheng S, Xing D, Call D F, et al. Direct Biological Conversion of Electrical Current into Methane by Electromethanogenesis[J]. Environmental Science & Technology, 2009, 43(10): 3953-3958.

[11] Xu H, Wang K, Holmes D E. Bioelectrochemical removal of carbon dioxide (CO₂): An innovative method for biogas upgrading[J]. Bioresource Technology, 2014, 173: 392-398.

[12] Palacios P A, Philips J, Bentien A, et al. Relevance of extracellular electron uptake mechanisms for electromethanogenesis applications[J]. Biotechnology Advances, 2024, 73.

[13] Rowe A R, Xu S, Gardel E, et al. Methane-Linked Mechanisms of Electron Uptake from Cathodes by Methanosarcina barkeri[J]. Mbio, 2019, 10(2).

[14] Zhang Z, Song Y, Zheng S, et al. Electro-conversion of carbon dioxide (CO₂) to low-carbon methane by bioelectromethanogenesis process in microbial electrolysis cells: The current status and future perspective[J]. Bioresource Technology, 2019, 279: 339-349.

[15] Zheng S, Liu F, Wang B, et al. Methanobacterium Capable of Direct Interspecies Electron Transfer[J]. Environmental Science & Technology, 2020, 54(23): 15347-15354.

[16] Zhen G, Lu X, Kobayashi T, et al. Promoted electromethanosynthesis in a two-chamber microbial electrolysis cells (MECs) containing a hybrid biocathode covered with graphite felt (GF)[J]. Chemical Engineering Journal, 2016, 284: 1146-1155.

[17] Mayer F, Enzmann F, Lopez A M, et al. Performance of different methanogenic species for the microbial electrosynthesis of methane from carbon dioxide[J]. Bioresource Technology, 2019, 289.

[18] Pawar A A, Karthic A, Lee S, et al. Microbial electrolysis cells for electromethanogenesis: Materials, configurations and operations[J]. Environmental Engineering Research, 2022, 27(1).

[19] Zheng X, Lin R, Xu J, et al. Enhanced methane production by bimetallic metal-organic frameworks (MOFs) as cathode in an anaerobic digestion microbial electrolysis cell[J]. Chemical Engineering Journal, 2022, 440.

[20] Kracke F, Wong A B, Maegaard K, et al. Robust and biocompatible catalysts for efficient hydrogen-driven microbial electrosynthesis[J]. Communications Chemistry, 2019, 2.

[21] Kracke F, Deutzmann J S, Jayathilake B S, et al. Efficient Hydrogen Delivery for Microbial Electrosynthesis via 3D-Printed Cathodes[J]. Frontiers in Microbiology, 2021, 12.

[22] Cai W, Cui K, Liu Z, et al. An electrolytic-hydrogen-fed moving bed biofilm reactor for efficient microbial electrosynthesis of methane from CO₂[J]. Chemical Engineering Journal, 2022, 428.

[23] Shang G, Cui K, Cai W, et al. A 20 L electrochemical continuous stirred-tank reactor for high rate microbial electrosynthesis of methane from CO₂[J]. Chemical Engineering Journal, 2023, 451.

[24] Huang Y, Cai B, Dong H, et al. Enhancing anaerobic digestion of food waste with granular activated carbon immobilized with riboflavin[J]. Science of the Total Environment, 2022, 851.

[25] Hu X, Vandamme P, Boon N. Co-cultivation enhanced microbial protein production based on autotrophic

nitrogen-fixing hydrogen-oxidizing bacteria[J]. Chemical Engineering Journal, 2022, 429.

[26] Liu C, Sun D, Zhao Z, et al. Methanothrix enhances biogas upgrading in microbial electrolysis cell via direct electron transfer[J]. Bioresource Technology, 2019, 291.

[27] Liu X, Shu Z, Sun D, et al. Heterotrophic Nitrifiers Dominate Reactors Treating Incineration Leachate with High Free Ammonia Concentrations[J]. Acs Sustainable Chemistry & Engineering, 2018, 6(11): 15040-15049.

AUTOMATED TWO-STAGE PARTIAL NITRIFICATION/ANAMMOX SYSTEM FOR TREATING ACTUAL DEWATERED LIQUID FROM FOOD WASTE METHANE FERMENTATION: PILOT-SCALE PERFORMANCE AND CONTROL STRATEGY OPTIMIZATION

Yuanyuan Ren [a,b], Shen Cui [b], Shenghao Ji [b], Yu-You Li [b*]

[a] Department of Environmental Engineering, School of Energy and Environmental Engineering, University of Science and Technology Beijing, Beijing 100083, China

[b] Department of Civil and Environmental Engineering, Graduate School of Engineering, Tohoku University, 6-6-06, Aramaki Aza Aoba, Aoba-ku, Sendai, Miyagi 980-8579, Japan

* Corresponding author: Yu-You Li, e-mail: gyokuyu.ri.a5@tohoku.ac.jp

ABSTRACT:

Large amount of organic waste generated annually, making its efficient resource utilization a key pathway toward building a decarbonized, circular society. Methane fermentation has gained attention in recent years due to its dual benefits of carbon emission reduction and energy recovery by converting organic waste into biogas. However, the large-scale application of this technology faces significant challenges. The resulting dewatered liquid from digestate contains high concentrations of nitrogen and phosphorus pollutants, requiring advanced treatment to meet discharge standard. This study proposes a two-stage PNA system integrated with an automatic control strategy. In long-term operation, the system achieved efficient synergistic nitrogen removal between the PN and anammox process. Sufficient alkalinity provided by the dewatered liquid from food waste methane fermentation supported both HAP formation and PNA reactions, achieving an impressive NRE about 90 % at an exceptionally high influent NH_4^+-N concentration of 3520 mg/L (anammox NLR of 9.47 g-N/L/d) without excessive dilution. Continuous and stable operation over a period of 110 days validated the feasibility and application potential of this system for treating high-ammonia wastewater.

Study on detection method of waste disposal sites using object detection technology (YOLO) with satellite remote sensing in Japan

Yasuhiro Sugisaki[1], Taiki Kamitaki[1], Leeme Arther Baruti[1], Hirofumi Nakayama[1], Takayuki Shimaoka[2]
1 Department of Urban and Environmental Engineering Faculty of Engineering Kyushu University, 744 Motooka Nishi-ku, Fukuoka, Japan
2 Kyushu Environmental Evaluation Association, 1-10-1 Matsukadai Higashi-ku, Fukuoka, Japan

Abstract

Understanding and managing the location and number of disposal sites in developing countries is an urgent priority. Therefore, in this study, we aimed to clarify a method to identify disposal sites and attempted to detect disposal sites from satellite remote sensing image data using object detection technology.

As a result, the following conclusions were obtained in this study. (1) In a study using the object detection technology YOLO, a model was constructed that could detect 68% of controlled landfill sites and 18% of Stable type landfill sites. (2) When the constructed model was applied to Nishi-ku, Fukuoka City, it was able to detect disposal sites with 66% accuracy. Most of the places that were incorrectly detected were quarries and land in forest gaps.

Introduction

In developing countries such as those in Asia and Africa, the volume of waste has been increasing annually due to rapid economic development and population growth in recent years, leading to the construction of disposal sites. However, many areas lack basic waste collection systems, and the precise locations and numbers of disposal sites remain unknown in numerous regions. Leachate flowing from unmanaged disposal sites can pollute the environment, potentially causing adverse effects on human health. Furthermore, waste emits significant greenhouse gases like CO_2 and CH_4, particularly CH_4 with its high global warming potential, contributing to climate change. These factors underscore the critical importance of identifying and managing the number and locations of disposal sites.

Satellite remote sensing offers a potential solution. This research employs object detection technology to identify disposal sites using satellite imagery data. While targeting developing countries, this study focused on Japan, where disposal site locations are known and a larger volume of training data can be collected.

Methodology

Object Detection

Object detection is a function that identifies the location and type of specific objects present within an image. It is currently utilized in various fields such as medicine and construction. Figure 1 shows an example of the system in operation. The object detection algorithm employed is YOLO V8 [1]. YOLO, which stands for 'You Only Look Once', used in this study is a popular object detection and image segmentation method. YOLO, proposed by Redman et al. in 2016 [2] has impacted the world of object detection due to its high speed of detection. In comparison to another systems, YOLO makes real-time use of object detection more realistic.
YOLO divides the input image into multiple grid cells and detects bounding boxes that is sub-area surrounding an object. At the same time, probability of the type of object present in each grid cell is calculated. And multiply the trust level of the bounding box by the probability of the type in each cell to determine the position of the object and its type.

Characteristics of disposal site in satellite images

Disposal site are man-made structures, and their shape as seen from satellites differs from natural landforms. Furthermore, material consists primarily of waste, such as plastic and incineration ash, which likely results in distinct colors when viewed from satellites.

Figure1: Example of detecting a disposal site using object detection from satellite imagery.
Map: Esri Japan, Esri

Satellite image data

This study used “World Imagery” as data for training and validation. “World Imagery” consists of satellite imagery and aerial photographs provided by ESRI, offering global satellite coverage. The resolution for major metropolitan areas worldwide is 0.3 m, while other regions have a resolution of 0.6 to 1.2 m. The data acquisition date is June 6, 2024.

Process Overview

Procedure is as follows: First, collect image data. Next, annotation that labels the collected data (adding information about the location of each disposal site to each image) for training and verification. Then, perform machine learning to build a model, and finally evaluate these.

This study focused on disposal(landfill) sites in Japan. In Japan landfill site is classified into three types that isolated landfill site, controlled landfill site, and stable-type landfill site (Figure 2). Isolated landfill sites are excluded because they have roofs and are the same as other buildings. Controlled landfill sites are divided into two types: municipal solid waste and industrial waste. And we added school grounds and bare land these areas very similar to disposal sites - as comparison targets. Table 1 lists the target types and training and validation data number.

Figure2 Landfill Sites in Japan
(left: controlled landfill site, right: stable-type landfill site)
Map: Esri Japan, Esri

Table1 Target types and number of data

land class	training	validation
all	282	78
controlled landfill site (MSW)	144	35
controlled landfill site (industrial waste)	9	5
stable type landfill site	65	13
school ground	45	20
bare land	19	5

Annotation

When creating a dataset for training in object detection, a labeling process called annotation is required. Annotation is an indication of the extent of an object's area in the image, that is bounding box for each paper product. This task was performed using the annotation tool “labelimg” [3], which is commonly used in object detection tasks. Annotation was performed by one person.

Training

In YOLO, various parameters can be set that determine how training proceeds. The Number of training sessions was set to 300, the size of the input image was set to 1024 x 1024 to match the pixels of the created image, and the learning rate (lr) was set to 0.01, which is the default.

Validation

After the training phase, object detection is performed on image data for verification using the obtained model in training, and its accuracy is evaluated.

Evaluation Method

The results of object detection are divided into four categories: True Positive (TP), False Positive (FP), False Negative (FN) and True Negative (TN). Each of these is classified and illustrated in Table 2. Using the number of cases of TP, FP, and FN in these indices, Precision and Recall can be calculated. Precision is the percentage of correct responses when an object is detected from an image. Recall is the percentage of correct responses when an object exists in the image. Precision and Recall are expressed using TP, FP and FN as follows.

$$Precision = \frac{TP}{TP + FP}$$

$$Recall = \frac{TP}{TP + FN}$$

Table2 4 types of object detection results

		Predicted class	
		A	Not A
True class	A	True Positive (TP)	False Negative (FN)
	Not A	False Positive (FP)	True Negative (TN)

The curve with data plotted as Precision on the vertical axis and Recall on the horizontal axis is called the Precision Recall Curve. AP (Average Precision) is the area bounded by the Precision Recall Curve and is expressed by the following equation.

$$AP = \int_0^1 p(r)dr$$

p: Precision
r: Recall

AP is often used as an evaluation metric for object detection, with closer to 1 indicating a better learned model. And mAP is obtained by averaging this AP for all classes. In this study, mAP50 is used as the evaluation index. This variable is the mAP when the IoU (Intersection over Union) represents the ratio of the area of overlap between the predicted bounding box and the true value bounding box. is bigger than 0.5.

RESULTS

Validation results are shown in Table3 and Figure3. Table3 shows the Precision, Recall, and mAP50 values for each class. In Fig.3, the confusion matrix is shown. The confusion matrix represents the actual true class on the horizontal axis and the class detected by YOLO on the vertical axis. The numbers in the figure are the ratio of the number of objects detected by YOLO to the total number of objects in target class.
The validation results for all the classes showed an mAP50 of 0.45 from Table3. For controlled landfill site (MSW) mAP50 is 0.45 and accuracy rate is 68%. But Others show low accuracy. In particular, stable type landfill site mAP50 is 0.29 and accuracy rate is 18%.

Table3 object detection (yolo) results

Class	Precision	Recall	mAP50
all	0.60	0.45	0.45
controlled landfill site (MSW)	0.44	0.57	0.45
controlled landfill site (industrial waste)	0.46	0.2	0.29
stable type landfill site	0.34	0.31	0.29
school ground	0.75	0.59	0.61
bare land	1	0.59	0.6

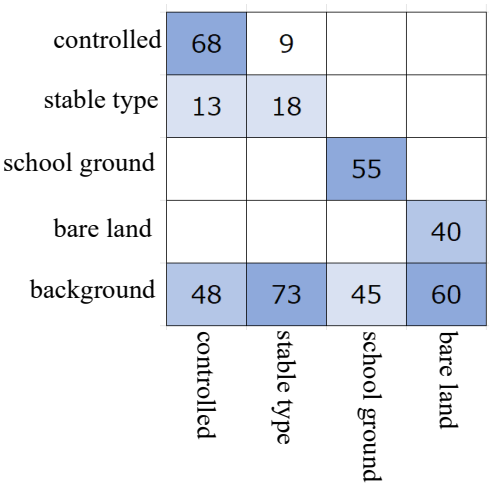

Figure3 confusion matrix (%)

For this cause, Figure3 shows that 73% of stable type landfill sites are detected as background. An example of an image that could not be detected is shown in Figure4. From this figure, cause of this result was thought to lie in the visual similarity to the surrounding land near the landfill site, such as in shape and color.

Figure4 Example of mis-detection
Landfill site is located within red-lined circular area.

Additional Validation

Constructed model was applied to an actual area Fukuoka City Nishi Ward (83.83 km²) to verify detection accuracy. This area contains one controlled landfill site (MSW) and one stable type landfill site. 56 images were used for this validation. Results showed that stable type landfill site was identified as controlled landfill site (MSW), but both landfill sites were successfully detected (Figure5). However, misdetections occurred in 30 locations across 19 other images. Therefore, the detection accuracy regarding the presence of disposal sites was 66% (37/56). Since misdetections were frequent in quarries, agricultural land, and gaps in forested areas, further model accuracy improvement is possible by adding new classes or increasing the training data.

Figure5 Result of additional validation

CONCLUSION

This study aimed to detect disposal (landfill) sits Japan using the YOLO object detection model applied to satellite imagery. The main findings are summarized as follows:

1.Model performance
- Controlled landfill sites (MSW):
  The mAP50 was 0.45, and the accuracy rate was 68%.
- Stable-type landfill sites:
  The mAP50 was 0.29, and the accuracy rate was 18%. This relatively low accuracy is likely due to the visual similarity between landfill sites and their surrounding areas in terms of shape and color.

2.Application to Fukuoka City Nishi Ward
When applied to satellite images of Fukuoka City's Nishi Ward, the model detected landfill sites with an accuracy of 66%. Most false positives occurred in areas such as quarries, farmland, and forest gaps.

In future work, we plan to improve model performance by introducing additional classes and increasing the volume of training data. We also intend to extend the application of our model to landfill site detection in developing countries.

ACKNOWLEDGEMENTS
This work was supported by JSPS KAKENHI Grant Number JP23K04091.

References

1. Ultralytics: Ultralytics YOLO Docs, available at: https://docs.ultralytics.com/ (last access: 5 November 2024), 2024.

2. Redmon J, Divvala S, Girshick R, Farhadi A (2016) You Only Look Once: Unified, Real-Time Object Detection. 2016 IEEE Conf. on Computer Vision and Pattern Recognition, pp.779-788

3. Label Studio community: HumanSignal/labelImg, available at: https://github.com/HumanSignal/labelImg/ (last access: 5 November 2024), 2024.

STUDY ON SYNTHESIS OF ETHYL LACTATE BY MICROBIAL-ENZYME COUPLING ESTERIFICATION

Yaxin Zhang[1]，Yongsheng Li[2]，Qi Yang[1]，Xiaona Wang[2]，Yuanyuan Ren[2]，Qunhui Wang[2*]

1. School of Water Resources and Environment, China University of Geosciences (Beijing) Beijing, 100083, China
2. School of Energy and Environmental Engineering, University of Science and Technology Beijing, Beijing, 100083, China

ABSTRACT: Anaerobic fermentation technology, as an effective approach for the resource utilization of organic waste, plays a significant role in reducing waste volume and promoting resource recycling. However, during the later stage of the fermentation process, the accumulation of metabolic products often occurs, with the production of lactic acid and ethanol no longer increasing and the metabolic activity of the system significantly decreasing. These accumulated metabolic precursor substances can be converted into high-value ethyl lactate through esterification reactions under suitable conditions. In this study, a microbial-enzyme coupled catalytic system was constructed to achieve the targeted conversion of precursors in the later stage of fermentation by introducing an exogenous catalytic module. The experimental results showed that under the conditions of an initial glucose concentration of 15% in the medium, inoculating 10% (v/v) of the seed liquid of Candida anomala, and performing pasteurization at 84 h of fermentation to terminate biological activity, followed by the addition of 1% of Candida antarctica lipase B, the ethyl lactate yield reached 630 mg/L, which was approximately 17 times higher than that of the basic fermentation system (35 mg/L). This coupled strategy effectively overcomes the bottleneck of the plateau phase in the fermentation process by reducing the feedback inhibition effect of the product and promoting the reaction equilibrium to shift towards ester synthesis, providing a new technical path and theoretical basis for the high-value utilization of organic waste such as corn cobs and kitchen waste.

KEYWORDS: fermentation; esterify; ethyl lactate; candida antarctica lipase

INTRODUCTION

As an important way to utilize organic waste, anaerobic fermentation technology plays a key role in achieving waste reduction and resource recovery. This technology converts organic matter into platform compounds such as lactic acid and ethanol with economic value through the metabolic activities of microorganisms, providing a feasible path for establishing a circular economy model. However, in the actual fermentation process, especially in the later stage of fermentation, there is a phenomenon of product accumulation and saturation, which ultimately limits the economy and feasibility of the overall process. The formation mechanism of this plateau is complex, involving the joint action of multiple physiological and biochemical processes[1]. First, as the fermentation process progresses, the substrate concentration gradually decreases, and the carbon sources and nutrients available to microorganisms are continuously depleted, resulting in limited cellular metabolic activities. Secondly, high concentrations of lactic acid and ethanol can have feedback inhibition and toxic effects on microbial cells. Lactic acid accumulation will cause the pH value of fermentation broth to drop, change cell membrane permeability, affect the absorption of nutrients and the excretion of metabolites; As a protoplasmic poison, ethanol can damage the structure of cell membranes and inhibit the activity of key enzymes, ultimately leading to cell growth arrest and reduced metabolic activity[2]. However, from the perspective of reaction engineering, the lactic acid and ethanol generated in the fermentation system can be further esterified under suitable conditions and converted into ethyl lactate ester with higher added value[3]. As an environmentally friendly green solvent and fragrance ingredient, ethyl lactate has a wide range of application prospects in the food, pharmaceutical and cosmetics industries due to its low toxicity, biodegradability and pleasant fruity aroma. Compared with lactic acid and ethanol, ethyl lactate has significantly higher economic added value and market competitiveness, which provides new opportunities to break through the economic bottleneck of traditional fermentation processes[4].

Based on the above analysis, this study proposed to convert the lactic acid and ethanol accumulated in fermentation into ethyl lactate ester in a timely manner

by introducing esterification catalysts in the fermentation process[5]. In order to verify the feasibility of this technical route, this study first used a synthetic medium system to systematically optimize the ester production conditions of abnormal Wickham's yeast, focusing on the feasibility of enzyme catalysis and microbial catalysis coupling to promote the synthesis of ethyl lactate[6], and then using corn cob and food waste as actual substrates to verify it, so as to overcome the plateau period limitation of product accumulation and provide new technical path and theoretical support for the high-value transformation of waste biomass.

1 MATERIALS AND METHODS

1.1 Experimental strains

The strain used in this experiment is Wickerhamomyces anomalus 2.470, which was purchased by our laboratory at the General Microbiology Center of the China Microbial Strain Conservation and Management Committee. The medium used was wort agar substitution medium, and the main components were glucose 10.0 g/L, peptone 10.0 g/L, and yeast extract 5.0 g/L.

1.2 Experimental instruments and reagents

The main experimental instruments and equipment used in this research include BS110S electronic analytical balance, SW-CJ-1D single-person aseptic workbench, LC-20 high performance liquid chromatography, GC-2010 plus gas chromatography, HZQ-C air bath shaker, TDZS-WS low-temperature high-speed centrifuge. The main reagents used include sodium hydroxide, cellulose disaccharides, glucose, xylose, arabinose, lactic acid, ethanol, ethyl lactate, peptone, yeast extract, acetone, Candida antarctica lipase (CALB lipase, enzyme activity 10,000 PLU/g).

1.3 Experimental methods

The wort agar substitution medium was used as the ester-producing yeast medium. After adding glucose and 5 g/L L-lactic acid to the medium, they were sterilized at 115 ℃ for 15 min in a sterilization pot, then connected to 10% (v/v) ester-producing yeast seed liquid, and incubated at 120 rpm at a constant temperature of 28 ℃. After 84 h of culture, it was sterilized by pasteurization, followed by CALB lipase for enzymatic esterification, and the changes of sugar, lactic acid, ethanol and ethyl lactate concentrations were measured during fermentation at 120 rpm for 72 h in a constant temperature shaking incubator at 40 ℃.

1.4 Analysis methods

1.4.1 Fermentable sugar, lactic acid, ethanol

The concentrations of fermentable sugars (cellulose disaccharides, glucose, xylose and arabinose), lactic acid, and ethanol in the samples were determined by Shimadzu LC-20 HPLC. The system is equipped with the Shodex Sugar SH 1011 Glycan Column (300 mm × 8.0 mm) and the Index Refractive Detector (RID-10A, Shimadzu Corporation). After centrifuging the sample at 12000 rpm for 10 minutes, use 0 After filtering with 22 μm microporous membrane filtration, the filtrate was properly diluted and mixed with ultrapure water, and then quantitatively analyzed by liquid chromatograph at a column temperature of 60 °C, a flow rate of 1.0 mL/min, and an injection volume of 10 μL.

1.4.2 Ethyl lactate

Shimadzu GC-2010 Plus gas chromatograph was used to determine the concentration of ethyl lactate in the samples. The system is equipped with a DB-FFAP column (30.0 m x 0.53 mm x 0.50 μm) and a (Flame ionizationdetector) detector. After centrifuging the sample at 12000 rpm for 10 minutes, use 0.22 μm microporous filter membrane is filtered, and the filtrate is properly diluted with ultrapure water and mixed evenly, and then tested by gas chromatograph.

2 RESULTS AND ANALYSIS

2.1 Effect of initial glucose concentration on the esterification process

Glucose can provide sufficient carbon source and energy for ester-producing yeasts, promote the growth of bacteria and the expression of their own esterases, which is conducive to the synthesis of ethyl lactate. However, excessive initial glucose concentration may lead to the carbon metabolism flow mainly flowing to ethanol fermentation[7], competing with esterification reaction for substrate lactate, and the osmotic stress caused by high sugar may also continue to function as a cell active agent of exogenous esterase, which reduces the esterification efficiency[8]. At the same time, under low sugar conditions, microorganisms will give priority to the limited carbon source for basic life activities rather than catalytic esterification, resulting in insufficient driving force for the conversion of lactic acid and ethanol, and ultimately leading to a significant decrease in the synthesis rate and yield of ethyl lactate. Therefore, it is necessary to balance the relationship between cell growth, substrate supply and product inhibition by optimizing the initial glucose concentration (5%, 10%, 15%, 20%) to maximize the esterification reaction rate and yield, as shown in Fig. 2-1 and Fig. 2-2.

From Fig. 2-1, it can be seen that the ethanol yield increases significantly and then flattens with the increase of initial glucose concentration. When the initial glucose concentration increased from 5% to 10%, the ethanol yield increased significantly from 18.05 g/L to 34.73 g/L. The concentration was further increased to 15%, and the ethanol yield reached 51.01 g/L. When the concentration continued to increase to 20%, although the yield increased slightly to 66.54 g/L, the increase slowed down significantly. From Fig. 2-2, it can be seen that the yield of ethyl lactate increases significantly and then decreases sharply with the

change of glucose concentration: when the initial glucose concentration is 5%, 10%, 15% and 20%, the yield of ethyl lactate is 35 mg/L, 47 mg/L, 122 mg/L and 45 mg/L, respectively. Yield peaked when glucose concentration rose to 15%, and when concentration increased further to 20%, yield decreased significantly to a level comparable to that of the low concentration group[9]. This trend is closely related to the change of ethanol production in this system. As mentioned earlier, ethanol, as one of the key substrates for esterification reactions, maintained high yields in the 15%-20% concentration range[10], but the increase slowed down, suggesting that the overall cellular metabolism has begun to be adversely affected by the high-sugar environment. The significant decrease of ethyl lactate at 20% glucose concentration is mainly due to the multiple inhibitory effects brought about by high glucose concentration: on the one hand, excessive substrate concentration leads to a sharp increase in the osmotic pressure of the medium, which seriously affects the stability of yeast cell membrane and material transport efficiency, and inhibits cell growth and key enzyme activities[11]. On the other hand, substrate overload exacerbates the Crabtree effect, resulting in the accumulation of organic acids and other by-products, which changes the metabolic balance of the intracellular acid synthesis pathway. At the same time, ethanol as a product inhibits yeast activity when accumulated to higher concentrations inside and outside the cell[12], and may affect the stability and function of key enzymes that catalyze ester synthesis, such as esteryltransferase. Therefore, despite the abundance of ethanol substrates, the ester anabolic network was significantly inhibited at 20% glucose concentration, which ultimately led to a decrease in ethyl lactate production instead of an increase. In conclusion[13], the 15% glucose concentration is the optimal choice for considering the substrate supply and avoiding inhibitory effects under the experimental conditions.

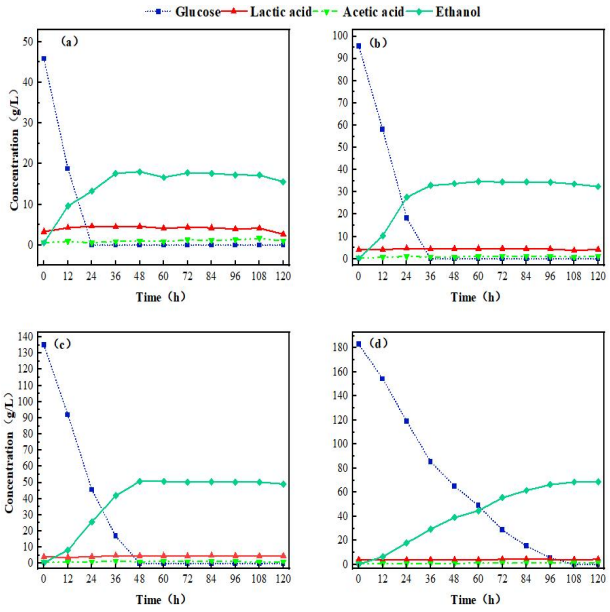

Fig.2-1 Variation curves of concentrations of various substances in the fermentation process with different initial glucose concentrations (5% for A, 10% for B, 15% for C, and 20% for D)

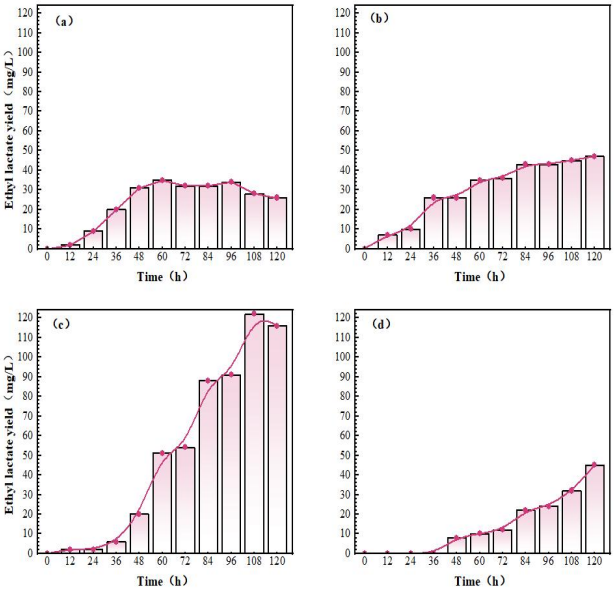

Fig.2-2 Variation curves of ethyl lactate concentration during fermentation with different initial glucose concentrations (5% for A, 10% for B, 15% for C, and 20% for D)

2.2 Effect of enzyme and bacterial compounding on esterification process

In the process of synthesizing ethyl lactate by microbial fermentation, it was observed that the yield of ethyl lactate was low and did not reach the ideal level when relying only on the bacteria's own metabolic system, which may be related to the lack of catalytic efficiency of the enzyme system in the bacteria or the presence of bottlenecks in the metabolic pathway[14]. In order to effectively improve the esterification efficiency, we introduce CALB lipase as an exogenous catalytic aid. CALB lipase has high esterification and transesterification activity, excellent operational stability and broad substrate adaptability, which can significantly enhance the catalytic conversion process between lactic acid and ethanol, as shown in Table 2-1, and the experimental results are shown in Fig. 2-3 and Fig. 2-4.

Table 2-1 Experimental conditions of the effect of enzyme bacteria on ethyl lactate yield

Constituencies	Vaccination ratio (%)	Amount of lactic acid added (g/L)	Enzyme amount added (g)	Amount of added ethanol (g)
a	10	8	0	0
b	0	8	2	5.4
c	0	8	5	5.4
d	10	8	2	0
e	10	8	5	0

Figs. 2-3 and 2-4 showed that there were significant differences in ethyl lactate yield between groups. The yield of the control group inoculated with ester-producing yeast alone was 226 mg/L. The yield increased to 330 mg/L when 2 g of CALB enzyme was added alone and ethanol was added, while the yield decreased to 234 mg/L when 5 g of CALB enzyme was added alone. When CALB enzyme and ester-producing yeast were added at the same time, the yield of ethyl lactate was significantly inhibited, and the yield of 2 g of CALB enzyme and the bacteriome decreased to 175 mg/L, and the yield of 5 g of enzyme and bacteriome was significantly reduced to 60 mg/L. The above results showed that exogenous CALB enzyme could effectively catalyze esterification in a cell-free system, and an appropriate amount of enzyme (2 g) could increase the yield of the product, but the catalytic efficiency may decrease due to steric hindrance or substrate competition when the enzyme addition amount was increased to 5 g. This may be due to the lipid components of lipase acting on the surface of yeast cell membranes, disrupting the integrity of cell structure and interfering with its normal metabolic function, and the catalytic process of exogenous enzymes may lead to changes in the local microenvironment[15], such as pH fluctuations and intermediate product accumulation, affecting yeast growth and the activity of intracellular lide synthase lines. At the same time, there may be substrate competition between enzymes and bacteria, especially interfering with the utilization of key precursors lactic acid and ethanol, thereby weakening the ability of microorganisms to synthesize esters. Based on the above results, the direct use of the "enzyme synergy" one-step fermentation strategy is not only difficult to increase efficiency, but will seriously interfere with the normal metabolism and ester synthesis function of bacteria. Therefore, in order to take into account the advantages of microbial fermentation and enzyme catalysis, we propose a step-by-step treatment process: first, ester-producing yeast is used for fermentation, and the precursor substance is generated by its complete metabolic network and part of the ethyl lactate ester is synthesized. Subsequently, the fermentation broth was sterilized to eliminate the physical and biochemical interference of viable bacteria in the enzyme catalytic process[16]. Finally, CALB lipase was added to efficiently transform the remaining precursors inside and outside the cell under the optimal enzymatic reaction conditions,Under optimal enzymatic reaction conditions, this system can efficiently convert residual lactic acid and ethanol in the fermentation broth while effectively utilizing metabolic precursors released extracellularly due to membrane transport or cell lysis. By precisely controlling the timing of enzymatic reactions[17], it can fully exert its effects during the stable growth phase or decline phase of the cells, avoiding interference with the metabolism of actively growing cells while achieving deep utilization of remaining substrates. This strategy, based on maintaining microbial cell activity and system metabolic balance, elevates enzymatic catalytic efficiency to its theoretical maximum, thereby significantly enhancing the synthesis flux of ethyl lactate and ultimately achieving systematic optimization of the overall yield.

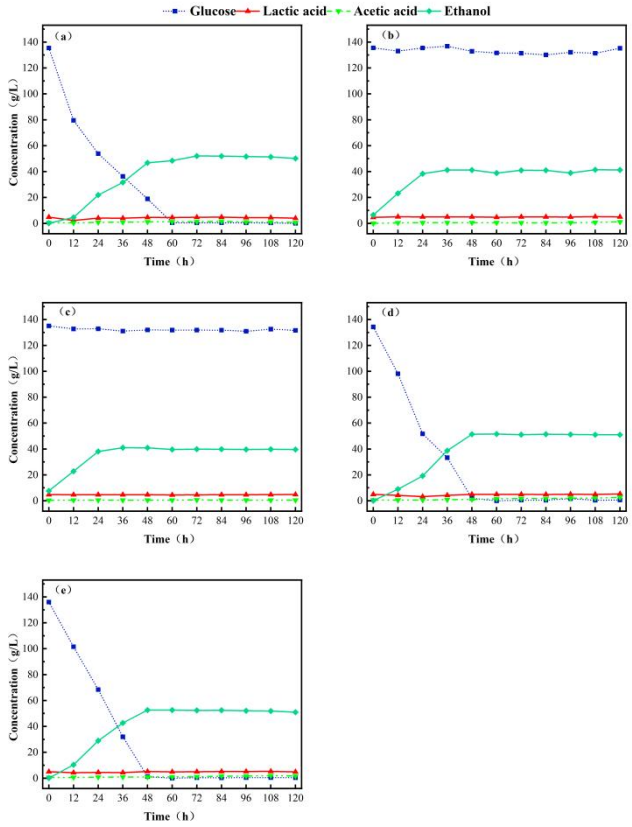

Fig.2-3 Concentration curves of various substances in the compound fermentation process of enzyme bacteria (A is the control group, B is the enzymatic reaction group -2 g, C is the enzymatic reaction group -5 g, D is the fermentation-enzymatic coupling group -2 g, and E is the fermentation-enzymatic coupling group -5 g)

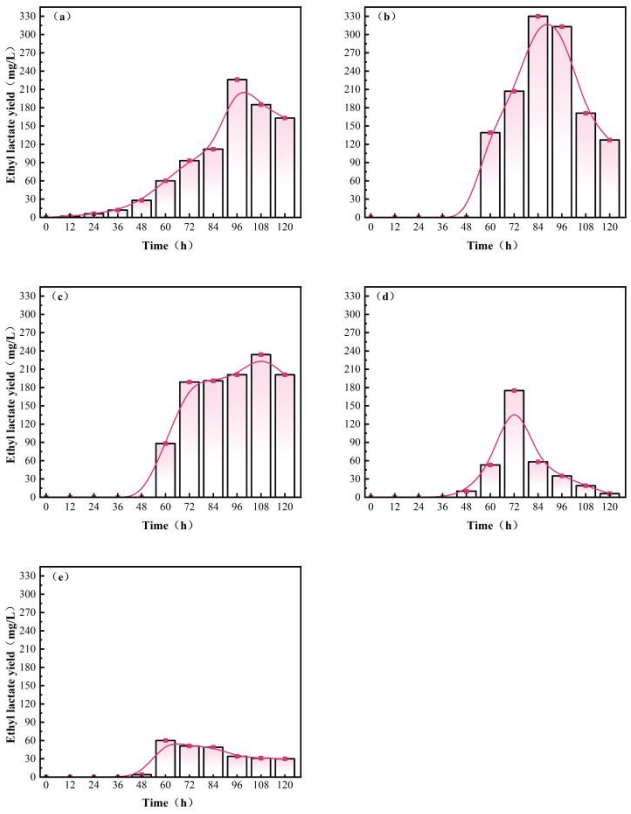

Fig.2-4 Variation curves of ethyl lactate concentration during compound fermentation of enzyme bacteria (A is the control group, B is the enzymatic reaction group -2 g, C is the enzymatic reaction group -5 g, D is the fermentation enzymatic coupling group -2 g, E is the fermentation-enzymatic coupling group -5 g)

2.3 Effects of bacteria first and then enzymes on esterification process

In practical applications, the enzyme addition concentration has a decisive impact on the reaction efficiency, and when the concentration is too low, the active site is insufficient and the reaction kinetics are limited, resulting in a decrease in conversion rate and a prolonged cycle[18]. Although excessive addition may increase the initial rate, it is not only economically poor, but also easy to cause enzyme molecule aggregation, interface saturation and non-specific side reactions (such as reverse hydrolysis)[19], which reduces the purity and yield of the product and increases the burden of subsequent separation. Therefore, it is necessary to systematically optimize the enzyme loading (0.5%, 1%, 2%, 3%) to achieve the best balance between reaction efficiency and economy, the experimental conditions are shown in Table 2-2, and the experimental results are shown in Figures 2-5 and 2-6.

From Figs. 2-5 and 2-6, it can be seen that the enzyme addition concentration has a significant effect on the final ester yield, and shows a trend of increasing first and then decreasing. The yield of ethyl lactate in the 0.5% CALB enzyme group was 330 mg/L, and the yield of 1% CALB enzyme group increased to 630 mg/L, reaching a peak. When the CALB enzyme concentration continued to increase to 2% and 3%, the yield decreased to 556 mg/L and 426 mg/L. This result showed that the optimal balance between catalytic efficiency and economy was achieved at the concentration of CALB enzyme at 1%, and the active site of the enzyme was insufficient below this concentration, and the reaction kinetics were slow, limiting the conversion of substrates[20,21]. Although excessive enzyme amounts may increase the initial reaction rate, the catalytic efficiency is reduced due to excessive aggregation of enzyme molecules, increased steric resistance and interfacial saturation effects, and may trigger non-specific side reactions, such as the hydrolysis reverse reaction of esters, thereby reducing the yield and purity of the product[22]. In addition, high concentrations of enzymes can easily cause the viscosity of the system to increase, the mass transfer resistance to increase, and may promote heteroprotein

interactions and interfere with the target esterification process. Therefore, the optimization of enzyme loading is crucial for efficient esterification, and the optimal addition concentration of 1% for CALB lipase can maximize the yield of ethyl lactate while avoiding enzyme waste and side reactions, which provides a key parameter basis for subsequent process scale-up[23-25].

Table 2-2 Experimental conditions of the effect of bacteria and enzymes on the yield of ethyl lactate

Constituencies	Vaccination ratio （%）	Enzyme amount added after 48 hours （%）	Temperature before enzyme addition （℃）	Enzyme Temperature （℃）
a	10	0.5	28	40
b	10	1	28	40
c	10	2	28	40
d	10	3	28	40

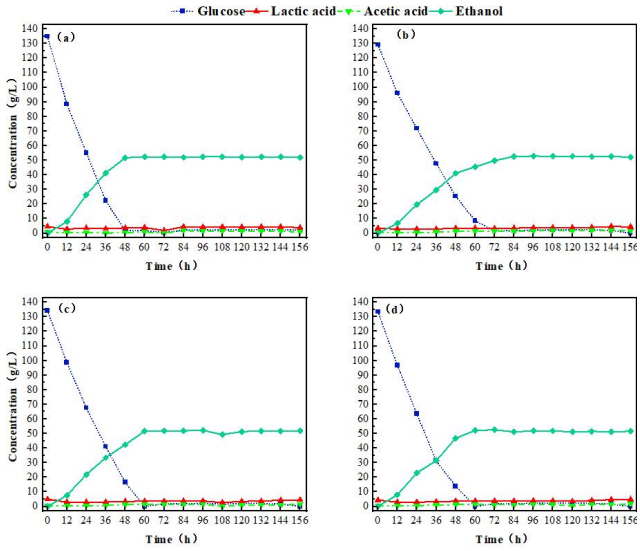

Fig.2-5 Concentration curves of various substances in the fermentation process of bacterial and then enzyme (0.5% for A, 1% for B, 2% for C, and 3% for D)

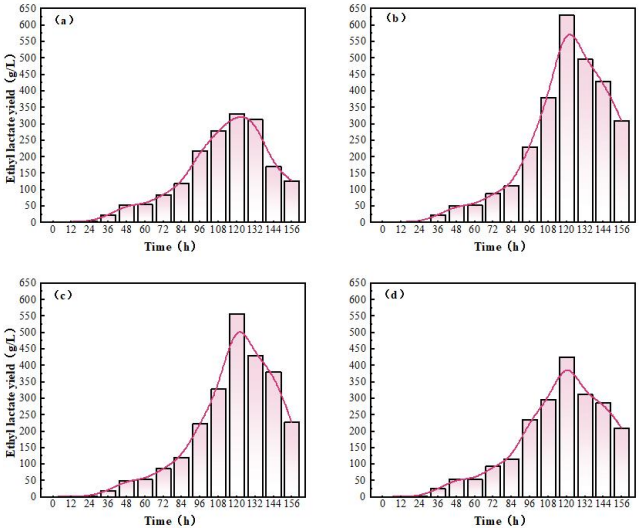

Fig.2-6 Variation curve of ethyl lactate concentration during enzymatic fermentation (0.5% for A, 1% for B, 2% for C, and 3% for D)

3 CONCLUSION

In this study, the efficient conversion of lactic acid and ethanol to ethyl lactate was successfully realized by constructing optimizing the fermentation-esterification coupling system based on abnormal Wickham yeast and CALB lipase. The results showed that the yield of ethyl lactate could reach 630 mg/L under the optimal conditions of initial glucose concentration of 15%, pasteurization after 84 hours of fermentation and addition of 1% CALB lipase, which was significantly improved compared with the traditional fermentation process. By removing lactic acid and ethanol from fermentation products in time, the coupling strategy effectively relieved the product feedback inhibition, restored the metabolic activity of the system, and pushed the reaction balance to the esterification direction. It not only breaks through the technical bottleneck of metabolic stagnation caused by product accumulation during anaerobic fermentation, but also provides a new process path for in-situ conversion of lactic acid and ethanol, which shows a good application prospect in the fields of biomass refining and green bio-manufacturing.

ACKNOWLEDGEMENT

This work was supported by the National Natural Science Foundation of China (Grant NO. 52470137 and 52170121)

REFERENCE

[1] A-K Rana, Thakur V-K. Advances and new horizons in metabolic engineering of heterotrophic bacteria and cyanobacteria for enhanced lactic acid production[J]. Bioresource Technology, 2025, 419.

[2] X Li, Zhang X, Jian H, et al. Biocycle Fermentation Based on Lactic Acid Bacteria and Yeast for the Production of Natural Ethyl Lactate[J]. ACS Omega, 2019, 4(14): 16009-16015.

[3] Sheila Montipo, Ballesteros Ignacio, Fontana Roselei-Claudete, et al. Bioprocessing of rice husk into monosaccharides and the fermentative production of bioethanol and lactate[J]. Cellulose, 2019, 26(12): 7309-7322.

[4] Enrique Cubas-Cano, Gonzalez-Fernandez Cristina, Ballesteros Mercedes, et al. Biotechnological advances in lactic acid production by lactic acid bacteria: lignocellulose as novel substrate[J]. Biofuels, Bioproducts and Biorefining, 2018, 12(2): 290-303.

[5] Di Cai, Chen Huidong, Zhang Changwei, et al. Carbonized core-shell diatomite for efficient catalytic furfural production from corn cob[J]. Journal of cleaner production, 2021, 283(Feb.10): 125410-125411.

[6] Rodrigues-TV Dias, Amore T-D, Teixeira E-C, et al. Carotenoid Production by Rhodotorula mucilaginosa in Batch and Fed-Batch Fermentation Using Agroindustrial Byproducts[J]. Food Technol Biotechnol, 2019, 57(3): 388-398.

[7] Vaishali Gupta, Odaneth Annamma-A, Lali Arvind-M. Continuous fermentation using high cell density cell recycle system for L-lactic acid production[J]. Preparative biochemistry & biotechnology: An international journal for rapid communication, 2024, 54(1/5): 668-679.

[8] H-Y Su, Li H-Y, Xie C-Y, et al. Co-production of acetoin and succinic acid by metabolically engineered Enterobacter cloacae[J]. Biotechnol Biofuels, 2021, 14(1): 26.

[9] T Cheng, Liang X, Wang Y, et al. Co-Production of Isoprene and Lactate by Engineered Escherichia coli in Microaerobic Conditions[J]. Molecules, 2021, 26(23).

[10] H Liu, Zhen F, Wu D, et al. Co-production of lactate and volatile fatty acids through repeated-batch fermentation of fruit and vegetable waste: Effect of cycle time and replacement ratio[J]. Bioresour Technol, 2023, 387129678.

[11] Yufei Fan, Ji Hairui. Corncob Fractionations Toward Two Purposes: Furfural Production and Papermaking[J]. BioEnergy Research, 2023, 17(1): 359-368.

[12] Bhavana-B K, Mudliar Sandeep-N, Bokade V-V, et al. Effect of furfural, acetic acid and 5-hydroxymethylfurfural on yeast growth and xylitol fermentation using Pichia stipitis NCIM 3497[J]. Biomass Conversion and Biorefinery, 2022, 14(4): 4909-4923.

[13] Y Zhang, Dong J, Xu G, et al. Efficient production of hyaluronic acid by Streptococcus zooepidemicus using two-stage semi-continuous fermentation[J]. Bioresour Technol, 2023, 377128896.

[14] Y Li, Zhu H, Zhou F, et al. Enhanced bioconversion of kitchen food waste into aquaculture feed using a mixed culture of Bacillus licheniformis and Yarrowia lipolytica[J]. Sci Rep, 2025, 15(1): 16497.

[15] J-Y Ren, Liu G, Chen Y-F, et al. Enhanced Production of Ethyl Lactate in Saccharomyces cerevisiae by Genetic Modification[J]. J Agric Food Chem, 2020, 68(47): 13863-13870.

[16] Jin-ying Ren, Liu Gang, Chen Ye-fu, et al. Enhanced Production of Ethyl Lactate in Saccharomyces cerevisiae by Genetic Modification[J]. Journal of Agricultural and Food Chemistry, 2020, 68(47): 13863-13870.

[17] Alexandra-Cristina Blaga, Ciobanu Corina, Cascaval Dan, et al. Enhancement of ergosterol production by Saccharomyces cerevisiae in batch and fed-batch fermentation processes using n-dodecane as oxygen-vector[J]. Biochemical Engineering Journal, 2018, 13170-76.

[18] Luis-A Roman-Ramirez, Powders Mark, McKeown Paul, et al. Ethyl Lactate Production from the Catalytic Depolymerisation of Post-consumer Poly(lactic acid)[J]. Journal of Polymers and the Environment, 2020, 28(11): 2956-2964.

[19] S Yzturk, Yalik P, Yzdamar T-H. Fed-Batch Biomolecule Production by Bacillus subtilis: A State of the Art Review[J]. Trends Biotechnol, 2016, 34(4): 329-345.

[20] Vinicius-Fabiano Dos Passos, Marcilio Rafaella, Aquino-Neto Sidney, et al. Hydrogen and electrical energy co-generation by a cooperative fermentation system comprising Clostridium and microbial fuel cell inoculated with port drainage sediment[J]. Bioresource Technology: Biomass, Bioenergy, Biowastes, Conversion Technologies, Biotransformations, Production Technologies, 2019, 27794-103.

[21] Jun Cheng, Li Hui, Ding Lingkan, et al. Improving hydrogen and methane co-generation in cascading dark fermentation and anaerobic digestion: The effect of magnetite nanoparticles on microbial

electron transfer and syntrophism[J]. Chemical Engineering Journal, 2020, 397.
[22] Patrick-Othuke Akpoghelie, Edo Great-Iruoghene, Ali Ali-B-M, et al. Lactic acid bacteria: Nature, characterization, mode of action, products and applications[J]. Process Biochemistry, 2025, 1521-28.
[23] J Zhang, Xu T, Wang X, et al. Lignocellulosic xylitol production from corncob using engineered Kluyveromyces marxianus[J]. Front Bioeng Biotechnol, 2022, 101029203.
[24] Juan-Gilberto Martinez-Miranda, Chairez Isaac, Duran-Paramo Enrique. Mannitol Production by Heterofermentative Lactic Acid Bacteria: a Review[J]. Applied Biochemistry and Biotechnology, 2022, 194(6): 2762-2795.
[25] Juan-Gilberto Martinez-Miranda, Chairez Isaac, Duran-Paramo Enrique. Mannitol Production by Heterofermentative Lactic Acid Bacteria: a Review[J]. Applied Biochemistry and Biotechnology, 2022, 194(6): 2762-2795.

ENHANCEMENT OF ANAEROBIC FERMENTATION FOR ACID PRODUCTION AND SYNERGISTIC CO_2 FIXATION BY GRANULAR ACTIVATED CARBON (GAC) IN DISTILLERY'S GRAINS

Wenwen Chen[1], Dezhi Sun[1], Yan Dang[1]
[1]College of Environmental Science and Engineering, Beijing Forestry University, No. 35 Qinghua East Road Haidian District, Beijing, China

ABSTRACT
Anaerobic fermentation (AF) of lignocellulosic waste offers a promising route for volatile fatty acid (VFA) production and carbon recovery, yet its efficiency is often limited by slow hydrolysis and intermediate inhibition. This study investigates the enhancement of acidogenesis and CO_2 fixation in distillery's grains (DGR) via the addition of granular activated carbon (GAC) without pretreatment. Batch reactors with (GDG) and without (DG) GAC (15 g/L) were operated under anaerobic conditions. Results demonstrated that GAC supplementation significantly promoted acetate and propionate production, increasing their yields by 40.0% and 175.0%, respectively, and elevating the maximum VFAs/sCOD ratio to 59.5% compared to 49.7% in the control. Volatile solids (VS) removal efficiency also improved, reaching 25.3% in GDG versus 19.3% in DG group. Microbial analysis revealed a shift from Firmicutes to Bacteroidota dominance, indicating enhanced polysaccharide degradation and electron transfer. Furthermore, the GDG system exhibited a 41% higher cumulative CO_2 uptake than DG over 15 days. These findings underscore the role of GAC in facilitating microbial metabolism and acidogenic efficiency, providing a feasible strategy for waste valorization and carbon mitigation in anaerobic fermentation.

KEYWORDS
Anaerobic fermentation; Distillery's grains; VFAs; GAC; CO_2 fixation; Microbial community.

1. INTRODUCTION

Escalating environmental pollution from agricultural and industrial activities has made the resource recovery of organic solid wastes and the mitigation of greenhouse-gas emissions global priorities (Lanfranchi et al., 2025). Compared with the conventional biogas production, the acidogenic fermentation (AF) stage of anaerobic digestion can selectively converts organic substrates into volatile fatty acids (VFAs), which find extensive applications as carbon sources in wastewater treatment and as platform chemicals in the food, pharmaceutical, and chemical industries (Ramos-Suarez et al., 2021; Zhang et al., 2021). AF is therefore recognized as a key platform process underpinning the circular bioeconomy (Zhang et al., 2025).

Distillery's grains (DGR), as one type of the lignocellulosic biomass, are the principal solid byproduct generated during the distillation process. Its global annual output is substantial; in China alone, the 2024 production of Chinese liquor is estimated at approximately 4.1 million t, corresponding to about 12.4 million t of DGR (https://www.stats.gov.cn/). Current management practices include direct disposal, incineration or composting. These approaches often lead to resource underutilization and environmental burdens. Given its rich nutrients (e.g., starch, lipids, proteins), DGR holds considerable potential for conversion to VFAs.

However, lignocellulosic substrates such as DGR are constrained by recalcitrant cell-wall architectures and derivative inhibitors (e.g., phenolics, furans), which limit hydrolysis rates and thereby become the bottleneck to valorization (Monlau et al., 2014; Sawatdeenarunat et al., 2015). Conventional solutions primarily rely on pretreatment methods such as acid/alkali/thermal/enzymes to improve microbial accessibility (Chevalier et al., 2025). However, these approaches typically entail operational complexity or costly reagents, increasing process costs and environmental footprints and thus limiting engineering scalability (Zhang et al., 2025). Accordingly, avoiding complex pretreatments and developing low-cost conversion strategies for effective DGR valorization is of considerable interest.

In recent years, conductive material-mediated microbial interactions have emerged as a cost-effective approach to enhance anaerobic processes. GAC combines high specific surface area, appreciable electrical conductivity, and adsorption/buffering capacities (Lovley, 2017; Yang et al., 2020). It can (i) provide attachment sites for the enrichment of hydrolytic/acidogenic consortia, (ii) improve the distribution of electron flow during fermentation, and (iii) adsorb lignin-derived inhibitors to alleviate substrate toxicity. Thereby it may boost acidogenesis without resorting to complex pretreatments. Beyond its widespread verification in methanogenic

digestion, our previous work demonstrated that GAC increased VFA yields from garden waste and upregulated glycoside hydrolases and key fermentative functional genes, corroborating its direct stimulation during the hydrolysis–acidogenesis stage (Chen et al., 2023). Nevertheless, research on extracellular polymeric substances (EPSs) dynamics, electron transfer capacity, and microbial community succession remains limited. Moreover, the lignocellulosic matrix contains functional groups with CO_2 fixation potential, making it important to conduct preliminary investigations into the CO_2 fixation capacity of this system (Abdelaziz et al., 2016).

Taken together, employing GAC as a functional material to intensify hydrolysis–acidogenesis of high-solids DG without other complex pretreatments, and subsequently supplying exogenous CO_2 during the late acidogenic phase to preliminarily evaluate the system's CO_2-fixation potential, holds clear scientific and engineering significance. This study is expected to provide technical support and theoretical guidance for DG valorization and carbon mitigation.

2. MATERIALS AND METHODS

2.1. Substrate and Inoculums

DGR was collected from a Chinese liquor distillery in Southwest China. The DGR was oven-dried at 60°C, ground using a high-speed multifunctional mill (CHAORAN, CR-100, China), and sieved through a 30-mesh screen (Tyler Standard Screen Scale). The processed DG was then sealed in plastic bags and stored at ambient temperature until use. The inoculum with pH of 7.6±0.1 was collected from a full-scale up-flow anaerobic sludge bed (UASB) reactor in our laboratory and stored at 4°C. Table 1 showed the characteristics of the DGR and inoculum used in this study.

Table 1 Characteristics of distillery grain and inoculum

	Total Solid (%)	Volatile Solid (%)	Cellulose (%)	Hemicellulose (%)	Lignin (%)
DGR	98.9 ±0.2	90.5±1.6	15.1 ± 0.3	49.0± 0.6	3.9± 0.2
Seed	10.4 ±0.1	8.0±0.1	—		—

2.2. Reactor Set-up and Operation Conditions

Two treatment sets of batch anaerobic reactors were established: a GAC-dosed group (GDG; GAC at 15 g/L) and a GAC-free control (DG), with all other conditions identical. The GAC used in this experiment was purchased from Changge Tanernuo Catalytic Technology Co., Ltd. (China), with individual particle volumes of 35-170 mm^3 and geometric surface areas of 50-180 mm^2. Each reactor consisted of a 1-L serum bottle operated at a working volume of 0.7 L and sealed with rubber stoppers equipped with a sampling line and a gas-outlet line connected to a gas bag; the sampling line was clamped during operation. Dry DGR solids were dosed at 10% total solids (TS). For each bottle, 200 mL of anaerobic sludge inoculum and 10 mmol/L sodium 2-bromoethanesulfonate (BES) were added, and the contents were topped up with tap water to 0.7 L and homogenized. The headspace was deoxygenated by sparging with a CO_2/N_2 mixture (20/80, v/v) for 15 min prior to sealing, and then both reactors were incubated in a thermostatic shaking water bath at 35 C and 115 rpm. Liquid and gas samples were collected at scheduled intervals for analyses. To preliminarily assess CO_2 uptake/fixation, from day 35 to day 50, the gas bags were replenished every 5 days with pure CO_2, and the decrease in CO_2 content was quantified every 5 days.

2.3 Analytical Methods

The composite samples were retrieved from the serum bottles at predetermined intervals and subsequently centrifuged at 10,000 rpm for 6 min. The supernatant was filtered through a 0.45-μm membrane for the subsequent analysis of soluble chemical oxygen demand (sCOD) and filtered through a 0.22-μm membrane for the analysis of VFAs. The COD, TS, and volatile solids (VS) were determined with standard methods (APHA, 2005). VFAs were measured by high-performance liquid chromatography (HPLC) (Bio-Rad, Hercules, California) using 5 mM H_2SO_4 as the mobile phase (Huang et al., 2022). The total VFAs were the sum of acetate, propionate, iso-butyrate, and n-butyrate during fermentation. pH was measured with a pH meter (HACH, United States). The gas volume collected in a sampling bag was measured using an air pum, and then, the gas was transferred back into the bag. The CO_2 content in the gaseous samples in the sampling bag was measured using gas chromatography apparatus equipped with a thermal conductivity detector (TCD) (Tianmei, GC7900, China). Cyclic voltammetry (CV) was performed with current (A) -potential (V) in the range of -1.0 V-1.0 V (vs. Ag/AgCl) at a scanning rate of 5 mV/s. The extraction method for EPSs, including soluble EPS (S-EPS), loosely bound EPS (LB-EPS), and tightly bound EPS (TB-EPS), followed the recommended procedures reported in the literature (Jin et al., 2022). The quantified methods are shown in previous study (Chen et al., 2025).

2.4 DNA Extraction and Microbial Community

To assess the dynamic succession of microbes in the fermentation reactors, DNA was extracted from 2 mL sludge samples collected from seed sludge and reactors at day 15 and day 35 using RNeasy PowerSoil DNA Elution kit. The method followed that described in the previous study, using the primer set (338F/806R) for bacteria (Liu et al., 2019).

3. RESULTS AND DISCUSSION

3.1. Reactor's Performance

As shown in Fig. 1(a-b), both the GDG and DG reactors exhibited similar trends in pH and sCOD variations. The pH decreased rapidly within the first 5 days and then stabilized around 5.5 in both reactors. The sCOD reflects the dissolution of organic matter in DGR. As illustrated in Fig. 1(b), the sCOD concentration in both groups increased rapidly during the initial 5 days, followed by a slow rise thereafter. The lower sCOD level observed in the GDG group may be attributed to the adsorption effect of GAC (Yang et al., 2020; Zusman et al., 2020), which resulted in the adsorption of a portion of sCOD generated from DGR hydrolysis.

The VFA compositions were identical in both reactors, consisting of acetate, propionate, iso-butyrate, and n-butyrate. The addition of GAC enhanced the production of acetate and propionate (Fig. 1(c-f)). Compared to the DG group, the acetate yield in the GDG group increased by 40.0% on day 9. A significant difference ($p<0.05$) was observed in propionate production between the two groups, with the GDG group showing a 175.0% increase on day 35.

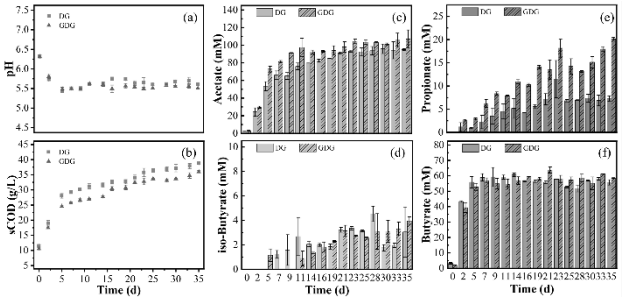

Fig. 1 Temporal variations of different parameters during anaerobic fermentation in both reactors: (a) pH, (b) sCOD, (c) acetate, (d) iso-butyrate, (e) propionate, (f) butyrate.

The VFAs/sCOD ratio served as a key parameter, reflecting the efficiency of conversion from soluble organic matter to VFAs (Fang et al., 2019). As shown in Fig. 2(a), the GDG reactor demonstrated a higher VFAs/sCOD ratio compared to the DG reactor. Based on quantitative analysis, the maximum ratio observed in the GAC-amended group was 59.5%, exceeding the value of 49.7% recorded in the control group, which suggests enhanced acidogenic performance due to GAC addition . Nevertheless, this value remained lower than the 70.0% reported in our previous investigation (Chen et al., 2023), likely owing to the reduced GAC dosage employed here (15 g/L vs. 50 g/L). Furthermore, as presented in Fig. 2(a), the promotional effect of GAC also led to increased total VFA production, with peak concentrations of 11.4 g acetate/L and 10.0 g acetate/L in the GDG and DG reactors, respectively.

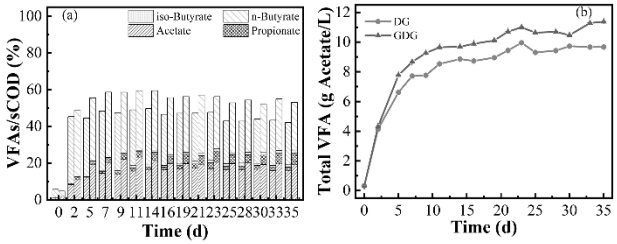

Fig. 2 (a) VFAs/sCOD ratio (Left: DG reactor; Right: GDG reactor), (b) temporal variation of the total VFA concentration.

Fig. 3(a and b) depict the concentrations of polysaccharides and proteins in sludge. During the initial phase, both metrics were lower in the GDG group than in the control group (DG). This could be attributed to the high porosity and adsorption capacity of GAC, which can rapidly adsorbed S-EPS released from the substrate, preventing excessive accumulation, alleviating mass-transfer limitations, and improving substrate accessibility. This observation was also consistent with the lower sCOD observed in GDG reactor (Fig. 1(b)). By the mid-fermentation stage (day 15), polysaccharides declined sharply in both groups—from 4.1 g COD/L to 0.5 g COD/L in the DG group, and from 3.5 g COD/L to 0.2 g COD/L in the GDG group. Meanwhile, protein concentrations increased relative to the initial level on day 15 by 9.4% in DG and 10.5% in GDG, and then decreased again by day 35. This phenomenon can be explained as follows: as DGR continued to degrade, the cellulose and hemicellulose structures were progressively broken down, leading to rapid hydrolysis of soluble polysaccharides and their conversion into VFAs and other products, causing a sharp decrease in concentration. And a transient rise in protein caused by cell lysis or extracellular enzyme release during peak microbial activity, followed by further conversion by acidogenic-producing consortia, leading to a renewed decline (Sheng et al., 2010). Notably, the protein peak in GDG was lower than in DG, indicating superior buffering of intermediate accumulation and facilitation of downstream metabolism by GAC.

VS removal efficiency is a core indicator that quantifies the biodegradability of lignocellulosic organic matter in AF (Wei et al., 2015). VS removal efficiency reached 15.8% (DG) and 22.1% (GDG) on day 15, and 19.3% (DG) and 25.3% (GDG) on day 35 (Fig. 3(c)), demonstrating that GAC enhanced the degradation of organic solids in DGR and increased substrate conversion. Moreover, Fig. 3(d) shows a broader current-density distribution in GDG, evidencing strengthened electron-transfer capability in the presence

of the system.

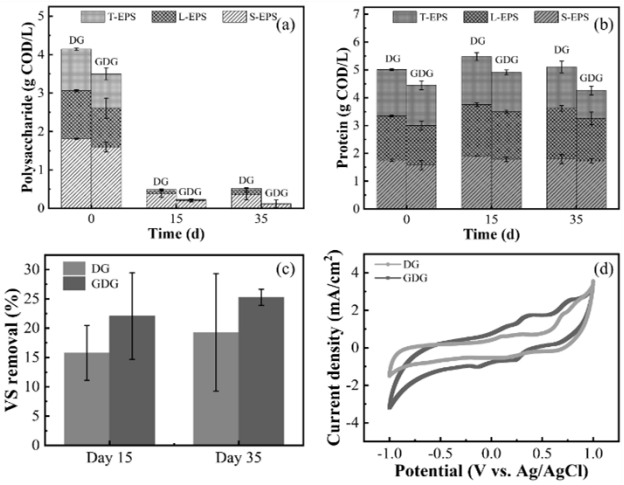

Fig. 3 Variation in (a) polysaccharide content, (b) protein content (c) VS removal efficiency, (d) CV scan of sludge from the reaction system on day 35.

3.2 The Potential of CO_2 Fixation

To preliminarily investigate the CO_2 fixation potential of the anaerobic fermentation system using DGR, pure CO_2 was used to replace the gas in the attached bags every 5 days starting from day 35, and the reduction in CO_2 was monitored. As shown in Fig. 4, CO_2 consumption occurred in both groups during the three intervals (35-40 d, 40-45 d, and 45-50 d), with the GDG group consistently exhibiting significantly higher consumption than the DG group: 105 vs. 73 mmol, 86 vs. 65 mmol, and 77 vs. 52 mmol, corresponding to increases of approximately 44%, 32%, and 48%, respectively. The cumulative CO_2 consumption over 15 days was 268 mmol for the GDG group and 190 mmol for the DG group, representing an overall increase of about 41%. A gradual decrease in CO_2 uptake was observed in both groups over time. Collectively, these results preliminarily suggest that the system possesses CO_2 fixation capacity, and GAC addition further strengthens this capability.

3.3 Microbial Community Structure

Fig. 5(a and b) show the changes in microbial community structure at the phylum and genus levels in the reactors during different operational periods. At phylum level, starting from the inoculated sludge (Seed), Firmicutes rapidly became dominant in both treatments by day 15 (M_DG: 48.7%, M_GDG: 45.2%). Various acidogenic bacteria within Firmicutes are well-known producers of proteases, lipases, and extracellular enzymes that biodegrade macro-molecular organic compounds into VFAs (Li et al., 2022). A notably higher relative abundance of Bacteroidota at day 15 was observed in the GAC-amended system (M_GDG: 31.1% vs. M_DG: 10.1%), and it became absolutely dominant by the end of the operation at day 35 (E_GDG: 45.1%), compared to only 16.8% in the control group. Relevant studies indicate that Bacteroidota can hydrolyze proteins and produce VFAs during organic substrate metabolism (Ma & Huang, 2024). In contrast, Firmicutes continued to increase and remained dominant in the control group by day 35 (E_DG: 59.0%), while its relative abundance in E_GDG was 41.2%. Additionally, Proteobacteria showed a slight increase in the GDG group during the mid-term (3.45% vs. 1.04% in DG), whereas Fermentibacterota and Desulfobacterota decreased more markedly in the GDG reactor (to 1.19% and 0.96%, respectively; compared to 2.38% and 2.64% in the control). These results indicate that the addition of GAC shifted the microbial community from a "Firmicutes-dominant" to a "Bacteroidota-dominant" structure in the later phase, suggesting that GAC promotes a metabolic network characterized by enhanced polysaccharide degradation and sugar fermentation. This shift may also imply suppression of certain sulfate-reducing bacterial communities, which was consistent with the increased conversion of carbohydrates into VFAs during acidogenesis.

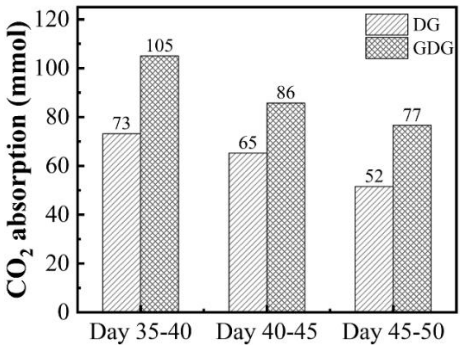

Fig. 4 Temporal profile of CO_2 absorption measured at 5-day intervals in the DG and GDG reactors from day 35 to day 50.

At genus level (Fig. 5(b)), *Prevotella*, belonging to the phylum Bacteroidota, was a dominant genus in the GDG group, with relative abundances of 25.2% in M_GDG (day 15) and 38.5% in E_GDG (day 35), compared to only 2.45% and 3.31% in the control group. As *Prevotella* is known as a polysaccharide-fermenting taxon linked to acetate/propionate formation, its enrichment suggests that GAC enhances the accessibility of sugar-based substrates and promotes acidification pathways favoring acetogenesis and propionogenesis (Zhang et al., 2023). In contrast, *Clostridium sensu stricto 1* (phylum Firmicutes), a butyrate producer (Lv et al., 2022), was significantly

more abundant in the control group (M_DG: 22.5%; E_DG: 38.6%), while it remained around 19% in the GDG group. The result indicates that GAC somewhat suppressed the overdominance of typical butyrate-producing pathways. *Caproiciproducens* maintained a moderate abundance in the later phase in the GDG group (E_GDG: 5.54% > E_DG: 1.62%) but did not become a dominant genus. These results demonstrate that GAC addition altered the microbial community structure and further shifted electron flow during acidogenesis.

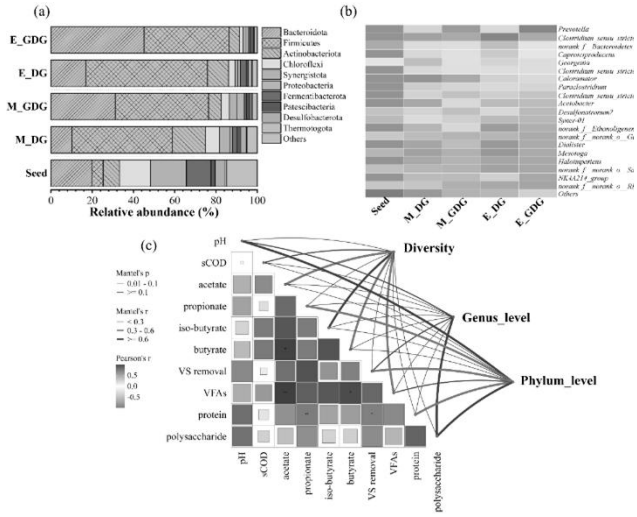

Fig.5 Microbial composition and Mantel analysis: (a) phylum level, (b) genus level, (c) correlation between environmental factors and community structure

As shown in Fig. 5(c), mantel tests revealed significantly strong correlations between microbial diversity (Diversity) and acetate, VS removal efficiency, and total VFA concentration. At the phylum level, community structure was strongly correlated with propionate, VS removal, and protein content. VFAs were positively correlated with sCOD and VS removal, but negatively correlated with protein and polysaccharide content. Additionally, pH was negatively correlated with VFA levels, indicating that persistently low pH may, in turn, suppress further VFA production.

4. CONCLUSION AND OUTLOOK

In summary, the addition of GAC (15 g/L) demonstrated a regulatory effect on the microbial community structure and enhanced hydrolysis and acidogenesis during the anaerobic fermentation of DGR. It particularly promoted the production of acetate and propionate and improved the VS removal efficiency, providing a theoretical basis for enhancing waste valorization efficiency. However, the relatively low dosage of GAC used in this study led to limited improvement in acid production from untreated DGR. Therefore, further investigation is warranted into the effects of GAC dosing levels or synergistic strategies combining GAC with complementary materials on the acidogenic fermentation of DGR. Additionally, preliminary results indicate that this anaerobic fermentation system has CO_2 fixation potential. Follow-up studies employing methods such as $^{13}CO_2$ isotope tracing and metagenomics are recommended to elucidate the underlying mechanisms.

5. REFERENCES

Abdelaziz, O.Y., Brink, D.P., Prothmann, J., Ravi, K., Sun, M., García-Hidalgo, J., Sandahl, M., Hulteberg, C.P., Turner, C., Lidén, G., Gorwa-Grauslund, M.F. 2016. Biological valorization of low molecular weight lignin. Biotechnology Advances, 34(8), 1318-1346.

Chen, W., Zeng, Y., Liu, H., Sun, D., Liu, X., Xu, H., Wu, H., Qiu, B., Dang, Y. 2023. Granular activated carbon enhances volatile fatty acid production in the anaerobic fermentation of garden wastes. Frontiers in Bioengineering and Biotechnology, 11, 1330293.

Chen, W.W., Li, H.Y., Liu, C.Q., Li, Y.Q., Sun, D.Z., Qiu, B., Li, P.S., Xu, H.Y., Wu, H.B., Dang, Y. 2025. Optimizing anaerobic digestion of Chinese liquor brewing wastewater: A cost-effective and high-performance approach. Chemical Engineering Journal, 506, 160028.

Chevalier, A., Evon, P., Monlau, F., Vandenbossche, V., Sambusiti, C. 2025. Extrusion as a pretreatment for lignocellulosic agricultural byproducts to improve biogas production: A review. Bioresource Technology Reports, 29, 102063.

Fang, W., Zhang, P., Zhang, T., Requeson, D.C., Poser, M. 2019. Upgrading volatile fatty acids production through anaerobic co-fermentation of mushroom residue and sewage sludge: Performance evaluation and kinetic analysis. Journal of Environmental Management, 241, 612-618.

Huang, Y., Cai, B., Dong, H., Li, H., Yuan, J., Xu, H., Wu, H., Xu, Z., Sun, D., Dang, Y., Holmes, D.E. 2022. Enhancing anaerobic digestion of food waste with granular activated carbon immobilized with riboflavin. Science of The Total Environment, 851, 158172.

Jin, H., He, Z., Ren, Y., Tang, C., Zhou, A., Chen, F., Liang, B., Liu, W., Wang, A. 2022. Role and significance of co-additive of biochar and nano-magnetite on methane production from waste activated sludge: Non-synergistic rather than synergistic effects. Chemical Engineering Journal, 439, 135746.

Lanfranchi, A., Magdalena, J.A., Cavinato, C., Trably, E. 2025. Highly selective acetate production from wine lees through acidogenic fermentation. Journal of Environmental Management, 373, 123532.

Li, J., Xin, W., Liang, J., Shang, P., Song, Y., Wang, Q., Gamal El-Din, M., Arslan, M., Guo, S., Chen, C. 2022. Alkaline fermentation of refinery waste activated sludge mediated by refinery spent caustic for volatile fatty acids

production. Journal of Environmental Management, 324, 116317.
Liu, C., Sun, D., Zhao, Z., Dang, Y., Holmes, D.E. 2019. *Methanothrix* enhances biogas upgrading in microbial electrolysis cell via direct electron transfer. Bioresource Technology, 291, 121877.
Lovley, D.R. 2017. Happy together: microbial communities that hook up to swap electrons. The ISME Journal, 11(2), 327-336.
Lv, N., Cai, G., Pan, X., Li, Y., Wang, R., Li, J., Li, C., Zhu, G. 2022. pH and hydraulic retention time regulation for anaerobic fermentation: Focus on volatile fatty acids production/distribution, microbial community succession and interactive correlation. Bioresource Technology, 347, 126310.
Ma, S., Huang, X. 2024. Volatile fatty acid (VFA) production from sludge and chicken manure co-fermentation: Role of acid/alkali-treatment and microbial characteristics. Journal of Environmental Chemical Engineering, 12(2), 112215.
Monlau, F., Sambusiti, C., Barakat, A., Quéméneur, M., Trably, E., Steyer, J.P., Carrère, H. 2014. Do furanic and phenolic compounds of lignocellulosic and algae biomass hydrolyzate inhibit anaerobic mixed cultures? A comprehensive review. Biotechnology Advances, 32(5), 934-951.
Ramos-Suarez, M., Zhang, Y., Outram, V. 2021. Current perspectives on acidogenic fermentation to produce volatile fatty acids from waste. Reviews in Environmental Science and Bio/Technology, 20(2), 439-478.
Sawatdeenarunat, C., Surendra, K.C., Takara, D., Oechsner, H., Khanal, S.K. 2015. Anaerobic digestion of lignocellulosic biomass: Challenges and opportunities. Bioresource Technology, 178, 178-186.
Sheng, G.-P., Yu, H.-Q., Li, X.-Y. 2010. Extracellular polymeric substances (EPS) of microbial aggregates in biological wastewater treatment systems: A review. Biotechnology Advances, 28(6), 882-894.
Wei, Y., Li, X., Yu, L., Zou, D., Yuan, H. 2015. Mesophilic anaerobic co-digestion of cattle manure and corn stover with biological and chemical pretreatment. Bioresource Technology, 198, 431-436.
Yang, L.B., Si, B.C., Zhang, Y.H., Watson, J., Stablein, M., Chen, J.B., Zhang, Y.L., Zhou, X.F., Chu, H.Q. 2020. Continuous treatment of hydrothermal liquefaction wastewater in an anaerobic biofilm reactor: Potential role of granular activated carbon. Journal of Cleaner Production, 276(276), 122836.
Zhang, B., Fan, F., Guo, C., Yu, M., Zhao, M., Song, Y., Li, Y. 2021. Evaluation of maturity and odor emissions in the process of combined composting of kitchen waste and garden waste. Applied Sciences-Basel, 11(12).
Zhang, B., Lingga, C., De Groot, H., Hackmann, T.J. 2023. The oxidoreductase activity of Rnf balances redox cofactors during fermentation of glucose to propionate in *Prevotella*. Scientific Reports, 13(1), 16429.
Zhang, G., Li, J., Liu, S., Hou, P., Tao, X., Gao, W., Sun, L., Lv, L., Liang, J. 2025. Recent advances in bioconversion of lignocellulosic biomass for volatile fatty acid production with rumen microorganisms. Biotechnology Advances, 83, 108654.
Zusman, O.B., Kummel, M.L., De la Rosa, J.M., Mishael, Y.G. 2020. Dissolved organic matter adsorption from surface waters by granular composites versus granular activated carbon columns: An applicable approach. Water Research, 181, 115920.

Poster

Title: Straw-Induced Carbon Dynamics in Saline Soils: Insights from CO_2 Emissions to Soil Organic Carbon Sequestration

Cailing Shi, Yinglu Tao, Wenjun Xie, Lei Xu, Gaoqi Li, Xiangrui Wang

School of Environmental and Municipal Engineering, Qingdao University of Technology, 266520, China.

Abstract

Straw is an abundant and renewable resource worldwide. Straw application is a widely adopted strategy for reclaiming saline soils and enhancing soil organic carbon (SOC) accrual. However, the fate of straw carbon under salinity stress—whether it is mineralized into CO_2 or conversed into SOC pool fractions—remains poorly understood, limiting our ability to predict the carbon sequestration potential and environmental impacts of straw amendment in saline land. ^{13}C-labeled maize straw was used in this study to track exogenous organics turnover in soils with different salinity. Results showed that salinity decreased straw decomposition and CO_2 emissions significantly. The intensity of priming effect reduced while the duration increased significantly with increased soil salinity. High salinity decreased the activities of soil dehydrogenase and straw-decomposed enzymes, then favored straw conversion into free particulate organic carbon (fPOC). However, the quantity of mineral-associated organic carbon (MAOC) derived from straw decreased with salinity rising significantly. Our findings suggested that straw transformation and the composition of soil organic carbon pool can be influenced by soil salinization.

Construction and Technological Progress of a Comprehensive Carbon Reduction System for CCUS in the Steel Industry

Yang Zheng[1, 2], Rongrong Lei [1,2], Wei Su[1, 2, *], Yi Xing[1,2]

[1] School of Energy and Environmental Engineering, University of Science and Technology Beijing, Beijing, 100083, China

[2] State Key Laboratory of Advanced Metallurgy, University of Science and Technology Beijing, Beijing, 100083, China

Abstract: The development characteristics of carbon capture, utilization, and storage (CCUS) technologies in the steel industry, the establishment of a comprehensive carbon reduction system, and technological advancements have been explored. The characteristics of carbon emissions in the steel industry, the current status of carbon reduction technology development, and the distinctive features of CCUS technology have been elucidated. As a significant component of heavy industry, the combustion of fossil fuels such as coal during steel production leads to substantial carbon emissions. Although China has increasingly recognized the importance of CCUS in recent years, the overall progress remains in the early stages, and there is still a need for further improvement in technology and policy support. A "6C" system is proposed to create an integrated CCUS solution encompassing the entire process, detailing the technologies, strategies, and application cases across six aspects: carbon capture, utilization, storage, verification, monitoring, and assets. It discusses how optimization can help achieve the goal of reducing carbon emissions, while also providing valuable experiences and references for carbon emission control in other industrial sectors. The progress of CCUS technology in typical steel industry scenarios has been analyzed, and three carbon reduction pathways have been proposed. The traditional blast furnace CCUS route involves capturing and separating part of the blast furnace gas source to recycle CO and utilize CO2. Addressing the current challenges of high energy consumption and costs in carbon capture, a direct solid carbon route from end-of-pipe flue gas has been proposed to lower the purity of captured CO2. The hydrogen metallurgy coupled with CCUS route aims to produce green methanol through the integration of hydrogen

production from renewable energy with CCUS. The implementation of these three carbon reduction pathways will promote traditional long-process decarbonization, reduce carbon source inputs, enhance the utilization of carbon resources, and achieve high value-added utilization of products. Future large-scale demonstration projects will facilitate the internal cycling of CO2 in the steel industry and its cross-industry utilization. Recommendations and outlook for advancing CCUS technology in the steel industry have also been presented.

Research on Social Implementation of Lithium-Ion Batteries(LIBs) Detection Methods Using RFID Tags

Koji Sakakibara[1], Eriko Aibara[1], Hirofumi Nakayama[1], Kazuki Suehiro[2], Haruichi Kanaya[2], Takayuki Shimaoka[3]

[1]Department of Urban and Environmental Engineering, faculty of Engineering, Kyushu University,744 Motooka, Nishi-ku, Fukuoka, Japan

[2]Department of Electronics Graduate School of Information Science and Electrical Engineering, Kyushu University,744 Motooka, Nishi-ku, Fukuoka, Japan

[3]Kyushu Environmental Evaluation Association, 1-10-1 Matsukadai Higashi-ku, Fukuoka, Japan

ABSTRACT

Numerous fire incidents have been reported due to Lithium-Ion Batteries (hereinafter referred to as LIBs) inadvertently mixed with non-combustible waste. This study investigates a fundamental approach to detecting LIBs containing products in waste streams, based on the application of Radio Frequency Identification (RFID) tags affixed to LIBs. RFID is widely utilized as an automatic identification technology. The unidirectional RFID tag antennas employed in this research, currently under development, are designed to enable communication with a reader/writer (hereinafter referred to as R/W) even when attached to metal products.

In previous experiments, tag affixed to mobile battery were tested under various conditions. The results confirmed that the tag could be detected reliably in environments with ambient radio waves, such as Wi-Fi, and even when mixed with non-combustible waste such as empty cans. Moreover, detection performance was found to improve significantly when tag were located within metal-enclosed spaces due to enhanced electric field strength.

The present study extends these findings by demonstrating LIBs detection during the waste collection stage, with a focus on future practical implementation. Specifically, multiple detection methods were examined and verified in two scenarios: small electronic device collection boxes and the loading ports of collection vehicles. Based on these experiments, optimal detection methods are proposed for both settings.

1. Introduction

In recent years, fire accidents caused by LIBs mixed in municipal solid waste have frequently occurred in garbage collection vehicles, waste treatment facilities, and recycling plants. When LIBs are present at the loading ports of packer trucks or in crushing equipment at recycling facilities, excessive compression or crushing may trigger ignition.[1-4] Such fire incidents pose a serious safety concern.

Current countermeasures primarily involve the early detection of abnormal temperature rises, smoke, or flames, followed by the use of automatic fire extinguishing systems.[5] However, these measures are reactive, as they address fires only after they have begun. To reliably reduce the number of such accidents, proactive measures are required—specifically, the detection and removal of LIBs mixed with refuse before collection and processing.

One recently studied approach involves measuring dimethyl carbonate (DMC) concentrations leaking from LIBs using two-wavelength optical absorption spectroscopy.[6] DMC, an electrolyte used in LIBs, has an explosion limit of 4.2–12.9%. The method aims to detect concentrations below the lower explosion limit (4.2%). While effective for identifying LIBs that have already released gas due to crushing or other damage, this method cannot detect intact LIBs prior to gas generation.

This study aims to evaluate the detection performance of RFID tags currently under development. These tags are designed to be affixed to LIBs and LIB-containing products, enabling their identification within mixed waste streams. At our previous research presentation, we reported the following key findings:

1) Owing to the unidirectional properties of the RFID tag used in this study, detection was achieved even when tag was directly attached to LIBs enclosed in metal cases. (In contrast, general-purpose tags fail under such conditions.)
2) Detection was possible in typical Wi-Fi environments (laboratories, hallways, and outdoor settings), although detection distance varied with interference.
3) The tag affixed to mobile battery was successfully detected even when mixed with empty cans or other non-combustible waste.
4) In metal-enclosed spaces, suppression of radio wave diffusion enhanced electric field strength, thereby improving detection performance.

Building on these results, the present study verifies detection performance under practical conditions at the

waste collection stage, with an eye toward future social implementation. Specifically, two cases were investigated: detection in small electronic device collection boxes and at the loading ports of packer trucks.

2. Materials and methods

2.1 Detection experiment in small electronic device collection box

The experiment focused on small electronic device collection box installed at the community facility "SAITOPIA" in Fukuoka City's Nishi Ward. As shown in Figure 1, the collection box resemble mailbox in structure. Discarded small electronic devices are inserted through the top opening on the side and stored in a plastic collection container inside the box. In practice, the collection container held various electronic devices such as mobile batteries, game consoles, cables, mobile phones, digital cameras, and e-cigarettes. While batteries like LIBs and dry cell batteries are supposed to be collected separately in dedicated battery containers, the box also contained products like mobile phones and e-cigarettes that had LIBs built-in.

The experimental method involved placing a tagged mobile battery among the electronic devices originally in the collection container and then verifying detection performance by waving a R/W near the collection container. Detection tests were conducted in two scenarios: with the collection box door open and the container remaining inside the box(Case1), and with the container removed from the box(Case2). Given that the electronic devices inside the container reached a height of approximately 40 cm, the mobile battery was placed in two positions: the center (20 cm from the bottom) and the bottom.(Figure 2)

Collection container installed inside the box

Small electronic devices contained in the box

Figure1 Small electronic device collection box

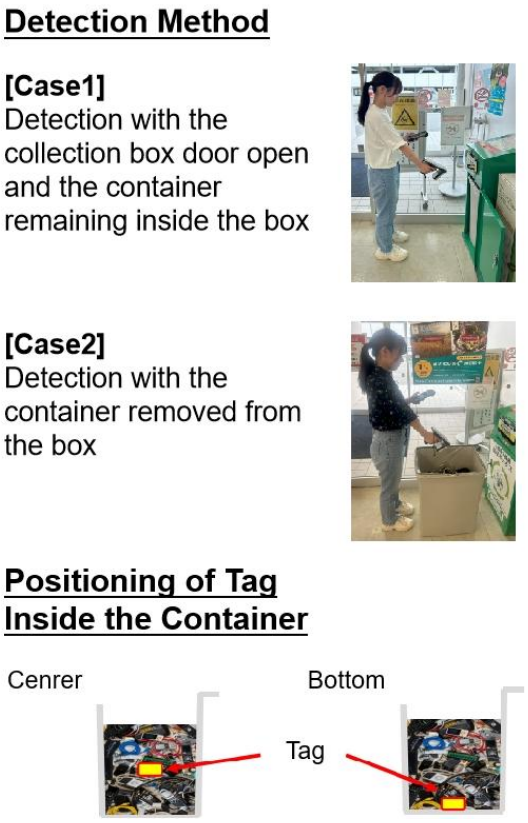

Figure2 Experiment at small electronic device collection box

2.2 Detection experiment at packer truck inlet

An experiment was conducted using a 4-ton rotary plate packer truck. The truck's waste inlet dimensions were 1670 mm wide × 890 mm high. Due to its elongated width, two R/W units were employed.The experimental conditions comprised the following three cases, as shown in Figure 3.

1) Positioning two R/W units either at the top of the inlet (400 mm inward from each end) or on the left/right sides (500 mm above the bottom of the inlet)
2) Setting the position of the garbage bag containing empty cans with attached mobile battery tags inside the inlet to the left, center, or right side
3) Simulating the garbage bag placement actions of collection workers, the bag positions were set both in front of the opening before insertion and inside the opening after insertion.

The R/W used in the experiment was the SP1 model manufactured by Denso Wave Incorporated. Detection performance was evaluated based on the detection time required and the detection rate.

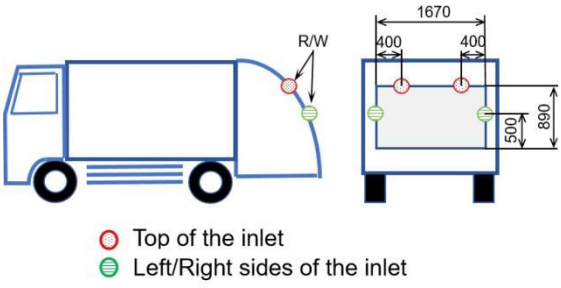

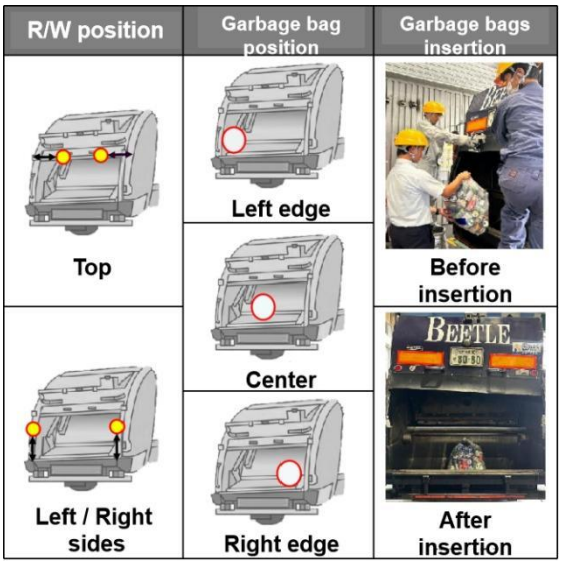

Figure3 Experiment at packer truck inlet

3. Results and discussion

3.1 Detection experiment in small electronic device collection box

The experimental results are shown in Figure 4. Detection performance was evaluated by conducting each experiment 10 times. When the mobile battery was placed in the center of the collection container, detection occurred within 1 second in all 10 cases when the collection container was inside the collection box. However, when the collection container was removed, detection took 1 to 4 seconds. Furthermore, when the mobile battery was at the bottom of the collection container, detection was successful in all 10 trials while the container was inside the collection box, though detection times varied. Conversely, when the container was removed, detection failed in 2 out of 10 trials. Therefore, the most effective detection method was to open the collection box door and detect the container while it remained inside the box. This is likely because the steel construction of the collection box creates a metal cavity when the container is inside. This increases the electric field strength around the tag, improving detection performance.

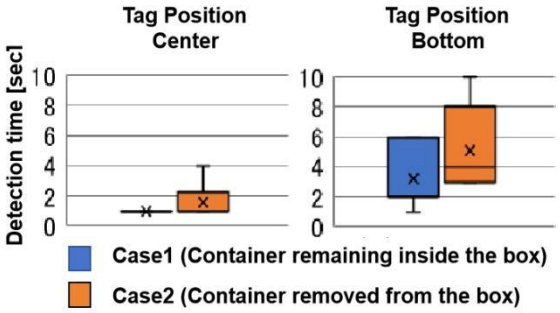

Figure4 Comparison of detection time based on measurement method and tag position

3.2 Detection experiments at the packer truck inlet

Each experiment was conducted five times to evaluate detection performance. Figure 5 shows a comparison of detection times based on the R/W installation position when the garbage bag was placed on the left, center, or right side. When the R/W was installed on either side of the opening, detection occurred within one second by one of the R/Ws regardless of the bag's position. However, when the R/W was installed at the top, detection generally occurred within approximately 1 second, but there were cases where detection failed when the garbage bag was on the right side. This indicates that installing the R/W on either side of the inlet is effective.

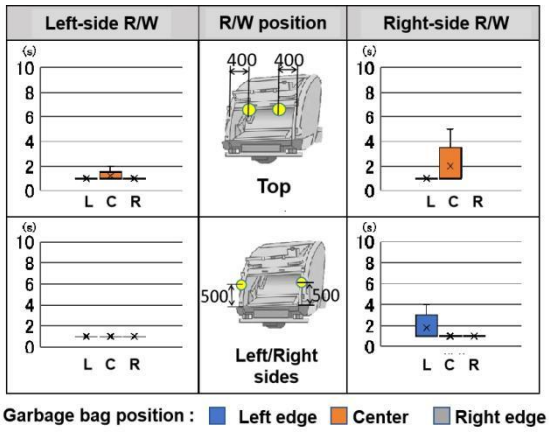

Figure5 Comparison of detection times based on the R/W installation position

Detection time results for the position of the garbage bag before and after insertion shows Figure 6. Before insertion, detection times varied between 1 and 10 seconds. After insertion, detection occurred within 1 second on either R/W in all 5 trials. Furthermore, while detection might fail before

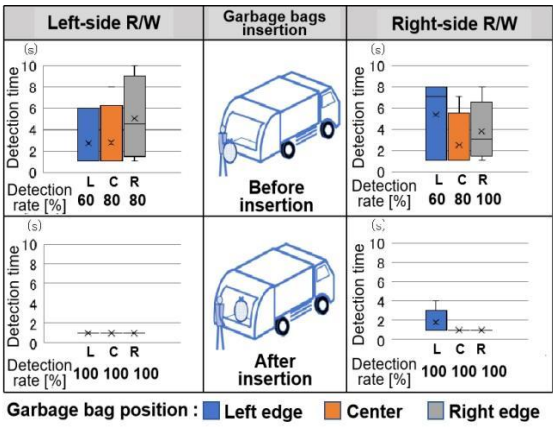

Figure6 Comparison of detection time results for the position of the garbage bag before and after insertion

insertion depending on the bag's position, after insertion, detection succeeded in all 5 trials regardless of position.

Figure7 shows the simulation results of the electric field distribution inside the garbage bag before and after insertion. The electric field strength inside the garbage bag was generally higher after insertion than before. The Received Signal Strength Indicator (RSSI) on the tag surface inside the bag was -92.5 dBm before insertion and -39.2 dBm (average of the two R/W units) after insertion, indicating a higher value after insertion. The loading port of the packer truck is constructed of steel plates. After loading, the tags exist within a metal-enclosed space, which is believed to have improved reception performance.

4. Conclusion

The following detection methods proved effective during the actual waste collection stages utilizing this system:

1) Small electronic device collection box; Detection when the box door is opened and the collection container is fully seated inside the box
2) Packer trucks; Installed R/W units on both sides of the packer inlet, detection when waste bags are fully seated inside the loading port after insertion.

Acknowledgments

The authors would like to express their sincere gratitude to theFukuoka City Environmental Bureau, the community facility “Saito Pia” in Fukuoka City's Nishi Ward, Fukuoka Research Commercialization Center for Recycling Systems, and Nishihara Shoji Holdings Co., Ltd.

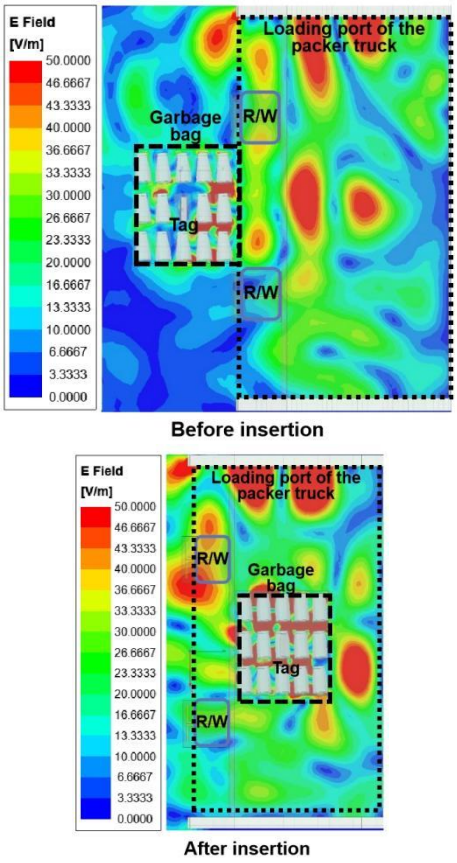

Figure7 Simulation results of the electric field distribution of the garbage bag before and after insertion

Reference

1)The Japan Containers and Packaging Recycling Association, “Smoke and fire problems caused by lithium-ion batteries and other ignition materials”, https://www.jcpra.or.jp/municipality/dangerous/tabid/757/index.php

2)US EPA, “An Analysis of Lithium-ion Battery Fires in Waste Management and Recycling”, EPA 530-R-21-002,July 2021, https://www.epa.gov/system/files/documents/2021-08/lithium-ion-battery-report-update-7.01_508.pdf

3) Lingxi Kong, Chuan Li, Jiuchun Jiang, Micheal G. Pecht, “Li-Ion Battery Fire Hazards and Safety Strategies”, Energies 2018, 11, 2191

4) Atsushi Terazono, “Fire and Other Incidents/Challenges surrounding the Recycling and Disposal Process of Lithium-ion Batteries, Material Cycles and Waste Management Research, vol33, No.3, pp.214-228, 2022

5)Atsushi Terazono, Masahiro Oguchi, Hiroyuki Akiyama, Hiromitsu Tomozawa, “Ignition and fire-related incidents caused by lithium-ion batteries in waste treatment facilities in Japan and countermeasures”, Resources, Conservation & Recycling 202 (2024) 107398

6)Tomoharu Konishi, Iwao Mizumoto, Yotsumi Yoshii, “Optical absorption measurement system for fire detection of lithium ion battery”, Studies in Science and Technology, vol. 8, Number 1, 2019

PROCESS OPTIMIZATION FOR DISSOLVING HEMICELLULOSE FORM CORN BRAN IN DILUTE ACID PRETREATMENT

Wenyan Yang[1], Dayi Qian[1,2 *], Chang Liu[1], Xiaona Wang[1], Yuanyuan Ren[1], Qunhui Wang[1]
1 School of Energy and Environmental Engineering, University of Science and Technology Beijing, Beijing, 100083, China
2 Key Laboratory of Pollutant Chemistry and Environmental Control, College of Chemistry and Environmental Science, Yili Normal University, 835000, China

ABSTRACT: In this study, the process of dissolving hemicellulose in dilute sulfuric acid pretreatment was optimized to improve the solubility of hemicellulose and xylose recovery to support subsequent biofuel and high-value utilization. The experiment was designed by $L_9(3^3)$ orthogonal test, and three factors (reaction temperature: 110, 120, 130°C; Reaction time: 20, 40, 60 min; Sulfuric acid concentrations: 0.25%, 0.75%, 1.25%) on hemicellulose solubility and xylose concentration. The results showed that the primary and secondary factors affecting the solubility of hemicellulose were sulfuric acid concentration> reaction temperature> and reaction time. Under the optimized conditions (130 °C, 40 min, 0.75% sulfuric acid concentration), the verification experiment showed that the solubility of hemicellulose was as high as 99.97%, and the xylose concentration in the pretreatment solution reached 30.694 g/L. This process verifies the feasibility of dilute acid pretreatment in the efficient recovery of corn bran hemicellulose and xylose, and provides a cost-effective pretreatment strategy for the biorefining of lignocellulose biomass.

KEYWORD： lignocellulose, dilute acid pretreatment, xylose, orthogonal experiments

INTRODUCTION

As a typical representative of the second generation of biofuels, lignocellulosic biomass has a wide range of raw material sources covering agricultural waste, forestry residues, energy crops and municipal solid waste and other crop residues. Lignocellulose, a complex composed of different inorganic and organic pollutants, is a key component of plant biomass, accounting for between 15% and 40% of plant dry biomass. It contains three main polymers, cellulose, hemicellulose and lignin, which are used in paper, biofuel, livestock feed and other industries, and are renewable resources with great development potential, which can be converted into bioenergy, high-value chemicals and functional materials through biorefining and other technologies. Efficient use of lignocellulose is key to achieving sustainable management and resource recovery of this industrial waste. (Mandeep et al., 2020; Rubin, 2008)

Corn bran is a multi-layer thin leaf-like structure wrapped on the outside of corn ears, which is a typical agricultural waste generated during corn planting and processing, and is also one of the important sources of lignocellulose biomass. From the perspective of structure and composition, it is mainly composed of cellulose (31.66%), hemicellulose (34.50%) and lignin (5.16%), and contains a small amount of pectin, protein and ash, which form a fiber structure with certain mechanical strength through close microscopic combination.

Through a series of pretreatments, the dense structure is broken, and then the mutual constraints between components are broken, giving full play to the potential value of each component and laying a key foundation for subsequent energy conversion or high-value utilization.

Lignin is an amorphous aromatic polymer rich in oxyphenylpropyl alcohol structure or its derivative structural units in molecular structure, which can be removed by dilute alkalis, organic solvents, dilute acids, etc(Sun et al., 2014). The removal of lignin can improve the pretreatment efficiency of hemicellulose and cellulose and increase the yield of reducing sugars. Cellulose to dry matter is a homogeneous polymer formed by the linear connection of glucose units by β-1,4 glycosidic bonds. Hemicellulose is a heteropolysaccharide composed of different types of monosaccharides, of which xylose accounts for about 50%. Cellulose and hemicellulose can be separated by

dilute acid and low eutectic solvent (DES) to achieve targeted utilization of different reducing sugars in the future. Tang et al(Tang et al., 2019) compared the pretreatment effects of dilute acid, dilute alkali, and ferric chloride on pennisetum and found that alkali treatment could significantly remove lignin, while acid and ferric chloride treatment mainly removed hemicellulose. Zhu et al(Zhu et al., 2025)found that Na_2CO_3 pretreated wheat straw effectively removed lignin (7.17-11.61%) and xylan (17.28-28.89%), but the loss rate of cellulose was less than 10.30%. Zhang et al(Zhang et al., 2018)pretreated bagasse with ferric chloride ($FeCl_3$) combined with surfactant, and the hemicellulose removal rate was 91.2%, cellulose recovery was 89.1%, and the glucose yield after enzymatic hydrolysis was 80.1%. Li et al(Li et al., 2010)performed dilute acid pretreatment and ionic liquid pretreatment on switchgrass, focusing on their effects on biomass degradation resistance, deligninization efficiency, and enzymatic glycation. Ionic liquid pretreatment had a more significant effect of delignination than diluted acid, but the hemicellulose residue was higher. Alkaline pretreatment of lignocellulose can significantly remove lignin and part of hemicellulose, but the yield of reducing sugars is low and difficult to utilize. Ionic liquid can indeed significantly separate hemicellulose as a green solvent pretreatment, but it has the problems of high cost, biotoxicity inhibition, process and operation complexity. Dilute acid pretreatment can efficiently dissolve lignin and hemicellulose within the range of suitable temperature, acid concentration, treatment time, etc., while retaining cellulose, which has a higher yield and subsequent utilization rate of reducing sugar.

In this study, corn bran were pretreated with sulfuric acid, and the sulfuric acid concentration, reaction time and reaction temperature were optimized by orthogonal design, and the solubility of hemicellulose and the xylose concentration in the treatment solution were used as selection indicators.

1 MATERIALS AND METHODS

1.1 Materials

Corn bran, Yili Henghui Starch Co., Ltd., are dried and sealed and stored. The main reagents include sulfuric acid, fiber disaccharides, glucose, xylose, arabinose, etc.

1.2 Main instruments

Constant water bath, autoclave, low-speed centrifuge, electronic balance, HPLC, muffle furnace.

1.3 Experimental methods

Weigh corn bran with a dry weight of 5 g in a 100 mL blue-cap bottle with a solid-liquid ratio of 1:8, add different concentrations of H_2SO_4 solution, and put them into an autoclave to react at different temperatures. After the pretreatment, the reaction material is taken out, and the reduced sugar content of the liquid part is determined after centrifugation. The solid part was washed to neutral and then dried, and the content of cellulose, hemicellulose and lignin in the solid was determined.

1.4 Analysis methods

1.4.1 Determination of cellulose, hemicellulose and lignin content

The levels of cellulose, hemicellulose, and lignin in corn bran before and after pretreatment were determined according to the standard methods of the National Renewable Energy Laboratory (NREL) in the United States(Sluiter et al., n.d.).

1.4.2 Pretreatment fluid

The concentration of reducing sugars (cellulose disaccharides, glucose, xylose and arabinose) in the pretreatment solution was determined by high performance liquid chromatography.

1.5 Orthogonal experimental design of corn bran pretreated with sulfuric acid

The orthogonal experimental table was designed by SPSS software, and the reaction temperature (°C), reaction time (min) and sulfuric acid concentration (v/v, %) were selected as the optimization factors, and the level settings of each factor were shown in **Table 1** to generate an orthogonal design table.

Table 1 $L_9(3^3)$ Orthogonal test factor level table

level	A temperature °C	B time min	C Sulfuric acid %
1	110	20	0.25
2	120	40	0.50
3	130	60	0.75

2 RESULTS AND ANALYSIS

The results of orthogonal tests **(Table 2)** showed that the primary and secondary factors affecting the solubility of hemicellulose and the xylose concentration in the pretreatment solution were C>A>B, that is, sulfuric acid concentration> reaction temperature > reaction time. According to the experimental results, when the sulfuric acid concentration is C2 and C3, the results of k2 and k3 are not significant, and C2 is selected as the best sulfuric acid concentration considering the cost and the impact on the equipment. In the same way, B2 was selected as the optimal reaction time, and the optimal combination

was A3B2C2, that is, the reaction temperature was 130°C, the reaction time was 40min, and the sulfuric acid concentration was 0.75%.

Table 2 Orthogonal experimental results

Experiment serial number		A	B	C	Actual combination	Hemicellulose Solubility %	Xylose concentration g/L
1		A1	B1	C1	110℃，20min、0.25%	70.213	5.1035
2		A1	B2	C2	110℃，40min、0.75%	94.722	25.6215
3		A1	B3	C3	110℃，60min、1.25%	99.0079	28.9215
4		A2	B1	C2	120℃，20min、0.75%	99.0539	28.1505
5		A2	B2	C3	120℃，40min、1.25%	100	28.7255
6		A2	B3	C1	120℃，60min、0.25%	94.9157	18.434
7		A3	B1	C3	130℃，20min、1.25%	99.2477	30.722
8		A3	B2	C1	130℃，40min、0.25%	97.1167	24.915
9		A3	B3	C2	130℃，60min、0.75%	99.7788	28.8125
Hemi-cellulose Solubility %	k1	87.9810	89.5049	87.4151	C>A>B		
	k2	97.9899	97.2796	97.8516			
	k3	98.7144	97.9008	99.41851			
	R	10.7334	8.39593	12.0034			
Xylose con-centration g/L	k1	19.8822	21.3253	16.1508	C>A>B		
	k2	25.1033	26.4207	27.5282			
	k3	28.1498	25.3893	29.4563			
	R	8.26767	5.0953	13.3055			

Table 3 Optimal condition validation experiments

Temperature/°C	Time/min	Sulfuric acid concentration/%	Hemicellulose Dissolution %	Xylose concentration g/L
130	40	0.75	99.98	31.051
			99.95	30.336
average value			99.97	30.694

The verification experiment proved **(Table 3)** that the combination (A3B2C2) optimized by the orthogonal experiment was as expected, and the orthogonal test was established. The solubility of hemicellulose reached 99.97% and the xylose concentration in hydrolysate reached 30.694 g/L when the corn bran was pretreated with a reaction temperature of 130°C, a reaction time of 40 min and a sulfuric acid concentration of 0.75%.

Table 4 Research content of dilute acid pretreatment lignocellulose biomass

Biomass	Acid types	Acid concentration	Temperature (°C)	Time (min)	Conclusion	Bibliography
straw	sulfuric acid	3%	130	20	Hemicellulose solubility 95.8% Cellulose solubility 14.1%	(Kim et al., 2011)
corn stalks	nitric acid	0.6%	150	1	xylose 22 g/L, arabinose 2.9 g/L, glucose 1.9 g/L	(Zhang et al., 2011)
oil palm empty fruit	sulfuric acid	2%	116	20	Xylose yield 91.2%	(Tan et al., 2013)
hemp fiber	sulfuric acid	1%	180	10	Solid phase: 95% cellulose, 25% hemicellulose; Liquid phase: 2.5% cellulose, 55% hemicellulose	(Kuglarz et al., 2014)
olivine	sulfuric acid	0.025 M	195	5	Liquid phase: 89.7% xylose recovery Solid phase: 55% enzymatic hydrolysis yield	(Saleh et al., 2014)
wheat straw	sulfuric acid	0.4%	140	60	Solid phase: glucose 25.0g/L Liquid phase: Xylose 13.26g/L-acetic acid 1.31g/L-Furfural 0.35g/L	(Morikawa et al., 2014)

Compared with the previous study **(Table 4)**, the optimized pretreatment conditions in this study are more-mild, and although the reaction time is slightly extended, the reaction temperature is significantly reduced, which effectively reduces energy consumption and is more suitable for practical engineering applications. From the perspective of key indicators, the solubility of hemicellulose and the yield of xylose in this study were better than those reported in the above literature. In conclusion, the efficient dissolution of

hemicellulose and the high yield of xylose in the process of dilute sulfuric acid pretreatment of corn bran were achieved through the optimization of the process parameters determined by orthogonal experiments, which provided a better process reference for the subsequent resource utilization of the raw material.

3 CONCLUSION

The process conditions for dissolving hemicellulose in corn bran pretreated with sulfuric acid were optimized by orthogonal experiments. The optimal process conditions were 130 °C, 40 min, and 0.75% sulfuric acid concentration. Under these conditions, the solubility of hemicellulose in corn bran reached 99.97%, and the xylose concentration in hydrolysate reached 30.694 g/L. It was shown that the pretreatment of corn bran with dilute acid could dissolve almost all hemicellulose and obtain a high concentration of reducing sugars, which was conducive to the subsequent biotransformation of xylose.

ACKNOWLEDGEMENT

Xinjiang Uygur Autonomous Region Key R&D Program (2022B02021)

REFERENCE

Kim, J.-W., Kim, K.S., Lee, J.-S., Park, S.M., Cho, H.-Y., Park, J.C., Kim, J.S., 2011. Two-stage pretreatment of rice straw using aqueous ammonia and dilute acid. Bioresource Technology 102, 8992–8999. https://doi.org/10.1016/j.biortech.2011.06.068

Kuglarz, M., Gunnarsson, I.B., Svensson, S.-E., Prade, T., Johansson, E., Angelidaki, I., 2014. Ethanol production from industrial hemp: Effect of combined dilute acid/steam pretreatment and economic aspects. Bioresource Technology 163, 236–243. https://doi.org/10.1016/j.biortech.2014.04.049

Li, C., Knierim, B., Manisseri, C., Arora, R., Scheller, H.V., Auer, M., Vogel, K.P., Simmons, B.A., Singh, S., 2010. Comparison of dilute acid and ionic liquid pretreatment of switchgrass: Biomass recalcitrance, delignification and enzymatic saccharification. Bioresource Technology 101, 4900–4906. https://doi.org/10.1016/j.biortech.2009.10.066

Mandeep, Kumar Gupta, G., Shukla, P., 2020. Insights into the resources generation from pulp and paper industry wastes: Challenges, perspectives and innovations. Bioresource Technology 297, 122496. https://doi.org/10.1016/j.biortech.2019.122496

Morikawa, Y., Zhao, X., Liu, D., 2014. Biological co-production of ethanol and biodiesel from wheat straw: A case of dilute acid pretreatment. RSC Adv. 4, 37878–37888. https://doi.org/10.1039/C4RA07251K

Rubin, E.M., 2008. Genomics of cellulosic biofuels. Nature 454, 841–845. https://doi.org/10.1038/nature07190

Saleh, M., Cuevas, M., García, J.F., Sánchez, S., 2014. Valorization of olive stones for xylitol and ethanol production from dilute acid pretreatment via enzymatic hydrolysis and fermentation by Pachysolen tannophilus. Biochemical Engineering Journal 90, 286–293. https://doi.org/10.1016/j.bej.2014.06.023

Sluiter, A., Hames, B., Ruiz, R., Sluiter, J., Templeton, D., Crocker, D., n.d. Determination of structural carbohydrates and lignin in biomass: Laboratory analytical procedure (LAP) (Technical Report No. No. DE-AC36-08GO28308). National Renewable Energy Laboratory, Denver West Parkway Golden, Colorado 80401.

Sun, Q., Foston, M., Sawada, D., Pingali, S.V., O'Neill, H.M., Li, H., Wyman, C.E., Langan, P., Pu, Y., Ragauskas, A.J., 2014. Comparison of changes in cellulose ultrastructure during different pretreatments of poplar. Cellulose 21, 2419–2431. https://doi.org/10.1007/s10570-014-0303-6

Tan, H.T., Dykes, G.A., Wu, T.Y., Siow, L.F., 2013. Enhanced xylose recovery from oil palm empty fruit bunch by efficient acid hydrolysis. Appl Biochem Biotechnol 170, 1602–1613. https://doi.org/10.1007/s12010-013-0298-8

Tang, S., Xu, C., Vu, L.T.K., Liu, S., Ye, P., Li, L., Wu,

Yuxuan, Chen, M., Xiao, Y., Wu, Yue, Wang, Y., Yan, Q., Cheng, X., 2019. Enhanced enzymatic hydrolysis of pennisetum alopecuroides by dilute acid, alkaline and ferric chloride pretreatments. Molecules 24, 1715. https://doi.org/10.3390/molecules24091715

Zhang, H., Lyu, G., Zhang, A., Li, X., Xie, J., 2018. Effects of ferric chloride pretreatment and surfactants on the sugar production from sugarcane bagasse. Bioresource Technology 265, 93–101. https://doi.org/10.1016/j.biortech.2018.05.111

Zhang, R., Lu, X., Sun, Y., Wang, X., Zhang, S., 2011. Modeling and optimization of dilute nitric acid hydrolysis on corn stover. Journal of Chemical Technology & Biotechnology 86, 306–314. https://doi.org/10.1002/jctb.2529

Zhu, R., Yang, M., Yin, J., Wu, Z., Li, M., Zhao, L., Wang, X., Ren, J., 2025. Mild sodium carbonate pretreatment of wheat straw for improving cellulose and xylan enzymatic hydrolysis. Industrial Crops and Products 227, 120728. https://doi.org/10.1016/j.indcrop.2025.120728

Porous polymethyl methacrylate monolith fabricated without organic solvent for cationic pollutant removal: A preliminary study

Tomoko Shirahase[1], Fumitake Takahashi[2]
1 Tokyo Metropolitan Industrial Technology Research Institute, 1-20-20 Minamikamata, Ohta-ku, Tokyo, 144-0035, Japan
2 Department of Transdisciplinary Science and Engineering, School of Environment and Society, Institute of Science Tokyo, G5-13, 4259, Nagatsuta, Midori-ku, Yokohama, 226-8503 Japan

INTRODUCTION

Porous materials like activated carbon have been widely used for pollutant removal in wastewater, aquatic environment, exhaust gas, and the atmosphere. In particular, activated carbon has great advantages in terms of low fabrication cost, wide availability of feedstocks, and excellent characteristics like large specific surface area. On the other hand, activated carbon also has some disadvantages like non-uniform characteristics, moderate difficulty of designed surface modification and non-granular shape formation. There are many researches on inorganic and organic adsorbents like zeolite[1], metal organic framework (MOF)[2], and porous polymer monolith[3]. Porous polymer monolith might be promising owing to high flexibility of designed fabrication methods and high applicability at industrial scale. The fabrication of polymer monoliths is categorized to polymerization, phase separation, selective removal of one block in self-organized block copolymers, and selective removal of one component in polymer blends. Owing to highly ordered pore structure of self-assembled copolymer, the monolith fabrication using copolymers is promising for nanoscale pore formation. However, copolymer synthesis usually requires non-easy multi-steps using organic solvents. Due to hazards of organic solvents to human being and the ecosystem, monolith fabrication via the decomposition of polymer blends is attractive. It makes the selective degradation of polymer blends possible using non-organic solvent like enzyme, phosphate buffer solution, alkaline solution, pure water. In this method, the fabrication of well-mixed polymer blends plays a significant role on pore structure of porous polymer monolith. The first author has focused on the selection of miscible polymers for polymer blend, which enables well-mixed polymer blend using only mechanical blending without any organic solvents[4]. The first author reported the degradation characteristics of miscible polymers, in particular polylactide (PLLA) and polymethyl methacrylate (PMMA) blend[5]. The first author has also developed organic solvent-free fabrication of porous PMMA monolith via hydrolytic degradation using NaOH solution and subsequent freeze-dry treatment[6]. In this conference, the authors would report the basic characteristics of porous polymethyl methacrylate monolith and preliminary results of model pollutant removal using the monolith.

METHODS

Fabrication of porous PMMA monolith via selective degradation of PLLA

The details of the monolith fabrication method can be referred to Shirahase et al[6]. In this study, PLLA (Uz's S-09; Mw = 163,400; Toyota Motor Corporation), PMMA (Acrypet VH; Mw = 100,000; Mitsubishi Rayon Co., Ltd.), and PMMA-H (Mw = 350,000; Sigma Aldrich Co. LLC) were used as feedstock polymers. Sodium hydroxide was analytical grade (Kanto Kagaku Co., Ltd). Both polymers (PLLA and PMMA) were firstly dried at 80 °C for 24 h under vacuum condition. They were melt-blended using a two-roll mill (Nishimura machinery Co., Ltd.) at 190 °C for 15 min. Polymer blend (PLLA/PMMA) was compressed at 190 °C and 19.6 MPa for 5 min to form polymer blend film with 0.5 mm thicknesses. To make the films amorphous, they were quenched quickly into iced water. Specimens of polymer blend films were cut to 5.0 mm square for SEM observation and nitrogen adsorption measurements or 10 mm square for other analyses. The polymer blend films were treated by 1 N NaOH aqueous solution at 50 °C. After PLLA in the films was completely degraded, the samples were washed twice and additionally immersed in distilled water for 3 days. Subsequently, the samples were frozen with 1 ml of distilled water using liquid nitrogen and freeze-dried at −40 °C under a pressure of 100 Pa for 1 day.

Model pollutant removal using porous PMMA monolith

Electrostatic attraction is one of significant driving forces in pollutant adsorption process. In this study, methyl orange and methylene blue were tested as model pollutants. Methyl orange represents a model anionic pollutant and methylene blue was used as a model cationic pollutant. The adsorption performances were observed visually by color disappearance. It should be noted that exact concentrations of these dye after the adsorption onto porous PMMA monolith were not measured in this time.

RESULTS AND DISCUSSIONS

Characteristics of porous PMMA monolith fabricated by selective degradation of PLLA/PMMA blend

The cross-section SEM images of the porous PMMA monolith are shown in **Fig. 1**. Co-continuous mesopores with around 6–50 nm pores were clearly observed. According to further SEM observations, the sizes of PMMA skeletons of all fabricated PMMA monoliths ranged from 10 to 60 nm, which were the same with the previous research. The average skeleton size was around 20 nm. As presented in the previous research[6], the porosity of the PMMA monolith was not equal to PLLA weight fraction of PLLA/PMMA blend. After freeze-dry treatment, volume shrinkage of porous PMMA monolith were observed, which decreased real porosity smaller than the expected one (PLLA weight fraction). As the same with the previous research[6], average pore size and specific surface area were changed depending on blending ratio of PLLA. When PLLA blending ratio was ranged from 50% to 90%, the ranges of average pore and specific surface area are 7-32 nm and 90-200 m^2/g, respectively.

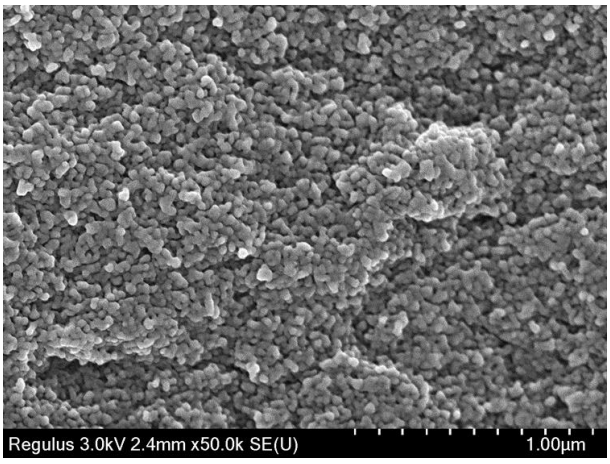

Fig. 1 Cross-section SEM image of the fabricated PMMA monolith

Removal of model pollutants (methyl orange and methylene blue) using porous PMMA monolith

The color changes after the adsorption of methyl orange and methylene blue are shown in **Fig. 2**. **Fig. 2** clearly shows that the porous PMMA monolith is useful for methylene blue removal but useless for methyl orange adsorption It proposes that the porous PMMA monolith might be effective to remove cationic pollutant like heavy metals likely due to negative surface charge. On the other hand, the surface modification is absolutely necessary for the removal of anionic pollutant like nitrate, nitrite, and phosphate.

CONCLUSIONS

This study fabricated porous PMMA monolith without organic solvent. This study confirmed repeatability of the characteristics of fabricated PMMA monolith. The monolith showed good removal performance for methylene blue but no removal for methyl orange. It proposes that the surface of the fabricated PMMA monolith were likely negatively charged. Further researches are necessary for in-depth analysis of cationic pollutant adsorption onto the monolith.

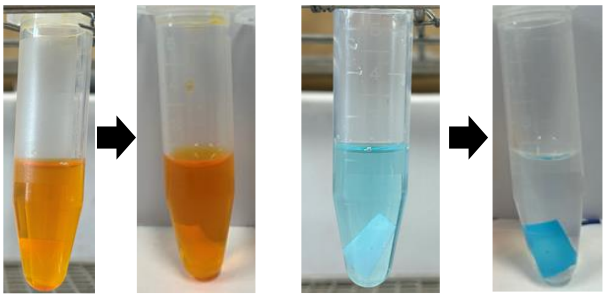

Fig. 2 Color change after methyl orange and methylene blue adsorption

ACKNOWLEDGEMENT

This study was supported financially by JSPS KAKENHI Grant numbers 16K16211 and 24K15350. The authors appreciate them greatly.

REFERENCES

1. Wang S.B., Peng Y.L. (2010) Natural zeolites as effective adsorbents in water and wastewater treatment, Chemical Engineering Journal, 156(1), 11-24.
2. Li J., Wang X.X., Zhao G.X., Chen C.L., Chai Z.F., Alsaedi A., Hayat T., Wang X.K. (2018) Metal-organic framework-based materials: superior adsorbents for the capture of toxic and radioactive metal ions, Chemical Society Reviews, 47(7), 2322-2356.
3. Sözbir M., Simsek E.B., Mert H.H., Kekevi B., Mert M.S., Mert E.H. (2023) Renewable terpene-based highly porous polymer monoliths for the effective removal of persistent pharmaceuticals of tetracycline and ibuprofen, Microporous and Mesoporous Materials, 354, 112509.
4. Shirahase T., Komatsu Y., Marubayashi H., Tominaga Y., Akasaka S., Asai S., Sumita M. (2007) Miscibility and hydrolytic degradation in alkaline solution of poly(L lactide) and poly(p-vinyl phenol) blends, Polymer Degradation and Stability, 92(8), 1626- 1631.
5. Shirahase T., Komatsu Y., Asai S., Sumita M. (2007) Miscibility and hydrolytic degradation in alkaline solution of poly(L lactide) and poly(methyl methacrylate) blends , Polymer, 47(13), 4839-4844.
6. Shirahase T., Akasaka S., Asai S. (2020) Organic solvent free fabrication of mesoporous polymer monolith from miscible PLLA/PMMA blend,

Polymer , 122742.

ROOT-MEDIATED OXYGEN TRANSFER DRIVES METHYLOBACTER ENRICHMENT AND SECONDARY ALCOHOL METABOLISM TO STRENGTHEN CHLOROBENZENE DEGRADATION IN RHIZOSPHERE SYSTEMS

Zhilin Xing, Liangjie Li, Kun Cao, Tiantao Zhao

School of Chemistry and Chemical Engineering, Chongqing University of Technology, Chongqing 400054, China

*Corresponding author: Zhilin Xing (xingzhilin@cqut.edu.cn)

\Abstract

Vegetation covers were tested for their ability to enhance methane (CH_4) oxidation and co-metabolic degradation of chlorobenzene (CB) in landfill cover soils. Using a three-dimensional simulated landfill column system, we compared White clover (herb), Castor plant (shrub) and Paper mulberry (tree). Experiments combined gas profiling, 16S rRNA microbial community analysis and non-targeted rhizosphere metabolomics. Paper mulberry and Castor plant markedly increased O_2 availability across the profile, which translated into higher CH_4 and CB removal: CH_4 removal increased by 14.43% (Paper mulberry) and 7.41% (Castor); CB removal increased by 40.67% (Paper mulberry) and 22.17% (Castor) relative to unvegetated controls. White clover slightly increased CB removal (+4.52%) but reduced CH_4 removal (−17.37%). Vegetation reshaped microbial communities: Paper mulberry enriched Methylobacter, Castor enriched Pseudoxanthomonas, and White clover favored Chryseolinea. Metabolomics indicated Paper mulberry uniquely secreted compounds that could activate dehalogenases and enhance quinone cycling in degraders. We propose a zonal Paper mulberry–Castor planting strategy to synergistically reduce landfill greenhouse gas and CB emissions.

Keywords: landfill cover; vegetation; rhizosphere microbiome; chlorobenzene; methanotroph; Paper mulberry

1. INTRODUCTION

Landfill gas (LFG), primarily CH_4 with trace chlorinated VOCs such as chlorobenzene (CB), threatens air quality and public health. Methanotrophs oxidize CH_4 and can co-metabolize chlorinated aromatics, but oxygen limitation often restricts their activity. Root systems modify rhizosphere redox, increase O_2 transport and supply exudates that stimulate pollutant-degrading microbes. This study systematically compared herb (White clover), shrub (Castor plant) and tree (Paper mulberry) impacts on CH_4 and CB co-degradation, linking gas profiles, microbial community shifts and rhizosphere metabolomics to remediation performance.

2. MATERIALS AND METHODS

Soil and plants were sampled from a Chongqing MSW landfill. Vertical PVC column reactors (140 cm height, 30 cm i.d.) replicated cover profiles: 90 cm soil layer + 40 cm growth zone (Figure 1). Four treatments (Control, White clover, Castor, Paper mulberry) with triplicates were tested. Simulated biogas (CH_4:CO_2 = 1:1) and CB vapor (target 2.21 mg L^{-1}) were fed after N_2 purging. O_2, CH_4 and CB vertical profiles were measured, mid-layer soils taken for 16S rRNA (V4–V5) sequencing and non-targeted UHPLC-MS metabolomics. Differential metabolites were identified by OPLS-DA (VIP>1, $P<0.05$).

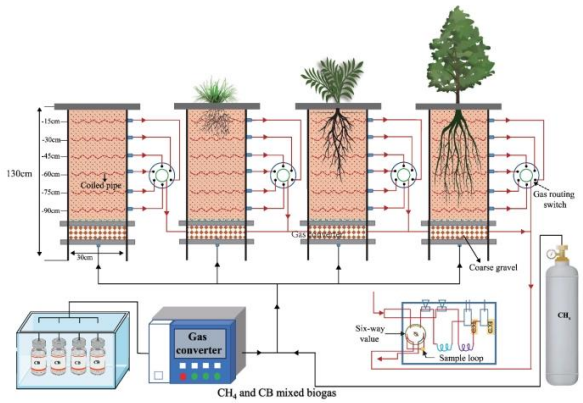

Figure 1 Vegetation-microbe synergistic enhancement system for CH_4-CB co-degradation in landfill cover. a, bare soil; b, White clover cover; c, Castor plant cover; d, Paper mulberry cover.

3. RESULTS AND DISCUSSION

3.1 Vegetation altered O_2 and CH_4 vertical profiles

Paper mulberry produced an aerobic profile across 0–90 cm (O_2 >10% at depth; O_2 = 17.17% at −15 cm), removing anaerobic/hypoxic zones. Castor reduced the anaerobic zone by ~30 cm and expanded a hypoxic mid-layer. White clover modified only shallow layers and generated a prolonged transition zone. These root-mediated O_2 patterns governed CH_4 oxidation spatially: deep-rooted Paper mulberry promoted systemic CH_4 oxidation.

3.2 Vegetation effects on CH_4 oxidation and CB degradation (key outcomes)

Average removal efficiencies: CH_4 — Control 63.4%; Paper mulberry 77.83% (+14.43%); Castor 70.81% (+7.41%); White clover 46.03% (−17.37%). CB — Control 18.48%; Paper mulberry 59.15% (+40.67%); Castor 40.65% (+22.17%); White clover 23.05% (+4.52%). Paper mulberry combined deep O_2 delivery and exudates favoring aerobic dehalogenation; Castor enhanced facultative zones supporting co-metabolism; White clover's labile C stimulated heterotrophs, increasing O_2 competition and reducing methanotrophy.

3.3 Microbial community shifts and functional recruitment

Vegetation reshaped taxonomy and functional guilds. Dominant phyla included Proteobacteria, Bacteroidota, Chloroflexi, Firmicutes and Actinobacteriota. Paper mulberry enriched Methylobacter (methanotroph); Castor enriched Pseudoxanthomonas; White clover favored Chryseolinea. Functional degraders Bacillus (anaerobic reductive dehalogenation) and Pseudomonas (aerobic ring-cleavage) were differentially distributed along depth gradients. Vegetation increased positive co-occurrence interactions by ~8–18%, indicating strengthened cooperation among degraders.

3.4 Rhizosphere metabolomics-metabolites that promote CB degradation

Paper mulberry showed the largest metabolic shift (75 up / 170 down). Unique compounds included 8,8-dimethoxy-2,6-dimethyl-2-octanol and 1-(11Z-eicosenoyl)-glycero-3-phosphate. Acetal-type compounds likely activate microbial dehalogenases; phospholipid precursors may act as electron shuttles in quinone cycling, facilitating downstream catechol dioxygenase activity. KEGG enrichment (ABC transporters, arginine/purine metabolism) supported enhanced stress tolerance and pollutant handling.

3.5 Mechanistic synthesis: Vegetation–Microbe Synergy Model

A dual mechanism was proposed: (1) root-mediated axial O_2 transport creates aerobic niches for dehalogenation and methanotrophy; (2) root exudates supply co-substrates, electron carriers and enzyme modulators that accelerate dechlorination and ring-cleavage, funneling intermediates into central metabolism.

4. APPLICATION POTENTIAL AND MANAGEMENT IMPLICATIONS

LandGEM-based modeling suggests 50 ha of Paper mulberry could reduce CH_4 by ~2,587 $m^3 \cdot ha^{-1} \cdot yr^{-1}$

(total ~129,400 $m^3 \cdot yr^{-1}$), with significant CO_2-eq benefits. Recommended strategy: Paper mulberry in core oxygenation zones (800–1,000 trees·ha^{-1}) + Castor on slopes/margins (200 plants·ha^{-1}), combined with gas-distribution engineering and targeted Methylobacter inoculation (Figure 2).

5. CONCLUSIONS

Deep-rooted Paper mulberry significantly improved CH_4 (~14.43%) and CB (~40.67%) removal by increasing O_2 availability and secreting metabolites that enhanced dehalogenation and quinone cycling. Castor provided moderate benefits; White clover increased labile C but reduced CH_4 oxidation. Vegetation reshaped microbiomes and strengthened cooperative networks, supporting effective co-removal. A Paper mulberry–Castor zonal planting strategy integrated with engineering controls is recommended for large-scale landfill LFG mitigation.

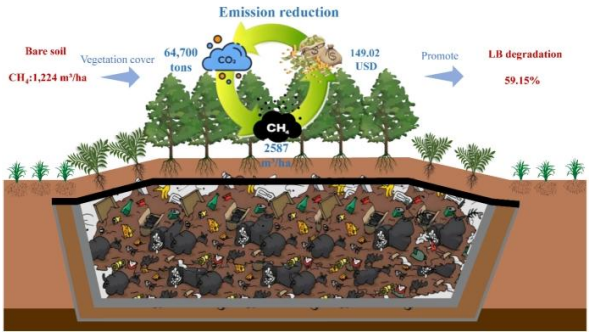

Figure 2 Projected CH_4 mitigation benefits under vegetative cover scenarios

Sponsored by

Kanadevia
Technology for people and planet

JFE

三ツ星ベルト

125 Years & Beyond
PENTA-OCEAN

人と自然を、技術でむすぶ。
奥村組
OKUMURA CORPORATION

Kubota

KURITA

九環協 地球を知り、未来につなぐ。
一般財団法人 九州環境管理協会

Be a ChangeBuilder.
安藤ハザマ
HAZAMA ANDO CORPORATION

GeoWaste Tech.
NPO法人廃棄物地盤工学研究会

ESRG
環境・遮水管理センシング技術研究会